On the glass transition of bulk and confined polyamorphic liquids: A molecular dynamics simulations study

Der Glasübergang von polyamorphen Flüssigkeiten in Bulk und in Confinement: Eine Molekulardynamik-Simulationsstudie
Zur Erlangung des Grades eines Doktors der Naturwissenschaften (Dr. rer. nat.)
Genehmigte Dissertation von Robin Thomas Horstmann aus Heppenheim
Datum: 19.06.2023, Tag der Einreichung: 07.02.2023, Tag der Prüfung: 17.04.2023

1. Gutachten: Prof. Dr. Michael Vogel
2. Gutachten: Prof. Dr. Nico van der Vegt
Darmstadt 2023

TECHNISCHE
UNIVERSITÄT
DARMSTADT

Physics Department
Institute for Condensed Matter Physics
AG Vogel

On the glass transition of bulk and confined polyamorphic liquids: A molecular dynamics simulations study
Der Glasübergang von polyamorphen Flüssigkeiten in Bulk und in Confinement: Eine Molekulardynamik-Simulationsstudie

Accepted doctoral thesis by Robin Thomas Horstmann

1. Review: Prof. Dr. Michael Vogel
2. Review: Prof. Dr. Nico van der Vegt

Date: 19.06.2023
Date of submission: 07.02.2023
Date of thesis defense: 17.04.2023

Darmstadt 2023

Bitte zitieren Sie dieses Dokument als:
URN: urn:nbn:de:tuda-tuprints-urn:nbn:de:tuda-tuprints-240462
URL: http://tuprints.ulb.tu-darmstadt.de/240462

Erklärungen laut Promotionsordnung

§8 Abs. 1 lit. c PromO

Ich versichere hiermit, dass die elektronische Version meiner Dissertation mit der schriftlichen Version übereinstimmt.

§8 Abs. 1 lit. d PromO

Ich versichere hiermit, dass zu einem vorherigen Zeitpunkt noch keine Promotion versucht wurde. In diesem Fall sind nähere Angaben über Zeitpunkt, Hochschule, Dissertationsthema und Ergebnis dieses Versuchs mitzuteilen.

§9 Abs. 1 PromO

Ich versichere hiermit, dass die vorliegende Dissertation selbstständig und nur unter Verwendung der angegebenen Quellen verfasst wurde.

§9 Abs. 2 PromO

Die Arbeit hat bisher noch nicht zu Prüfungszwecken gedient.

Darmstadt, 07.02.2023

Robin Thomas Horstmann

Abstract

Supercooled liquids and the glass transition are not satisfactorily understood to date. The temperature dependence of dynamical properties eludes theoretical prediction. No model can be successfully applied to all liquids. One liquid is particularly complex in its supercooled regime – water. This seemingly simple liquid exhibits the most anomalies of any neat liquid, and most of these are thought to be related to the existence of two distinguishable liquid phases with different density in the supercooled regime, i.e., water exhibits polyamorphism. However, most of the relevant temperature range lies in the so-called *no-man's land*, a region of the phase diagram in which bulk water rapidly crystallizes and which is therefore experimentally inaccessible to the bulk liquid. Therefore, experimental studies often exploit the fact that crystallization of water is suppressed in nanoscopic confinements or water mixtures. The present work deals with both areas of research, water's polyamorphism and dynamics of supercooled liquids, confined and mixed, with the use of molecular dynamics simulations. They allow for detailed analysis and systematic variation of the liquid and enable easy supercooling.

Partial charges of the TIP4P/2005 and SPC/E water models were scaled which led to strong shifts of dynamics in temperature. These were reconciled by using the high-temperature activation energy as the relevant energy scale as long as structural properties were the same. For the TIP4P/2005 model and a set of reduced charges, isochore crossing in the phase diagram confirmed the existence of a liquid-liquid critical point (LLCP) in the supercooled regime at positive or negative pressures, depending on the molecular polarity. The two-structure equation of state (TSEOS) formalism was used to describe the data and determine the location of the LLCP. In addition, reduction of the partial charges accelerated dynamics at the LLCP and simulations with elongated boxes in the double metastable regime allowed for the coexistence of high-density (HDL) and low-density (LDL) liquid phases and the determination of their dynamics as a function of temperature. The results are in agreement with observations from isochoric and isobaric simulations and translational motion was observed for all state points. It was found that the temperature dependence of the dynamics at a constant fraction of the low-density state (LDS) is Arrhenius-like. Thus, the presumed fragile-to-strong transition (FST) of water is not caused by a transition from fragile HDL to strong LDL but by the fast transition between these liquid states when the system is cooled through the Widom line at constant pressure. This is consistent with experimental observations slightly above water's glass transition temperature T_g and reinforces the question of whether HDL or LDL on their own exhibit an FST. Models for the temperature dependence of reactive mixtures were tested but were unable to describe simulation results at the lowest studied temperatures.

A family of functional forms for the temperature dependence of dynamical properties of supercooled liquids was derived. These functions allow their description over the entire temperature range from the boiling point to the glass transition and with or without an FST. The second-order functions predict a high and low-temperature Arrhenius regime connected by an intermediate fragile regime. Knowledge of the path in the phase diagram of charge-scaled water-like systems, whether they cross the Widom line at increased charges or not, allowed for more rigorous testing of these functional forms. They are sensitive to deviations from Vogel-Fulcher-Tammann (VFT) behavior and apply well to data from charge-scaled water and silica simulations, which have a pronounced FST, as well as to real liquids. The possibility that supercooled liquids in general have a low-temperature Arrhenius regime and the characteristics of such FSTs were discussed.

Simulations of charge-scaled water models in chemically neutral pores were performed and static and dynamic length scales associated with changes of water's structure and dynamics near the pore wall were extracted. These correlation lengths were used to test theories of the glass transition and discussed in the context of water's two phases. Signs of crossing the Widom line could not be found in the temperature dependence of the correlation lengths within the moderately supercooled temperature range. The slowdown at the pore wall relative to the pore center was characterized using two empirical functions for additional activation energies caused by the liquid-confinement interface. Furthermore, the potential energy landscape (PEL) imprinted on the liquid was quantified using a novel approach based on Boltzmann statistics and predicted and measured mobility gradients are in agreement.

Lastly, the origin of slow solvent processes observed in dielectric spectroscopy studies of dynamically asymmetric binary mixtures was determined in simulations. For mixtures of picoline and polymethylmethacrylate and of water and polylysine, fractions of slow solvent molecules were not found. Instead, the PEL imprinted by the slow polymer molecules causes preferred locations and orientations for the solvent molecules. A mechanism was proposed in which the solvent molecules exchange fast compared to the relaxation of the polymer molecules but have correlated orientations. This causes long-lived cross correlations that can be misinterpreted as slow solvent contributions in coherent measurements. Other sources of cross correlations were quantified and the dependency on measured molecular property and correlation function were discussed. The dynamical heterogeneity of solvent dynamics was traced back to the variation of the local solvent concentration and it is broad but unimodal. The same observations, slowly decaying cross correlations and absence of self correlation on these time scales, were made for other binary mixtures, suggesting that these effects are relevant to a wide range of systems.

Zusammenfassung

Unterkühlte Flüssigkeiten und der Glasübergang sind bis heute nicht zufriedenstellend verstanden. Die Temperaturabhängigkeit der dynamischen Eigenschaften entzieht sich einer theoretischen Vorhersage. Kein Modell lässt sich erfolgreich auf alle Flüssigkeiten anwenden. Eine Flüssigkeit ist in ihrem unterkühlten Zustand besonders komplex – Wasser. Diese scheinbar einfache Flüssigkeit weist die meisten Anomalien aller reinen Flüssigkeiten auf, und man nimmt an, dass die meisten dieser Anomalien mit dem Vorhandensein von zwei unterscheidbaren flüssigen Phasen mit unterschiedlicher Dichte im unterkühlten Bereich zusammenhängen, d. h. Wasser weist Polyamorphismus auf. Der größte Teil des relevanten Temperaturbereichs liegt jedoch im so genannten *no-man's land*, einem Bereich des Phasendiagramms, in dem Wasser im Bulk rapide kristallisiert und der daher experimentell im Bulk unzugänglich ist. Daher wird in experimentellen Studien häufig die Tatsache ausgenutzt, dass die Kristallisation von Wasser in nanoskopischen Confinements oder Wassermischungen unterdrückt wird. Die vorliegende Arbeit befasst sich mit beiden Forschungsbereichen, der Polyamorphie des Wassers und der Dynamik unterkühlter Flüssigkeiten, sowohl im Confinement als auch in Mischungen. Hierfür kommen Molekulardynamik-Simulationen zum Einsatz. Sie ermöglichen eine detaillierte Analyse und systematische Variation der Flüssigkeit und leichtere Unterkühlung.

Die Partialladungen der Wassermodelle TIP4P/2005 und SPC/E wurden skaliert, was zu starken Verschiebungen der Dynamik in der Temperatur führte. Diese konnten durch die Verwendung der Hochtemperatur-Aktivierungsenergie als relevante Energieskala reskaliert werden, solange die strukturellen Eigenschaften gleich blieben. Für das TIP4P/2005-Modell und eine Reihe von reduzierten Ladungen bestätigte das Kreuzen von Isochoren im Phasendiagram die Existenz eines flüssig-flüssig kritischen Punktes (LLCP) im unterkühlten Bereich bei positivem und negativem Drücken. Der *two-structure equation of state* (TSEOS) Formalismus wurde zur Beschreibung der Daten und zur Bestimmung der Lage des LLCP verwendet. Darüber hinaus ermöglichte die Reduzierung der Teilladungen eine beschleunigte Dynamik am LLCP und Simulationen mit länglichen Boxen im doppelt metastabilen Regime mit Koexistenz von flüssigen Phasen mit hoher Dichte (HDL) und niedriger Dichte (LDL) und die Bestimmung ihrer Dynamik als Funktion der Temperatur. Die Ergebnisse stimmen mit Beobachtungen aus isochoren und isobaren Simulationen überein und für alle thermodynamischen Zustände wurde auch Translationsbewegung beobachtet. Es wurde festgestellt, dass die Temperaturabhängigkeit der Dynamik bei einem konstanten Anteil des Zustands niedriger Dichte (LDS) Arrhenius-artig ist. Der vermutete fragil-zu-stark Übergang (FST) von Wasser wird also nicht durch einen Übergang von fragilem HDL zu starkem LDL verursacht, sondern durch den schnellen Übergang zwischen diesen Flüssigkeitszuständen, wenn die Widom-Linie bei konstantem Druck überschritten wird. Dies stimmt mit experimentellen Beobachtungen etwas oberhalb der Glasübergangstemperatur T_g von Wasser überein und unterstreicht die Frage, ob HDL oder LDL für sich genommen einen FST aufweisen. Es wurden Modelle für die Temperaturabhängigkeit reaktiver Mischungen getestet, die jedoch nicht in der Lage waren die Simulationsergebnisse bei den niedrigsten untersuchten Temperaturen zu beschreiben.

Für die Temperaturabhängigkeit der Dynamik in unterkühlten Flüssigkeiten wurde eine Familie von Funktionen hergeleitet. Diese Funktionen ermöglichen die Charakterisierung der Dynamik über

den gesamten Temperaturbereich, vom Siedepunkt bis zum Glasübergang und mit oder ohne FST. Die Funktionen zweiter Ordnung sagen ein Hoch- und ein Tieftemperatur-Arrhenius-Regime voraus, welche durch einen dazwischen liegenden fragilen Temperaturbereich verbunden sind. Die Kenntnis über den Pfad im Phasendiagramm von ladungsskalierten wasserähnlichen Systemen, ob sie die Widom-Linie bei erhöhten Ladungen überqueren oder nicht, ermöglichte eine genauere Prüfung dieser Funktionen. Sie sind sensibel für Abweichungen von Vogel-Fulcher-Tammann (VFT) Verhalten und lassen sich gut auf Daten aus Simulationen mit Ladungsskalierung von Wasser und Siliziumdioxid, welche einen ausgeprägten FST zeigen, sowie auf reale Flüssigkeiten anwenden. Die Möglichkeit, dass unterkühlte Flüssigkeiten im Allgemeinen ein Tieftemperatur-Arrhenius-Regime haben, und die Eigenschaften solcher FSTs wurden diskutiert.

Es wurden Simulationen von ladungsskalierten Wassermodellen in chemisch neutralen Poren durchgeführt und statische und dynamische Längenskalen extrahiert, die mit Änderungen der Wasserstruktur und -dynamik in der Nähe der Porenwand verbunden sind. Diese Korrelationslängen wurden verwendet, um Theorien des Glasübergangs zu testen, und im Zusammenhang mit den zwei Phasen des Wassers diskutiert. Anzeichen für ein Überschreiten der Widom-Linie konnten in der Temperaturabhängigkeit der Korrelationslängen innerhalb des mäßig unterkühlten Temperaturbereichs nicht gefunden werden. Die Verlangsamung an der Porenwand relativ zur Porenmitte konnte durch zwei empirische Funktionen für zusätzliche Aktivierungsenergien, die durch die Flüssigkeits-Confinement-Grenzfläche verursacht werden, charakterisiert werden. Außerdem wurde die der Flüssigkeit aufgeprägte potentielle Energielandschaft (PEL) mit Hilfe eines neuartigen, auf der Boltzmann-Statistik basierenden Ansatzes quantifiziert, und die vorhergesagten und gemessenen Mobilitätsgradienten stimmen überein.

Und schließlich konnte der Ursprung langsamer Lösungsmittelprozesse, die in dielektrischen Spektroskopiestudien an asymmetrischen binären Mischungen beobachtet wurden, in Simulationen ermittelt werden. Für Mischungen aus Picolin und Poly-Methylmethacrylat sowie aus Wasser und Polylysin wurden keine langsamen Lösungsmittelmoleküle gefunden. Stattdessen verursacht das von den langsamen Polymermolekülen aufgeprägte PEL bevorzugte Orte und Orientierungen für die Lösungsmittelmoleküle. Es wurde ein Mechanismus vorgeschlagen, bei dem die Lösungsmittelmoleküle im Vergleich zur Relaxation der Polymermoleküle schnell austauschen aber korrelierte Orientierungen aufweisen. Dies verursacht langlebige Kreuzkorrelationen, die bei kohärenten Messungen als langsame Lösungsmittelbeiträge fehlinterpretiert werden können. Andere Quellen von Kreuzkorrelationen wurden quantifiziert und die Abhängigkeit von der gemessenen molekularen Eigenschaft und der Korrelationsfunktion wurde diskutiert. Die dynamische Heterogenität der Lösungsmitteldynamik wurde auf die Variation der lokalen Lösungsmittelkonzentration zurückgeführt und ist zwar breit, aber unimodal. Die gleichen Beobachtungen, nämlich langsam zerfallende Kreuzkorrelationen und das Fehlen von Selbstkorrelation auf dieser Zeitskala, wurden auch bei anderen binären Mischungen gemacht, was darauf hindeutet, dass diese Effekte für ein breites Spektrum von Systemen relevant sind.

Contents

1. Introduction

Matter exists in many states, most commonly known are the solid, liquid, and gaseous phases of molecules. While for example plasmas can also occur naturally on earth, most other more exotic states of matter, such as Bose-Einstein condensates, require extreme conditions. However, there are other liquid and solid states of matter which have less severe requirements. One of them is the amorphous solid, also called glass. This state of matter, unlike a crystal, has no long-range order of the atoms comprising the solid and can in theory occur for any atoms or molecules, although it may be difficult to produce. A liquid system may become an amorphous solid upon cooling but this often depends on the cooling process itself and whether crystallization can be avoided. Furthermore, the properties of the thus obtained glass depend on its history which is usually not the case for other states of matter and is related to its metastable nature. The glass transition temperature T_g marks the crossover from the liquid to the solid state. The liquid becomes so viscous upon cooling that it behaves as a solid on typical experimental time scales, and so both states of matter have much in common. Hence, the study of glasses is often preceded by studying the liquid state and the transition to the glass. And because most liquids at these temperatures are below the melting temperature and in a metastable state, they will all be referred to as supercooled liquids within this work.

The study of supercooled liquids is a broad field with far-reaching consequences. Despite the supposed simplicity and wide accessibility of various supercooled liquids and glasses, their theoretical description is still incomplete. Predicting the properties of supercooled liquids and glasses fundamentally requires solving a many-body problem, a notoriously difficult class of tasks. Nevertheless, a very generally applicable predictive model would not only solve this by now 100-year-old problem, but would also help in the development of new materials and support research in areas with transferable concepts. While silica based glasses are widely known and used since thousands of years, their improvement is often an empirical process. In addition, amorphous metals have unique properties such as higher elasticity or even higher critical temperature for superconductivity. The conditions under which liquids are studied are not limited to the actual supercooled regime and are therefore insightful for liquids under a lot of other conditions. Water for example often participates in mixtures, may be confined between larger molecules within cells or exist under extreme conditions in astronomical bodies.

The majority of the results in this work are on pure water and water-like systems. Water exhibits many anomalies compared to other liquids:[1] a density maximum and a crystalline phase with lower density than the liquid, an anomalous pressure dependence of dynamics, and many crystalline structures to name a few. Its ability to form hydrogen bonds is thought to be responsible for many of them. Furthermore, its anomalous behavior becomes more severe in the supercooled regime where thermophysical properties appear to diverge.[2] However, water's strong tendency to crystallize prevents bulk measurements in the so-called *no-man's land*, the temperature range of ∼150–230 K where homogeneous crystallization is unavoidable without possibly altering the observations too significantly. Simulations are on short enough time scales that nucleation can be avoided allowing one to enter the *no-man's land*.[3,4] They showed evidence of the existence of two liquid phases that are possibly separated by a liquid-liquid phase transition (LLPT) line which terminates in a critical point

(LLCP).[5] In the proposed two-phase regime in its phase diagram, water is in the low density liquid (LDL) phase with tetrahedral local structure at sufficiently low pressure while at elevated pressures it is in a high density liquid (HDL) phase with compressed local structure.[6] This phenomenon is known as liquid polyamorphism and quite rare[7] with evidence for, e.g., carbon, phosphorus and sulfur as well as theoretical models.[8–12]

The existence of two liquid phases of water is supported by the finding of at least two amorphous phases at temperatures below the *no-man's land*.[13] Furthermore, the glass transition temperatures associated with both amorphous states differ suggesting that both phases have different dynamics. However, the inability to further investigate water in the *no-man's land* with most experimental methods leaves the details of water's liquid-liquid phase transition highly controversial.[14,15] Even the details of the measured molecular dynamics near the glass transition temperatures, whether it is translational or only rotational motion or only a secondary relaxation is observed, are unclear.[16–18] Experimental evidence of translational motion is still rare[19–21] and polyamorphism is generally not sufficiently understood. The two phases are each mixtures of two constituents that are comprised of the same molecules or atoms that can interchange, i.e., they are reactive binary mixtures with only on average constant concentration. How this affects molecular dynamics, in particular around the phase transition, is not fully understood. While simulations have already proven useful in demonstrating the existence of an LLPT in water for a number of water models, they have had trouble with the slow dynamics at the temperatures in the two-phase regime. The liquid-liquid critical point lies deep in the supercooled regime and at negative pressures where water anomalously slows down. An example is the SPC/E model for which the critical point was predicted to be located in a computationally inaccessible temperature and pressure range of the phase diagram.[22] This is where charge scaling comes in.

Simulations offer the advantage that variable model systems can be prepared under well-controlled thermodynamic conditions. Classical molecular dynamics (MD) simulations can nowadays be used to simulate systems with up to millions of particles and in extreme cases on millisecond time scales.[23] While it is not yet possible to traverse the experimental glass transition, they are sufficient for an exploration of the moderately supercooled regime. And whenever a system is too difficult to simulate or analyze it may be advantageous to simplify or modify it and, hence, to refrain from the attempt of a chemically fully realistic description. This allows the research field to advance into experimentally inaccessible regimes. In MD simulations of water and its LLPT, systematically modified water-like systems may be helpful. The relatively strong Coulomb interactions of this small molecule are the most influential parameter, and hence scaling the partial charges has strong influence on the Hamiltonian of the system. Previous work on water and other systems has already shown strong effects on the local structure, density and the location of the glass transition.[24] For silica, Lascaris et al. showed with simulations of a model with polyamorphism that the location of the LLCP can be shifted or even removed entirely.[25] Therefore, the idea of the present work is to use charge scaling for a systematic study of the existence and location of the LLCP in water-like liquids and more importantly for the investigation of molecular dynamics in the two-phase regime. In particular, the capabilities of MD simulations will allow the separate analysis of both phases in coexistence.

The enormous slowdown of liquid dynamics when cooling down to the glass transition temperature T_g is an intriguing phenomenon on its own. Many models attempt to describe the temperature dependence of dynamical properties, such as viscosity, diffusivity, or the decorrelation of molecular orientation with time. There should exist some underlying mechanism that if understood allows the prediction of these properties in general. And in particular for water and its many anomalies, it is of interest to understand how the supercooled phase gives rise to general dynamical behavior that even water largely complies with. However, such a theory remains elusive despite decades of work.[26,27] Several promising ideas have emerged over time, for example entropy theory,[28–30] elastic models,[31] mode-coupling theory[32] or a Langevin equation approach.[33] One of their shortcomings is the inability to make predictions for the dynamics in broad temperature and pressure ranges, from the boiling point to the glass transition, for all liquids. Hydrogen-bonded liquids have proven particularly difficult to include.

One of the open questions is the functional form of the temperature dependence of the structural relaxation, for which most theories make different predictions.[34,35] In an Arrhenius plot of the structural relaxation time, one can distinguish strong liquids, which obey the Arrhenius law, from fragile liquids, which do not. For fragile liquids, the slope steadily increases with decreasing temperature and can be quite high at T_g. The most common empirical description of this temperature dependence is the Vogel-Fulcher-Tammann (VFT) equation. Liquids are thus often compared in terms of their fragility, a measure of the slope at T_g, with strong and fragile liquids having low and high slopes, respectively. However, there is increasing evidence of the existence of a crossover from VFT behavior to Arrhenius behavior at strong supercooling.[36] There exists no non-empirical functional form that satisfactorily characterizes the dynamics of the liquid from the boiling point to the glass transition when such a fragile-to-strong transition (FST) occurs. However, functional forms with these characteristic regimes can be derived naturally from a simple ansatz and assumptions, as shown in this work. It even reveals a common mathematical origin of two functional forms that have been proposed and successfully used in the last two decades – one approach by Schmidtke et al.[37] for regular liquids and one by Tanaka et al.[38] specifically derived for the dynamics of water. But there may be something more general to dynamics having a strong, fragile, and again strong regime. In fact, entropy models predict a second Arrhenius regime for a non-vanishing and nearly constant configurational entropy.[39]

Here again, simulations of water-like systems are useful. Experimental studies of dynamics below the *no-man's land* and just above T_g revealed a strong temperature dependence, which will only be consistent with observations above the *no-man's land* if water has an FST.[40] Aside from the above question of the nature of the relaxation observed near T_g, it has been suggested that HDL and LDL are fragile and strong liquids, respectively. The transition from the former to the latter then explains the observed temperature dependence above and below the *no-man's land*. While it is impossible to study this with experimental methods in true bulk systems, simulations of charge-scaled models allow for a systematic variation of the location of the LLCP and the prominence of the FST. Using these simulations, theoretical models for the structural relaxation of supercooled liquids and its temperature dependence can be tested and the dynamics in previously inaccessible regions of the phase diagram, in particular, in the two-phase regime below the LLCP can be analyzed.

Another topic of this work is the glass transition of confined liquids. It is quite common for liquids to be confined on nanoscopic length scales. Water in particular can be confined in micelles, between lipid layers or proteins in biological cells, in clays, zeolites, or mesoporous silica. These confinements vary in geometry and interaction between the liquid and the confining matrix. Hence, there have been extensive studies to understand the properties of liquids under such conditions.[41,42] Applications range from modifications of the interface to affect the liquid behavior[43] to suppression of crystallization.[44] However, in addition to the geometrical restriction, liquid-matrix interactions can introduce deviations from bulk behavior, e.g., microphase separation,[45–47] which reduces transferability of observations.[41,42] In particular, it was found that mobility at the interface can be orders of magnitude slower depending on the confinement.[46,48] MD simulations allow for the construction of so-called neutral confinements where the matrix consists of the same molecules and has the same structure as the confined liquid.[48,49] This allows better disentangling of geometric and surface effects from intrinsic behavior of the liquid. Additionally, the full microscopic information available in simulation studies allows for the analysis of observables that are position resolved with respect to the confinement. These have shown steep gradients in the properties of confined liquids[48] that are caused by the static potential energy landscape (PEL) imposed on the liquid by the matrix.[46] Such gradients exist for many properties, e.g., structural or dynamical, of the liquid and correlation lengths, which describe the range of the confinement effects, can be extracted.[50] These length scales are thought to also be relevant to bulk systems where dynamical and structural heterogeneity increase in the supercooled regime. There exist several theories of the glass transition which explain the super-Arrhenius temperature dependence of dynamical properties with activation energies for molecular mobility that depend on length scales growing upon supercooling the liquid. By calculating various correlation lengths from simulations of neutral confinements, these theories can be tested and it can in general be investigated which length scales are relevant and related to the slowdown in supercooled bulk liquids, if any. Additionally, the analysis of temperature- and spatially-resolved mobility and structure of the liquid in neutral confinements enables new approaches to characterize the temperature dependence of the slowdown at the liquid-matrix interface or its distance dependence.

The last part of this work deals with the glass transition of dynamically asymmetric liquid mixtures, which consist of smaller and more mobile molecules and larger less mobile molecules. Examples of such systems are binary mixtures of a solute and solvent with vastly different T_g in their neat systems. This is typical of polymer-plasticizer systems or protein solutions, and thus occurs in a variety of technical applications and biological systems.[51,52] But also mixtures of non-polymeric molecules with strongly different dynamics exhibit similar phenomena suggesting commonalities between various dynamically asymmetric binary mixtures and the discussion and interpretation of the observed relaxation scenarios is ongoing.[53–55] The common observation is an acceleration of solute dynamics and a slowdown of solvent dynamics in the mixtures. While the shapes of the correlation functions of molecular dynamics appear to be unaffected for the former, they broaden significantly for the latter implying that the solvent molecules experience a higher dynamical heterogeneity compared to neat systems. These effects are studied based on the fluctuating energy landscapes imposed by the slow solute molecules onto neighboring solvent molecules.

Observations in broadband dielectric spectroscopy (BDS) studies were taken as evidence that a small fraction of solvent molecules is severely hindered by the solute and that this causes a bimodal distribution of solvent mobility.[56] Moreover, it was concluded that the slow fraction grows with respect to the fast one with decreasing temperature. However, nuclear magnetic resonance (NMR) experiments do not confirm the existence of the fraction of slow solvent molecules or at least disagree on their amount in several systems.[53,57–59] A key difference between these experimental methods is the actual correlation function measured. While BDS measures coherent dynamics, NMR can be used to make incoherent measurements. MD simulations allow the calculation of either type and their direct comparison. Therefore, this work presents simulations of the asymmetric binary mixture of 2-methylpyridine and poly-methylmethacrylate, for which a slow solvent fraction was found in very recent coherent measurements. The results reveal that the slow solvent fraction does not exist and a mechanism is proposed, which is based on cross correlations together with the fluctuating energy landscape imposed by the slow solute molecules onto the solvent molecules.

This document is organized in the following way. Chapters 2-5 cover fundamentals of relevant topics and details of MD simulations and their analysis. Chapters 6 through 10 present the results and each chapter contains its own review of the literature and motivation and summary of the results. The results begin with the charge-scaled water systems and the discussion of deviations from ordinary water. Chapter 7 investigates the polyamorphism of water under charge scaling. The results for dynamical properties of water and other systems are then used to discuss general functional forms of the temperature dependence of the activation energy of relaxation processes and their implications for strong-fragile-strong transitions in Ch. 8. Then, results of charge-scaled water in neutral nanoscopic confinements are discussed in Ch. 9 in relation to water's polyamorphism but also generally in the context of the dynamical behavior of supercooled liquids. Finally, Ch. 10 discusses the differences between coherent and incoherent measurements and difficulties of their interpretation using the example of dynamically asymmetric binary mixtures. The main results of the thesis are summarized in Ch. 11.

2. Theories and the state of research

This chapter gives a short overview of the concept of supercooled liquids and glasses. It introduces the most common phenomena and some theories that attempt to characterize them. Furthermore, it discusses findings for supercooled water and open questions.

2.1. Supercooled liquids and the glass transition

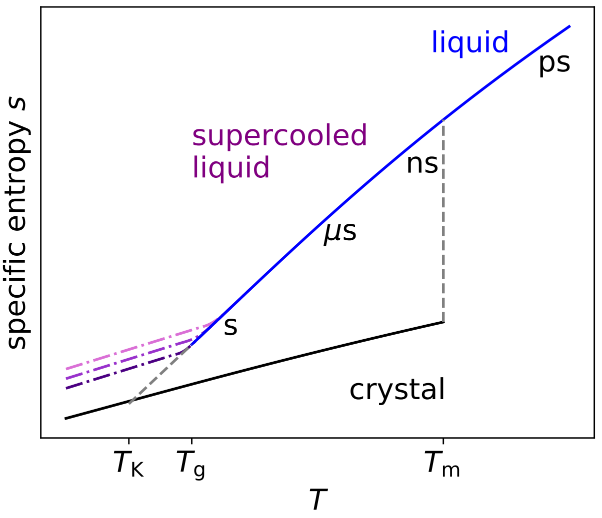

Figure 2.1.: Simplified sketch of the specific entropy of the liquid, crystal and glass as a function of temperature.

Supercooled liquids and glasses (also called amorphous solids) are both forms of condensed matter and belong to the group of liquids and solids, respectively. An initial distinction from the regular liquid and crystalline phase comes from thermodynamic observations. In general, cooling a liquid below its melting temperature T_m results in a first order phase transition to a crystal. The kinetics of crystallization are relevant for understanding liquid phases below T_m. This phase transition is accompanied by a drop in entropy, indicated in Fig. 2.1. The previously amorphous arrangement of molecules is replaced by order and, with exceptions such as water, denser packing. The molecules lose most of their mobility and are only able to perform local vibrations. The solid responds only elastically to stress while the liquid flows. The cause of the phase transition is the difference in Gibbs free energy between the liquid and the crystalline solid, $\Delta G = G_\text{crystal} - G_\text{liquid} < 0$. The ordered arrangement of the crystal is favored by enthalpy and crystallization releases heat to the environment. This fulfills the second law of thermodynamics. However, the process of crystallization is hindered by an activation energy barrier, and thus requires nucleation. The interface between amorphous liquid and crystal is energetically unfavorable. Considering a spherical crystallization nucleus, the gain ΔG scales with its radius cubed while the interfacial energy scales only with the radius squared. The consequence is a critical nucleus size: smaller nuclei shrink while larger ones continue to grow. The free energy for this radius is the energy barrier to overcome. The probability of a critical nucleus occurring through thermal fluctuations is given by the Boltzmann factor. With the degree of supercooling, $T - T_\mathrm{m} < 0$, both the energy barrier and the thermodynamic fluctuations decrease, leading to a nucleation rate that is non-monotonic in T and has a maximum below T_m. In addition to the rate at which critical nuclei occur, the growth of the crystal depends on the mobility of the molecules, i.e., how fast they can arrange into the crystalline structure, and on the thermal conductivity. Altogether, the rate at which a liquid sample crystallizes has its maximum at supercooled temperatures. The mechanism described above is called homogeneous nucleation. Heterogeneous nucleation occurs in the presence of impurities. Foreign particles in the liquid can allow nuclei to form on their surface and effectively reduce the critical size and energy barrier. Impurities thus facilitate faster crystallization. Because of crystallization kinetics, it is possible to study liquids below their melting point, i.e., in the supercooled regime. Such a supercooled liquid is in a metastable state – the crystal is the true thermodynamic equilibrium. Besides a pure sample, two time scales are relevant to allow observations at supercooled temperatures: the experiment happens on shorter time scales than crystallization and the cooling rate is fast enough to avoid nucleation.

Not only is the supercooled liquid still liquid it also exhibits different thermodynamic properties than the crystal. In particular, its specific heat is higher, since not only phonons, as in a solid, but also configurational changes determine the internal energy. The consequence is a steeper temperature dependence of the entropy, sketched in Fig. 2.1. The extrapolation to lower temperatures suggests a crossing at the so-called Kauzmann temperature, the so-called Kauzmann paradox.[60] Very few systems that exhibit the phenomenon of inverse melting,[61,62] crystallization upon heating, appear to exhibit this behavior. However, this is only a theoretical scenario for the vast majority of liquids and experimentally not observed. Instead, the liquid becomes increasingly viscous upon further supercooling, a fact discussed in more detail in Sec. 2.2 and Fig. 2.4. Importantly, at some point the viscosity becomes so large that the sample no longer flows on experimental time scales and begins to behave like a solid. Despite this, the molecules do not have long-range order. Instead, the liquid vitrifies; it has become a glass. The specific heat is reduced and the Kauzmann paradox is avoided.

This vitrification phenomenon is called glass transition. The supercooled liquid is still in equilibrium, albeit metastable. However, the dynamics slow down: the viscosity increases rapidly with decreasing temperature and the time to reach equilibrium increases strongly.[63] The molecules need time to adjust structurally to external influences, e.g., shear stress or temperature changes. This structural relaxation time is indicated in Fig. 2.1 and increases by many orders of magnitude. Below T_g, the structural relaxation time exceeds the experimental time scale and the system falls out of equilibrium. It can no longer explore the entire phase space. The glass transition is therefore kinetic rather than thermodynamic in nature and does not involve discontinuities in thermodynamic properties. What further distinguishes the glass transition from typical first-order phase transitions is its dependence on the history of the system. The system responds differently to temperature changes depending on the time it spent at previous temperatures and the rate of cooling or heating. In particular, T_g depends on the cooling rate. Faster cooling causes the system to fall out of equilibrium at higher temperatures, while staying just below T_g for longer times anneals the sample, see Fig. 2.1.

The official definition of T_g incorporates a constant cooling rate (ISO 11357-2:2020). T_g is determined by analysis of the step in specific heat in a differential scanning calorimetry (DSC) measurement. Since a DSC measurement is not always available, especially for simulations because of the computational cost, other practical definitions exist. The acceptable time for an experiment to wait for equilibrium defines an upper end for the dynamics of the system of about $\tau(T_\mathrm{g}) \sim 100 - 1000\,\mathrm{s}$. Measurements of the viscosity near the glass transition give about $\eta(T_\mathrm{g}) \sim 10^{12}$ Pa·s. For comparison, the viscosity of water at 20 °C is about 1 mPa·s. However, all of these definitions are arbitrary. It remains an open question whether or not a true thermodynamic transition exists below T_g.

Some systems are more easily supercooled and transformed into a glass than others. Silicate glasses or polymers are good glass formers. Sterically hindered crystalline phases as in mixtures of ions of different sizes are often suppressed. Even many molecular liquids can be stored at supercooled temperatures down to T_g for days. However, when the structural relaxation time exceeds the crystallization rate the liquid can no longer be equilibrated and the supercooled liquid does effectively not exist. Rapid cooling can be used to skip the supercooled regime of poor glass formers and avoid crystallization. Methods for this include vapor deposition or melt spinning, which achieves cooling rates on the order of 10^6 K/s. Melt spinning is also used to produce amorphous metal alloys with unique properties that cannot be achieved with their crystalline counterparts. Once the system is below T_g, the high viscosity prevents subsequent crystallization. Finally, T_g is material specific and any liquid can be as fluid as water or as viscous as molten glass at the right temperature, unless crystallization cannot be avoided or the system undergoes chemical changes. Since several properties of supercooled liquids are general, e.g., the rapid increase in viscosity, the designation as a supercooled liquid is used more freely in this work, i.e., even when T_m is unknown. Whenever the liquid is to be distinguished specifically from its supercooled state, it is referred to as a simple liquid.

Thus, supercooled liquids and glasses are widely relevant phenomena. Amorphous materials are the subject of current research and have many applications.[64] However, a general theory explaining all the properties of supercooled liquids and glasses is still missing. The experimental and theoretical study of the glass transition is challenging. Experiments not only require that crystallization is avoided, but are also limited by T_g and often cover only a fraction of the many orders of magnitude of dynamics, ranging from picoseconds to thousands of seconds. Theoretical models for many-body problems are notoriously difficult. A brief overview of some models for the dynamical properties is given in Sec. 2.2, after discussing the structural and dynamical observations in more detail.

2.1.1. On the structure of supercooled liquids and glasses

The structure of supercooled liquids and glasses on microscopic scales is one of their major common features. The arrangement of molecules is not periodic and there is no long-range order. Hence, they are homogeneous and isotropic on mesoscopic length scales, which gives them properties not found for single-crystal solids, such as an isotropic refractive index. However, molecules are not randomly arranged on microscopic length scales. There, preferred local configurations of neighboring molecules occur according to their interaction energy and statistical mechanics. Energetically favorable configurations are more likely to occur than others. However, they are generally incompatible to fill space with a repeating pattern. The local structure decorrelates on nanometer length scales.

Figure. 2.2 presents these observations using the radial pair-distribution function (RDF), see Sec. 5.1.1. Deviations from one indicate an increased or decreased probability of finding particles at distance r from each other as compared to a random particle arrangement. For amorphous systems, the RDF quickly decays to one, implying fast decorrelation of the local structure. At temperatures close to the boiling point, only next neighbor positions are correlated. With decreasing temperature, correlations are enhanced even beyond the next neighbors. The range to which deviations from one are significant increases until the system undergoes structural arrest at T_g. Long-range

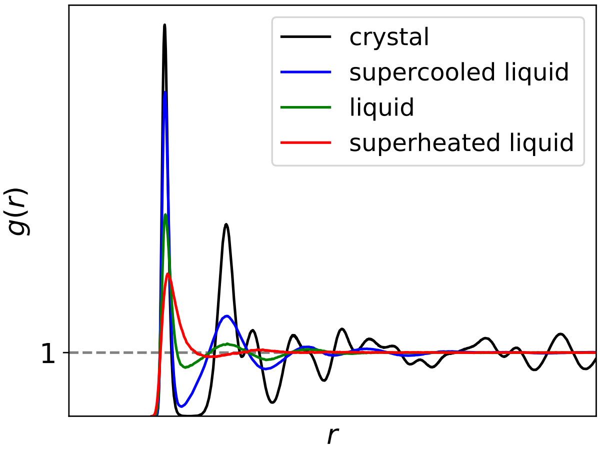

Figure 2.2.: Radial pair-distribution functions for oxygen atoms of simulated water in the crystal phase, the supercooled regime, the liquid phase, and close to the boiling point.

correlations are only found in crystals or otherwise inhomogeneous systems. The continuous transition from supercooled liquid to the glass makes both states structurally indistinguishable. Therefore, studying either system can be helpful in understanding both.

2.1.2. Correlations in time

Besides the structural characterization, the quantification of the dynamics in the system is also of significant interest. Correlation functions are a major aspect in this respect and are frequently used in this work. Therefore, they are discussed in more detail here – their mathematical basis and how to interpret them. The thermodynamic aspect of liquids inherently involves the existence of many properties that can be considered random variables. Unlike white noise, they are not necessarily uncorrelated with themselves or even with each other at all times. Correlations of random variables and how long they persist are of great interest. In general, the correlation of two random variables, x and y, can be calculated by their normalized covariance:

$$C_{x,y} = \frac{\langle xy\rangle - \langle x\rangle\langle y\rangle}{\sigma_x\sigma_y}, \tag{2.1}$$

with $\langle\dots\rangle$ denoting averages and the standard deviation σ.

In physical cases, a non-normalized calculation may be more appropriate. Furthermore, x and y are usually time dependent. If the system is in (metastable) equilibrium and ergodic, all times are equivalent time origins and only the time differences t are relevant. Averages $\langle\dots\rangle$ over several time origins t_0 are then performed:

$$C_{x,y}(t) = \frac{\langle x(t_0)y(t+t_0)\rangle - \langle x\rangle\langle y\rangle}{\sigma_x\sigma_y}. \tag{2.2}$$

If ergodicity is not satisfied, the expectation values and standard deviations also depend on the time origin. If x and y are different quantities, cross correlations are measured, while for $x = y$ the correlation function simplifies to a so-called autocorrelation function, more precisely the auto-covariance function:

$$C(t) = \frac{\langle x(t_0)x(t+t_0)\rangle - \langle x\rangle^2}{\sigma_x^2}. \tag{2.3}$$

Again, depending on the physical property the normalization can be omitted. This function can be used to autocorrelate any scalar property in time. These can be single-particle, multi-particle, or macroscopic properties such as internal energy or pressure. The use of transformations $f : \mathbb{R}^n \to \mathbb{R}$ allows for more complex correlation functions, e.g., rotational correlation functions in Sec. 5.2.3. They are qualitatively identical and are treated and analyzed in the same way in this work. In equilibrium, the Wiener-Khinchin theorem[65] relates the autocorrelation of a time series to its spectral density:

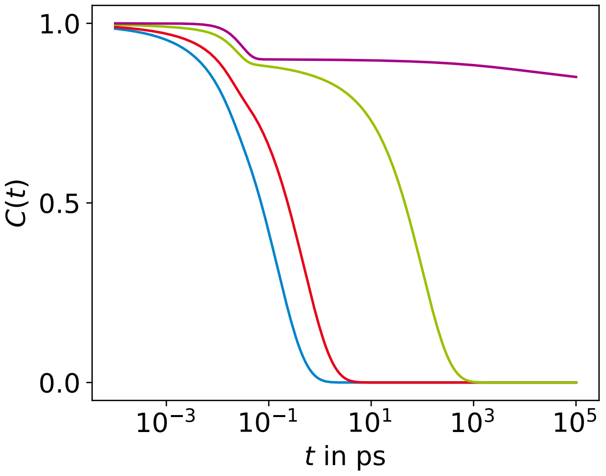

Figure 2.3.: Typical decays of correlation functions in simple liquids (blue) and liquids at various degrees of supercooling.

$$C(t) = \mathcal{F}^{-1}\left(|\mathcal{F}(x(t))|^2\right) , \tag{2.4}$$

where $\mathcal{F}$ stands for the Fourier transform.

In simple situations, autocorrelation functions feature an approximately exponential decay characterized by the correlation time, a measure of how long the property is correlated with itself. An example is shown in Fig. 2.3. Properties subjected to thermal fluctuations or vibrations of particles within their local potential share a rapid decay on sub-picosecond time scales. This partial decorrelation is followed by one or more (stretched) exponential decays. To quantify the time scale of the main terminal decay, it is often fitted with a scaled Kohlrausch-Williams-Watts (KWW) function:[66,67]

$$A \exp\left[-\left(\frac{t}{\tau_{\mathrm{kww}}}\right)^{\beta_{\mathrm{kww}}}\right]. \tag{2.5}$$

The prefactor A quantifies the correlation loss of this decay, which can be less than one due to vibrational motion. The correlation time is determined by τ_{kww} and β_{kww}, the time constant and the stretching parameter of the KWW function. The mean correlation time $\langle\tau\rangle = \frac{1}{A}\int_0^\infty C(t)\,\mathrm{d}t$ is calculated with $\langle\tau\rangle = (\tau_{\mathrm{kww}}/\beta_{\mathrm{kww}})\Gamma(1/\beta_{\mathrm{kww}})$, where $\Gamma(x)$ denotes the gamma function. However, at high temperatures, the vibrational and terminal decay are often not sufficiently separated. In such cases, the definition $C(\tau_{\mathrm{e}}) = 1/e$ is used for consistent results.

Because many different microscopic processes contribute the shape of correlation functions is the subject of countless studies in the literature.[68,69] The underlying processes are usually designated by their order. The α-process is the slowest and leads to the terminal decay, with the notable exception of polymer melts. Its correlation time τ_α is usually on the order of 100 s at T_{g} and is therefore considered as an indicator of the structural relaxation time and viscosity. In detail, this is not an exact definition because the α-process of different correlation functions or different molecular degrees of freedom varies, see Sec. 2.1.3 and 5.2.3. In general, the α-process is identified with significant displacements or reorientations of individual molecules. In contrast, faster processes such as the Johari-Goldstein β-process are caused by internal or local degrees of freedom. Their amplitude is not sufficient to cause complete decorrelation, and they are only readily observable when the α-process is sufficiently slower than the vibrational motion. Hence, they appear in the supercooled regime and are more clearly observed below T_{g}, when the α-process has arrested. Processes between the β-process and vibrational motion are rare but possible and not of interest in this work. Finally, it should be noted that certain correlation functions that characterize multi-particle motion may even in non-polymeric systems show a terminal decay slower than the α-process. An example is the Debye process caused by cross correlations of hydrogen-bonded monohydroxy alcohols.[70] Chapter 10 addresses a recent identification of cross correlations in mixtures and their interpretation.

In addition to the correlation times of these processes, their shape is also of significant interest. For example, the function necessary to model a decay and its shape parameters, e.g., the KWW function and β_{kww}, provide information about the heterogeneity of the system. Deviations from an exponential decay indicate that the motions of the molecules are stochastic processes which are not independent of each other and that the correlation times have a broad distribution.

This is only a brief overview of what can be expected from correlation functions and neglects numerous special cases. Their importance is emphasized by the fact that many experimental methods probe a correlation function directly or indirectly. Its Fourier transform yields the spectral density $J(\omega)$ and susceptibility $\chi(\omega)$, properties measured in frequency space by, for example, nuclear magnetic resonance (NMR) and broadband dielectric spectroscopy (BDS).[68] On the other hand, depolarized dynamic light scattering (DDLS) provides access to an autocorrelation function. Moreover, frequency-dependent viscoelastic measurements complement this way of characterizing the dynamics of the system under study.

2.1.3. Relations between different dynamical properties

Using different experimental methods to characterize the dynamics may seem counterintuitive. An optimal method would be desirable. The shear viscosity η and the self-diffusion coefficient D are promising candidates along with a selection of τ. However, not all of these quantities are experimentally available over the entire temperature range, especially in more complex systems. Their temperature dependence is theoretically linked by the Stokes-Einstein (SE) relation,[71]

$$D_{\mathrm{T}} = \frac{k_{\mathrm{B}}T}{6\pi\eta R_{\mathrm{H}}}\,, \tag{2.6}$$

where k_{B}, T, and D_{T} are the Boltzmann constant, the temperature, and the translational self-diffusion coefficient of a spherical particle in a liquid of viscosity η. It was derived using hydrodynamics and Brownian motion and R_{H} denotes the effective hydrodynamic radius. The Stokes-Debye (SD) relation analogously gives for rotational diffusion D_{R}:[72]

$$D_{\mathrm{R}} = \frac{k_{\mathrm{B}}T}{8\pi\eta R_{\mathrm{H}}^3}\,. \tag{2.7}$$

From the above equations η can be eliminated, leading to the Stokes-Einstein-Debye (SED) relation. They can be linked to rotational correlation times τ. For rotational diffusion holds $D_{\mathrm{R}} = \frac{1}{\tau_\ell \ell(\ell+1)}$, where ℓ is the rank of the Legendre polynomial used in the correlation function, see Sec. 5.2.3. Together with Eqs. (2.6) and (2.7), a constant product $D_{\mathrm{T}} \cdot \tau_l$ is predicted:

$$D_{\mathrm{T}} \cdot \tau_l = \frac{4}{3l(l+1)} R_{\mathrm{H}}^2\,. \tag{2.8}$$

However, deviations are often observed for supercooled liquids. The most common case, an increase in R_{H} upon cooling, is attributed to the different weighting of the dynamical heterogeneity in D and τ.[73–75] While diffusion determines a rate average and, thus, weights fast dynamics more strongly, correlation times are a time average. Different temperature dependencies are obtained when the distribution of correlation times changes shape with temperature. In particular, as heterogeneity increases, as may occur with severe supercooling, τ is expected to slow down more relative to D, increasing R_{H}. However, the actual cause, dependence, and strength of the decoupling depends on the system and may also exhibit the opposite temperature dependence.[76] Hence, supercooled liquids are not so simple and measuring multiple dynamical properties actually increases the understanding of a given system.

2.2. Models of dynamics in the supercooled regime

So far, the dynamical aspects of the supercooled liquid and glass transition have been discussed only qualitatively. However, they are far more complex and exhibit a temperature dependence that eludes a satisfactory model. In this section, general observations are discussed and various models of the glass transition are used to introduce concepts relevant to the rest of this work.[27,64,77]

The steep temperature dependence of, for example, τ_α in the supercooled regime is best studied in an Arrhenius plot, $\log_{10}(\tau_\alpha)$ versus $1/T$. Alternatively, the temperature can be rescaled by T_{g} to obtain what is known as an Angell plot, which allows comparison of different glass formers, see Fig. 2.4. In general, a super-Arrhenius behavior, i.e., an increasing slope with decreasing temperature, is observed. While some liquids cross from perfectly fluid to the glass in a narrow temperature range with a strong curvature that can be characterized reasonably well by the Vogel-Fulcher-Tammann (VFT) equation,[63,78,79] Eq. (2.10), others show almost Arrhenius behavior, Eq. (2.9):

$$\text{Arrhenius: } \tau_\alpha = \tau_\infty e^{\frac{E}{T}} \tag{2.9}$$

$$\text{VFT: } \tau_\alpha = \tau_\infty e^{\frac{B}{T-T_0}} \tag{2.10}$$

Here, τ_∞ is a prefactor, E is the activation energy of the Arrhenius law, and T_0 is the temperature of divergence.

The slope at T_g in the Angell plot is called the fragility and has been useful in characterizing various systems. It is defined as

$$m = \left(\frac{\delta \log_{10} \eta}{\delta(T_\mathrm{g}/T)}\right)_{T=T_\mathrm{g}} . \tag{2.11}$$

Liquids with high fragility are called *fragile* and follow a VFT-like behavior, while liquids with low fragility are called *strong* and approximate an Arrhenius behavior. Although the terms fragile and strong are defined in conjunction with T_g, in this work they are also applied to regimes far from the glass transition, i.e., whether the liquid follows an Arrhenius or a VFT behavior in a given temperature range.

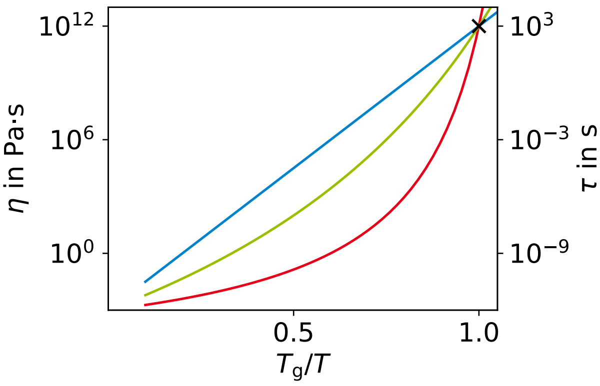

Figure 2.4.: Angell plot of artificial viscosities of strong and fragile glass formers.

Observing Arrhenius and super-Arrhenius behaviors requires rejecting a simple picture of an activated process with a constant activation energy for all liquids. Instead, each molecule experiences an inhomogeneous energetic potential with different energy barriers that changes with time and temperature as the system as a whole traverses the macroscopic potential energy landscape. These changes extend beyond the vibrational degrees of freedom of a solid. The local configuration of molecules becomes more efficiently packed and the energy barriers increase significantly upon further cooling. In particular, there is no longer sufficient free volume for relaxation processes of individual molecules. Instead, many neighboring molecules have to rearrange. Hence, relaxation in the supercooled regime is often called cooperative. This inherent multi-particle problem makes the formulation of a successful model difficult. Nevertheless, the following models and theories had some success and have helped to deepen the understanding of supercooled liquids.[27,80]

2.2.1. Entropy theories – Adam-Gibbs

One of the earlier theoretical successes was based on the work of Flory, who calculated the number of disordered configurations available to a polymer on a lattice.[81] He found that this number becomes less than one at some finite temperature, a problem comparable to the Kauzmann temperature. This similarity did not go unnoticed and Gibbs and Di Marzio associated it with the glass transition and a second-order phase transition.[28] Adam and Gibbs developed what is known as Adam-Gibbs (AG) theory.[29] Following the cooperative picture of relaxation in supercooled liquids, they assume the existence of cooperatively rearranging regions (CRR) consisting of many particles. Their size grows upon cooling as the particles become increasingly correlated. Subsets of a CRR cannot rearrange independently and, thus, do not contribute to the actual available number of states Ω that a CRR can assume. However, CRRs interact weakly with each other and can rearrange independently.

Since each CRR consists of n particles, the total number of states $\mathcal{N}$ of a system of N particles is $\mathcal{N} = \Omega^{N/n}$.[27] Therefore, the configurational entropy S_c of the system is

$$S_\mathrm{c} = \frac{1}{N}\log\mathcal{N} = \frac{\log\Omega}{n} . \tag{2.12}$$

As suggested, the entropy decreases as the number of correlated particles n increases. Moreover, the size of the CRRs can be estimated as $\xi^d \sim n(T) = \frac{\log\Omega}{S_\mathrm{c}(T)}$ for d dimensions. ξ is also known as the correlation length, a reoccurring concept in other theories. AG theory states that the activation energy for relaxation events scales with the number $n \sim 1/S_\mathrm{c}$ of cooperatively rearranging particles. Assuming an Arrhenius ansatz, the structural relaxation time can then be written as

$$\tau = \tau_0 e^{\frac{A}{TS_\mathrm{c}}} , \tag{2.13}$$

with a system-dependent prefactor τ_0 and energy scale A. Finally, $S_\mathrm{c}(T)$ near T_k can be approximated by the difference in specific heat Δc_p of liquid and crystal as $S_\mathrm{c} \sim \Delta c_\mathrm{p}\frac{T-T_\mathrm{k}}{T_\mathrm{k}}$.[27] The resulting temperature dependence of τ,

$$\tau_\alpha = \tau_0 e^{\frac{AT_\mathrm{k}}{\Delta c_\mathrm{p} T(T-T_\mathrm{k})}} , \tag{2.14}$$

is approximately equal to the VFT equation when T is close to T_k.

AG theory has several interesting results. It links configurational entropy and dynamics, makes estimates for the correlation length, produces fragile behavior, and approximately justifies the VFT equation. However, it assumes a constant Ω and proposes a second-order phase transition. The latter can be avoided by modifications made after the original theory was proposed.[82–84] Furthermore, recent theoretical calculations predict a residual entropy for the liquid at all temperatures.[39,85] For further insight into entropy theories, see Dudowicz et al. (2008).[30]

2.2.2. Mode-coupling theory

A different theoretical approach to dynamics in supercooled liquids is given by mode-coupling theory (MCT).[86–88] In the supercooled regime, processes occur on different time scales, see Fig. 2.3. Accordingly, the phase space variables of the system contain fast fluctuations caused by vibrational motion and slower changes, for example the α-process. The Mori-Zwanzig formalism is then used to project from the full phase space to a set of slowly varying variables. The time dependence of the set $\mathbf{A}$ of slowly varying variables can then be expressed by

$$\frac{\mathrm{d}\mathbf{A}(t)}{\mathrm{d}t} = i\mathbf{\Omega}\cdot\mathbf{A}(t) - \int_0^t d\tau\mathbf{M}(\tau)\cdot\mathbf{A}(t-\tau) + \mathbf{f}(t) , \tag{2.15}$$

where $\mathbf{M}(t)$ is the so-called memory function, $f(t)$ is a fluctuating force, and $i\mathbf{\Omega}$ is a frequency matrix. $\mathbf{M}(t)$ couples the slowly varying variables, also called modes, which gives the theory its name. For supercooled liquids, the variable of choice is the particle density in momentum space $\rho(\vec{k},t)$. The corresponding correlation function is then the coherent intermediate scattering function, see Sec. 5.2.1, and measures the dynamics of particles at different length scales. The memory function then couples the modes of density corresponding to the different wave vectors. The only input MCT requires is static information about the structure factor and the bulk density of the system. It correctly predicts the two-step behavior of correlation functions and the shape of the regime of the β-process.[88]

The enhancement of local structure with decreasing temperature, see Fig. 2.2, leads to a slowdown of dynamics. MCT predicts a power law for the correlation time,

$$\tau = \tau_0 \frac{T_\mathrm{c}}{(T - T_\mathrm{c})^\gamma} \, , \tag{2.16}$$

with a divergence at the finite mode-coupling critical temperature T_c. However, the significance of denser packing in the local structure is overestimated and T_c is above T_g, i.e., the correlation function does not decay between T_g and T_c. MCT lacks activated dynamics, which become the dominant mechanism of relaxation below T_c. Many attempts have been made to remedy this premature dynamical divergence. For example, hierarchically stacked memory functions in the generalized MCT avoid the approximation of the standard MCT.[89] As the order of the memory functions increases, the agreement between prediction and measurement improves at deeper supercooling and the divergence can be avoided altogether with infinite order.[90] Nevertheless, MCT does not predict thermodynamic variables and requires prior knowledge, the structure factor, about the system at each temperature.

2.2.3. Random first-order transition theory

The mosaic or random first-order transition (RFOT) theory has similarities with the AG theory.[27,91–93] The system again consists of CRRs in different states – a mosaic, see Fig. 2.5. However, their interaction is not neglected. In particular, the interface between CRRs is not ideal and causes surface tension. This increases the free energy barrier that must be overcome to move from one state to another. This additional cost is offset by the number of states available to a CRR. A region of size R has an exponentially large number of possible states. While the overall free energy is in equilibrium, visiting other states by rearrangement increases the configurational entropy. Remaining in one of many equally likely states is not favored by statistical mechanics. In the end, thermal fluctuations and entropy drive the dynamics of the system.

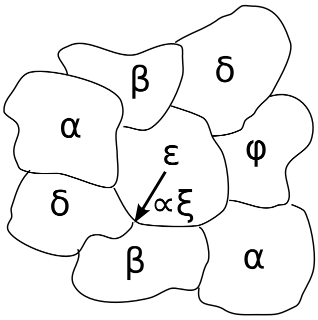

Figure 2.5.: Mosaic of CRRs with different states.

The RFOT theory acknowledges that the surface of amorphous regions does not necessarily have dimension $d-1$, where d is the dimension of the system. In particular, it may be reduced and fractal during a rearrangement event. Hence, the free energy barrier is described as

$$\Delta F = \underbrace{\gamma(T) R^\theta}_{\text{cost}} - \underbrace{T s_\mathrm{c} R^d}_{\text{driving}} \, . \tag{2.17}$$

Here, γ is the surface tension, θ the unknown dimensionality of the interface, and s_c is the configurational entropy per unit volume. Analogous to the nucleation theory of crystals, the barrier decreases above a certain size and even vanishes for sizes larger than

$$\xi = \left(\frac{\gamma(T)}{T s_\mathrm{c}(T)} \right)^{\frac{1}{d-\theta}} \, . \tag{2.18}$$

Regions larger than ξ are unstable against rearrangement. However, the probability of such an event decreases with the number of particles involved and, thus, RFOT suggests that CRRs are typically of size ξ. Furthermore, the liquid cannot rearrange when confined to volumes smaller than $\sim \xi^d$ and consequently is in a glassy state. Note that this correlation length ξ increases more with decreasing temperature and configurational entropy in RFOT than in AG.

Finally, the structural relaxation time can be estimated by calculating the barrier height from the maximum of Eq. (2.17). Following several assumptions near T_k, $\theta = d/2$ can be proposed, in which case structural relaxation times follow the same VFT, Eq. (2.14), as in AG theory.[91] More generally, the structural relaxation time follows

$$\tau = \tau_0 e^{B\frac{\xi^\phi}{T}} , \tag{2.19}$$

where ϕ is an unknown exponent likely to be less than d.[92] The RFOT theory does not assume validity for all temperatures. In particular, the surface tension is assumed to vanish in the simple-liquid regime. The upper limit of validity is T_c and RFOT adopts MCT for higher temperatures.

2.2.4. Free-volume and elastic models

Two directions of models are summarized here because they have some ideas in common. The observation that many supercooled liquids have higher thermal expansion than their respective crystal suggests that the increasingly denser packing of molecules with cooling is significant. This reduces the ”free volume” available to individual molecules for rearrangement. Early on, it was found that the viscosity of a liquid can indeed be related to the expansion of the liquid as

$$\eta = \eta_0 e^{B\frac{v_0}{v_\mathrm{f}}} , \tag{2.20}$$

where η_0 and B are constants, v is the specific volume, v_0 is the specific volume at absolute zero, and $v_f = v - v_0$ is the temperature-dependent free volume.[94] Free-volume models have been further refined, leading for example to Eq. (8.22).[95–97] However, free-volume models are not applicable to associated liquids, i.e., liquids with hydrogen-bond networks. The density anomaly of water, for example, is incompatible with the monotonic slowdown of dynamics in free-volume models. Furthermore, the definition and determination of the free-volume in the different models is inconsistent. For example, Voronoi tessellation can be used in simulations to calculate the volume of individual molecules.[98] In the same study, $v_\mathrm{f}^{2/3}$ was found to be more accurate and there is a linear relation between it and the Debye-Waller factor $\langle u^2 \rangle$, the vibrational displacement at short times, see Sec. 5.2.2. In other words, $\langle u^2 \rangle$ is a measure of the expansion of the free volume.

This Debye-Waller factor is also a parameter in many elastic models.[31] Their main feature is the connection of fast vibrational dynamics and slow structural relaxation despite the separation by orders of magnitude. The dense packing in the supercooled regime leads to the so-called caging of molecules. The translational motion of the particles changes from ballistic on very short time scales to diffusive on long time scales. In the supercooled liquid, this transition is hindered by the neighboring molecules, which form a cage and cause a significant energy barrier for translation. As a result, the respective decays of correlation functions due to vibrational motion and structural relaxation separate in time, see Fig. 2.3. It was originally proposed that the molecules probe and, thus, quantify the surrounding potential energy landscape of the cage via local vibrations.[99] The amorphous structure leads to complicated potentials that are approximated by harmonic functions for small displacements. The resulting spring constants determine $\langle u^2 \rangle$, which in turn acts as a probe for the local potentials and defines the elastic behavior of the system. This leads to the prediction known as the harmonic approximation,[99]

$$\eta = \eta_0 e^{\frac{a^2}{\langle u^2 \rangle}} , \tag{2.21}$$

with a as the constant inter-molecular distance. Despite their differences, the free-volume models and the elastic models have similar results.

Another example of elastic models is the shoving model, which assumes that relaxation events in the supercooled regime require the nucleation of a free volume into which a molecule can move.[100,101] The cost associated with such a rearrangement is caused by shearing of neighboring molecules and, since the shoving model views viscous liquids as solids which flow, is given by the instantaneous elastic shear modulus G_∞:

$$\tau \sim e^{\frac{V_\mathrm{c} G_\infty(T)}{k_\mathrm{B} T}} , \tag{2.22}$$

where V_c is a temperature-independent microscopic volume. The increase of G_∞ upon cooling causes the super-Arrhenius temperature dependence of τ. Recent studies have argued that instead G_p, the height of the post-vibrational plateau in the transient elastic modulus, is a better choice.[102,103] In fact, they propose a non-linear relation between the activation energy and G_p.

The localization model generalizes Eq. (2.21) by assuming non-isotropic and possibly fractal shapes of the free volume.[104] Including the finding of a possible onset temperature T_A, which qualitatively separates the simple-liquid and viscous regimes by their dynamical behavior,[105] leads to a simple relation:

$$\ln \frac{\tau(T)}{\tau(T_\mathrm{A})} = \left(\frac{\langle u^2(T_\mathrm{A}) \rangle}{\langle u^2(T) \rangle} \right)^{\gamma/2} - 1 , \tag{2.23}$$

with the generalized exponent γ. The exact functional form is still unsettled, as for example Puosi et al. propose a generalization using higher moments of $\langle u^2 \rangle$.[106]

Finally, a more analytical model is the elastically collective nonlinear Langevin equation (ECNLE) theory.[107,108] It attempts to overcome the limitations of MCT by calculating energy barriers for collective rearrangements below T_c. Each particle i is caged by its neighbors and is thus subject to a potential modeled by the so-called dynamic free energy $F_{\mathrm{dyn},i}(r_i(t))$, where $r_i(t)$ is its displacement $|\vec{r}_i(t) - \vec{r}_i(0)|$. F_dyn incorporates a barrier ΔF that must be overcome and a minimum inside the cage that characterizes the localization of the particle on short time scales. In addition, a free volume beyond the energy barrier must be created. ECNLE theory proposes small but collective displacements which decay in amplitude with r^{-2}. Hence, all other particles pay a dynamic free energy cost in their respective potentials $F_{\mathrm{dyn},i}(r_i(t))$. This displacement is small and elastic and can be approximated by harmonic potentials. The total barrier for rearrangement consists of the initial barrier ΔF and the integral over the elastic displacement field F_elastic. The ECNLE theory adopts Kramers' theory and predicts:[109,110]

$$\frac{\tau}{\tau_\mathrm{s}} = \frac{2\pi}{\sqrt{K_0 K_\mathrm{B}}} \exp\left(\frac{\Delta F + F_\mathrm{elastic}}{k_\mathrm{B} T} \right) . \tag{2.24}$$

τ_s is a short-time process and K_0 and K_B are curvatures of F_dyn. At higher temperatures, ΔF dominates, while F_elastic grows faster upon cooling or increasing packing fractions. While the model does not explicitly derive one, it raises the question of the existence of an elastic correlation length that characterizes the extent of collective participation of particles in rearrangement events.[111]

This brief overview shows the relevance and success of theories based on concepts of elastic or free volume, but also that they are still the subject of active research and that there are further but divergent developments.

2.2.5. Empirical model by Schmidtke et al.

Finally, there are empirical models, or rather functions, that characterize the temperature dependence of viscous liquids without being derived from physical arguments, for example the model by Schmidtke et al.[37] As shown in the previous sections, several models are often applicable only to a certain temperature range. For example, MCT works above T_c, while the VFT equation in the AG model is derived near T_g. Instead, this empirical model characterizes the entire temperature range from the "boiling point to the glass transition".[112] The authors criticize the lack of attention to the high-temperature regime, which can be well described by an Arrhenius law. Hence, deviations in the temperature dependence in the supercooled regime are attributed to the cooperative nature of relaxation events, which are represented as a temperature-dependent activation energy $E_\mathrm{c}(T)$ that vanishes at high temperatures. The ansatz is

$$\tau = \tau_\infty e^{\frac{E_\infty + E_\mathrm{c}(T)}{T}} , \tag{2.25}$$

where τ_∞ and E_∞ are the parametrizations of the high-temperature Arrhenius regime. Splitting the total activation energy in this way has been used successfully in other models before, for example to separate the influence of pressure and temperature.[113] E_c can be obtained from the available data by rewriting the formula,

$$E_\mathrm{c}(T) = T \cdot \ln\left(\frac{\tau}{\tau_\infty}\right) - E_\infty . \tag{2.26}$$

Combining dielectric spectroscopy and dynamic light scattering data revealed an exponential temperature dependence for $E_\mathrm{c}(T)$ for a large number of molecular glass formers and even polymers:[37,112,114,115]

$$E_\mathrm{c}(T) = E_\infty \cdot e^{-\mu(T/T_\mathrm{x}-1)} . \tag{2.27}$$

Here, μ can be interpreted as a generalized fragility parameter and T_x is a reference temperature. In the above case, this temperature is the isoenergetic point at which E_c is as large as the high-temperature activation energy E_∞.

The ratios E_∞/T_g were found to be about 11 for a variety of molecular glass formers and 16 for polymers.[37,115] This suggests a deeper connection of the interaction strength of particles in the simple-liquid and in the supercooled regime, and even allows rough estimates of the glass transition temperature from measurements in the simple-liquid regime alone. However, this ratio depends on the dynamical property probed and the thermodynamic ensemble.[116] Subsequent studies found an exponential temperature dependence of E_c also for associated liquids, water and silica.[117,118] This is only true for the moderately supercooled regime because both liquids appear to transition from fragile to strong behavior upon further supercooling, see Sec. 2.3.4.[118–121] In this case, E_c becomes more complex than Eq. (2.27) and requires an additional parameter.[38,120] These observations are the subject of Ch. 8, where this family of empirical models is studied.

2.3. Supercooled water and polyamorphism

Since water makes up the majority of the studied liquids, this section introduces its anomalous properties relevant to this work.

2.3.1. Supercooled water

Water is a truly special liquid.[1]* It has the lowest molecular weight of all molecules that form a liquid phase under atmospheric conditions. It has a very high dielectric constant and defies melting and boiling point expectations[1] for its weight. In fact, it occurs on Earth in the crystalline, liquid and gaseous phase. Its most famous anomalies are the density maximum at 277 K and a crystalline

---

*An extensive collection of information on water and references can be found on `https://water.lsbu.ac.uk/water/`

phase with lower density than the liquid.[122] This allows bodies of water to freeze over while liquid water with a temperature of 4 °C exists at their bottom. Water exhibits extreme polymorphism with currently 20 different known crystalline phases.[123,124] Water has a very high heat capacity, heat of vaporization, and surface tension.[1] When water is compressed, dynamical properties speed up in contrast to the slowdown common to other liquids, i.e., water has an anomalous pressure dependence of dynamics. And this list of anomalies is not exhaustive. It is believed that the ability of water to form a hydrogen-bond network is responsible for most of these anomalies.[1,125] And all these phenomena arise from the many-particle physics of the small and simple H_2O molecule. This does not even include the overwhelming numerous phenomena that occur when water is mixed with other molecules, such as in the hydration of proteins in living cells. In fact, several of water's anomalies, such as the high polarity and density anomaly, are thought to be responsible for the possibility of the existence of life.[1]

Initially, it appears that water can be supercooled like most other glass formers. However, its anomalous behavior becomes more pronounced in the supercooled regime.[2] In fact, it is currently believed that the origin of many of the anomalies of water lies deep within its supercooled regime. Extensive research is being conducted, and a wide range of phenomena and findings has been reported.[2,126] However, the study of water's supercooled regime is far from straightforward and to date defies comprehensive description. Water can be moderately supercooled by reducing the probability of heterogeneous nucleation with distilled water in clean containers. Interestingly, measurements of thermodynamic response functions found temperature dependencies for density, viscosity, isothermal compressibility, and other observables that are consistent with their divergence upon further cooling.[127] However, the lowest temperature that can be reached is about 235 K, even with careful experimentation. At this point, the homogeneous nucleation rate becomes so high that measurements cannot be performed before the sample freezes. This is about the same temperature at which supercooled water occurs in nature, at ~236 K in micrometer-sized droplets in convective clouds.[128] Similar experiments with evaporative cooling of droplets in a vacuum chamber reduced the homogeneous nucleation temperature T_H to 228 K.[129,130] Also, T_H is reduced at elevated pressures and has a minimum of 181 K at 2 kbar,[131] but experiments performed by cooling pure water below this homogeneous nucleation line in the phase diagram are impossible.

Therefore, water's supercooled regime was also approached from below. Glassy water was initially produced via vapor deposition and hyperquenching.[132,133] Upon heating, a glass transition was found at $T_\mathrm{g} \approx 136\,\mathrm{K}$. Supercooled water is achieved with further heating until it inevitably freezes again at about $T_\mathrm{x} \sim 150\,\mathrm{K}$. Nevertheless, measurements can be performed within this narrow temperature range. The region in-between, ~150–230 K, has been termed *no-man's land*, see Fig. 2.6. Attempts have been made to enter the *no-man's land*, e.g., with nanoporous confinements,[134,135] laser heating,[20] or eutectic solutions.[136,137] All of these have in common that they potentially alter the behavior of water and the observations may not be representative of the bulk phase. Findings within the *no-man's land* are discussed in the following sections.

Subsequent experiments with glassy water and its glass transition at different pressures and with different preparations surprisingly revealed multiple amorphous phases with different T_g.[138,139] If water has multiple amorphous glassy phases, it may as well have distinguishable liquid phases. In fact, scientists such as Harold Whiting and Wilhelm Röntgen attempted to explain anomalies of water over 135 years ago by describing it as a mixture of liquid and ice-like molecules.[140,141] And 30 years ago, it was proposed based on simulations that water might have not only two liquid phases, but even a liquid-liquid phase transition (LLPT) that terminates in a second critical point (CP) at elevated pressures in the *no-man's land*, see Fig. 2.6.[5]

2.3.2. Water's two liquid phases

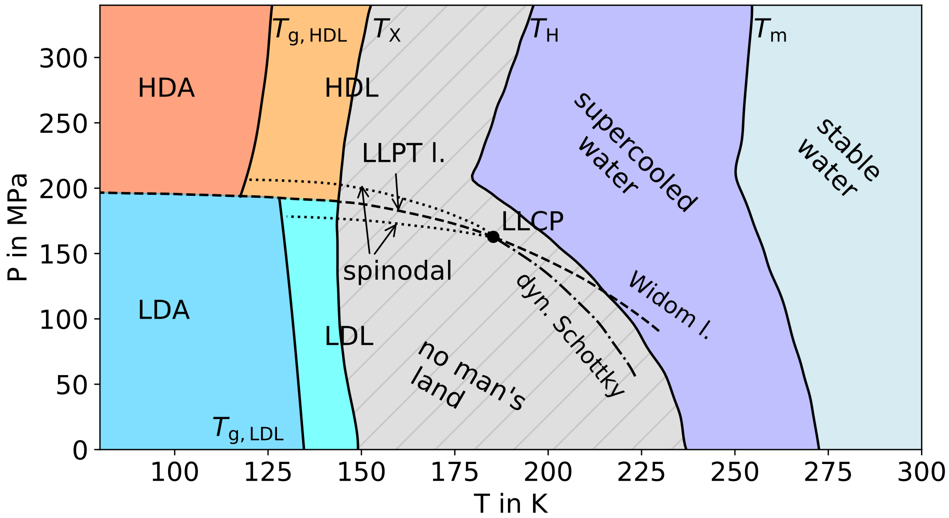

Figure 2.6.: A sketch of the phase diagram of amorphous water, inspired by Stanley et al. (2000)[142] and extended along the lines of Tanaka et al. (2020).[7]

Water has the potential for up to four energetically favorable hydrogen bonds with neighboring molecules. This favors tetrahedral local structures and a hydrogen-bond network that spans the entire liquid, see Fig. 2.7. Such tetrahedral local structures have large voids, resulting in lower density compared to sphere packing. The repulsive forces between the oxygen atoms due to the Pauli exclusion principle and their electrons would allow even denser packing if the Coulomb interaction and hydrogen bonds did not interfere. Hence, pressurizing the liquid distorts these tetrahedral structures and eventually increases the coordination number above four.[143] In addition, ambient temperatures are sufficient for defects in the hydrogen-bond network and tetrahedral structures, resulting in some of the water molecules not participating in four H-bonds. Based on this already existing observation of different local structures in water and their pressure dependence, the proposition of the existence of two amorphous states may seem reasonable. Water molecules can participate in a low-density structure (LDS) or a high-density structure (HDS), see Fig. 2.7. Water can then be a low-density liquid (LDL) or a high-density liquid (HDL) for a high or low concentration of LDS, respectively.[6,125,139,142,144] This phenomenon is known as liquid polyamorphism,[7] see Sec. 2.3.3, and not to be confused with the polymorphism of the ice phases of water.

There are several additional indications of the existence of the two phases of water. One is the finding of the amorphous phases.[6,13,145] They are called low-density amorphous ice (LDA) and high-density amorphous ice (HDA). In fact, experiments showed a pressure induced first-order like phase transition between LDA and HDA.[145] Depending on pressure and preparation, there exist several other amorphous states: hyperquenched glassy water (HGW) from splat cooling, amorphous solid water from vapor deposition, very high-density amorphous ice (vHDA), transformation of hexagonal ice to unannealed HDA (uHDA), and the expanded HDA (eHDA) by relaxation of uHDA.[139] Depending on the preparation of HDA, it was also questioned whether it truly represents HDA or just a collapsed form of ice.[123] In general, the categories LDA, HDA, and vHDA are states distinguishable by their pair-distribution functions with zero, one, and two interstitial neighbors.[139] Moreover, unlike the transformation between LDA and HDA, the transformation between HDA and vHDA is continuous, and thus vHDA is unlikely to be associated with a third liquid phase separated by a phase transition.[139,146] Evidence of a first-order phase transition between LDL and HDL, and, thus, an LLPT, is scarce. For example, when HDA is heated above its T_g and the pressure is reduced, it can also transform into hexagonal ice. Nevertheless, X-ray scattering revealed two values for water dynamics during this transition.[21] Furthermore, X-ray scattering on HDA samples heated with femtosecond infrared laser pulses detected the transformation to LDL within the *no-man's land* before crystallization sets in.[129]

The existence of two phases in the supercooled regime of water would be a reasonable explanation of water's anomalies and the apparent divergence of thermophysical properties. The length scales of the fluctuations between LDL and HDL would grow close to the LLCP and LLPT line where they diverge. The continuation of the LLPT line, called the Widom line, into the one-phase region of the phase diagram is probably much closer to T_H.[40,147–150] One would observe a maximum in the correlation length on the Widom line, which often coincides with maxima in thermodynamic response functions which can be observed.[151] The magnitude of this effect depends on the distance from the LLCP. However, fluctuations in LDS and HDS concentrations without an LLPT can lead to similar observations.

Several scenarios for the apparent critical behavior of water in its supercooled regime have been proposed in the past.[125] The first is a retracing liquid-vapor spinodal or stability limit conjecture of Speedy[152] causing the divergent behavior. This has been refuted since it does not agree with newer experimental observations.[2] The second-critical-point scenario was proposed by Poole et al. about 30 years ago.[5] An alternative was the critical-point free scenario, which proposes that the LLPT line enters negative pressures where it meets the liquid-vapor spinodal (LVS) without terminating in a second CP.[153,154] And finally, the singularity-free scenario of Sastry et al., in which the existence of a density maximum and other anomalies are explained without the need for a singularity in the supercooled regime.[2,155] The most favored scenario today is the second-critical-point scenario which remains consistent with experimental observations. However, the truth is unfortunately hidden in the *no-man's land* and the existence of the LLPT of water remains controversial, in particular, because it is often difficult to fully exclude effects from an onset of crystallization.[14]

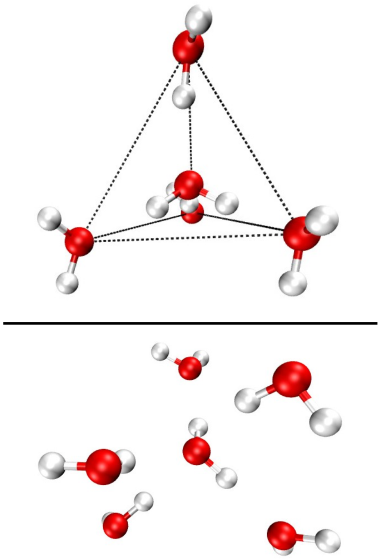

Figure 2.7.: Open tetrahedral configuration (top) and dense configuration with five next neighbors (bottom) from MD simulations.

Besides experimental evidence, numerous observations from simulations also support the second-critical-point scenario. While it is possible to freeze water in MD simulations,[156] the small volume, purity, and short time scales allow supercooling well below the experimental T_H, i.e., into the *no-man's land*.[3,4,157] There is no single water model that matches all experimental observations perfectly and can be relied upon to extrapolate to experimentally inaccessible regimes. However, an LLPT or even LLCP has been found for a number of water models: TIP4P/2005,[158–162] TIP4P/Ice,[162] TIP5P,[161] WAIL,[163] E3B3,[164] and ST2.[5,165–168] An LLCP was also found in simulations for atomistic liquid silica, which also forms tetrahedral local structures of silicon atoms linked by oxygen atoms.[4,25,169] The observations are often unambiguous, e.g., phase flipping between LDL and HDL, crossing of isochores and discontinuities in the density of isobars, or two minima in the free energy landscape. Of course, the simulation results have also been challenged with the discussion of crystal-like clusters,[170–172] and the coarse-grained mW water model has no LLCP because the entropy of mixing of LDS and HDS is too high.[173] And in the case of the SPC/E model, the existence of an LLCP was deemed likely but predicted at computationally inaccessible temperatures.[22]

Some further insights could be gained from the study of water at negative pressure. This state of stretched liquids can be achieved for example by the so-called Berthelot tube method.[174,175] The LVS can then be found as the line of lowest pressures at which the liquid remains stable against cavitation.[174] Tracing the LVS and water's anomalies to negative pressures completes the phase diagram of water at least above T_H.[175,176] For example, the line of density maxima exists even at negative pressures down to -140 MPa,[177] Considering the additional data also refines thermodynamic models of water.[176] Of course, experimental observations are again particularly difficult because it is double metastable at negative temperatures and pressures, when it is simultaneously supercooled and stretched.

2.3.3. Polyamorphism

In contrast to polyamorphism, the polymorphism of crystals is more commonly known, the best example of which is water.[123,124] Rather special transitions are, for example, superfluidity of H_2 or the superconductivity of amorphous metals. Polyamorphism and transitions between simple amorphous states without such special properties have not been studied as much and as long. Early ideas invoked the existence of local crystal structures and defects in the liquid phase.[178] Most commonly, transitions between amorphous states induced by pressure are observed.[179] Hence, density is often used like an order parameter. It would be more accurate to quantify a microscopic state as an order parameter. However, local crystal structures should not be used because crystal structures are not required in some of the following examples.

More specifically, these amorphous transitions are observed in single-component liquids extending to liquids that cannot phase separate, e.g., ionic liquids.[180] In some regions of the phase diagram they appear to be first-order like. But even without a discrete transition, polyamorphism can lead to phenomena similar to those observed in water.[181] One difference between polyamorphic transitions in glasses and liquids is that the former are far from equilibrium. A second glassy phase could also be only dynamically stable with respect to a crystalline phase. Transitions in the liquid phase must be reversible and require at least metastability.

How polyamorphism is thermodynamically allowed in equilibrium and can have a first-order phase transition is shown in the following theoretical description. In a mean-field approximation, the Gibbs energy per molecule can generally be written as follows:[182]

$$G(P,T,\phi) = G_0(P,T) + k_\mathrm{B}T f(\phi) - h\phi \,, \tag{2.28}$$

where P, T, and k_B are pressure, temperature, and the Boltzmann constant, respectively. The order parameter ϕ of the transition enters in combination with a thermodynamic ordering field h and a function $f(\phi)$ which converts the order parameter into thermodynamic quantities. Since liquids are amorphous and isotropic, ϕ can be assumed to be scalar, although it may be a vector in the case of symmetry breaking, e.g., with magnetization. In the case of polyamorphic liquids, the ordering field is probably a function of temperature and pressure.

In the case of liquids and with the observation of different microscopic structures in mind, the order parameter can be defined as a quantitative measure of different local states A and B, e.g., the fraction $x = \phi$ of state B. These states may be different arrangements of next neighbors or types of inter-molecular bonding. This leads to the so-called two-structure equation of state (TSEOS) formalism, which has been successfully applied to water in the past.[161,168,173,182–188]

In chemical reactions, the conversion $A \rightleftharpoons B$ would involve the breaking of covalent bonds. This is not necessary in polyamorphism. Given the equal stoichiometry, the Gibbs energy can then alternatively be written as

$$G(P,T,x) = G^{\mathrm{A}}(P,T) + xG^{\mathrm{BA}}(P,T) + G^{\mathrm{mix}}(P,T) \ . \tag{2.29}$$

$G^{\mathrm{BA}} = G^{\mathrm{B}} - G^{\mathrm{A}}$ is the difference of the Gibbs energies of the pure states and equivalent to $-h$ in Eq. (2.28) while the Gibbs energy of mixing G^{mix} represents $k_{\mathrm{B}}Tf(\phi) - h\phi$. Replacing G^{mix} with a form containing the symmetric entropy of mixing yields a form typically used to describe binary mixtures,

$$\begin{aligned} G(P,T,x) = {} & G^{\mathrm{A}}(P,T) + xG^{\mathrm{BA}}(P,T) \\ & + k_{\mathrm{B}}T\left[x\ln x + (1-x)\ln(1-x) + \omega x(1-x)\right] \ . \end{aligned} \tag{2.30}$$

The nonideality of mixing ω can be enthalpic[168] or entropic[185] in nature or both depending on its temperature dependence. In the above definition, a purely entropic nonideality would be found for a temperature-independent ω. The determination of G^{A}, G^{BA} and ω remains and an empirical modeling for the polyamorphism of water can be found in Sec. 7.2.2. For liquids in equilibrium, the concentration x takes on its equilibrium value, which is given by the condition $\frac{1}{k_{\mathrm{B}}T}\left(\frac{\partial G}{\partial x}\right)_{P,T} = 0$. This leads to the condition

$$-\frac{G^{\mathrm{BA}}(P,T)}{k_{\mathrm{B}}T} = \ln K(P,T) = \ln\frac{x}{1-x} + \omega(1-2x) \ , \tag{2.31}$$

where $K(P,T)$ is the reaction equilibrium constant. A phase transition can occur on the line of $\ln K(P,T) = 0$, i.e., where G^{BA} vanishes, when two solutions for x exist, which requires $\omega > 2$. For $\omega \leq 2$, the two liquid phases cannot separate and a continuous transition is observed upon crossing $\ln K(P,T) = 0$. These conditions define the LLPT line and the Widom line, respectively. Polyamorphic transitions in the above model are simply paths in the phase diagram where the concentration of states A and B changes rapidly. In such cases, anomalies such as maxima in density or heat capacity can occur.

The phenomenological similarities with chemical reactions, the interconversion $A \rightleftharpoons B$, mean that single-component liquids with polyamorphism can be thought of as reactive mixtures. Conversions occur and the macroscopic concentration of A and B is not constant with temperature or pressure. At the same time, A and B may mix or phase separate. Another approach by Tanaka and coworkers focusing on bond ordering as the order parameter is also insightful but will not be discussed further as it goes beyond what is required for the present work.[7]

The picture derived above can be applied to water. In this scenario, two local structures, one spacious and with low energy the other compressed and with higher energy, compete. Their difference in Gibbs energy leads to phenomena of polyamorphism and, if large enough, a true phase transition. This could be demonstrated even with a very minimal model.[181] The two states are LDS and HDS, i.e., local structures consisting of several molecules, and the two liquids are LDL and HDL with some equilibrium concentration of LDS and HDS depending on the thermodynamic state (P,T). Of course, water is not the only liquid for which polyamorphism has been found.[7] Silicon and $\mathrm{Al_2O_3}$-$\mathrm{Y_2O_3}$ glasses exhibit polyamorphism.[189] Evidence of a first-order phase transition has been found for carbon at 5.6 GPa and for gallium.[8,190] Liquid phosphorus also has a transition to a dense liquid at about 1 GPa and 1000 °C where it reversibly polymerizes.[9,10] The same phenomenon is found for sulfur.[11] Even the comparatively large molecule D-mannitol has two amorphous phases with a density difference of only 2.1 %.[191,192]

Recent advances in the study of LLPTs are also due to the increase in computing power.[193] Simulations can reproduce findings for many systems, such as water, silicon, germanium, and silica and can often enter regions in the phase diagram that are difficult to access for experiments.[3,4,169,194,195] Polyamorphism is also found in simple theoretical models[12,196] and in model systems such as tetrahedrally functionalized particles or the spherically symmetric Jagla model.[197,198] And polyamorphism in simulations of confined water monolayers leads to a whole new phase diagram.[199]

In addition, simulations allow systematic manipulations. The LLPT of silicon, simulated with the Stillinger-Weber potential, vanishes when the three-particle repulsion parameter is reduced.[200–202] And charge scaling of the Woodcock-Angell-Cheeseman model for silica led to the existence of an LLPT in the accessible phase space.[4,25,169] And for water, tuning of the HOH bond angle can make the LLPT more or less pronounced.[203] Hence, simulations together with a systematic variation of the model parameters can be useful in studying liquid-liquid polyamorphism.

Despite the growing evidence in the last decades, there remain many challenges, experimentally and theoretically.[7,204] And constantly new observations of polyamorphism in different systems may mean that it is less rare than previously thought.

2.3.4. Water dynamics in the supercooled regime

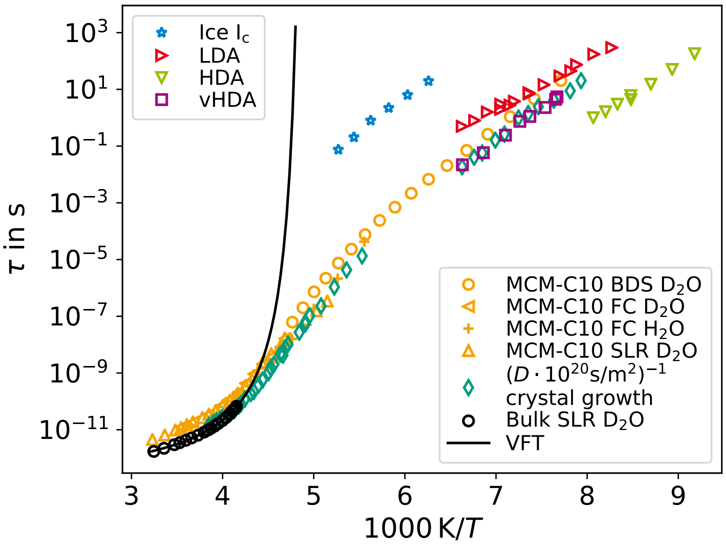

Figure 2.8.: Relaxation map of water under different thermodynamic conditions and in various nanoscopic environments. The data was taken from the following literature: bulk water from Qvist et al. (2012),[205] ice I$_c$, HDA and LDA from Amann-Winkel et al. (2013),[13] vHDA from Andersson et al. (2006),[206] self-diffusion coefficients from crystal growth from Xu et al. (2016).[20] MCM-C10 denotes confinement in silica pores with a diameter of 2.1 nm from Steinrücken et al.[207] The solid black line is a fit with the VFT equation to the bulk data.

Not only are the thermodynamic and structural properties of water complex, as discussed above, but measurements of dynamics also reveal anomalous behavior. The first problem arises when one attempts to reconcile the glass transition at 136 K with measurements of the α-relaxation time τ_α above the *no-man's land*. Above 235 K, the temperature dependence of τ_α can be described by the VFT equation, but extrapolation to 100 s gives a much higher glass transition temperature than 136 K, see Fig. 2.8. It follows from this extrapolation that water is a very fragile glass former, in fact one of the most fragile liquids.[40] The discrepancy in T_g could be resolved if the temperature dependence of dynamics in water changes in the *no-man's land*. For example, a transition from super-Arrhenius to Arrhenius behavior above T_g was proposed.[40,208] This type of crossover in dynamical behavior is also called a fragile-to-strong transition (FST). In support of such an interpretation is an Arrhenius behavior of relaxation times measured with BDS for HDA and LDA just above their T_g.[13] In addition, the step at T_g indicative of the glass transition was found to be small and to extend over a broad temperature range. Small differences in specific heat capacity are commonly found in strong liquids.[138,209] Indeed, observations of dynamic crossovers in LiCl solutions could be made[136] in simulations of water models.[210] On the other hand, these findings may also argue against a connection between the dynamics of water above the *no-man's land* and its glassy counterpart. Such controversies are discussed in more detail below.

Conveniently, silica, SiO_2, and water have many similarities.[211] Both are tetrahedral network formers and silica shares polyamorphism,[4,212] it shows signs of an FST in simulations,[149,213,214] and it is a super-strong liquid near its T_g.[215] A simultaneous explanation of both therefore argues for a connection to the LLPT.[154,213]

Liquid-liquid polyamorphism can indeed lead to unusual dynamical behavior. It was argued that the LDL phase has high tetrahedral order and lower and less temperature dependent entropy while the more disordered HDL phase has higher entropy.[208] Adam-Gibbs theory predicts that these liquids are strong and fragile, respectively. While this idea was proposed by Austen Angell to explain water in particular,[154,208] a second low temperature Arrhenius regime is generally expected for any liquid with non-vanishing and nearly constant configurational entropy.[39] If water is in an HDL-like phase around its melting temperature above the Widom line while it is LDL and LDA near T_g at atmospheric pressure, a liquid-liquid transition would automatically produce an FST. This would introduce a so-called dynamical Schottky line,[7,120,121] a line in the phase diagram where dynamical fluctuations have a maximum and the slope of τ_α is highest in the Arrhenius plot. At temperatures below this line, the slope decreases and the dynamical behavior becomes strong.

Experimental evidence of different dynamics of LDL and HDL exists. Primarily, the glass transition temperatures of LDA and HDA are different.[13,216] T_g of HDL is lower than for LDL, 122 K vs 136 K,[209] implying that molecular mobility in HDL is higher in the temperature range above T_g. There is a temperature range near T_g where the transformation kinetics to ice are slow enough that relaxation processes can be studied.[18] BDS measurements on LDA and HDA heated above their T_g showed Arrhenius behavior for both with similar activation energy but separated by two orders of magnitude, see Fig. 2.8.[13] Thus, both LDL and HDL are strong liquids, which is not consistent with the explanation of the FST above. The τ_α of heated vHDA at 1 GPA has a similar temperature dependence but lies in-between HDA and LDA at this pressure,[206,217] possibly because at such high pressures water returns to the pressure dependence of dynamics of regular liquids.

Empirical functional forms have been derived to characterize the temperature dependence of water. Caupin and coworkers successfully described the temperature dependence of the dynamical properties of water in the moderately supercooled regime by treating water with a two-state model.[218,219] Similar to the thermodynamical treatment above, a temperature-dependent concentration models the transition from HDL to LDL across the Widom line. In their model, LDL and HDL are described by an Arrhenius and VFT equation, respectively. They argue that the very fragile behavior above the *no-man's land* cannot be attributed to either phase and is a consequence of the liquid-liquid transition.

Tanaka and coworkers treat HDL with an Arrhenius equation instead of a VFT equation but arrive at the same conclusion for the FST.[119–121,220] Both models are capable of describing the dynamics of water over a wide range of temperatures but are not consistent with the finding of Arrhenius behavior for HDL with similar activation energy as LDL above T_g. A more detailed discussion of these models can be found in Sec. 7.6.

Overall, progress has been made in understanding the dynamics of water in its supercooled regime. However, the FST remains hidden in the *no-man's land* and the true temperature dependence of the dynamics in HDL and LDL in the entire supercooled regime cannot yet be determined. The determination of diffusion coefficients from recrystallization after laser heating of ice has partially closed the gap and results are compatible with other measurements of dynamics.[20] However, it is questionable whether they represent the bulk dynamics of liquid water under these conditions. In fact, many of the above claims have been questioned. In particular, it has been argued that above 136 K only rotational mobility remains and passes experimental time scales upon cooling, and thus this is not the true glass transition where structural relaxation arrests. The true T_g is thought by some to be at much higher temperatures. Unfortunately, experiments, e.g., ^{17}O field-gradient NMR, that directly determine the self-diffusion coefficients of oxygen atoms are difficult or impossible at temperatures where dynamics are so slow or before the onset of homogeneous crystallization. Slow diffusion of protons can also occur by other mechanisms, e.g., the Grotthuss mechanism.[221]

Assuming that translational motion associated with structural relaxation does not occur, the scenario of a shadow glass transition was proposed.[208,222] The step in DSC upscans at 136 K is weak and broad compared to other glass formers and it appears that the enthalpy of the hyperquenched glassy water is not fully relaxed before crystallization sets in at $\sim$150 K. Thus, it was suggested that T_g is higher, at about 165 K, and hidden by crystallization. A higher T_g is also supported by the simplification of the explanation of the dynamics of water since an FST and polyamorphism would no longer be necessary to explain the observations. However, the same broad and small step of $\Delta c_p \approx 1\,\mathrm{JK^{-1}mol^{-1}}$ can be used to argue for the strong behavior of water above its T_g.[138,209] Later measurements with water mixtures argue against a T_g above 160 K.[223] A small Δc_p is also found at the rotational glass transition, the freezing of rotational mobility, in some ice phases of water and is close to that for LDA. However, lower estimates for Δc_p of HDA are 3.6 to 4.8 $\mathrm{JK^{-1}mol^{-1}}$, about five times larger than the values for ices.[13,138] An onset of translational motion in the HDA-HDL glass transition is therefore likely. Note that typical values for Δc_p of fragile glass formers are about 100 $\mathrm{JK^{-1}mol^{-1}}$.[13]

Further controversy was caused by DSC measurements of isotope effects. Deuterated water should have a higher moment of inertia than protonated water while $H_2^{18}O$ has higher inertia only with respect to translation. For example, the expected isotope effect on the dynamics of water is $\sqrt{20/18}$ for rotation vs $\sqrt{2}$ for translation in $H_2^{18}O$ and D_2O, respectively.[224] Accordingly, the rotational glass transition of hydrogen-disordered ice VI is shifted to higher temperatures with respect to H_2O for D_2O but not for $H_2^{18}O$. The same observation was made in DSC measurements above the glass transition of LDA and eHDA and a rotational glass transition was concluded.[16] The same shifts, or the lack thereof, were also observed for tripropylene glycol and pentaethylene glycol water solutions.[224] These findings are contradicted by the absence of proton/deuteron isotope effects in the HDA/LDA transformation.[18] This was interpreted as a rearrangement of the oxygen structure. Furthermore, quantum effects are thought to be responsible for the large isotope shifts in water above its T_g.[225] Finally, hydrogen bonds dominate the inter-molecular interactions and isotope effects for transport properties are larger for D_2O compared to $H_2^{18}O$ above the *no-man's land*.[1,226]

Direct experimental evidence of translational dynamics is still rare. Diffusion between $H_2^{16}O$ and $H_2^{17}O$ doped layers above T_g was observed.[19] The growth rate of ice after laser heating in the *no-man's land* was taken as evidence of diffusion and the calculated self-diffusion coefficients are consistent with expectations for an FST.[20] Moreover, X-ray photon-correlation spectroscopy revealed diffusive characteristics on nanometer length scales during the HDL-LDL transition.[21] A lot of questions are still open the study of dynamics of supercooled water. Given the difficulties in the bulk, experiments have turned to water in more complex systems to avoid crystallization.

2.3.5. Water in confinement

Besides salty solutions or other aqueous mixtures, nanoscopic confinements are another method to supercool water and enter the *no-man's land*. Examples of such confinements are micelles, proteins, clays, zeolites, or mesoporous silica. Numerous studies have been performed with various liquids in confinement in the recent past.[41,42,44] While this improves the general understanding of liquids in confinement, which are actually common in nature, the relevant purpose for this work is the suppression of the melting point for many liquids in severe confinement.

In particular, water has been studied extensively in mesoporous silica. The surface of these cylindrical silica pores features silanol groups and is hydrophilic. Typical pore diameters range from about 2.1 nm to 6 nm or even larger sizes.[134,135] Calorimetric studies revealed a suppression of the melting point with decreasing pore size which can be described with a modified Gibbs-Thomson relation.[135,227] No calorimetric signature of freezing was found for pore diameters below 2.2 nm, i.e., liquid water can be studied within the *no-man's land*.[134]

Experimental measurements of dynamics with quasielastic neutron scattering found a clear crossover of dynamics at 220-230 K,[228] which was reproduced several times.[134,229] It was concluded that this crossover is caused by a high to low density transition of the confined water.[134] Interestingly, this temperature roughly corresponds to the temperature of divergence of thermodynamical properties above the *no-man's land*. However, the analysis of the experimental data was criticized and no crossover was found in other systems such as hydrated proteins.[230–232]

On the other hand, a second dynamic crossover around 180 K was observed by BDS and NMR in confinement within graphite oxide, silica nanopores, clays, molecular sieves, gels, and hydrated proteins.[233–235] Proposed explanations range from a glass transition of the macromolecule to a transition specific to the surface layer of water in contact with the confinement. Moreover, this second crossover temperature was found to be dependent on the size of the confinement.[234] Besides the discussion of potential glass transition temperatures as cause of the apparent FST, partial freezing in the confinements has also been considered as a possible reason. A freezing of the inner core of the water in silica pores would cause a transition to surface water dominated dynamics even for confinements with length scales larger than 2 nm.[236,237]

More importantly, the nature of the measured relaxation processes was questioned similarly to the rotational glass transition scenario at 136 K above. From BDS data of water in silica pores, clays, and molecular sieves, and from BDS and ^{2}H NMR measurements of protein hydration water, it was concluded that the α-relaxation arrests well above 136 K and that the measured molecular mobility results from a localized β-process.[230–232,238–240] The BDS data are consistent with the characteristics of an α-process at higher temperatures, while the lower temperatures are consistent with observations for β-processes.[230] The temperature dependence of τ_β is an Arrhenius behavior that separates from the α-process only at sufficient supercooling. An additional argument for a β-process may be the sometimes reported crossover at $\sim$180 K. When the α-process arrests at T_g, τ_β commonly exhibits a change in slope. Furthermore, ^{2}H NMR results showed that the reorientation below 200 K becomes mildly anisotropic and consists of jumps about the tetrahedral angle, i.e., rotations in the tetrahedral network.[232] Recent NMR results for water in silica pores of 2.1 nm size at 155-160 K suggest that any anisotropy, if existent, is very weak.[207] Therefore, the following scenarios have been proposed to explain the temperature dependence of measured relaxation times.[17,241] It could be caused by the polyamorphism of water and be a true FST. Another explanation is that translational and rotational motion in water decouple anomalously somewhere in its *no-man's land*. A third scenario is the arrest of the α-relaxation at higher temperatures and the transition to measuring a β-process. All these observations in confined water make the nature of the relaxation in heated LDA and HDA above T_g even more disputable.

There is no question that confinements increase the complexity of liquid system and introduce new phenomena.[241] The above conclusions have not even taken into account the complex freezing of water in confinement. It was argued that it freezes into stacking disordered layers of hexagonal and cubic ice and there is ongoing conversion of molecules between ice and liquid.[242,243] All of this makes the finding of an apparently universal activation energy of the low temperature Arrhenius law even more intriguing. Water dynamics measured in a large variety of aqueous systems have a value of about 0.46 to 0.54 eV.[17,229,234,238,240,241,244–247] Furthermore, the activation energy agrees quite well with that of the process measured with BDS in HDA and LDA above their T_g, see Fig. 2.8, and the relaxation times are in-between those of HDA and LDA.[13] Understanding the relaxation process of water and its nature within the *no-man's land*, a local rotational β-process or an actual α-process, in either bulk or in confinement may reveal much about its characteristics in the other.

3. Molecular dynamics simulations

In physics, advances are usually achieved by the interplay of theory and experiment. Theoretical models are accepted once predictions have been confirmed experimentally. Likewise, experiments may observe phenomena that require modifications of existing theories or entirely new models. Each approach is often complemented by simulations, a long existing method that has only grown in importance over the last decades. Simulations can only show phenomena that can emerge from their underlying theoretical models. At the same time, they produce data comparable to experimental measurements. However, they are usually simplified or incomplete and many reproduce the true observations from nature only qualitatively. Nevertheless, they offer many advantages over pure theory and experiment. Simulations can provide data for systems that have no analytical solution, such as most many-body problems. Their simplifications and well-defined nature allow for easier disentanglement of cause and effect compared to experiments. Furthermore, model systems inaccessible to experiments are available and theoretical models can be scrutinized in an effective way. Although they are limited by their computational cost, their potential will grow with computational power over time.

In this work, classical molecular dynamics simulations,[23,150,248] MD simulations in short, were employed. As the name suggests, they generate the time evolution of a many-body system on the microscopic scale. Several levels of detailedness exist: In principle, ab initio simulations are the most accurate and require only the theoretical models relevant for the system. At the level of MD and Monte-Carlo (MC) simulations, electrons and nuclei are merged into atoms.[23,150] Merging atoms into single particles is what is commonly referred to as ”coarse graining” and is also performed with MD simulations. In each of these steps, degrees of freedom and details are lost in favor of a significant decrease of the computational cost. Phenomena associated with the glass transition and studied in this work occur for all kinds of molecules and, thus, detailed ab initio simulations are not necessary. Still, interesting processes like chemical reactions or exchange of protons are also missing and would require more sophisticated but time consuming simulations. The most significant limitation is that it will remain impossible to cover 15 orders of magnitude in time, as is the case for dynamics in the supercooled regime, and to investigate processes in the range of seconds for probably several more decades into the future.

The simulations in this work are performed with the free open-source software package GROMACS,[150,249–254] developed and maintained by researchers worldwide. It provides an optimized implementation for numerically solving Newton’s equation of motion, features many tools for manipulation of data or analysis and is compatible with most force fields. The next sections will deal with the relevant basics and applied algorithms of classical MD simulations. In-depth details and proofs can be found in the cited literature.[23,150,248,255]

3.1. Newton's equations of motion

In principle, solving the time-dependent Schrödinger equation

$$i\hbar \frac{\mathrm{d}}{\mathrm{d}t} |\Psi(t)\rangle = \hat{H} |\Psi(t)\rangle \tag{3.1}$$

for the Hamiltonian $\hat{H}$ of the system with ab initio simulations would be most accurate. This is computationally too expensive and unnecessary for the purposes of most studies. Instead, it is assumed that velocities are non-relativistic and that atoms are always in their ground state. The Born-Oppenheimer approximation allows for the separate treatment of electrons and atomic nuclei.[256] It states that the large difference in the masses between nuclei and electrons leads to separated time scales of their motion and, thus, that the electrons immediately adjust to the motion of the nuclei. By calculating the potential energy landscape for the electron wave function and then the effective energy landscape of the nucleus, the Schrödinger equation can be simplified numerically. For MD simulations, the electrons are finally dropped entirely and their negative charges are included into the nuclei of the molecule according to the electron density, which leads to partial charges. With the potential energy landscape,

$$\Phi(\vec{r}_1, \vec{r}_2, \ldots, \vec{r}_N), \tag{3.2}$$

the force acting on an atom i can be derived,

$$\vec{F}_i = -\vec{\nabla}_{\vec{r}_i} \Phi(\vec{r}_1, \vec{r}_2, \ldots, \vec{r}_N). \tag{3.3}$$

Finally, Newton's equations of motion,

$$m_i \frac{\delta^2 \vec{r}_i}{\delta t^2} = \vec{F}_i\,, \tag{3.4}$$

replace the Schrödinger equation. Alternatively, Langevin dynamics can be obtained by adding a noise and friction term or Brownian dynamics can be applied to over-damped systems. An analytical solution to this many-body problem is impossible and numerical integration is necessary. Even then, system sizes range only from hundreds to several hundreds of thousands of particles, depending on the purpose of the study. The spatial extend of the system is on the order of nanometers in each dimension and simulations longer than microseconds are rare.

Integrators The leapfrog integrator is the algorithm applied in this work to solve Eq. (3.4),[248] though other algorithms, e.g., the velocity Verlet integrator,[257] exist. It iteratively updates the velocities and positions of all particles according to:

$$\vec{v}_i(t + \Delta t/2) = \vec{v}_i(t - \Delta t/2) + \frac{\Delta t}{m_i} \cdot \vec{F}_i(t) \tag{3.5}$$

$$\text{and } \vec{r}_i(t + \Delta t) = \vec{r}_i(t) + \Delta t \cdot \vec{v}_i(t + \Delta t/2)\,. \tag{3.6}$$

Unlike Euler integration, the leapfrog integrator is of second order and can be stable for oscillations in local potentials. The effective speed of the simulation, the achieved simulation time per real time, is proportional to the step size Δt. However, the largest possible step size is limited by the fastest dynamical processes, e.g., harmonic oscillations of bonds on time scales $t \sim 2\sqrt{m/k}$ with k as the spring constant. The details of the force field, the potential energy landscape of single molecules and pair interactions of atoms, and the degree of coarse graining are therefore a compromise between accuracy and speed.

Energy minimization is an important additional application of Eq. (3.4) but does not produce trajectories. Steepest descent iteratively updates positions according to

$$\vec{r}_{i,n+1} = \vec{r}_{i,n} + \frac{F_{i,n}}{\max(|\vec{F}_n|)} d_n \,, \tag{3.7}$$

where d_n is the maximum allowed displacement. Steepest descent or conjugate gradient can be used to find a local minimum in the potential energy landscape and prepare the configuration for runs with one of the integrators above.

MC simulations are not applied in this work, because they do not generate true dynamics.[23,150] Rather than solving Newton's equation of motion, the configuration is modified with small stochastically sampled displacements of particles. The energy difference before and after the displacement determines whether the new configuration is accepted or discarded. Negative energy differences are always accepted while positive differences may be accepted with the probability given by the Boltzmann factor. Therefore, MC simulations still sample the microstates correctly and give correct ensemble averages.

3.2. Thermodynamics

The following sections introduce basics about thermodynamic ensembles and methods to control them in simulations.

3.2.1. Ensembles

The above definitions and algorithms simulate the system in the microcanonical ensemble, that is with constant particle number, volume and total energy (NVE). This requires that only conservative forces are applied. The temperature is free to change. The NVE ensemble rarely applies to experimental conditions. Of interest in this work are instead the isothermal-isobaric (NPT) and canonical (NVT) ensemble. The former corresponds to most common experimental conditions. Temperature and number of particles are constant while the density relaxes to its equilibrium value for a given pressure, in most cases atmospheric pressure. In contrast, the NVT ensemble has a fixed density and the average pressure approaches the corresponding equilibrium value. The grand-canonical ensemble, which would require insertion and deletion of particles, is not applied in this work. In order to keep temperature or pressure constant, the system has to interact with a heat or pressure reservoir. This is achieved with algorithms for a thermostat and barostat, see Sec. 3.2.2 and 3.2.3.

Each ensemble and finite energy or temperature allow for an infinite number of microstates in phase space the system may visit. Their probability depends on the Hamiltonian of the system. Observables are correct only if the simulation properly samples the microstates. Improper algorithms may lead to correct average thermodynamic properties but incorrect fluctuations and, thus, wrong thermodynamic derivatives of higher order. The following sections deal with ways to adequately satisfy statistical mechanics.

Ergodicity In contrast to purely quantum mechanical systems, it takes infinite time to visit all available microstates. Since this is not feasible in practice, it is assumed that sampling a large enough number of microstates will eventually give the correct result within acceptable errors. This can be achieved by multiple independent simulations or long simulation times. The latter have to be significantly longer than correlation and relaxation times present in the system. For single-particle properties, a larger system can be equivalent to several independent simulations of a smaller system as long as correlation lengths are small. Both give a statistical ensemble to be averaged over. An important concept here is ergodicity. It states that given enough time a dynamical system will visit all available microstates with their respective probabilities. For ergodic systems, the average over independent particles is equivalent to an average over one particle in time. Therefore, long simulations suffice for accurate measurements of observables in most cases.

System geometry The above equations of motion are in theory sufficient. However, N is usually small and it is useful to have a limited phase space available, i.e., limited volume. The latter is important, for example, for a liquid in a vacuum. Evaporation leads to a loss of particles making this a non-equilibrium simulation. Walls may be introduced with artificial potentials creating a box that confines the particles. Both, a vacuum and artificial walls introduce significant surface effects in small systems. Surface effects as well as small system sizes can be avoided by application of periodic boundary conditions (PBC). Particles leaving the box are replaced by a periodic image entering from the opposite side. Interactions for each particle are calculated as if it was surrounded by infinitely many periodic images of the same box. Triclinic unit cells fulfill the condition of tiling space. In most cases, cubes or rectangular cuboids suffice. Unit cells leading to rhombic dodecahedra have properties useful in special cases.

3.2.2. Thermostat

With time, the system explores the phase space and potential and kinetic energy are rapidly interconverted by all particles. This leads to a correct average and huge fast fluctuations of temperature that only decrease with increasing system size. However, drifts of the average temperature occur when for example a simulation does not start in thermal equilibrium. Additionally, the numerical nature of Eq. (3.5) allows for inaccuracies in velocities that add up over time in either direction, increasing or decreasing the total energy. Furthermore, details of the interactions described in Sec. 3.3 are relevant: potentials are not harmonic, constraints lead to small errors, and the buffer of the next neighbor list is not perfect. Hence, an NVE simulation over very long times is practically impossible.

The temperature is defined by the kinetic energy and the equipartition theorem,

$$E_{\text{kin}} = \frac{1}{2}\sum_{i=1}^{N} m_i \vec{v}_i^2 = \frac{1}{2} N_{\text{f}} k_{\text{B}} T\,. \tag{3.8}$$

Here, m_i is the mass of each particle, N_{f} the number of degrees of freedom in the system and k_{B} the Boltzmann constant. Often, N_{f} is equal to $3N$ but it can be reduced, e.g., by constraining bonds (Sec. 3.3.2). Following this definition, temperature coupling can be achieved by adjusting velocities. The simplest algorithm is the Berendsen thermostat,[258]

$$\frac{\mathrm{d}T}{\mathrm{d}t} = \frac{T_0 - T}{\tau}\,, \tag{3.9}$$

with time constant τ and reference temperature T_0, which introduces a weak coupling to a heat bath. A corresponding scaling factor is applied to the velocities v_i. This suppresses fluctuations in an exponential manner but does not properly sample the thermodynamic ensemble. A better algorithm is the Nosé-Hoover thermostat.[259–261] It modifies Eq. (3.4) by an additional time dependent friction parameter,

$$m_i \frac{\delta^2 \vec{r}_i}{\delta t^2} = \vec{F}_i - m_i \frac{p_\xi}{Q} \frac{\delta \vec{r}_i}{\delta t}\,. \tag{3.10}$$

Here, the coupling to the heat bath is time dependent as $\mathrm{d}p_\xi/\mathrm{d}t = (T - T_0)$ and Q is an adjustable parameter scaling the oscillatory behavior of the temperature. This modification becomes more accurate when several heat baths are coupled in succession,[262] a feature not implemented in the used version of GROMACS. A newer alternative is the velocity-rescaling thermostat.[263] It extends the Berendsen thermostat, Eq. (3.9), by a stochastic process:

$$\mathrm{d}E_{\mathrm{kin}} = (E_{\mathrm{kin},0} - E_{\mathrm{kin}}) \cdot \frac{\mathrm{d}t}{\tau} + 2 \cdot \sqrt{\frac{E_{\mathrm{kin}} E_{\mathrm{kin},0}}{N_{\mathrm{f}}}} \cdot \frac{\mathrm{d}W}{\sqrt{\tau}} \,. \tag{3.11}$$

Here, $E_{\mathrm{kin},0}$ is the target kinetic energy related to the desired temperature and $\mathrm{d}W$ represents Wiener noise. This thermostat gives the proper canonical ensemble. In contrast to the Nosé-Hoover thermostat, it does not enable oscillations making it a more robust thermostat applicable to all systems. Which thermostat was applied is given in the details of the simulations in Ch. 4. Lastly, velocities of the particles can be randomized according to a Maxwell-Boltzmann distribution at the start of the simulation when for example the initial conditions do not specify them.

3.2.3. Barostat

The pressure of the system is a tensor **P** and calculated as the difference between the kinetic energy tensor $\mathbf{E}_{\mathrm{kin}}$ and virial tensor Ξ,

$$\mathbf{P} = \frac{2}{V}(\mathbf{E}_{\mathrm{kin}} - \Xi) \tag{3.12}$$

$$= \frac{1}{V}\sum_{i=1}^{N}\left[-m_i\big(v_i^\alpha - \langle v^\alpha\rangle\big)\big(v_i^\beta - \langle v^\beta\rangle\big) + \frac{1}{2}\sum_{j=1}^{N}\left(r_i^\alpha - r_j^\alpha\right)F_{ij}^\beta\right] \,. \tag{3.13}$$

V is the volume of the system, α and β denote the components of the vectors in Cartesian coordinates, and $\vec{F}_{ij}$ is the force between particles i and j. Hence, the pressure tensor quantifies whether particles tend to push inwards or outwards and the pressure is negative or positive, respectively. The barostat algorithm adjusts the box size accordingly. Weak coupling with a Berendsen barostat similar to Eq. (3.9) is a robust solution but suffers from the same limitation when more accurate statistical mechanics are desired. Instead, the Parrinello-Rahman barostat allows for fluctuations and oscillations and produces proper sampling in the NPT ensemble.[264,265] Similar to the Nosé-Hoover thermostat, the equations of motion are modified by a virtual friction term caused by the rescaling of the unit cell vectors,

$$m_i\frac{\delta^2\vec{r}_i}{\delta t^2} = \vec{F}_i - m_i\frac{p_\xi}{Q}\frac{\delta\vec{r}_i}{\delta t} - \mathbf{M}\frac{\delta\vec{r}_i}{\delta t} \,. \tag{3.14}$$

M is a time dependent scaling factor derived from the equations of motion for the unit cell vectors.

3.3. Force fields

The force field defines the potential Φ and other interactions of particles that determine forces and energies in the system. It contains functional forms, e.g., harmonic, of the potentials and parametrizations that lead to an approximation of the true Hamiltonian. It may be derived by matching reference data: forces from quantum mechanical calculations or experimental observations; like structure via the pair-distribution function (Sec. 5.1.1), dynamics, enthalpy etc. Combinations of this non-exhaustive list are advantageous. Several refinement steps with comparison to reference data are required to obtain the final force field. Because of these degrees of freedom, force fields for MD simulations are only empirical. The force field also defines the degree of coarse graining, e.g., united-atom force fields merge aliphatic hydrogen atoms with their carbon atoms, and whether or not atoms are polarizable. Ideally, the force field is created in a way that allows the transfer to chemically different systems and a wide range of thermodynamic conditions not contained in the reference data.

The potential commonly consists of bonded and non-bonded interactions,

$$\Phi_{\text{total}} = \underbrace{\Phi_{\text{bond}} + \Phi_{\text{angle}} + \Phi_{\text{dihedral}}}_{\Phi_{\text{bonded}}} + \underbrace{\Phi_{\text{Coulomb}} + \Phi_{\text{LJ}}}_{\Phi_{\text{nonbonded}}} . \tag{3.15}$$

These interactions and their potential forms will be defined in the following sections.

3.3.1. Non-bonded interactions

The implementation of MD simulations used in this work only supports pairwise-additive interactions that are isotropic, $\Phi(r_{ij})$. Higher functions with asymmetric forces will thus not be discussed. Because the calculation of all pair contributions grows with $\sim N^2$, non-bonded interactions are the computationally most expensive step. Therefore, they are only calculated up to a cutoff radius r_c beyond which corrections with more efficient algorithms are applied. One fast algorithm is the Ewald summation: The periodicity of the actual system and its copies related by the PBC is used for a spatial Fourier transform that allows for the separation of the sum of interactions with $r_{ij} > r_\text{c}$ into a constant and two quickly converging terms. The particle-mesh Ewald (PME) summation speeds up the Fourier transform by placing the particles on a discrete grid beforehand.[266] For small system sizes, the cutoff serves a second purpose: A cutoff smaller than half the shortest box dimension ensures that a particle directly interacts only with the closest image of other particles, also known as the minimum image convention. This reduces artifacts introduced by the PBC. For increased performance, the list of next neighbors within the cutoff radius r_c includes an additional buffer Δr and is updated less frequently.

Coulomb potential Ions and covalently bonded atoms with different electronegativity have whole or partial charges, respectively. Partial charges of the atoms in covalent bonds are usually determined using quantum chemical simulations. The potential contains all pairwise interactions between atoms i and j,

$$\phi_{\text{Coulomb}}(r_{ij}) = \frac{1}{4\pi\epsilon_0} \frac{q_i q_j}{r_{ij}} , \tag{3.16}$$

where ϵ_0 is the vacuum permittivity. Convergence for long distances is slow, because forces scale with $\sim r^{-2}$ while particle count grows as $\sim r^2$. Still, Coulomb interactions converge for systems without long-range order, e.g., liquids and glasses. Long-range interactions beyond the cut-off can be calculated with the PME method, when the system is neutral, or with reaction-field methods and permittivity ϵ_r.

Lennard-Jones potential The van der Waals force, more specifically the London dispersion force, is the attractive force between polarizable atoms. Fluctuations of the electron cloud of an atom induces correlated fluctuations in its neighbors that lead to a reduction of potential energy. This potential has a very short range and scales with r^{-6}. Note, that the dispersion force has to be considered especially when the force field does not include polarizability. Furthermore, the Pauli principle causes strong repulsive forces when the electron clouds of two atoms overlap. Its treatment with an exponential function would be more appropriate than a power function. However, squaring r^{-6} is computationally faster and suffices qualitatively. This allows for the combination of both, van der Waals forces and Pauli principle, into the Lennard-Jones (LJ) potential,[267]

$$\phi_{\mathrm{LJ}}(r_{ij}) = \frac{C_{ij}^{(12)}}{r_{ij}^{12}} - \frac{C_{ij}^{(6)}}{r_{ij}^{6}} \,. \tag{3.17}$$

The coefficients $C_{ij}^{(12)}$ and $C_{ij}^{(6)}$ depend on the electron cloud of both atoms. The chemical environment and covalent bonds may change these. Hence, several atom types of each element exist in the force field, each with its own parametrization to account for different bonding partners. Coefficients for interactions between different atom types can be specified but are for the most part calculated using mixing rules. An alternative form is

$$\phi_{\mathrm{LJ}}(r_{ij}) = 4\epsilon_{ij}\left(\left(\frac{\sigma_{ij}}{r_{ij}}\right)^{12} - \left(\frac{\sigma_{ij}}{r_{ij}}\right)^{6}\right) \tag{3.18}$$

with σ and ϵ giving the position and depth of the minimum.

The short range of the LJ potential allows for treatment with a cutoff alone. However, long-range dispersion forces are always attractive. They can be treated with PME or added analytically as

$$E_{\text{lr. disp.}} = -\frac{2}{3}\pi N n C^{(6)} r_{\mathrm{c}}^{-3} \,, \tag{3.19}$$

where n is the particle density. This applies only to homogeneous systems with no correlation beyond the cutoff r_{c}.

3.3.2. Bonded interactions

Intramolecular interactions are very strong and are a many-body problem in itself. They are not pairwise-additive since quantum mechanical effects are relevant on this scale. The potential energy landscape is better approximated by using an individual potential for each degree of freedom between particles separated by up to three bonds. Non-bonded interactions are applied when atoms are separated further. The degrees of freedom are bond lengths, bond angles, and dihedral angles and depend on two, three, and four particle positions, respectively. For each of these, several functional forms exist. Most common for bond lengths and bond angles are harmonic potentials,

$$\phi_{\text{bond}}(r_{ij}) = \frac{k_{ij}}{2}\left(r_{ij} - r_{ij,0}\right)^2 \tag{3.20}$$

$$\phi_{\text{angle}}(\vartheta_{ijk}) = \frac{\kappa_{ijk}}{2}\left(\vartheta_{ijk} - \vartheta_{ijk,0}\right)^2 \,. \tag{3.21}$$

ϑ_{ijk} is the angle spanned between the bonds ij and jk, $r_{ij,0}$ and $\vartheta_{ijk,0}$ are the equilibrium values of the bond length and bond angle, respectively, and k_{ij} and κ_{ijk} are the corresponding spring constants. Potentials for dihedrals may also be harmonic to prevent torsions of the plane. However, cases with multiple potential minima, for example for torsions of the C–C bond in ethane, exist. Such potentials have the form

$$\phi_{\text{dihedral}}(\varphi_{ijkl}) = \varkappa_{ijkl}\left(1 + \cos[n\varphi_{ijkl} - \varphi_{ijkl,0}]\right) \,. \tag{3.22}$$

φ_{ijkl} is the dihedral angle between the two planes spanned by ijk and jkl, $\varkappa_{ijkl}$ is a constant, and n is the multiplicity of the potential.

Constraints Vibrations of bonds have the highest frequency in the system, in particular when hydrogen atoms are involved. Therefore, it can be useful to constrain such internal degrees of freedom to their equilibrium position. This reduces the detail of the simulation but allows for larger time steps Δt of the integrator and, thus, increased performance. Algorithms for this purpose are LINCS and SHAKE which are applied in between integration steps.[268,269] For the special case of water, the SETTLE algorithm analytically solves for constraints of both, the OH bond length and the HOH angle, giving significantly increased performance.[270]

3.4. Simulation protocol

The typical simulation protocol is outlined here. Several steps can be taken to improve the quality of the results and ensure reproducibility.[271,272] For a new system, a starting configuration is randomly initialized followed by a simulation in the NPT ensemble with the Berendsen thermostat and a temperature corresponding to the liquid regime. In some cases, energy minimization is required prior to the propagation of the system because of large forces from the randomized configuration. For bulk systems, the number of particles is chosen such that the system size is at least $4 \times 4 \times 4\,\mathrm{nm}^3$ or a thousand molecules. This ensures that finite-size effects are small but does not substitute for a study of finite-size effects, which is necessary in some cases.

The simulation that generates the trajectory to be analyzed is called the production run. It is often preceded by an equilibration run that allows the system to relax to the thermodynamic state point (T,P). In particular, for isobaric simulation series the equilibration run applies the Parrinello-Rahman barostat while the production run is in the NVT ensemble. Both ensembles are equivalent in the thermodynamic limit and even for small but ergodic systems observables can be the same. However, constant box dimensions allow for simplifications of the analysis code and the sampling of microstates does not require fluctuations in density, which can become very slow in the supercooled regime. This improves the data quality even if the average pressure in the NVT simulation deviates slightly. Different state points are simulated in succession, starting each equilibration run with a configuration from the closest state point. In this way, the local structure of the starting configuration does deviate as little as possible from the new equilibrium.

The starting configuration for the production run is a frame from the NPT equilibration run with a density close to the average value and at later times in the equilibration trajectory. It is found by iteratively skipping parts from the start of the trajectory until the relative slope of the density is below some small threshold. Because trajectories without velocities are saved, the NVT simulation is initialized with randomized velocities. A fraction of the trajectory, approximately 10 %, is skipped in the analysis.

Simulation lengths are adjusted to the dynamics at each state point. To ensure that the equilibration is sufficient and that the production runs are representative, e.g., can be considered ergodic, simulations are as long as 100 times the α-relaxation time. Alternatively, a minimum mean-squared displacement, Sec. 5.2.2, of $5\,\mathrm{nm}^2$ or larger can be required.

The most used GROMACS versions in this work were 2016.3 and 2018.3. The newer version fixes a bug concerning multiple time stepping with the Parrinello-Rahman barostat and Nosé-Hoover thermostat. Specifically, the choice of parameters for both has different effects in older and newer versions of GROMACS and thermodynamic sampling was not perfectly reproducible with the newer version. Consequently, the simulation series are performed entirely with one of the two version and Ch. 4 contains the corresponding information.

4. Systems

This chapter presents the details of the simulations. The information necessary to reproduce the data includes the force field, system composition and GROMACS input parameters (thermostat etc.). Modifications made to the original force fields are presented. If not mentioned otherwise, simulations followed the protocol detailed in Sec. 3.4.

4.1. Water models

Water's anomalous behavior and extreme properties make it notoriously hard to model in MD simulations. For example, water molecules form hydrogen bonds, which in various systems have covalent character to some degree,[273] and protons can hop between molecules via the Grotthuss mechanism.[221] Such effects are not taken into account in classical MD simulations. A 3-site model with one particle for each atom in the water molecule has a small number of parameters that can be adjusted. With this limitation not all experimental observations can be matched. 4- or 5-site models with dummy particles introduce additional degrees of freedom to better match experimental data. Dummy particles can be used for example for the two lone electron pairs of the oxygen atom. Additionally, models may be rigid or flexible and can include polarizability. However, this increases the computational cost at little increase of accuracy. On the other hand, coarse grained models of water, e.g., the mW model,[274] speed up simulations significantly but lose microscopic information. In this work, the SPC/E (single point charge extended) and TIP4P/2005 water model were used.[275,276]

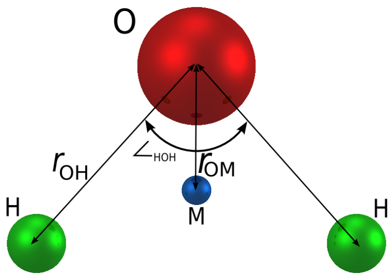

Figure 4.1.: 4-site model as used in the TIP4P/2005 water model.

Created by Car McBride and published on www.sklogwiki.org under license Creative Commons Attribution Non-Commercial Share Alike (08.06.2009)

Table 4.1.: Parametrization of the SPC/E and TIP4P/2005 water models.

	SPC/E	TIP4P/2005
σ in Å	3.166	3.1589
ϵ in kJ/mol	0.650	0.7749
r_{OH} in Å	1.0	0.9572
r_{OM} in Å		0.1546
$\angle_{\mathrm{HOH}}$	109.47°	104.52°
q_{O} in e	-0.8476	0
q_{H} in e	0.4238	0.5564
q_{M} in e		-1.1128

A comprehensive comparison of water models was performed by Vega et al.[277] In this comparison of phase behavior, thermodynamic and dynamical properties, both, SPC/E and TIP4P/2005, perform as well as other 3- to 5-site models. In particular, SPC/E outperforms some of the more complex models in several properties, e.g., diffusivity, relevant to the present study. Both models are widely used in the literature and TIP4P/2005 may unofficially be regarded as the most reliable model. To date, simulation results and experimental bulk data in the supercooled regime below 230 K, the *no-man's land*, cannot be compared and it is unknown how well these models perform outside of the thermodynamic regimes for which they were optimized. However, a perfect water model is not required for the general study of the glass transition and behavior under charge scaling, detailed below.

Table 4.2.: Parameters and simulations details with the SPC/E and TIP4P/2005 water models.

Parameter	SPC/E	TIP4P/2005	TIP4P/2005 (Ch. 7)
GROMACS	2016		2018
Δt in fs	2		
r_c in nm	1.2		1.0
PME grid in nm^{-1}	0.12		0.16
Long-range LJ	–		PME
Ensemble	NPT→NVT		NPT$\vert$NVT
Thermostat	Nosé-Hoover		
τ_t in ps	0.4		
Barostat	Parrinello-Rahman		
p in bar	1		-1000 …1500
τ_p, κ	5 ps, 4.5e-5 bar^{-1}		
N_atoms	$12000 \cdot 3$	$2000 \cdot 4$	
Size	$\approx 7.3 \times 7.3 \times 7.3\,\mathrm{nm}^3$	$\approx 4 \times 4 \times 4\,\mathrm{nm}^3$	
q-range	0.7 …1.25	0.7 …1.5	0.86 …0.91

Both models are rigid with LJ interactions only between oxygen atoms. Intramolecular interactions are, thus, non-existent. SPC/E is based on the SPC model with modified partial charges to account for the missing polarizability. The opening angle between the OH bonds is perfectly tetrahedral, 109.47°, instead of the experimentally observed 104.52°. It matches dynamical properties quite well but its density maximum is at 240-250 K.[277–280] Also, its melting temperature of 215 K is among the lowest of all water models.[277] Still, its low computational cost and widespread acceptance make this a useful model. In particular, it has been used in previous studies of water in neutral confinements.[50,281]

The TIP4P/2005 water model is a reparametrization of the TIP4P water model. It is also rigid but introduces a dummy atom that carries the negative charge. The opening angle is adjusted to the experimental value of 104.52°. It reproduces dynamical quantities well and in contrast to SPC/E matches the experimental temperature of the density maximum.[277] Its melting temperature is at 252 K. Another reparametrization, TIP4P/Ice,[282] matches the melting temperature of real water but performs worse overall.

Both models were mostly simulated without treatment of long-range LJ interactions beyond the cutoff distance. However, simulations for the thermodynamic study of the two-phase behavior in Ch. 7 require their calculation in order to be comparable to the literature. The simulation parameters are presented in Tab. 4.2. These two simulation series with and without long-range LJ interactions have little overlap and are analyzed separately.

Charge scaling A major topic of this work is the behavior of the water models under charge scaling. As the name suggests, the partial charges on the atoms were scaled linearly with a charge-scaling factor q. An alternative modification of water models would be adjustments to the geometry, e.g., changing the opening angle in a study of the ST2 water model.[203] However, charge scaling is more common and very effective in changing the system's behavior.[25,118,283] The single particle structure remains unaltered for atomistic systems, rigid molecules, or dominating bonded interactions. Structural changes are then solely caused by multi-particle effects from the modified inter-molecular interactions. At the same time, the energy scale is strongly affected even if the structural differences are minor. Hence, these systems provide insight into the dynamics of similar molecules with the same mass but at different thermal energy when q is small and into structural changes when q is varied over a wider range. The energy scale can also be changed with geometric modifications to a molecule, but the effects are usually weaker and this cannot be done with atomistic systems. Charge scaling has been successfully applied for example in studies of water,[46,117] silica,[25,118] an ionic liquid,[283] and a Kob-Andersen mixture.[116]

4.2. Other bulk systems

The following molecular glass formers complement the charge-scaled systems.

4.2.1. Glycerol

Glycerol $C_3H_8O_3$ is a polyol and because of its three hydroxyl groups miscible with water. It has a weak tendency to crystallize which makes glycerol a good glass former, i.e., a liquid that can be easily supercooled and studied. This and the fact that it can be studied with many methods, e.g., NMR, BDS, and DDLS, make it an often measured liquid since the early times of experiments on supercooled liquids. However, its relaxation mechanisms show uncommon behavior. Correlation times for rotational dynamics are significantly shorter than expected with the Stokes-Einstein-Debye relation.[284,285] This is attributed to the hydrogen-bond network present in the liquid. Hence, while this molecule provides a solid base for many different experiments it also exhibits unexpected behavior in the supercooled regime which can be used to more rigorously test models of the glass transition.

The parametrization of glycerol is based on the all-atom description by Chelli et al.[286,287] which was reparameterized by Blieck et al.[288] and later made charge-neutral by Egorov et al.[289] This last one is the version used in this study. Parameters of the simulation series with GROMACS are given in Tab. 4.3. While all bond lengths have been constrained, the molecules were flexible with respect to bond angles and torsions.

Table 4.3.: Simulation parameters and simulation details for glycerol.

Parameter	
GROMACS	2018
Δt	2 fs
r_c	1.2 nm
PME grid	0.12 nm^{-1}
Thermostat	v-rescale
τ_t	0.5 ps
Ensemble	NPT$\rightarrow$NVT
Barostat	Parrinello-Rahman
p	1 bar
τ_p, κ	5 ps, 4.5e-5 bar^{-1}
nst(p/t)couple	1
Temperature range	290-610 K
Longest simulation	2.24 µs
N_atoms	39200
Size	$\approx 7.1 \times 7.1 \times 7.1\,\mathrm{nm}^3$

4.2.2. LJ (model) systems

The following three liquids were simulated in bulk and use the LJ potential exclusively. All molecules are stiff by setting constraints for the bonds. While two of the three are based on real liquids, their abstraction lets them only barely resemble their real counterpart and quantitative agreement is therefore poor. However, their simplicity and comparatively short-range interactions make them a good complement to the water-like systems. Furthermore, simulations without Coulomb interactions are significantly faster which makes these systems computationally more efficient. Simulation details for all LJ systems are given in Tab. 4.5, and sketches of them are in Fig. 4.2.

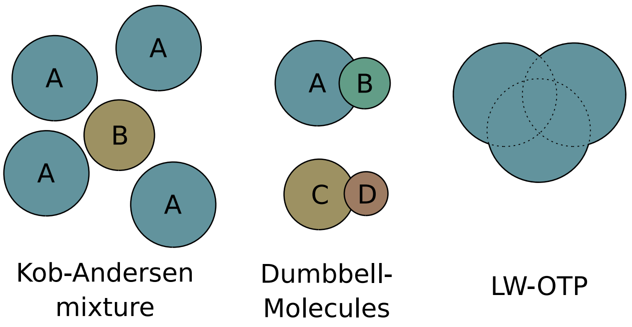

Figure 4.2.: Sketches of the three LJ systems. The relative size of the particles approximately represents their LJ radius σ.

Kob-Andersen mixture The first LJ liquid was introduced by W. Kob and H.C. Andersen and is based on the metallic system $\mathrm{Ni}_{80}\mathrm{P}_{20}$.[290,291] It is thus atomistic and consists of an 80:20 mixture of A and B particles. It is defined in reduced units with

$$\begin{aligned}\text{length } \tilde{r} &= \frac{r}{\sigma_{\mathrm{AA}}},\\ \text{time } \tilde{t} &= t\sqrt{\frac{\epsilon_{\mathrm{AA}}}{m\sigma_{\mathrm{AA}}^2}},\\ \text{temperature } \tilde{T} &= \frac{k_{\mathrm{B}}T}{\epsilon_{\mathrm{AA}}},\\ \text{energy } \tilde{E} &= \frac{E}{\epsilon_{\mathrm{AA}}},\\ \text{and pressure } \tilde{P} &= \frac{P\sigma_{\mathrm{AA}}^3}{\epsilon_{\mathrm{AA}}}.\end{aligned}$$

Here, σ_{AA} and ϵ_{AA} are the LJ parameters of the A particle. In these units, the rest of the parameters are $\sigma_{\mathrm{BB}} = 0.88$, $\sigma_{\mathrm{AB}} = 0.8$, $\epsilon_{\mathrm{BB}} = 0.5$, and $\epsilon_{\mathrm{AB}} = 1.5$, i.e., the parameters for particles A and C in Tab. 4.4. Their masses are $m = 1\,\mathrm{u}$ and $\sigma_{\mathrm{AA}} = 1\,\mathrm{nm}$ in the GROMACS simulations. If desired, the results can be transferred to real systems, e.g., helium or $\mathrm{Ni}_{80}\mathrm{P}_{20}$.[292,293] However, the absolute values for these systems are not relevant for the present work. Instead, they were scaled to $T = 500\,\mathrm{K}\cdot\tilde{T}$ and $D = \frac{1}{5}\frac{\mathrm{nm}^2}{ps}\cdot\tilde{D}$, where $\tilde{D}$ are self-diffusion coefficients in reduced units. This places them among typical molecular glass formers and the charge-scaled water-like systems. More precisely, the Kob-Andersen mixture has the same high-temperature regime as the original TIP4P/2005 water model at atmospheric pressure with this scaling.

This system's simplicity and very low computational cost compared to real molecules with partial charges have earned it a spot among the most often simulated systems to date. It can be easily supercooled and crystallizes only at very long simulation times.[294] More importantly, it has shown crossovers in the temperature dependence of several thermodynamic and dynamical properties at strong supercooling.[294,295] In particular, the dependence of the activation energy of dynamic observables on the reciprocal temperature appears to decrease at the lowest temperatures.

Roland's Dumbbell-Mixture The next step are the smallest possible molecules, two bonded atoms. These dumbbell-like shapes can either be symmetric or asymmetric with two different atom types. Unfortunately, their tendency to crystallize is high, since they easily arrange on a cubic lattice. This can be overcome in model systems where the size-to-distance ratio and the parametrization of both atom types can be varied. Even then unimolecular systems crystallize easily, which is the reason why Fradiagakis et al. created a mixture of two different asymmetric dumbbell molecules.[296,297] They based the parametrization on the Kob-Andersen mixture, details are given in Tab. 4.4. One small difference to the parametrization in the literature is that instead of the factor 0.4255 the not rounded value $0.8/(1+0.88)$ was used for the mixing term of σ for AC, AD, BC and BD and σ was then rounded to six decimal places. A 80:20 mixture as well as a pure system consisting of the larger dumbbell molecule were simulated. Two different size-to-distance ratios, 0.45 and 0.6, were tested. Of the two ratios, 0.6 was easier to supercool.

Despite their apparent simplicity, dumbbell molecules can show widely varying behavior depending on their parametrization. They can show isomorph scaling, i.e., invariance of static and dynamic observables in a phase diagram with reduced units.[298] On the other hand, they can be tuned to show a very pronounced three-step decay, i.e., a β-process between the vibrational and terminal decay, which was interpreted as the Johari-Goldstein relaxation.[297,299] In this case, dynamical heterogeneity is further pronounced and above the glass transition temperature only a fraction of the molecules perform this secondary process.

Table 4.4.: Lennard-Jones potential parameters for the four atom types in the dumbbell mixtures.[297] Reduced units as defined for the Kob-Andersen mixture are used.

σ_{ij}	A	B	C	D
A	1.0			
B	0.65	0.5		
C	0.8	0.587234	0.88	
D	0.612766	0.4	0.66	0.44

ϵ_{ij}	A	B	C	D
A	1.0			
B	1.0	1.0		
C	1.5	1.5	0.5	
D	1.5	1.5	0.5	0.5

Lewis-Wahnströhm – Ortho-terphenyl Ortho-terphenyl (OTP) is a well-studied fragile glass former. It consists of three connected benzene rings and has a for most purposes negligible polarity. It has a melting temperature of 329 K and glass transition temperature of 245 K[300] and can be easily supercooled, which promoted its use in experimental studies. From a simulation perspective, the molecule consists of more atoms and consequently pair interactions than necessary to understand the emergence of its basic structural and dynamic behavior. Hence, Lewis and Wahnström derived a simplified representation in which the molecule consists of three beads with rigid geometry and opening angle of 75°.[301] A single atom type with 76.768 u, $\sigma = 0.483\,\text{Å}$, and $\epsilon = 4.98868\,$kJ/mol is used for all three beads. These simplifications allow for significant reduction in computational cost while retaining the basic behavior of the liquid. Like the dumbbell molecules above, the Lewis-Wahnström OTP (LW-OTP) exhibits isomorph scaling.[298]

While the real OTP can be easily supercooled, the simplified LW-OTP is known to be able to crystallize at low temperatures and for long simulation times.[302] The temperature regime is therefore limited to temperatures at which the system remained in the liquid state. The original parametrization was developed with a fixed cutoff radius for pair interactions and neglects long-range LJ interactions. To assure a more natural contraction with temperature, long-range LJ interactions were taken into account in the present simulation series. Hence, the results may be even further from experimental results in the literature.

Table 4.5.: Parameters and details of bulk simulations with LJ liquids. The lowest temperatures for the Kob-Andersen mixture and the LW-OTP were limited by crystallization.

Parameter	KA mixture	Dumbbell systems	LW-OTP
GROMACS	2019.4		
Δt in fs	5		
r_c	$4\,\sigma$		$1.932\,\mathrm{nm}$
PME grid in nm^{-1}	$1\,\sigma/\mathrm{nm}^2$		0.483
Long-range LJ	PME		
Ensemble	NPT→NVT		
Thermostat	v-rescale		
τ_t in ps	0.5		1.0
Barostat	Parrinello-Rahman		
p in bar	1		
τ_p, κ	$1.0\,\mathrm{ps}$, $1.0\mathrm{e}\text{-}4\,\mathrm{bar}^{-1}$		$10.0\,\mathrm{ps}$, $1.0\mathrm{e}\text{-}3\,\mathrm{bar}^{-1}$
Temperature range	$0.394\text{-}1.333\,\epsilon_\mathrm{AA}$	$0.357\text{-}2.0\,\epsilon_\mathrm{AA}$	$300\text{-}1020\,\mathrm{K}$
N_atoms	4000	$2000 \cdot 2$	$6000 \cdot 3$
Size	$\approx 15.5 \times 15.5 \times 15.5\,\sigma^3$	$13 \times 13 \times 13\,\sigma^3$	$13 \times 13 \times 13\,\mathrm{nm}^3$

4.3. Neutral confinements

In this work, neutral confinement refers to nanoscopic geometries restricting the available space of guest molecules without introduction of spurious interactions. In order to achieve this, neutral confinements consist of the same molecules and composition as the confined liquid. These molecules have restricted mobility such that they form a solid matrix with the desired geometry. The interactions with the matrix are thus the same as those within the liquid. Or in the special case of water, the matrix is, in theory, neither more nor less hydrophilic.

Such neutral confinements allow for the study of confinement and finite-size effects on liquids with less interference from matrix-liquid interaction.[303] Moreover, liquid properties themselves, such as correlation lengths used in the RFOT and ECNLE theory of the glass transition, may be extracted. For example, the mobility of liquid molecules are altered when in contact with an immobile interface. Furthermore, the confinement imposes a partially static energy landscape onto the liquid. Thus, the structure of the liquid does not average over independent configurations in time. How these effects are propagated into the liquid reveals information about supercooled liquids themselves.

Within this work, two geometries will be applied – cylindrical pores and solid spheres. Other geometries like slit, spherical or randomly pinned pores[49] have been studied in the literature but will not be part of this work. In both cases, the procedure follows the equilibrated mixture protocol.[49] First, the liquid is equilibrated at the desired thermodynamic state. Then, the molecules that will compose the matrix are identified and their mobility is reduced using artificial potentials. More specifically, all neutral confinements within this work are for the charge-scaled SPC/E water models and use the equilibrated bulk simulations of Sec. 4.1 as basis. Thus, their parametrization and size is the same as detailed in Tab. 4.1 and 4.2 and the results are directly comparable to those from the respective bulk simulations. The solid fraction of water-like molecules is position restrained by

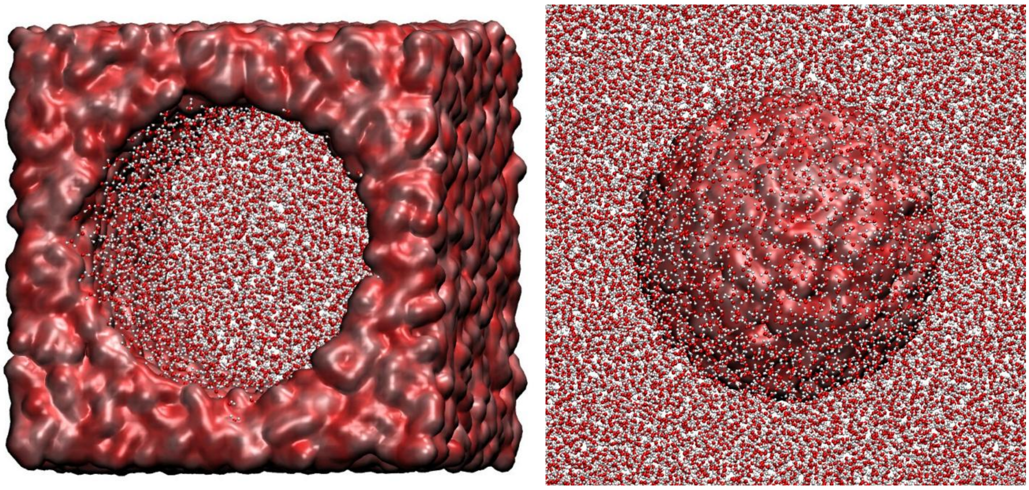

Figure 4.3.: The cylindrical (left) and inverted (right) neutral confinement with SPC/E water molecules. Oxygen atoms are red, hydrogen atoms are white and the matrix is represented with a surface mesh.

applying harmonic potentials with spring constant $\kappa = 10^6 \frac{\mathrm{kJ}}{\mathrm{mol\,nm}^2}$ to the oxygen atoms only. This value is quite high, covalent bonds usually have spring constants from 5 to $20 \cdot 10^6 \frac{\mathrm{kJ}}{\mathrm{mol\,nm}^2}$, and with thermal energy at 300 K corresponds to displacements on picometer length scale. Nevertheless, it assures that liquid molecules cannot penetrate the matrix.

The cylindrical pore is parallel to the z-axis of the simulation box and has a radius of 2.5 nm. Oxygen atoms outside of this radius are identified with the solid fraction. Because of PBC, the pore has infinite length. The size of the initial bulk system has to be large enough such that the interaction of liquid molecules of different pore images in x and y direction is negligible, i.e., that the thickness of the pore wall is large compared to the range of interactions. The pore radius of 2.5 nm is comparable to silica pores MCM41-C12 to 14 and SBA-15 pores in size and allows for the recovery of bulk-like behavior in the pore center. Silica pores however consist of an SiO_2 matrix with hydroxyl groups (-OH) on the surface. They are thus hydrophilic instead of neutral.

The second set of neutral confinements, the solid spheres, have a convex interface in contrast to the concave interface of cylindrical pores. Because of this and because a single sphere does not lead to a confinement between surfaces, they are also denoted as inverted confinement within this work. With PBC, the liquid moves within a matrix of solid spheres of arbitrary volume fraction. Several radii, 0.5, 1, 1.5, 2, and 2.5 nm, were simulated. Because of the fixed box size, the volume fraction and distance between spheres decreases with increasing radius. Because only one sphere is created per simulation and ensemble averages over multiple simulations are computationally expensive, the procedure for finding the solid fraction of molecules was extended. 25^3 different centers of the sphere were evaluated and the number of oxygens within the sphere, the number of hydrogens of the solid fraction reaching outside of the sphere as well as its absolute dipole moment were recorded. Then, a sphere with the lowest total relative deviation from the average value of each of these three properties is selected. Thus, the final system is not an outlier and represents the average sphere. This does not truly replace sampling from all possible spheres and averaging the results but is a good solution when computational costs are taken into account.

4.4. Asymmetric binary mixtures

Figure 4.4.: Chemical formulas of the repeat unit of the polymer PMMA with modified partial charges (left) and the solvent 2-methylpyridine (right). Hydrogen atoms not explicitly shown are merged with their respective carbon atoms in the united atom force field. Created with BKchem by Beda Kosata.

Table 4.6.: Simulation parameters and simulation details. Coupling to only one heat bath causes temperature gradients between solute and solvent of about 1 K and is not recommended in the future. However, these gradients are far smaller than in many cases in the literature.[304,305]

Parameter	
GROMACS	2018
Δt	1 fs
r_c	1.2 nm
PME grid	$0.12\,\mathrm{nm}^{-1}$
Thermostat	v-rescale
τ_t	0.5 ps
Ensemble	NPT
Barostat	Parrinello-Rahman
p	1 bar
τ_p, κ	2 ps, 4.5e-5 bar^{-1}
nst(p/t)couple	1
Temperature range	250-500 K
Longest simulation	17.5 µs
N_atoms	9020
Size	$\approx 5.4 \times 5.4 \times 5.4\,\mathrm{nm}^3$

The binary mixture investigated in Ch. 10 consists of picoline, specifically 2-methylpyridine, as the solvent and poly-methylmethacrylate (PMMA) as the macromolecule or solute, see Fig. 4.4. The pyridine ring is a basic organic compound and occurs in many agrochemicals and pharmaceuticals and 2-methylpyridine is an intermediate compound in the synthesis of pharmaceutical drugs. The polymer PMMA is more widely known as perspex. With a $T_\mathrm{g} \approx 138\,\mathrm{K}$ for picoline and $T_\mathrm{g} \approx 320 - 400\,\mathrm{K}$ for PMMA, depending on tacticity and molecular weight, the difference is high with about 200 K.[306–308] Hence, this is an excellent example of so-called dynamically asymmetric mixtures, systems comprising two constituents with strongly separated individual T_g.[51,309,310]

The web service "automated topology builder" was used to obtain united atom topologies[*] for both molecules.[311,312] They are used together with the updated GROMOS 54A7 force field provided by the web service. The parametrization of bonds and LJ interactions are defined by the force field while the partial charges are determined by the methods in Malde et al.[311] The partial charges of picoline are based on quantum mechanical calculations at the B3LYP/6-31G* level of theory while the PMMA molecule is based on semi-empirical calculations because of its size. From this topology, a version of a single charge-neutral repeat unit was derived. The parameters for bonded interactions were adopted while the partial charges were adjusted by a few percent, given in Fig. 4.4. The polymer chain is terminated by uncharged united atom methyl groups at both ends. The chirality of segments along the chain was randomized to

---

[*] See molid 367617 and hash 572dd for PMMA, and molid 990 and hash 32862 for picoline.

obtain an atactic polymer. The cubic system is comprised of 500 2-Methylpyridine molecules and 10 PMMA chains with a length of 50 repeat units.

Because of the slow PMMA and weak amplitude of the effects discussed in Ch. 10 long simulation times at low temperatures have higher priority than accuracy of the quantities. In contrast to the simulation protocol in Sec. 3.4, production runs in the NVT ensemble were omitted and instead long NPT simulations were evaluated. 10% of the trajectories were discarded before data acquisition. Because GROMACS produces a slow artificial drift that is not compensated by removal of center-of-mass motion when using a barostat the trajectories were corrected after the simulation. The drift at lower temperatures is about $0.2\,\mathrm{nm/\mu s}$ and therefore higher than the average displacement of PMMA during the simulation time.

Additionally, several other binary mixtures are briefly analyzed in Ch. 10. Information on these simulations is given in the appendix, App. A.5.2.

5. Observables

This chapter presents the applied definitions of common observables that are evaluated from MD trajectories. They are sorted by structural, or resp. static, and dynamical properties followed by general definitions. Observables like thermodynamic variables have already been introduced in Sec. 3. The list of observables is by no means exhaustive and only covers those used in this work. Observables or analysis routines specific and limited to a certain chapter are defined there.

The already mentioned advantage of MD simulations is the access to all N atom positions and their trajectories in time, $\vec{r}_i(t)$ with $i \in \{1, N\}$. Additionally, meta information like the mass and partial charge is available. Furthermore, it is assumed in most cases that the simulations are in thermal (metastable) equilibrium and ergodic, i.e., the ensemble and time average coincide. Averages are therefore performed over all particles and various times. Statistical errors are not derived since unknown systematic errors, e.g., the difference between simulation and experiment or non-ergodicity of the simulation, are usually larger. The analysis performed in this work was implemented with the Python package mdevaluate,[†] originally created by Matthias Bartelmeß and extended together with Niels Müller.[313,314]

5.1. Structure

Underlying the calculation of several of the following quantities is the particle density $n(\vec{r})$ which consists of delta functions for the position of each particle i:

$$n(\vec{r}) = \sum_i \delta(\vec{r} - \vec{r}_i). \tag{5.1}$$

5.1.1. Radial pair-distribution function

The short-range order of condensed matter, correlations of particle positions, can be studied using the radial pair-distribution function (RDF), see Fig. 2.2. It quantifies the particle density, normalized by the average density n_0, in infinitesimally thin spherical shells around a reference particle at the center. The RDF sums over pairs ij with $r_{ij} = |\vec{r}_i - \vec{r}_j|$,

$$g(r) = \frac{1}{n_0} \left\langle \sum_{j \neq i} \frac{\delta(r_{ij} - r)}{4\pi r^2} \right\rangle . \tag{5.2}$$

The angular brackets $\langle \cdot \rangle$ denote the ensemble average using $\frac{1}{N} \sum_i$ and averaging over multiple configurations in time. In practice, a histogram with finite bin width is calculated. Additionally, the RDF can be calculated between two subsets by letting each sum run over two different subsets and

---

[†] github.com/mdevaluate/mdevaluate

adjusting n_0, e.g., for subsets A and B

$$g_{\mathrm{AB}}(r) = \frac{1}{n_{0,\mathrm{B}} N_{\mathrm{A}}} \left\langle \sum_{i \in \mathrm{A}} \sum_{\substack{j \in \mathrm{B} \\ j \neq i}} \frac{\delta(r_{ij} - r)}{4\pi r^2} \right\rangle . \tag{5.3}$$

The most relevant RDF for the study of water is that between oxygen atoms, g_{OO}.

The RDF quantifies the probability relative to the average of finding particles at distance r to a reference particle. Note, that the absolute number of particles at r scales with $4\pi r^2$. The number of neighbors up to a distance r is given by

$$\mathcal{N}(r) = 4\pi n_0 \int_0^r g(r) r^2 \mathrm{d}r. \tag{5.4}$$

5.1.2. Structure factor

Related to the RDF via Fourier transform (FT) is the structure factor $S_{\vec{k}}$, a quantity typically measured in neutron scattering experiments:

$$S(\vec{k}) = \left\langle \sum_j e^{-i\vec{k}\cdot[\vec{r}_i - \vec{r}_j]} \right\rangle . \tag{5.5}$$

The wave vector $\vec{k}$ defines the length scale on which the structure is probed. The structure factor is related to the particle density via its FT,

$$\mathcal{F}(n(\vec{r}))(\vec{k}) = \sum_i e^{i\vec{k}\cdot\vec{r}_i}. \tag{5.6}$$

and its absolute square, $S(\vec{k}) = \mathcal{F}(n(\vec{r})) \cdot \mathcal{F}(n(\vec{r}))^*$. That is, it measures the amplitude and phase of waves scattered from the atoms.

For isotropic systems, the structure factor only depends on the wavenumber $k = |\vec{k}|$. A useful simplification is the average over all angular orientations of $\vec{k}$,

$$\begin{aligned} S(k) &= \left\langle \sum_j \frac{1}{4\pi} \int_0^{2\pi} \int_{-1}^{1} \cos\left(k r_{ij}\right) \mathrm{d}\cos\theta \, \mathrm{d}\varphi \right\rangle && (5.7) \\ &= \left\langle \sum_j \frac{\sin\left(k r_{ij}\right)}{k r_{ij}} \right\rangle . && (5.8) \end{aligned}$$

Even if the system is not isotropic, the sample may be present as a powder and this so called powder average is still performed. In the simple case of an isotropic system, the structure factor and RDF can be calculated from each other using

$$S(k) = 4\pi n_0 \int_0^{\infty} r^2 \frac{\sin(kr)}{kr} (g(r) - 1) \mathrm{d}r. \tag{5.9}$$

The RDF is computationally less time consuming and Eq. (5.9) is the preferred method to calculate $S(k)$ instead of via Eq. (5.8), which requires calculations for each wavenumber k. However, small k require large pair distances and only those within a sphere with radius R of half the box length are complete and free of artifacts. The assumption that no long-range structure beyond R exists, i.e., $g(r > R) = 1$, is often reasonable for liquids. In that case, a good approximation for length scales $2\pi/k < R$ is given by

$$S(k) = 1 - \frac{4\pi n_0}{k^2}\left(\frac{\sin(kR)}{k} - R \cdot \cos(kR)\right) + \left\langle \sum_{\substack{j\\ r_{ij}<R}} \frac{\sin(kr_{ij})}{kr_{ij}} \right\rangle . \tag{5.10}$$

5.1.3. Tetrahedral order parameter

How tetrahedrally five particles, e.g., oxygen atoms in case of water, are arranged can be quantified with the tetrahedral order parameter,[315]

$$Q_i = 1 - \frac{3}{8}\sum_{j=1}^{3}\sum_{k=j+1}^{4}\left[\cos(\Phi_{jik}) + \frac{1}{3}\right]^2 . \tag{5.11}$$

The sums run over the four neighbors closest to the reference particle i. The angle Φ_{jik} is between the vectors connecting i with two of its neighbors. Thus, Q_i sums the squared differences to the perfect tetrahedral angle of $\cos(\theta_{\text{tetra}}) = -1/3$. A value of one means perfect agreement while random configurations lead to a vanishing ensemble average. This definition has two shortcomings. First, the distance to particle i is irrelevant and, thus, the four neighbors can be anywhere on the centroid-edge connection vectors. And secondly, the fifth and further neighbors are not taken into account despite them being quite relevant to the local structure and behavior of the system.

5.1.4. Local structure identifiers

To distinguish the high and low density local structures, HDS and LDS respectively, of water in Ch. 7, three local structure identifiers are defined here. They are based on the fact that more than four neighbors exist in HDS in contrast to the tetrahedral LDS. The tetrahedral order parameter cannot properly represent this difference. For the calculations, the distances r_{ij} of neighbors j to molecule i are determined for the respective oxygen atoms and ordered by increasing distance. The number of neighbors within a cutoff radius $r_{ij} < 0.37\,\text{nm}$ is denoted as n_i.

The first identifier, the local structure index (LSI),[316] is defined as

$$I(i) = \frac{1}{n_i}\sum_{j=1}^{n_i}\left[\Delta_{ij} - \overline{\Delta}_i\right]^2 . \tag{5.12}$$

Here, $\Delta_{ij} = r_{i,j+1} - r_{i,j}$ and $\overline{\Delta}_i$ is the average of these differences over all n_i neighbors. The second structural identifier N_4 is much more primitive in that it is based on the number n_i of next neighbors alone,

$$N_4(i) = \begin{cases} 1 & n_i \leq 4 \\ 0 & \text{else} \end{cases} . \tag{5.13}$$

The third structural identifier is d_5.[160] Here, the distance to the fifth closest neighbor is compared to a cutoff of $r_{ij} < 0.35\,\text{nm}$:

$$d_5(i) = \begin{cases} 1 & r_{i5} \geq 0.35\,\text{nm} \\ 0 & \text{else} \end{cases} . \tag{5.14}$$

For the case of LDS, the first four closest neighbors are tetrahedrally arranged and have similar distances r_{ij}. The fifth closest neighbor, however, is clearly separated into the second coordination shell and the density is low. Hence, Δ_{ij} has a broad distribution and the LSI is large for LDS. Analogously, N_4 and d_5 are on average closer to one for predominantly tetrahedral or low density regions. In contrast, next neighbors in HDS have more continuously increasing distances r_{ij} and, thus, a narrower distribution of Δ_{ij} and small LSI. Corresponding regions with higher density and more HDS than LDS will have a small average N_4 and d_5. Despite the simplicity of N_4 and d_5, they well quantify the structural tendency as was also found in previous studies.[210] Removing vibrational displacements by using an energy minimized trajectory accentuates separation of the first and second next neighbor shell and, thus, increases the accuracy of all three identifiers significantly.

5.1.5. Local concentration

In mixtures, the concentration of its constituents may be heterogeneous and fluctuate in space. These fluctuations of the local concentration ϕ are measured with spheres of radius r_c, where r_c is large enough to encompass several molecules. They are quantified as

$$\phi_i = \sum_j H(r_\mathrm{c} - r_{ij}) = \bar{\phi} + \delta\phi_i \,, \tag{5.15}$$

where i denotes either a particle or an arbitrary position $\vec{r}_i$, H is the Heaviside step function, and $\bar{\phi}$ is the system averaged concentration.[317] For small cutoffs, fluctuations of the local concentration caused by vibrations can be large. To reduce such noise, the positions of the heavy atoms rather than the center of mass of molecules were used in Ch. 10. The local concentration can be correlated in time or space.

5.2. Dynamics

Temporal analysis leads to a time dependent particle density, Eq. (5.1), $n(\vec{r}, t)$. Density-density correlations are quantified by the van Hove correlation function

$$\begin{aligned} G(\vec{r}, t) &= \left\langle \frac{1}{N} \int n(\vec{r}, 0) \cdot n(\vec{r} + \vec{r}', t)\, \mathrm{d}^3\vec{r}' \right\rangle && (5.16) \\ &= \left\langle \sum_j \delta\left(\vec{r} - [\vec{r}_i(t) - \vec{r}_j(0)]\right) \right\rangle && (5.17) \\ &= \underbrace{\langle \delta\left(\vec{r} - [\vec{r}_i(t) - \vec{r}_i(0)]\right) \rangle}_{G_\mathrm{self}(\vec{r},t)} + \underbrace{\left\langle \sum_{\substack{j \\ j \neq i}} \delta\left(\vec{r} - [\vec{r}_i(t) - \vec{r}_j(0)]\right) \right\rangle}_{G_\mathrm{distinct}(\vec{r},t)} && (5.18) \end{aligned}$$

Isotropic systems allow the simplification to $G(r, t)$. The van Hove correlation function is essentially a probability distribution of displacements and is related to the propagator, the probability of finding particles at another location after a given time. It can be separated into a so called self and distinct part which contain information about the correlations of particles with themselves and cross correlations, respectively. This distinction will be relevant in further observables. In most cases however, the Fourier transform of $G(\vec{r}, t)$, the intermediate scattering function, is calculated instead.

5.2.1. Intermediate scattering function

The intermediate scattering function is the FT of the van Hove correlation function and corresponds to the structure factor in the limit $t = 0$. The scattering function is analogous to Eq. (5.5) defined as

$$S_{\vec{k}}^{\mathrm{coh}}(t) = \left\langle \sum_j e^{-i\vec{k}\cdot[\vec{r}_j(t)-\vec{r}_i(0)]} \right\rangle , \tag{5.19}$$

where the scattering vector $\vec{k}$ is a subscript to emphasize the time dependence. The superscript *coh* indicates that this is the coherent intermediate scattering function (CSF), i.e., cross correlations between different atoms are taken into account. In contrast to crystals, coherent scattering is weak in liquids and glasses and often the dynamics of individual particles is of interest. Then, the FT of the self part $G_{\mathrm{self}}(\vec{r}, t)$, the incoherent intermediate scattering function (ISF), can be determined. Analogous to Eq. (5.8), the expression can be simplified for isotropic systems to

$$S_k(t) = \left\langle \frac{\sin\left(kr_i(t)\right)}{kr_i(t)} \right\rangle , \tag{5.20}$$

where $r_i(t) = |\vec{r}_i(t) - \vec{r}_i(0)|$ and, throughout this work, the subscript k denotes the wavenumber in $[k] = \mathrm{nm}^{-1}$. For a liquid, this function decays from one to zero in a roughly exponential fashion comparable to other correlation functions. This decay quantifies translational motion on length scales given by the wavenumber. Smaller k correspond to longer length scales and a slower decay. In studies of the structural (α) relaxation, k corresponds to the first peak in the structure factor, i.e., the next neighbor peak in the RDF. For water, the ordering of extensive voids between oxygen atoms in the tetrahedral network causes a pre-peak at smaller k in the oxygen structure factor.[318,319] The minimum between the first two peaks at $k = 22.7\,\mathrm{nm}^{-1}$ corresponds to the next neighbor peak in $g(r)$ and, thus, is used to quantify the structural relaxation instead. For the sake of consistency, this wavenumber is also used for all charge-scaled variants of the water models despite shifts in the next neighbor position. Fitting the terminal decay with the KWW function, Eq. (2.5), gives a measure of the structural relaxation time. At high temperatures, it merges with the vibrational decay and, therefore, τ_{e} is preferred.

The length scale of displacement measured for a given k is usually given as $2\pi/k$. However, the average distance traveled at time τ_{e} differs and depends on the distribution of displacements. For a random-walk, the chi distribution, and in the special case of three dimensions the Maxwell-Boltzmann distribution, describes the probability of finding particles with displacement $r(t) = |\vec{r}(0) - \vec{r}(t)|$. For time difference τ_{e}, the parameter a of the probability distribution function has to solve

$$S_k(\tau_{\mathrm{e}}) = \int_0^\infty \frac{\sin(kr)}{kr} \underbrace{\left(\frac{2}{\pi}\right)^{\frac{1}{2}} \frac{r^2}{a^3} \exp\left[\frac{-r^2}{2a^2}\right]}_{\text{Maxwell-Boltzmann dist.}} \mathrm{d}r = \frac{1}{e} , \tag{5.21}$$

which gives $a = \sqrt{2}/k$. The average displacement is then $\langle r(\tau_{\mathrm{e}})\rangle = 2a(2/\pi)^{1/2} = 4/\sqrt{\pi}/k$. Using $2\pi/k$ overestimates the average displacement by a factor of $\pi^{3/2}/2 \approx 2.78$. The above mentioned value $k = 22.7\,\mathrm{nm}^{-1}$ then corresponds to average displacements of about $0.1\,\mathrm{nm}$. The chi distribution is actually incorrect for length scales on the order of the step size of the random-walk, i.e., the hopping motion of molecules in the supercooled regime. Still, the actual value of $\langle r(\tau_{\mathrm{e}})\rangle$ from simulations matches quite well.

5.2.2. Mean-squared displacement

Alternatively, the translational motion can be quantified with the mean-squared displacement (MSD) defined as

$$r^2(t) = \left\langle |\vec{r}_i(t) - \vec{r}_i(0)|^2 \right\rangle . \tag{5.22}$$

It quantifies the distance of particles after time t with respect to their original location. For small molecules, the MSD exhibits in general three different regimes. The time dependence of these regimes follows a power law $r^2 \sim t^\theta$, where the exponent θ can be calculated as $\theta = \mathrm{d}\ln(r^2)/\mathrm{d}\ln(t)$. For very short time scales, the particles have ballistic motion. The length scale is shorter than the size of the cage imposed by neighboring molecules. In this ballistic regime, the approximate relation $r^2(t) \sim t^2$ holds. The proportionality constant scales with $3k_\mathrm{B}T/m$, where k_B is the Boltzmann constant, T is the temperature, and m is the mass of the particle.

Once the particle collides with its neighbors, it ”slows down”, i.e., θ becomes less than two. In particular, in supercooled liquids the particles are trapped in their local cage for some time, giving rise to a plateau in the MSD. The vibrational motion within these cages is measured in scattering experiments as a loss of intensity by the Debye-Waller factor. Assuming harmonic potentials it is described by $\exp[-k^2\langle u^2\rangle/3]$, where $\langle u^2\rangle$ is the MSD at short times in the plateau and k the wavenumber.[320] Hence, the Debye-Waller factor and the MSD at short times contain information about the local potential explored by the particles. For brevity, Debye-Waller factor will refer to $\langle u^2\rangle$ instead of the actual attenuation of the intensity within this work.[98]

In a supercooled liquid, particles are subject to diffusive motion which on a microscopic scale consists of caging followed by jumps after some waiting time. In the long-time limit, they perform a random-walk and the propagator, the probability of displacements in x, y and z, becomes Gaussian and, as noted above, follows a Maxwell-Boltzmann distribution,

$$p(r,t) = \frac{1}{(4\pi Dt)^{3/2}} \exp\left[-\frac{r^2}{4Dt}\right] . \tag{5.23}$$

The expectation value for mean-squared displacements is given by the Einstein relation,

$$r^2(t) = 6Dt , \tag{5.24}$$

where D is the self-diffusion coefficient. Hence, the diffusive regime may be identified by $\theta = 1$. The proportionality factor is two times the number of dimensions available for free diffusion, e.g., six, four, and two in the case of three, two, and one dimensions, respectively. When the ISF is calculated for length scales large enough that the assumption of a random-walk becomes acceptable, then both, D from the MSD and τ from the ISF, are inversely proportional to each other. The solution to Eq. (5.21) determines the width parameter of Eq. (5.23) to be $a = \sqrt{2D\tau_\mathrm{e}} = \sqrt{2}k$ and leads to the relation $D\tau_\mathrm{e} = k^{-2}$.

The self-diffusion is subject to finite size effects caused by hydrodynamic interaction. The true value is,[321]

$$D = D_L + 2.837297\frac{k_\mathrm{B}T}{6\pi\eta L}, \tag{5.25}$$

where L is the length of the cubic box and η the viscosity of the liquids. A simulation series with several system sizes allows for the calculation of D.

5.2.3. Rotational correlation functions

Several experimental techniques for studying dynamics over a broad dynamical range, e.g., NMR, BDS, or DDLS, probe microscopic reorientation of a molecular vector $\vec{v}_i$ with respect to a reference axis $\vec{R}$. In general, the rotational correlation function (RCF) contains terms of the form,

$$\langle P_\ell(\cos\theta_i(0)) \cdot P_\ell(\cos\theta_i(t))\rangle \ , \tag{5.26}$$

where P_ℓ is the Legendre polynomial of rank ℓ, $\vec{u}_i = \frac{\vec{v}_i}{|\vec{v}_i|}$ the unit vector of the considered molecular vector, and θ_i the angle between $\vec{u}_i$ and the reference axis $\vec{R}$. Furthermore, the result is proportional to that for the deflection of $\vec{u}_i$ itself in case of isotropic systems or powder averages over $\vec{R}$, i.e., the integral over a sphere $\iint_S P_\ell(\vec{R}(\vartheta,\phi)\cdot\vec{u}(0)) \cdot P_\ell(\vec{R}(\vartheta,\phi)\cdot\vec{u}(t)) \sin\vartheta \, \mathrm{d}\vartheta \mathrm{d}\varphi$,

$$C(t) \overset{\text{isotropic}}{\sim} \langle P_\ell(\vec{u}_i(0)\cdot\vec{u}_i(t))\rangle \ . \tag{5.27}$$

Depending on the experimental technique different molecular vectors are correlated and also cross terms, for example, between molecules i and j may be relevant. The correlation function is written as

$$F^{\text{coh}}_{\ell,\vec{v}}(t) = \left\langle \sum_j P_\ell(\vec{u}_i(0)\cdot\vec{u}_j(t)) \right\rangle \ . \tag{5.28}$$

This definition gives a system size independent correlation function. In analogy to scattering functions, one can denote this as the coherent correlation function and distinguish the incoherent correlation function,

$$F^{\text{inc}}_{\ell,\vec{v}}(t) = \langle P_\ell(\vec{u}_i(0)\cdot\vec{u}_i(t))\rangle \ , \tag{5.29}$$

and the cross correlations,

$$F^{\text{cross}}_{\ell,\vec{v}}(t) = \left\langle \sum_{\substack{j \\ i\neq j}} P_\ell(\vec{u}_i(0)\cdot\vec{u}_j(t)) \right\rangle \ . \tag{5.30}$$

This way, the relation $F^{\text{coh}}_{\ell,\vec{v}} = F^{\text{cross}}_{\ell,\vec{v}} + F^{\text{inc}}_{\ell,\vec{v}}$ is fulfilled. In this work, sub- and superscripts are dropped whenever they are unchanged within a larger context.

These distinctions become relevant when simulation results are compared with experiments. Both, BDS and DDLS, are coherent measurements and, thus, include collective molecular orientations. However, they differ in the correlated property, dipole moment and polarisability tensor, and rank of the Legendre polynomial, $\ell = 1$ and $\ell = 2$, respectively. In contrast, ^{2}H NMR experiments are dominated by the ^{2}H bond-vector reorientation and can be regarded as an incoherent measurement with $\ell = 2$. In the case of water, BDS and ^{2}H NMR experiments can be mimicked by using the dipole moment $F^{\text{coh}}_{1,\vec{\mu}}$ and the OH-bond vector $F^{\text{inc}}_{2,\text{OH}}$. Note, that the above definitions are normalized. However, the measured correlation may include some proportionality factor, e.g., the strength of the dipole moment $|\vec{\mu}|$. Therefore, it may be necessary to weight the ij terms to match the experimental situation. In the simple case of $F_{1,\vec{\mu}}$, they can be written as $\vec{\mu}_i(0)\cdot\vec{\mu}_j(t)$.

Because the incoherent correlation function measures reorientation of vectors independently, it is also often called the self correlation function. Additionally, F^{inc}_1 is in many cases referred to as an auto-correlation function because of its mathematical similarity. Further analysis is performed for example by fitting with a KWW function, Eq. (2.5), and determining a correlation time τ. In case of rotational diffusion, correlation times for different ranks ℓ follow the relation $\frac{\tau_{\ell_1}}{\tau_{\ell_2}} = \frac{\ell_2(\ell_2+1)}{\ell_1(\ell_1+1)}$, see

Sec. 2.1.3. For example, τ for $\ell = 1$ is three times longer than for $\ell = 2$. However, rotational motion usually changes from diffusion to large angle jump motion in the supercooled regime.

Instead of probing the correlation function in the time domain, many experiments measure the dynamic susceptibility $\chi(\omega) = \chi'(\omega) - i\chi''(\omega)$. It follows from the fluctuation-dissipation theorem, that the imaginary part is connected to the correlation function via Fourier transform:

$$\chi''(\omega) \sim \frac{\omega}{k_\mathrm{B}\,T} \int\limits_0^\infty \cos(\omega\,t)\;C(t)\,\mathrm{d}t. \tag{5.31}$$

Configuration overlap correlation function The configuration overlap correlation function (OCF) quantifies the similarity of particle configurations.[322,323] Specifically, small spheres with radius r_c are defined at several positions. The occupancy $n_i(t)$ of a sphere is one if any particle is within the cutoff radius and zero otherwise. While their positions can be chosen arbitrarily, of particular use is placing them at the positions $\vec{r}_i$ of the particles at a given time and comparing configurations at different times. Then, the occupancy is defined as

$$n_i(t) = \begin{cases} 1 & |\vec{r}_i(0) - \vec{r}_j(t)| \leq r_\mathrm{c} \text{ for any } j \\ 0 & \text{else} \end{cases}. \tag{5.32}$$

Furthermore, a decomposition into self and distinct part, with conditions $i = j$ and $i \neq j$ respectively, is possible analogous to the van Hove correlation function and RCFs. The correlation function itself is then the autocorrelation of the occupancy

$$Q(t) = \frac{\sum_i^N \langle n_i(t) n_i(0)\rangle}{\sum_i^N \langle n_i(0)\rangle}. \tag{5.33}$$

In the case of water, only the oxygen atoms are used and the cutoff radius is chosen as $r_\mathrm{c} = 0.11\,\mathrm{nm}$. This ensures that a sphere can never be occupied by more than one molecule while vibrational motion leads only to minor correlation decay. A difference to several other correlation functions is that the distinct part of $Q(t)$ does not decay to zero for systems with finite particle density at all times, i.e., the volume covered by the spheres is not empty. This leads to a finite plateau Q_∞ at long times and the correlation function is in most cases fitted by a sum with a KWW function

$$Q(t) = (1 - Q_\infty) \cdot \exp\left[-\left(\frac{t}{\tau_\mathrm{kww}}\right)^{\beta_\mathrm{kww}}\right] + Q_\infty\,. \tag{5.34}$$

The analytical value for a system without static density correlations is $Q_\infty = 4/3\pi r_\mathrm{c}^3 n_0$, for cutoff radii r_c of half the distance at which the RDF becomes larger than zero.

5.3. Spatially resolved analysis

In inhomogeneous or anisotropic systems the observables as calculated above perform ensemble averages at the loss of information. Instead, the spatial variation of properties can be resolved by averaging the observables accordingly:

$$C(\mathbf{x}, t) = \left\langle \frac{\sum_i f_i(t)\delta(\mathbf{x} - \sigma(\vec{r}_i(0)))}{\sum_i \delta(\mathbf{x} - \sigma(\vec{r}_i(0)))} \right\rangle. \tag{5.35}$$

Here, the sum is performed over N particles i with positions $\vec{r}_i(0)$ at the time origin. The correlation function f_i can be any observable that can be ascribed to the particle i. The spatial assignment **x** can be positions $\vec{r}$ in space or any arbitrary spatial requirement, reflected by the mapping $\sigma(\vec{r}) : \mathbb{R}^n \to \mathbb{R}^m$. Of interest in this work are mostly the distance to reference particles or the radius in cylindrical or spherical coordinates. In practice, the delta function is replaced by bins of small but finite width. For example, with the set S_d of N_d particles that fall into the bin at distance d to the interface of a confinement at the time origin, the correlation function simplifies to:

$$C(d,t) = \left\langle \frac{1}{N_d} \sum_{i \in S_d} f_i(t) \right\rangle . \tag{5.36}$$

The number of particles $\langle N_d \rangle$ of the spatially resolved correlation functions may be required when further analysis is performed, e.g., the relative occurrence of spatially resolved correlation times is not equal.

The spatially resolved correlation functions in Ch. 9 are calculated in this way. More specifically, d is the distance of the oxygen atoms of liquid molecules to any atom, oxygen or hydrogen, of the position restrained matrix molecules. Alternatively, a radially resolved analysis is performed. The cylindrical coordinate system is aligned to the symmetry axis of the cylindrical confinement and Eq. (5.36) uses the radial coordinate r_i of the oxygen atoms instead. A third variation, denoted as the constrained distance resolved analysis, is a stricter distance resolved analysis with the constraint $r_i < 2.4\,\mathrm{nm}$.

6. Charge-scaled water models

This chapter presents basic observations made for the charge-scaled water models, see Sec. 4.1. It serves two purposes: as an introduction to common observables of simulations and to present the main effects that charge scaling can have. First, structural and static properties are investigated. In particular, observables that characterize the local structure of water are compared for different degrees of charge scaling. It is found that reducing the partial charges below $q = 0.9$ causes major changes in the first two next neighbor shells. The tetrahedral local structure can no longer be developed and its density reducing effect is missing. Hence, these systems lack the density anomaly. For increased charges, the local structure is qualitatively preserved.

Furthermore, it is found that charge scaling has, at first glance, the same effect on dynamics as temperature. Reducing q speeds up the system while increasing q strongly slows down molecular mobility. In particular, the temperature range covered by differently scaled water models easily shifts by more than a factor of five. The reason for this is the energy scale of interactions that strongly depends on the Coulomb potential. Qualitative differences between the charge-scaled variants with $q < 0.9$ and $q \geq 0.9$ occur when the Stokes-Einstein-Debye relations are tested. Most of the data shown for the SPC/E model was generated in a previous study.[24] Comparison with new charge-scaling data for the TIP4P/2005 water model reveals that the results are consistent and qualitatively independent of the choice between the two models.

6.1. Structural changes

The local structure and associated anomalies distinguish water from most other liquids. Therefore, static and structural properties are investigated first for their dependence on the charge-scaling factor q.

6.1.1. Density at atmospheric pressure

In particular the density anomaly, a maximum at 4 °C, is a feature associated with water's abnormal behavior. Figure 6.1(a) and (b) present the temperature-dependent density of the charge-scaled SPC/E and TIP4P/2005 water models, respectively, at atmospheric pressure. The accessible temperature range is limited by slow dynamics and long equilibration times at the lowest temperatures and by evaporation at the highest temperatures. For the original parametrization, density maxima are found at 249 K and 279 K for the SPC/E and TIP4P/2005 water model, respectively. This is in agreement with previous studies considering the different treatment of long-range interactions.[277–280] Besides the original models, most of the charge-scaled variants exhibit a density maximum as well. In particular, increasing the partial charges preserves this feature. Only for the highest charge-scaling factors the maximum vanishes. However, as will become more evident in the following, these systems are still structurally equivalent to water.

By decreasing the partial charges below $q = 0.9$, the density maximum also vanishes or at least leaves the accessible temperature range. Hence, these systems do not behave similar to water at

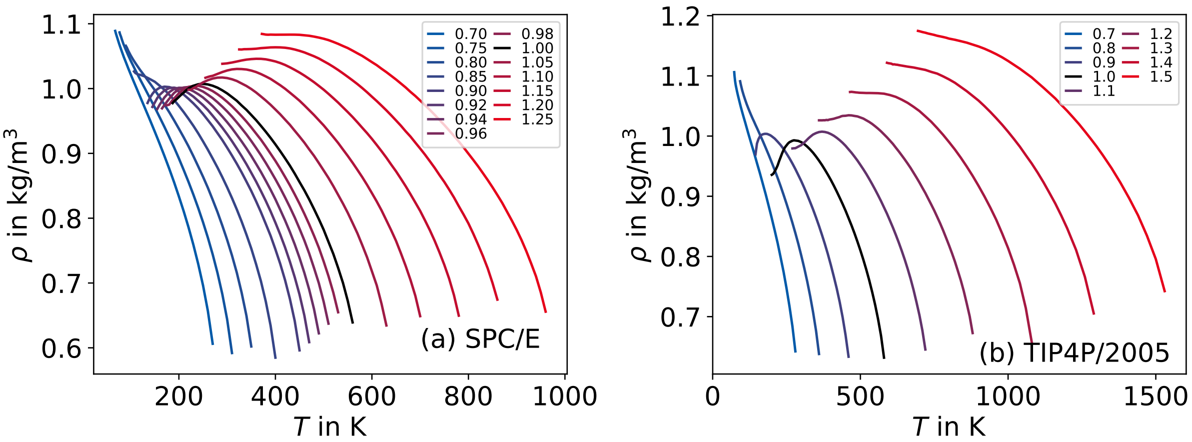

Figure 6.1.: Isobaric density for the charge-scaled variants of the (a) SPC/E and (b) TIP4P/2005 water models at atmospheric pressure. The charge-scaling factor q is given in the legend.

atmospheric pressure and can be expected to deviate in other structural properties as well.

6.1.2. Radial pair-distribution function (RDF)

For insights into the local structure and in consideration of experimentally accessible structure factors from neutron scattering, the radial pair-distribution function $g(r)$, see Sec. 5.1.1, can be investigated. The oxygen-oxygen $g(r)$ is presented in Fig. 6.2(a). It quantifies the occurrence of finding an oxygen atom at distance r of another relative to the probability for an uncorrelated homogeneous particle distribution. The typical situation for liquids is found: a prominent next-neighbor peak at short distances, followed by decaying oscillations to longer distances. For tetrahedral structures, the position of the second peak is expected to be at $\sqrt{8/3} \approx 1.63$ times that of the first peak, which is in good agreement with the data. Increasing the partial charges preserves $g(r)$ qualitatively but shifts the features to shorter distances r. This matches the observation in Fig. 6.1 of increasing density, i.e., stronger Coulomb interactions further compensate the repulsive part of the LJ potential and the molecules pack more densely. This also means that intermolecular distances are not the same among charge-scaled variants which may be relevant in studies using fixed length scales. Note, that $g(r)$ is qualitatively the same for all $q \geq 1$, even when no density maximum exists.

For reduced partial charges, the positions of the peaks shift to longer distances down to $q < 0.9$, where the second peak expected at the position for tetrahedral structure disappears. Instead, a small peak close to the next-neighbor shell appears. Hence, the local structure of the charge-scaled variants with $q < 0.9$ does not represent water at atmospheric pressure anymore. These observations also apply to the charge-scaled variants of the SPC/E water model, see Fig. A.1 in the appendix.

To ensure that the differences between the charge-scaled variants are not the result of different degrees of supercooling, the evolution of $g(r)$ with temperature is presented in Fig. 6.2(b) and (c) for the lowest and highest presented charge-scaled variants, respectively. For the water-like variant with $q = 1.5$, cooling amplifies the formation of the first and second next-neighbor shells at 0.25 nm and 0.42 nm, respectively. Distances in-between, at around 0.3 nm, are energetically unfavorable and are barely occupied at sufficient supercooling. In contrast, the system with $q = 0.7$ does not share this local structure at any temperature. The next-neighbor shell is not well separated from the second one and the latter is significantly broadened and ill-defined. These distinct local structures

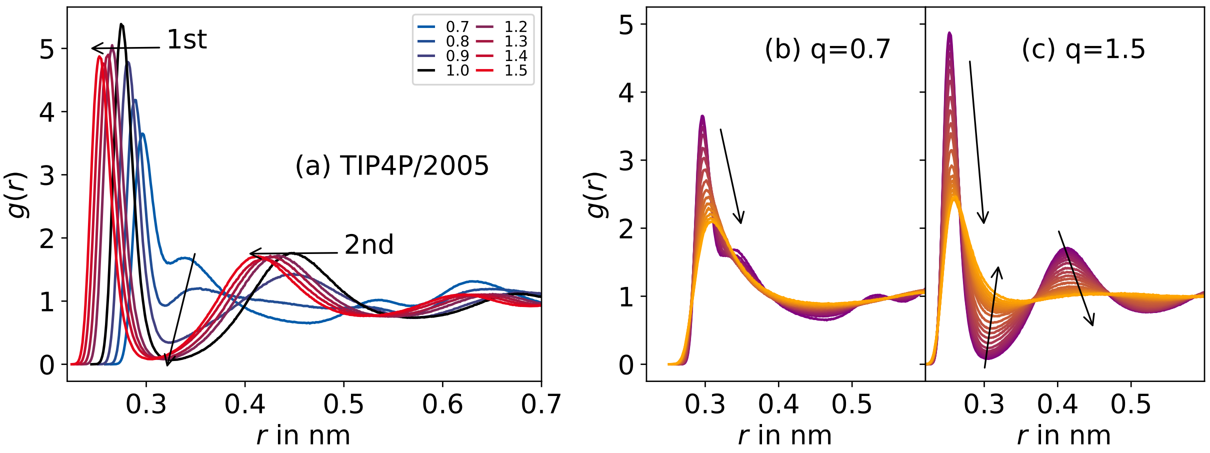

Figure 6.2.: (a) Oxygen-oxygen radial pair-distribution functions $g(r)$, see Sec. 5.1.1, for the charge-scaled variants of the TIP4P/2005 water model at atmospheric pressure and the lowest simulated temperatures. The respective graph for the SPC/E water model can be found in Fig. A.1(a) of the appendix. The charge-scaling factor q is given in the legend. (b) and (c) show the temperature dependence of the radial pair-distribution function for the lowest and highest partial charges. The temperatures are indicated with color gradients from cold in purple to hot in orange and range from 73 K to 280 K and from 695 K to 1530 K for $q = 0.7$ and $q = 1.5$, respectively. The black arrows in the graphs indicate the trend with increasing q and T, respectively.

are of further relevance in the context of water's two liquid phases.

6.1.3. Tetrahedral order

The tetrahedral order can be quantified using the tetrahedral order parameter Q, see Sec. 5.1.3. It measures the angular deviation from tetrahedral arrangement of the four next neighbors of each oxygen atom where a value of one denotes perfect agreement. The ensemble average $\langle Q \rangle$ is presented in Fig. 6.3(a) for charge-scaled variants of the TIP4P/2005 water model. With decreasing temperature, this parameter of local order increases for all systems, even for those with $q < 0.9$ that do not exhibit a density maximum. However, the value at the lowest temperature of these systems is increasingly lower with decreasing polarity. For larger q, the value at the lowest temperature is approximately $\langle Q \rangle \approx 0.9$. Again, the analysis of the charge-scaled variants of the SPC/E water model produces qualitatively consistent results, see Fig. A.1 in the appendix.

As for the RDF, the temperature dependence of two charge-scaled variants can be compared. Figure 6.3(b) and (c) presents results for TIP4P/2005 variants with $q = 0.7$ and $q = 1.5$, respectively. Both systems have broad distributions around $Q = 0.5$ at the highest temperature. However, systems with $q \geq 0.9$ develop a narrow distribution with a peak near $Q = 1$, indicating high tetrahedral order, while the distributions of systems with $q < 0.9$ remain broad and bimodal down to the lowest temperature. A comparable bimodal distribution can also be found for $q \geq 0.9$ at intermediate temperatures. However, the RDFs in Fig. 6.2(b) and (c) reveal that they do not actually share the same local structure and that the second peak of a tetrahedral structure is missing. Hence, systems with reduced partial charges are not expected to reach a similar tetrahedral order as the rest even for stronger supercooling. Comparing the RDFs and tetrahedral order parameters, it becomes obvious

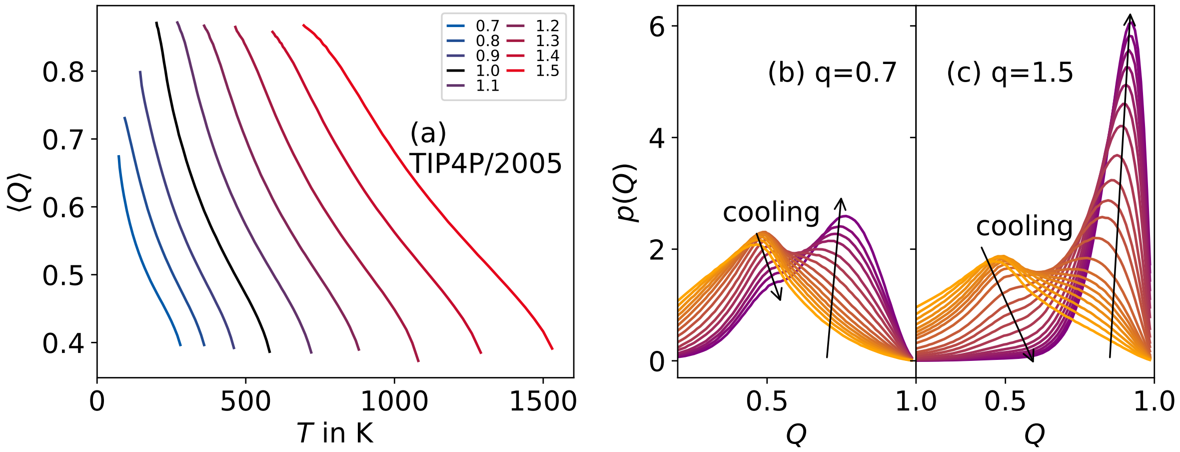

Figure 6.3.: (a) The average tetrahedral order parameter $\langle Q\rangle$, see Sec. 5.1.3, for the charge-scaled variants of the TIP4P/2005 water model at atmospheric pressure. The respective graph for the SPC/E water model can be found in Fig. A.1(b) in the appendix. The charge-scaling factor q is given in the legend. (b) and (c) show the temperature dependence of the probability distribution of Q for the lowest and highest partial charges. The temperatures are indicated as color gradients from cold in purple to hot in orange and range from 73 K to 280 K and from 695 K to 1530 K for $q = 0.7$ and $q = 1.5$, respectively. The black arrows indicate the trend upon cooling.

that the local structure of water-like molecules is not easily projected to a one-dimensional parameter. Therefore, several other identifiers of the local structure of water are employed in Ch. 7. There, the combined effects of charge scaling, temperature, and pressure will be investigated in the context of water's proposed two liquid phases.

6.1.4. Next-neighbor distances

The distribution of the distances to the oxygen atoms of next neighbors is assumed to have high relevance for water's anomalies.[324–326] They are useful for a simple understanding of the existence and absence of a density maximum for $q \geq 0.9$ and $q < 0.9$, respectively. Assuming a tetrahedral arrangement, the coordination number should be four. Figure 6.4(a) presents the average distance of the first four and fifth to eighth next neighbors, respectively. These supposedly represent the first coordination shell, the first peak in the RDF in Fig. 6.2, and the left flank of the second peak. The distance of the first four neighbors monotonically decreases upon cooling as in regular bulk liquids with no evidence of the density anomaly. However, distances to molecules in the second coordination shell show a minimum except for charge-scaled variants without a density anomaly. The local tetrahedral structure becomes more pronounced and the fifth and further neighbors are pushed away below the minimum to allow for an optimal arrangement. The temperature dependence of this effect becomes weaker with increasing q, in agreement with the finding that these systems do not show a density maximum. But to be accurate, the SPC/E variant with $q = 0.85$ does have a second next-neighbor shell that weakly increases in distance upon cooling, see Fig. A.1(c), but the effect is too weak to cause a negative thermal expansion coefficient.

The distance to the n-th next neighbor can be investigated in detail: Figure 6.4(b) and (c) compare the variants with the lowest and highest charge scaling, respectively. While the neighbors behave

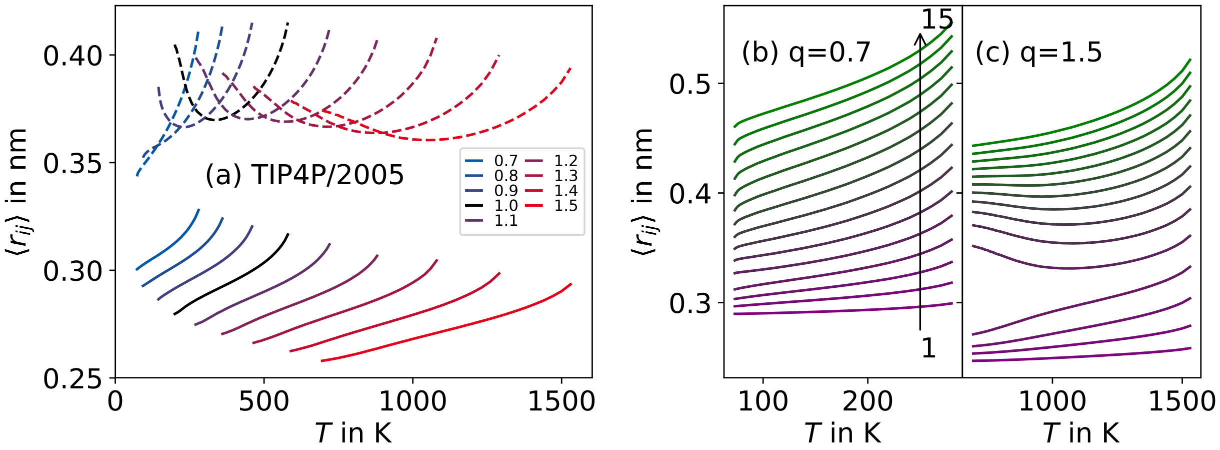

Figure 6.4.: (a) The average oxygen-oxygen distance $\langle r_{ij} \rangle$ for the charge-scaled variants of the TIP4P/2005 water model at atmospheric pressure. The index j runs over the first four (solid lines) and fifth to eighth (dashed lines) next neighbors of oxygen i. The respective graph for the SPC/E water model can be found in Fig. A.1(c) in the appendix. The charge-scaling factor q is given in the legend. (b) and (c) present the temperature dependence of the average distance to each of the next 15 neighbors for the lowest and highest partial charges. The ordering from 1 to 15 is indicated as color gradients from purple to green.

alike for the former, the latter shows a growing gap between the fourth and fifth next neighbor upon cooling. This occurs for all charge-scaled variants but strongly diminishes in strength below $q = 0.9$. This gap allows for the definition of several simple identifiers of the local structure, see Sec. 5.1.4. The difference of the distance of the fourth and fifth neighbors or lack thereof is the characterizing quantity. However, as can be seen from the different intermolecular distances in Fig. 6.4(a) the cutoffs have to be adjusted for significant charge scaling q.

The anomalies in these structural properties at atmospheric pressure can be understood in detail with the investigations of the following chapter. Finally, it is reassuring that the above observations are qualitatively equivalent for both water models, SPC/E and TIP4P/2005.

6.2. Dynamics

The study of structural properties of the charge-scaled variants revealed a significant temperature dependence for many features, e.g., the position of the density maximum. Furthermore, the available temperature range varied strongly as a consequence of the strong dependence of the dynamics of the system on the charge scaling q. Long-range translational dynamics at 300 K slows down with increasing q, see Fig. 6.5(a). More so, the shifts on a logarithmic scale increase by constant changes in q and, thus, the slowdown is super-exponential.

Reduction of q speeds up the system and it enters the diffusive regime with $r^2(t) \sim t$ immediately after the ballistic regime with $r^2(t) \sim t^2$ at subpicosecond times. For higher q, the system exhibits a glassy plateau before it becomes diffusive.

Local dynamics are studied based on the rotational correlation function of the OH-bond vector $F_{1,\mathrm{OH}}$ in Fig. 6.5(b). Consistent with the result for translational diffusion, the correlation decay shifts

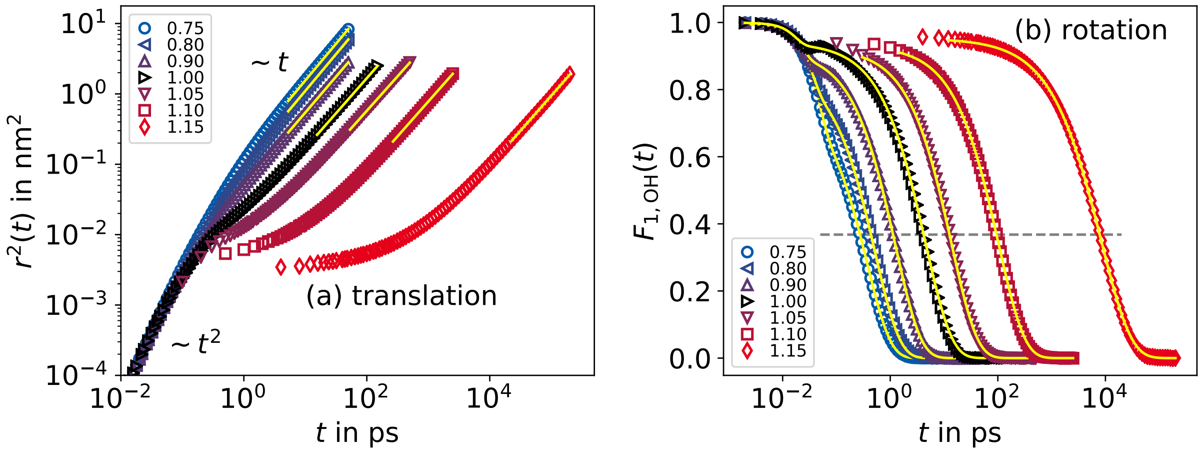

Figure 6.5.: Measures of dynamics at 300 K for several charge-scaled variants of SPC/E: (a) translation probed with the MSD of the oxygen atoms and (b) rotation probed by $F_{1,\mathrm{OH}}$, see Sec. 5.2.2 and 5.2.3, respectively. The charge-scaling factor q is given in the legend. In (a), solid yellow lines indicate fits to Eq. (5.24), yielding the self-diffusion coefficients D. In (b), solid yellow lines are fits to a KWW function, Eq. (2.5), and to a sum of two KWW functions for $q \leq 1$. The gray dashed line indicates the criterion for the determination of the correlation time τ_e. Results are presented here for the SPC/E variants because of the finer resolution in time and charge-scaling factor. The respective results for the TIP4P/2005 variants are shown in Fig. A.2 in the appendix.

to longer times with increasing q and a plateau of about 0.95 exists for intermediate times. Thus, long range and local dynamics are affected by charge scaling at least qualitatively in the same way. These changes of dynamics by orders of magnitude despite constant kinetic energy and mass underline the importance of intermolecular interactions such as hydrogen bonding and their strength.

The dynamical properties, self-diffusion coefficient D and correlation time τ_e, can be determined with fits of the data. However, in order to reduce the size of the trajectories, the time difference between stored frames was adjusted to the dynamics. Hence, the data of systems with increased charges is missing short times, i.e., the ballistic regime in the MSD and the vibrational decay of the correlation function. While the determination of D is unaffected, the fit of $F_{1,\mathrm{OH}}$ or any other correlation function of local dynamics can only include the vibrational decay if it is resolved. In this work, this is irrelevant in most cases because correlation functions are, as discussed in Sec. 2.1.2, mostly quantified by τ_e, the time at which they decay to e^{-1}. The reason for this is the merging of the vibrational and terminal decay and the therefore ill-defined fit of the latter at higher temperatures or reduced partial charges.

6.2.1. Temperature dependence

Of great relevance in this work is the temperature dependence of dynamical quantities. As for simple glass formers, dynamics slow down in a non-Arrhenius fashion upon cooling for all charge-scaled variants of the SPC/E and TIP4P/2005 water models when measured by any of the observables introduced in Sec. 5.2. As an example, the ISF for a wavenumber of $k = 22.7\,\mathrm{nm}^{-1}$ is shown in Fig. 6.6. Only one merged decay is observable at high temperatures while a plateau exists at lower temperatures and the long-time decay associated with the structural relaxation shifts to longer times.

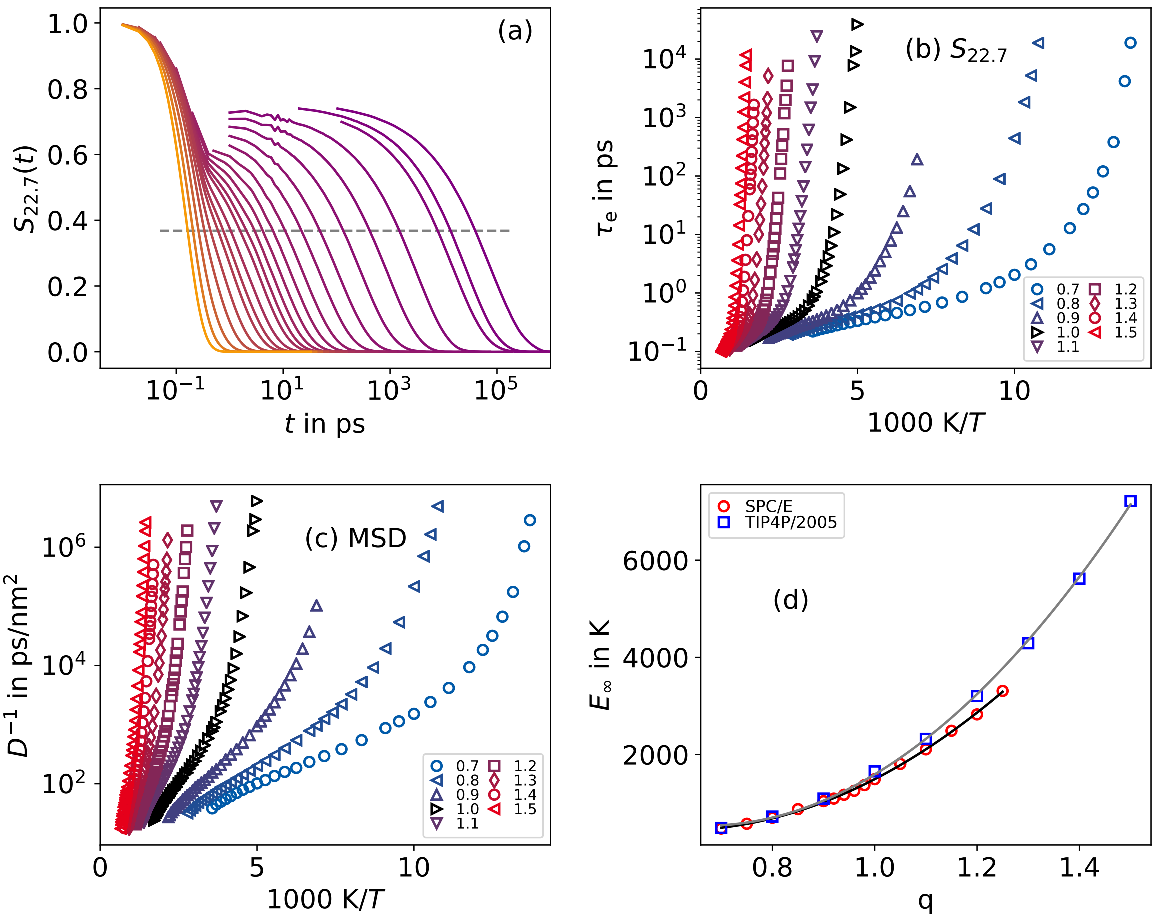

Figure 6.6.: (a) The incoherent intermediate scattering function $S_{22.7}(t)$ for the original TIP4P/2005 water model. The presented temperatures range from 200 K (purple) to 550 K (orange) and most temperatures are omitted to improve visibility. Dynamical quantities for all charge-scaled variants of the TIP4P/2005 water model: (b) Translational correlation times τ_e of $S_{22.7}$ and (c) reciprocal self-diffusion coefficient D. The charge scaling q is given in the legend. The equivalent graphs to (b) and (c) for the SPC/E water model can be found in Fig. A.3 in the appendix. (d) High temperature activation energy E_∞ for D. The black and gray solid lines are fits with a polynomial of second order.

Hence, charge scaling under isothermal conditions is qualitatively similar to a variation of temperature. In a first approximation, the energy scale of dynamics shifts with q.

The strong dependence of the dynamics on the charge scaling factor q can be observed in particular in the Arrhenius plot of dynamical quantities, see Fig. 6.6(b) and (c) for translational observables and Fig. A.3(c) for rotational correlation times. The steepness of the high-temperature Arrhenius regime, E_∞, and its location in temperature increase by an order of magnitude from $q = 0.7$ to $q = 1.5$ for the charge-scaled variants of TIP4P/2005. Extrapolating the fragile regime to the glass transition by eye suggests similar shifts for T_g.

Both, E_∞ and T_g will be investigated in more detail in Ch. 8. Here, only the charge dependence of E_∞ is investigated in Fig. 6.6(d). It is comparable for the SPC/E and TIP4P/2005 variants for minor charge scaling around $q = 1.0$, but increases slightly stronger for the TIP4P/2005 variants. For both data sets, the charge dependence can be characterized by a second order polynomial, consistent with Coulomb's law. Note however, that its minimum does not lie at $q = 0$. Instead, the low-q limit is that of a simple LJ liquid with finite E_∞. In general, the q dependence of E_∞ is different for various liquids. A parabolic function with minimum at $q = 0$ was found for a charged Kob-Andersen mixture while charge-scaled variants of the BKS model of silica follow linear behavior over a wide range of q.[116,118] Nevertheless, the relation between interaction strength and activation energy in the simple-liquid regime follow simple expectations independent of the structural differences at lower temperatures.

6.2.2. Stokes-Einstein-Debye relation and the hydrodynamic radius

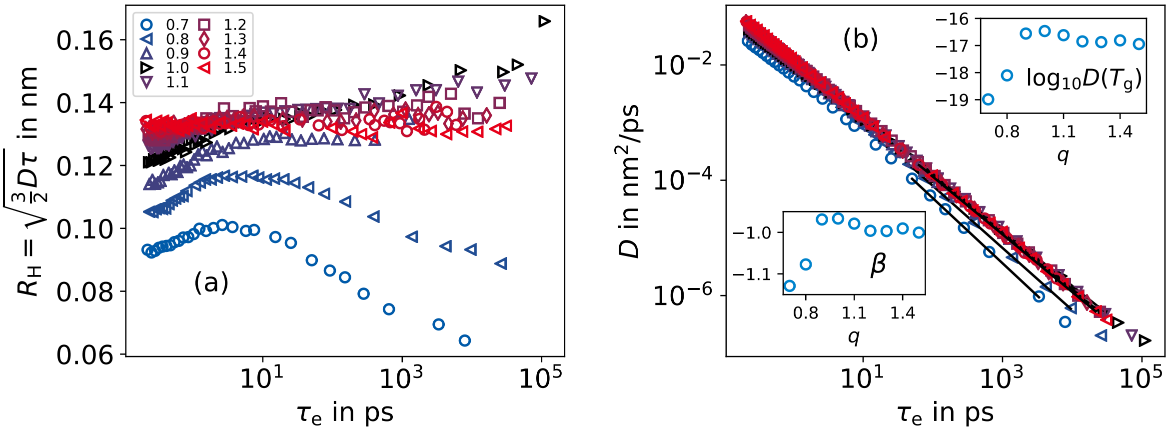

Figure 6.7.: (a) The hydrodynamic radius, Eq. (2.8), for the charge-scaled variants of the TIP4P/2005 water model as a function of the correlation time τ_e from the RCF $F_{1,\mathrm{OH}}$. For the SED analysis, $\tau = \tau_\mathrm{e}$ was used. The charge-scaling factor q is given in the legend. (b) Relation between self-diffusion coefficient D and correlation time τ_e with power law fits (black solid lines), see main text. The fit is limited to $2 \cdot 10^{-4}\,\frac{\mathrm{nm}^2}{\mathrm{ps}} > D > 5 \cdot 10^{-7}\,\frac{\mathrm{nm}^2}{\mathrm{ps}}$ to ensure supercooled dynamics and avoid data of poor statistics. The left and right inset present the exponent β of the power law fits and their extrapolation to T_g as a function of q, respectively.

How charge scaling affects translational and rotational dynamics can be investigated in more detail with the Stokes-Einstein-Debye (SED) relation, see Sec. 2.1.3. D and τ are inversely proportional to each other if the systems comply. Figure. 6.7(a) presents the hydrodynamic radius R_H as a function of rotational correlation times τ_e, see Fig. A.3(c), of the charge-scaled variants of TIP4P/2005. This representation avoids the large shifts in temperature and allows for a comparison at isokinetic points. For most systems, R_H is about $0.13\,\mathrm{nm}$. Strong deviations are found in particular for the two least polar systems which also differ the most in structural properties. In these cases, R_H starts to decrease upon cooling, i.e., towards longer correlation times. R_H grows slightly for intermediate values of q around the original model while it is essentially constant for larger q. Furthermore, the high-temperature regime is not flat in most cases. This implies that the high-temperature activation energy does not perfectly agree between both quantities, D and rotational τ_e. However, these deviations are small.

The data for D and τ_e can be characterized by a power law, $D \propto \tau_\mathrm{e}^{\beta}$, at supercooled temperatures, see Fig. 6.7(b). The exponent β is expected to be -1 if the SED relations hold. However, it holds only for $q \geq 1.2$ and exhibits a peculiar q dependence for $q < 1.2$. This SED breakdown was also found in other experimental and simulation studies of water.[74,327,328] Detailed investigations in Sec. 7.4 reveal that the origin lies in two liquid phases and the proposed second critical point (LLCP) of water. The SED breakdown depends on the distance to the LLCP and on which side of the phase transition line the system is. The power law can be extrapolated to $\tau_\mathrm{e}(T_\mathrm{g}) = 1000\,\mathrm{s}$ to find $D(T_\mathrm{g})$. The right inset of Fig. 6.7 shows that over so many orders of magnitude small differences in β can lead to deviations of several orders of magnitude. Differences of R_H of the charge-scaled variants at high temperatures become negligible in comparison. However, whether or not the power law is valid down to T_g cannot be confirmed with MD simulations.

It is important to note, that the observations in Fig. 6.7 depend on the choice of the correlation function. For the ISF, the SE breakdown becomes severe for all values of q if the wavenumber is large and it does not share the charge dependence found with $F_{1,\mathrm{OH}}$. Results for rotational correlation functions of different rank $\ell = 1, 2$ or for different vectors have qualitatively the same charge dependence but the exponent β is shifted to higher values, see Fig. A.4(a) in the appendix.

6.2.3. On the limits of water model charge scaling

The partial charge of the water models cannot be scaled arbitrarily without encountering problems. The reduction of q has strict limits. For SPC/E and $q = 0.6$, the system spontaneously crystallizes at $51\,\mathrm{K}$ with a cubic lattice structure. Correlation times are shorter than ns at this temperature and, thus, the liquid cannot be sufficiently supercooled. This happens because the Coulomb interactions become too weak compared to the unaltered LJ interactions. At $q = 0$ only a soft-sphere liquid which easily crystallizes remains. Negative pressures may allow for stronger supercooling but this is beyond the goals of the present work. For TIP4P/2005 and $q = 0.6$, the liquid also underwent a rapid transformation at $T = 58\,\mathrm{K}$ with dynamics on the order of $100\,\mathrm{ps}$. While the system did not crystallize, dynamics slowed down by orders of magnitude and the density increased discontinuously. Further equilibration proved computationally too expensive. While this system is also not helpful to this work, it might be of interest in future studies. For both water models and $q < 0.6$, the systems crystallized more easily and, thus, charge scaling has a lower boundary beyond which equilibration of the metastable liquid becomes impossible.

So far, a similar restriction was not found for increased partial charges. In particular, test simulations at much higher $q \geq 2$ have been no problem for both water models. Because the relevant energy scale increases, thermal energy and vibrations increase accordingly. This requires a reduced time step Δt of the integrator and adjustment of thermodynamic parameters to prevent nonphysical interactions. However, the density maximum disappeared already at the highest q presented in this chapter, Fig. 6.1. This suggests that the origin of water's anomalies is located at a greater distance in the phase diagram or that the range or strength of the anomalies decreased. Either way, such systems are not of interest to this work.

6.3. Summary

In this chapter, simple structural and dynamical properties were investigated for charge-scaled variants of the SPC/E and TIP4P/2005 water model. While real water exhibits a vast number of anomalies, investigating all of them is beyond the scope of this work and may even be impossible with MD simulations. However, many of them are assumed to have a similar origin, e.g., the tetrahedral local structure caused by hydrogen bonding. Here, the density maximum was used as a simple indicator of anomalous behavior. For both decrease and increase of q, it disappears. However, the RDF showed qualitatively the same local structure for all systems with the original and increased partial charges. The same is found for the tetrahedral order parameter and the next-neighbor resolved distances. The temperature dependence of the latter shows that the next-neighbor shell contracts as for regular liquids, whereas the second next-neighbor shell expands, leading to a negative thermal expansion and the density maximum. However, the temperature dependence of these two effects changes with q. The expansion can no longer compensate the contraction at the highest studied partial charges and, thus, the density maximum does not occur despite equivalent local structure.

For $q < 0.9$, the local structure was not preserved. The RDF does not resemble that of the original water models at any temperature except close to the boiling point. This discrepancy is not as evident with the tetrahedral order parameter, which suggests that further supercooling could lead to the same local structure. The next-neighbor distances also reveal that the water-specific coordination number of four and spatially separated first and second neighbor shells are not found in the accessible temperature regime. While it might be true that the water structure is restored at sufficient supercooling of these systems, this regime in the phase diagram could be beyond the glass transition temperature. Furthermore, reducing q too far leads to rapid crystallization into a cubic phase and, thus, makes a tetrahedral network unreachable. Hence, a simple distinction can be made: The liquids behave water-like for $q \geq 0.9$ and not water-like for $q < 0.9$. This will be investigated further in the context of water's proposed two liquid phases, low-density and high-density liquid, in the next chapter. In particular, observations of this chapter were made at atmospheric pressure and neglect the complexity of water's phase diagram.

Translational and rotational dynamics were strongly affected by charge scaling. At 300 K, increasing the partial charges by 15 % caused a decrease of the mobility by three orders of magnitude with respect to the original TIP4P/2005 water model. Reduction of q speeds up the system. These observations are weakly dependent on the observable, long-range translation, or local rotation. The high-temperature activation energy approximately increases as a function of q^2 and varies from the lowest to highest studied charge scaling by a factor of more than 6 and 14 for SPC/E and TIP4P/2005, respectively. The dynamically accessible temperature range and glass transition temperature shift accordingly and, thus, charge scaling and temperature have qualitatively a similar effect on dynamics in first approximation.

Detailed comparison of dynamical quantities reveals a dependence of the hydrodynamic radius and degree of the SED breakdown on the charge scaling. In particular, systems with $q < 0.9$ have a reduced R_{H} that decreases upon further supercooling, in contrast to the more common finding of a growing R_{H}. Long-range translation slows down less than rotational motion with temperature for these systems. On the other hand, systems with $q \geq 1.1$ show consistent and unremarkable behaviors. Hence, dynamics and structure are indeed connected in some way. What role water's proposed second critical point plays will be investigated in the next chapter.

7. Polyamorphism in charge-scaled TIP4P/2005

This chapter deals with polyamorphism of supercooled water-like models. It presents a study on the relation of thermodynamics, structure and dynamics of the TIP4P/2005 water model with systematically reduced partial charges, and thus weakened hydrogen bonding. The observation of isochore crossing in the P-T diagram shows that these water-like models exhibit an easily accessible liquid-liquid critical point (LLCP), followed by a liquid-liquid phase transition (LLPT) line between a high-density liquid (HDL) and low-density liquid (LDL) phase. A two-structure equation of state (TSEOS) is used to determine the critical parameters, temperature T_c, pressure P_c, and density ρ_c, and their dependence on charge scaling. With simulations of elongated rectangular geometries the phase separation into stable HDL and LDL regions is facilitated and the study of their respective structure and dynamics made possible. For the dynamics, it is found that the fragility of isochores varies only slightly while their composition differs greatly but changes only moderately with temperature. On the contrary, strong variations of fragility and significant temperature dependence of the composition are found for isobars. Thus, the origin of the dynamical transition from fragile to strong behavior for cooling along isobars is not the existence of two phases with significantly different temperature dependencies of their respective dynamics. Instead, the results show that rapid conversion from HDL-like water with fast dynamics to LDL-like water with slow dynamics is the origin of the apparent highly fragile behavior. Furthermore, the dynamics are studied by employing two models based on the two-structure model. Their validity in the phase diagram is limited. In conclusion, theoretical challenges for the description of dynamics in a reactive binary mixture are discussed.

7.1. Motivation

Many-particle physics are a rich field leading to many phenomena of which the anomalies of water are a well-known example. At the origin of these anomalies is the competition of hydrogen bonding and other intermolecular interactions which are most prominent in the supercooled regime.[2] There, the thermodynamic response functions have been predicted to diverge.[127] In particular, simulations indicated that the anomalies of water are caused by a liquid-liquid phase transition (LLPT) line at low temperatures and above atmospheric pressures and that a second critical point (CP) marking the end of the LLPT line exists.[5] The two phases differ in density and are, thus, denoted as high-density liquid (HDL) and low-density liquid (LDL).[6,125,139,142,144] As a consequence, the short-range structure differs between both phases, with LDL arguably having higher tetrahedral order. Additionally, they are expected to have different dynamics.[18]

A significant problem is the very rapid crystallization of water below the homogeneous nucleation temperature T_H. Raman scattering of evaporating micrometer-sized droplets determined this to be $T_H \approx 231\,K$.[329] Hence, in the temperature range of $\sim$150–230 K crystallization prevents the experimental study of structure and dynamics of bulk water, and thus, the two liquid phases. This so-called *no-man's land* still hinders experimental evidence of the LLPT line despite some progress in exploring it.[129,330–332] While multiple amorphous ice phases, i.e., glasses, that are separated by first-order like phase transitions and have different glass transition temperatures T_g have been found,[6,13,125,139,142,144] the LLPT line and LLCP are still inaccessible and controversial.[14,15]

Such polyamorphism in liquids is not limited to water. Simple theoretical approaches and simulations with model systems,[12,196] e.g., tetrahedrally functionalized particles or the spherically symmetric Jagla model, have shown that polyamorphism can be introduced with certain inter-molecular interactions.[197,198] Furthermore, experimental evidence of polyamorphism has been found for carbon, phosphorus and sulfur, among others.[8–11] A broad overview can be found in a recent review.[7] The literature implies that an LLCP can occur when spacious and ordered local structures of low energy, such as tetrahedral arrangements, exist. In such systems, cooling favors the low-density structure (LDS) while increasing the pressure leads to an increase in high-density structures (HDS) with denser packing. These local structures are generated by a small group of molecules and attributed to this group or to the central molecule, as is done within this work. They should not be confused with LDL and HDL, which are regions consisting of a larger number of molecules in many local structures. In particular, LDL and HDL are rarely pure phases, but mixtures of predominantly LDS and HDS, respectively, whose concentrations depend on the thermodynamic state.

As has been exploited in the previous chapter, the crystallization is suppressed in simulations because of the high cooling rates and small system size. This makes MD simulations very suitable for studying the polyamorphism of water.[3,4,169,194,195] The literature on evidence of LLPTs in simulations of several water models is already quite extensive.[157] Among those that show indications of an LLPT are the TIP4P/2005,[158–162] TIP4P/Ice,[162] TIP5P,[161] WAIL,[163] E3B3,[164] and ST2 model.[5,166–168] In contrast, the mW model does not have an LLPT because the entropy of mixing is too high for phase separation.[173] Not in all cases is the LLCP computationally accessible, i.e., equilibration at the LLCP can be performed within reasonable time.[158–161] So deep in the supercooled regime and at negative pressures, at which water anomalously slows down, the structural relaxation can be quite slow. One such example is the SPC/E model, for which the LLCP was predicted at currently inaccessible temperatures.[22] Additionally, the influence of crystal-like clusters, in particular in systems of finite size, is still debated.[170,171]

The systems and corresponding literature mentioned above show that liquid polyamorphism may be more common than one might think. A fundamental understanding of the LLCP, how its existence and location depend on the particle interactions, is still lacking and would help in the search for further systems with this phenomenon. MD simulations offer two major advantages in this respect. First, the thermodynamic conditions, temperature, pressure, and density, can be controlled and easily adjusted. Experimentally, negative pressure is achievable, e.g., with the so-called Berthelot tube method.[175] Detailed experimental measurements in this region of the phase diagram, where water is double metastable, are still rare. Simulations with the TIP4P/2005 water model agree with experimental data at these conditions, but are much more stable and can be analyzed as usual.[175]

Second, MD simulations allow for continuous variation of particle interactions and exploration of model systems. For example, decreasing the three-particle repulsion parameter of the Stillinger-Weber potential for silicon led to a disappearance of the LLPT.[200–202] A more pronounced LLPT was found for variations of the bond angle in the ST2 model of water.[203] An approach possible with most chemically realistic models is the scaling of partial charges. While for the WAC model for silica no LLCP was found in the accessible phase space,[4] it was shown by the crossing of isochores in the P-T phase diagram and by extensive free energy calculations that an LLPT exists when the partial charges of the model are reduced.[25,169] As with silica, no unique accepted model exists for water and an exploration of the parameter space helps in assessing the implications for real water. Charge scaling has also been helpful in studying the glass transition in water,[46,117] silica,[118] an ionic liquid[283] and a charged Kob-Andersen mixture[116,290,291] and has been investigated in the previous chapter. It already changed the liquid behavior significantly, e.g., removing the density anomaly at atmospheric pressure and reduced charges. Thus, charge scaling is applied again in favor of other options for variation of the strength of hydrogen bonds and the degree of tetrahedral order.[46,117]

To complement the standard analysis of simulations a theoretical description for polyamorphism is needed. The two-structure equation of state (TSEOS) formalism has been successfully applied in several studies.[161,168,173,182–188] Within it, the liquid is represented as a mixture of HDS and LDS in all regions of the phase diagram. A mean-field approximation allows for the calculation of the Gibbs energy analogous to binary mixtures. It consists of a concentration-dependent weighted sum of the pure phases and an non-ideal mixing term of entropic[173,185,333] or enthalpic[160,168,176,334] origin. This approach has been successfully applied in the literature for interpolation and moderate extrapolation,[182] and the built-in parametrization of the LLCP allows for a robust determination.

Moreover, liquid polyamorphism could lead to unusual dynamic behavior. The dynamical anomaly of water, that viscosity decreases with increasing pressure,[2] is thought to originate in its proposed polyamorphism. If structural relaxation is sufficiently different between HDS and LDS, the dynamics of the mixture will vary with their concentration, which in turn varies with pressure. Given that the HDS concentration grows with pressure, its mobility is higher than that of LDS. This is consistent with the experimental finding that T_g of HDL is lower than for LDL.[13] However, it is still controversial whether this glass transition is related to translational or just rotational motion,[16] as the nature of the dynamics in the *no-man's land* is difficult to study. Also with extensive simulations using the TIP4P/2005 water model, two different glass transition temperatures were found of which LDL/LDA exhibits anomalous pressure dependence of T_g while HDL/HDA shows normal behavior.[216]

Furthermore, water exhibits a very fragile temperature dependence of dynamics in the mildly supercooled regime while a strong temperature dependence is required at even lower temperatures to match the experimentally found T_g. Thus, it may belong to the class of liquids that exhibit a fragile-to-strong transition (FST).[40] More specifically, HDL and LDL are assumed to be fragile and strong liquids, respectively, and an FST is expected when the Widom line is crossed in temperature. The Widom line is the continuation of the LLPT line into the single-phase region above the LLCP where the thermodynamic response functions of the liquid exhibit a maximum and the change in HDS/LDS concentration with temperature is high.[147–150] Nevertheless, there exist other explanations for the observed dynamic crossover, e.g., that only a β-process remains.[17] MD simulations have already been used to investigate the dynamical behavior near the LLPT with the ST2 water model and the WAC model for silica among others.[210,213]

Therefore, this chapter deals with MD simulations specifically performed to investigate thermodynamic, structural, and dynamical properties of the TIP4P/2005 water model over a large region of the phase diagram. Charge-scaling is used to reach regimes that are not as accessible with the original model and to systematically study the resulting phase diagram. Crossing of isochoric data in the P-T phase diagram is observed. Hence, the systems possess an LLCP and the TSEOS can be employed to analyze its position. Furthermore, the dependence of its parametrization on charge scaling can be investigated and used to test the accuracy of this method and to compare with literature data. Because the mobility at the critical point accelerates with reduced charges, dynamical properties can be studied across the LLCP and the systems can be equilibrated below the critical point. Furthermore, simulations which promote phase separation into HDL and LDL regions in the metastable regime are performed allowing for the study of both phases directly. Finally, the FST of water can be rationalized with the rapid transition from HDL to LDL in a narrow temperature range. Models that characterize water's dynamics in this way are then thoroughly tested.

7.2. Methods

The following sections contain information on simulations and analyses specific to this chapter.

7.2.1. Simulation details

Listed here are the studied systems and important details only. For further details about the water model and simulation parameters see Sec. 4.1. As described in Sec. 4.1, the partial charges of the original TIP4P/2005 water model[276] are scaled by a factor q, in this case from $q = 0.86$ to $q = 0.91$, while all other parameters of the model remain unchanged. Thus, the polarity and strength of the hydrogen bonds is reduced. The model was parameterized with long range LJ interactions taken into account. The contributions of the LJ potential at large distances are always attractive and give a negative contribution to pressure and energy. Hence, PME is employed for the LJ potential as well to determine pressure correctly and comparable to the literature. Results are therefore slightly different from simulations in Chap. 6 and 8.

The majority of the simulations in this chapter, as in the majority of the water simulations in this thesis, were performed with cubic boxes and $N = 2000$ molecules, resulting in an edge length of $\sim 4\,\mathrm{nm}$. Comparable studies were often performed with less molecules.[25,219] While this is not relevant in the one phase region, it should become crucial in the two-phase region where the volume fraction of a proposed liquid-liquid interface would scale with $N^{2/3}$ instead of N. For simulations in the isothermal-isobaric (NPT) ensemble of this chapter, the density equilibration was not followed by production runs in the NVT ensemble. Instead, data for isobars was obtained from trajectories in the NPT ensemble and it was assured that a fraction of the trajectory sufficient for equilibration was omitted in the data acquisition for isochores and isobars. Isochores end at temperatures where the simulation lengths necessary for equilibration exceed $2\,\mu$s.

To promote phase separation, simulations were performed with elongated rectangular boxes. These allow for a smaller ratio of surface area to volume in the case of phase separation than their cubic counterparts at the same computational cost.[169,335] These coexistence simulations were also performed in the NVT ensemble for $q = 0.86$ and $q = 0.88$. The edge lengths had a ratio of $L_\mathrm{x} : L_\mathrm{y} : L_\mathrm{z} \equiv 1 : 1 : 3$ for systems with $N = 2000$ molecules and $1 : 1 : 6$ for further simulations with $N = 12000$ molecules. With these parameters, the size of the box of the small system is $L_\mathrm{x} = L_\mathrm{y} \geq 2.7\,\mathrm{nm}$ and $L_\mathrm{x} = L_\mathrm{y} \geq 4.0\,\mathrm{nm}$ for the large system. For the large system, the influence of a biased starting configuration was investigated. Flat bottomed potentials were applied to artificially promote separation into one high-density and one low-density region and the system was equilibrated at a temperature close to T_c. The simulation protocol of cooling down in succession was applied once low enough temperatures for stable phases were reached.

7.2.2. Two-structure equation of state

The TSEOS, two-structure equation of state, formalism has been very successful in describing and analyzing data from simulations and real water in many previous studies.[160,161,168,188] Therefore, it is used to determine the location of the LLCP for the isochoric data set. This approach considers the liquid to consist of two mutually convertible high-density and low-density local structures A and B with fractions $1 - x$ and x, respectively. Thus, contrary to common binary mixtures it is a reactive mixture with a concentration, which is constant only on average. Still, the thermodynamic description features many similarities. As a starting point, the molar Gibbs energy is written as[160,161,168,182,188]

$$G = G^\mathrm{A} + xG^\mathrm{BA} + RT\left[x\ln x + (1-x)\ln(1-x) + \omega x(1-x)\right] \ . \tag{7.1}$$

Here, G^{A}, G^{B}, R and ω are the Gibbs energies of the pure A and B phases, the molar gas constant and the non-ideal mixing parameter, see Eq. (7.4). By using the concentration x and the difference of the Gibbs energies, $G^{\mathrm{BA}} = G^{\mathrm{B}} - G^{\mathrm{A}}$, one avoids explicit parametrization of the low density phase. The more easily accessible high density phase is modeled in more detail while the difference G^{BA} will be approximated. Similarly to binary mixtures, a contribution by the entropy of mixing of A and B structures is included. It consists of two terms describing ideal mixing and a term for non-ideal contributions. Because the determination of the LLCP is of interest, it is convenient to represent the temperature and pressure as dimensionless quantities, $\Delta\hat{T} = \frac{T-T_{\mathrm{c}}}{T_{\mathrm{c}}}$ and $\Delta\hat{P} = \frac{P-P_{\mathrm{c}}}{\rho_{\mathrm{c}} R T_{\mathrm{c}}}$. G^{A} is effectively modeled as a Taylor series with terms up to third order,

$$G^{\mathrm{A}} = RT_{\mathrm{c}} \sum_{m,n} \hat{c}_{mn} \Delta\hat{T}^{m} \Delta\hat{P}^{n}, \tag{7.2}$$

with $\hat{c}_{mn}$ as adjustable coefficients. Some of these can be interpreted, e.g., at the LLCP $\hat{c}_{10}$ is the zero point entropy and $\hat{c}_{01}$ characterizes the volume. The coefficient $\hat{c}_{10}$ is set to zero in the literature and in this study. For a reactive mixture model, the equilibrium of the reaction $A \rightleftharpoons B$ is determined by the equilibrium constant $K(T, P) = \exp(-G^{\mathrm{BA}}/RT)$. In this case $-\ln K$ is approximated by a first order expansion:

$$\frac{G^{\mathrm{BA}}}{RT} = \lambda(\Delta\hat{T} + a\Delta\hat{P} + b\Delta\hat{T}\Delta\hat{P}). \tag{7.3}$$

The free parameters λ, a, and b describe the entropy difference of A and B at the LLCP, the slope of the LLPT line or the Widom line in the P-T diagram and their curvature.[160] The LLCP and LLPT are defined by the condition $\ln K(T, P) = 0$ where its continuation for temperatures above the LLCP is the Widom line. More specifically, the LLPT line is the region with $\omega > 2$ while the Widom line applies to $\omega < 2$.

It is assumed here that the non-ideal contribution to the entropy of mixing, $\omega x(1-x)$, is symmetric in x. The parameter ω determines the strength of this effect. While a temperature-independent ω describes entropic causes, one finds $\omega \propto \frac{1}{T}$ when the nonideality has enthalpic origin. Previous work with the TIP4P/2005 water model has shown that the data can be well described with[160,188]

$$\omega = \frac{2 + \omega_0 \Delta\hat{P}}{\hat{T}}, \tag{7.4}$$

with $\hat{T} = T/T_{\mathrm{c}}$ and ω_0 as a free parameter. Therefore, this form was also used in this study for all charge-scaled systems.

The concentration at equilibrium x_e is defined by the condition

$$\frac{1}{RT}\left(\frac{\partial G}{\partial x}\right)_{P,T} = \frac{G^{\mathrm{BA}}}{RT} + \ln\left(\frac{x}{1-x}\right) + \omega(1-2x) = 0\,. \tag{7.5}$$

Solutions to this equation must be found numerically. To describe isochoric data, the reduced volume $\hat{V} = \rho_{\mathrm{c}}/\rho$ can be determined by partial derivation of the dimensionless Gibbs energy $\hat{G} = \frac{G}{RT_{\mathrm{c}}}$ with respect to $\hat{P} = \frac{P}{\rho_{\mathrm{c}} RT_{\mathrm{c}}}$:

$$\begin{aligned} \hat{V} = \frac{\partial \hat{G}}{\partial \hat{P}} = \sum_{m,n>0} & n \cdot \hat{c}_{mn} \Delta\hat{T}^{m} \Delta\hat{P}^{n-1} \\ & + x\lambda(a + b\Delta\hat{T}) \cdot \hat{T} \\ & + x(1-x)\omega_0. \end{aligned} \tag{7.6}$$

The pressure that satisfies the given density, and thus the given volume, must be determined. At the same time x must correspond to the equilibrium concentration x_e, and thus satisfy Eq. (7.5). Therefore, the solution is a (P, x) vector that simultaneously satisfies Eq. (7.5) and $\rho = \rho_\mathrm{c}/\hat{V}$ via Eq. (7.6). A constraint is that $\hat{V}_\mathrm{c} = 0.25\omega_0 + \hat{c}_{01} + 0.5\lambda a = 1$ has to be fulfilled at the LLCP.

This optimization problem is solved for each measured state point (T, P, ρ) independently but with the same set of parameters. The parameters of the TSEOS are then determined by a global fit using the calculated and measured pressures. The constraint is not taken into account during the fit. Instead, ρ_c^* is fixed and the real value is calculated as $\rho_\mathrm{c} = \rho_\mathrm{c}^*/V_\mathrm{c}^*$ afterwards. All parameters are scaled accordingly. Below T_c, two solutions with different x are possible. To account for this and to assure convergence, the optimization step is performed twice with a small and large initial guess for x. In case of two solutions, the one closest to the measured pressure is chosen. This is problematic close to the LLCP where the spinodals are close in pressure but not an issue once they are separated by more than the statistical uncertainty of P. Including other thermodynamic variables, e.g., the specific heat capacity c_V, could improve the fit and extend what the fitted model can predict. Because the present study uses only derivatives of $\hat{G}$ with respect to pressure but not to temperature, only parameters occurring in Eq. (7.6) and Eq. (7.5) are determined.

Isochores at low density or isobars at strongly negative pressure can enter the vicinity of the liquid-vapor spinodal where the derivative $\partial P/\partial V|_T$ vanishes. This introduces additional terms into the TSEOS description and has been done recently.[176,188] It increases the accuracy and region of the phase diagram that can be described. In this study, the data is restricted to temperatures and pressures within the vicinity of the LLCP. Explicitly, only temperatures $T < 1.25T_\mathrm{c}$ are used. Higher temperatures can be included, however, their interpretation in terms of HDS and LDS is questionable as perhaps neither is dominating in the disordered simple-liquid regime. Therefore, such additional terms are not used in the present approach.

7.2.3. Observables

Structure Three local structure identifiers, LSI, N_4, and d_5, from Sec. 5.1.4 are used to distinguish between HDS and LDS. For the calculation of all three of them only the distances of neighboring oxygens are relevant. The local structure index (LSI),[316] Eq. (5.12), is a widely proven and accepted measurement to distinguish between separated or joined first and second next-neighbor shells. Small values indicate a narrower distribution of distance differences of next neighbors, and thus identifies HDS. Larger values indicate separated shells and therefore spacious LDS. One may extract the LDS fractions from the probability distribution $p(I)$ as the fraction of values with $I \geq 0.0006\,\mathrm{nm}^2$, denoted in the following with x_LSI. The simple structural identifier N_4 distinguishes HDS from LDS with the number of neighboring molecules within the cutoff alone. Four or less next neighbors indicate a spacious LDS environment while five or more are found for HDS. Values of N_4 of zero and one represent HDS and LDS, respectively. A similar approach was taken previously for water to investigate the LLCP.[210] Additionally, the distance to the fifth neighbor is analyzed and d_5 indicates whether the fifth neighbor is inside or outside the cutoff as zero and one, again representing HDS and LDS.[160] The cutoff distances are $r_{ij} < 0.37\,\mathrm{nm}$ and $r_{ij} < 0.35\,\mathrm{nm}$ for N_4 and I and for d_5, respectively. As found for charge scaling of the SPC/E water model the next-neighbor distances change slightly with strong charge scaling.[117] Here, only a small range of scaling parameters is investigated and, thus, it is assumed that these differences in distances are small enough to not require charge scaling dependent cutoffs. More parameters have been investigated with MD simulations of water in detail, for example ζ by Shi et al.,[336] but their advantages appear when single molecules and temperatures further from the presumed LLCP are investigated. Here, averages over subsets are calculated and temperatures probe deep into the supercooled regime and, thus, the simplest structural identifiers with the least assumptions suffice. For higher temperatures, N_4 and d_5 will falsely identify local structures with 3 next neighbors as LDS while they naturally appear in the disordered liquid state. The tetrahedral order parameter is not employed because of its broad distribution of values and, thus, inaccuracy in distinguishing structure, as is shown in Sec. 6.1.

Dynamics One expects for the water-like molecules growing fluctuations of local structure with decreasing distance to the LLCP and, hence, possibly significant dynamical heterogeneity. The mean-square displacement (MSD), see Sec. 5.2.2, is analyzed to characterize the long-range translational motion. The self-diffusion coefficient D is thus averaged over all dynamical heterogeneities.
Local dynamics is probed with the reorientation of the O–H bond vectors of the water-like molecules by computing the rotational correlation function (RCF), see Sec. 5.2.3, with the Legendre polynomial of rank 1, $F_{1,\mathrm{OH}}(t)$. Because the vibrational decay and the dynamical heterogeneity vary between different thermodynamic paths, fits of the RCF beyond the vibrational regime to a scaled Kohlrausch-Williams-Watts (KWW) function are used to calculate the mean correlation time, see Sec. 2.1.2. This allows for comparable dynamics between the different thermodynamic paths but limits the analysis to temperatures where vibrational and terminal relaxation are well separated.

Spatially-resolved analysis In the vicinity and below the LLCP in the metastable region one observes spatial structuring of HDS-rich and LDS-rich regions into layers in the xy plane. In this study, these spatial and temporal structural fluctuations are analyzed with layers of thickness $\Delta z = 1\,\mathrm{nm}$, aligned with the xy plane. Determining the layer-averaged density and structural identifiers along the trajectory one can investigate their evolution in time. Here, it is distinguished between following a reference molecule or a position fixed in space. The former measures the change of the environment as experienced by the particles in time and takes into account a change of the environment by translation. The latter corresponds to the macroscopic observation in the laboratory system.

To analyze the structural fluctuations in time, the layer-averaged quantities $\xi_{\mathrm{L}}(t)$, where ξ is the density ρ or a structural identifier, i.e., ρ_{L}, $x_{\mathrm{LSI,L}}$, I_{L}, $N_{4,\mathrm{L}}$, and $d_{5,\mathrm{L}}$ are defined. One averages over all molecules or reference positions z to obtain z- and t-dependent values of the layer-averaged structural properties. For $N = 2000$, layer averages contain about 250 molecules. While this is comparable to ensemble averages of some simulation studies, it is still small enough to cause artifacts because of discretization. To analyze the temporal aspect of the fluctuations as a whole, the autocorrelation functions of the layer-averaged quantities are calculated,

$$C_\xi(t) = \frac{\langle \xi_{\mathrm{L}}(t+t_0)\xi_{\mathrm{L}}(t_0)\rangle - \langle \xi_{\mathrm{L}}\rangle^2}{\sigma_\xi^2}\,, \tag{7.7}$$

where ξ_{L} is the respective random variable, σ_ξ is its standard deviation, and averages are over molecules or reference positions. Consistent with the rotational correlation function $F_{1,\mathrm{OH}}$, fits of KWW functions to the terminal decay are used to determine the average correlation time τ_ξ of these fluctuations. Vibrations and the numerical precision and small number of particles lead to rapid changes of the structural properties within these layers. For example, particles leaving and entering the layer volume because of vibrations already leads to broadening of the local density on the vibrational time scale. Higher volume to surface ratios would suppress this effect. Here, the structural properties are averaged over the time scale of molecular vibration. As these artificial fluctuations should be irrelevant for local dynamics more accurate results are expected. To investigate the relation between local structure and dynamics, $F_{1,\mathrm{OH}}(t)$ is averaged over subsets of molecules with different local environments. For example, molecules are distinguished by different layer-averaged properties at the time origin t_0 and during the time scale of vibration with the layer centered around the molecule as defined above.

7.3. TSEOS analysis

The investigation begins with the P-T diagram of isochoric data of the charge-scaled TIP4P/2005 system, with the pressure calculated from the virial stress tensor. Typically, liquids show a monotonic decrease in pressure P when the temperature T is reduced at constant density. For all charges, one observes that the pressure decreases with temperature for all isochores as long as density or temperature is sufficiently high, see Fig. 7.1 and Fig. A.5. However, it increases at lower temperatures for isochores with sufficiently small densities. This phenomenon can be found in systems of two competing liquid phases with different densities. In particular, a crossing of isochores in the P-T diagram indicates an LLPT.[4,25,169,337] Indeed, such isochore crossing is found for appropriate intermediate densities and the lowest temperatures. The metastable region, where isochores cross, can be studied to some extent. The highest temperature for which isochore crossing is observed and the corresponding pressure and density mark the LLCP. The same qualitative behavior is observed for all studied charge scalings.

With the crossing of isochores as evidence of the existence of two competing liquid states, one may now use the TSEOS approach to examine the simulation data in more detail. The TSEOS is fit to pressures close to the LLCP and the results are shown as solid lines in Fig. 7.1. One observes for all charges that the TSEOS describes the simulation data very well near the LLCP, consistent with previous studies for various tetrahedral liquids.[160,161,168,188] The parameters from fitting the TSEOS to the data and the respective locations of the LLCPs are summarized in Tab. 7.1. Parameters of smaller order in $\hat{T}$ and $\hat{P}$, i.e., ω_0, λ, a, b, and $\hat{c}_{01}$, have similar values for different charge scaling factors q but scatter without a notable trend. On the other hand, the location of the LLCP shifts significantly and monotonically. Hence, the properties at the LLCP and the shape of the LLPT in the immediate vicinity are not influenced significantly by this approach. However, they do not quite agree within their scattering with results for the original TIP4P/2005 model.[160] Parameters relevant in higher order terms vary strongly. This is unsurprising, since the temperatures and densities studied are close to the LLCP and no higher thermodynamic derivatives are included and the TSEOS is slightly overparameterized. The high uncertainty of these parameters is not of concern here, because only the accurate determination of the LLCP and description within its vicinity are relevant to this study.

Next, the dependence of the location of the LLCP, as identified by the critical temperature T_c, pressure P_c, and density ρ_c, is studied as a function of the charge-scaling factor q, see Fig. 7.2. The results for all three properties show monotonous reduction with reduced polarity. A similar observation was made for the WAC model of silica for which the partial charges of the ions were reduced.[25] Hence, these findings are explained with the dependence of the critical parameters on the strength of the Coulomb interactions. For water and these water-like models, a significant fraction of the potential energy is caused by hydrogen bonding. Reducing the partial charges reduces the binding energy and the scale of relevant thermal energies and, hence, T_c. With the hydrogen bonds and, thus, the tetrahedral local configurations weakened, less energy or force is required to disturb the local order with a fifth molecule within the next-neighbor shell. This means that P_c is expected to decrease with the partial charges and, in particular, it moves to negative pressure when the partial charges are reduced by more than 10 %. For the density it is important to note that the LJ potential for two oxygen atoms has its minimum at larger distances than found for the next-neighbor distance

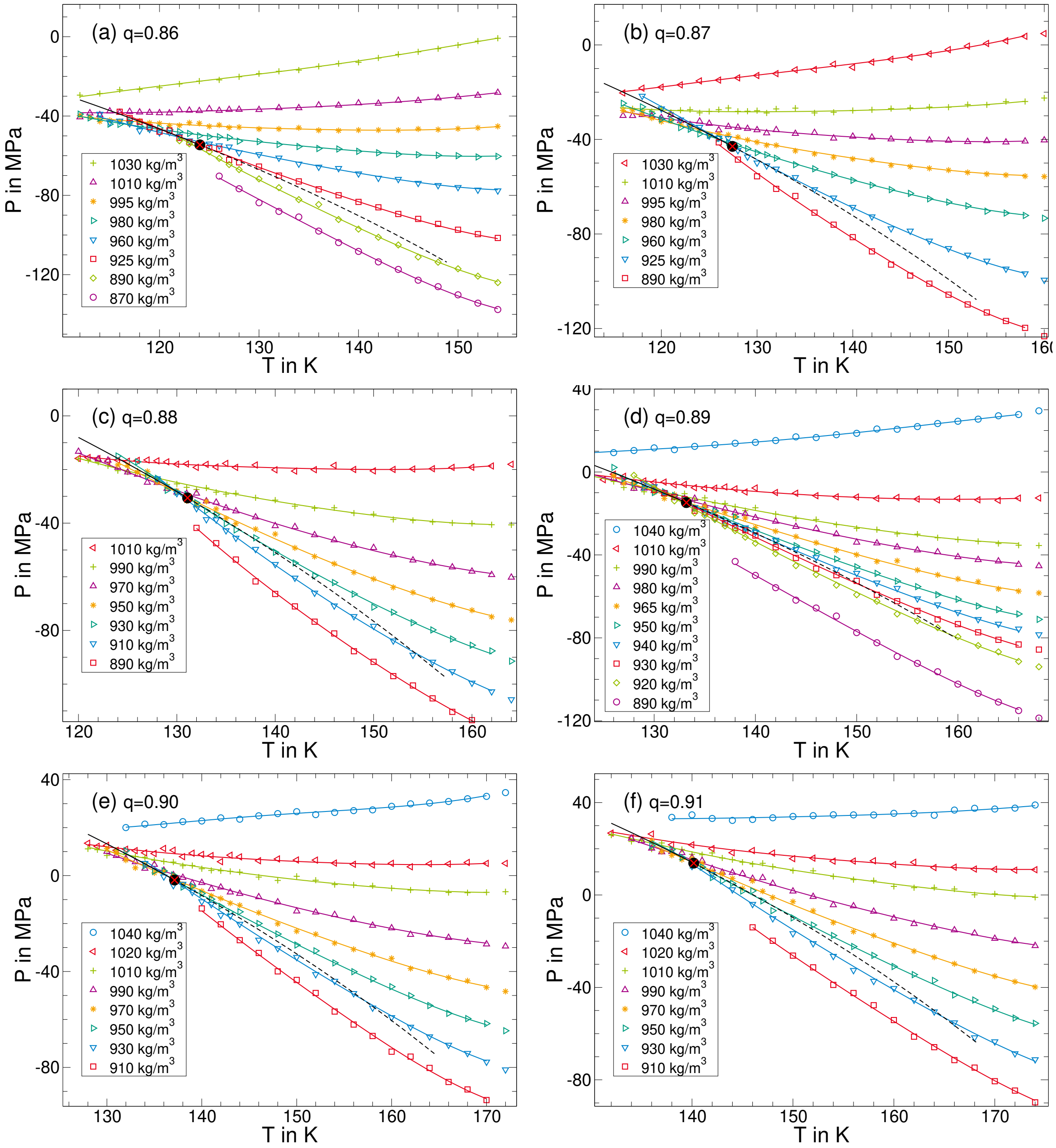

Figure 7.1.: Isochore data of the charge-scaled TIP4P/2005 water model in the P-T diagram in ascending order from $q = 0.86$ (a) to $q = 0.91$ (f). The respective densities are given in the legend. The colored solid lines are the result of the TSEOS analysis and indicate the data points that were included in the fit routine. The red crosses on black circles mark the position of the LLCP, the black solid lines are the LLPT, and the black dashed lines the Widom line. Note, that the axis range varies between the graphs. For a wider range of temperatures and pressures, see Fig. A.5 in the appendix.

Table 7.1.: Parameters of the TSEOS and locations of the LLCPs for charge-scaled TIP4P/2005 with scaling factors $q = 0.86$–0.91. Only parameters $\hat{c}_{mn}$ that occur in fitting the pressure are shown.

Parameter	0.86	0.87	0.88	0.89	0.90	0.91
T_c in K	124.1	127.4	131.1	133.2	137.1	140.2
P_c in MPa	-54.54	-42.94	-30.6	-14.75	-1.86	13.78
ρ_c in kg/m^3	923.2	928.2	935.9	947.2	948.3	955.8
ω_0	0.09164	0.1106	0.1056	0.06734	0.1025	0.1072
λ	1.478	1.551	1.538	1.434	1.563	1.602
a	0.211	0.1994	0.1996	0.2107	0.1984	0.1977
b	-0.161	-0.1551	-0.1518	-0.163	-0.1647	-0.1925
$\hat{c}_{01}$	0.8211	0.8177	0.8201	0.8321	0.8193	0.8148
$\hat{c}_{02}$	0.00321	0.005705	0.009058	0.002807	0.008431	0.01531
$\hat{c}_{11}$	0.1339	0.1536	0.1594	0.1029	0.1579	0.2198
$\hat{c}_{12}$	-0.06196	-0.07647	-0.08927	-0.05013	-0.06727	-0.1654
$\hat{c}_{21}$	-0.2146	-0.2262	-0.2965	0.001027	-0.2012	-0.4412
$\hat{c}_{22}$	0.2848	0.2742	0.2343	0.1773	0.0872	0.5909
$\hat{c}_{31}$	0.6568	0.5172	0.6825	0.09845	0.4062	0.8121
$\hat{c}_{23}$	-0.008097	-0.01679	0.004091	-0.01736	-0.05696	0.006732
$\hat{c}_{32}$	-0.6706	-0.5275	-0.3187	-0.3932	-0.01522	-0.927
$\hat{c}_{33}$	0.06347	0.1267	0.01144	0.07191	0.2536	0.008787

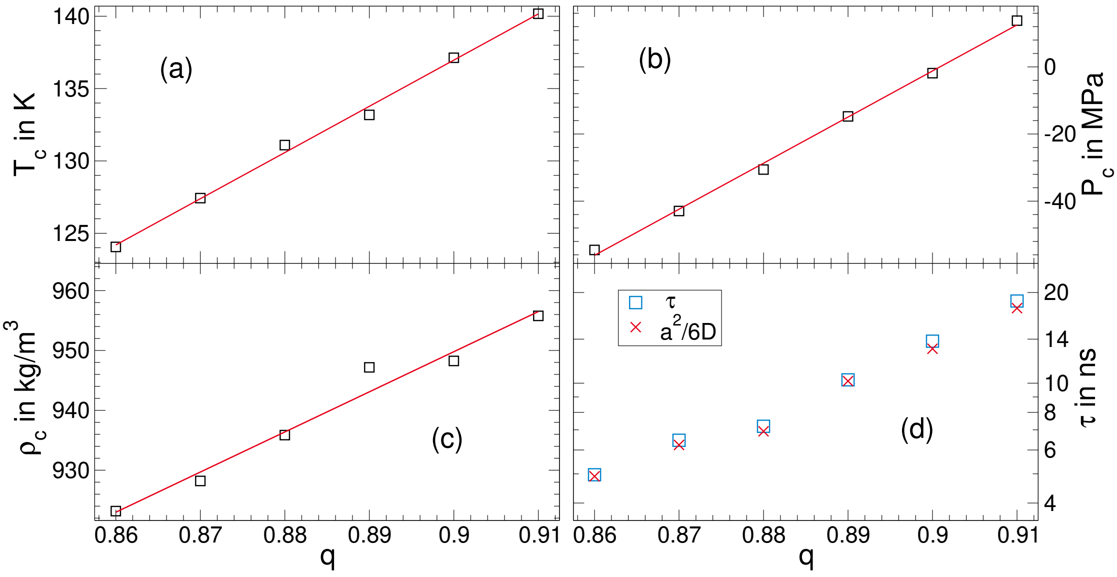

Figure 7.2.: Critical parameters from the TSEOS analysis as a function of the charge-scaling factor q: (a) critical temperature T_c, (b) critical pressure P_c, and (c) critical density ρ_c. The solid lines are linear fits. (d) Rotational correlation times τ and jump times $a^2/6D$ at the LLCP. A jump length of $a = 0.325$ nm, which is between the first and second neighboring shells, is used to calculate the jump time from the self-diffusion coefficient. D and τ at the LLCP were determined by interpolation, see text for further details.

in water. The attractive Coulomb interactions pull the molecules closer than they would be without them. Thus, the local tetrahedral order stretches and the density ρ_c decreases with decreasing q.

To verify the TSEOS result, the density ρ during isobaric cooling at atmospheric pressure is examined in Fig. 7.3. As expected, one finds that ρ decreases very rapidly for higher charges while such jumps are not observed for lower q. For the lower charge scalings, $q < 0.89$, the critical pressure P_c is far enough below the atmospheric pressure, see Tab.7.1, for the system to enter the HDL phase and ρ to increase continuously in the studied temperature range. For $q = 0.91$, P_c is above 1 bar and, thus, the system crosses the Widom line. Rapid increase of the fraction of LDS leads to a decrease in ρ upon cooling. In particular, P_c is only just below 1 bar for $q = 0.9$ and the metastable region is entered upon cooling leading to a jump from HDL to LDL and a discontinuity in density. Because of its proximity to P_c the jump occurs at $T = 137\,\mathrm{K} \approx T_c$, see Tab. 7.1. The results for $\rho(T)$ at atmospheric pressure confirm the results of the TSEOS analysis.

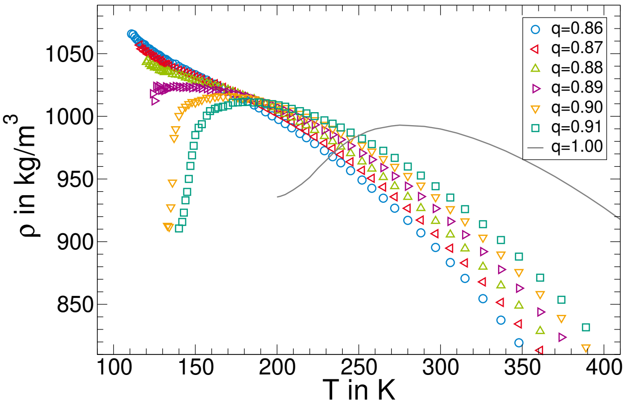

Figure 7.3.: Temperature-dependent density ρ of the charge-scaled TIP4P/2005 water models for isobars at atmospheric pressure, $P = 1$ bar. The scaling factors q are given in the legend. The gray line is the original TIP4P/2005 model but without long-range LJ interactions and, thus, effectively at reduced pressure.

Table 7.2.: Location of the LLCP of the regular TIP4P/2005 model as found by different studies.

Study	T_c in K	P_c in MPa	ρ_c in kg/m^3
Abascal 2010[158]	193	135	1012
Sumi 2013[159]	182	158-162	1020
Yagasaki 2014[338]	185	–	1020
Singh 2016[160]	182	170	1017
Handle 2018[339]	175	175	997
Debenedetti 2020[162]	177	175	–
Extrapolation	169	136	1017

One may extrapolate the apparently linear dependence of the critical parameters on the scaling factor to $q = 1$ to determine the respective values for the original TIP4P/2005 model. $T_c = 169\,\mathrm{K}$, $P_c = 136\,\mathrm{MPa}$ and $\rho_c = 1017\,\mathrm{kg/m^3}$ are obtained this way. The values for T_c and P_c are smaller but still close to those found in the literature for the TIP4P/2005 model, see Tab. 7.2.[158–160,162,338,339] The critical density ρ_c lies within the range of the critical densities found. The deviations are most probably a consequence of the extrapolation of q over twice the range studied and the assumption of a linear dependence over a larger parameter range of q might not be adequate.

7.3.1. The specific heat anomaly

Before focusing on the microscopic structure and the effects on the dynamics of the system, it can be shown that other expectations for thermodynamic properties are well observable in the simulations. For example, the thermodynamic derivative c_P, the specific heat, can be calculated from fluctuations of the enthalpy $H = U + PV$,

$$c_P = \frac{\langle H - \langle H \rangle \rangle^2}{k_\mathrm{B} T^2} \,. \tag{7.8}$$

Figure 7.4(a) presents the results at atmospheric pressure and for reduced partial charges. Consistent with Fig. 7.3, systems with $q < 0.89$ do not cross the Widom line and, accordingly, a moderate increase of c_P upon cooling is observed. However, the Widom line is crossed for $q \geq 0.9$ and a sharp peak appears at low temperatures. There, fluctuations in enthalpy are larger when interconversion of HDL and LDL is prominent. The peak is higher for the system with $q = 0.9$, for which the distance to the LLCP is smaller at atmospheric pressure. For $q = 0.89$, a sharp increase to $c_P > 600\,\mathrm{J/(mol{\cdot}K)}$ is found. However, dynamics are slow and the system is difficult to equilibrate increasing the uncertainty. It is possible that the system is close to its LLPT line. At high temperatures an increase in c_P is observed when the systems approach their boiling point.

Figure 7.4(b) presents the data for several isobars. Equivalently, a peak at low temperatures is found when the pressure is below $P_\mathrm{c} = -55\,\mathrm{MPa}$ and the Widom line is crossed. Again, the peak height increases with decreasing distance to the LLCP. The isobars above the critical pressure never cross the LLPT or Widom line in the simulated temperature range, see Fig. 7.1(a), and, thus, exhibit monotonous growth of c_P. Note, that increasing P and compressing the system even further increases c_P. These observations are consistent with water's anomalies upon crossing the Widom line.

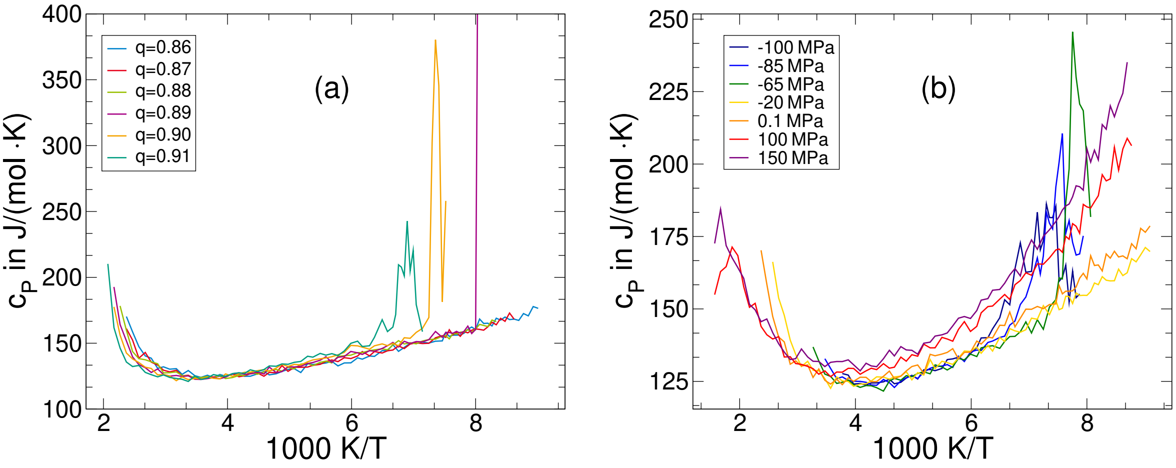

Figure 7.4.: (a) The temperature-dependent isobaric specific heat c_P per mole molecules of the charge-scaled TIP4P/2005 model (a) for different charge-scaling factors and atmospheric pressure and (b) $q = 0.86$ and several pressures.

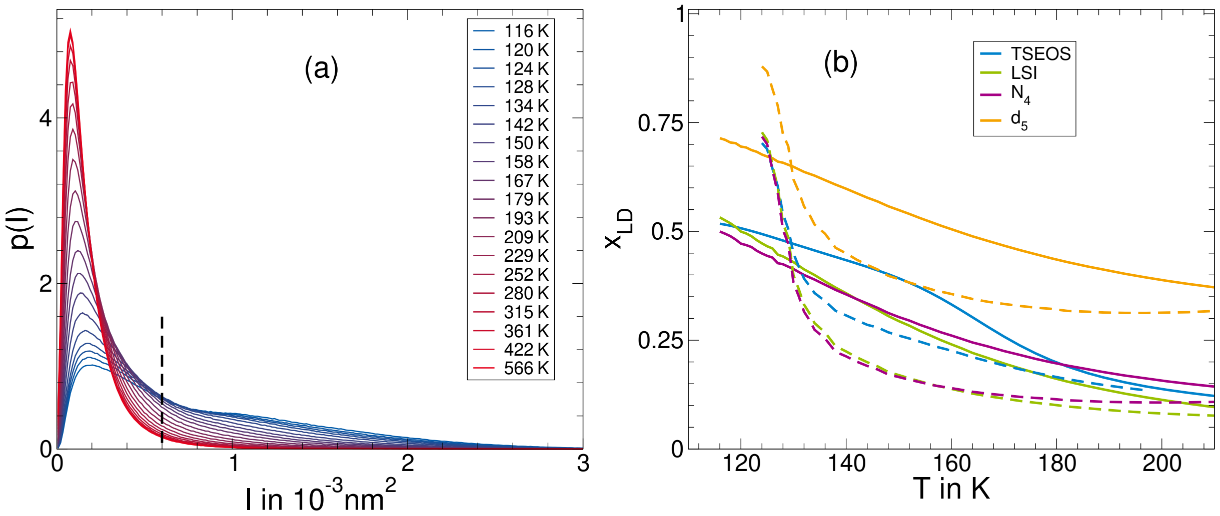

Figure 7.5.: Temperature dependence of the local structure identifiers for the charge-scaled TIP4P/2005 model with $q = 0.86$ along the isochore with the density $\rho = 925$ kg/m^3 $\approx \rho_c$. The critical temperature is $T_c = 124$ K. (a) Probability distribution of the LSI $p(I)$ at the indicated temperatures. The dashed line separates I values typical of HDS and LDS. (b) Temperature dependence of fractions of LDS x_{LD}. In particular, the equilibrium concentration from the TSEOS analysis and LDS fractions determined with the criteria $N_4 = 1$, $I \geq 0.0006$ nm^2 and $d_5 > 0.35$ nm are shown. The results obtained for the isochores with $\rho = 925$ kg/m^3 (solid lines) are compared to the data from the isobars with $P = -65$ MPa (dashed lines), which is close to the critical density $P_c = -55$ MPa.

7.4. Structure and dynamics

After determining the LLCP of the charge-scaled TIP4P/2005 water models, their structure is studied. Shown are the results for structural identifiers using the example of $q = 0.86$ and the density closest to the critical density, $\rho = 925\,\text{kg/m}^3 \approx \rho_c$, in Fig. 7.5.

The distribution of the structural identifier LSI is weakly bimodal, see Fig. 7.5(a). A second peak at larger values $I \approx 0.0011\,\text{nm}^2$, corresponding to the more spacious LDS appears for lower temperatures and grows at the cost of the HDS peak at $I \approx 0.0002\,\text{nm}^2$. Both have broad distributions due to the fact that trajectories of real dynamics were analyzed instead of inherent structures, i.e., energy-minimized configurations. For these, the separation of the two peaks is more prominent and they shift to larger values.[326] Still, these results show that at high temperatures only structures with continuously increasing next-neighbor distances are preferred and that upon cooling down to the LLCP and into the metastable regime LDS becomes relevant and its fraction increases. However, phase separation into extended HDL and LDL phases is not observed in the case of cubic systems at any of the temperatures studied.

In order to analyze the conversion from an HDL-like to an LDL-like liquid in more detail, the temperature dependence of the LDS fraction is determined. To do so, one distinguishes HDS and LDS with the criteria $N_4 = 1$, $I \geq 0.0006\,\text{nm}^2$, and $d_5 > 0.35\,\text{nm}$, where $I = 0.0006\,\text{nm}^2$ lies approximately between the peaks in $p(I)$. Figure 7.5(b) shows that the fraction of LDS x_{LD} obtained from the different structural identifiers and from the TSEOS analysis slowly increases as the temperature is decreased along the shown isochores with $\rho \approx \rho_c$. That x_{LD} grows with cooling also holds for all studied

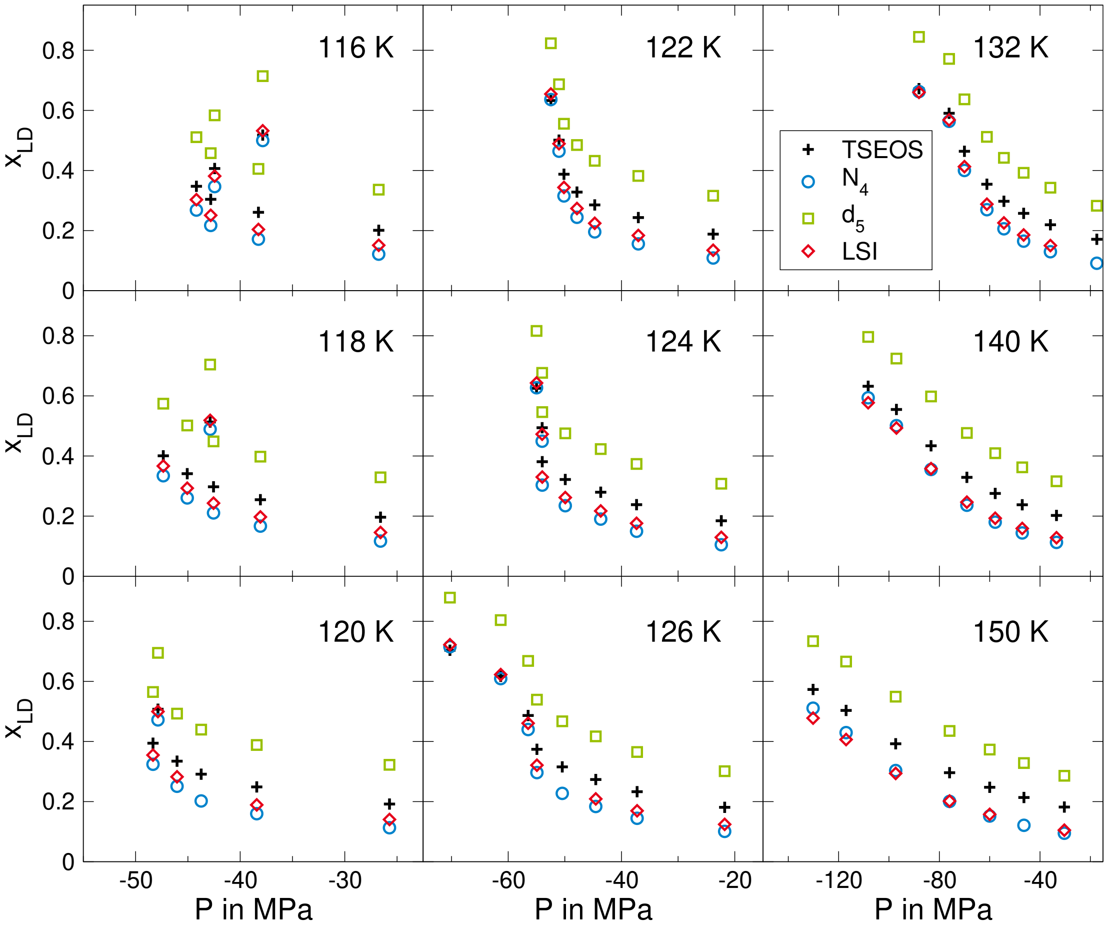

Figure 7.6.: Pressure dependence of the fraction of LDS, x_{LD}, for the charge-scaled TIP4P/2005 water model with $q = 0.86$ at the indicated temperatures. The critical pressure is $P_{\mathrm{c}} = -55$ MPa and the critical temperature is $T_{\mathrm{c}} = 124$ K, see Tab. 7.1. The fractions are determined with the criteria $N_4 = 1$ (blue circles), $d_5 > 0.35$ nm (green squares) and $I \geq 0.0006$ nm^2 (red diamonds) and are shown together with the fraction as determined from the TSEOS analysis (black pluses).

densities but may be violated for more extreme cases. In contrast, a rapid increase of x_{LD} near T_{c} occurs when a system with $P \approx P_{\mathrm{c}}$ is cooled under isobaric conditions. The pressure dependence of x_{LD} at characteristic temperatures is presented in Fig. 7.6. The various properties differ quantitatively but show qualitatively consistent behavior. For most studied state points, the values of x_{LD} obtained with I and N_4 are smaller than those of the TSEOS analysis while the values for d_5 are larger. However, it should be noted here that the absolute values depend on the chosen limits. The pressure dependence changes qualitatively with temperature. Significantly above T_{c}, x_{LD} gradually decreases with increasing pressure and near T_{c} one observes a sharp step as the pressure is increased above P_{c}. Significantly below T_{c}, a re-entrant behavior of x_{LD} is found for all structural quantities as a function of pressure because of the existence of two possible compositions, HDL and LDL, with minima in the Gibbs energy. This means that the pressure as a function of x_{LD} or ρ is no longer injective, unlike in a normal liquid. Exploring states below the LLCP for the original TIP4P/2005 water model is computationally more expensive and, thus, these results have not been found for previous studies on it. This is a further argument for the presented charge scaling approach which allows the study of the LLPT in more detail.[160]

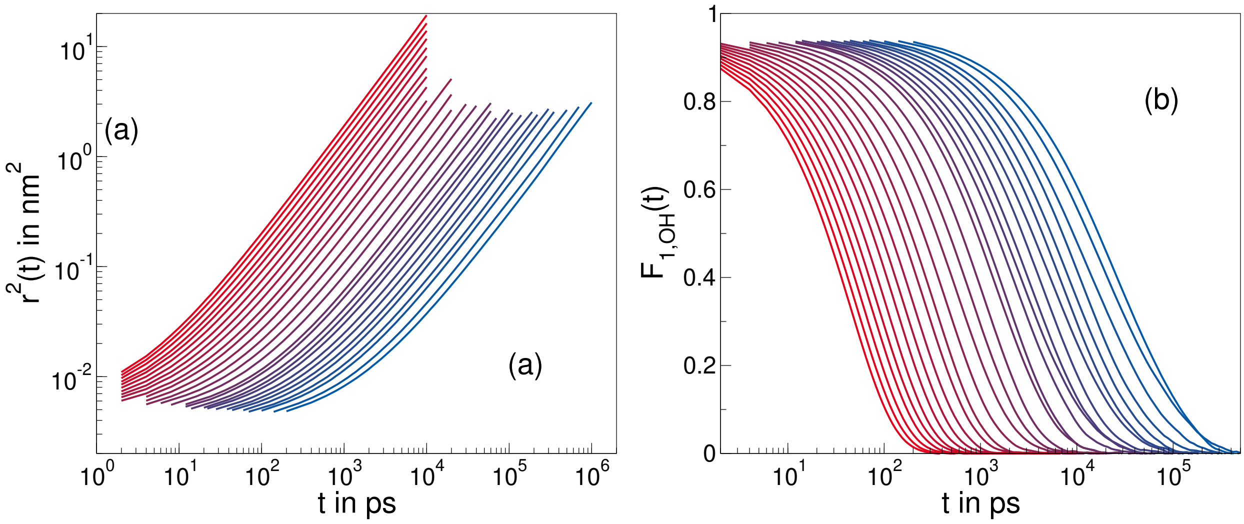

Figure 7.7.: The (a) MSD $r^2(t)$ and (b) RCF $F_{1,\mathrm{OH}}(t)$ exemplary for the charge scaled TIP4P/2005 water model with $q = 0.86$. Data for the isochore with density $\rho = 925\,\mathrm{kg/m^3} \approx \rho_\mathrm{c}$ for temperatures from $158\,\mathrm{K}$ (red) to $116\,\mathrm{K}$ (blue) are shown. The critical temperature of this system is $T_\mathrm{c} = 124\,\mathrm{K}$.

One observes a significant slowdown of translational and rotational dynamics with decreasing temperature, as measured by the MSD and RCF respectively, see Fig. 7.7. To quantify the dynamics, the self-diffusion coefficient D and the mean correlation times τ, as described in Sec. 2.1.2, are determined from $r^2(t)$ and $F_{1,\mathrm{OH}}(t)$, respectively. The same analysis was performed for all isochores and isobars. Evidence of bimodal dynamics, as expected for coexisting HDL and LDL regions with differing mobility, is not found for any of the systems with cubic geometry. This is consistent with the finding that no phase separation was observed. In detail, it was investigated in App. A.2.3 whether or not $F_{1,\mathrm{OH}}(t)$ must be described with one or two components, i.e., a biexponential behavior. A single KWW function appropriately characterizes the correlation function while the same is not the case for elongated systems, studied in Sec. 7.5.

The determined self-diffusion coefficients and correlation times of the charge-scaled TIP4P/2005 water model with $q = 0.86$ obtained for different isochores and isobars are presented in Fig. 7.8. One finds that the translational and rotational dynamics slow down significantly when the density is reduced near ρ_c. This is consistent with the dynamical anomaly as found for real water and other tetrahedrally ordered systems such as silica.[2,25] No evidence of changes in the temperature behavior near the LLCP when cooling along isochores is found. In particular, no FST for the density $\rho = 925\,\mathrm{kg/m^3} \approx \rho_\mathrm{c}$ exists in the studied temperature range. In fact, all self-diffusion coefficients and correlation times of the shown isochores can be described sufficiently by a Vogel-Fulcher-Tammann (VFT) equation, where τ_0, B, and T_0 are second-order polynomial functions of the density. This is contrasted by a high-temperature dependence for cooling under isobaric conditions with pressures below but close to $P_\mathrm{c} = 55\,\mathrm{MPa}$.

In particular, the temperature dependence of $D(T)$ for isochores and isobars is similar for sufficiently high or low temperatures while it is significantly stronger under isobaric conditions and $P < P_\mathrm{c}$ near the LLCP. A sigmoidal shape is observed, see Fig. 7.8(b). The same features were also

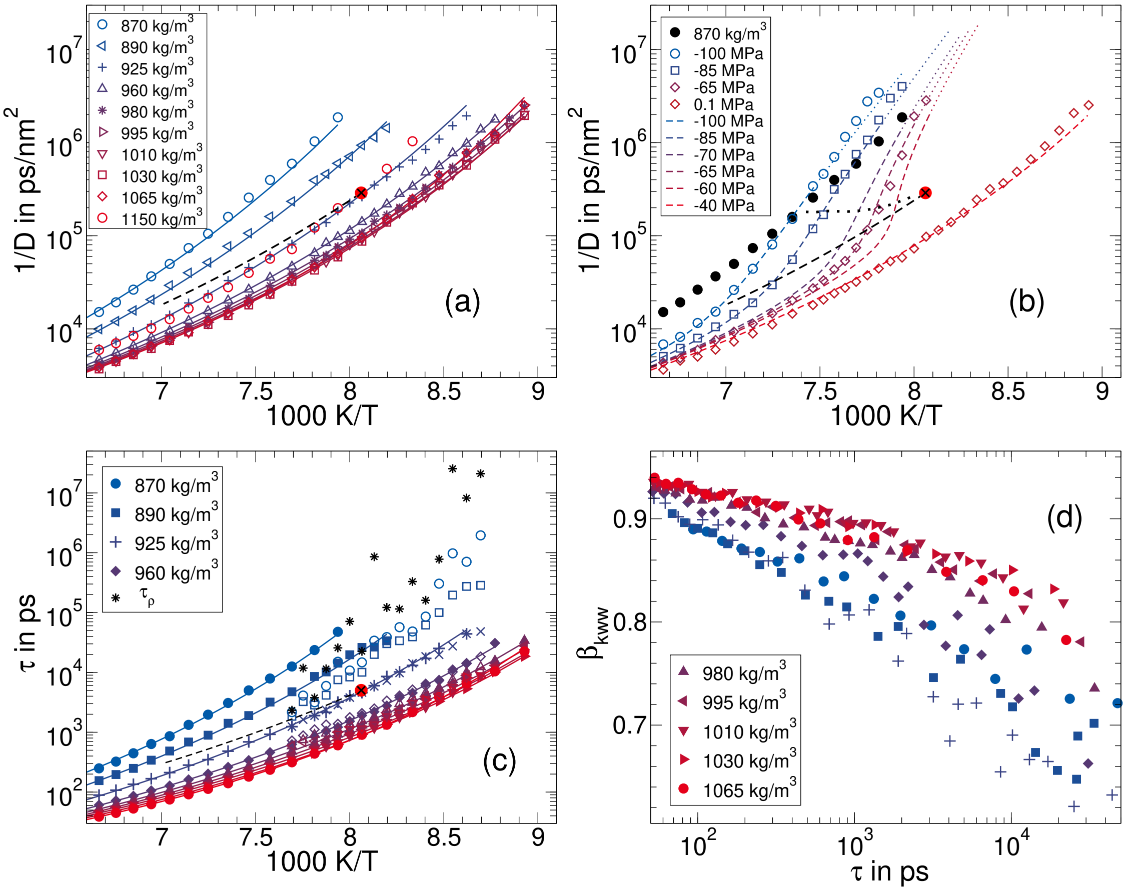

Figure 7.8.: The temperature dependence of dynamics for charge-scaled TIP4P/2005 with $q = 0.86$ near the LLCP. The reciprocal self-diffusion coefficients $1/D$ are presented (a) along isochores and (b) along isobars. The isochore closest to the critical density is 925 kg/m^3 $\approx \rho_{\text{c}}$. The solid lines in (a) and (c) are fits with VFTs, see text. In (b), the colored dashed lines are $1/D$ at the indicated pressures P interpolated from the observed behavior along the isochores and the information from the TSEOS analysis, see text. The colored dotted lines are extrapolations of these behaviors. The black dotted line marks the location of inflection points for isobars calculated from the TSEOS and the VFT fits.
(c) Mean rotational correlation times τ determined from KWW fits to $F_{1,\text{OH}}$ correlation functions. For the stretched systems with phase separation, spatially resolved correlation times τ_{L} (open symbols) were determined for layers with mean density equal (± 5 kg/m^3) to the simulated isochores of the cubic systems (filled symbols). The time scales τ_ρ on which layer-averaged densities ρ_{L} fluctuate are calculated with the autocorrelation functions $C_\rho(t)$. In this case, the centers of the layers follow the reference molecules. The crosses show the results along isochores with density $\rho = 925$ kg/m^3 $\approx \rho_{\text{c}}$.
(d) Stretching parameters β_{kww} of the same KWW fits to $F_{1,\text{OH}}$ as in (c). In (a)–(c), $1/D$ and τ at the LLCP are marked by a black cross on a red circle and the black dashed lines show the interpolated values on the Widom line. The legends in (c) and (d) apply to both graphs.

found for rotational correlation times $\tau(T)^{340}$ and they have also been found for ST2 model of water.[341] Comparing the results for different pressures P, one observes that the onset of the enhanced temperature dependence is within the vicinity of the Widom line. These observations are consistent with findings of a stronger temperature dependence of the self-diffusion coefficients along isobars compared to isochores near the LLCP.[121,210,213,219] The moderate and rapid transition from an HDL-like liquid to an LDL-like liquid upon isochoric and isobaric cooling, respectively, below T_c are accompanied by corresponding changes in translational and rotational dynamics. This is a strong indication of a structural origin of the FST.

The shape of the terminal decay $F_{1,\mathrm{OH}}(t)$ contains information about how broadly distributed or inhomogeneous the rotational dynamics of the molecules are. The stretching parameters β_kww of KWW fits to the data are shown in Fig. 7.8(d) for isochores of the charge-scaled TIP4P/2005 water model with $q = 0.86$. This analysis is only possible in the supercooled regime where vibrational and α-relaxation are well separated. Hence, β_kww is shown only for $\tau > 50\,\mathrm{ps}$. By plotting β_kww as a function of the correlation time one can compare isokinetic points and is independent of the strong slowdown with decreasing density. This better represents the degree of supercooling from a dynamical point of view. For all isochores a decrease of the stretching parameter with cooling is found. The non-exponentiality of the decays increases as the dynamics slows down. Close to the LLCP the structural heterogeneity of mixed and fluctuating LDS and HDS and their respective dynamics should enhance the signs of dynamical heterogeneity, e.g., a significant drop of $\beta_\mathrm{kww}(\tau)$ or even a minimum.[336] No strong indication of such behavior is found and $\beta_\mathrm{kww}(\tau)$ decreases monotonically. The slight increase for the isochore with density $\rho = 890\,\mathrm{kg/m^3}$ is within error and does not appear for isochores with other scaling parameters q. However, it should be taken into account that for the cubic systems the phase separation remains suppressed while it causes biexponentiality for the elongated systems, see Fig. 7.12. Hence, the structural and dynamical heterogeneity may be suppressed to some degree as well. One finds that for a given τ the stretching parameter decreases with density. The density dependence of $\beta_\mathrm{kww}(\rho)$ does not appear to be monotonic and shows a weak minimum at $\rho \approx \rho_\mathrm{c}$. Thus, these results indicate that the dynamical heterogeneity increases with increasing LDS fraction and maximizes for a 50:50 mixture, though the limited temperature range beyond the LLCP prevents conclusive evidence. It is the concentration rather than fluctuations that determine the dynamical heterogeneity.

Next, the knowledge of the VFT parameters as functions of density ρ, $\tau_0(\rho)$, $B(\rho)$, and $T_0(\rho)$, from the previous analysis is exploited to interpolate the self-diffusion coefficient D_c and the correlation time τ_c at the LLCP. Translational and rotational dynamics at the critical point become significantly faster for smaller scaling parameters q and, hence, weaker hydrogen bonding, see Fig. 7.2. This means that the charge scaling approach leads to a more easily accessible LLCP. This is taken advantage of later on when phase separated elongated systems are studied. Additionally, one finds that the q dependence of the self-diffusion coefficients at the LLCP can be translated into correlation times with the relation $a^2 = 6D_\mathrm{c}\tau_\mathrm{c}$. Here, the jump length is $a = 0.325\,\mathrm{nm}$, a distance between the first and second neighboring shells. This means that short- and long-range dynamics at the critical point have the same relation for all water-like models. Differences in length scale a arising from the reduction of the critical density are about 3%, and are thus not significantly larger than the inaccuracy of the dynamical quantities, see Fig. 7.9.

The Stokes-Einstein Debye relation, Sec. 2.1.3, can be used to compare the temperature dependence of diffusion and correlation times. The hydrodynamic radius $R_\mathrm{H} = \sqrt{\frac{3}{2}D\tau}$ is a measure that follows directly from the equation. In Fig. 7.9(a), the jump lengths, proportional to the hydrodynamic radius, are shown as an example for the TIP4P/2005 model with the smallest scaling factor studied $q = 0.86$. Values in the literature for the jump length with rotational correlation times measured with $F_{2,\mathrm{OH}}(t)$

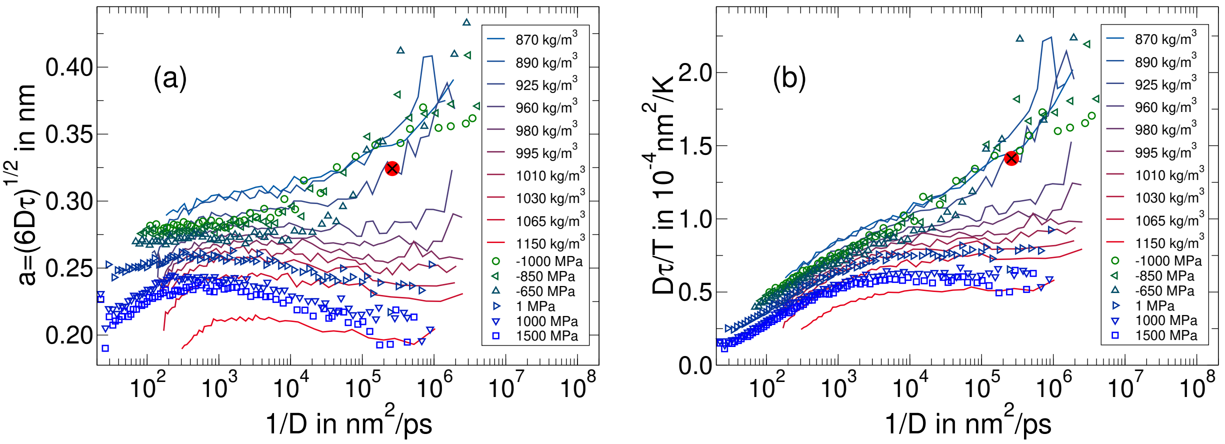

Figure 7.9.: The jump length $a = \sqrt{6D\tau}$ (a) and the alternative test of the SED relation with $D\tau/T$ (b), calculated from self-diffusion coefficients D and rotational correlation times τ measured with $F_{1,\mathrm{OH}}(t)$, as function of the dynamics $1/D$ for charge-scaled TIP4P/2005 with $q = 0.86$. For clarity, solid lines are connections of points for isochores with the indicated densities. Symbols are results for isobars at the indicated pressures. The value closest to the LLCP, with $T = 124$ K$\approx T_\mathrm{c}$ and $\rho = 925$ kg/m$^3 \approx \rho_\mathrm{c}$, is marked by a black cross on a red circle.

are 0.289 nm, 0.253 nm, 0.219 nm and 0.257 nm for water in bulk solution, in silica pores, in mixture with a polysaccharide and with an ionic liquid, respectively.[342,343] Rotational correlation times with Legendre polynomials of different rank are only comparable when large-angle jumps are performed instead of rotational diffusion, which is the observed trend towards the lowest temperatures for example in Fig. 9.22(b). Considering that atmospheric pressure is below the suspected critical point and similar isobars for the charge scaled water have $a \approx 0.275$ nm in the one-phase regime,[342] the range of values covered by the different isochores and isobars is not unreasonable. Alternatively, in some systems, viscosity and correlation time are found to have the same temperature dependence. For completeness, the temperature dependence of $D\tau/T$, Fig. 7.9(b), is studied as well. For comparison at isokinetic state points, both quantities are shown as a function of $1/D$. A monotonic increase of a and $D\tau/T$ with decreasing density is found for similar dynamics. This means that the short-range rotation slows down stronger than the long-range translation with decreasing density. For isochores with densities much higher than ρ_c, one observes a slight decrease in the jump length upon supercooling whereas for densities with $\rho < \rho_\mathrm{c}$, a pronounced increase in a is found. Under isobaric conditions, the corresponding behavior is found for $P < P_\mathrm{c}$ and $P > P_\mathrm{c}$, respectively. Towards very high temperatures, the jump length decreases for all densities. However, one observes a plateau under isobaric conditions, possibly because the expansion during heating compensates for the effect at constant density. Note the high similarity of Fig. 7.9(a) and Fig. 6.7(a) which shows the qualitative equivalence of moving the location of the LLCP by charge-scaling or shifting the path in the phase diagram with pressure or density. $D\tau/T$ shows some qualitative differences. For example, no plateau is seen at high temperatures even under isobaric conditions. Instead, the data for isobars and isochores shows a plateau at low temperatures and sufficiently above P_c and ρ_c, respectively. This observation has also been found previously for the ST2 water model.[327]

Commonly, in supercooled liquids, one finds that, as temperature decreases, the jump length and $D\tau/T$ increase, which is attributed to the growth of dynamical heterogeneity, see also Sec. 2.1.3.[73–75]

For now, this is consistent with the observation that the violation of the SED relation at the same dynamics is stronger for lower densities where the stretching parameter of the correlation functions is also smaller at similar dynamics, see Fig. 7.8(d). But despite the higher densities having a decreasing stretching parameter as well, the SED relation is not violated in the same way for isochores or isobars above the LLCP in density or pressure, respectively. In fact, the jump length further decreases with temperature. This case, unusual for supercooled liquids, has also been found for binary mixtures of soft spheres[344] and ionic liquids.[76] The possibility that for $\rho > \rho_\mathrm{c}$ an increase at even lower temperatures occurs cannot be ruled out, similar to the study of soft spheres. These results also show that for a suitable density or pressure of about 980 kg/m^3 or -200 MPa for $q = 0.86$ the SED relation should be satisfied for a large dynamic range. Therefore, previous attempts to classify the SED breakdown in water, e.g., by inserting the caging regime,[74] with data on one side of the LLCP in the phase diagram give an incomplete picture or even lead to incorrect conclusions. However, qualitative agreement with the literature finding that the SED relation is strongly violated upon crossing of the Widom line and, hence, growing LDS fraction exists.[327,328] The interpretation of increasing heterogeneity must be used with caution in the case of water because the jump length in LDL and HDL differs quantitatively and the transition from HDL to LDL may be superimposed on the violation of the SED relation, depending on the thermodynamic pathway.

Analogously to the interpolation of dynamics at the LLCP one may calculate data for isobars and compare it with the findings for isochoric and isobaric cooling. $\rho(T)$ for isobars is found by calculating the densities ρ needed to achieve a desired pressure from the TSEOS. Using the density dependence of the VFT parameters dynamics in the supercooled regime are inter- and extrapolated. The self-diffusion coefficients determined in this way agree very well with those from the NPT simulations, see Fig. 7.8(b). These results and especially the predictions from extrapolations to lower temperatures lead to a sigmoidal temperature dependence of $\log(1/D)$. This behavior is able to reconcile dynamics with the low glass transition temperature and has been predicted for decades from the Adam-Gibbs theory and entropy.[29,147,208] Recent estimations of the diffusivity of water within the *no-man's land* from laser heating and the following crystal growth have supported this prediction.[20,120] Here, bulk dynamics are followed into the *no-man's land* and supporting results are found. More importantly, these results show that the fragile temperature regime is caused by a rapid transition from HDL with fast dynamics to LDL with slow dynamics. HDL itself, as seen for isochores with densities $\rho > \rho_\mathrm{c}$ or isobars with $P > P_\mathrm{c}$, is in comparison only moderately fragile. In particular, all isochores show comparable fragility in the supercooled regime. Thus, the FST is not truly a transition from a fragile to a strong liquid but rather the consequence of a transition from the strong high-temperature regime to a strong or moderately fragile supercooled regime of LDL.

The sigmoidal temperature dependence leads to a maximum in the derivative $1/D(1/T)$ or $\tau(1/T)$ with respect to $1/T$, see also Sec. 8.2.3. This inflection point is shown in Fig. 7.8(a,b). For further reduced pressure and, hence, increased distance to the LLCP the inflection point shifts to higher temperatures and the sigmoidal shape as well as the apparent fragility are less pronounced. The Widom line and the line of inflection points do not agree, which was also found in a recent study.[121]

This apparent FST can be explained as the result of a rapid transition from an HDL-like to an LDL-like liquid, each with different mobilities. Such a transition has been modeled using a two-state model for water in previous studies. Tanaka and coworkers[119–121,220] suggested that it is not a true FST between liquids with vastly different fragility but the simple-liquid regime and LDL both follow an Arrhenius law with different activation energies. The rapid transition from one Arrhenius law to the other is where fragile behavior occurs. Caupin and coworkers[218,219] concluded as well that the fragile behavior near the Widom line cannot be attributed to either phase and that it results from a mixture of two liquid's behaviors. Instead of an Arrhenius law, they used VFT behavior for the high-temperature and high-pressure regime, i.e., they modeled it as a fragile liquid. Both models are examined and compared in more detail in Sec. 7.6.

7.5. Spatially resolved analysis

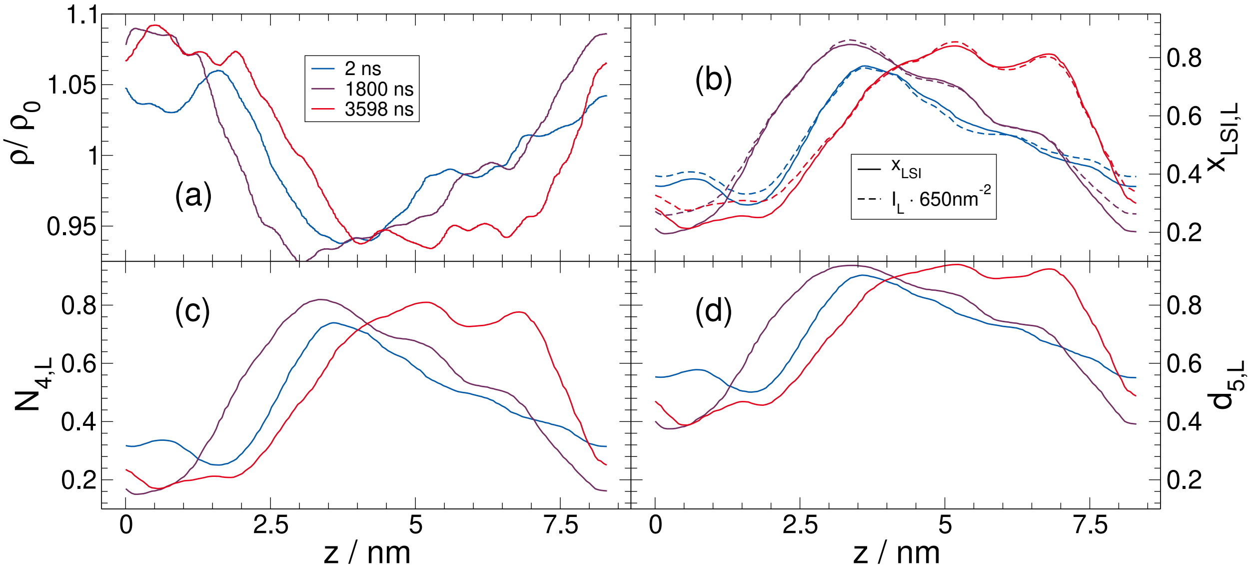

Figure 7.10.: Spatially resolved structural properties of the charge-scaled TIP4P/2005 water model with $q = 0.88$ simulated at $\rho = 940\,\mathrm{kg/m^3}$, $T = 125\,\mathrm{K}$ and in elongated geometry with $L_\mathrm{x} : L_\mathrm{y} : L_\mathrm{z} \equiv 1 : 1 : 3$ and $N = 2000$ molecules: (a) ρ_L/ρ, (b) I_L and $x_\mathrm{LSI,L}$, (c) $N_\mathrm{4,L}$, and $d_\mathrm{5,L}$. Presented is data at the beginning, middle and end of the trajectory. The structural identifiers were averaged over $\delta z = 1\,\mathrm{nm}$ thick layers centered on each oxygen and perpendicular to the z-axis. To reduce noise the properties were averaged over short periods of time and a low-pass filter was applied to further reduce artifacts caused by the discretization of the number of particles in a layer. Figure A.7 in the appendix presents data for the larger system with $N = 12000$.

This section switches from the cubic system, which showed no stable phase separation despite entering the metastable regime, to the elongated systems to further verify the existence of the two liquid phases and to study their properties. There, one exploits that the energetically unfavorable interface of actual HDL and LDL phases and its volume ratio to phase separated regions is reduced when it is aligned parallel to the smallest surface of the simulation box. Phase separation below the LLCP is thus enhanced. These simulations are performed for charge scaling of $q = 0.86$ and $q = 0.88$ for two reasons: Dynamics speed up with lower scaling factors, see Fig. 7.2(d), but thermodynamic drive to phase separate might be weakened. It was assured in Fig. A.6 in the appendix that the pressure P at a given state point is the same within the error margins in the simulations for the cubic and elongated boxes.

Next, the fluctuations of density and structural identifiers in space are investigated for a $4\,\mu\mathrm{s}$ simulation with $q = 0.88$, $\rho = 940\,\mathrm{kg/m^3}$, and $T = 125\,\mathrm{K} < T_\mathrm{c}$ at the beginning, midway, and end of the simulation, Fig. 7.10. Consistent with the construction of the elongated systems, layers parallel to the xy plane and of thickness $\delta z = 1\,\mathrm{nm}$ centered around the respective position z of each oxygen are analyzed. With this layer thickness it is assured that the normalized density ρ_L/ρ and the structural identifiers $x_\mathrm{LSI,L}$, $N_\mathrm{4,L}$, and $d_\mathrm{5,L}$ are averaged over several layers of molecules. Visual inspection of the results shows that the system separates into two regions with distinct structural properties. The relative difference of the layer-averaged density between the center and the edges of the simulation box is about 10%, which is comparable to values found for studies with the ST2 and TIP4P/2005 models.[338,341,345] The structural identifiers are anticorrelated to the density. Since these supposedly measure the LDS fraction the combined result confirms the separation into a low-density phase in the center and a high density phase on the edges, consisting of LDS and HDS respectively, and that the structural identifiers measure structures of the respective phases. The interface layer between the two regions changes only slightly during the simulation time. This temporal stability on the order of μs will be important for the analysis of dynamics within these regions. These observations suggest that the system separates into extended and stable LDL and HDL phases.

In the appendix, see Fig. A.7, the analogous analysis at $T = 132\,\mathrm{K} > T_\mathrm{c}$ is shown, which shows that the corresponding fluctuations in the structural quantities exist in the one-phase region above the LLCP as well. This is expected for critical phenomena where fluctuations and their respective length scales grow with decreasing distance to the critical point where they diverge. Figure A.7 also shows weaker spatial distinction and shorter time scales for the HDL and LDL regions. These properties and their temperature dependence are investigated in more detail in the following. Note here, that without an external field, e.g., gravity, there is no driving force for having only two regions of each phase other than the energetic gain of minimizing the energetically unfavorable interface. If the long time limit consists of two phases then barriers have to be overcome by fluctuations to achieve this state. However, because of the periodic boundary conditions and the small box size, the system with $N = 2000$ molecules immediately separates into one HDL and LDL region, meaning the size of the regions is artificially influenced here. The same is not necessarily true for much larger systems.

Having investigated qualitatively the phase separation one can continue with quantifying its significance. The probability distribution of these layer-averaged properties, as determined per reference oxygen, is calculated and shown in Fig. 7.11 for the charge-scaled model with $q = 0.88$ for several temperatures above and below the critical point. One finds for all properties uni- and bimodal distributions depending on the temperature. In particular, shapes similar to normal distributions are found for temperatures around the LLCP and at least bimodal distributions appear for temperatures sufficiently below the LLCP. The unimodal distributions at higher temperatures are not trivial. Inspection of e.g., the LSI in the one-phase regime shows bimodal behavior, see Fig. 7.5. The difference is that in the presented data the local structural identifiers are averaged over larger volumes. The length scale of fluctuations at higher temperatures is thus below the size of the layers and averaged results are obtained. For even larger volumes the distributions are expected to be narrower. Note here, that the histograms are biased. A layer containing mostly LDS contains fewer molecules because of their more spacious configuration than a layer consisting mostly of HDS. For cooling below the LLCP, the free energy difference gained by developing a planar interface and separation into two phases becomes sufficient to produce more distinct regions. This means that the length scale of the structural fluctuations grows to at least the nanometer scale, as seen in Fig. 7.10. The three peaks observed for 124 K may be a relaxation problem as the system may have continued development of phase separation during the simulation or might be just on the edge of forming well separated phases. Stronger separation of the bimodal behavior for the layer averaged structural identifiers is expected in larger systems where the interface takes up a smaller fraction of the volume. Indeed, the data for the larger system with $N = 12000$ molecules in Fig. A.8 exhibits bimodal distributions at higher temperatures than the small system. Phase separation occurs already close to the LLCP. However, the increase in computational cost makes ergodicity and acquiring good statistics equally

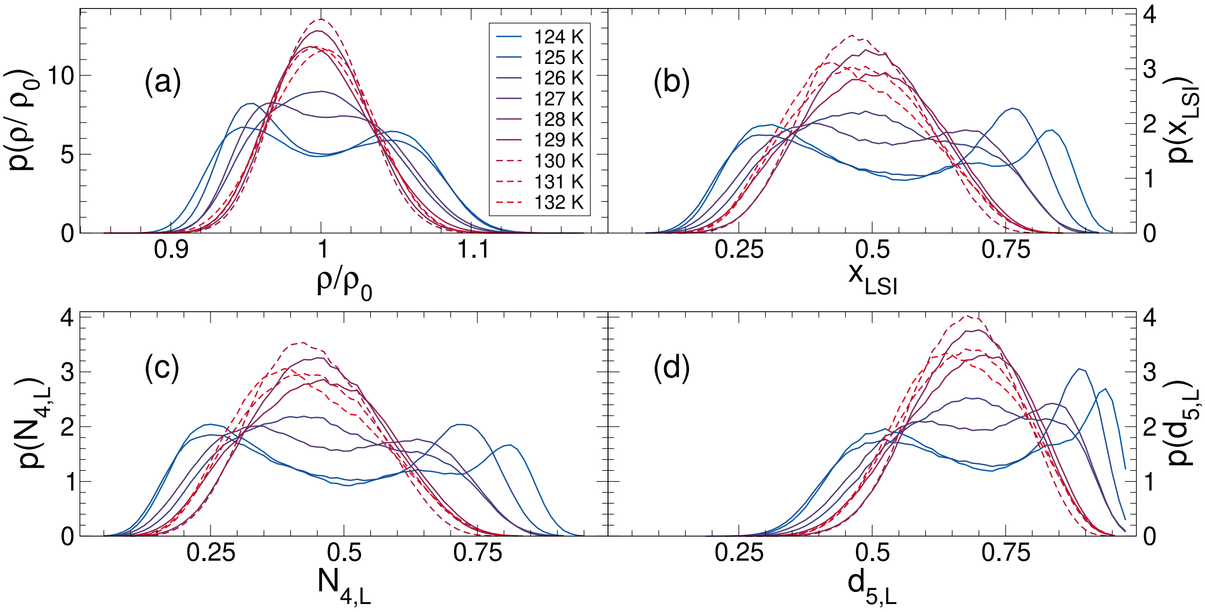

Figure 7.11.: Probability distributions of the layer-averaged properties for the charge-scaled TIP4P/2005 water model with $q = 0.88$ and $\rho = 940\,\mathrm{kg/m^3}$ at the indicated temperatures: (a) ρ_L/ρ, (b) I_L, and (c) $N_{4,\mathrm{L}}$ d_5. The results were determined for the elongated system with aspect ratio $1:1:3$ and $N = 2000$ molecules. The critical temperature is $T_\mathrm{c} \approx 131\,\mathrm{K}$ and dashed lines indicate results at and above this value in the one-phase region. For $N_{4,\mathrm{L}}$, $x_{\mathrm{I,L}}$, and $d_{5,\mathrm{L}}$ a moving average was applied to reduce artificial noise due to their discretized values. Figure A.8 in the appendix presents data for the larger system with $N = 12000$.

problematic at strong supercooling. That the small system can already show the same phenomena decreases the still accessible temperatures.

Having investigated the structural properties, their dynamical properties and the relation of both are studied next. For this purpose, the molecules are distributed into subsets according to their layer-averaged structural identifiers. If the inspected dynamical property, e.g., the rotational correlation function, is faster than the fluctuation in average local structure, the dynamics within LDL and HDL regions can be determined. The small thickness of the layers of 1 nm allows for a higher resolution than larger values, yet it is still larger than the jump length of $a \approx 0.33\,\mathrm{nm}$ that connects the rotational correlation time τ and translation D. In this way, it is assured that in case of stable HDL and LDL phase separation the local environment does not change significantly on the time scale of the RCF. For sufficient cooling below the LLCP, the results are expected to be representative of the dynamics in phases with the respective average properties. Still, dynamical heterogeneity will broaden dynamics in the respective phases as it does in bulk and the systems with cubic geometry.

The results are presented in Fig. 7.12 for the elongated system with $q = 0.88$, $\rho = 940\,\mathrm{kg/m^3}$, and $N = 2000$ molecules at a temperature below the critical point. Compared is the RCF $F_{1,\mathrm{OH}}$ for subsets of molecules distinguished by their layer averaged value $N_{4,\mathrm{L}}$. One finds that the terminal relaxation shifts to longer times with increasing $N_{4,\mathrm{L}}$ and, thus, increasing LDS fraction. The stretching as well as the vibrational decay of the subsets is not identical. Their mean correlation times τ_L are presented as a function of the structural identifier in Fig. 7.12(b). Note, that only results for values of the

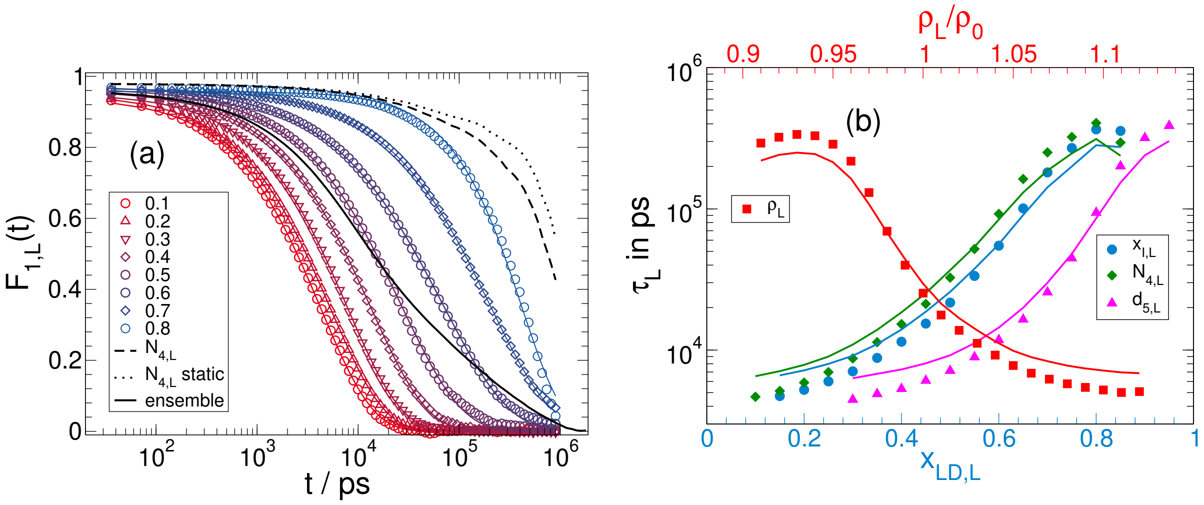

Figure 7.12.: Dynamics as a function of structure for the charge-scaled TIP4P/2005 water model with $q = 0.88$ and $\rho = 940\,$kg/m^3 at $T = 125\,$K: (a) rotational correlation function $F_{1,\mathrm{OH}}(t)$ for molecules characterized by different layer-averaged values $N_{4,\mathrm{L}}$ at the time origin t_0 and over the time scale of the plateau preceding the α relaxation. The legend indicates the center of the bins with bin width 0.05 for $N_{4,\mathrm{L}}$. The colored solid lines are fits to KWW functions. The black solid line is the RCF $F_{1,\mathrm{OH}}(t)$ for the ensemble average. The black dashed line is the correlation function $C_{\mathrm{N4}}(t)$ of the layer-averaged quantity $N_{4,\mathrm{L}}$, see Eq. (7.7), and the black dotted line is the corresponding result for layers static in space. (b) Corresponding correlation times τ_L as a function of the layer-averaged quantities ρ_L/ρ_0 (red squares), $x_{\mathrm{I,L}}$ (blue circles), $N_{4,\mathrm{L}}$ (green diamonds) and $d_{5,\mathrm{L}}$ (pink triangles). Solid lines show mean correlation times with S_{10} for the oxygen atoms for comparison at the same respective layer-averaged values.

structural properties for which a reasonable amount of statistics exists are shown. One finds that LDL environments cause dynamics that are almost two orders of magnitude slower than for HDL environments. Consistently, the same slowdown is found when molecules are discriminated by their layer averaged density ρ_L or the structural identifiers $x_{\mathrm{I,L}}$ and $d_{5,\mathrm{L}}$. A strong dependence on the LDS fraction is found for intermediate values while asymptotic behavior appears for $N_{4,\mathrm{L}} > 0.7$ and $N_{4,\mathrm{L}} < 0.3$. As a consequence of this strong dependence of dynamics on the structure of the local environment and the bimodal distribution of the structural properties, the ensemble average shows a stretched biexponential decay. Because the interfacial regions take up a significant fraction of the box volume, the intermediate LDS fractions smear out this biexponentiality. The correlation function of the elongated system is compared with the result for cubic systems in detail in App. A.2.3.

Furthermore, biexponential decays are only possible when the layer-averaged properties measured with correlation functions, e.g., $C_{\mathrm{N}_{4,\mathrm{L}}}$, decay slower than $F_{1,\mathrm{OH}}$ in the LDL region. This is in particular true for the case of static layers. If the rearrangement of some molecules causes a structural relaxation of their surrounding regarding LDS and HDS, then the slower component is suppressed. Here, $C_{\mathrm{N}_{4,\mathrm{L}}}$ decays later than correlation functions for all values of $N_{4,\mathrm{L}}$. This means that correlation times for low and high values of $N_{4,\mathrm{L}}$ may be representative of stable HDL and LDL phases. The weaker dependence of τ_L on the local environment in these regimes in Fig. 7.12(b) supports this conclusion.

Translational dynamics exhibits a consistent dependence on the local environment, as seen for the ISF in Fig. 7.12(b). Correlation times with $F_{1,\mathrm{OH}}$ and S_{10} are almost the same, implying that rotational decorrelation happens on the same length scales as defined by the wavenumber $k = 10\,\mathrm{nm}^{-1}$, which corresponds to displacements of 0.23 nm on average. The SED relation appears to be weakly and systematically violated when the LDS fraction is varied, in agreement with Fig. 7.9. More importantly, regular translational motion is found in HDL and LDL environments.

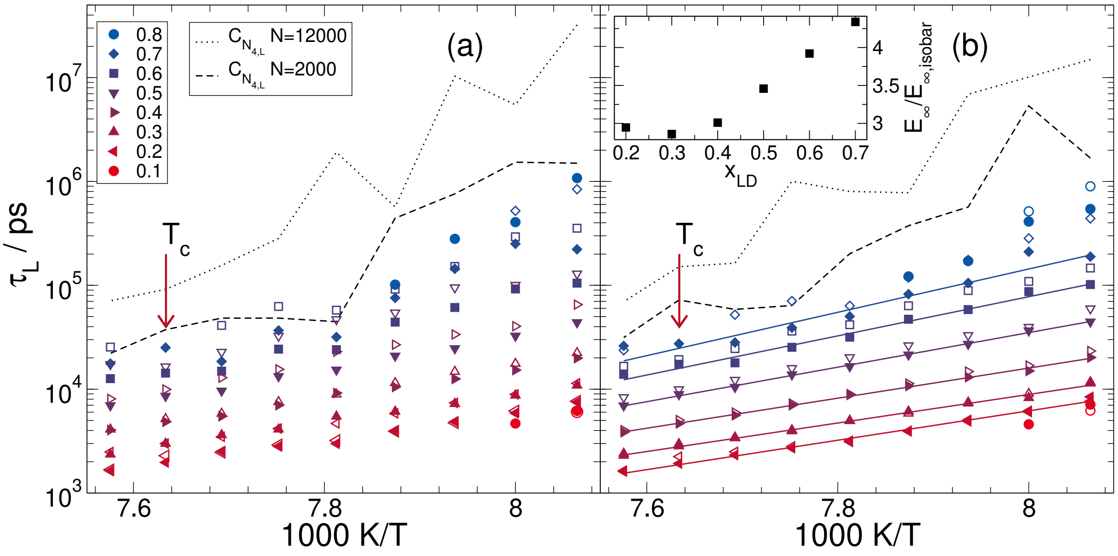

Figure 7.13.: The temperature dependence of mean rotational correlation times τ_{L} measured with $F_{1,\mathrm{OH}}(t)$ for environments with the indicated layer-averaged structural identifier $N_{4,\mathrm{L}}$. The data is for charge-scaled TIP4P/2005 systems with $q = 0.88$ and elongated geometry with with $N = 2000$ molecules and aspect ratio $1:1:3$ (solid symbols) and $N = 12000$ and $1:1:6$ (open symbols). On the left (a), results are presented for simulations with density $\rho = 940\,\mathrm{kg/m^3}$. On the right side (b) results are averaged geometrically over several simulations: densities of $935\,\mathrm{kg/m^3}$, $940\,\mathrm{kg/m^3}$, and $944\,\mathrm{kg/m^3}$ for the small system and simulations with randomized and biased, i.e., one LDL and HDL phase, starting configurations for the large system. For comparison, the time scale τ_{N_4} of $N_{4,\mathrm{L}}$ fluctuations from fits of $C_{\mathrm{N}_{4,\mathrm{L}}}(t)$ to KWW functions is shown: (dashed) $N = 2000$ and (dotted) $N = 12000$. The arrow marks the critical temperature $T_{\mathrm{c}} \approx 131\,\mathrm{K}$. Solid lines are fits with Arrhenius laws to data of the small system. The inset presents their activation energies relative to the high temperature activation energy of isobar simulations at atmospheric pressure. Poor statistics for the rarer cases of $N_{4,\mathrm{L}} = 0.1$ and $N_{4,\mathrm{L}} = 0.8$ allow their investigation only far below the LLCP.

Before concluding this section, the temperature dependence of rotational dynamics in environments characterized by their local LDS fraction is investigated in more detail. Mean correlation times τ_{L} are shown as a function of the layer-averaged structural identifier $N_{4,\mathrm{L}}$ in Fig. 7.13(a). Corresponding data for charge scaling of $q = 0.86$ is shown in the appendix, Fig. A.9. This extracts what might be called isomorphs, i.e., lines in the phase diagram with constant structure. The Arrhenius plot reveals Arrhenius-like behavior for all local environments with only moderate differences in the activation energy but relative differences of up to two orders of magnitude for the lowest temperatures. While an Arrhenius law may always fit a small enough temperature range, this observation is still noteworthy when compared with the temperature dependence of isobars in Fig. 7.8(b). There, structural properties are not constant and slopes are vastly different depending on which side of the

LLPT line the isobar lies. The isomorphs instead have similar activation energies E_∞ of three to four times the high-temperature activation energy of isobaric simulations at atmospheric pressure, see the inset of Fig. 7.13(b). E_∞ increases with $N_{4,\mathrm{L}}$. Note however, that the correlation time of $N_{4,\mathrm{L}}$, which characterizes the subsets, is comparable to τ_L of subsets with $N_{4,\mathrm{L}} > 0.7$ at high temperatures. This means that the determined correlation function for LDL environments decays prematurely for temperatures above or close to the LLCP. Thus, dynamics in this case are not representative. The increased temperature dependence across $127\,\mathrm{K}$, when the time scales of rotational dynamics and fluctuations of the environment separate, is thus not to be trusted. In addition it is found that only at sufficiently low temperatures, when the phase separation becomes more stable, the highest and lowest values of $N_{4,\mathrm{L}}$, 0.8 and 0.1, appear.

To scrutinize these results simulations with $N = 12000$ molecules and increased elongation of $1 : 1 : 6$ were performed. The phase separation should be stabilized even further and the relative occupied volume of the two phases to the interfacial region should be increased. Presented in Fig. 7.13(a), the fluctuation of the layer-averaged structural identifier $N_{4,\mathrm{L}}$ shifts to longer times. Thus, the temporal stability appears to improve with system size. Perfect agreement with the smaller system is found for rotational correlation times at LDS fractions of $N_{4,\mathrm{L}} = 0.4$ and lower. For LDS-rich environments, the rotational correlation times increase for the larger system. Hence, the correlation time of the slower LDS-rich environments is indeed reduced in case the time scale of the structural fluctuations is not sufficiently separated. Unfortunately, the increased computational cost for the increased system size prevents the study of temperatures further below the LLCP. Ergodicity is already lost since the HDL and LDL phases do not occupy each position in the box equally often for periodic systems with finite size and zero momentum. A reliable determination of the temperature dependence of the LDL phase is, thus, not easily feasible with either the large system because of computational cost or the small system because of reduced stability and length scale of the phase separation. Still, the combined results show that for HDL no significant changes in the temperature dependence occur upon cooling below the critical temperature T_c.

These findings can be further supported by performing several simulations at temperatures for which dynamics is still fast. The small system with $N = 2000$ molecules was simulated at $\rho = 935\,\mathrm{kg/m^3}$, $940\,\mathrm{kg/m^3}$, and $944\,\mathrm{kg/m^3}$. Inspection of the results shows no systematic dependence on the average density. The resulting $\tau_{\mathrm{N}_{4,\mathrm{L}}}$ are geometrically averaged and shown in Fig. 7.13(b). For the large system, averaging over randomized and biased systems introduced no notable differences. Overall, the behavior as discussed above holds for the data but higher accuracy is achieved.

Finally, the correlation times from isochores in the cubic system are compared with the results $\tau_{\rho,\mathrm{L}}$ obtained for environments with the respective layer-averaged densities ρ_L for the elongated system. The results are presented in Fig. 7.8(c) and the correlation times of isochores with high densities $\rho \geq \rho_\mathrm{c}$ agree well with those determined for the respective layer-averaged densities. This confirms that the correlation times of HDS-rich environments characterized by the average density are representative. One finds disagreement for densities smaller than ρ_c. The results from elongated systems underestimate the correlation time of the cubic systems above and close to T_c. Upon further cooling the difference decreases and the apparent higher temperature dependence suggests that agreement could exist at lower temperatures. These deviations are attributed to the comparably fast fluctuations of the local environment and, thus, premature decorrelation of $F_{1,\mathrm{OH}}$ in LDS-rich environments. Note, that the density of the slowest isochore does barely occur in the probability distributions, see Fig. 7.11, and is most likely beyond the minimum of LDL in the Gibbs energy. Results calculated from the elongated systems for this density might never be correct. The same discrepancies would occur for much higher densities.

7.6. Two-structure models of dynamics

Since the TSEOS and similar approaches for water are very successful in describing thermodynamic properties, models that use two states to describe the dynamics of water are now tested. In the previous section, it was found that in a certain range of density and pressure the dynamics depends monotonically on the density and, hence, on the fraction of HDS and LDS. Within this range, one may assume that the dynamics can be described by a monotonous function of x. For mixtures, which separate in phases with different self-diffusion coefficients D_i, one expects that the self-diffusion coefficient of a component, which occurs with the probability p_i ($\sum_{i=1}^{N} p_i = 1$) in the respective phases, is the rate average $D = \sum_{i=1}^{N} p_i D_i$ over the different phases. Note however, that phase boundaries may constitute diffusion barriers. The simplest extension for the one-phase regime would be that the self-diffusion coefficient is a linear function of x. This approach was unsuccessful here independent of the choice of x, from the TSEOS or one of the structural identifiers. The relation of D and x is non-linear, see Fig. A.11 in the appendix. Of course, the reason for this may be that no phase separation occurs in the cubic systems. In any case, even for the layer-averaged dynamics in Fig. 7.12, it can be observed that the dynamics is not a simple function of the LDS fraction. In particular, it already saturates for phases that do not consist only of HDS or LDS.

To account for the strong dependence on x, the energy barrier that must be overcome for relaxation events can be considered instead. One approach is that when particles repeatedly switch between HDS and LDS, they sense an energy barrier consisting of both structures on average. In general, this can be written as $E(T,P) = (1-x)E_{\text{HDS}}(T,P) + xE_{\text{LDS}}(T,P)$. Tanaka and coworkers and Caupin and coworkers have each taken this approach.[119,120,218] Both assume an Arrhenius law for LDS, consistent with many observations for strongly supercooled water in confinement or for LDL above the glass transition.[13,245] However, they differ in their description of HDS, or rather the high-temperature regime. While Tanaka assumes another Arrhenius that fits well with the simple-liquid regime, Caupin follows the phenomenological observation that water always exhibits fragile behavior in the supercooled regime and, hence, uses a VFT behavior.[218,219] Thus, Tanaka uses

$$1/D = 1/D_\infty \exp\left([1 - s(T,P)]\frac{E_\infty}{T} + s(T,P)\frac{E_0}{T}\right) , \tag{7.9}$$

$$s(T,P) = \left[1 + \exp\left(\frac{\Delta E - T\Delta\sigma + P\Delta v + P^2 b}{T}\right)\right]^{-1} \tag{7.10}$$

while Caupin applies

$$1/D = 1/D_\infty \left(\frac{T}{T_{\text{ref}}}\right)^{-0.5} \exp\left([1 - f(T,P)]\frac{B + P\Delta v_{\text{HDS}}}{T - T_0} + f(T,P)\frac{E_0 + P\Delta v_{\text{LDS}}}{T}\right) . \tag{7.11}$$

Here, s and f are the fraction of LDS and not necessarily the same in both approaches. In Tanaka's case, s is given by fitting the data to Eq. (7.10), where ΔE, $\Delta\sigma$, and Δv are the energy, entropy, and volume differences of pure HDL and LDL. It incorporates a second order term in pressure with prefactor b. Caupin assumes a predetermined fraction f, e.g., from the TSEOS. Of course, any choice for x_{LD}, f or s, can be applied with either model. Furthermore, E_∞, B, and E_0 are parameters for the high and low temperature activation energies, respectively, where in Caupin's model a VFT equation describes the high-temperature regime. Both models start with a prefactor $(T/T_{\text{ref}})^\nu$ with arbitrary T_{ref}, which is intended to preserve the SED relation when adjusted for diffusion, viscosity, and rotational correlation time on the one hand and to account for the temperature dependence of the velocity of the particles on the other. However, Tanaka and Caupin chose $\nu = 0$ and $\nu = 0.5$

for D, respectively. As discussed in Sec. 8.2, these differences are often masked by the much more influential parameters in the exponent. Equation (7.9) can be simplified to Eq. (8.9) for constant pressure. With prior knowledge about the LDS fraction, one has three free fit parameters for Eq. (7.9) and six (four for constant pressure) free fit parameters for Eq. (7.11). At the same time, Eq. (7.11) does not describe the commonly found Arrhenius in the high-temperature regime, but should be particularly good at describing data in the slightly supercooled region. However, the advantage of Eq. (7.9) for the high-temperature regime is only valid as long as the Arrhenius behavior is the same for all P or ρ. Without knowledge about the LDS fraction, Eq. (7.10) can be used in Eq. (7.11) which, however, introduces four more fit parameters. It should be mentioned here that in older publications the parameters b and Δv_{LDS} were missing and were added to characterize a wider range of the phase diagram in more recent publications.

Both equations replicate the observation made in Fig. 7.13. For isomorphs, data along constant x_{LD}, the temperature dependence of the apparent activation energy is weak. Tanaka's formula leads to an Arrhenius for constant s while in Caupin's case the sum of a constant to a VFT contribution allows for some temperature dependence. At first glance, both seem to be suitable to characterize the data.

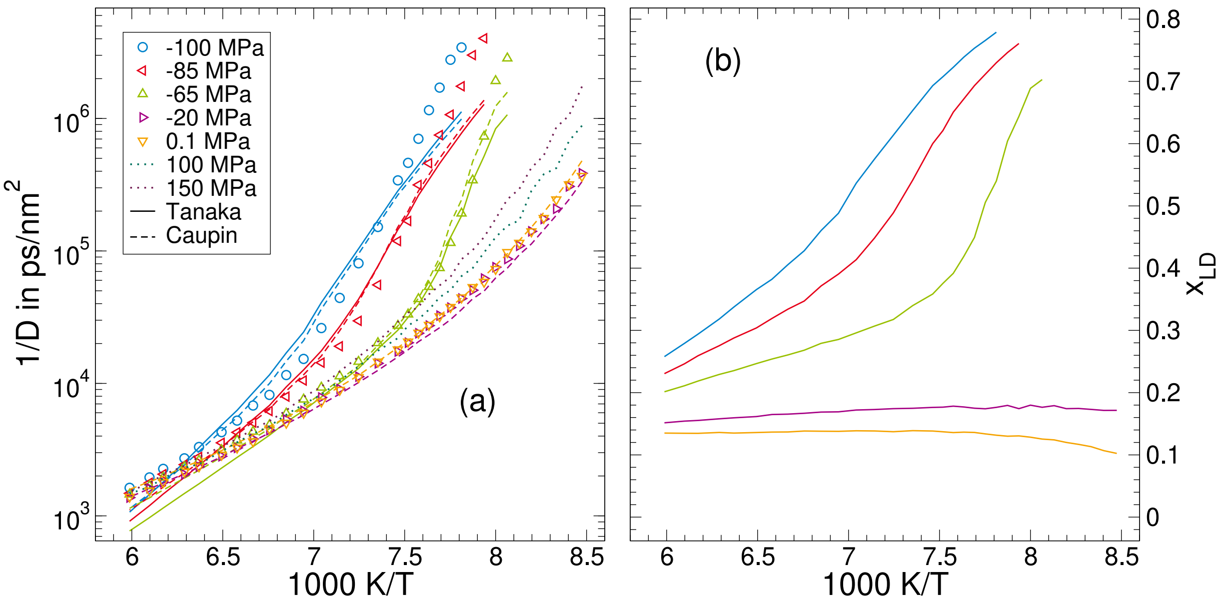

Figure 7.14.: (a) The temperature-dependent self-diffusion coefficients $1/D$ of the charge-scaled TIP4P/2005 model with $q = 0.86$ at the indicated isobars (colored symbols and dotted lines). Solid lines are global fits of Eq. (7.9) to data for pressures $P < P_{\mathrm{c}}$ while dashed lines are fits to data for pressures $P \leq 0.1$ MPa with Eq. (7.11). The LDS fraction s or f is given by the equilibrium concentration x_{LD} of the TSEOS for the same charge-scaled system. (b) Equilibrium concentration x_{LD} of the LDS component calculated from the TSEOS. Isobars with $P \geq 100$ MPa are not shown because they are too far from the range of validity of the TSEOS. The colors in the legend apply to both graphs.

First, the knowledge about the concentration x_{LD} from the TSEOS is used to test the two models. For the fits with Eq. (7.9) and (7.11), the fraction of LDS was taken as given. Since the fraction is constant or even decreasing for pressures above the LLCP, only data with $P < P_{\mathrm{c}}$ were considered for

Eq. (7.9). The moderate fragility of pressures above the LLCP cannot be represented by a combination of two Arrhenius laws and constant or even decreasing LDS fraction. Tanaka's approach is thus more restricted in the phase space near the LLCP than Caupin's approach, but has the potential to describe the high-temperature regime correctly. Since the dynamics slow down again at very high pressures as in normal liquids, only pressures up to 1 bar are considered for fits to Eq. (7.11). In principle, the contribution $P\Delta v_{\mathrm{HDS}}$ can accommodate this slowdown but was found to be insufficient. Very high temperatures are also not considered, as these require uncertain extrapolations of the TSEOS. Despite these limitations, the present data set is more extensive than those used in the literature,[119–121,218,219] i.e., the self-diffusion coefficients reach down to $3 \cdot 10^{-7}$ nm^2/ps and a wide range of pressures and temperatures and, thus, densities is available.

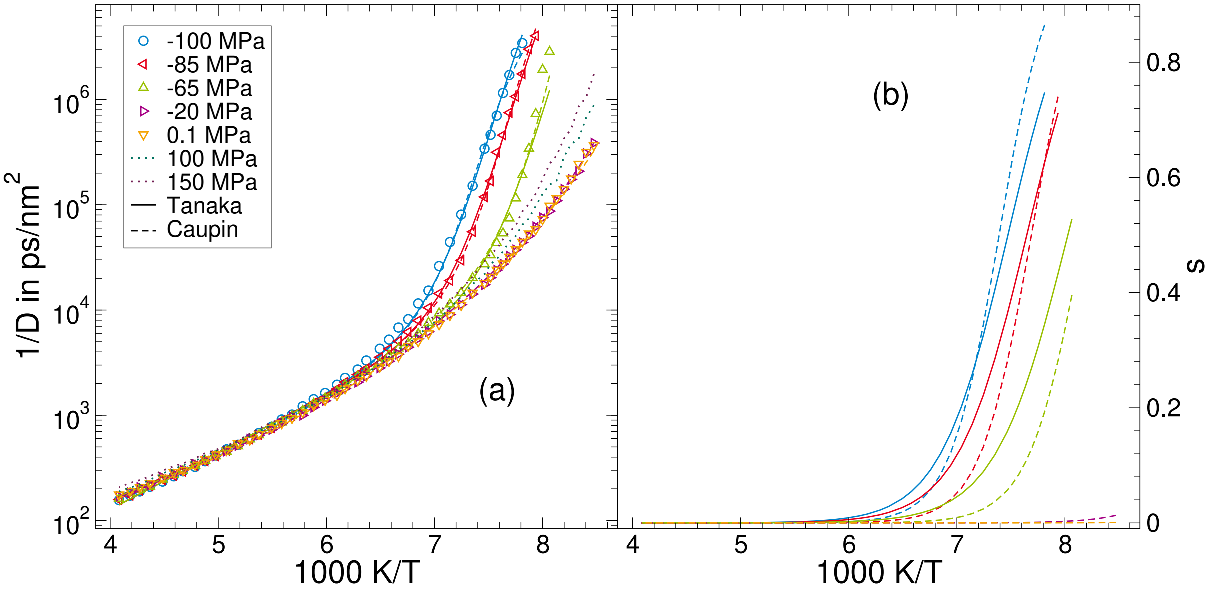

Figure 7.15.: (a) The temperature-dependent self-diffusion coefficients $1/D$ of the charge-scaled TIP4P/2005 model with $q = 0.86$ at the indicated isobars (colored symbols and dotted lines). Solid lines are global fits with Eq. (7.9) to data for pressures $P < P_\mathrm{c}$ while dashed lines are fits with Eq. (7.11) to data for pressures $P \leq 0.1$ MPa. Here, the LDS fraction s or f is described by Eq. (7.10) and is part of the fitting procedure. (b) LDS fraction s of Eq. (7.10) determined by the fits in (a). Only pressures for which data was included in the fit are shown. The colors in the legend apply to both plots.

Figure 7.14 shows the self-diffusion coefficient for isobars and the corresponding x_{LD} as well as the fits with Eq. (7.9) and (7.11) for the charge-scaled TIP4P/2005 with $q = 0.86$. One finds acceptable descriptions for Tanaka's approach for the temperature range around the Widom line. However, it deviates strongly at high and low temperatures despite the limited high-temperature regime, which leaves more freedom to the fit parameters. The slowdown to low temperatures is underestimated, which is likely caused by the prematurely reduced slope of x_{LD} and a sign that within this model x_{LD} does not equal s. In fact, Shi et al. have already found that the Widom line, the location for $x_{\mathrm{LD}} = 0.5$ and in their case called the static Schottky line, and the dynamical Schottky line, the location of the largest slope in the Arrhenius plot and in their model the location of $s \approx 0.5$, are not identical. The same is observed same in Fig. 7.8(b). They argue that the local structure has to be coarse grained.

An LDS molecule only shows LDL dynamics if neighboring molecules are LDS as well.

Caupin's model is more successful because it better describes the high-temperature regime and at the same time it is also fitted to data with $P > P_\mathrm{c}$. However, the fit deviates from the data at slow dynamics and low pressure. This remains the case even when pressures above the LLCP are neglected. The most important finding here is that both models have problems following the temperature dependence of the dynamics for low temperatures and low pressures or densities. That is, for high LDS fractions, the dynamics are not successfully characterized. This is also particularly visible in the appendix in Fig. A.12. There, the data for the same system but for isochores are fitted to Eq. (7.11). Also in this case, deviations arise for low temperatures and high LDS fractions. The model works well up to self-diffusion coefficients of $10^{-5}\,\mathrm{nm}^2/\mathrm{ps}$, which is also about the limit of the data on which this model was tested in the literature.[218,219] Even there, it has already been observed that deviations occur when temperature and pressure are low.

To verify that the basic principle of the models, the linear combination of two temperature-dependent activation energies, works, Eq. (7.10) is used instead of the LDS concentration from the TSEOS. This formula, which resembles the Fermi distribution, was motivated via Boltzmann statistics for two states with different energy and volume.[220] A major difference to the LDS concentrations from the TSEOS is that pure states are expected for high and low temperatures. The TSEOS does not agree with this, see Fig. 7.14(b). Moreover, the transition is much more discrete and does not incorporate the slow variation with temperature of x_LD for low pressures. In Fig. 7.15(a), the fits with this function to the same data as in Fig. 7.14 are shown. The only difference in the data is that the independence from the range of validity of the TSEOS allows higher temperatures to be included. It is found that low temperatures and low densities are also sufficiently described. The moderate fragility at $P > P_\mathrm{c}$ is characterized by the VFT contribution in the case of Eq. (7.11). The fraction s, Fig. 7.15(b), follows the expected behavior for both models. LDS vanishes for high temperatures and increases rapidly upon cooling and for pressures below the LLCP. It is negligible for pressures above the LLCP. This shows that, in principle, the temperature dependence of the dynamics can be described by a sum of activation energies of two competing states. However, some weaknesses do exist:

i Equation (7.10), although physically motivated, could not produce results comparable to any of the structural identifiers for the LDS fraction. The introduction of coarse graining can in principle solve this issue. Moreover, Eq. (7.10) cannot be applied to data from isochores. In the metastable region, two liquids with different LDS fractions exist for each pressure. Thus, the formula would have to be extended to include density or be modeled similarly to the TSEOS with two solutions. For isobars, one expects a first order phase transition, which is not taken into account.

ii Tanaka's approach with two Arrhenius laws does not work significantly better than Caupin's in the supercooled regime. The latter has the advantage of being able to characterize pressures and densities above the LLCP as well. A difference is that the high temperature Arrhenius regime cannot be attributed to either phase in the supercooled regime. In contrast, the VFT equation adequately describes HDL in the temperature range considered here. Thus, for a successful model, it is necessary for the temperature dependence of HDL to be included adequately.

iii At very high pressures, water again behaves like a normal liquid and viscosity increases with increasing pressure. In order to describe water in the full phase diagram, the above models would have to be extended. Caupin's model already allows an increase of the activation energy in the VFT equation with pressure. However, this is still insufficient to include higher pressures in the fit in Fig. 7.15.

iv The VFT equation has a divergence at T_0. Here and also in the literature, this is above T_g of LDL and LDA.[219] One conclusion is that HDL crosses the dynamics of LDL at low temperatures but above T_g. However, this is incompatible with experimental findings of strong behavior above T_g.[13,206,217] In the context of an approach with additive activation energies, the VFT equation dominates the Arrhenius for LDL already above the T_g of pure LDL. The question arises as to what the temperature dependence of HDL really is.

Points (i)-(iii) lead to an extension of the mathematical form of the models. However, this only results in extensive quantitative description of the water dynamics without necessarily being a representation of the underlying physics. It would be much more instructive to determine the dynamics on the basis of the real LDS fraction or at least a quantity with a simple relation to it, e.g., N_4. However, the problem remains that dynamics slow down strongly for high LDS fractions. There may be several reasons for this. First, as already found in the previous section, the dynamics of LDS is not conserved in the mixture. In the notion of cooperatively relaxing regions on some length scale, the dynamics of LDS can be obtained only for sufficiently high concentration in extensive regions. Relaxation events of HDS change the local structure and lead to premature relaxation of the previously LDS molecule. The mixture could even enable or prevent relaxation mechanisms for LDS and HDS which may be non-existent in the respective pure phases. The energy barriers for relaxation events would be affected by such effects. The approaches by Caupin and Tanaka are also not exempt from this. Thus, higher order perturbations would have to be introduced in Eqs. (7.9) and (7.11). Here, the challenge for the theory is to find a model that predicts the activation energy relevant for molecular dynamics in reactive mixtures. The approach of Tanaka and coworkers to consider only a coarse grained local structure for the LDS fraction is one possible solution.

For water in particular, it is still unclear how the temperature dependence of the dynamics of HDL and LDL is from the high-temperature regime down to the glass transition, see point (iv). For the latter, the high-temperature regime cannot be fully investigated because the liquid-vapor spinodal (LVS) becomes relevant and cavitation is inevitable, even in simulations. The more important supercooled temperature regime seems to be well characterized by an Arrhenius law. Although it would still be intriguing to see whether or not LDL shows an FST even at constant high LDS fraction. This may not be clarified or only with suitable model systems in which the LVS is avoided as much as possible. A solution would be to use increased partial charges and shift the LLCP to elevated pressures. However, this approach loses the accessibility of the LLCP at feasible relaxation times.

For HDL, current simulation results show no deviation from the super-Arrhenius behavior in the supercooled regime. Temperatures at which the extrapolated dynamics of LDL and HDL are expected to cross are still outside the range achievable within reasonable computational time. For both liquid phases, the question remains which fractions of HDS and LDS are representative. For example it can be seen in Fig. 7.12(b) that the dynamics saturate before pure HDS or LDS is reached. Figure. 7.8(a)-(c) shows the same for HDL-like isochores. Below the LLCP, where the Gibbs energy has two minima, they are commonly not at the extreme values of the order parameter. The fact that the distributions of the structural identifiers in Fig. 7.11 do not assume both extreme values is possibly a consequence of this. Very high pressures further reduce the LDS fraction but lead to the behavior common to liquids – dynamics slow down with increasing pressure. Thus, the fastest dynamics are not found in systems with the lowest LDS fraction.

Thermodynamic paths with instructive results for future studies could be with constant fraction x to clarify the temperature dependence of dynamics for constant structure or along the two minima of the free energy G for state points on the LLPT to scrutinize the temperature dependence of LDL and HDL found for coexistence simulations.

7.7. Summary

In this chapter, MD simulations were performed to determine the thermodynamic, structural and dynamical properties of water-like models in the supercooled regime. In particular, the effects of weakened Coulomb interaction and, hence, hydrogen bonding on the polyamorphism of water-like systems were investigated based on the TIP4P/2005 water model. This charge-scaling approach enabled the study of the relation of local structure and dynamics in the context of distinguishable liquid phases in more detail. The presented results are relevant for all liquids in which compressed high-energy and spacious low-energy local structures compete, in particular for water for which a complete model is still missing.

The existence of an LLPT and the related LLCP have been proposed as possible explanations for the anomalous behavior such liquids commonly show. But, it has been shown that the existence of competing local orders with different density alone can lead to these anomalies, e.g., in the case of the BKS and WAC model of silica or the mW model of water,[4,173] and, thus, the existence of an LLPT cannot be inferred from these phenomena. To investigate the existence of an LLPT, it was exploited that charge scaling shifts these phenomena to computationally accessible dynamics. Similar results for the WAC model have been found where charge scaling provided access to the LLCP.[25] For all studied scaling factors crossing of isochores in the P-T diagram was found, which proves the existence of an LLPT. The TSEOS formalism was applied successfully to characterize the data. Even despite its mean field approach it proves very useful in determining the LLCP for a wide range of systems. One finds that an LLCP exists in the given range of scaling parameters and that it shifts by 16 K. Including the LLCP of the overstructured water model ST2 at $T_\mathrm{c} = 237\,\mathrm{K}$ and the modified TIP4P/2005 model,[166] the parameter range for which an LLCP can exist in water-like models is significant and includes a temperature range of more than 100 K. The phenomenon of LLPTs in water-like systems is, thus, not limited to a narrow region in parameter space. Therefore, it is not unlikely that an LLCP exists also in real water.

Having determined the location of the LLCP, the critical temperature T_c, pressure P_c, and density ρ_c, it is found that these properties shift to lower values with decreasing scaling factor q. In particular, they have a near linear dependence on q for the studied range of $q = 0.86$–0.91 but non-linear behavior is expected in a wider parameter space. The linear extrapolation of T_c and P_c to the original TIP4P/2005 water model underestimates results found by previous studies.[158–160,162,338,339] The extrapolation of the critical density is within the expected range. For charge scaling with $q < 0.9$, the critical pressure assumes negative values. This means that studies at atmospheric pressure will not cross the Widom line for these systems and, hence, might not notice the anomalies caused by competing local structures as clearly as for normal water. For example in Ch. 6, the density anomaly of water was missing for systems with significantly reduced partial charges. However, the density anomaly and divergence of specific heat, Fig. 7.4, could be shown for $q = 0.86$ once pressure is sufficiently reduced. In nature, more systems might exhibit liquid polyamorphism at negative pressures and, thus, undetectable by common experiments. A more extended exploration of the phase space would be necessary.

One also finds that a reduction of the scaling parameter and weakening of hydrogen bonding leads to shallower isochores in the P-T diagram above the LLCP. This scenario is similar to results for the WAC model where the LLCP disappears below the LVS,[25] which also happened for simulations with a model of silicon.[195] These findings and that the critical pressure for $q = 0.86$ assumes strongly negative values allow for the speculation that the LLCP disappears below the LVS as well not far below the studied q.

Dynamics of the studied models are consistent with the dynamical anomaly of water and slow down when the pressure or density are reduced in the vicinity of the LLCP. The presented results for the rotational correlation functions $F_{1,\mathrm{OH}}$ reveal an increased dynamical heterogeneity for state points close to the LLPT. An apparent decreasing heterogeneity for densities below ρ_c suggests that the dynamical heterogeneity is large for mixed systems while it could be smaller in the liquid phases with high HDS or LDS fraction, respectively. Examination of the SED relation revealed that rotational and translational dynamics are not related in the same way in HDL and LDL. For thermodynamic paths crossing the Widom line, the Stokes-Einstein breakdown is superimposed by the transition from low to high LDS fraction. Hence, extra care has to be taken in the case of water when self-diffusion coefficients D and rotational correlation times τ are compared in different regimes of the phase diagram.

When comparing self-diffusion coefficients and rotational correlation times for isochores and isobars, prominent differences consistent with results for the ST2 water model are found.[210] The deviation from Arrhenius behavior along isochores is moderate and similar for all densities. No significant deviation is found upon crossing the LLPT line for cubic systems. In contrast, cooling along isobars with $P < P_\mathrm{c}$ leads to a strong temperature dependence in the vicinity of the LLCP. For larger distance to the LLCP, $T \gg T_\mathrm{c}$ and $T \ll T_\mathrm{c}$, the temperature dependence weakens and approaches that of the closest isochores. For thermodynamic paths above the critical point that avoid entering the metastable regime, dynamics of isobars with high pressure and isochores with high density agree. These remarkable differences between isochoric and isobaric conditions are also present in the temperature dependence of the LDS fractions and could be confirmed by calculating temperature dependent dynamics for isobars using the data for isochores and the TSOES analysis.

To scrutinize this connection of structure and dynamics the dynamics of extended and stable HDL and LDL regions were analyzed. Here, it was exploited that phase separation into such regions is possible in elongated systems. The unfavorable interface of both phases can be minimized by parallel alignment to the smallest surface of the simulation box (xy-plane). Significant changes were found upon cooling below the LLCP. The density and structural properties show bimodal distributions when measured on 1 nm length scales. This implies phase separation into extended HDL and LDL regions. These systems entered their metastable region with respect to their polyamorphism. In fact, water in this region can even be triple metastable, i.e., it resists crystallization, phase separation, and cavitation at negative pressures.

The phase separation was exploited to characterize the structural and dynamical properties of layers perpendicular to the elongated axis and with thickness $\Delta z = 1\,\mathrm{nm}$ centered about the z position of reference molecules. One finds that structural properties of such layers are stable on a microsecond and nanometer scale for sufficiently low temperatures. This way, it could be ensured that structural distinctions are stable on the time and length scale on which dynamics are probed. Previous studies in the literature have been performed above T_c and only used the local structure instead of extended environments. Measures of the local structure have faster and short range fluctuations which lead to partially averaged dynamics.[336,346] Here, the same effect is found for environments with high LDS fractions and temperatures close to the critical point. The temporal fluctuations of the structural properties lead to premature decay of the correlation functions and, hence, dynamics not representative of LDL. Upon further supercooling the time scales separate and determination of LDL dynamics appears to become possible.

This spatially-resolved analysis was performed for charge-scaling factors of $q = 0.86$ and $q = 0.88$ to take advantage of the speedup of dynamics at the LLCP while still having a pronounced LLPT. One observes a slowdown of rotational dynamics of approximately two orders of magnitude between HDL and LDL environments. Experimental results for heating HDA and LDA above their respective glass transitions show Arrhenius behavior separated by two orders of magnitude as well.[13,206,217]

Agreement between τ from cubic systems with constant density and spatially-resolved analysis of layers with corresponding densities in an elongated system proved that these results are representative of environments with the respective structural properties. These results allow for an explanation of the anomalous pressure dependence of D and τ – it can be understood as a transition from an LDL-like liquid with slow dynamics to an HDL-like liquid with fast dynamics.

The dynamical transition found for water and other tetrahedral network formers under isobaric conditions can be further clarified. This phenomenon was commonly interpreted as an FST resulting from an LLPT. The argument states that HDL and LDL are fragile and strong liquids respectively and that an FST appears as the composition changes from one to the other upon cooling. Instead, only weakly fragile behavior was found for isochoric cooling and hardly any deviations from strong behavior are observed for isomorphs calculated with spatially resolved analysis in a limited temperature regime. Thus, the dynamic transition is not caused by liquids with significantly different fragilities. More importantly, the dynamical properties of HDL and LDL can only be observed at sufficient distance to the LLCP. The dynamical properties on the Widom line and in the vicinity of the LLCP cannot be attributed to either liquid. Additionally, the structure of the high-temperature or simple-liquid regime is a simple disordered phase that is not representative of HDL. As temperature is increased, the average coordination number decreases again and a local structure that is neither HDS nor LDS takes over. The high-temperature dependence upon crossing the Widom line can be understood as the rapid passing over lines of constant LDS fraction and their respective $D(T)$ and $\tau(T)$. The distance to the LLCP in the one-phase region of the phase diagram determines how rapid this conversion happens and, hence, how fragile the temperature dependence of dynamics appears. Approaching the LLCP in pressure leads to a steeper increase in dynamics. In other words, the observed temperature dependence in the crossover region should not be related to a fragility, neither of HDL nor of LDL. Accordingly, no dynamical transition is found for isochores since they show no rapid change of the HDS and LDS fractions with temperature.

This interpretation has similarities with two two-state models for water dynamics developed by Tanaka and coworkers and Caupin and coworkers.[119,120,218] They also proposed that the FST is caused by a crossover between two phases of water that have dynamics on very different time scales. However, strong deviations between the models and the data occur at low temperatures and low pressures or densities, i.e., high LDS fractions. The slowdown of dynamics is underestimated, in part because the slope of the LDS fraction flattens out earlier than the slowdown of the dynamics. Previous tests of these models have not had equally high LDS fractions, and thus may not yet have been able to observe this shortcoming. However, they have also recognized that the location of the maximum slope in the Arrhenius plot and the Widom line are not identical, and thus the fraction x of the TSEOS cannot be readily used.[121] It was found that, in principle, a linear combination of the respective activation energies can be successful. However, higher order terms would have to be introduced for values of the LDS fraction as found from the TSEOS or local structure identifiers to be viable. Thus, the fundamental understanding of how the average dynamics of a reactive mixture are determined by the respective pure phases is still lacking. A solution to this problem would be relevant to all polyamorphic systems. While the high-temperature regime cannot be assigned to either phase, HDL or LDL, it helps to properly represent the supercooled region of HDL to cover as much of the phase space as possible. The extrapolated intersection of the dynamics of HDL and LDL at low temperatures but above T_g and the disagreement with experiments on HDL above T_g raises the question of what the true temperature dependence of HDL is. It would be possible that HDL itself has an FST, a theory that can neither be proven nor discarded here. The implication would be interesting, because then both water phases would belong to the class of liquids with strong-fragile-strong behavior, see Sec. 8.5.

8. Functional forms of $E(T)$

The following sections present and discuss the temperature dependence of dynamical properties in the supercooled regime and possible parametrizations. Because of the shortcomings of most existing functional descriptions, several functional forms are derived from a simple ansatz in this work. Some of them have been used before, but their common mathematical origin, and thus possibly more general applicability, is shown here. They are applied to data sets of systems with regular temperature dependence or with an FST. For the regular case, common relations between the fit parameters are discussed. In the case of an FST or a suspected FST, the functions appear to probe the deviation from fragile behavior, consistent with the expectations for the charge-scaled water systems, Ch. 7, and describe the data over the entire temperature range in the case of silica. In addition, experimental data is investigated and the possibility of a general low-temperature Arrhenius regime is discussed.

8.1. Motivation

The enormous slowdown of liquid dynamics in the supercooled regime down to the glass transition is an intriguing phenomenon. Despite substantial progress, its complicated origin in many-particle physics denies a complete description to this day.[26,27,80,93,150,347,348] There exist various approaches, e.g., entropy theory,[28–30] elastic models,[31] mode-coupling theory[32] or a Langevin equation approach,[33] advancing the field, none of them satisfactorily describes all liquids or all regimes of the glassy slowdown.[80]

Recent reviews still list a variety of open questions, from the shape of correlation functions and susceptibilities to the very basic question of the functional form of the temperature dependence itself.[34,35] In particular, the widely used Vogel-Fulcher-Tammann (VFT) equation, Eq. (2.10), is empirical at best. Although Adam and Gibbs were able to derive this functional form from entropy theory, the result depends on the existence of T_k, the Kauzmann temperature.[29] There the difference in configurational entropy between the glass and the crystal vanishes. While it has been found in the past that the temperature of divergence T_0 of the VFT equation coincides with T_k,[349] indicating an ideal glass transition, deviations have been found in numerous cases as well.[350] A study of 42 liquids found little evidence of such a divergence.[351]

In particular, many liquids show deviations from VFT behavior under strong supercooling. The very sensitive Stickel plot, a representation of the temperature-dependent dynamics linearizing the VFT equation, raised the awareness of this finding.[36,352,353] A study of 84 liquids found deviations from VFT behavior and trends toward an Arrhenius regime at low temperature, suggesting a general importance of this phenomenon.[354] Aging experiments on a 20 Ma old amber also showed a strong deviation from VFT behavior.[355]

One challenge lies in the regimes of different temperature dependencies which can be observed in the liquid regime. In general, the high-temperature regime (HTR), or upper range of the simple-liquid regime (SLR), shows Arrhenius behavior, which will be referred to as the high-temperature Arrhenius (HTA). Upon cooling, the temperature dependence increases becoming super-Arrhenius often characterized by VFT behavior. At strong supercooling, the above-mentioned deviations occur.

In particular, there exist strong liquids with an extensive low-temperature Arrhenius (LTA) regime, e.g., liquids with strong directional bonds such as silica or water, as discussed in Ch. 7. A variety of formulas, derived from physical models or empirical, have been tested and found to be inadequate, for example the MCT, generalized VFT, an equation by Bässler, Avramov, and Milchev, parabolic functions, or the approaches of Mauro et al. or Souletie et al.[356–363] They are either limited by their low parametrization in the number of phenomena or regimes they can characterize, or they are empirical and have high parametrization. For example, the fragile-to-strong transition (FST) in silica has been described by a combination of two Arrhenius and one VFT regime.[118,214] Hence, the question of real temperature dependence and its characterization are the subject of ongoing studies.[34,35,80]

A recent empirical approach by Schmidtke et al., see Sec. 2.2.5, characterized the simple-liquid and supercooled regime of regular liquids exceptionally well despite its simplicity.[37,112,114,115,117,118] Another potential advantage is the absence of a divergence of dynamics. The super-Arrhenius temperature dependence is described by an exponentially increasing activation energy for relaxation events. A similar but more complex functional form was derived by Tanaka and coworkers for the description of water dynamics in the entire temperature regime, see Sec. 7.6.[38,120,121,220] This equation, based on a two-state model, is able to describe the HTR and an FST at stronger supercooling. Recently, the same functional form has been used to characterize dynamics across the glass transition temperature, where liquids typically exhibit a weaker temperature dependence, and thus Arrhenius behavior.[364] These very specific applications of this functional form leave the question of its possible application to other liquids in the liquid regime unanswered. A model qualitatively in-between these two was derived from free-volume theories by Cohen and Grest (CG model).[97] However, its physical interpretation, the pressure and free-volume dependence, was found to be inadequate.[365,366] Still, it is a very potent functional form, especially in cases where deviations from VFT behavior are observable.[356,367]

With these different functional forms and behaviors, e.g., regular vs FST, the question of universality or simplicity among all liquids remains. Some insights in this regard have been obtained for the activation energy E_∞ of the HTA. Experimental data for several molecular glass formers suggests a common ratio of $E_\infty/T_\text{g} \approx 11$.[37,115] Such a common ratio is consistent with a common ratio of 24 when the cooperative contribution to the activation energy is used.[368,369] The SLR and the supercooled regime may be more deeply linked by the typical interaction energies between the particles. However, these ratios differ for polymers[115] as well as for the used dynamical property and the thermodynamic ensemble.[116] Nevertheless, common ratios may exist for subsets of glass formers and the relevance of the interactions in the simple-liquid regime and their influence on the entire temperature range could be further investigated. Systematic studies such as those with the charge-scaled variants of water models could help to scrutinize such relations.

Lastly, the divergence of dynamics in entropy models mentioned above can be avoided by modifications[82–84] or evidence of nonvanishing configurational entropy.[39] The latter implies a constant activation energy at low temperatures in the liquid, if it can be equilibrated. Simulations showed no thermodynamic transition even in the non-ergodic regime.[370] In particular, theoretical calculations of the topological landscape of a mixture of soft spheres showed ergodicity for all finite temperatures.[85] A true ground state at $T = 0$ can be achieved, although the entropy does not vanish for $T > 0$. Simulations also found evidence of a deviation from VFT behavior for the very similar Kob-Andersen mixture.[294,295] Thus, the question arises whether a low-temperature limit for entropy and an Arrhenius-like temperature dependence apply to liquids in general and are only masked by the glass transition in most cases.[356,367]

With these open questions in mind, this chapter presents the formal derivation of several functional forms that can characterize regular and FST behavior. Two of these are the aforementioned models by Schmidtke et al. and Tanaka and coworkers whose common mathematical origin is revealed. These functional forms are tested on results from regular glass formers and then, in particular, on simulation data from charge-scaled water models for which an FST can be related to configurational changes in the liquid, see Sec. 7. Additionally, simulation data of silica with a pronounced FST[118] and various experimental data sets are characterized.

8.2. Derivation of empirical models

In general, functions describing the temperature-dependent dynamics in the supercooled regime are based on physical observations. The VFT equation can be derived from the Adam-Gibbs theory and the vanishing configurational entropy at the Kauzmann temperature, while the power law of mode-coupling theory is a prediction from the mathematical model.[29,32] Here, functions are derived from simple principles and investigated for their possible physical interpretation afterwards. The general idea, that a temperature-dependent dynamical property X can be described by an exponential function of the temperature-dependent activation energy $E(T)$, or E for short, leads to the common ansatz

$$X = X^*_\infty \left(\frac{T_\mathrm{r}}{T}\right)^\theta \exp\left(\nu \frac{E}{T}\right) , \tag{8.1}$$

where X^*_∞ and T_r are a system-dependent prefactor and an arbitrary reference temperature or energy, respectively. The exponent θ corresponds to the effect of thermal energy on the particle velocity and can be used to satisfy the SED relation (Sec. 2.1.3), i.e., $|\varDelta\theta = 1|$ between the descriptions of the viscosity η and the rotational correlation time τ or the self-diffusion coefficient D. This becomes relevant when viscosity and self-diffusion or correlation time have the same activation energy. The sign of the exponent is ν, e.g., $+1$ for τ and -1 for D. For simplicity, energy is defined in Kelvin, $[E] = \mathrm{K}$. In the supercooled regime, temperature generally changes by a factor of two down to the glass transition temperature T_g. Thus, its effect on the dynamics is weak compared to the influence of the exponent when dynamics slow down by more than ten orders of magnitude. Hence, the factor $(T_\mathrm{r}/T)^\theta$ can often be omitted and the description of $E(T)$ includes this contribution to the temperature dependence. Moreover, one can omit the sign ν by inverting the dynamical property, e.g., using $1/D$, which allows for the simplified form

$$X = X_\infty \exp\left(\frac{E}{T}\right) \tag{8.2}$$

in most cases. However, at temperatures up to the boiling point and above, the prefactor can become relevant and the situation is not always that simple, as found for example for isobaric and isochoric cooling of charged LJ particles.[116] With the exception of these very high temperatures, it is of particular importance in the following derivation that the functional form of E describes as much of the available temperature range as possible. Any model that does not follow the common strong-fragile crossover, i.e., HTA to supercooled super-Arrhenius, is not viable. As will be seen later, the derived functions produce not only strong-fragile but also strong-fragile-strong behavior, as found for tetrahedral network formers such as water, Ch. 7,.[120,147,208]

It has proven useful to split the activation energy into two parts, a constant contribution at high temperatures E_∞ and E_c, a contribution often attributed to cooperative effects.[37,112,113]

$$E(T) = E_\infty + E_\mathrm{c}(T) \tag{8.3}$$

E_∞ is fixed as the temperature-independent contribution in the simple-liquid regime. It remains to describe the cooperative contribution E_c. This restricts functions for E_c to those that (i) vanish at high temperatures and (ii) increase monotonically with decreasing temperature. The existence of an ideal phase transition and divergence at finite temperature, a feature exhibited by the very popular VFT equation, would imply a divergence of E_c for finite temperatures. However, there is no experimental evidence of a true divergence of glassy dynamics and instead there is evidence of finite relaxation times at all finite temperatures.[39,85,350,370] Thus, an optional condition (iii) is that E_c should be continuous for all temperatures.

A simple approach to approximate E_c would be a series expansion in T up to a certain order. However, polynomial functions can lead to nonphysical results if the data is extrapolated far from the interpolation, e.g., growing E_c for $T \to \infty$. Instead, series expansion in orders of E_c itself is performed.* There are two options for the derivative: with respect to real or to reciprocal temperature. While the latter follows the typical study of glass formers, e.g., with Arrhenius plots, neither will be preferred for now. To introduce dimensionless parameters and functional forms, E_c and T are expressed on the scale of E_∞, $\hat{E}_\mathrm{c} = E_\mathrm{c}/E_\infty$ and $\hat{T} = T/E_\infty$. The series expansions are

$$\frac{\mathrm{d}\hat{E}_\mathrm{c}}{\mathrm{d}\hat{T}} = \alpha\hat{E}_\mathrm{c} + \beta\hat{E}_\mathrm{c}^2 + \mathcal{O}(\hat{E}_\mathrm{c}^3) \text{ and} \tag{8.4}$$

$$\frac{\mathrm{d}\hat{E}_\mathrm{c}}{\mathrm{d}1/\hat{T}} = \alpha\hat{E}_\mathrm{c} + \beta\hat{E}_\mathrm{c}^2 + \mathcal{O}(\hat{E}_\mathrm{c}^3). \tag{8.5}$$

Here α and β are the relevant parameters that determine the behavior of $\hat{E}_\mathrm{c}$. A constant term would prevent the occurrence of an Arrhenius regime and contradicts the construction of Eq. (8.3). Orders of power 3 or greater are neglected since they prevent an analytical solution of the differential equations. Thus, it remains to study the combinations of $\alpha, \beta = 0$ with $\mathrm{d}\hat{T}$ and $\mathrm{d}1/\hat{T}$ that satisfy conditions (i) and (ii) for all temperatures. For relevant solutions of the differential equations, shown in Tab. 8.1, the integration constant is introduced as $\mathcal{C}$ and the signs of α and β in Eq. (8.4) and (8.5) are adjusted so that both parameters are positive. Other solutions are possible, but allow for violations of (i) and (ii) in combination with $\mathcal{C}$.

Trivially, two types of solutions can be found, hyperbolic and exponential. Solutions containing only the first-order term, $\beta = 0$, are simple exponential functions. Note that $\exp(\alpha(1/\hat{T} + \mathcal{C}))$ does not vanish for $T \to \infty$ and violates condition (i). However, for $\mathcal{C} \ll 0$ it becomes negligible in the high-temperature regime. On the other hand, the solution $\exp(\alpha(1/\hat{T} + \mathcal{C}))$ has a low-temperature limit, i.e., the functional form leads to an LTA for sufficiently small temperatures $T \ll \mathcal{C}$. Using only the second-order term in the differential equation, i.e., setting $\alpha = 0$, leads to functions with possible divergences, and thus to the violation of condition (iii).

The solutions for first and second-order terms of $\hat{E}_\mathrm{c}$ lead to two exponential functions, one of which resembles the Fermi distribution. With $\beta > 0$, they have a continuous temperature dependence. Interestingly, they also have a low-temperature limit. The activation energy of this LTA, in addition to E_∞, is $\hat{E}_\mathrm{c} = \alpha/\beta$ for the derivative with respect to $\mathrm{d}1/T$ while this value is only approximately assumed for $\mathrm{d}T$ when $\mathcal{C} \ll 0$. This complements the solution for only first-order terms and $\mathrm{d}1/T$ for which $\hat{E}_\mathrm{c}$ does not truly vanish in the HTR.

Including X_∞ and E_∞, the functions have four or five adjustable parameters. This makes them more complex than most other functional forms in the literature. However, the freedom of these parameters is limited by the above conditions for which the solutions were filtered. Accordingly, the

---

[*] One of the resulting functional forms of second order was found through empirical reasoning first and correspondence with V. N. Novikov lead to the ansatz of series expansion in E_c, for which I am very grateful.

Table 8.1.: Solutions to Eq. (8.4) and (8.5) for $\hat{E}_{\mathrm{c}}$. The signs of the terms in Eq. (8.4) and (8.5) are adjusted such that $\alpha, \beta \geq 0$ and conditions (i) and (ii) are fulfilled.

	$\mathrm{d}\hat{T}$	$\mathrm{d}1/\hat{T}$
order	$\hat{E}_{\mathrm{c}}$	
1st	$e^{-\alpha(\hat{T}+\mathcal{C})}$	$e^{\alpha(1/\hat{T}+\mathcal{C})}$
2nd	$\frac{1}{\beta(\hat{T}+\mathcal{C})}$ $\hat{T}>-\mathcal{C}$	$-\frac{1}{\beta(1/\hat{T}+\mathcal{C})}$ $1/\hat{T}<-\mathcal{C}$
1st & 2nd	$\frac{\alpha}{\beta+e^{\alpha(\hat{T}+\mathcal{C})}}$	$\frac{\alpha}{\beta+e^{-\alpha(1/\hat{T}+\mathcal{C})}}$

data sets should contain the HTA and supercooled super-Arrhenius regime to give the fit parameters their respective meanings. For incomplete data sets, these functional forms are overparameterized.

8.2.1. Applicability of the solutions

The solutions to the differential equations listed in Tab. 8.1 are applied to test data to investigate their ability to fit the data and their compliance with conditions (i)-(iii). Figure 8.1(a) shows the reciprocal self-diffusion coefficients for the charge-scaled TIP4P/2005 water model with charge-scaling factor $q = 0.7$ and isobaric cooling at $P = 1\,\mathrm{bar}$. A HTA is clearly visible and the VFT equation cannot adequately describe this temperature regime. In contrast, all the functions from Tab. 8.1 describe the data very well. The additional requirement to also describe the SLR is made possible by the additional parameters.

Figure 8.1(b) shows the reduced cooperative contribution $\hat{E}_{\mathrm{c}}$ to the activation energy as described by the functions. For the exponential functions, $\hat{E}_{\mathrm{c}}$ grows upon supercooling and diminishes rapidly for higher temperatures, which is not the case for the hyperbolic functions. The consequence for these functions is a reduced value for the fit parameter E_∞ compared to an Arrhenius fit to the HTR alone, see Fig. 8.1(c). Both hyperbolic functions have the same temperature of divergence, $T = 67\,\mathrm{K}$, which is surprisingly close to the temperature of divergence $T_0 = 65\,\mathrm{K}$ of the VFT equation fitted to the supercooled regime. While this is an intriguing finding, the hyperbolic functions lead to a deviation of E_∞ and the violation of (iii), a divergence of $\hat{E}_{\mathrm{c}}$. For these reasons, they will be omitted from here on.

As for the functional forms with first and second-order terms, the parameter β is zero for the fits to the present data set. Hence, the first-order approximation is sufficient to describe simple cases ranging from a strong HTA to the fragile low-temperature super-Arrhenius regime. However, the importance of the second-order term will become apparent in later sections and these functional forms are not dropped.

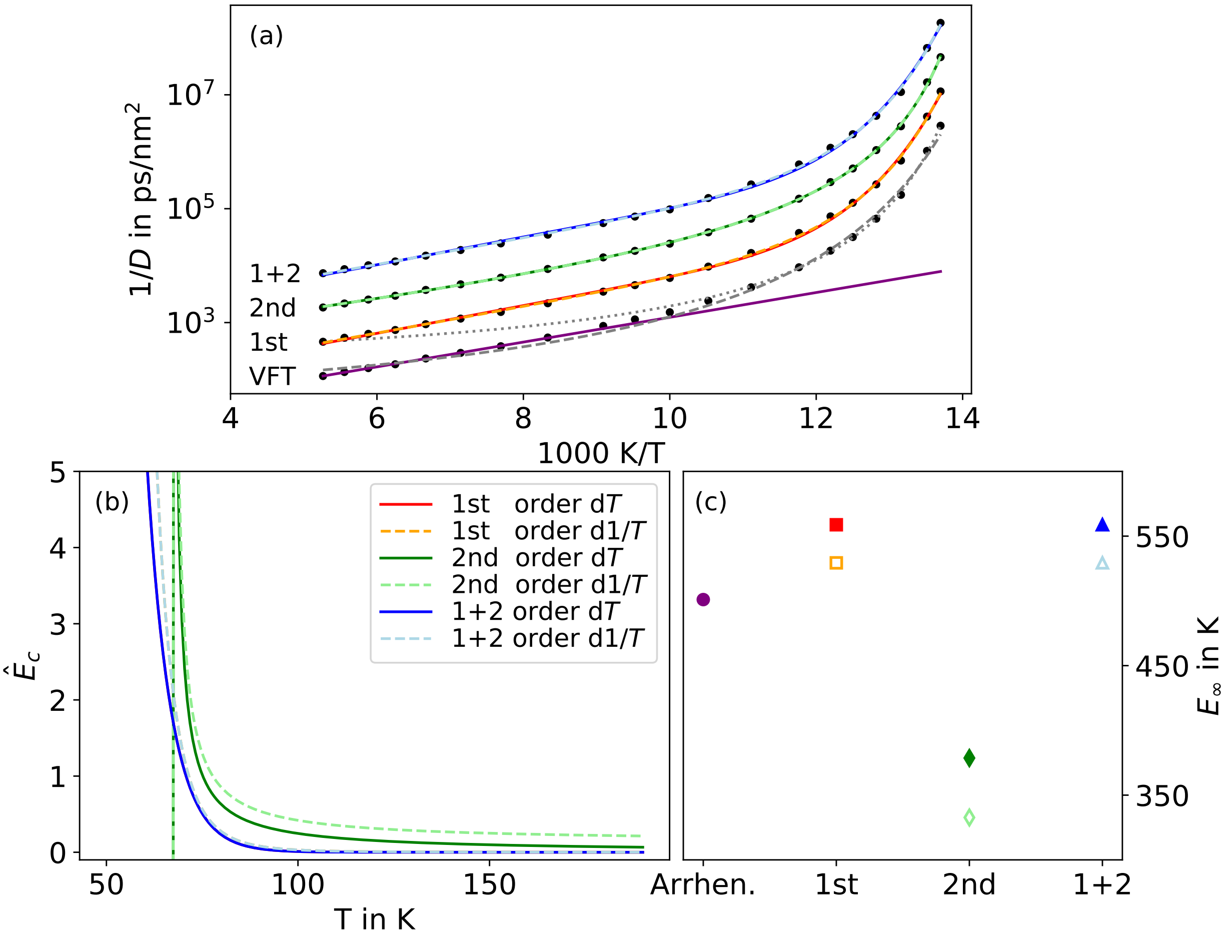

Figure 8.1.: Test of the solutions to the differential equations in Tab. 8.1. (a) The black dots are self-diffusion coefficients D of the charge-scaled TIP4P/2005 water model with $q = 0.7$ and are repeated and shifted upwards by a factor of two for clarity. The solid purple line is an Arrhenius fit to the SLR. The dashed and dotted gray lines are fits with the VFT equation to the entire data set and the supercooled regime only, respectively. The colored solid and dashed lines are fits of the different solutions for derivatives with respect to $\mathrm{d}T$ and $\mathrm{d}1/T$, respectively. The included orders of the terms in the differential equations are given next to the HTR of the shifted data sets. (b) The reduced cooperative contribution to the activation energy $\hat{E}_\mathrm{c}$ as a function of temperature for the fits in (a). Vertical lines mark a divergence of $\hat{E}_\mathrm{c}$. The lines for first-order terms are hidden beneath the respective lines for first- and second-order terms. (c) The activation energy E_∞ from the fits. The color code of the legend applies to all panels.

8.2.2. Final functional forms

The solutions in Tab. 8.1 are now rewritten into more convenient forms by subsuming terms into $\mathcal{C}$ and redefining α and β with μ and $\lambda \geq 0$.

$$E_{\mathrm{c}^1} = E_\infty e^{-\mu(T-T_\mathrm{x})/E_\infty} \tag{8.6}$$

$$E_{\mathrm{c}^1_\dagger} = E_\infty e^{\mu E_\infty(1/T-1/T_\mathrm{x})} \tag{8.7}$$

$$E_{\mathrm{c}^2} = \frac{E_\infty}{\lambda + e^{\mu/E_\infty(T-T_\mathrm{x})}} \tag{8.8}$$

$$E_{\mathrm{c}^2_\dagger} = \frac{E_\infty}{\lambda + e^{-\mu E_\infty(1/T-1/T_\mathrm{x})}} \tag{8.9}$$

The subscripts denote these activation energies as the cooperative contribution in Eq. (8.3) as solutions to series expansions up to order 1 and 2. The absence and addition of † to the subscript denotes the derivative in the series expansion with respect to $\mathrm{d}T$ and $\mathrm{d}1/T$, respectively.

$\mathcal{C}$ has the meaning of a temperature or energy and is renamed to T_x. This is the temperature at which $E_\mathrm{c} = E_\infty$ in Eqs. (8.6) and (8.7). However, its meaning can be arbitrarily changed by changing the prefactor in E_c from E_∞ to another value. μ can be interpreted as a generalized fragility parameter that mostly governs the super-Arrhenius temperature dependence.[37] Its value differs strongly between E_{c^2} and E_{c^1} due to the inversion of T/E_∞ to E_∞/T. Comparable values can be obtained by scaling with $(T_\mathrm{x}/E_\infty)^2$, which has not been done in the above equations for brevity. The activation energy of the LTA is characterized by λ. Note that E_{c^2} and $E_{\mathrm{c}^2_\dagger}$ simplify to E_{c^1} and $E_{\mathrm{c}^1_\dagger}$ for $\lambda \to 0$, respectively.

Two of the above functional forms have been discovered earlier. Schmidtke et al. empirically found $\hat{E}_{\mathrm{c}^1}$,[37] recently referred to as the constant two barrier (CTB) model,[116] while Shi et al. modeled the FST of water effectively using $\hat{E}_{\mathrm{c}^2_\dagger}$, see Eq. (7.9). The latter is physically motivated by a two-state model and the transition from one Arrhenius to another, Sec. 7.6. However as shown here, the functional form can be derived without prior knowledge of the system and its local structures or states.

Substitution with Eq. (8.6)-(8.9) in Eq. (8.3) and (8.1) leads to the final functional forms, which from here on will be abbreviated as first-order (FOF), reciprocal first-order (rFOF), second-order (SOF) and reciprocal second-order function (rSOF).

8.2.3. Features and internal comparison

Before applying the functional forms to real data, they are compared with each other, see Fig. 8.2. Since SOF and rSOF are extensions of their lower-order variants, only functions within the same order need to be compared. A dummy data set is calculated using the FOF and SOF and the reciprocal functions are fitted to the result. Figure 8.2(a) shows that both variants, expansion in $\mathrm{d}T$ and expansion in $\mathrm{d}1/T$, agree well for a significant dynamical range with barely noticeable deviations. The SOFs with $\lambda > 0$ lead to a clearly visible FST. The cooperative contributions E_c are shown in Fig. 8.2(b). They are zero for high temperatures as constructed and increase exponential-like for $\lambda = 0$. However, for $\lambda > 0$, E_c is a smooth step function consistent with the FST of the dynamic quantity. Differences between the dummy data and the fit are more apparent for E_c where the rFOF and rSOF both overestimate it compared to the amount in the FOF and SOF. This difference is compensated by differences in the fit parameters X_∞ and E_∞.

To further scrutinize the differences between the variants and investigate this FST, the first and second derivative $\frac{\mathrm{d}\ln X/X_\infty}{\mathrm{d}1/T}$ and $\frac{\mathrm{d}^2\ln X/X_\infty}{\mathrm{d}1/T^2}$ can be studied. The first derivative is the apparent

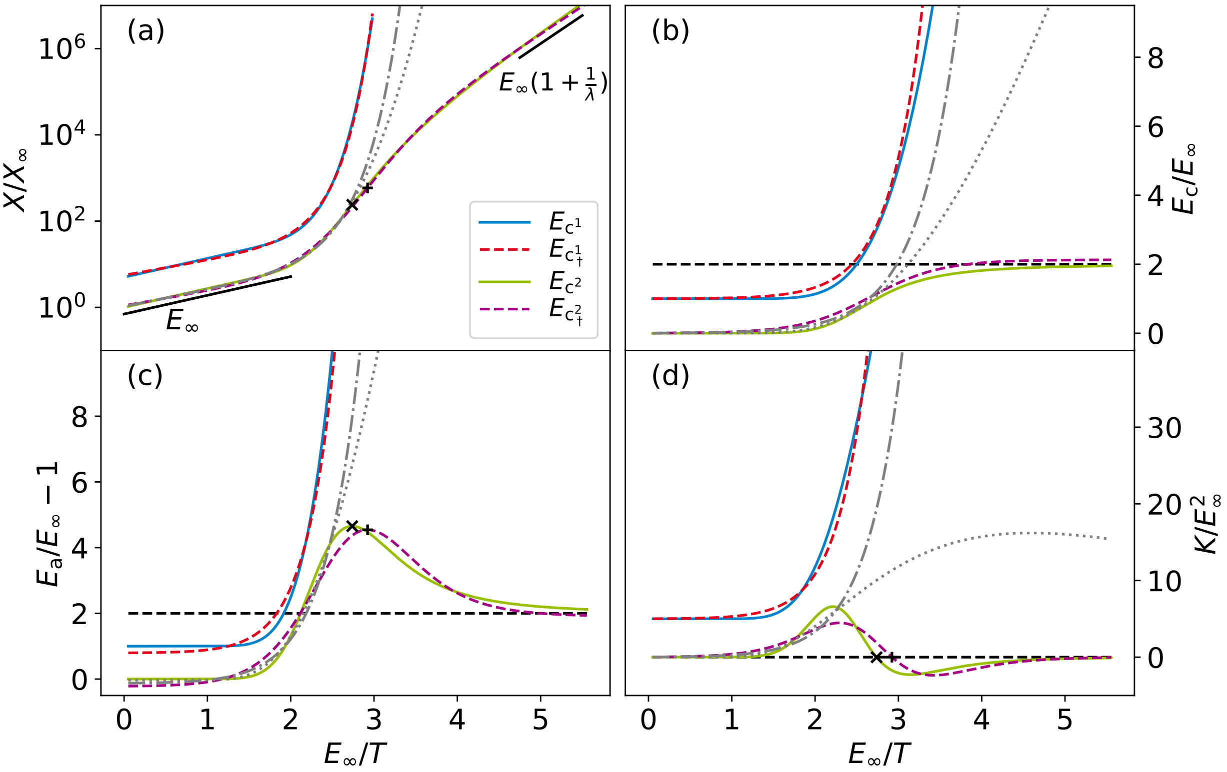

Figure 8.2.: The derived functions, Eq. (8.6)-(8.9), are compared with each other in conjunction with Eq. (8.2). (a) Arrhenius plot of the dynamical property X. The solid lines are calculated using the FOF and SOF with $\mu = 20$, $T_\mathrm{x} = 2/5E_\infty$, and $\lambda = 0.5$. The dashed lines are fits with the rFOF and rSOF to the respective calculated data. The data for the FOF is shifted upwards by a factor of 5 for clarity. (b) The cooperative contribution to the activation energy. Data for the FOF is shifted upward by 1. The black dashed line indicates the low-temperature limit for the SOF. (c) The apparent activation energy E_a of the data in (a) as a function of temperature. The black dashed line indicates the low-temperature limit for the SOF. The result for the FOF and rFOF are shifted upward by 1. (d) The curvature K of the respective data. Data for the FOF is shifted upward by 5.
The results are scaled by the values of X_∞ and E_∞ used in the calculation of the original data with the FOF and SOF. The dotted and dash-dotted gray lines are the corresponding result for fitting the FOF and rFOF to the calculated data from the SOF for temperatures above the inflection point T_i. Black crosses and plus signs mark T_i for the SOF and rSOF, respectively.

activation energy E_a and the second derivative the curvature K.[120] The derivatives for the FOF and SOF are:

$$E_{\mathrm{a,c}^1} = E_\infty + e^{-\Phi}(\mu T + E_\infty) \qquad K_{\mathrm{c}^1} = e^{-\Phi}\frac{\mu^2 T^3}{E_\infty} \tag{8.10}$$

$$E_{\mathrm{a,c}^2} = E_\infty + \frac{e^{\Phi}(\mu T + E_\infty) + \lambda E_\infty}{(\lambda + e^{\Phi})^2} \qquad K_{\mathrm{c}^2} = \frac{\mu^2 T^3 e^{\Phi}\left(e^{\Phi} - \lambda)\right)}{E_\infty\left(\lambda + e^{\Phi}\right)^3} \tag{8.11}$$

The formulas are shortened using $e^{\Phi} = E_\infty / E_{\mathrm{c}^1} = e^{\mu(T - T_\mathrm{x})/E_\infty}$. The derivatives for the rFOF and rSOF are:

$$E_{\mathrm{a,c}^1_\dagger} = E_\infty + e^{-\Theta}E_\infty(1 + \mu\frac{E_\infty}{T}) \qquad K_{\mathrm{a,c}^1_\dagger} = e^{-\Theta}\mu E_\infty^2(2 + \mu\frac{E_\infty}{T}) \tag{8.12}$$

$$E_{\mathrm{a,c}^2_\dagger} = E_\infty + \frac{E_\infty e^{\Theta}(1 + \mu\frac{E_\infty}{T}) + \lambda E_\infty}{(\lambda + e^{\Theta})^2} \qquad K_{\mathrm{a,c}^2_\dagger} = \frac{\mu E_\infty^2 e^{\Theta}(\lambda(2 - \mu\frac{E_\infty}{T}) + e^{\Theta}(2 + \mu\frac{E_\infty}{T}))}{(\lambda + e^{\Theta})^3} \tag{8.13}$$

Here $e^{\Theta} = E_\infty / E_{\mathrm{c}^1_\dagger} = e^{-\mu E_\infty (1/T - 1/T_\mathrm{x})}$ is used to shorten the formulas.

The corresponding results for the first-order cases follow for $\lambda \to 0$. According to the construction with condition (i), E_a is equal to E_∞ for high temperatures and increases upon cooling. Only for $\lambda > 0$, the second-order case, does K have a root and then asymptotically approaches zero. This implies a maximum in E_a followed by an asymptotic value of $\lim\limits_{T \to 0} E_\mathrm{a} = E_\infty(1 + 1/\lambda)$ at lower temperatures. In contrast, the activation energy increases strictly monotonically in the first-order case. As mentioned earlier, K also vanishes for the FOF and $T \to 0$ and E_a is finite at $T = 0$, unlike the rFOF for which these properties diverge.

Both E_a and K can be compared for the dummy data and the fitted functions, see Fig. 8.2(b) and (c). The expected features of monotonic increase or maximum in E_a occur for the first- and second-order functions, respectively. E_∞ of the fitted functions does not perfectly match the calculated data. Because the models are not completely identical, the fit of both, the high and supercooled temperature regime, leads to compromises. For the application of these models, it may be advantageous to fix the parameters corresponding to the HTA if they can be reliably determined.

The peak in E_a is narrower for the SOF than for the rSOF and shifted to higher temperatures. Accordingly, the root of the curvature K is also shifted to higher temperatures, see Fig. 8.2(c). That the models "overshoot" in E_a compared to E_c as $E(T)$ approaches the LTA is a nontrivial consequence of their construction. For example, a sigmoidal shape in E_a and the FOF would also lead to an FST, but with the LTA as a direct continuation of the fragile regime. For which liquids this scenario is relevant will be discussed in Sec. 8.5.

Both the peak of E_a and the root of K define the inflection point T_i in the Arrhenius plot. It can be calculated analytically for the SOF and numerically for the rSOF:

$$\text{SOF: } T_\mathrm{i} = T_\mathrm{x} + \frac{E_\infty}{\mu}\ln\lambda, \tag{8.14}$$

$$\text{rSOF: } 0 \overset{!}{=} 2\lambda + 2e^{\Theta} + \mu\frac{E_\infty}{T_\mathrm{i}}(e^{\Theta} - 1). \tag{8.15}$$

As long as temperatures above T_i are studied, an FST may not be visible and functions with fewer parameters may describe the data.[340] On the other hand, an FST of this kind is only observable when T_i lies above T_g.[213]

To test this, the FOF and rFOF were fitted to the data generated with the SOF for temperatures above T_i, Fig. 8.2. The dynamical property can be well described in this temperature range and the deviations in E_c and E_a are minor. The curvature as a higher-order derivative is of course more sensitive and deviations are more apparent. Lastly, note that the extrapolation for the fitted FOF to the data shows its maximum in K within the presented temperature range. However, extrapolation to $X/X_\infty = 10^{15}$ leads to $E_\infty/T_\mathrm{g} \approx 4.35$. At this temperature, K is close to its maximum value and E_a is still strongly temperature dependent. It is unlikely that any parametrization of real liquids with the FOF leads to this LTA at T_g or above.

The above discussion shows that the derived functional forms have a variety of features. In summary, they exhibit a strong regime at high temperatures followed by a fragile regime upon cooling, they can have an FST with (or without with the FOF) a maximum in E_a upon further cooling, they can have asymptotes and extrema in E_a and K, and even a root in K. The derived family of functional forms should therefore be useful in describing a variety of liquid dynamics.

8.3. Functional forms in the literature

Table 8.2.: Functional forms for the temperature dependence of dynamics in the supercooled regime from the literature.

	$\ln\left(X(T)/X_\infty\right)$
VFT[63,78,79]	$\frac{B}{T-T_0}$
Mauro et al.[359]	$\frac{K}{T}\exp\left(\frac{C}{T}\right)$
Bässler, Avramov Milchev[360,361]	$\frac{C}{T^\alpha}$
Parabolic[362]	$\left(\frac{J}{T_0}\right)^2 \cdot \left(\frac{T_0}{T} - 1\right)^2$
Arrhenius + VFT	$\frac{E}{T} + \frac{B}{T-T_0}$
Cohen & Grest[97]	$\frac{2B}{T-T_0+[(T-T_0)^2+\alpha T]^{1/2}}$
MCT[86,87]	$X = X_\infty\left(\frac{T_\mathrm{c}}{T-T_\mathrm{c}}\right)^\gamma$
Souletie & Bertrand[363]	$X = X_\infty\left(\frac{T}{T-T_\mathrm{c}}\right)^\gamma$

After comparing the derived functions with each other, they are now compared with other functional forms from the literature. Table 8.2 shows many possible functions and the corresponding literature. It is noticeable that most functions in the literature have only three fit parameters. Hence, they provide more conservative fits than the FOF and SOF with four and five parameters, respectively, and are less likely to overfit the data. The MCT theory and Souletie & Betrand functions have a possible divergence at a low but finite temperature T_c and therefore do not satisfy the optional condition (iii). Most importantly, most functions in the literature do not seem to characterize an Arrhenius regime for any temperature range.

To visually test the performance of the fit, the functions are fitted to a data set of self-diffusion coefficients from the TIP4P/2005 water model with charge scaling $q = 1.1$, see Fig. 8.3(a) and (e). With the exception of the MCT and parabolic functions, all describe the data reasonably well. The functions by Bässler, Avramov and Milchev and by Mauro et al. do not perform well in the long HTA regime but perform better in the fragile regimes for which they were derived. The power law from MCT theory, see Sec. 2.2.2, performs well only in a limited temperature range.

To better visualize the deviations, the ratio of fit and data is presented in Fig. 8.3(c) and (f). As expected, the functions with four or more parameters have smaller errors than those with fewer. The VFT equation and the equation by Mauro et al. are good contenders with three parameters. However, all functions except the SOF and rSOF with five parameters systematically overestimate or

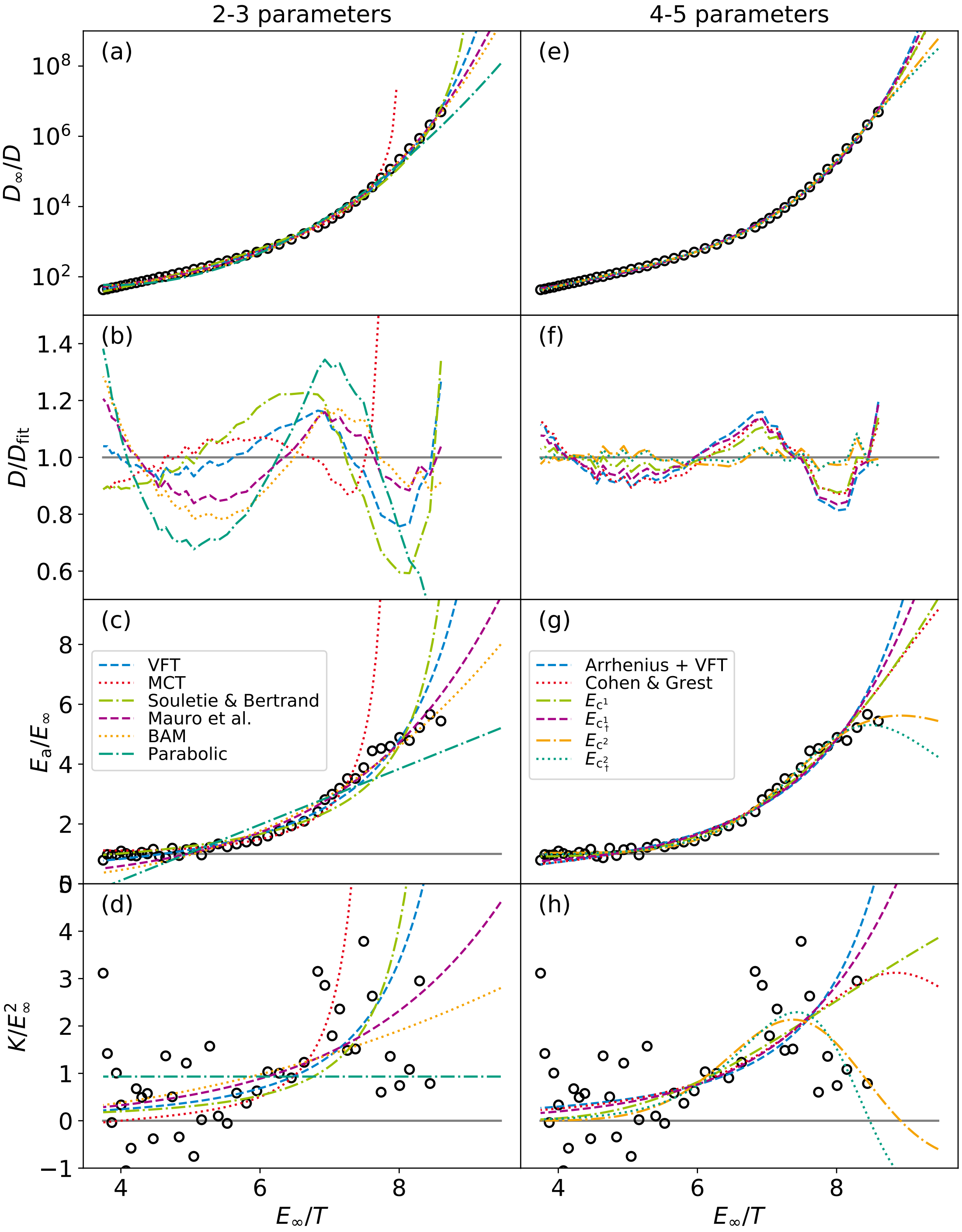

Figure 8.3.: The functions in Tab. 8.2 and the derived functions are fitted to the self-diffusion coefficients of the charge-scaled TIP4P/2005 water model with $q = 1.1$ from Ch.6. Shown are the Arrhenius plot (a,e), the prediction of the fit relative to the data (b,f), the apparent activation energy E_a (c,g), and the curvature K (d,h). The plots are rescaled by the parametrization of the high-temperature regime, E_∞ and $1/D_\infty$ determined by an Arrhenius fit to the data. The black circles are the original data. The legends apply to the respective columns.

underestimate the data in different temperature regimes. These functions cannot truly characterize the temperature dependence of this data set and the fit is only a compromise. Of course, increasing the number of fit parameters generally improves the quality of the fit. However, the features of the derivatives E_a and K reveal whether a functional form is appropriate or not.

Figure 8.3(c) and (g) show the apparent activation energy of the data set and the functional forms. The constant E_a in the high-temperature regime of the data is reproduced only by some functions. In the case of this data set, the upward curvature of E_a appears to decrease towards lower temperatures. This is likely due to the polyamorphism of water discussed in the previous chapter. Most fit functions cannot reproduce this feature because their curvature K is always positive and increases monotonically with decreasing temperature. Only the SOF, rSOF, and the CG model allow K to vanish at stronger supercooling. While K does vanish for the FOF, it does so only in the limit $T \to 0$ and there is no indication of this behavior within the temperature range of the data set.

The second derivative is too noisy to draw meaningful conclusions from this data set alone. Nevertheless, the functions from the literature are not able to produce a maximum in K and an asymptotic approach to zero, which is necessary for an FST. Only the CG model has this feature as well. In the following sections, the FOF and rFOF are studied for the regular case of strong-to-fragile temperature dependence, and then the SOF and rSOF are applied to cases with an FST.

8.4. Strong-to-fragile behavior

It was shown by Schmidtke et al. that the FOF,

$$X = X_\infty e^{\frac{E_\infty}{T}(1+\exp[-\mu(T-T_\mathrm{x})/E_\infty])}\,, \tag{8.16}$$

describes very successfully the most common temperature dependence of liquid dynamics, a transition from strong-to-fragile behavior (SFB) upon cooling. The function describes rotational correlation times for many molecular glass formers down to T_g.[37,112,114,115] The complementary rFOF,

$$X = X_\infty e^{\frac{E_\infty}{T}(1+\exp[\mu E_\infty(1/T-1/T_\mathrm{x})])}\,, \tag{8.17}$$

has not yet been tested for similar data. Hence, this regular case of SFB is analyzed for several data sets. However, most of the simulation data is for water and water-like models. As shown in Ch. 7, these systems can exhibit an FST at lower temperatures. Nevertheless, a description with the FOF and rFOF should be possible as long as the distance to the potential inflection point is large enough. In particular, comparison of systems with only LJ or LJ and Coulomb interaction can provide insightful results.

8.4.1. Determination of the high-temperature parametrization

The routine for analyzing the data is presented in Fig. 8.4 using four liquids as examples. The self-diffusion coefficient D is studied because its temperature dependence is independent of processes on the particular length scale defined by most other methods and it is available for all systems, molecular or atomistic. For a definition of the glass transition temperature for these data sets, see Sec.A.3.1 in the appendix. For the purpose of clarity and comparison, the data in Fig. 8.4 is rescaled by the parametrization of the HTA.

The usual behavior of a strong temperature dependence in the simple-liquid regime is observed followed by a significant slowdown upon further cooling. Deviations from the Arrhenius law occur

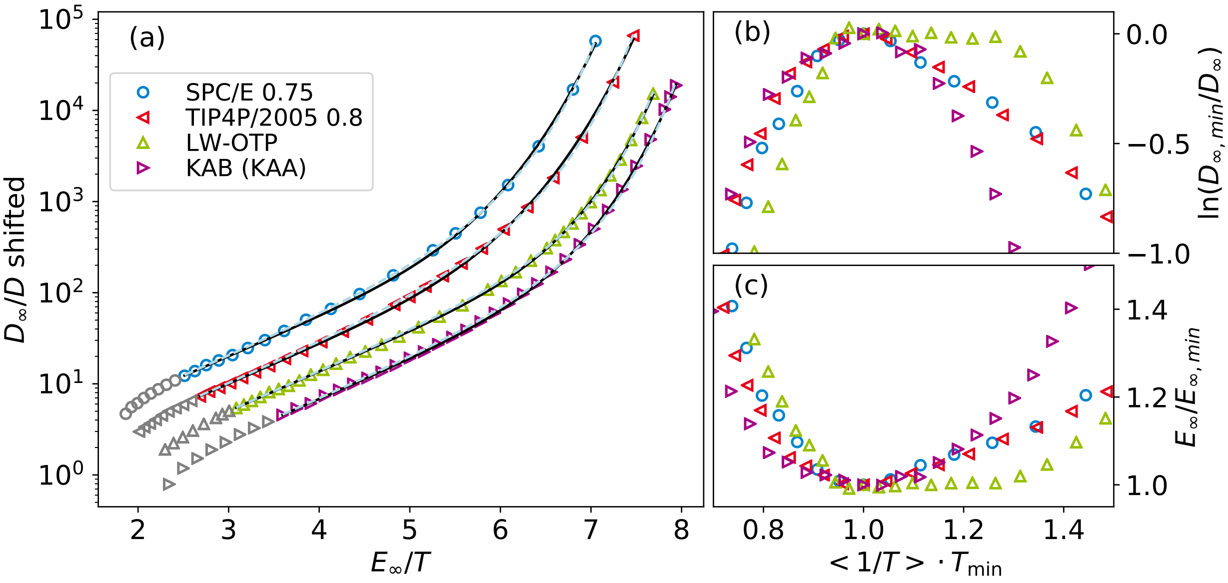

Figure 8.4.: (a) Scaled temperature dependence of the reciprocal self-diffusion coefficient for four examples: charge-scaled SPC/E and TIP4P/2005 at 1 bar and q=0.75 and q=0.8, respectively, LW-OTP, and the larger A particles of the Kob-Andersen mixture. The data is scaled with the fit parameters D_∞ and E_∞ of the HTR and shifted by powers of two for clarity. The solid black and dashed light blue lines are fits with the FOF and rFOF, respectively. Gray symbols mark temperatures beyond the high-temperature Arrhenius regime and are not included in the fit, see the main text. (b) The prefactor $1/D_\infty$ and (c) the activation energy E_∞ of Arrhenius fits to subsets of the data on the left, scaled to the minimum in E_∞. Each subset includes 5 to 8 consecutive temperatures, depending on the resolution of the data set. The reciprocal temperature $\langle 1/T \rangle$ is the average of each subset. The legend applies to all panels.

also at the highest temperatures studied. This feature can appear in simulations for atomistic and molecular systems alike,[116,283] but is not usually observed in experimental measurements. Common experimental techniques such as dielectric spectroscopy have difficulty measuring at such high frequencies and in some cases the dynamics on ps time scales has to be supplemented with light scattering measurements.[112] In addition, temperatures may be high enough to cause chemical reactions or decomposition. Correlation functions at these temperatures decay on sub-ps time scales and are not separated from vibrational motion, see Sec. 2.1.2. In simulations of water and water-like systems, superheating above the critical point is possible and leads to an increased temperature dependence of the density. Evaporation can be rare enough for modest superheating and the system is in a metastable equilibrium, similar to supercooling below the melting temperature. In experiments, superheating is not possible to the same extent. Hence, experimental results for dynamics of this extended high-temperature regime (eHTR) are lacking. In some cases, this temperature dependence can be reconciled by using the temperature-dependent prefactor, Eq. (8.1).[116] This is not the case for the data presented here. The understanding of the eHTR is still insufficient and may be the subject of future studies. Similarities or, more likely, differences to the relaxation mechanisms in the supercooled regime could contribute to a better understanding of the latter.

Here, the simple-liquid and supercooled regime are of interest and the data is systematically reduced, i.e., the eHTR is discarded. To this end, E_a is studied. Because real data is noisy, Arrhenius laws are fitted to subsets of the data in the HTR. Their length in consecutive data points depends on the resolution of the data set. The resulting fit parameters $E_\infty(T)$, a local E_a, and $X_\infty(T)$ are then examined. Figure 8.4 shows the activation energy of the subsets as a function of their average temperature. A minimum and parabolic shape are observed, consistent with the inspection of the eHTR. Accordingly, the prefactor $1/D_\infty$ shows a maximum and an inverted parabolic shape. To characterize the SLR, the parametrization of the Arrhenius law with the lowest activation energy is determined by interpolation. It is assumed that the contributions from cooperative effects, such as those occurring in the supercooled region, and effects from the eHTR are minimized in this way. The highest temperature of the subset with the lowest activation energy is the highest temperature included in fits to the simple-liquid and supercooled regime. Higher temperatures are grayed out and ignored in the following evaluation. Furthermore, this activation energy may be considered the "true" E_∞ of the liquid. When fitting functions to data, the parametrization of E_∞ and X_∞ can be fixed, which is the case here, reducing the free fit parameters of Eq. (8.16) and (8.17) by two. However, this is only possible for data that exhibits an asymptotic or parabola like temperature dependence of E_∞, which is usually not the case for experimental data sets. Reasons are the above-mentioned limitations in frequency or time scale and chemical instability. In addition, combination of different experimental methods leads to discontinuous data sets which are problematic for detailed analysis.

The characterization of the HTA is then used in fitting the SLR and supercooled regime. Excellent agreement between the data and the fits is found for both functions, FOF and rFOF, and all systems, water-like and LJ particles. The dynamics can be described over five orders of magnitude. For experimental data, good agreement was shown for up to 13 orders.[37] Small deviations between the two functions occur, consistent with theoretical observations in Sec. 8.2.3. However, fixing the HTA parametrization may not always lead to satisfactory results, especially when the HTR is only partially resolved and no minimum is found in E_∞. Therefore, fits of the functions to data in the following sections may have fixed or free HTA parametrization depending on the data set.

8.4.2. Typical glass formers - simulations

The investigation is extended to several LJ liquids and a typical glass former, glycerol. For details on the systems see Sec. 4. Consistently, super-Arrhenius behavior in the eHTR, which was excluded from fits to the data, followed by Arrhenius and super-Arrhenius temperature dependence upon cooling is observed, Fig. 8.5(a). The data can be well described by the FOF and rescaling with the parametrization of the HTA collapses the HTR onto a master curve. Deviations from Arrhenius behavior are observed starting at approximately $T = E_\infty/6$ with some variation among the systems. Thus, the energy scale for the onset of cooperative contributions to the activation energy of relaxation appears to be related to the high-temperature activation energy. In particular, they do not play a role at very high temperatures relative to E_∞. This is hardly surprising because the interaction energies that lead to intermolecular bonding and determine the energy scale at which the substance is in a liquid state instead of the gaseous phase are likely also related to the activation energy. For charge-scaled water-like models and LJ particles, a strong dependence of the activation energy on the partial charges and, hence, Coulomb interactions was found, Fig. 8.9.[116,117,283] However, entropy, a property independent of simple geometry-preserving parameter scaling, has varying impact depending on the energy scale and thermodynamic potential, e.g., Gibbs energy $G = U + pV - TS$. Hence, differences are expected when the activation energy is not exclusively enthalpic in nature but has also entropic character, which is at the origin of some models of the glass transition.

If the FOF is well suited to describe the supercooled regime, then it should be possible to collapse

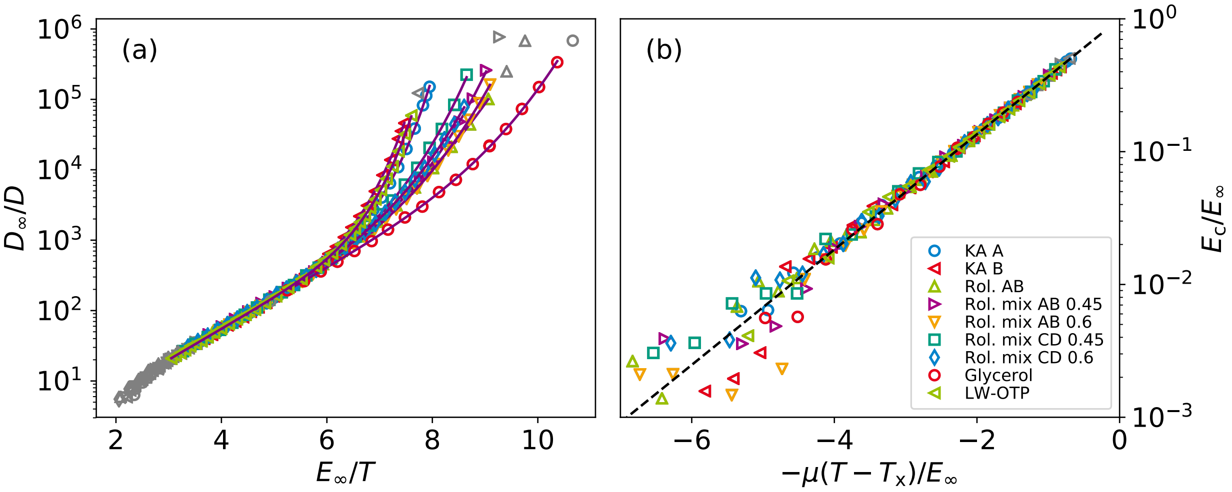

Figure 8.5.: (a) Temperature dependence of the reciprocal self-diffusion coefficient $1/D(T)$ for several model LJ liquids, the Lewis-Wahnströhm model for OTP, and glycerol. The data is rescaled by the parametrization of the HTA and the raw data can be found in Fig. A.14(a) in the appendix. (b) Master curve of the data on the left with the FOF, Eq. (8.16). E_c is calculated from the data and shown as a function of the exponent in Eq. (8.6). Solid purple lines are fits to Eq. (8.16) and the black dashed line is a guide to the eye. Gray symbols mark the eHTR and data points with $D \geq 10^{-6}$ nm^2/ps, and are excluded from the fit to avoid data of poor quality. The legend applies to both plots. The size-to-distance ratios of Roland's dumbbell mixtures are given in the legend.

the data onto a single master curve. This is tested by calculating the cooperative contribution E_c from the data using the parametrization of the HTA and plotting it against the exponent in Eq. (8.6), see Fig. 8.5(b). The data nicely collapses onto a single curve up to temperatures at which E_c amounts to 2% of E_∞. The same master curve for the rFOF is shown in Fig. A.14 in the appendix. The data also collapses but deviations at higher temperatures are systematic. The quality of master curves is further investigated in Sec. 8.4.5.

Both functional forms are fitted to the data with free and fixed parametrization of the HTA. The fit parameters and typical glass transition properties are shown in Fig. 8.6 for fits to the data in Fig. 8.5. Four variations are distinguished, the FOF and rFOF each with free and fixed HTA parametrization, and their relative differences to the result with the FOF and fixed parametrization are shown. Most notable is the good agreement for all fit parameters and even the extrapolations to T_g for both fits with the FOF. The relative differences are small and scatter around zero. Thus, its description for the HTR, as a constructed with an HTA and vanishing E_c, works well even when the HTA parametrization is determined independently.

However, for the rFOF large differences arise already in $1/D_\infty$ and E_∞. A larger value for the prefactor and a smaller high-temperature activation energy are required to describe the data. As a consequence, fixing the parametrization leads to a much larger generalized fragility μ. Another discrepancy is the temperature T_A at which E_∞ and E_c are assumed to be equal. This temperature is much higher for the rFOF than for the FOF. In addition, the extrapolated temperature dependence of the self-diffusion coefficients is much more fragile for the rFOF. The fragility can be calculated for both functional forms according to the definition, Eq. (2.11), and E_a, Eq. (8.11) and (8.13):

$$m_{\mathrm{c}^1} = \frac{1}{\ln 10}\left[\ln\left(\frac{X(T_\mathrm{g})}{X_\infty}\right) + \mu\frac{E_{\mathrm{c}^1}(T_\mathrm{g})}{E_\infty}\right] \tag{8.18}$$

$$m_{\mathrm{c}^1_\dagger} = \frac{1}{\ln 10}\left[\ln\left(\frac{X(T_\mathrm{g})}{X_\infty}\right) + \mu\frac{E_{\mathrm{c}^1_\dagger}(T_\mathrm{g})E_\infty}{T_\mathrm{g}^2}\right] . \tag{8.19}$$

The higher fragility with the rFOF leads to 10 to 15% higher glass transition temperatures which is certainly not trivial. Hence, extrapolation over many orders of magnitude leads to different description of dynamics above the glass transition. For all properties and parameters investigated, results for fitting with the FOF are less dependent on the fitting routine than with the rFOF. However, no general claim can be made for data that does not require extrapolation.

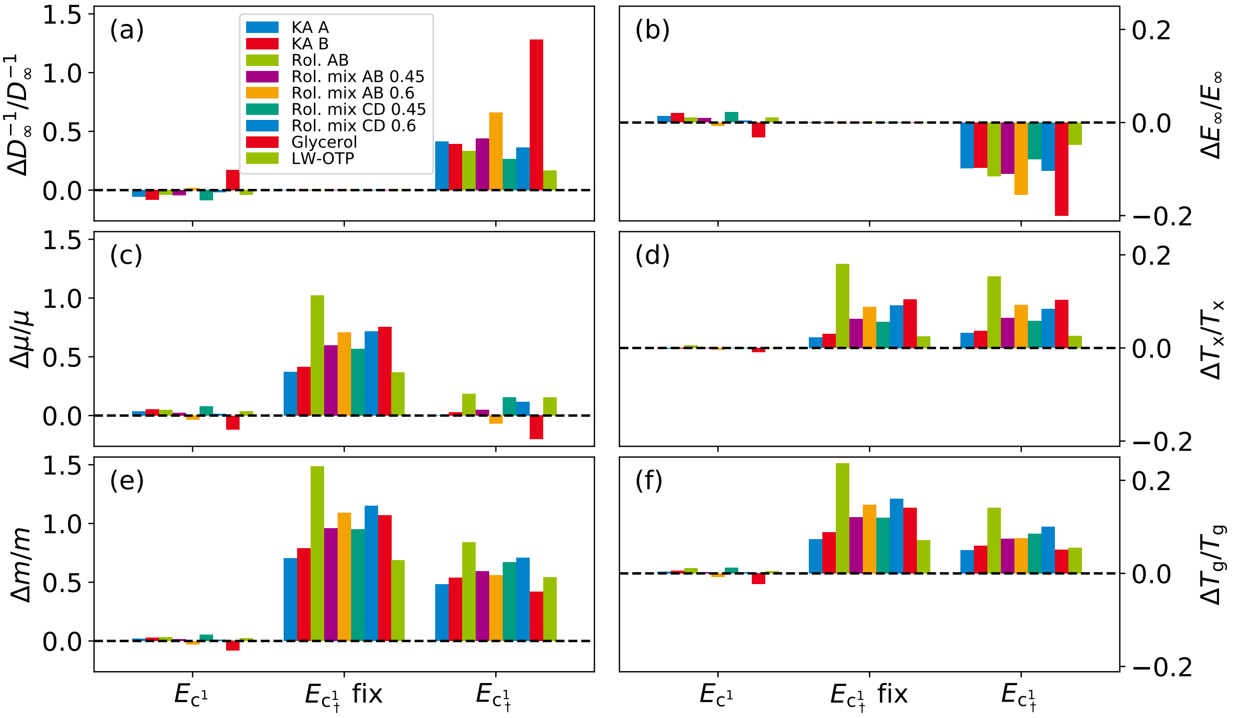

Figure 8.6.: The relative differences $\Delta p/p$ for several fit parameters and properties p determined by fitting the FOF and rFOF, Eq. (8.16) and (8.17), to the same data as in Fig. 8.5 with free and fixed parametrization of the HTA. The differences are always with respect to the fit of the FOF with fixed HTA parametrization, which is therefore not shown, and the parameters are (a) $1/D_\infty$, (b) E_∞, (c) μ, and (d) T_A. For the rFOF, μ is rescaled with $(T_\mathrm{x}/E_\infty)^2$. The fits are extrapolated to the glass transition temperature T_g (e) and the fragility m (f) is determined. The legend applies to all graphs.

8.4.3. Typical glass formers - experimental data

The FOF has already been successfully used by Schmidtke et al. to describe experimental data from the boiling point to the glass transition.[37,112] To ascertain the viability of the rFOF, it is fitted to experimental data from the same literature and the result and a master curve are shown in Fig. 8.7. Visually, the rFOF performs well and the data can be described over 15 orders of magnitude by it. A master curve that covers the supercooled regime can also be created. Deviations occur already earlier in the supercooled regime than for the data from simulations in Fig. 8.5. Note, however, that the experimental data sets are from different methods that are not necessarily perfectly compatible. In particular, the high-temperature regime had to be supplemented with data from light scattering experiments.

The stability of the fits and their extrapolation with increasing distance of the data points to the glass transition was investigated. More specifically, the lowest temperatures were iteratively dropped and the functional forms fitted to the remaining data. The observed trends match those for the simulation data, i.e., underestimation of E_∞ and overestimation of T_g and the fragility by the rFOF. However, the inconsistencies and quality of the data sets prevent further conclusions. Lastly, the master curves for the FOF and rFOF and fixed parametrization of the HTA can be compared in the appendix, Fig. A.15. In this case, the FOF performs better and has less systematic deviations at high temperatures, consistent with the findings in Fig. 8.6.

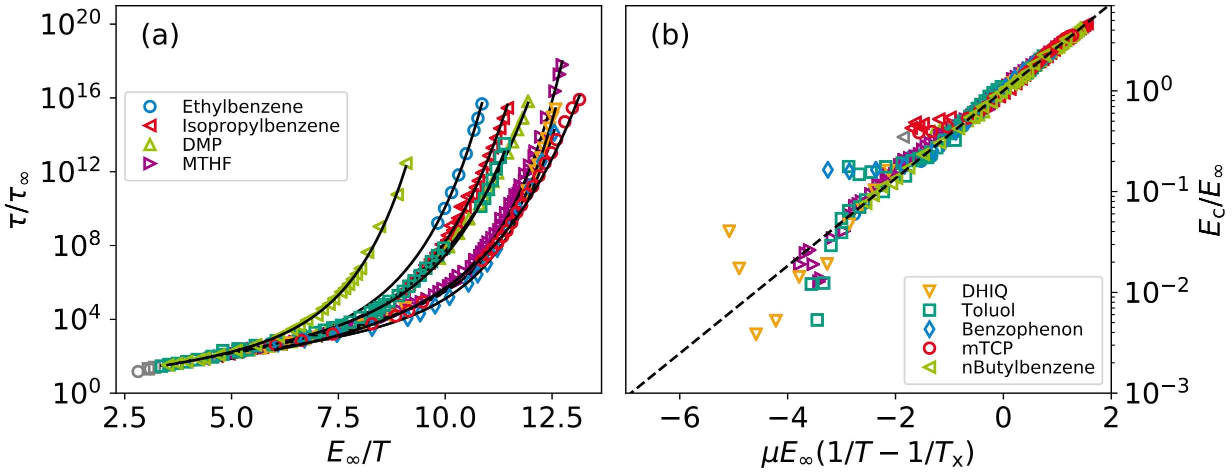

Figure 8.7.: (a) Rotational correlation times for various molecular glass formers from dielectric spectroscopy and light scattering experiments taken from the literature.[112] The data is rescaled by the parametrization of the HTA. Solid black lines are fits the rFOF, Eq. (8.17). (b) Master curve of the data and fits on the left. E_c is calculated from the data and shown as a function of the exponent in Eq. (8.7). The black dashed line is a guide to the eye. The legends apply to both plots. Complementary plots with the FOF and with fixed parametrization of the HTA can be found in Fig. A.15 in the appendix.

8.4.4. Regular temperature dependence for water and water-like systems

Water in its supercooled regime above the *no-man's land* exhibits super-Arrhenius behavior that makes it one of the most fragile systems. Data sets from simulations can reach significantly into the supercooled regime and also show super-Arrhenius behavior. Ch. 7 investigates in detail when and how an FST appears for water-like systems. The FOF and rFOF are not able to characterize such a temperature dependence. In order to investigate these functional forms with data from simulations of water-like systems, the self-diffusion coefficients are limited to values greater than 10^{-6} nm^2/ps. As shown in Sec. 8.2.3, the first-order functional forms are capable of describing data sets with an FST as long as the distance to the inflection point is large enough.

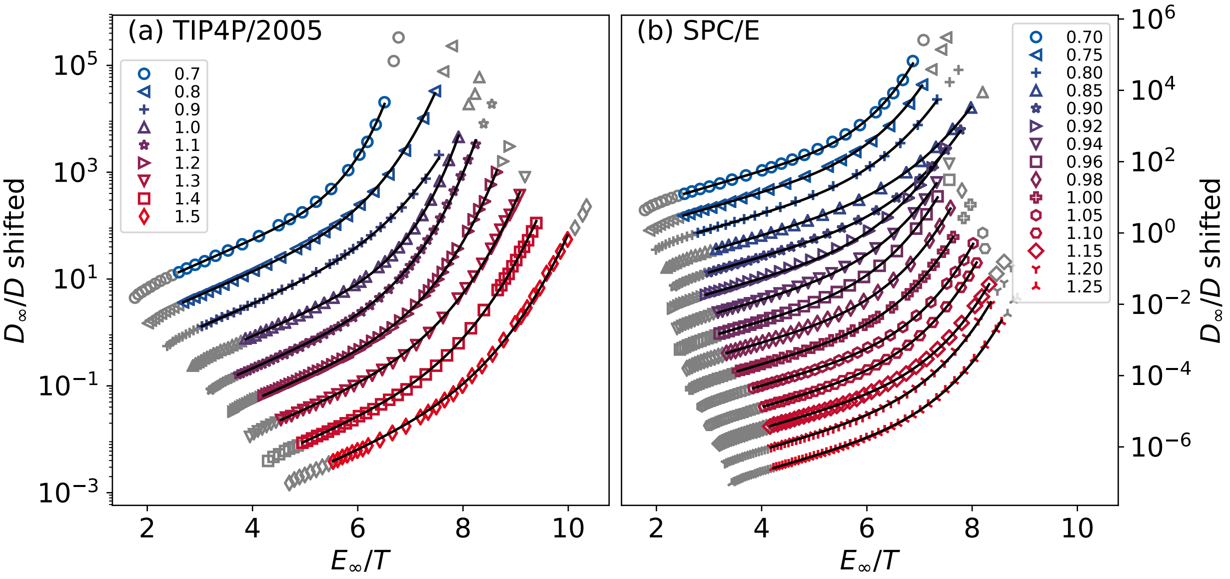

Figure 8.8.: Temperature dependence of the reciprocal self-diffusion coefficient $1/D(T)$ for the charge-scaled TIP4P/2005 (a) and SPC/E (b) water models. The charge-scaling factor q is given in the legend. The data is rescaled in temperature by the high-temperature activation energy E_∞. D is rescaled by the prefactor D_∞ and then shifted by factors of four for clarity. The unscaled data is presented in Fig. 6.6(c) and in Fig. A.3(b) in the appendix. Solid black lines are fits with the FOF, Eq. (8.16), and fixed parametrization of the HTA. Gray symbols mark data points excluded from the fit. On the low-temperature end, data are limited to $D > 10^{-6}$ nm^2/ps to avoid data of poor quality and reduce the influence of the possible FST in these water-like systems.

The self-diffusion coefficients for charge-scaled variants of the TIP4P/2005 and SPC/E water models are shown in Fig. 8.8. Fits with the FOF can successfully describe the data. A complementary study with rotational correlation times of the molecular dipole moment can be found in Horstmann et al. J. Chem. Phys. (2017).[117] A common super-Arrhenius behavior does not seem to be the case. In particular, the curves for SPC/E with $q = 0.92$ and $q = 0.9$ cross despite being shifted. Furthermore, the onset of deviations from the HTA shifts to lower temperatures with increasing charge-scaling factor q. This effect is more pronounced for the charge-scaled TIP4P/2005 variants. However, the highest reciprocal temperature E_∞/T for deviations is just above 6, consistent with the observations to Fig. 8.7.

The charge-scaled variants can be investigated in more detail using the fit parameters and extrapo-

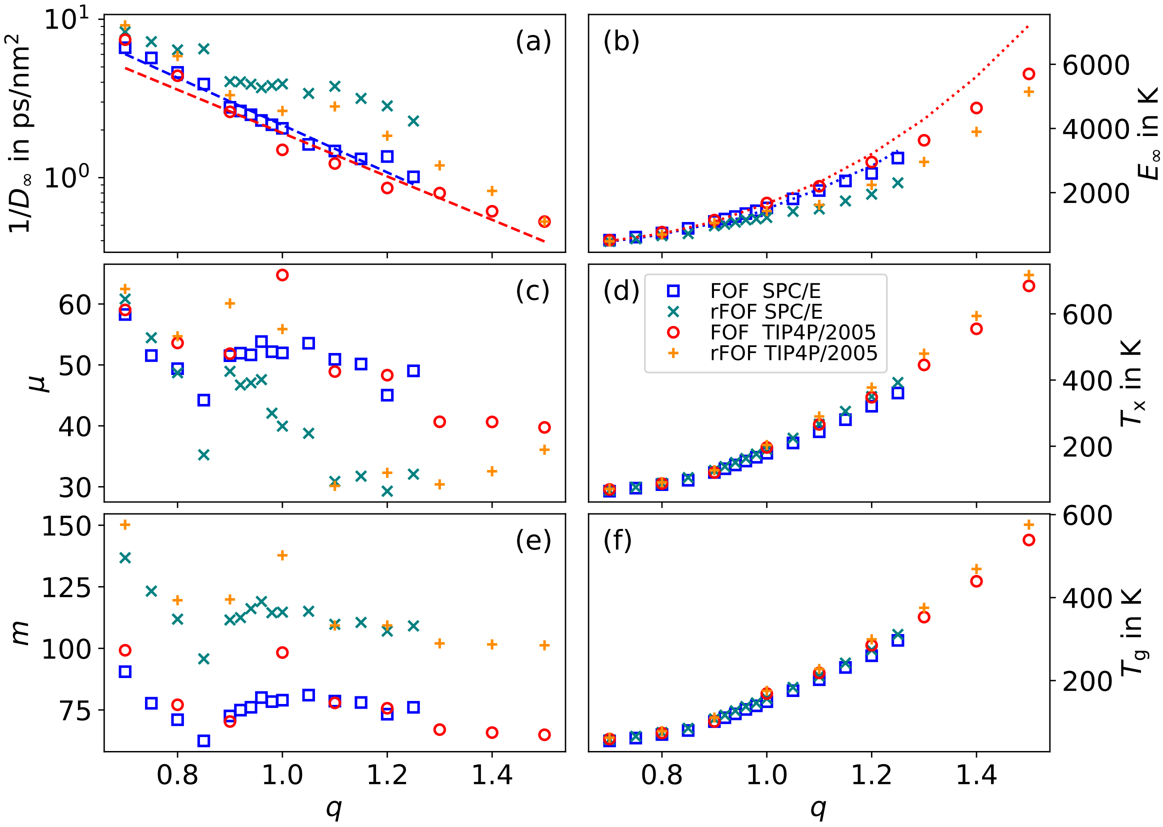

Figure 8.9.: Dependence of the fit parameters (a) $1/D_\infty$, (b) E_∞, (c) μ, and (d) T_x for the FOF and rFOF, Eq. (8.16) and (8.17), on the charge-scaling factor q for two water models, SPC/E and TIP4P/2005. The fits are extrapolated to the glass transition temperature T_g (e) and the fragility m (f) is calculated. The fragility parameter μ from Eq. (8.17) is scaled by $(E_\infty/T_\mathrm{x})^2$. $1/D_\infty$ and E_∞ are the same for the fits with both models and shown only once. The dashed lines in (a) are exponential fits to the data and serve as guides to the eye. The dotted lines in (b) indicate E_∞ from the fit only of the HTA.

lations to T_g, shown in Fig. 8.9 as a function of the charge-scaling factor q. The FOF and rFOF are both fitted with free HTA parametrization to allow them to describe the data as accurately as possible. As a consequence, E_∞ and $1/D_\infty$ may deviate from the best description of the HTR. E_∞ from fitting the FOF does agree with the separate determination for $q < 1.2$ while deviations for the rFOF occur at even lower charge-scaling factors. This difference in the stability of the HTA parametrization between both functional forms is consistent with findings in Sec. 8.4.2.

All properties except the fragilities have a strong monotonic dependence on q. The prefactor $1/D_\infty$ decreases almost exponentially with increasing partial charge. Theoretical derivations for the Enskog or binary-collision regime at high temperatures predict $D_\infty \sim T/\sigma$, where σ is the diameter of colloidal particles.[371] For the charge-scaled variants, σ should vary only weakly compared to E_∞. Since the latter characterizes the energy scale of the SLR, one may assume the simplified relation $D_\infty \sim E_\infty$. Figure A.16 in the appendix shows that this relation is weakly violated for parametrization of the HTA from free fits with the FOF. Independent determination of the HTA leads to even larger violations. Thus, the systems behave only close to the theoretical predictions.

The energy scale E_∞ and the temperatures T_x and T_g all increase almost quadratically with q.

An actual parabolic shape as for charge-scaled LJ particles is not found.[116] Furthermore, all three properties show comparable dependence on q and approximate ratios of $E_\infty/T \approx 10$, suggesting a deeper connection, which is further explored in Sec. 8.4.6. E_∞ is largely the same for both charge-scaled models but increases more for TIP4P/2005, possibly because of its higher absolute partial charges.

The generalized fragility scatters the most among all the properties. For the FOF, its charge dependence is qualitatively similar to that of the fragility m. There is a minimum just below $q = 0.9$ for both systems and μ increases for reduced charges. While the same behavior is found for reduced charges for the rFOF, it predicts charge-scaled variants with $q > 1$ as exceptionally strong. This strong decrease in fragility is not found in the true extrapolation to T_g.

Instead, extrapolation of the two functional forms to the glass transition temperature leads to qualitatively similar results. As with the previous systems, the rFOF predicts a higher T_g and fragility m. The charge dependence of m is similar for both charge-scaled water models, showing the same minimum and weakly decreasing fragility for charges $q > 1$. The location of the liquid-liquid critical point for some systems of the charge-scaled TIP4P/2005 water model is known from Ch. 7. It shifts to negative pressures for $q \leq 0.9$. Therefore, the fragilities on the left are on the HDL side of the LLPT in the phase diagram. Apparently, the fragility increases with the distance from the LLCP. This phenomenon is accompanied by the disappearance of the density anomaly for both water models, see Fig. 7.3 and 6.1. Although the existence of an LLPT is not known for the SPC/E variants, they still most likely have a high HDS concentration and are more representative of HDL than LDL with reduced charges.

The fragility of systems that are suspected to cross the Widom line in the phase diagram if a LLPT exists, is also higher, consistent with the high apparent fragility of water-like systems caused by a rapid transition from low to high HDS concentration with decreasing temperature in Sec. 7.6. However, it is not representative of the fragility of LDL at T_g since the data was intentionally limited to avoid the potential FST.

8.4.5. Master curves

An overview of the performance of the two functional forms, FOF and rFOF, and the fitting routines, with and without fixing the HTA parametrization, is shown in Fig. 8.10. The master curves compare the calculated E_c with the calculated exponent given the fit parameters μ, T_x, and E_∞. The results for the self-diffusion coefficients of the simulated systems in Fig. 8.5 and the charge-scaled variants of SPC/E and TIP4P/2005 are shown. All fits collapse the data in the supercooled regime. Deviations occur when E_c is only within a few percent of E_∞. This depends on the uncertainty of the data and the accuracy of determining E_∞.

The FOF describes all data sets well with and without fixed parametrization and the systems scatter nonsystematically, Fig. 8.10(a-c) and (g-i). Freely fitting the parametrization of the HTA leads to improved results for the water-like systems and good agreement can be found for E_c down to 2% of E_∞. Such improvement is not found for the simple glass formers and it may be related to the remaining presence of an FST in the data, which is discussed in more detail in the following sections.

The most noticeable errors are found for the rFOF and fixed parametrization. The prediction underestimates the actual values of E_c in the high-temperature regime, Fig. 8.10(j-l). Moreover, the master curve exhibits a slight curvature even in the moderately supercooled regime. Freely fitting of the rFOF resulted in a different shallower description of the HTA in all previous analyses of data sets. Hence, it is recommended to freely fit the rFOF. As a consequence, the value of E_∞ is not determined by the HTR alone.

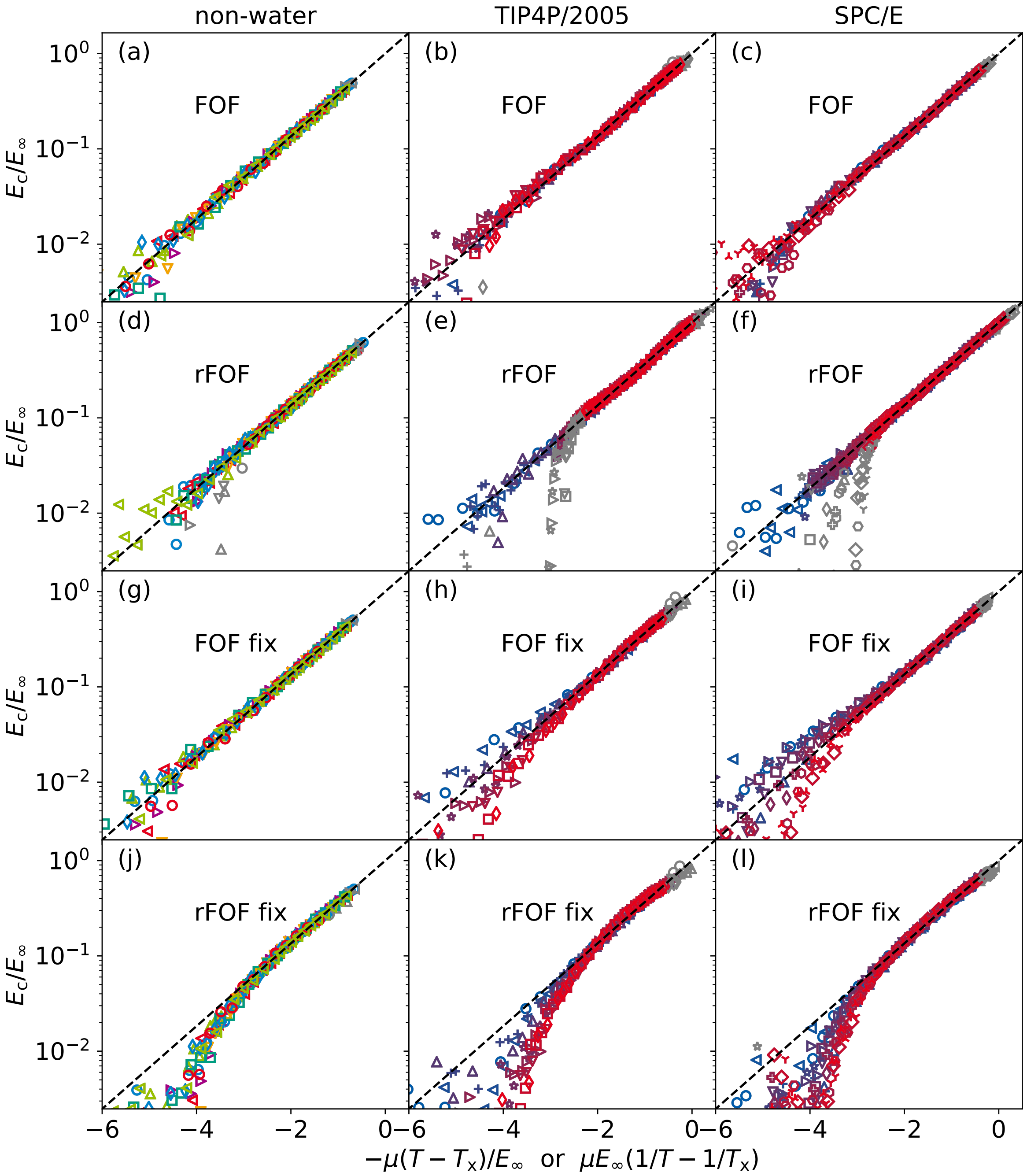

Figure 8.10.: Master curves for several model LJ liquids, the Lewis-Wahnströhm model for OTP, and glycerol (left), the charge-scaled variants of the TIP4P/2005 water model (middle) and the charge-scaled variants of the SPC/E water model (right). The FOF (a-c & g-i) and rFOF (d-f & j-l) are fitted to the data and E_c is calculated and shown as a function of the exponent in Eq. (8.6) and (8.7), respectively. Both functions are shown with (g-l) and without (a-f) fixed independently determined parametrization of the HTA. The black dashed lines mark perfect agreement and are guides to the eye. The colors and symbols are the same as in Fig. 8.5 and 8.8.

In contrast, the FOF is more robust and E_∞ is close the independent determination using the HTR alone, see Fig. A.17 in the appendix. It is the generally recommended functional form for the regular SFB of liquid dynamics. Further investigations that discuss relations with E_∞ will be performed only with the FOF. However, both models are empirical and the overall quality of the description of the data might be different if more extensive high quality data sets ranging from the high-temperature regime down to T_g were available.

8.4.6. Relation of the HTR and T_g

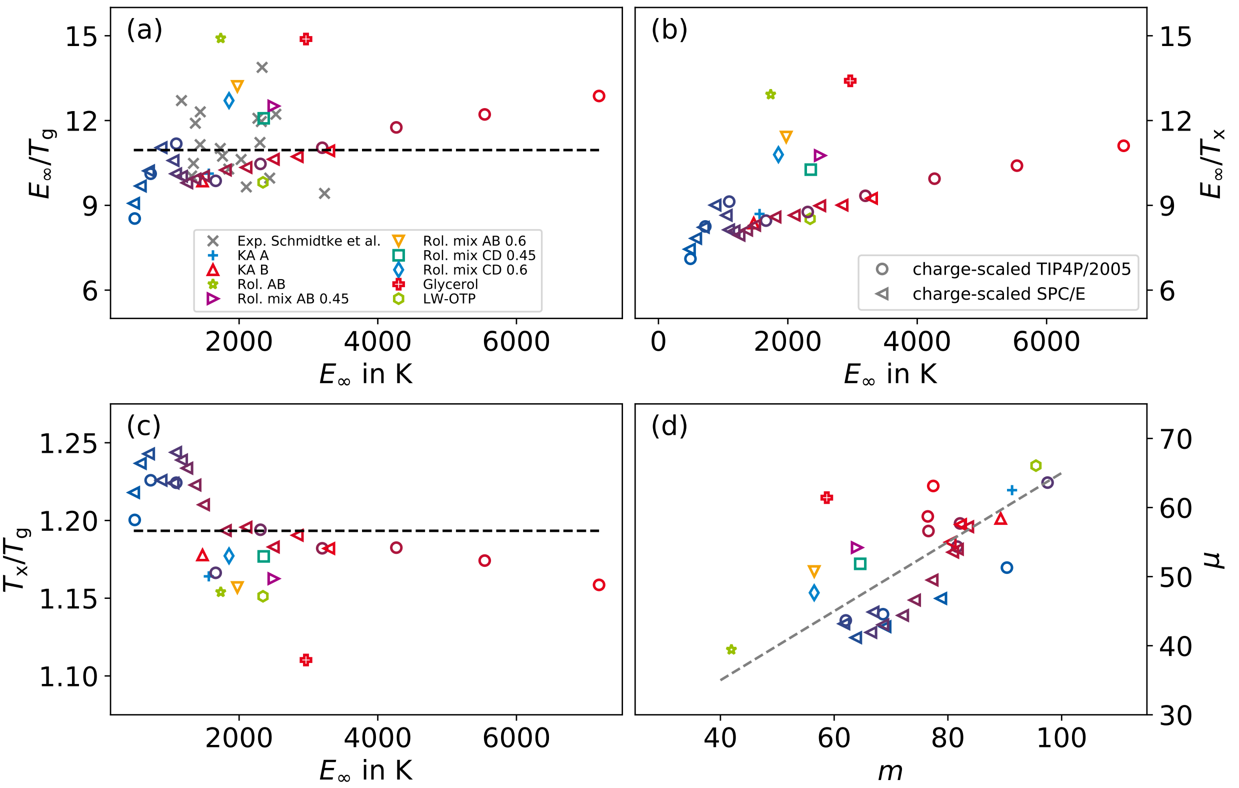

Figure 8.11.: The ratios (a) E_∞/T_g, (b) E_∞/T_x, and (c) $T_\mathrm{x}/T_\mathrm{g}$ shown as functions of E_∞. The values are obtained by fitting the FOF with fixed independently determined parametrization of the HTA to the data. Gray crosses are experimental results for molecular glass formers from Schmidtke et al. (2013).[112] The black dashed lines mark the average value of the simulated systems. (d) The generalized fragility μ is shown as a function of fragility m from extrapolation of the data to T_g. The gray dashed line is a guide to the eye. The data for charge-scaled variants of the SPC/E and TIP4P/2005 water models are shown with open circles and left-facing triangles, respectively, and the charge scaling factor is indicated by colors from blue to red from low to high q.

Having investigated the description of the simple-liquid and supercooled liquid regime with empirical models, possible relations between them are studied now. Figure 8.11 suggests common ratios of E_∞ and T_g, consistent with findings for molecular glass formers in the literature.[37,114,115] An average value of $E_\infty/T_\mathrm{g} \approx 10.9$ is found for the simulation data in this chapter, see Fig. 8.11(a). A very similar value was found for experimental of various molecular glass formers and data points down to T_g.[37,115] Note that self-diffusion coefficients were used here, while literature values represent rotational correlation times, and that the actual value depends within a few percent on the definition of T_g.

This common ratio suggests a link between the simple-liquid regime at high temperatures and the glass transition at low temperatures. The activation energy that controls relaxation at high temperatures is an intrinsic feature that sets the thermal energy scale even for strong supercooling when cooperative effects dominate. Knowledge of one of the two quantities, E_∞ or T_g, allows the other to be estimated without further knowledge. However, considerable scattering is found among the studied systems, with a standard deviation of $\sigma \approx 14\%$ of the mean. At T_g, the total activation energy is by definition given as $\ln X/X_\infty|_{T_\mathrm{g}} = \frac{E_\infty + E_\mathrm{c}}{T_\mathrm{g}} \approx \ln 10^{16} \approx 37$. Hence, inaccuracies on the scale of σ lead to a deviation of the dynamical property by two orders of magnitude. From the observation that E_∞/T_g has an approximately common value and the value of the total barrier, it follows that the ratio $E_\mathrm{c}(T_\mathrm{g})/T_\mathrm{g}$ is about 27, in reality 28 for the given data and the applied definition of T_g. A similar common ratio of 24 was found in the literature.[368,369] Hence, the total activation energy at T_g is less than four times the activation energy in the simple-liquid regime. In other words, the contribution to the activation energy by cooperative effects accounts for the majority of the activation energy but E_∞ is still relevant.

The ratio E_∞/T_x shows similar behavior, Fig. 8.11(b). On average, the cooperative contribution to the activation energy takes over at temperatures corresponding to about 11% of the high-temperature activation energy. Closer inspection reveals that the relative scattering is consistent with that for E_∞/T_g. The fact that the ratio to E_∞ is the same in both cases also indicates a correlation between the two temperatures. While the ratio $T_\mathrm{x}/T_\mathrm{g}$ averages 1.19, see Fig. 8.11(c), the scatter of the data is also quite significant.

Considering that the systems do not show the same relative slowdown from X_∞ to T_g, one might hope to reconcile some of the scatter by redefining T_g, e.g., as $\Xi(T_\mathrm{g})/X_\infty = 10^{16}$. However, the steep slope near T_g requires adjustments of only a few percent to account for an order of magnitude more or less in X. For the charge-scaled variants of TIP4P/2005 with $q > 1$, $1/D_\infty$ decreases by about an order of magnitude while the ratio E_∞/T_g does increase by 20%. Hence, the trends are not so easily compensated. Moreover, $1/D_\infty$ is monotonic in q, while the same is not true for E_∞/T_g. Nevertheless, as the rescaling of the data by E_∞ and X_∞ has shown, such a definition might be more appropriate for comparison of different models. It can be argued that the scatter of the data can be reduced if temperatures down to T_g are available and extrapolations are avoided. However, the experimental data of Schmidtke et al. shows comparable scatter.[112] They also found different ratios for polymers.[115] Thus, the results depend on the class of systems studied.

In the literature, the fit parameter μ has been called generalized fragility because of its weak correlation with the fragility m.[112] There is also a weak correlation for the present systems, see Fig. 8.11(d). However, the scatter is high and a systematic trend is found only for the charge-scaled variants of SPC/E, where m and μ increase approximately monotonically but not linearly with partial charge. Overall, no deeper relation between these parameters can be found in the present data.

Closer inspection of the data for the charge-scaled systems shows that both families of models share a common charge dependence. There are two regimes below and above $q \approx 0.9$ with the ratios E_∞/T_g and E_∞/T_x increasing with E_∞, or equivalently q, in both cases. They are separated by a sudden jump consistent with the qualitative change of the path in the phase diagram with respect to a possible LLTP. Hence, there appears to be an as of yet unexplained systematic trend in similar systems, those on the HDL and LDL side in the phase diagram, respectively. Furthermore, the values for reduced charges rapidly approach those found for charged LJ particles, which was about 7.5 for self-diffusion coefficients and isobaric cooling.[116] Note that in this study the fit to the HTR explicitly includes reciprocal temperature, as in Eq. (8.1), leading to reduced values for E_∞. As the partial charges are weakened, the water-like systems turn into spherical LJ particles, since only the oxygen atoms interact with LJ potentials in these force fields. However, real molecular systems have very different structures and interactions, e.g., glycerol forms a hydrogen bond network while OTP is a Van der Waals liquid.

8.5. Strong-fragile-strong behavior

The above investigations referred to data with the regular SFB. Now, liquids with a strong-fragile-strong behavior (SFSB) are investigated. For these, the solutions to the differential equations with first- and second-order terms, the SOF and rSOF, are necessary. Consistent with Eq. (8.16) and (8.17), the SOF and rSOF can be written as

$$X = X_\infty \exp\left[\frac{E_\infty}{T}\left(1 + \frac{1}{\lambda + e^{\mu/E_\infty(T-T_\mathrm{x})}}\right)\right] \quad \text{and} \tag{8.20}$$

$$X = X_\infty \exp\left[\frac{E_\infty}{T}\left(1 + \frac{1}{\lambda + e^{-\mu E_\infty(1/T-1/T_\mathrm{x})}}\right)\right] \,, \tag{8.21}$$

respectively. The former is an extended version of the empirical model by Schmidtke et al. while the latter is an equivalent form to the two-state model of dynamics for water by Tanaka and coworkers.[37,120]

8.5.1. Water's polyamorphism

The first system to be studied is the charge-scaled TIP4P/2005 water model with $q = 0.86$ and isobaric cooling from Ch. 7. The polyamorphism in this system is understood and the location of the LLCP at $P_\mathrm{c} \approx -54.5\,\mathrm{MPa}$ is known. Hence, the temperature dependence of properties can be related to paths in the phase diagram. The FST for isobars at lower pressures is caused by the rapid increase in HDS concentration and the crossing of isomorphs. The raw self-diffusion coefficients are shown in Fig. 8.12(c) and are fitted by the SOF and rSOF. The apparent activation energy E_a is then calculated from the data and shown along with the prediction by the fits in Fig. 8.12(a).

For systems with $P > P_\mathrm{c}$, E_a increases monotonically with decreasing temperature, i.e., the systems exhibit regular SFB. However, a maximum in E_a occurs for $P < P_\mathrm{c}$. This is consistent with the feature of the SOF and rSOF for $\lambda > 0$ and causes an apparent SFSB. The data can be well described by the functional forms. The maximum becomes higher and narrower the closer the pressure is to P_c, and thus the higher the transition rate in temperature from HDS-rich to LDS-rich. Only the extremely sharp maximum in E_a for $P = -65\,\mathrm{MPa}$ is not reproduced by the fits. They are either unable to describe the data or the data quality is poor this close to the LLCP. The strong fluctuations in density and LDS concentration, caused by the proximity to the LLCP, make the equilibration particularly computationally expensive. The residues in the fit are instead dominated by the long HTR. It remains to be seen whether data sets well beyond the inflection point will yield stable fits and can be well described by the SOF and rSOF.

For isobars above the critical point, an FST is not necessarily expected. Nevertheless, as discussed in the previous chapter, HDL may have its own FST. The SOF predicts no FST for $P > P_\mathrm{c}$, i.e., $\lambda = 0$, while the rSOF deviates from this, see Fig. 8.12(b). However, the quality of the fits is comparable and the distance to the predicted inflection point is still large. It is still questionable whether these systems have an FST and the SOF seems to be more conservative. On the other hand, the rSOF can

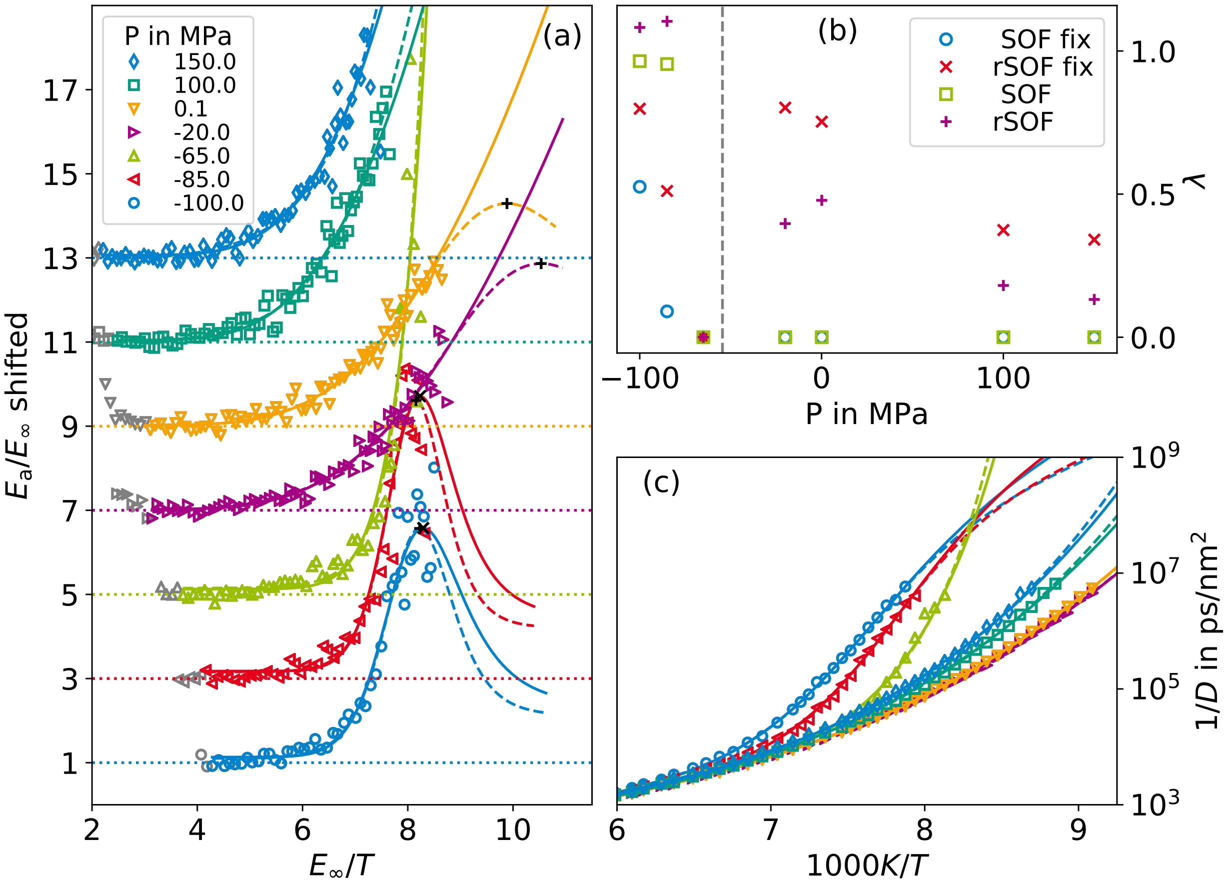

Figure 8.12.: (a) Temperature dependence of the apparent activation energy E_{a}, calculated numerically as the local gradient, for isobars of the charge-scaled TIP4P/2005 water model with $q = 0.86$ and at the indicated pressures. For clarity, the data is rescaled by the parametrization of the high-temperature Arrhenius and shifted on the y-axis by two for each system. The solid and dashed lines are results of free fits with Eq. (8.20) and Eq. (8.21) to the self-diffusion coefficients, respectively. The dotted lines indicate $E_{\mathrm{a}}/E_\infty = 1$ for each shift. The pressure of the isobars P is given in the legend. (b) Pressure dependence of the second-order parameter λ from fits to the data. The fitting routine is given in the legend. (c) Arrhenius plot of the self-diffusion coefficients including the respective fits in (a). The legend in (a) also applies to (c).

be considered more sensitive to deviations from SFB. In favor of the prediction by the rSOF is the experimental finding of strong behavior of HDA and LDA above their respective T_g and no crossing of the dynamics of HDL and LDL,[13] which would be the case for extrapolations with the SOF. Increasing the pressure to 100 MPa and above results in a regular slowdown of dynamics with pressure. In these cases, rSOF predicts lower values for λ than for isobars closer to the LLCP. This could mean that the system is farther from an FST at these pressures.

In the following sections, several other systems for which the existence of an LLPT is unclear will be studied. The above findings may help in interpreting the results.

8.5.2. Silica

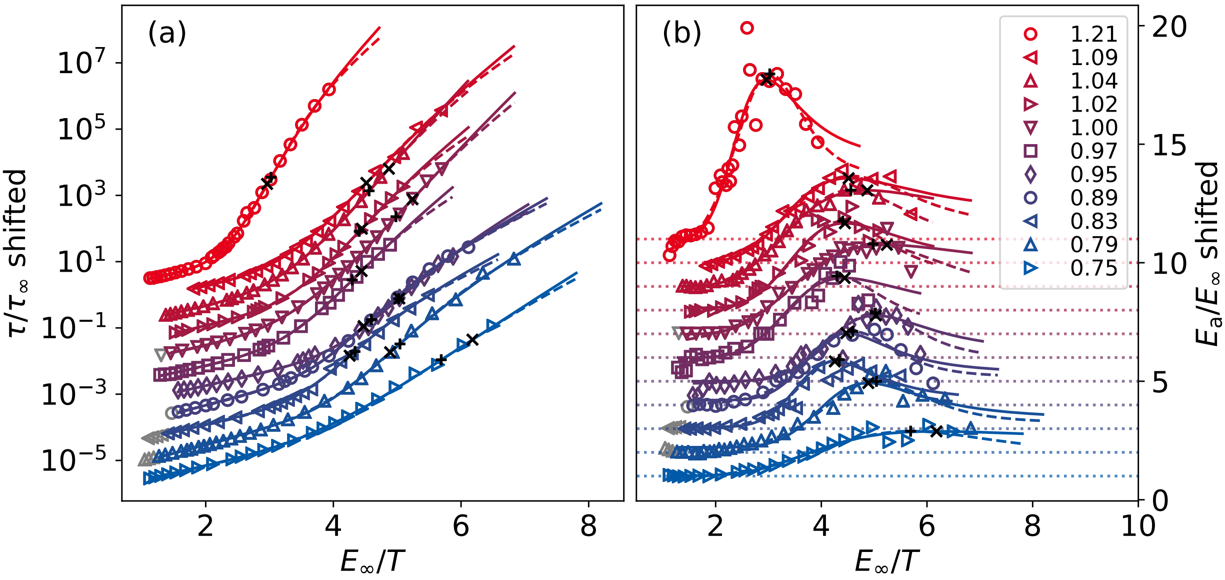

Figure 8.13.: (a) Temperature dependence of the correlation time τ of the ISF with $k = 20\,\mathrm{nm}^{-1}$ for the charge-scaled BKS model of silica, courtesy of Elvira Pafong and Julian Geske.[118,214] For clarity, the data is rescaled by the parametrization of the HTA and shifted on the y-axis by factors of four. The solid and dashed lines are fits to Eq. (8.20) and Eq. (8.21), respectively. (b) The apparent activation energy E_a, calculated numerically as the local gradient, as a function of reciprocal temperature. E_a is rescaled by the high-temperature activation energy and shifted upwards by one for increasing charge-scaling factors q. The dotted lines indicate $E_\mathrm{a}/E_\infty = 1$ for each q. Solid and dashed lines are E_a as calculated by the respective fits in (a). Black crosses and plus signs mark the inflection point T_i for the SOF and rSOF, respectively. The legend applies to both plots. Because of an insufficient eHTR, the HTA parametrization from fitting the SOF freely was used for $q = 1.21$, 0.97, and 0.95.

A system with a very pronounced FST is silica. The data are from simulations with the BKS model.[372] Figure 8.13(a) shows correlation times τ obtained from the incoherent intermediate scattering function (ISF), Sec. 5.2.1. Diffusion data is also available but is of poorer quality.

All systems exhibit Arrhenius behavior at high temperatures followed by super-Arrhenius temperature dependence at intermediate temperatures. Similar to the water-like systems crossing the Widom line in Fig. 8.12, the dynamics deviate at more severe supercooling and the super-Arrhenius behavior becomes weaker. More specifically, the curvature appears to change sign for some of the systems, e.g., for $q = 1.21$. Previously, the data was described by a combination of two Arrhenius functions joined by a VFT equation at intermediate temperatures, or by a combination of Eq. (8.16) followed by an Arrhenius function at lower temperatures. Both descriptions, including the transition temperatures, have nine and seven parameters, respectively, and are differentiable only if constructed correctly. The SOF and rSOF fit the data perfectly over the entire temperature regime with only five parameters and are always differentiable. Thus, they provide a good alternative for describing the data.

The data and the fits can again be investigated in more detail by calculating the apparent activation energy E_a directly for the data and for the functions, shown in Fig. 8.13(b). The features of E_a are in qualitative agreement with those of the theoretical investigation in Fig. 8.2(c) and for the water-like system crossing the Widom line. E_a is constant at high temperatures followed by an exponential-like increase upon cooling. It then exhibits a maximum and either levels off upon further supercooling or even decreases for some systems. The apparent activation energy is also described qualitatively and quantitatively by the fits of both functional forms to the correlation times. Accordingly, the curvature K should approach zero or even have a root. However, further numerical derivatives are not shown because of the noise in the data. The rSOF appears to describe the temperatures below the inflection point better than the SOF and the sum of residuals for E_a is lower for the rSOF. Note, however, that insufficient equilibration at the lowest temperatures generally leads to faster dynamics, and thus artificially reduced E_a. It is unclear overall how accurate the data is below T_i. However, all systems certainly show a deviation from super-Arrhenius behavior and a need for higher-order functional forms making it quite certain that an FST is occurring.

The temperature regime around T_i is approximately linear. Previous studies on water and silica attributed the location of the FST to a temperature between the apparent fragile and Arrhenius regimes.[118,214] However, the true second low-temperature Arrhenius regime appears only for $E_\mathrm{a} = const.$ at even lower temperatures. The transition is smooth and one can argue that it is simply a strong-strong transition. Hence, one may consider the inflection point to be the relevant temperature. It separates the liquid dynamics into two regimes. Above T_i a fragile behavior is observed. The second Arrhenius can only be observed sufficiently below T_i. When T_i is not within the temperature range of the data set, especially for $T_\mathrm{i} < T_\mathrm{g}$, the FOF and rFOF are sufficient to describe the data. In general, the derivatives E_a and K need to be examined to characterize the dynamics in terms of a possible FST.[356,367]

Finally, the FST of these silica-like systems can be discussed in the context of a possible polyamorphism in these systems. However, for the original BKS model, no LLCP could be found within the computationally accessible regime and the data showed no indication of being close to one.[4] Nevertheless, all charge-scaled BKS systems shown exhibit a density maximum.[118] The tetrahedral order increases with decreasing temperature and the fifth nearest Si-Si neighbor is pushed out of the first nearest-neighbor shell. Exactly the same observations were made for the charge-scaled variants of TIP4P/2005 in Sec. 6.1. Therefore, the picture of competing local structures of different density, which described the water-like systems well in Ch. 7, may also apply here. The existence of an FST within these systems may be associated with polyamorphism-like behavior, even in the absence of a true LLPT. The existence of the density maximum may imply that also for BKS a rapid change in the concentration of such local structures with temperature is at the origin of the FST.

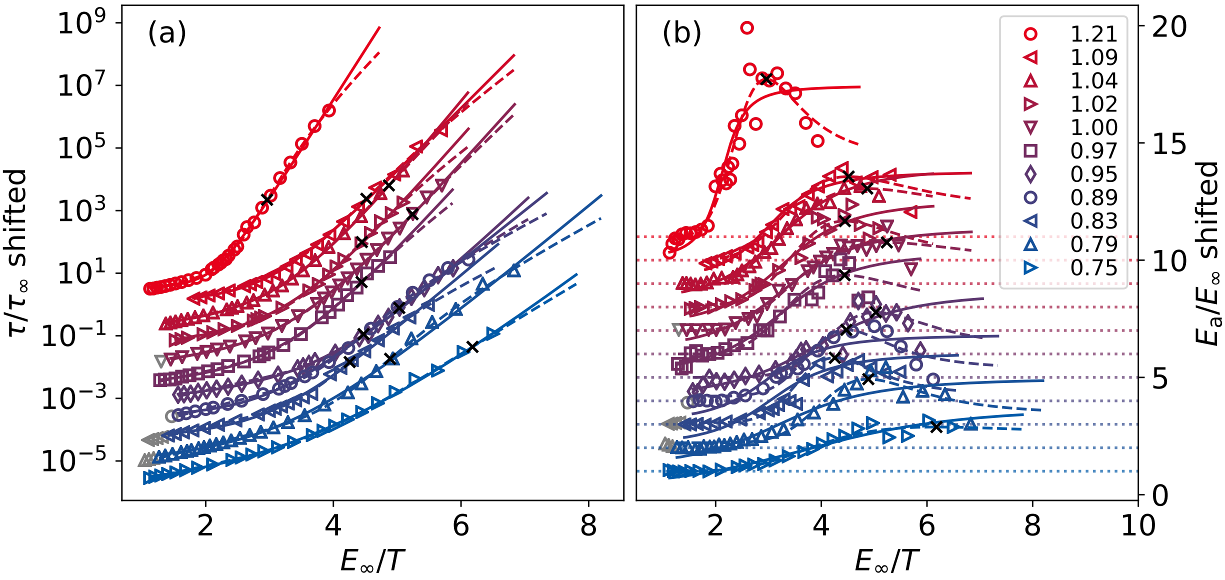

Figure 8.14.: Same plot as Fig. 8.13 but with fits of the CG model and the SOF, Eq. (8.22) and (8.20), shown as solid and dashed lines, respectively. (a) Temperature dependence of the correlation time τ of the ISF for the charge-scaled BKS model of silica, courtesy of Elvira Pafong and Julian Geske.[118,214] The charge-scaling factors q are given in the legend. For clarity, the data is scaled by the parametrization of the HTA and shifted on the y-axis by factors of four for each charge. (b) The apparent activation energy E_a, calculated numerically as the local gradient, as a function of reciprocal temperature. E_a is rescaled by the high-temperature activation energy and shifted upwards by one for increasing charge-scaling factor q. The dotted lines indicate $E_\mathrm{a}/E_\infty = 1$ for each q. Solid and dashed lines are E_a as calculated by the respective fits in (a). Black crosses mark the inflection point T_i for the SOF. The legend applies to both graphs. Because of an insufficient eHTR, the HTA parametrization from fitting the SOF freely was used for $q = 1.21, 0.97$, and 0.95.

8.5.3. Cohen-Grest model

Another model has been used in the literature to describe data sets with deviations from a simple VFT-like super-Arrhenius temperature dependence.[356,367] Cohen and Grest modeled the slowdown to the glass transition with a free-volume model and percolation leading to the functional form[97]

$$X = X_\infty \exp\left[\frac{2B}{T - T_0 + \sqrt{(T-T_0)^2 + \alpha T}}\right] . \tag{8.22}$$

The parametrization with B and T_0 is similar to the VFT equation. However, the divergence is shifted in temperature and can even be avoided. The parameter α accounts for anharmonicities of the local potentials experienced by the particles and the free volume can be extracted from it. However, the results from such an analysis are at odds with the estimates of free volume obtained from pressure-volume-temperature data.[366] Nevertheless, its qualitative features make it a good additional function to consider.[356,367] At sufficiently low temperatures, the $T - T_0$ terms become negligible compared to αT and one approaches a low-temperature Arrhenius.

The fits of the SOF and of the CG model to the silica-like systems data are shown in Fig. 8.14. While it visually describes the correlation times well over a wide temperature range, it of course cannot describe the maximum in E_a. Instead, Eq. (8.22) provides a smooth FST as a direct continuation of the fragile regime with an Arrhenius regime. It describes the data almost as well as the previously used combination of several Arrhenius and VFT regimes but with only four free fit parameters. Note, however, that E_a is not constant at high temperatures for several of the fits. The SOF or rSOF seem to be necessary to fully describe the data.

8.5.4. Water-like systems

The complementary analysis to the charge-scaled BKS systems is performed with self-diffusion coefficients D from the charge-scaled SPC/E and TIP4P/2005 systems, Fig. 8.15 and 8.16. Two phenomenological observations can be made for the charge-scaled systems. The apparent activation energy appears to increase exponentially for reduced charges while its temperature dependence appears to weaken for increased charges at the lowest temperatures. The crossover for TIP4P/2005 is at approximately $q = 0.9$, which is consistent with the finding for the fragilities of the charge-scaled systems and the shift of the LLCP to negative pressures.

The SOF and rSOF are fitted to the reciprocal self-diffusion coefficients $1/D$ and E_a is calculated. At increased charges, extrapolation with both functional forms often predicts a maximum in E_a. They disagree for intermediate charge scaling of $q = 0.9$ to $q = 1$ and the SOF predicts only SFB. For $q < 0.8$, both functional forms predict either no maximum or one at significant extrapolation from the data. The existence of the maximum depends on the second-order parameter λ. For vanishing values, the system apparently shows regular temperature dependence. The larger λ, the lower the slope of the low-temperature Arrhenius regime, i.e., the lower the plateau of E_a below the inflection point. The dependence of λ on q is shown in Fig. 8.15(b) and 8.16(b) for both functional forms and fitting routines with free and fixed HTA parametrization. Independent of the fitting routine and functional form, λ becomes small or even zero for $q \leq 0.8$ and $q \leq 0.9$ for SPC/E and TIP4P/2005 variants, respectively. Thus, these systems exhibit a close to regular temperature dependence of the dynamics.

In contrast, λ does not vanish for $q \geq 1.0$ in almost all cases. Thus, the functional forms predict an FST for these systems, although the data is inconclusive within the scatter at the lowest temperatures. This result is in agreement with the expectation that the LLCP is at elevated pressure for these systems, if it exists, and that they cross the Widom line at atmospheric pressure. This leads to a rapid transition in LDS concentration and, correspondingly, to a superficially increased fragility at intermediate temperatures. As discussed for the silica systems, such a transition may exist even if the systems do not have a true LLPT.

Another general finding is that λ is larger for the rSOF than for the SOF. Hence, the rSOF predicts a shallower slope $E_\infty(1 + 1/\lambda)$ for the LTA. The SOF is more conservative and the maximum in E_a is broader in temperature. A fit with unconstrained parameters for the HTA allows the rSOF to have values for λ comparable to those with the SOF while the deviations in the description of the HTA are acceptable.

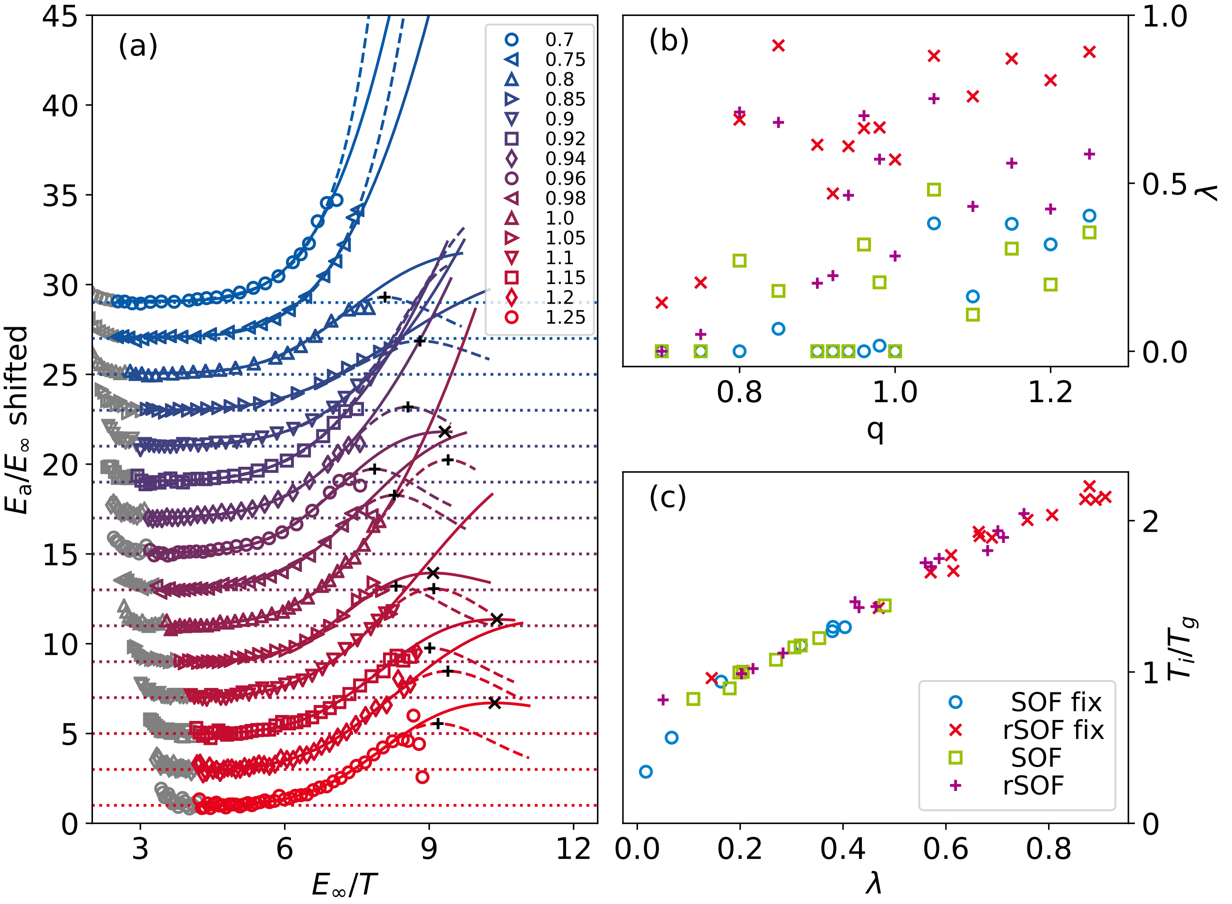

Figure 8.15.: (a) The apparent activation energy E_a calculated numerically as the local gradient as a function of reciprocal temperature, for the charge-scaled variants of the SPC/E water model. The charge-scaling factor q is given in the legend. For clarity, the data is rescaled by the parametrization of the high-temperature Arrhenius and shifted on the y-axis by two for each charge-scaling factor. Solid and dashed lines are results for fits with the SOF and rSOF, Eq. (8.20) and (8.21), to the self-diffusion coefficients, respectively. The dotted lines indicate $E_\mathrm{a}/E_\infty = 1$ for each shift. The charge-scaling factor q is given in the legend. Black crosses and plus signs mark the inflection point T_i for the SOF and rSOF, respectively. (b) Dependence of the second-order parameter λ on q for both functional forms and two fitting routines, with free and fixed HTA parametrization, denoted in the legend in (c). (c) Ratio of the inflection point T_i to the glass transition temperature T_g as a function of λ.

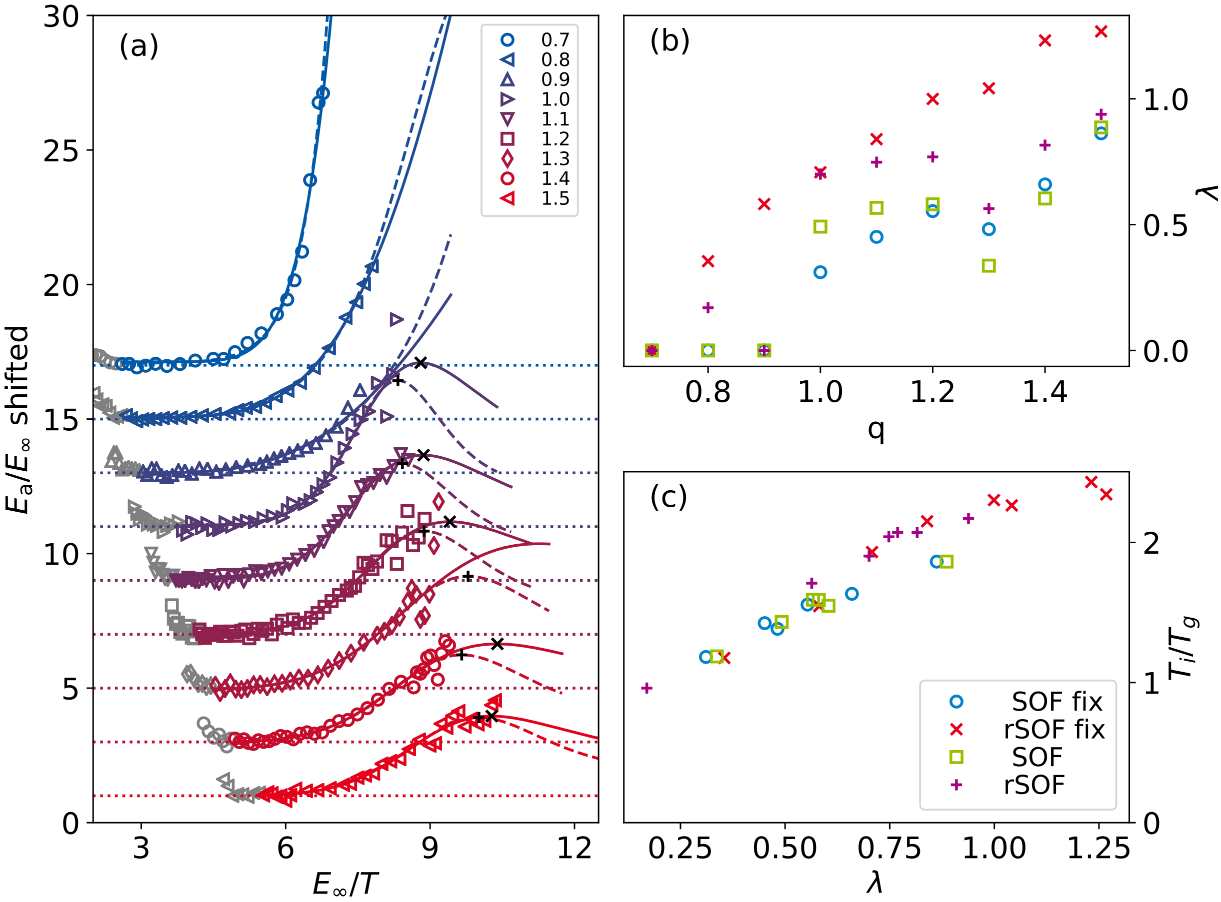

Figure 8.16.: Analogous results to Fig. 8.15 for the charge-scaled variants of the TIP4P/2005 water model.

Lastly, the location of the inflection point T_i is studied with respect to the extrapolated T_g, i.e., whether T_i could be observed directly in experiments or not. Figures 8.15(c) and 8.16(c) show good correlation between λ and the distance to T_g. The lower the activation energy of the LTA, i.e., the larger λ, the more readily the inflection point can be observed. For very small values of λ, the extrapolations predict the inflection point below T_g. The quantitative connection of course depends on all parameters, i.e., μ and T_x, but the result suggests that the most important parameter is the difference in activation energies of the two Arrhenius regimes.

The $\lambda > 0$ results for different charge-scaled variants are consistent with the expectation based on their path in the phase diagram, i.e., whether or not they cross the potential Widom line, from the findings in Ch. 7 for the charge dependence of the LLCP. This argument and the good description of the data suggest that the SOF and rSOF can serve as indicators for the existence of an FST. At the very least, $\lambda > 0$ indicates the necessity of second-order terms in the series expansion of E_c to describe the data, and thus a deviation from the simplest regular temperature dependence of dynamics.

8.5.5. Second-order effects in experimental data

Finally, the SOF and rSOF are tested on experimental data sets down to T_g from the literature which have been found to deviate from VFT behavior near T_g, shown in Fig. 8.17.[353,366] For comparison, the data is also fitted with the FOF and the CG model. Because not all data sets contain sufficient data in the HTR, the determination of E_∞ is inaccurate. Therefore, the parametrization of the HTA is fitted freely in all cases and T_g, taken from the literature, is used to rescale T and E_a.

The dynamics of 1-propanol, ethanol, and propylene carbonate can be described with the FOF within small errors. Deviations occur only at the lowest temperatures. Nevertheless, the CG model and the functional forms of second order perform better. The more sensitive rSOF suggests a necessity for second-order terms in all three cases. Salol, PDE, and PCB cannot be described by the FOF. The maxima in E_a predicted by the SOF and rSOF are at T_g and in some cases slightly above it. The data does not show a clear maximum in E_a for any of the data sets and so far agrees well with the CG model. However, it should be noted, that the CG model does not describe the highest temperatures as well as the SOF and rSOF.

Between the SOF and the rSOF, the narrower maximum in E_a of the rSOF seems to be less appropriate for the given data and, hence, the SOF could be preferable. However, either functional form can be used to describe the data or to probe for deviations from regular behavior with $\lambda > 0$.

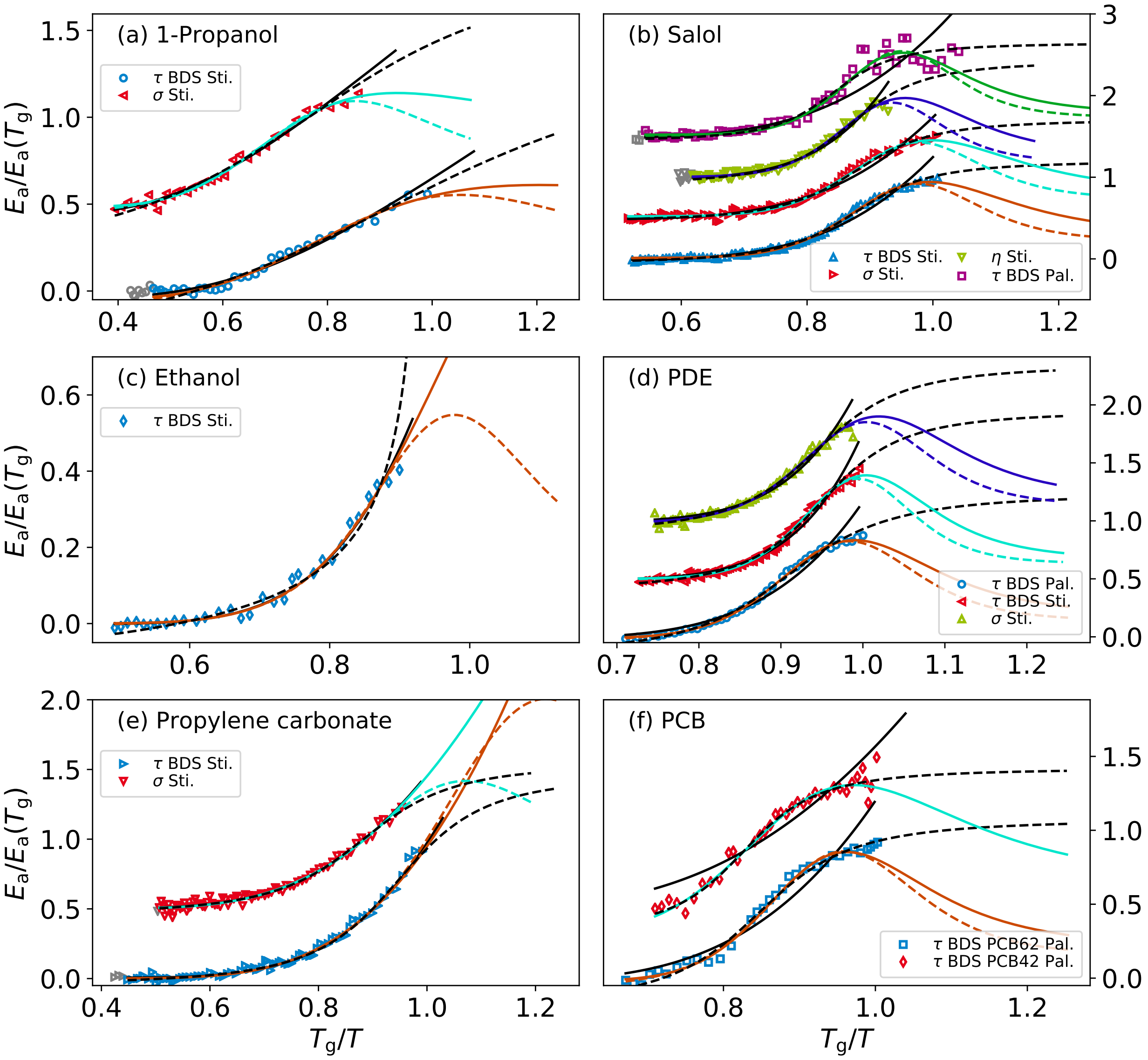

Figure 8.17.: Temperature dependence of the apparent activation energy E_{a}, calculated numerically as the local gradient, for various glass formers and correlation times τ from dielectric spectroscopy, DC conductivity σ, and viscosity η. The data was taken from publications by Stickel et al. and Paluch et al.[353,366] The glass transition temperatures T_{g} are also taken from the literature. E_{a} is scaled by its value at T_{g} for fits with the SOF. The solid and dashed lines in complementary colors to the data points are results for fits to the raw data with the SOF and rSOF, Eq. (8.20) and (8.21), respectively. The solid and dashed black lines are results for fits with the FOF and the CG model, respectively.

8.6. Summary

In this chapter, the temperature dependence of dynamical properties of liquids in the entire available temperature regime was investigated. The empirical finding of an exponential function with a temperature-dependent activation energy $E(T)$ was used as a starting point for the systematic construction of a family of functional forms. Following the observation of an Arrhenius behavior in the simple-liquid regime, the proven splitting of $E(T)$ into a temperature-independent contribution E_∞ and $E_\mathrm{c}(T)$ was employed. The latter is often attributed to the increasing cooperativity of motion in the supercooled regime.

Derivatives of $E_\mathrm{c}(T)$ can be expressed with a series expansion in orders of E_c itself, leading to two sets of differential equations depending on the derivative in real or reciprocal temperature. Considering only terms up to second order allows for analytical solutions, all of which can describe the regular temperature dependence of dynamics. The set of solutions was reduced to physically more meaningful functional forms by introducing three conditions for E_c: It vanishes at high temperatures, it increases monotonically upon cooling, and it is continuous. In particular, there is so far no experimental evidence of a divergence of, e.g., correlation times at finite temperatures, quantum effects left aside. Functional forms such as the VFT equation or the power law from the MCT have their applications but do not conform to this relevant observation.

Two of the four functional forms have been used successfully in earlier work, e.g., by Schmidtke et al. or Tanaka and coworkers. The derivation in this chapter reveals their common mathematical origin and complements them with two related functional forms. While the first-order functional forms, FOF and rFOF, can describe regular temperature dependence, the second-order parameter $\lambda > 0$ introduces an inflection point in an Arrhenius plot, i.e., a maximum in the apparent activation energy E_a, and a second Arrhenius regime at stronger supercooling. The former functional forms can describe a strong-to-fragile behavior while the latter can describe a strong-fragile-strong behavior. Both scenarios have often been described with combinations of Arrhenius laws and the VFT equations. The functional forms presented here use significantly fewer parameters. Still, as the number of features increases, e.g., strong or fragile regimes or roots in derivatives of the observed quantity with respect to reciprocal temperature, the number of parameters necessarily also increases.

The FOF and rFOF were used to study LJ liquids and simple glass formers and describe the self-diffusion coefficients very well. However, the solution for $\mathrm{d}1/T$ proved to be less robust in the parametrization of the high-temperature Arrhenius. Hence, the FOF, the model by Schmidtke et al., is recommended for the SFB of liquids. More extensive data sets of high quality and from a single observable down to T_g are necessary for a more detailed comparison. Application to data from charge-scaled water models gave good agreement for moderate supercooling or reduced partial charges. The charge dependence of several properties, e.g., the fragility, are consistent with the location of isobars in the phase diagram with respect to a possible LLPT. The charge dependence of the pressure of the LLCP found in Ch. 7 consistently separates the systems into isobars that do and do not undergo a transition from one preferred local molecular structure to another. Both functional forms are also capable of describing experimental data down to T_g.

The ratios of the activation energy of the HTA, E_∞, to the glass transition temperature, T_g, was found to be on the order of 11, consistent with findings for experimental data on various molecular glass formers.[115] The scatter is significant and the ratio can be used for an approximate estimate of either quantity when the other is unknown. The results for the charge scaling of the two water models depend on the region in the phase diagram with respect to the LLPT. A study of charged soft spheres also suggests largely common ratios.[116] Hence, the interaction strength determines E_∞ among classes of interactions, i.e., of similar directionality and local structure, and rescaling of temperatures by this energy scale leads to common behavior.

The charge-scaling data of the two water models and the BKS model of silica was used to study the SFSB of the SOF and rSOF. The silica systems showed a very pronounced FST in the accessible dynamical range. E_a exhibits a maximum and the overall dynamics are well characterized by the second-order functional forms. Hence, the Cohen-Grest equation, a four-parameter function without a maximum in E_a, does not qualitatively reproduce the temperature dependence. The LTA is not the continuation of the fragile regime, i.e., there is an inflection point separating two strong regimes. The inflection point T_i seems to be a relevant temperature. In particular, it is only possible to determine whether a liquid exhibits SFSB of this kind if T_i is above T_g. For the charge-scaled water models, T_i could not be identified with certainty. Still, fitting the functional forms reveals whether or not the characterization of the data requires the second-order parameter λ. The findings are again consistent with the location in the phase diagram, i.e., $\lambda > 0$ when the isobar is below the suspected critical point. Higher values of λ are related to higher T_i with respect to the glass transition. Hence, a small difference between the activation energies of the HTA and LTA is most important for the accessibility of the latter. It seems that for tetrahedral network formers with strong directional bonding, e.g., silica or water with hydrogen bonds, the interaction strength is close in the high and low-temperature regime. In the case of water, the average number of hydrogen bonds is less than four at high temperatures but quickly approaches its optimum upon cooling. Hence, if the energy barriers are dominated by hydrogen bonds compared to other sources of cooperativity in the relaxation mechanism, then it is not unreasonable to expect both activation energies to be on the same order of magnitude at high and low temperatures, as suggested by $\lambda > 0.2$. The SOF was more conservative with λ, and thus could be used as a test for SFSB.

It is unclear whether all silica- and water-like systems exhibit true LLPT and polyamorphism. However, they all share the competition of local structures with different density even if the two local structures mix easily and no LLPT exists. It could be that the mere existence of such local structures and an appropriate path in the phase diagram cause an SFSB in other systems as well. For the tetrahedral network formers, the question of the temperature dependence in a region of the phase diagram with high HDS concentration remains unresolved. Still, the less conservative rSOF predicts an inflection point beyond the covered temperature range also for systems that should not cross a Widom line.

For real molecular glass formers, deviations from VFT behavior at strong supercooling have been discussed for some time. Such data sets from the literature were used to test the second-order functional forms. Both are able to describe the entire available temperature range. Some of the data sets appear to have an inflection point near T_g. The FOF and rFOF cannot adequately describe these cases. However, the raw data does not show a clear maximum in E_a and the functional forms appear to overestimate its sharpness. The more conservative CG model also fits the data well, at least below the HTR. These systems may exhibit an FST but not with the same qualitative features as the tetrahedral network formers. Instead, E_a seems have a smooth step-like temperature dependence. Besides the CG model, the FOF also exhibits this feature. However, it cannot be parameterized to match this step in the experimental data. The SOF can always be used to fit the data and includes an indication of the relevance of second-order effects. Compared to the CG model, the former can correctly describe the full data set.

As can be seen from the theoretical results in the literature, an Arrhenius regime may be more common than expected at strong supercooling, perhaps even a general property of all liquids. Of course, these considerations apply to classical physics, since quantum effects and the freezing in of degrees of freedom become relevant at significant supercooling. Knowledge of whether or not the activation energy has a low-temperature limit would be an important step in understanding the glass transition, since only theories that account for this phenomenon would be viable. Another question is whether the origin for SFSBs with and without an inflection point is qualitatively different or whether they are manifestations of the same underlying physics. A functional form of $E(T)$ that satisfies both scenarios is nontrivial. While these questions may be difficult to address with experimental data and the limitation by T_g, simulations of suitable model systems and increasing computational power may tackle these challenges in the near future.

9. Water in neutral confinements

The following sections investigate dynamical and structural properties of charge-scaled SPC/E water models within neutral cylindrical pores. The matrix imposes a static potential energy landscape onto the liquid causing persistent structuring and reduced mobility. Several theories of the glass transition propose dynamically or structurally differing regions of growing length scale upon supercooling. Confinements are well suited for their determination. Hence, correlation times and configurational overlap were spatially resolved and characterized and the slowdown in the immediate vicinity of the pore wall was quantified. Several properties can be generalized among the charge-scaled variants using isokinetic representations or the energy scale E_∞. Manifestations caused by the suspected polyamorphism of the model are weak and appear only in some properties. Models of the glass transition that correlate vibrational motion and correlation times fail in the confinement. Instead, it was found that the energy barrier governing dynamics may be increased by a temperature independent amount at the pore wall and that it can be explained using Boltzmann statistics.

9.1. Motivation

Confined liquids are a quite common phenomenon in many areas such as biology, chemistry and physics. In particular, nanoscopic confinements have a strong influence on structure and dynamics and require further understanding. These systems have been topic of a vast amount of studies in the recent past,[41,42] using for example micelles[373] or proteins as soft confinement and clays, zeolites or mesoporous silica as hard confinement. Besides the rigidity, the size, geometry and dispersity is different among these confinements. Their diameter can range from a few to hundreds of nanometers. In addition to such geometrical features, the interaction of the liquid with the matrix can be particularly important. Chemically modifying the interface, e.g., varying the silanol-group density in silica pores,[374] can lead to structural and dynamical changes influencing the behavior of the entire liquid volume.[43] Especially in mixtures the liquid-liquid and liquid-matrix interactions can lead to significant structural changes with respect to the bulk, e.g., microphase separation.[44–47,375]

This entanglement of geometric and interaction effects and dependence on the liquid itself has hindered a precise understanding of confinement effects so far.[41,42] To reduce the complexity of this problem, neutral confinements can be employed in simulations.[48,49,303,376] By giving the matrix the same structure and composition as the bulk liquid, liquid-matrix interactions are simplified and well defined for each system. In MD simulations, such systems are easily constructed by restraining the movement of a fraction of particles, see Sec. 4.3. Ideally, the local structure of the confined liquid is unaltered across the interface and only dynamics are affected. While this may often be the case,[48,49,376] density fluctuations may still occur.[377] Previous studies found by several orders of magnitude reduced mobility at the interface, followed by steep mobility gradients and recovery of bulk behavior for sufficient distances to the matrix.[48,323,378] Underlying these phenomena is the potential energy landscape (PEL) that, in contrast to bulk, does not fully relax. The confinement imprints a static contribution onto the landscape of the liquid that is propagated some distance by the particle interaction.[46,229,379]

Several theories of the glass transition seek to explain the deviations from strong Arrhenius to fragile super-Arrhenius behavior by introducing length scales of dynamical or structural heterogeneity that grow upon supercooling and determine the structural relaxation. This increases the importance of cooperative motion for relaxation, and thus the energy barrier. Among these theories are for example the Adam-Gibbs model,[28,29] proposing growing length scales of cooperative motion, and the random-first-order transition (RFOT)[91] theory that introduces structurally distinguishable patches of increasing size. MD simulations have proven useful in this regard. Not only can dynamical and structural length scales be calculated from bulk but also from confinement simulations.[27,48,323,376,379–385] The latter enhance the heterogeneity and impose an upper limit to dynamical and structural length scales, allowing for further studies under well defined conditions. In particular, neutral confinements were employed in several cases, ranging from binary Lennard-Jones liquids,[376,380,381,384,386] binary mixtures of quasi-hard spheres,[383] silica,[379] to even water.[48,323,385] The expectation of growing dynamical and structural length scales was well met in these systems. However, the usually reduced mobility at the interface reduces the accessible temperature range to the weakly supercooled regime. Whether this method remains applicable for stronger supercooling or not remains to be seen. More importantly, which of the extracted length scales proves relevant and how they are related to the glassy slowdown of the bulk liquid is not fully understood.

This work focuses on the supercooled regime of the tetrahedral network former water and its charge-scaled variants to distinguish features caused by interaction strength from those caused by confinement properties. As discussed in the previous chapters, water models may have an LLPT that shifts in the phase diagram depending on the partial charges. In particular, the associated LLCP can be at positive or negative pressure and isobaric pathways in the phase diagram may enter the HDL or LDL regime upon cooling. Both cases exhibit significant differences in dynamics and structure. For another tetrahedral network former, silica, simulations have shown the existence of the corresponding fragile-to-strong transition (FST) in the BKS model and charge-scaled variants.[118,149,150,214,372,387–391] For SPC/E water, the FST could not be observed in the accessible temperature range.[117,275] The temperature dependence of length scales across the FST would be a good test of their relevance in models of the glass transition.[379] Nevertheless, the dependence of confinement effects on the variation of the water model may reveal or disprove common behavior within these models.

Therefore, extensive simulation series of water-like models in neutral confinements are investigated in this chapter. Specifically, the charge-scaled variants of SPC/E, used in bulk simulations in previous chapters, are confined in cylindrical neutral pores. A similar study was performed for silica-like systems based on the BKS potential.[392] By quantifying the range and degree of temperature dependent confinement effects for different interaction strengths and regions in the phase diagram, the relevance of length scales determined in confinement to the glass transition in bulk can be studied.

9.2. Particle density

A prerequisite to analyzing dynamics spatially resolved is an understanding of the particle distribution and structural inhomogeneities. The neutral pores by construction have a radius of $R = 2.5\,\mathrm{nm}$ which is applied to the instantaneous oxygen position of the water molecules, see Sec. 4.3. The interface is rough with hydrogen atoms reaching into the pore and small voids beyond the cutoff available to the liquid fraction. Hence, resolving the molecular positions, defined here by the position of the oxygen atom, by their distance r to the pore axis will average over the roughness of the interface. Alternatively, the shortest distance to the surface can be calculated. This way, the tetrahedral local structure of water is taken into account. Particle densities for both methods are shown in Fig. 9.1. The distance resolved particle density resembles the pair-distribution function $g(r)$. The first and second

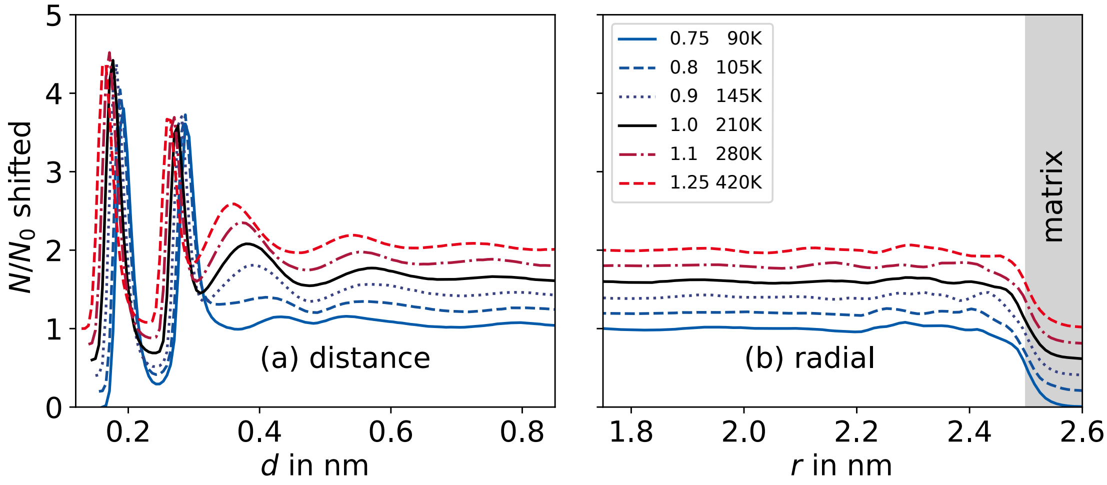

Figure 9.1.: Particle density of water oxygens within a neutral pore with radius $R = 2.5$ nm: (a) resolved over the shortest distance d to any wall atom and (b) radially resolved. The count N of atoms is normalized by the average N_0 for 1.1 nm $< d < 1.5$ nm and $r < 1.5$ nm, respectively, and shifted upwards by 0.2 for each data set for clarity. The bins for distance resolved counting are chosen such that they have equal volume for a smooth cylindrical wall. The scaling factors of the partial charges are given in the legend and the temperatures shown are chosen such that the correlation time τ_e in the pore center amounts to roughly 100 ps.

peak are the H–O and O–O next neighbor distances. Their position shifts to shorter distances with increasing charge scaling factor q, in accordance with the increasing density with stronger Coulomb interaction in Sec. 8. Further oscillations are mixtures of distances to hydrogen or oxygen atoms of the matrix, e.g., the third peak represents the H–O distance of the second next neighbor shell and decreases significantly in height and shifts to longer distances when the charges are reduced below $q = 0.9$. The local structure appears to be significantly altered by charge scaling, as found for the bulk systems. The previous chapters suggest for the polyamorphism of this water model that for charge scaling $q < 0.9$ and atmospheric pressure the Widom line is not crossed and the systems enter the HDL phase. Hence, interpretations of the results in the following will take into account the differences in local structure.

These details are absent in the radially resolved particle density, Fig. 9.1(b). Density is mostly flat with moderate modulations close to the pore wall. The rough interface leads to a smooth step and allows for minor penetration beyond $R = 2.5$ nm. At low temperatures, no particles were found to reside at larger distances within the pore wall. Previous radially resolved analysis of neutral pores found no difference in structure and density across the interface.[48,379] For the Kob-Andersen mixture in neutral confinement however, a more pronounced modulation of density was found.[377]

The analysis in the following sections shows that the structural features in Fig. 9.1(a) are also present in dynamical properties. Radially resolving the positions averages over these effects. Hence, this chapter focuses more on distance resolved analysis. Results for particles beyond the next neighbor distance are consistent between radial and distance resolved analysis.

9.3. Slowdown in confinement – spatially resolved

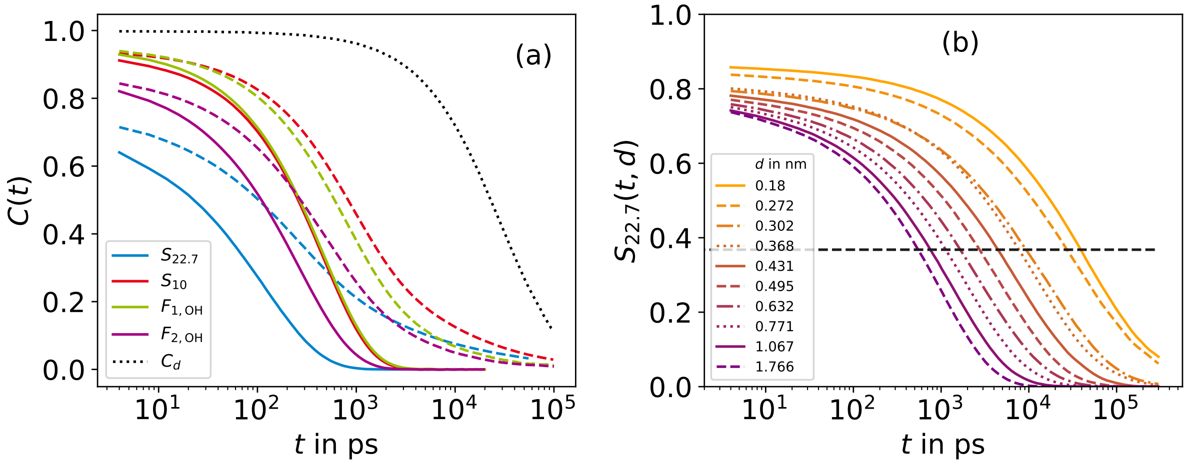

Figure 9.2.: Correlation functions of water dynamics in bulk and within a neutral pore with radius $R = 2.5$ nm. (a) Comparison of translational and rotational correlation functions in bulk (solid lines) and confinement (dashed lines) at 210 K for the original SPC/E model of water. Translation of the oxygen atoms is probed with the ISF, $S_q(t)$, for two wavenumbers, $S_{22.7}$ and S_{10}. Rotation is probed with the RCF of the OH-bond vector, $F_{1,\mathrm{OH}}$ and $F_{2,\mathrm{OH}}$. The black dotted line represents the autocorrelation of the distance to the pore wall, $C_d(t)$. (b) $S_q(t)$ for subsets at different distances to the pore wall, given in the legend, at 400 K and charge scaling $q = 1.25$. The black dashed line indicates the criterion used for the determination of correlation times τ_e, $C(\tau_\mathrm{e}) = 1/e$.

For spatially resolved studies of dynamics in confinement it is necessary that displacements on the time scale of the analysis are small compared to the confinement size and, as seen later, dynamical gradients. Observables that measure dynamics on a local scale, i.e., on the next neighbor distance, are preferred over self-diffusion coefficients. The incoherent intermediate scattering function (ISF, Sec. 5.2.1), with two wavenumbers S_{10} and $S_{22.7}$, and rotational correlation functions (RCF, Sec. 5.2.3) will be calculated. Figure 9.2(a) compares several ensemble averaged correlation functions for bulk and confinement obtained for the original SPC/E water model at 210 K. The ordering of the correlation decays, $S_{22.7} < F_{2,\mathrm{OH}} < F_{1,\mathrm{OH}} \leq S_{10}$, is mostly preserved in the confinement. $S_{22.7}$ and $F_{2,\mathrm{OH}}$ show the fastest dynamics and, thus, have the smallest translation and provide the most accurate spatial resolution. Comparison of $F_{1,\mathrm{OH}}$ with S_{10} shows that rotations measured this way occur for translation over the next neighbor distance. Ensemble averaged correlation functions in confinement show a prominent long time tail that is absent in bulk. They cannot be characterized by a KWW function and determination of a correlation time τ is not trivial. The Mittag-Leffler function roughly applies but is of no further use here. Instead, by binning particles according to their distance to the pore wall and averaging the correlation functions respectively, see Sec. 5.3, dynamics can be studied in a spatially resolved manner. These correlation functions can again, as in bulk, be characterized by KWW functions and only their superposition for all positions within the confinement leads to the broadly stretched decays in Fig. 9.2(a). For the ISF, the correlation decay shifts by orders of magnitude to shorter times with increasing distance to the pore wall, see Fig. 9.2(b). Hence, position and dynamics are correlated and their relation will be quantified in the following by determining the distance dependent correlation times $\tau_\mathrm{e}(d)$.

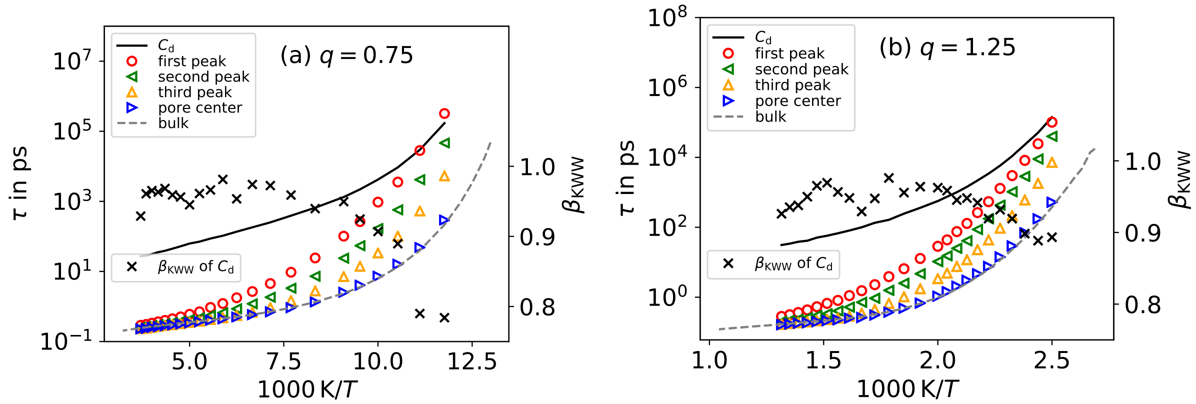

Figure 9.3.: Arrhenius plot with correlation times τ_e of SPC/E water dynamics in a neutral pore with radius $R = 2.5$ nm. Shown are results for the variants with the lowest $q = 0.75$ (a) and highest $q = 1.25$ (b) charge scaling. The correlation times are calculated from the distance resolved $S_{22.7}$ by averaging $\tau_\mathrm{e}(d)$ over some distances d. The black solid line presents $\tau_\mathrm{e,d}$ of the autocorrelation $C_\mathrm{d}(t)$ of the distance to the pore wall, see Eq. (2.3), and the gray dashed line is the result from bulk simulations. The colored symbols show correlation times for distances d corresponding to the first, second and third peak in Fig. 9.1(a) and the pore center. The black crosses are the stretching parameter k_kww of the KWW fit to $C_\mathrm{d}(t)$.
The distances to the pore wall are $d/\mathrm{nm} \in (0, 0.24), (0.24, 0.365), (0.365, 0.48)$ and $(1.7, \infty)$ for $q = 0.75$ and $d/\mathrm{nm} \in (0, 0.225), (0.225, 0.295), (0.295, 0.45)$ and $(1.7, \infty)$ for $q = 1.25$.

An Arrhenius plot of correlation times in confinement is presented in Fig. 9.3. $S_{22.7}$ for the oxygen atoms is averaged over distances to the matrix that correspond to the first to third peaks in the distance resolved density, Fig. 9.1(a), and the pore center. All of them show a super-Arrhenius temperature dependence and a slowdown of up to over two orders of magnitude at the pore wall with respect to the pore center. The latter agrees well with results from bulk simulations with minor deviations at stronger supercooling. Consistent with previous studies, the fragility, found by fitting the data for lower temperatures to the VFT equation and extrapolating to T_g, at smaller distances d is reduced.[229,378] The reasons for this are discussed further below, Sec. 9.5. The autocorrelation $C_\mathrm{d}(t)$ of the distance to the pore wall effectively quantifies the diffusion on the length scale of the confinement. For example, a random-walk in 1D confined to a length L trivially leads to correlation times $\tau \sim L^2$. Here, the geometry is cylindrical and a dynamical gradient exists. For high temperatures, $\tau_\mathrm{e,d}$ from $C_\mathrm{d}(t)$ is two orders of magnitude longer than the translation in the pore center as measured with the ISF. However, for stronger supercooling the dynamical heterogeneity increases and τ_e at the pore wall becomes comparable to or, in some cases of charge scaling, larger than $\tau_\mathrm{e,d}$. Because of the strong gradient, it is sufficient to leave the first layer at the pore surface and the increased mobility at larger distances leads to fast decorrelation. In case of $\tau_\mathrm{e} > \tau_\mathrm{e,d}$, the autocorrelation $C_\mathrm{d}(t)$ becomes non-exponential with $\beta_\mathrm{KWW} < 0.9$.

The meaning of τ_d is important in the context of ensemble averages. It characterizes the time scale on which a randomly selected molecule explores the structural and dynamical heterogeneities caused by the confinement and reproduces the ensemble average. Hence, ergodicity of observables is not achieved when the measurement is on shorter times than τ_d and this time scale corresponds approximately to the slowest particles at the pore wall in the strongly supercooled regime. For temperatures at that point and below, ergodicity can only be restored for times longer than the correlation time at the pore wall.

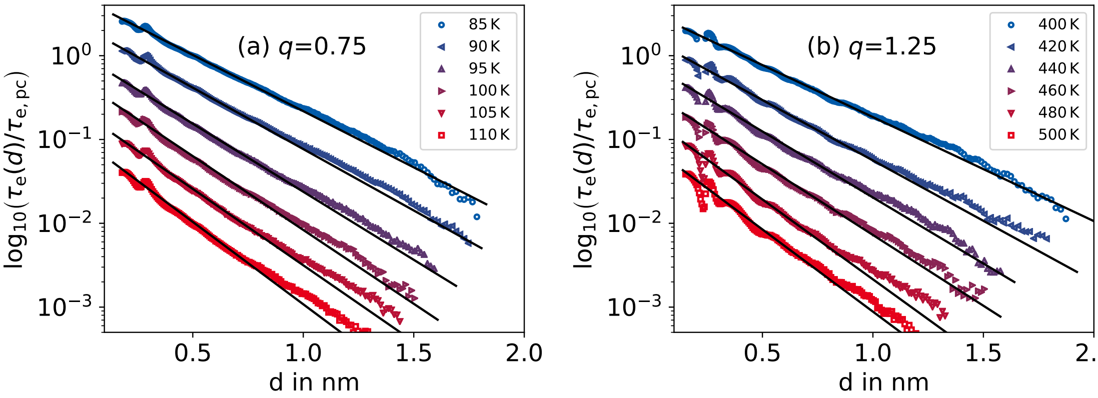

Figure 9.4.: Distance resolved correlation times $\tau_\mathrm{e}(d)$ in neutral pores of the SPC/E water model for two different charge scalings, $q = 0.75$ (a) and $q = 1.25$ (b). The correlation time τ_e is from $S_{22.7}(t)$. Higher temperatures are shifted by factors of 0.5 for clarity. The black lines are fits to Eq. (9.1). To demonstrate the double-exponential behavior, the logarithm $\log_{10}(\tau_\mathrm{e}(d)/\tau_\mathrm{e,pc})$ is shown, where $\tau_\mathrm{e,pc}$ is the correlation time in the pore center determined by the fit.

In the following, the propagation of the confinement effect from the first layer towards the pore center will be investigated. The roughness of the pore surface allows for pockets with particularly slow molecules that are of little interest for the propagation. Hence, the following sections use the constrained distance resolved analysis that ignores molecules with radial positions beyond 2.4 nm. The measured properties, e.g., the correlation times, at larger distances to the pore wall are unaffected. The dynamical profiles $\tau_\mathrm{e}(d)/\tau_\mathrm{e,pc}$ are shown in Fig. 9.4 in a representation that emphasizes the double-exponential decay found in previous studies on confined liquids.[48,323,376,379,380,383] The same behavior is found for the family of the charge-scaled SPC/E water model. Oscillations at short times exist which correspond to the density fluctuations in Fig. 9.1(a). The PEL imposed by the wall has more and less favorable positions. At preferred positions, the particles stay longer and have reduced mobility in contrast to less favorable positions, at which mobility is increased. Note, that the dynamical profile has to be weighted by the occurrence of the respective distances to reproduce the ensemble average. The data can be fit with a double exponential decay

$$\ln\left(\frac{\tau(d)}{\tau_\mathrm{pc}}\right) = A\exp\left(-\frac{d}{\xi_\mathrm{dyn.}}\right). \tag{9.1}$$

Here, τ_pc denotes the correlation time in the pore center and was found to be close to the bulk correlation time for all investigated temperatures and systems. The prefactor A captures the strength of the slowdown at the wall. The range of the influence of the matrix on the liquid is quantified by $\xi_\mathrm{dyn.}$, the dynamic correlation length. In this regard, all charge-scaled variants follow qualitatively the behavior found for Lennard-Jones mixtures,[380] binary mixtures of hard spheres,[376,383] regular SPC/E water,[48,323] and regular BKS silica.[379] This steep double exponential gradient may thus be a universal property of liquids in neutral confinements.

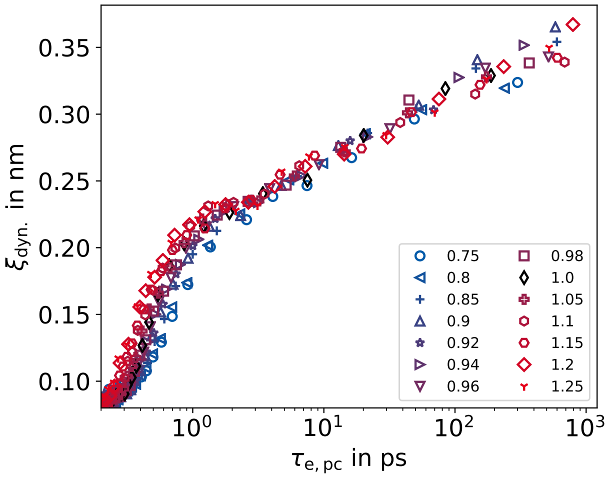

Figure 9.5.: Dynamic correlation lengths $\xi_{\mathrm{dyn.}}$ as a function of the correlation time $\tau_{\mathrm{e,pc}}$ in the pore center. The data is the result from fits with Eq. (9.1) to dynamical profiles $\tau_{\mathrm{e}}(d)$ from the ISF, as in Fig. 9.4, for the charge-scaled SPC/E water models in neutral confinements. The charge scaling q is given in the legend.

The correlation lengths, resulting from weighted fits to data from two independent simulations, are shown in Fig. 9.5. Because the investigated temperature range strongly depends on the dynamics and, thus, on the charge scaling, $\xi_{\mathrm{dyn.}}$ is shown as a function of the τ_{pc} instead of the respective temperatures. Hence, the systems are compared at isokinetic state points. The data shows two different regimes. At subpicosecond correlation times the dynamical process is neither cooperative nor predominantly activated, i.e., temperatures are above the Goldstein temperature. For temperatures with $\tau_{\mathrm{pc}} > 2\,\mathrm{ps}$, a linear relation between $\xi_{\mathrm{dyn.}}$ and $\ln \tau_{\mathrm{e,pc}}$ is found. Within the scattering of the data, no dependence of the slope on the charge scaling q can be found and the data collapses to a master curve. For charge scaling of silica, however, prefactors differed with partial charge and deviations from the linear relation at long correlation times appeared.[392] The slope of $\xi_{\mathrm{dyn.}}$ decreased upon further supercooling. Similar behavior for the SPC/E variants cannot be excluded. Nevertheless, linear extrapolation as function of $\ln \tau_{\mathrm{e,pc}}$ to T_{g}, with $\tau_{e,pc}(T_{\mathrm{g}}) = 100\,\mathrm{s}$, leads to dynamic correlation lengths of $0.93\,\mathrm{nm}$.

9.3.1. Configurational overlap

Apart from the confinement effect on the dynamics, its structural influence can be quantified. The PEL imposed by the matrix is static. Previous studies showed that favorable and unfavorable positions of the liquid molecules in neutral pores exist.[46,229,379] The resulting static density correlations can be analyzed with configuration-overlap correlation functions $Q(t)$, see Sec. 5.2.3. Figure 9.6(a) shows the spatially resolved results $Q(t, d)$. Consistent with the ISF, the decay shifts to longer time scales with decreasing distance d to the matrix. The long-time plateau $\lim_{t\to\infty} Q(t) = Q_\infty \approx 0.2$ in bulk corresponds to random distributions of particles and depends on the overlap criterion and particle density. The bulk value is obtained in the pore center indicating a full structural decorrelation. With decreasing distance to the pore wall, $Q_\infty(d)$ increases. The favorable and unfavorable positions in the static PEL imprinted by the confinement increase the probability of reoccurring configurations. The same oscillations observed for $\tau_{\mathrm{e}}(d)$ are found for very short distances, up to 0.6 nm in $Q_\infty(d)$, Fig. 9.6(b). To quantify the range of this effect, the static correlation length $\xi_{\mathrm{sta.}}$ can be obtained by

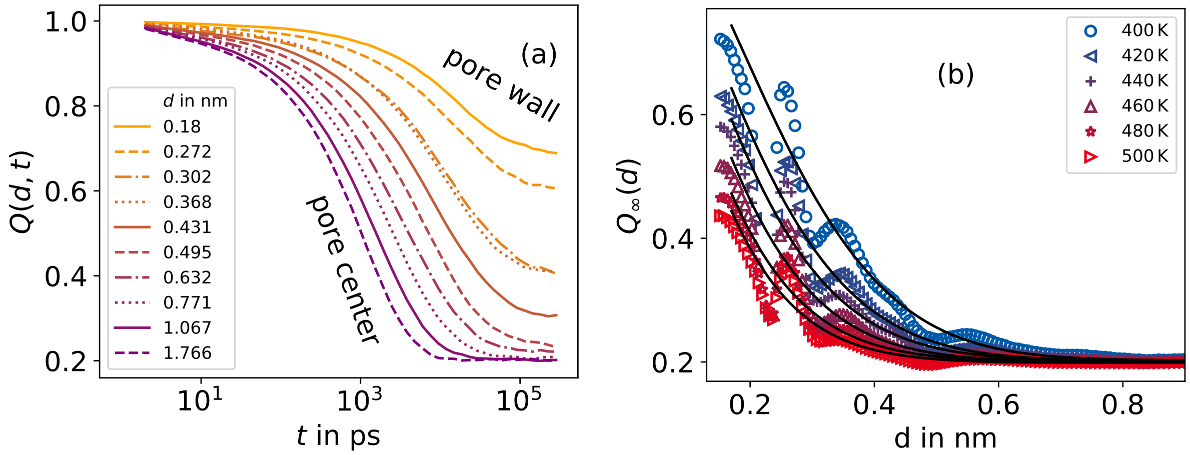

Figure 9.6.: (a) The overlap correlation function $Q(t)$ for subsets at different distances d to the pore wall, given in the legend, at 400 K and with charge scaling $q = 1.25$. (b) The configuration overlap at infinite times Q_∞ determined by fitting the data in (a) to Eq. (5.34) for the charge-scaled SPC/E water model with $q = 1.25$ and several temperatures. The black lines are fits with Eq. (9.2).

fitting with[323,376,382,384]

$$Q_\infty(d) = Q_{\text{pc}} + (1 - Q_{\text{pc}}) \exp\left(-\left(\frac{d}{\xi_{\text{sta.}}}\right)^\beta\right). \tag{9.2}$$

Here, Q_{pc} is the plateau height in the pore center and β allows for stretched or compressed exponential decays. Previous studies found $\beta > 1$, temperature independent in some cases.[323,376,382,384] The results for the fit parameters $\xi_{\text{sta.}}$ and β are presented in Fig. 9.7(a). Again, isokinetic state points are compared by showing $\xi_{\text{sta.}}$ as a function of $\tau_{\text{e,pc}}$. Similar to $\xi_{\text{dyn.}}$, the slope in the subpicosecond regime is different and this data is unlikely to be relevant for the glassy slowdown. However, not all results for $\xi_{\text{sta.}}$ collapse onto a master curve upon supercooling. Variants with $q < 0.9$ deviate, consistent with the proposition that these are HDL-like systems, while LDL-like systems collapse. Not only is the relation of $\xi_{\text{dyn.}}$ and $\xi_{\text{sta.}}$ regarding dynamics in the pore center different but the latter, $\xi_{\text{sta.}}$, appears to be significantly larger for lower q. Linear extrapolation of $\xi_{\text{sta.}}$ as a function of $\ln \tau_{\text{e,pc}}$ to T_{g} leads to slightly smaller values of $\xi_{\text{sta.}}$ than for $\xi_{\text{dyn.}}$ with on average 0.8 nm for charge scaling larger than 0.9 and larger values for $q < 0.9$. While the dynamic correlation length appears to be unaffected by the LLPT, when comparing isokinetic points, the static correlation length systematically varies.

The stretching parameter β of the decay was not found to be temperature independent. In particular, it increases with decreasing temperature indicating a compressed exponential decay. Just as $\xi_{\text{sta.}}$, β collapses onto a master curve for LDL-like systems while it deviates to even higher values for HDL-like systems. This means that the interfacial zone more narrowly transitions from affected to unaffected by the matrix. In other words, the structurally affected region becomes better defined with stronger supercooling. This is consistent with the idea of structurally distinguishable patches in the RFOT theory of the glass transition. For silica, β reached values of 2, corresponding to Gaussian shape, and larger.[392] Considering the temperature dependence of β, the quantification of the static correlation length from the fit parameter alone may be questionable. To take this into account, the

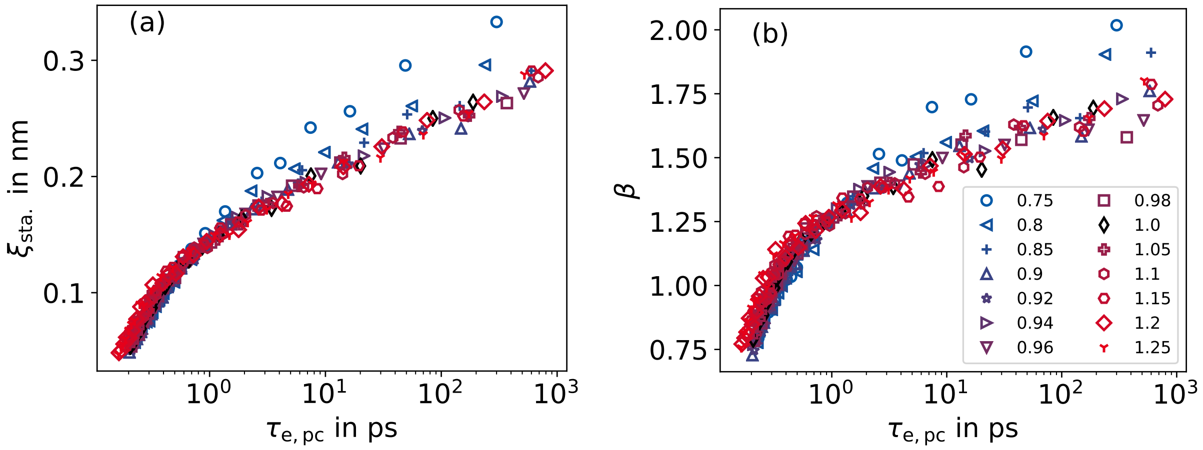

Figure 9.7.: (a) Static correlation lengths $\xi_{\mathrm{sta.}}$ as a function of the correlation time $\tau_{\mathrm{e,pc}}$ in the pore center. The data is the result from fits with Eq. (9.2) to overlap plateau profiles $Q_\infty(d)$, as in Fig. 9.6(b), for the charge-scaled SPC/E water model in neutral confinements. The charge scaling q is given in the legend. (b) The respective stretching parameter β of the same fits to $Q_\infty(d)$.

mean correlation length, $\langle \xi_{\mathrm{sta.}} \rangle = \xi_{\mathrm{sta.}}/\beta \cdot \Gamma(1/\beta)$, was calculated and is shown in Fig. A.18 in the appendix. While $\langle \xi_{\mathrm{sta.}} \rangle$ is slightly smaller than $\xi_{\mathrm{sta.}}$, the dependence on dynamics and charge scaling is qualitatively the same.

9.3.2. Debye-Waller factor

Next, the vibrational motion and its position dependence is investigated. Specifically, the MSD of the oxygen atoms at 1 ps, $u^2 = r^2(t = 1\,\mathrm{ps})$, is analyzed. At this time and for sufficient supercooling, the particles are caged by their neighbors and the MSD exhibits a plateau, separating ballistic and diffusive motion. These vibrations are experimentally accessible via the Debye-Waller factor, see Sec. 5.2.2.[320] Elastic models of the glass transition propose that the structural relaxation time depends on the short-time MSD, see Sec.5.2.2.[31] By substituting the prediction, $\ln \tau \sim 1/u^2$, into Eq. (9.1), the expected behavior of $u^2(d)$ is

$$\frac{u_{\mathrm{pc}}^2}{u^2(d)} - 1 \propto \exp\left(-\frac{d}{\xi_{\mathrm{vib.}}}\right). \tag{9.3}$$

Here, u_{pc}^2 is the short-time MSD in the pore center and $\xi_{\mathrm{vib.}}$ is the vibrational correlation length, quantifying the range of the effect of the matrix on the liquid. Figure 9.8 shows data for u^2 rescaled to demonstrate the exponential distance dependence. Except for the oscillations at short d, found at the same distances as for $\tau_{\mathrm{e}}(d)$ and $Q_\infty(d)$, $1/u^2$ decreases with increasing distance, i.e., the amplitude of vibrational motion is larger in the pore center than at the wall. Exponential behavior can only be found at sufficient distance to the wall, i.e., beyond a few next neighbor distances from the wall. However, the temperature dependence of the relative reduction of vibrations between pore wall and pore center, u_{pc}^2/u^2, at the first and second peak, is weak and almost nonexistent for $q = 0.75$. This effect will be investigated in Sec. 9.5 in terms of the PEL at the pore wall. It can be noted here, that the weak temperature dependence of u_{pc}^2/u^2 compared to that of $\ln(\tau_{\mathrm{e}}/\tau_{\mathrm{e,pc}})$ at the wall is incompatible with the predictions of elastic models. One cannot be constant while the

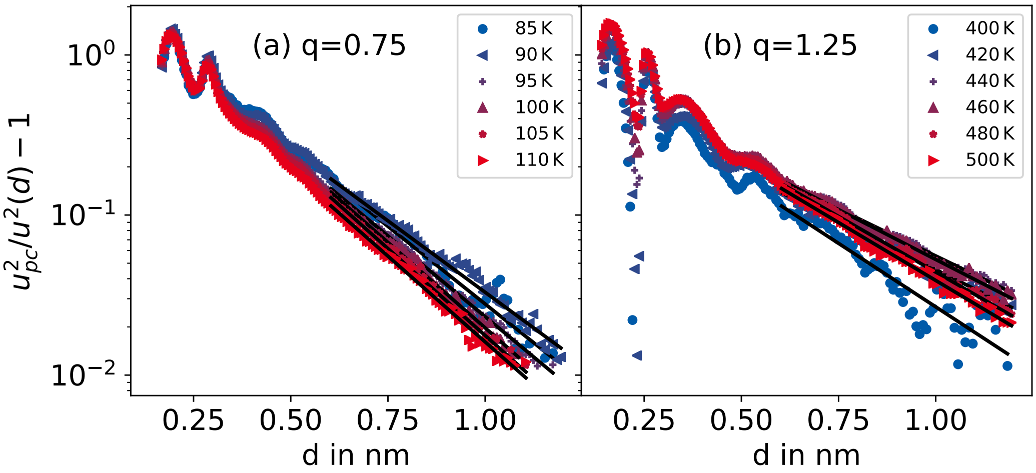

Figure 9.8.: Distance resolved short-time MSD $u^2(d)$, in reduced representation $u_{\mathrm{pc}}^2/u^2(d) - 1$, in neutral pores of the SPC/E water model for two different charge scalings, $q = 0.75$ (a) and $q = 1.25$ (b). u^2 is the MSD at $t = 1$ ps. To demonstrate the exponential behavior, the data is rescaled by the value in the pore center u_{pc} and subtracted by one. The black lines are fits to Eq. (9.3).

other is temperature dependent. The vibrational length scales $\xi_{\mathrm{vib.}}$ resulting from fits to the data at distances $d > 0.6$ nm are shown in Fig. 9.9 for all SPC/E variants and supercooled temperatures. In contrast to $\xi_{\mathrm{dyn.}}$ and $\xi_{\mathrm{sta.}}$, $\xi_{\mathrm{vib.}}$ does not collapse onto a master curve when shown as a function of vibrations in the pore center, $1/u_{\mathrm{pc}}^2$. No qualitative change is found when shown as a function of $\tau_{\mathrm{e,pc}}$. Instead, the vibrational correlation length increases with increasing partial charge and the temperature dependence is weak. This differs from the two other correlation lengths, which will be compared in the next section. The stronger scattering of the data makes this a less reliable length scale.

Because the local structure of water is highly directional, with hydrogen bonding and a tetrahedral network, the vibrations of molecule vectors might be a meaningful alternative. However, the short-time angular displacement $1/\theta^2$, shown in the appendix in Fig. A.19, was proven to not be qualitatively different from the vibrational displacement $1/u^2$. The temperature dependence is weak and the small relative slowdown towards the pore wall leads to shorter ranges of reliable data.

Comparison of length scales

All three correlation lengths, $\xi_{\mathrm{dyn.}}$, $\xi_{\mathrm{sta.}}$, and $\xi_{\mathrm{vib.}}$, are presented in Fig. 9.10 for the lowest and highest charge scaling and the original SPC/E model. Shown are only supercooled temperatures with correlation times of $\tau_{\mathrm{e,pc}} \geq 1$ ps. For all investigated temperatures and charge-scaled variants, the correlation lengths are on the order of the next neighbor distance of the tetrahedral network, ≈ 0.28 nm. The temperature dependence of $\xi_{\mathrm{dyn.}}$ and $\xi_{\mathrm{sta.}}$ is similar. Their absolute values are the same for variants with HDL structure but differ for those with LDL structure. When comparing $\xi_{\mathrm{dyn.}}$ and $\xi_{\mathrm{vib.}}$, not only does their temperature dependence differ but also their absolute values. The latter is reason enough to conclude that elastic models that rely on $\ln \tau \sim 1/u^2$ are incorrect in confinement.

Figure 9.11 presents the static correlation length as function of the dynamic correlation length. Indeed, their temperature dependence is quite similar. The LDL-like systems, with charge scaling

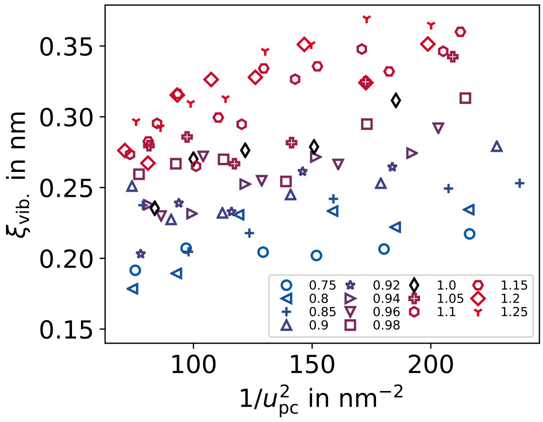

Figure 9.9.: Vibrational correlation lengths $\xi_{\text{vib.}}$ as a function of the reciprocal short-time MSD $1/u_{\text{pc}}^2$ in the pore center. The data is the result from fits with Eq. (9.3) to the long-distance tail, specifically $d > 0.6$ nm, of the profiles $u_{\text{pc}}^2/u^2(d) - 1$, as in Fig. 9.8, for the charge-scaled SPC/E water model in neutral confinements. The charge scaling q is given in the legend. Only temperatures with trajectories that resolve $t = 1$ ps are shown.

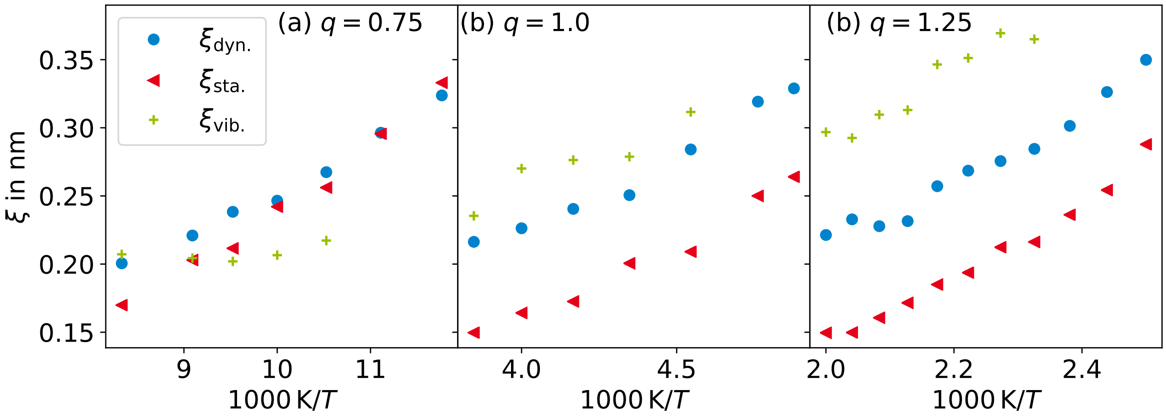

Figure 9.10.: Several correlation lengths of the SPC/E water model in neutral confinement as function of inverse temperature. Presented are the dynamic, static and vibrational correlation length, $\xi_{\text{dyn.}}$, $\xi_{\text{sta.}}$, and $\xi_{\text{vib.}}$, for the lowest, regular SPC/E and the highest charge-scaling factors, (a) $q = 0.75$, (b) $q = 1.0$ and (c) $q = 1.25$. For $\xi_{\text{vib.}}$, only temperatures with trajectories that resolve $t = 1$ ps are shown.

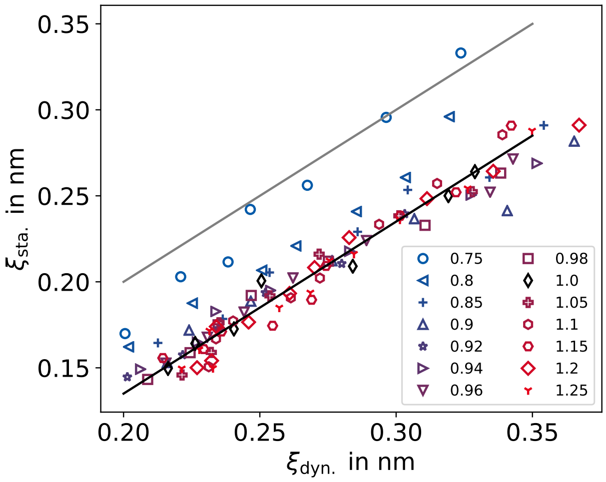

Figure 9.11.: The static correlation length $\xi_{\text{sta.}}$ as function of the dynamic correlation length $\xi_{\text{dyn.}}$ for charge-scaled SPC/E in neutral pores. The charge scaling is given in the legend. Only temperatures with $\tau_{\text{e,pc}} \geq 1$ ps are shown. The black and gray solid lines are guides to the eye. The latter follows $\xi_{\text{sta.}} = \xi_{\text{dyn.}}$ while the former indicates $\xi_{\text{sta.}} - 0.065\,\text{nm} = \xi_{\text{dyn.}}$.

$q \geq 0.9$, have a $\xi_{\text{sta.}}$ shorter by about $0.065\,\text{nm}$ than $\xi_{\text{dyn.}}$. Only for the lowest partial charge, $q = 0.75$, both correlation lengths are similar in size. In contrast, the static correlation length was found to be larger for all charge-scaled BKS silica variants.[392] Hence, various tetrahedral liquids do not show the same ratio of static and dynamic correlation lengths. Still, all charge-scaled variants with similar local structure have a common relation between $\xi_{\text{sta.}}$ and $\xi_{\text{dyn.}}$ regardless of interaction strength.

9.3.3. RFOT and charge scaling

The random first order transition (RFOT) theory of the glass transition,[91] Sec. 2.2.3, makes predictions about the relation of the structural relaxation and the size of structurally distinguishable regions with locally optimized structure. Specifically, it predicts for the α-relaxation $\ln \tau/\tau_0 \propto \xi^{\phi}_{\text{sta.}}/T$, where τ_0 is a prefactor and ϕ a fractional exponent for the static correlation length $\xi_{\text{sta.}}$. This combines the correlation time of the bulk system with the correlation length from confinement simulations. The following formula was used to fit and rescale the data:

$$\ln \frac{\tau}{\tau_0} = \left(\frac{\xi_{\text{sta.}}}{\xi_{\text{sta.},0}} \right)^{\phi} \frac{E_\infty}{T} \tag{9.4}$$

Here, the proportionality factor is introduced as $\xi_{\text{sta.},0}$ for dimensionality reasons and E_∞ is the high temperature bulk activation energy of the respective correlation time τ. When each charge-scaled variant is fitted with Eq. (9.4) individually, the number of free fit parameters and few data points lead to overfitting. Instead, the exponent ϕ is a global fit parameter and $\xi_{\text{sta.},0}$ and τ_0 are independent with respect to charge scaling. Figure 9.12(a) presents the master curve for fits to correlation times for $S_{22.7}$ and $F_{1,\vec{\mu}}$. Hence, Equation (9.4) is sufficient to characterize the temperature dependence of bulk dynamics in the mildly supercooled regime. Furthermore, the fit parameters $\xi_{\text{sta.},0}$ and τ_0 are independent of q for the LDL like systems and only increase for reduced charge scaling, Fig. 9.12(b). A global fit of all three parameters is possible for $q \geq 0.9$ with acceptable quality. The fact that rescaling the temperature with E_∞ again allows for a collapse of data further supports its role as the relevant

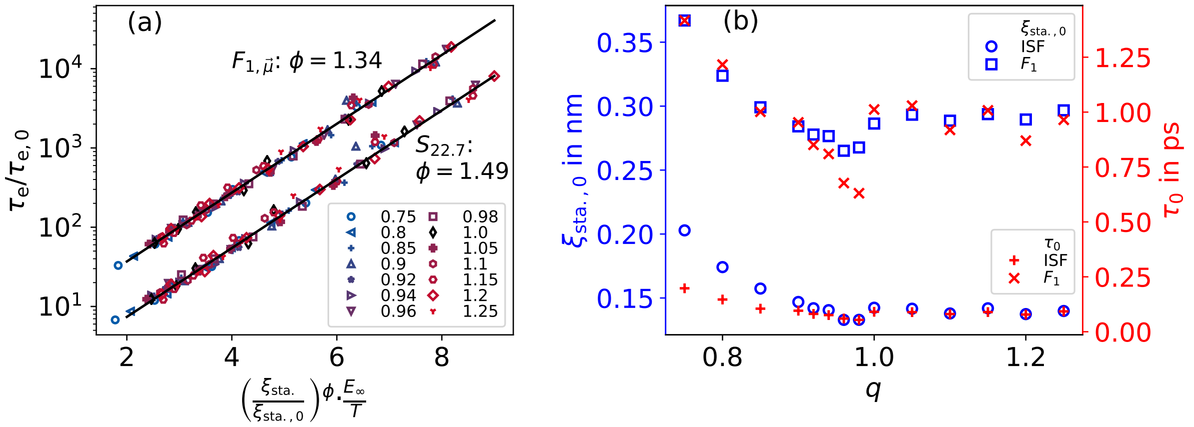

Figure 9.12.: A test of the prediction of the RFOT theory with data from the charge-scaled SPC/E water model. The correlation time τ_e from bulk and the static correlation length $\xi_{sta.}$ from confinement simulations are fit with Eq. (9.4). The correlation times are from $S_{22.7}$ and $F_{1,\vec{\mu}}$ and are rescaled with the result from the fit to achieve master curves (a). The data for $F_{1,\vec{\mu}}$ is shifted upwards by a factor of five for clarity. Only temperatures with $\tau_e^{S_{22.7}} \geq 1$ ps are included and the charge scaling q is given in the legend. In each case, the exponent ϕ is a global fit parameter while $\xi_{sta.,0}$ and τ_0 are charge dependent. The resulting fit parameters are shown in (b) as a function of q.

energy scale not only in the simple-liquid but also in the supercooled regime. Interestingly, the reference length $\xi_{sta.,0}$ is comparable to the average displacement found for the respective correlation time $\langle|\vec{r}(\tau) - \vec{r}(0)|\rangle$. For $S_{22.7}$, $\langle|\vec{r}(\tau) - \vec{r}(0)|\rangle = 0.11$ nm would be correct while the slower decay of $F_{1,\vec{\mu}}$ corresponds to average displacements similar to the next neighbor distance.

However, the exponent ϕ differs between both correlation functions. RFOT predicts a value of $\phi = 1.5$, which is close to the value found for τ from the ISF and but not from $F_{1,\vec{\mu}}$. In addition, τ_0 does not match the values for fits to the high temperature Arrhenius regime, as in Fig. 8.8, where a significant dependence on charge scaling is found. Fitting each charge-scaled variant independently leads to strong scattering of the fit parameters and does not resolve such discrepancies. These results should be interpreted qualitatively and show, that for LDL systems, which share a common local structure and relaxation mechanism, the relation of τ and $\xi_{sta.}$ is unaltered by charge scaling.

9.4. Influence of the confinement properties

So far, the dependence of the properties of the confined liquids on the charge scaling has been investigated for pores constructed with the same structural properties, pore geometry and wall rigidity. The following sections exploit that neutral pores allow also for systematic studies of the dependence on properties of the confinement.

9.4.1. Pore rigidity

First, the same pore geometry is applied but the wall rigidity is varied. Specifically, the spring constant κ defining the steepness of the harmonic potential, that traps the oxygen atoms of the matrix, is reduced. Since the charge scaling leads to high temperature activation energies varying by a factor of 5, κ might require adjustment to prevent penetration of the pore wall at higher temperatures and obtain comparable results for all charge-scaled variants.

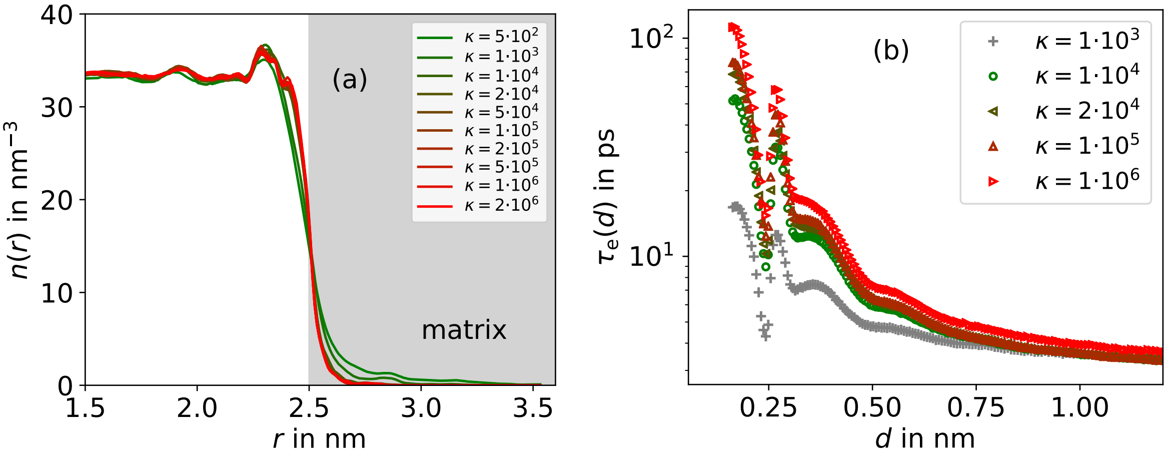

Figure 9.13.: (a) Particle density n of water oxygens as a function of distance to the pore axis r at 240 K within a neutral SPC/E pore with radius $R = 2.5$ nm for several spring constants κ. Their values given in the legend are in units of kJ/mol·nm^{-2}. All neutral pores are otherwise identical. (b) Constrained distance resolved correlation times $\tau_\mathrm{e}(d)$ for several values κ. The correlation time τ_e is from $S_{22.7}$.

Figure 9.13(a) presents the oxygen particle density of the liquid species as a function of the radial position for a neutral pore with radius $R = 2.5$ nm and the original SPC/E water model. In all studies presented up to here, κ was 10^6 kJ/(mol·nm^2). For the sake of brevity, the units of κ will be omitted in the following. Density profiles agree for reduced values of κ over several orders of magnitude. For the lowest rigidities, $\kappa \leq 10^3$, penetration of the pore wall occurs more often. This effect is more severe at higher temperatures and leads to a reduction of the density in the rest of the pore. In these cases, observables in the pore center deviate from previous results and bulk behavior.

The dynamical profile $\tau_\mathrm{e}(d)$ for $S_{22.7}$ is presented in Fig. 9.13(b) for several spring constants κ. The extent of slowdown towards the pore surface is stronger for stiffer walls. Systematic differences exist even for $\kappa \geq 10^4$ where penetration of the matrix is negligible. Stiffer walls have smaller vibrational displacement u^2 and the PEL imprinted on the liquid is sharper, i.e., the potential minima are deeper and energy barriers higher. Or, rationalized considering the findings for the Debye-Waller factor in Sec. 9.3.2, the reduction of u^2 caused by the matrix and propagated by the liquid simply starts off stronger for higher spring constants κ.

The dynamic and static correlation lengths can be determined to study their dependence on the pore rigidity. Figure 9.14(a) shows the plot corresponding to Fig. 9.4, but for a single temperature and several spring constants κ. The data sets are shifted in distance d such that the curves coincide in $\tau_\mathrm{e}(0)/\tau_\mathrm{e,pc} = 1$, i.e., they start with the same relative slowdown. The data sets with $\kappa \geq 10^4$ collapse onto a master curve and their common slope indicates that they have the same dynamic correlation length. The slope for $\kappa = 10^3$ deviates. The dependence of $\xi_\mathrm{dyn.}$ and $\xi_\mathrm{sta.}$ on κ exemplifies this effect, see Fig. 9.14(b). For all investigated temperatures, $\xi_\mathrm{dyn.}$ appears to be the same for $\kappa \geq 10^4$. Determination of the static correlation length fails completely for soft walls. There, the profile $Q_\infty(d)$ of the static overlap does not follow an exponential decay. Properties of the liquid determined by neutral confinement simulations as performed in this study are independent of pore rigidity for $\kappa \geq 5 \cdot 10^4$. This supports the interpretation of these length scales as being properties of the bulk

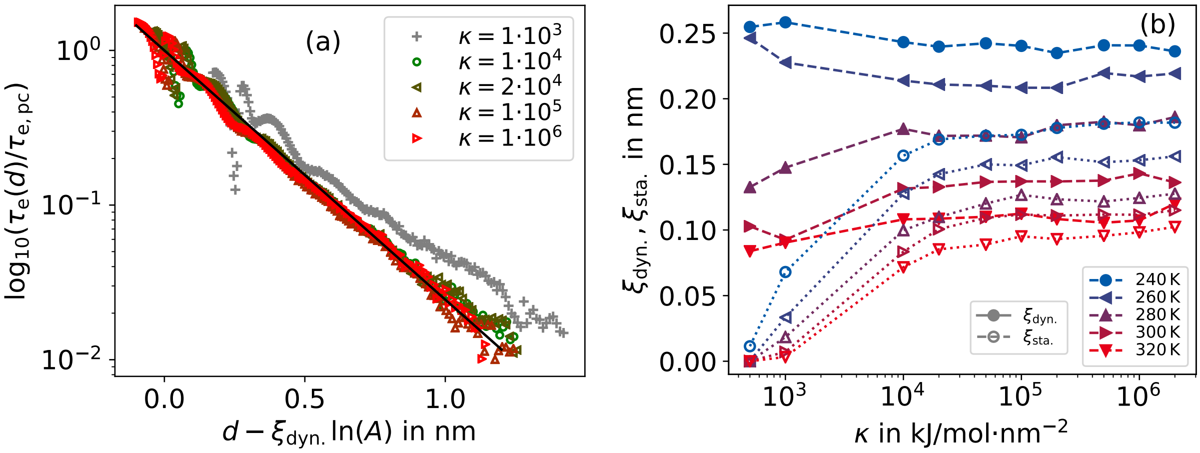

Figure 9.14.: (a) Constrained distance resolved correlation times $\tau_e(d)$ at 240 K within a neutral SPC/E pore with radius $R = 2.5$ nm for several spring constants κ, see Fig. 9.13(b). To demonstrate the double-exponential behavior, the logarithm $\log_{10}(\tau_e(d)/\tau_{e,pc})$ is shown, where $\tau_{e,pc}$ is the correlation time in the pore center determined by the fit. The data is fitted with Eq. (9.1) and shifted along the x-axis to collapse on $\tau_e(0)/\tau_{e,pc} = 1$. The black line is Eq. (9.1) for the average value $\xi_{dyn.}$, excluding $\kappa = 10^3$. (b) The dynamic and static correlation lengths, $\xi_{dyn.}$ and $\xi_{sta.}$, as determined with Eqs. (9.1) and (9.2), as a function of spring constant κ. The temperatures are indicated in the legend. Filled symbols connected by dashed lines present $\xi_{dyn.}$ while open symbols connected by dotted lines present $\xi_{sta.}$.

liquid. Thus, $\kappa = 10^6$ being two orders of magnitude larger should be sufficiently high to prevent penetration of the matrix for also the highest charge-scaled variants and temperatures. Depending on the study, softer or stiffer walls may be preferable. Softer confinement allows for slightly faster dynamics and stronger supercooling in equilibrium. Stiffer confinement enhances the slowdown at the surface and improves the study of confinement effects at mild supercooling.

9.4.2. Inverted pores and dependence on the radius of curvature

Next, the pore geometry is varied while the rigidity remains unaltered at $\kappa = 10^6$. Previous studies showed for cylindrical pores enhanced slowdown with decreasing pore diameter, while correlation lengths were unaffected.[48,323] For small convex confinements, the properties in the pore center do not recover bulk behavior. Here, concave confinements are studied. Specifically, a sphere of position restrained molecules with varying radius is used as ”inverted confinement”, see Sec 4.3. This allows for much smaller radii of curvature while both, concave and convex confinements, are expected to coincide when the radius approaches infinity. A patch of significantly slower molecules may affect surrounding molecules similar to a restrained sphere. This is relevant in theories of the glass transition in a dynamically heterogeneous bulk liquid or with larger and less mobile components of mixtures. However, the systems studied here use the high spring constant of $\kappa = 10^6$ instead of a softer restraint, which may be characteristic for the surface of less mobile regions. Simulations are limited to the original SPC/E model of water and radii from 0.5 to 3.0 nm.

The radial density of the oxygen atoms shows a small peak at the pore surface absent in results for cylindrical pores, see Fig. 9.15(a). Also, weak penetration beyond the cutoff radius of the solid

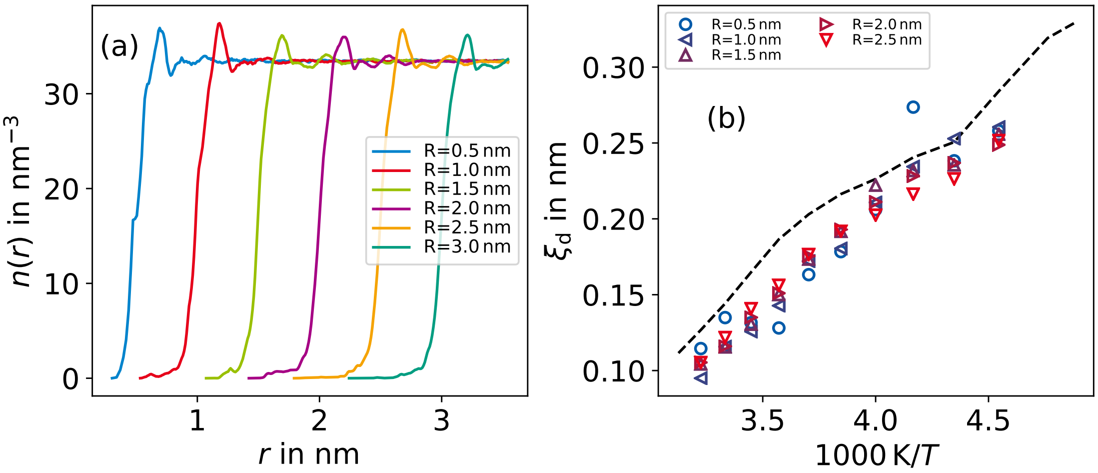

Figure 9.15.: (a) Particle density n of oxygen atoms of the SPC/E model of water as a function of the radial position r at 280 K. Shown is the density of the liquid fraction surrounding a sphere of a position restrained solid fraction with radii R given in the legend. (b) The dynamic correlation length $\xi_{\text{dyn.}}$ as a function of inverse temperature for several radii of solid fractions in (a). The black dashed line indicates the result from cylindrical neutral pores of radius $R = 2.5$ nm.

fraction exists. Likely, the roughness of the surface and corresponding pockets are energetically more easily exploited for a concave geometry. Besides that, the density in these systems is mostly unperturbed consistent with the cylindrical confinements. Again, the dynamical profile $\tau_{\text{e}}(d)$ for $S_{22.7}$ is calculated and fitted with Eq. (9.1). The dynamic correlation lengths $\xi_{\text{dyn.}}$ are shown in Fig. 9.15(b) alongside the result for the cylindrical pore. The results for inverted pores are identical within the accuracy of the method. For the smallest sphere with radius $R = 0.5$ nm the quality of the data suffers from poor statistics and would require a larger ensemble average over multiple configurations of the sphere. Agreement between concave and convex confinements would be expected for large radii. However, $\xi_{\text{dyn.}}$ is mildly but systematically shorter for inverted pores. The difference appears to be constant with temperature and, thus, the growth of $\xi_{\text{dyn.}}$ with decreasing temperature is consistent. It is possible, that the different steps during the construction, detailed in Sec. 4.3, or minor details in the spatially resolved analysis are reasons for this discrepancy. Overall, both methods lead to the same temperature dependence and the dependence on the confinement geometry is negligible compared to the effect of temperature.

9.5. Rationalization of the relative slowdown at the pore wall

So far, the ranges of the dynamical slowdown and enhanced configurational overlap were investigated. In other words, the consequence of the static PEL, imprinted by the matrix, and its propagation by the unrestrained molecules, which is a property of the liquid, were studied. Here, the quantification of the PEL is attempted. The short-time MSD u^2 probes the local potential well experienced by caged particles. In this static PEL, potential minima for oxygen atoms are always the same distance apart. Then, the facts that u^2 is reduced and τ longer at the pore wall imply that the potential wells are steeper and the energy barriers between local minima higher than in the pore center, or in bulk, respectively. For harmonic potentials, the potential at the pore wall is higher by a factor of $u_{\mathrm{pc}}^2/u_{\mathrm{pw}}^2$ than in the pore center. The energy barrier between two local minima scales by this value and, hence, is taken as a measure of the PEL at the pore wall. Here, u_{pw} is taken as the value at the second maximum in the particle density, see Fig. 9.1(a). Figure 9.16(a) presents the results for all charge-scaled variants as a function of inverse temperature.

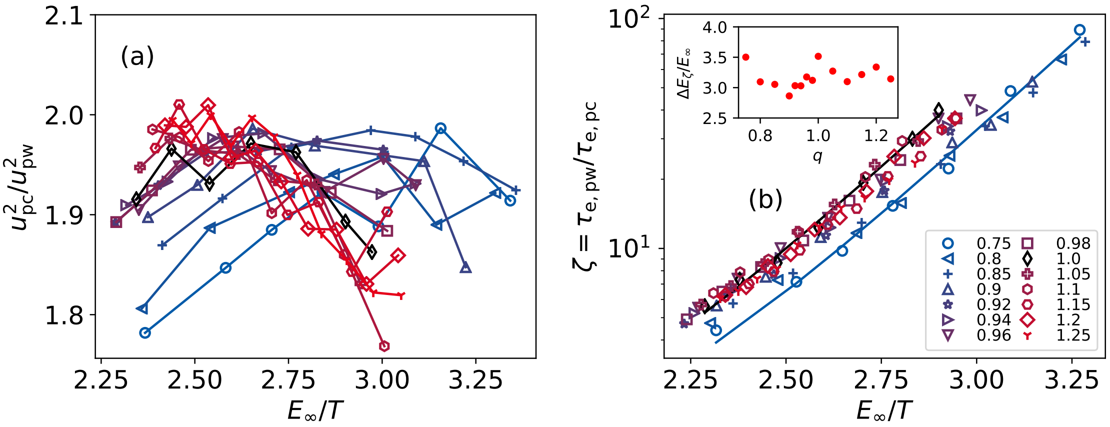

Figure 9.16.: (a) Relative short-time MSD $u_{\mathrm{pc}}^2/u_{\mathrm{pw}}^2$ between the pore wall and center. Specifically, u_{pw}^2 is the value at the position of the second maximum of the distance dependent oxygen particle density, see Fig. 9.1(a). (b) The relative slowdown between pore wall and center $\zeta = \tau_{\mathrm{e,pw}}/\tau_{\mathrm{e,pc}}$ for τ_{e} from $S_{22.7}$. To reduce noise, fits with Eq. (9.1) were used to interpolate $\tau_{\mathrm{e}}(d)$ at the same positions as in (a). The black and blue solid lines are fits with Eq. (9.5) to the data for $q = 1.0$ and $q = 0.75$, respectively. The insert shows the ratio of $\Delta E_\zeta/E_\infty$ as determined by the fits and the Arrhenius regime with E_∞ of τ_{e} at high temperatures in bulk simulations. The charge scaling q is given in the legend. Both panels show only temperatures with $\tau_{\mathrm{e,pc}} \geq 1\,\mathrm{ps}$.

For all charge-scaled variants, the potential at the wall and energy barriers are roughly 1.9 to 2 times steeper and higher, respectively, compared to the pore center. This ratio is weakly dependent on temperature in the investigated regime with a minor tendency to decrease upon further supercooling. HDL-like liquids appear to be shifted to lower temperatures. The comparison of vibrational motion implies that the difference of energy barriers between wall and center does not increase further. However, in the previous sections no straightforward agreement was found between dynamic/static and vibrational observables. Instead of the short-time MSD, the correlation time at the pore wall and in the pore center can also be compared. In the following, several models will be formulated and tested concerning the relative dynamical slowdown in the presence of a confining matrix. They all assume that the relative slowdown caused by the matrix can me modeled by an additional activation energy, i.e., that it follows $\sim \exp \frac{\Delta E}{T}$.

9.5.1. Constant additional activation energy

Figure 9.16(b) shows the relative slowdown at the wall $\zeta = \tau_{\mathrm{pw}}/\tau_{\mathrm{pc}}$. Specifically, it uses interpolation with fits of Eq. (9.1) at the position of the second maximum in the density in Fig. 9.1, considering charge scaling and temperature. On a reduced temperature scale, E_∞/T, the charge-scaled variants with lower q, i.e., HDL-like systems, almost collapse onto a master curve showing a reduced slowdown. ζ appears to follow an Arrhenius law for sufficient supercooling while it approaches unity at high temperatures. A simple empirical function that fulfills both constraints has only the two parameters required for the Arrhenius law and shifts it to one for $\lim_{T\to\infty}$,

$$\zeta = \frac{\tau_{\mathrm{pw}}}{\tau_{\mathrm{pc}}} = 1 - \exp\left(-\frac{\Delta E_\zeta}{T_0}\right) + \exp\left(\Delta E_\zeta\left(\frac{1}{T} - \frac{1}{T_0}\right)\right). \tag{9.5}$$

Here, ΔE_ζ quantifies the increased activation energy at the wall and the slope in Fig. 9.16(b) for sufficiently low temperatures. T_0 shifts the onset of this Arrhenius temperature dependence. Fits to Eq. (9.5) characterize the data well in the mildly supercooled regime and the resulting activation energy is shown in the inset of the figure in units of the high temperature activation energy E_∞. Approximately the same ratio $\Delta E_\zeta/E_\infty \approx 3$ is found for all charge-scaled variants. This is comparable to the cooperative contribution to the total activation energy at T_g in bulk systems, see Sec. 8.4.6,[37,112,115] and suggests that also in neutral confinement E_∞ is a relevant energy scale. Note that, while a study of the Kob-Andersen mixture in neutral confinement also found $\Delta E_\zeta/E_\infty \approx 3$,[377] the ratio was found to be ≈ 1.7 for silica in neutral confinement.[392] Hence, a value of 3 is only universal for the water-like models studied here. Furthermore, using rotational correlation times and their higher activation energies E_∞ leads to a ratio close to unity, see appendix Fig. A.21. This finding may have more important implications than the factor of 3 for the ISF, because E_∞ for RCFs is close to the value found for self-diffusion coefficients in bulk water and, thus, a more reliable measure of the underlying dynamics of the liquid. But, weaker slowdown, discussed in Sec. 9.6 further below, and spatial averaging make usage of RCFs less reliable in the present study.

The above analysis can be extended to any distance d to the pore wall and the real data with distance dependent $\Delta E_\zeta(d)$ and $T_0(d)$, presented in Fig. 9.17(a) and (b). The fits are shown on the example of $q = 1.0$ in the appendix, Fig. A.20. The data is noisy and superimposed by the oscillations of the distance resolved spatial analysis. The dynamical gradient within the pores is for the most part characterized by the temperature offset $T_0(d)$. The activation energy $\Delta E_\zeta(d)$ appears to be only

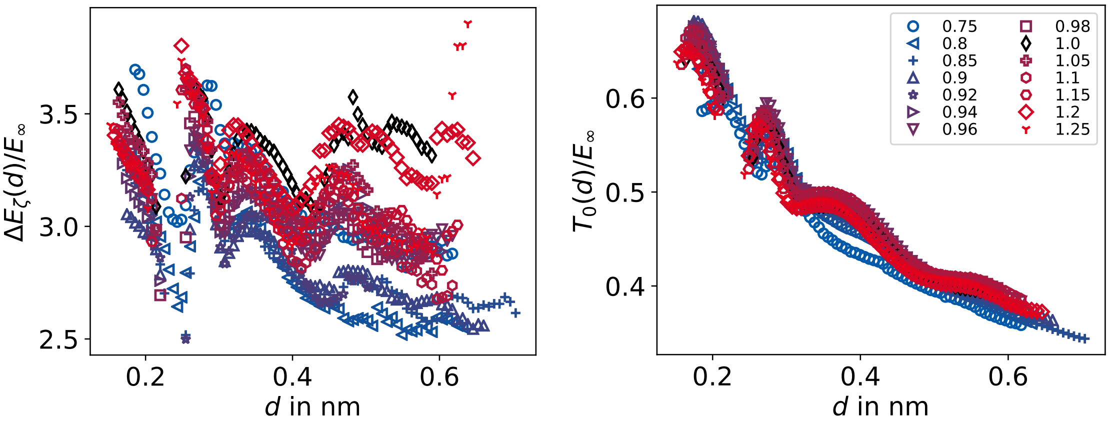

Figure 9.17.: The additional activation energy $\Delta E_\zeta(d)$ (a) of the Arrhenius law of the relative slowdown $\zeta(d) = \tau_{\mathrm{e}}(d)/\tau_{\mathrm{e,pc}}$ and the related onset temperature T_0 (b). The values are results from fits of Eq. (9.5) to the dynamical profiles $\tau_{\mathrm{e}}(d)$ for all charge-scaled variants of SPC/E in neutral confinement. The correlation times $\tau_{\mathrm{e}}(d)$ are calculated from $S_{22.7}$. The charge scaling q is given in the legend. Only distances with sufficient slowdown of $\zeta(d) \geq 2$ are shown. The analogous analysis with $F_{1,\mathrm{OH}}$ can be found in Fig. A.21 in the appendix.

weakly dependent on distance to the pore wall in comparison. Both fit parameters are superimposed by the density oscillations. The empirical assumption of $\lim_{T\to\infty}\zeta(d) = 1$ seems appropriate for greater distances to the pore wall. However, ζ is smaller and fewer data points are available. The characterization of the data for larger distances and mild supercooling has to be performed with caution.

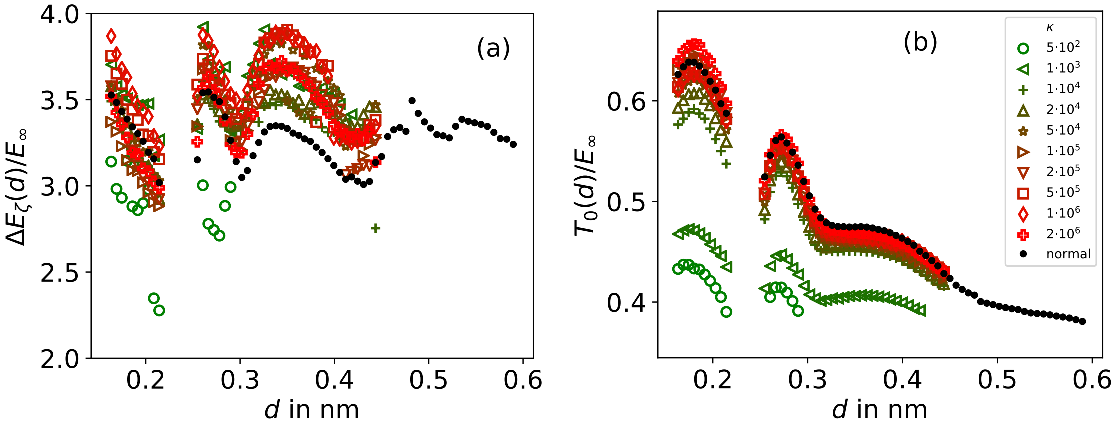

Figure 9.18.: The distance resolved fit parameters ΔE_ζ (a) and T_0 (b) in units of E_∞ from fits with Eq. (9.5) to the data for different pore rigidities in Sec. 9.4. The correlation times $\tau_\mathrm{e}(d)$ are calculated from $S_{22.7}$. The pore rigidity is given in the legend by the spring constant κ of the position restraints in units of kJ/mol·nm^{-2}. The black points are the result from averaging over two other simulations with $\kappa = 10^6$ with configurations differing from the colored data.

The simulations with different pore rigidities, Sec. 9.4, showed systematically varying slowdown ζ but consistent correlation lengths. In other words, the propagation of the wall effect by the liquid is independent of the pore properties. Within the variance of the data, the increased potential barrier $E_\zeta(d)$ is consistent among all pore rigidities and distances with sufficient slowdown, Fig. 9.18(a). The colored data is from identical pores, i.e., the same configurational snapshot and pinning of wall molecules, but different spring constants κ. Additionally, the averaged result of two different pores with $\kappa = 10^6$ is shown in black. The high variance of the data suggests that large ensemble averages over configurationally different pores would be required for sufficient accuracy of $\Delta E_\zeta(d)$. The reduced slowdown for softer confinement is also characterized by the temperature offset $T_0(d)$, which varies systematically with pore rigidity, Fig. 9.18(b).

One may propose that a qualitatively similar behavior underlies dynamics for strong dynamical heterogeneity in bulk. The slowdown of particles in contact with slow patches relative to the fastest fraction might simply depend on the rigidity of the slow patch, which greatly increases with dynamical heterogeneity and decreasing temperature.

9.5.2. Linearization of the slowdown

The assumption of a constant contribution ΔE_ζ to the activation energy by the matrix in Eq. (9.5) is only true in the low-temperature limit. This predicted temperature region, where $\ln\zeta \cdot T = \text{const.}$ is approximately valid, is not reached and cannot be confirmed. Furthermore, other empirical descriptions of the slowdown are possible. In particular, the contribution to the activation energy

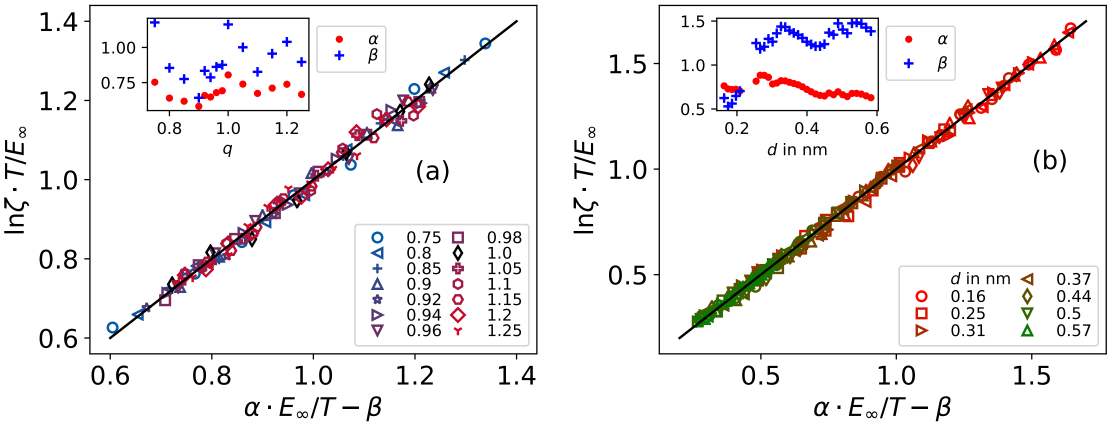

Figure 9.19.: The temperature dependent activation energy for the distance dependent relative slowdown $\zeta(d) = \tau_\mathrm{e}(d)/\tau_\mathrm{e,pc}$ with respect to the pore center for charge-scaled SPC/E in neutral confinement: (a) for the pore wall, $d \approx 0.28$ nm, and all charge-scaled variants and (b) for several distances d to the pore wall for the original SPC/E, given in the respective legends. Correlation times τ_e are from $S_{22.7}$ and the high temperature activation energy E_∞ is from the respective bulk liquids. The x-axis is rescaled to produce a master curve for a linear relation on reciprocal temperature. The parameters α and β, shown in the insets as function of charge scaling q and d, respectively, are the results of fits with Eq. (9.6) to the data. Only temperatures with $\tau_\mathrm{e,pc} \geq 1$ ps are shown.

could be a linear function of reciprocal temperature,

$$\ln\zeta \cdot \frac{T}{E_\infty} = \alpha\frac{E_\infty}{T} - \beta\,, \tag{9.6}$$

where α and β are constants. A master curve, presented in Fig. 9.19(a), is possible for all charge scalings q and temperatures with $\tau_\mathrm{e,pc} \geq 1$ ps. Evidently, $\ln\zeta \cdot T$ is far from the low-temperature limit of $3E_\infty$. Combining Eq. (9.6) with Eq. (8.2), assuming that $\tau_\mathrm{pc}(T)$ can be characterized this way, leads to the empirical description of $\tau_\mathrm{pw}(T)$ as

$$\tau_\mathrm{pw}(T) = \underbrace{\tau_\infty \cdot \exp\left[\frac{E_\mathrm{pc}(T)}{T}\right.}_{\tau_\mathrm{pc}(T)} \left. + \alpha\left(\frac{E_\infty}{T}\right)^2 - \beta\frac{E_\infty}{T}\right]\,, \tag{9.7}$$

with τ_∞ being the prefactor and E_pc the temperature dependent activation energy in the pore center, respectively. This master curve can also be created for larger distances to the matrix, see Fig. 9.19(b). The free fit parameters α and β are shown in the inset of Fig. 9.19. If $E_\mathrm{pc}(T)$ can be separated according to Eq. (8.3) into a temperature dependent contribution and E_∞, then $\beta \approx 1$ implies that this constant activation energy contribution is negated and $\tau_\mathrm{pw}(T)$ shows exceptionally strong temperature dependence. The additional term $\sim T^{-2}$ leads to increased fragility at the pore wall in contrast to the common finding of reduced fragility.[229,378] However, prediction of the fragility for either statement requires correct modeling that allows for extrapolating to longer time scales. Rather both, Eq. (9.5) and (9.7), characterize the available data satisfyingly in the supercooled regime which necessitates further tests for an ultimate decision.

9.5.3. Boltzmann factor energy landscape

The above attempts to find the difference in activation energy between pore center and pore wall employed dynamical quantities alone. But first and foremost, the matrix imposes a static PEL on the liquid that modulates the local density, as seen in Fig. 9.1(a). The latter can be interpreted as the result of Boltzmann factors weighting positions in the pore. Hence, the PEL may be partially reconstructed from the particle density. From it, preferred positions may be identified and the energy barrier, that has to be overcome to escape such positions, may be calculated.

The accessible volume of the liquid molecule fraction is covered with uniformly distributed spheres of radius $r_\mathrm{S} = 0.05\,\mathrm{nm}$. In particular, their positions are on evenly distributed radii and z-positions in cylindrical coordinates. Their distance is significantly smaller than r_S in order to cover the entire volume, leading to overlapping spherical volumes and over $2 \cdot 10^6$ spheres. For each sphere i the probability p_i of being occupied by oxygen atoms is calculated from the trajectories. This probability is associated with a potential energy ε_i. Next, local minima in the potential energy are identified by starting from each sphere and going to the closest neighboring sphere with larger probability p_i, i.e., following the steepest ascending path in probability or descending path in the potential energy, respectively. The thus obtained spheres j define the local energy minima ε_j. Their occupation probabilities are compared with those at distance $\delta r_{i,j}$, denoting the distance between the centers of spheres i and j. Their ratio of probabilities, the Boltzmann factor, gives the energy difference $\Delta\varepsilon_{i,j} = \varepsilon_i - \varepsilon_j$,

$$\frac{p_i}{p_j} = \exp\frac{-\Delta\varepsilon_{i,j}}{T}. \tag{9.8}$$

Averaging over all neighboring spheres at distance δr and all minima leads to the average local potential energy profile $\langle\Delta\varepsilon(\delta r)\rangle$.

However, the finite sample size leads to artifacts. The probability in bulk, and in the pore center of large pores, is expected to be homogeneous and the PEL flat when averaged over infinite times. In practice, p approximately follows a normal distribution with the average $\langle p\rangle$ depending on r_S and the standard deviation σ_p, which itself depends on r_S and the sample size, i.e., the number of frames in the trajectory. The consequences are artificial local minima and energy barriers with this method in the bulk and in the pore center that have no physical origin. Only at strong supercooling or small confinement sizes might the pore center be truly affected. Larger sphere radii r_S smooth out fluctuations in density while smaller radii lead to worse statistics and stronger artifacts. Therefore, r_S was varied and $\Delta\bar{\varepsilon}$, see further below, exhibits a maximum for $\approx 0.05\,\mathrm{nm}$ in the present study. Furthermore, only sites with $p_{\vec{r}} > \langle p\rangle + \sigma_\mathrm{p}$ were taken as starting points for the ascend into local maxima. The number of frames also varies among the simulations, with higher temperatures having less than half the number of frames as simulations at lower temperatures. This leads to a jump in the artificial energy barriers in the pore center for these less relevant temperatures.

Again, $\langle\Delta\varepsilon(\delta r)\rangle$ is studied spatially resolved to preserve information, shown in Fig. 9.20(a) for various radial positions within the confinement. The energy profile rises steeply within 0.1 nm and reaches a local maximum at distances $\delta r \approx 0.155\,\mathrm{nm}$. This corresponds roughly to half the next neighbor distance of $\approx 0.28\,\mathrm{nm}$ where the maximum would be expected if only the direct path between minima were considered. The height is strongly dependent on the radial position with the highest values found at the pore surface, consistent with the finding that the density modulations quickly tamper off towards the pore center. Beyond the maximum, the energy profile is modulated by a minimum and second maximum at around the next neighbor distance and between the first and second shell, respectively. The local minima are positioned relative to each other according to the local structure of the liquid. Furthermore, the energy profile differs for directions towards the pore center or the pore wall, with larger values towards the matrix, not shown.

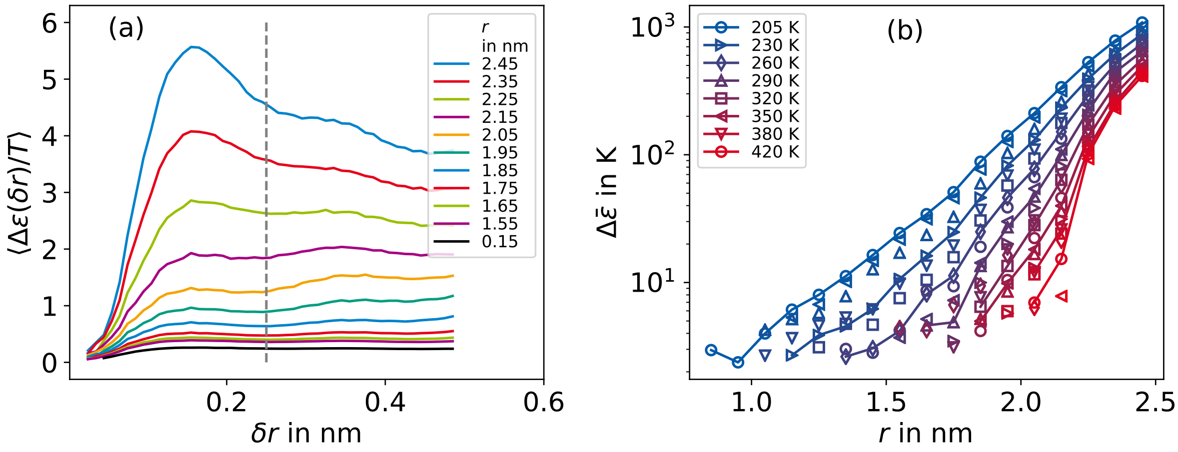

Figure 9.20.: (a) The average Boltzmann factors $\langle \Delta\varepsilon(\delta r)/T \rangle$ as function of distance δr to a local minimum of the PEL for SPC/E in a neutral pore at 205 K. The average is shown for various radial positions r in a neutral pore with radius $R = 2.5$ nm. The dashed line at 0.25 nm indicates the cutoff up to which the maximum value determines the energy barrier $\Delta\varepsilon$. The barrier $\Delta\varepsilon_{\text{pc}}$ in the pore center, shown in black, is subtracted to obtain $\Delta\bar{\varepsilon}$. (b) The barrier $\Delta\bar{\varepsilon}$ for different temperatures as a function of radial position in the pore. Only values $\Delta\bar{\varepsilon} > T/100$ are shown. Points of temperatures given in the legend are connected with lines while temperatures in between are not.

It is assumed here, that the rate of leaving a minimum relative to the rate of translation in bulk is given by this additional energy barrier caused by the matrix. Because the elementary translatory event in the supercooled regime is hopping on the next neighbor distance, the maximum for $\delta r < 0.25$ nm is taken as the energy barrier $\Delta\varepsilon$ that has to be overcome in order to escape the local minimum. Further translation depends on the barrier profile corresponding to the new position of the particle after hopping. Because the dynamical quantity of interest is the relative slowdown ζ, the difference $\Delta\bar{\varepsilon} = \Delta\varepsilon - \Delta\varepsilon_{\text{pc}}$, with $\Delta\varepsilon_{\text{pc}}$ being the value in the pore center, is used.

Figure 9.20(b) presents the energy barrier $\Delta\bar{\varepsilon}$ logarithmically as function of the radial position within the pore. Both, dependence on the radial position and temperature exist. With decreasing temperature, the barrier grows consistent with the growth of the configurational overlap plateau Q_∞. The Boltzmann factor already contains a temperature dependence. Thus, the multi-particle interactions in supercooled liquids or the reduced vibrations of the matrix apparently lead to an even stronger increase of the energy barriers. At high temperatures, the matrix affects only the first two layers. At these temperatures, dynamics are fast with $\tau < 1$ ps and the dynamic and static correlation lengths exhibit deviations from their low-temperature dependence or are not applicable. For temperatures in the supercooled regime, $T < 270$ K, an exponential decay of the energy barrier with decreasing radius is found, consistent with the double logarithmic decay of the correlation times in Fig. 9.4. In particular, the relation

$$\zeta(r) = \frac{\tau(r)}{\tau_{\text{pc}}} \sim \exp\left(-\frac{\Delta\bar{\varepsilon}}{T}\right) \tag{9.9}$$

may hold. Thus, Figure 9.21 presents the data for the lowest and highest charge-scaled and regular SPC/E in the supercooled regime. The barrier profiles suggest translation over the next neighbor distance and, thus, $\Delta\bar{\varepsilon}$ is compared to τ_e from S_{10}, which corresponds to hopping on this length scale. The relative slowdown ζ and Boltzmann factor share a linear relation, confirming Eq. (9.9). For high temperatures or small radii, only the slowdown increases and an offset in $\Delta\bar{\varepsilon}$ exists. It is possible, that the subtraction of the statistical contribution in the pore center is incorrect for larger radii. Simulations with increased sample size are necessary to reduce the influence of statistical inaccuracies.

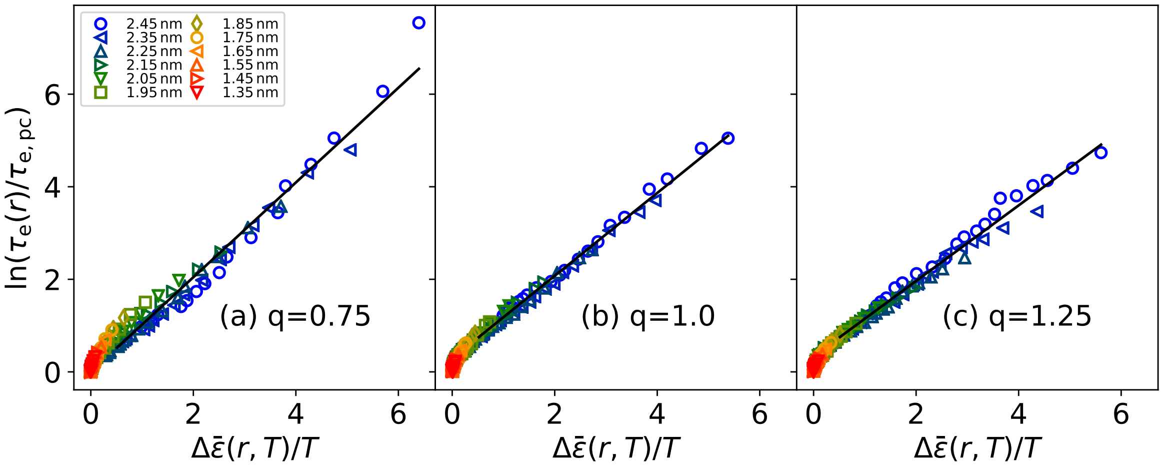

Figure 9.21.: The radially resolved relative slowdown $\tau_\mathrm{e}(r)/\tau_\mathrm{e,pc}$ versus the Boltzmann factor $\Delta\bar{\varepsilon}/T$ for escaping local minima in the PEL. Shown are the data for neutral pores of the lowest (a) and highest (c) charge-scaled variants and the original SPC/E (b). The correlation time is τ_e from S_{10}. The radial positions r are indicated in the legend. For each value of r, results for various sufficiently low temperatures are shown. Black solid lines are linear fits for values larger than 0.5 in both quantities.

The linear relation applies considerably worse to the lower charge scaling. This deviation occurs most prominently for charge-scaled variants $q \leq 0.9$ that enter the HDL-like regime upon supercooling. One reason might be that using the same cutoff parameters for all charge-scaled variants may not be appropriate. Alternatively, the competition of local structures explains the systematic dependence on charge scaling. For the higher charge-scaled variants, the liquid enters the LDL-like regime immediately upon supercooling while HDL-like systems require significant supercooling for the local structure to be fully developed. Reducing the data points to temperatures with stronger supercooling, e.g., $\tau > 20\,\mathrm{ps}$, gives good agreement between all charge-scaled variants. In other words, the linear relation holds once the local structure of the liquid is largely temperature independent or the competition between LDS and HDS is at least weak. The slope is not unity and decreases monotonically from 1 to 0.8 with increasing charge-scaling factor q, i.e., the energy barrier has a system dependent prefactor. Narrower confinements or stronger supercooling without recovery of bulk behavior could be investigated in the same way regarding the relative slowdown to bulk and extend the range of validity.

Still, the PEL imprinted onto the liquid by the matrix, a highly non-trivial cooperative effect propagated by the liquid, affects the particle density distribution and translational dynamics in a way that is consistent with the application of Boltzmann statistics. For the small molecular glass former of charge-scaled water molecules, either property can be used to predict the other.

9.6. Translational and rotational decoupling

As stated in the beginning of this chapter, Sec. 9.3, dynamics were investigated using the ISF and a short length scale on the order of the next neighbor distance. In some cases, e.g., atomistic liquids, only translational properties can be studied. However, for molecular liquids it may be worthwhile to be aware of potential differences between translational and rotational dynamics. Figure 9.22(a) presents the dynamical profiles $\tau_\mathrm{e}(d)$ of several translational and rotational correlation functions for the original SPC/E water model and two temperatures. Calculated were the ISF for two wavenumbers, $S_{22.7}$ and S_{10}, and the rotational correlation functions $F_{\ell,\vec{v}}$ for rank $\ell = 1$ and $\ell = 2$ with the OH bond vector and the dipole moment $\vec{\mu}$. Only $\ell = 1$ is shown for the latter. The bulk-like behavior far from the wall demonstrates the following ordering of the correlation time: $S_{22.7} < F_{2,\mathrm{OH}} < S_{10}, F_{1,\mathrm{OH}}, F_{1,\vec{\mu}}$. While all of them exhibit a slowdown towards the pore wall, this order is not preserved towards the wall. In particular, translational correlation times increase more upon approaching the wall with $S_{22.7}$ becoming as slow as $F_{2,\mathrm{OH}}$ for the higher temperature and even slower for the lowest temperature. Furthermore, among rotational correlation functions, the slowdown is stronger for $F_{1,\vec{\mu}}$ than for $F_{1,\mathrm{OH}}$. In previous studies, an enhanced occurrence of rotations around the c_2-symmetry axis of water, which coincides with its dipole moment, was found.[50] Hence, the mobility of the OH bond vector is higher at the pore wall than that of the dipole moment.

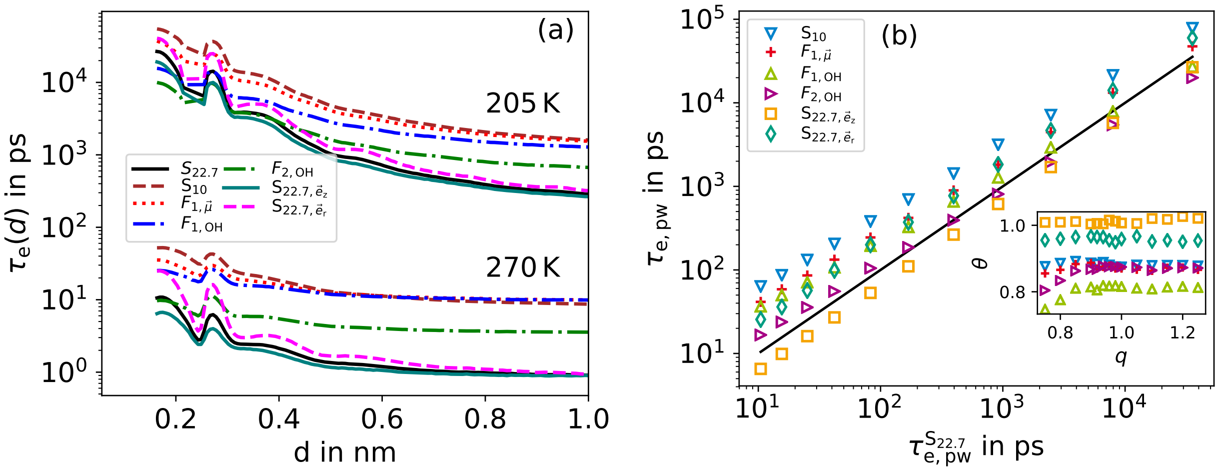

Figure 9.22.: (a) Dynamical profile $\tau_\mathrm{e}(d)$ in SPC/E neutral pores for two temperatures. The correlation times are from different correlation functions given in the legend. (b) A double logarithmic plot of the correlation time $\tau_\mathrm{e,pw}$ at the position of the second peak in Fig. 9.1(a). The result for different correlation functions in (a) are shown as function of $\tau_\mathrm{e,pw}$ from $S_{22.7}$. Only temperatures with $\tau_\mathrm{e,pc} \geq 1$ ps are shown. The inset shows the exponent θ of fits with power laws to the data for all charge-scaled variants q.

The double logarithmic representation of correlation times at the pore wall as a function of those for $S_{22.7}$ presents power laws, see Fig. 9.22(b). In this case, the interpolation of the actual data at the position of the second density maximum was used instead of an interpolation by fits with Eq. (9.1). The exponent θ of the power laws is below unity for most correlation functions and ranges between 0.82 and 0.92, see the inset of Fig. 9.22(b). Rotational and translational dynamics decouple at the pore surface. Hence, several rotational correlation times cross translation and become faster than short-range translation within the investigated temperature regime. Note, that S_{10} is not expected to follow this trend indefinitely, as it cannot become faster than $S_{22.7}$. The different temperature dependence implies differences in the increased energy barriers at the pore wall. The part of the PEL imposed by the neutral confinement responsible for reorientation may be weaker than that for translation. This is confirmed by Fig. A.21 in the appendix, showing the respective results of $\Delta E_{\zeta}(d)$ from Fig. 9.17 for $F_{1,\mathrm{OH}}$.

Lastly, a so far overlooked detail of measuring the translational dynamics with the ISF will be discussed. As calculated with Eq. (5.20), the ISF is a powder average, i.e., averages over all possible orientations of the pore with respect to the scattering vector $\vec{k}$. However, translation within the pores is anisotropic. In particular, particles at the surface of the cylindrical confinement have geometrically less than half the usual volume available for translation. Hence, Figures 9.22(a) and (b) include the decomposition of the ISF onto the unit vectors $\vec{e}_\mathrm{z}$ and $\vec{e}_\mathrm{r}$ in cylindrical coordinates, with the pore center as the origin. Specifically, $\vec{k}$ is parallel to $\vec{e}_\mathrm{r}$ or $\vec{e}_\mathrm{z}$ at the position of the particle at the time origin of the correlation function. For translation parallel to the pore surface, along $\vec{e}_\mathrm{z}$ and $\vec{e}_\phi$, the movement is not geometrically restricted as it is for radial motion. Thus, $\tau_{\mathrm{e,pw}}$ is shorter for the former than for the latter and the powder average. Still, they share approximately the same temperature dependence, i.e., the exponent from fitting a power law is very close to unity. Correlation times for surface-parallel motion may also eventually become longer than those for several rotational correlation functions. The overall slowdown towards the pore wall is however reduced. Future studies could investigate the dynamic correlation length for rotational and surface parallel translational motion.

9.7. Summary

In this chapter, the effects of cylindrical confinement on a liquid were studied with variation of one force field parameter, the strength of the Coulomb interaction, and under conditions that retained bulk-like structure. The latter was achieved by the use of so called neutral pores, the confinement consisting of the same molecules strongly restrained in their mobility. Furthermore, confinement properties like the geometry and rigidity were varied. The charge scaling allows for the study of confinement effects under variation of interaction strength and relevant energy scales. If the findings for TIP4P/2005 and its LLPT dependence on charge scaling in Ch. 7 and 8 apply also qualitatively to SPC/E, then charge scaling also allows for discerning discrepancies or commonalities between water-like liquids entering the HDL-like or LDL-like region of the phase diagram. At least qualitatively, a difference seems to occur between charge scaling with $q < 0.9$ or with $q \geq 0.9$ but neither the LLPT nor this threshold are confirmed.

Previous studies showed negligible effects of neutral confinement on the structure, density and tetrahedral order parameter, of water.[48,379] Consistently, the radially resolved density of oxygen atoms is only weakly modulated by the confinement for all charge-scaled systems. However, radially resolved properties average over the rough pore surface. Distance resolved spatial analysis proved to include more detail at the liquid-matrix interface. The interaction leads to more and less preferable positions relative to the pore surface corresponding to the local structure in bulk. In particular, the first two peaks in the distance resolved density of oxygen atoms are the hydrogen bond acceptor and donator distances, respectively. All charge-scaled variants as well as a similar study on the BKS model of silica share this feature. Beyond that, the charge-scaled variants differ structurally in that the third peak disappears for HDL-like systems.

As in previous studies,[48,323,380] correlation functions probing dynamics were found to be severely stretched and more long-lived than their counterparts in bulk systems but showed no sign of separable terminal decays, i.e., dynamically distinguishable species or bimodality of dynamics. Dynamics, spatially resolved by the distance to the pore wall and measured with the ISF for short length scales, slows down by 2-3 orders of magnitude towards the pore wall in the investigated temperature range. The configurational overlap, the similarity of liquid oxygen positions in time, increases with decreasing distance to the wall and temperature. The amplitude of the short-time MSD at the wall is about half of that in the pore center. These phenomena are the result of the static PEL imposed by the wall onto the liquid, which is not the same for all charge-scaled systems but similarly influences all properties. For a molecule in contact with the pore wall, a part of its local potential is static, caused by the position restrained wall molecules. In contrast to bulk, spatial broadening of this potential in time, caused by vibrational motion, is greatly suppressed and the volume occupied by wall atoms is inaccessible at all times. Hence, energy barriers are higher and more stable in time making translational or rotational relaxation events less likely. The local cage becomes more stable and is less broadened because of the lacking vibrational displacements of some of the neighboring molecules. Hence, the short-time MSD is reduced in amplitude. Models of the glass transition, e.g., the facilitation model, which expects relaxation of neighboring particles, or the shoving model, which connects structural relaxation and vibrational motion, predict qualitatively the influence of the confinement on the liquid dynamics. The reverse is observed for unfavorable positions. Energy barriers are reduced making relaxation events more and the occupation less likely. For larger distances to the wall, these effects weaken and the short ranged local structure of liquids leads to averaged properties. The confinement effect in distance resolved analysis is characterized by oscillations, consistent with the density profiles, superimposed on structurally averaged simpler decays, consistent with findings in previous studies.[48,323,376,379,380] The latter are, for example, double exponential for correlation times $\tau(d)$, compressed exponential for the configurational overlap $Q_\infty(d)$ and exponential for the short-time MSD $1/u^2(d)$. These are representative for the collective response of the liquid to the confinement and were quantified by their respective correlation lengths ξ.

Because the charge-scaled variants span a wide temperature range, the results were compared at isokinetic points, specifically the correlation time in the pore center. The dynamic correlation length $\xi_{\text{dyn.}}$ behaved qualitatively and quantitatively indistinguishable for all charge-scaled variants. The confinement effect on dynamics appears to be strongly connected to the temperature dependence of the dynamics in the pore center and, for large enough pores, in bulk. Interestingly, results for another tetrahedral network former, the BKS model of silica, show a more significant dependence on charge scaling.[392] There, $\xi_{\text{dyn.}}$ decreased with increasing charge despite the higher expected cooperativity of tetrahedral liquids and longer range of Coulomb interactions. It may be, that the independent motion of oxygen and silicon atoms compared to the rigid H_2O molecules causes qualitative differences between water- and silica-like systems. Alternatively, this behavior is expected for more severe charge scaling, as q for the BKS model was as low as 0.65 and the liquids will turn into soft-sphere systems. The static correlation length $\xi_{\text{sta.}}$ is independent of the charge-scaling factor q at $q \geq 0.9$ but increases upon reduction at lower values of q. The same is found for the stretching parameter β, indicating a narrower decay of the confinement effect. The decay tends towards a Gaussian shape of the wall effect with $\beta = 2$. For silica, the values were generally larger but were not found to increase further with stronger supercooling.[392] All systems might have a constant shape in the deeply supercooled regime. A stronger dependence on charge scaling was found for the vibrational correlation length $\xi_{\text{vib.}}$. Its absolute values and temperature dependence increased significantly with increasing partial charges. Hence, the dynamical profiles $\tau(d)$ and $1/u^2(d)$ are not reconcilable within several models of the glass transition. The effect of confinement on the liquid does not follow bulk properties entirely.

Several models of the glass transition, e.g., the ECNLE and RFOT theory,[91,107,108] employ length scales to predict the liquid behavior in the supercooled regime. Here, the static correlation length $\xi_{\text{sta.}}$ was used within the prediction of the RFOT theory and it was found that the model works with universal parameters for all structurally comparable systems, those with charge scaling $q \geq 0.9$ in the LDL-like region of the phase diagram. However, the HDL-like systems with reduced charges do not comply and the scattering and limited temperature range of the data do not allow further conclusions.

The relative slowdown ζ at the matrix with respect to the pore center, and roughly to bulk, was found to approximately increase with an Arrhenius law for sufficient supercooling. Hence, a temperature independent activation energy ΔE_ζ, in addition to the activation energy in bulk $E(T)$, and the onset temperature T_0 suffice to characterize the dynamics at the pore wall. The finding of less fragile behavior at interfaces compared to the bulk can therefore be rationalized by the comparably lower temperature dependence of the total activation energy. Still, for significant supercooling the bulk behavior will dominate. ΔE_ζ was found to be about three times or equal to E_∞, for τ from the ISF and F_1 respectively. Hence, the high-temperature regime is also relevant for the interaction within neutral pores. The cooperative contribution to the activation energy $E_\mathrm{c}(T)$ reaches about 2.5 times E_∞ at T_g, see Ch. 8. In comparison, $\Delta E_\zeta \approx 3E_\infty$ is of significant size in the entire dynamically accessible regime. Unfortunately, these values are different for a comparable study of silica.[392] Furthermore, the values for the first layer may depend on the matrix when non-neutral confinements are used. Still, changing properties of neutral confinements mostly influenced the onset temperature T_0 but not the activation energy. When compared to the short-time MSD u^2, a similar indicator for the local potential, the results do not agree. The potential depth is changed by a factor of 1.9 with weak dependence on temperature and charge. With this, however, the relative reduction of u^2 does not at all follow an Arrhenius law. Furthermore, the limited temperature range does allow for other equally good functional forms. ΔE_ζ is not yet perfectly constant in the studied temperature regime and may as well be characterized by a linear dependence on reciprocal temperature. This leads to a temperature dependence of τ_pw containing a term $\sim \exp[(a/T)^2]$ and leading to strongly increasing differences in mobility between pore center and wall upon supercooling. A physical model explaining this is missing and it does not allow for the prediction of spatially resolved dynamics without determination of the parameters. It remains to be tested which, if any, of the two is applicable in the entire supercooled regime.

Alternatively, the static density fluctuations within the confinement were used to reconstruct the PEL assuming Boltzmann statistics. Energy minima and the energy barrier to overcome the average neighborhood using Boltzmann factors were identified. This energy barrier was also temperature dependent and characterizes the difference to the pore center, where a homogeneously flat PEL is expected. It correlates well with ΔE_ζ implying that both static and dynamical properties are affected by the matrix in a similar way. More precisely, the mobility gradients within the confinement can be rationalized entirely with Boltzmann statistic.

In the context of polyamorphism, investigated for charge-scaled TIP4P/2005 in Ch. 7, one may expect similar behavior for the charge-scaled SPC/E variants. Because systems with charge scaling $q \geq 0.9$ exhibit a density maximum they could cross their respective Widom lines if an LLPT exists.[117] But, even if no LLPT exists within these systems, the competition of LDS and HDS is apparent and causes phenomena similar to those of the charge-scaled TIP4P/2005 systems with a true LLPT. Even more so, the charge-scaled BKS models of silica show a pronounced dynamical transition within the accessible temperature regime. However, neither system shows indications of the polyamorphism in the temperature dependence of correlation lengths or slowdown. For a fragile-to-strong transition (FST), the low temperature Arrhenius regime should be associated with a constant correlation length, if the activation energy scales with any ξ as proposed. The extrapolation of $\xi_\mathrm{dyn.}$ and $\xi_\mathrm{sta.}$ to T_g would then be wrong. Unfortunately, the simulated temperatures of the charge-scaled SPC/E variants are not close to their respective FST, if the prediction in Ch. 8 holds. Still, quantitative differences between the HDL-like and LDL-like liquids could be found, i.e., larger $\xi_\mathrm{sta.}$ and other parameters for the description of $\tau(T)$ within the RFOT theory for lower partial charges.

Finally, many follow-up investigations of liquids in neutral confinement can be performed in the future. The reliability and meaning of translational correlation functions at the pore surface could be investigated. More specifically, the decoupling of rotational and translational motion at the pore wall could have implications for the Stokes-Einstein breakdown of dynamics in bulk. The choice of the correlation function influences the value of the additional activation energy $\Delta E_\zeta / E_\infty$ found for dynamics at the pore wall. This Arrhenius behavior Eq. (9.5) and its alternative Eq. (9.7) should be tested for a wider range of systems and stronger supercooling to determine which if either is true at all. With longer correlation lengths, the spatially resolved $\Delta E_\zeta(d)$ and $T_0(d)$ could be studied for larger distances to the pore wall. In the present study, finding a constant or distance dependent $\Delta E_\zeta(d)$ depends on whether or not the data is reduced to sufficient slowdown or not. If $\Delta E_\zeta(d)$ is constant and $T_0(d)$ is dependent on the rigidity of the wall, and in extension on the dynamical gradient $\frac{\partial \tau(d,T)}{\partial d}$, a self-consistent set of equations characterizing $\tau(d,T)$ could be constructed. Of course, this could only quantify average dynamics ignoring the oscillations at short distances to the pore wall. Alternatively, predicting the temperature dependence of the correlation lengths and slowdown at the interface would characterize dynamics as well.

10. Cross correlations in asymmetric binary mixtures

Proceeding from idealized static pores, more natural systems are studied and matrix and solvent dynamics in the mixture of PMMA and picoline are investigated. Binary asymmetric mixtures, i.e., mixtures with largely different glass transition temperatures for both components, exhibit a slow matrix formed by the solute and a fast solvent. In general, molecules are slowed down at immobile interfaces (with exceptions) and a mobility gradient appears. For mixtures however, broadband spectroscopy, e.g., BDS, finds two processes, separated by several orders of magnitude, that can be attributed to the solvent. Hence, an interpretation so far is the existence of a slow solvent fraction in contact with the matrix and a fast bulk-like fraction. The findings presented in this chapter challenge this interpretation for a wide variety of systems, from polymer-plasticizer mixtures to hydrated proteins.

Results for coherent and incoherent measurements are compared and the slow solvent process is identified as cross correlations that decay on the time scale of the matrix. Consistent results are found for oligomerized styrene in benzene and poly-ϵ-lysine in water. A mechanism of replacements of solvent molecules in locally preferred orientations caused by the energy landscape imprinted by the matrix is discussed. Finally, the heterogeneity of dynamics is investigated. Solvent mobility is broadly distributed but not bimodal.

10.1. Motivation

Dynamically asymmetric binary mixtures are characterized by their large difference in T_g of the neat systems of the two components. The low-T_g component is typically a small molecule and is referred to as the solvent while the high-T_g component is the solute and typically a macromolecule.[307,393–395] Examples include polymer-plasticizer mixtures or hydrated proteins.[51,52] Their complex behavior and highly heterogeneous dynamics have been the ongoing subject of studies for decades.[51,309,310] The high customizability of the mixtures, e.g., by variation of solute and solvent and the concentration, makes these types of systems important in technical applications and their relevancy in biological systems leads to them frequently occurring in studies.

A consequence of the very different T_g is the observation of two structural relaxation processes in the mixture that are separated in time by several orders of magnitude. The fast process is then attributed to the solvent while the slow process is thought to be caused by the solute. A general effect is that the dynamics of the solute and solvent are accelerated and slowed down, respectively, compared to the bulk. An asymmetric effect on the distribution of relaxation times is observed. While the shape of the distribution, or the measured susceptibility, remains unchanged for the solute, the distribution of the solvent dynamics is strongly broadened indicating increased heterogeneity experienced by the smaller molecules.[309,396] In particular, the two relaxation processes each have their own glass transition.[307,394,395] Above T_g of the solute process the solvent molecules experience a PEL caused by a slowly varying solute. This PEL is static below T_g and the heterogeneity of the solvent process is even more pronounced. Because of these similarities with other nanoscopic confinements, the macromolecule will be referred to as matrix in this work when general conclusions are drawn. These properties of asymmetric mixtures are rather general which can be concluded from the fact that such observations have also been made for solvent molecules mixed with polymers,[51,56] oligomers[394,395] and non-polymeric macromolecules,[54,55,57,397] aqueous peptide solutions[53,58] and hydrated proteins.[52] Thus, these phenomena are not limited to specific molecular sizes, structures, concentrations of the mixture, or particular solvent-solute interactions.

Given the broad time and temperature range covered by asymmetric binary mixtures the most commonly used experimental methods are broadband dielectric spectroscopy (BDS), nuclear magnetic resonance (NMR) spectroscopy, or depolarized dynamic light scattering (DDLS), which are usually employed to measure molecular reorientation. These methods can be used to selectively analyze one of the components, depending on the system. BDS can be applied to mixtures of polar and nonpolar components, NMR allows isotopic labeling of the molecules, and DDLS is sensitive to the anisotropy of the molecular polarizability tensor. However, ongoing research on these mixtures and the application of these methods has led to controversial results.

A BDS study of the mixture of the polar solvent 2-methyl tetrahydrofuran (MTHF) and the nonpolar solute polystyrene (PS) revealed contributions from MTHF to the fast and slow processes despite them being separated by nine orders of magnitude at the high-temperature T_g.[56] This contribution to the relaxation strength observed with BDS grew upon cooling and contributed up to 10% of the total relaxation strength. The data was interpreted as a fraction of solvent molecules being severely restrained by the matrix and that the distribution of solvent dynamics is bimodal. Similar slow solvent dynamics were also found for other polymer solutions.[398,399] However, solvent-selective NMR experiments could not confirm this fraction of slow MTHF molecules. From ^{2}H NMR spectra the fraction of molecules relaxing faster than the inverse coupling constant was determined as a function of temperature.[400] The resulting fraction is much lower than that calculated from BDS measurements. However, agreement can be achieved if the slow solvent process in BDS is ignored and the fraction of molecules slower than the inverse coupling constant of ^{2}H NMR is calculated using the fast structural relaxation process alone. Similar discrepancies have been found for mixtures with non-polymeric solute molecules,[57] aqueous peptide solutions,[53,58,59] and even hydrated proteins.[52] In particular, the slow water process in aqueous poly-ϵ-lysine and its absence in ^{1}H and ^{2}H NMR were extensively discussed.[53,58,59]

A hint to the origin of the discrepancies between observations by different experimental methods is their sensitivity to exchange of identical particles. BDS and DDLS are insensitive to instantaneous exchange of molecules with respect to their position and orientation. The correlation function does not decay under such an operation because both methods make coherent measurements and the cross correlation of the exchanged particles compensates for the loss of self correlation. Similar insensitivity of fluorescence Stokes shift (FSS) experiments to exchange of water molecules in the protein hydration shell has been discussed by Nilsson et al.[401] The same is not true for ^{1}H and ^{2}H NMR. In particular ^{2}H NMR performs incoherent measurements and correlation is lost upon particle exchange. Cross correlations are nonexistent in this case. Hence, a contribution to relaxation processes that is visible in coherent measurements but invisible in incoherent methods is likely due to cross correlations. Proper quantification of molecular dynamics requires disentanglement of cross and self correlations, otherwise false or conflicting interpretations could be made. Given the amount of research being performed with these experimental methods, a better understanding would have significant impact. MD simulations can support the investigation of cross correlations quite easily. The direct calculation of coherent and incoherent correlation functions makes the determination of the origin of slow solvent processes and the fraction of slow solvent molecules straightforward.

Even the origin of possible cross correlations can be investigated. Also, rotational and translational dynamics can be measured and correlations can be spatially resolved.

In this chapter, MD simulations of a mixture of picoline, specifically 2-methylpyridine, as solvent and poly-methylmethacrylate (PMMA), see Sec.4.4, are analyzed. They complement experimental measurements with BDS and DDLS on the same system. Results from simulations and experiments were discussed collectively in the collaboration with Böhmer et al.[400] Here, the focus is on the simulations which are analyzed in more detail. First, incoherent and coherent rotational correlation functions as well as incoherent and coherent scattering are discussed in the context of slow solvent processes. Then, simultaneous cross correlations of location and orientation of solvent molecules are quantified. Contributions to cross correlations are discussed, in particular with respect to the measured property of the molecule and the correlation function used. Then, the broadened distribution of correlation times as a function of local concentration and time scales of ergodicity are determined. The final relaxation map shows the enormous complexity that asymmetric binary mixtures can exhibit. Finally, preliminary results for cross correlations in other mixtures are discussed.

10.2. Coherent vs incoherent measurements

First, coherent and incoherent correlation functions of the binary mixture of PMMA and picoline, details in Sec. 4.4, are investigated. More specifically, the rotational correlation function $F_{1,\vec{\mu}}(t)$, Eq. (5.28), of the dipole moment $\vec{\mu}$ of picoline molecules and PMMA segments with the Legendre polynomial of rank 1, see Sec. 5.2.3, is studied. In particular, the scalar product $\vec{\mu}_i \cdot \vec{\mu}_j$ is taken to account for the strength of the dipole moments. Figure 10.1(a) shows the coherent result for the dipole moment of picoline. Note, that the dipole moments of both components can be analyzed selectively. The vibrational decay, which is not resolved, is followed by a fast decay of most of the correlation and a stretched slow decay at longer times. The amplitude of the latter grows with decreasing temperature. Figure 10.1(d) displays a Fourier transform of a fit with a sum of two KWW functions, Eq. (2.5). The simulations qualitatively reproduce the experimental results found for light scattering, a fast and slow process in the susceptibility.[400] To study the dynamics as experienced by individual molecules, Fig. 10.1(b) shows the self part of the correlation function for picoline. The same fast process is found suggesting that this is the α-relaxation for the majority of the picoline. However, it is followed by a long time tail for lower temperatures. In depth investigations in the appendix, App. A.5.1, reveal a more complex relaxation including anisotropic reorientation. In the context of this chapter, this anisotropic reorientation is neither problematic nor of interest. The inset also shows the Fourier transform of the self part. While the peaks at higher frequencies coincide for the coherent and incoherent measurement, the intensity at lower frequencies, or longer times, is underestimated in the self part which shows a ω^1 power law at low frequencies. The incoherent susceptibility is lower than the coherent one for all frequencies indicating significant contributions from cross correlations. The cross correlations are determined by subtraction, Eq. (5.28) and (5.28), and shown in Fig. 10.1(c). Again, two decays are found: a fast decay on the time scale of the α-relaxation followed by a plateau and a decay at longer times. This reveals that the coherent correlation function contains a stretched exponential decay at long times which is not simply the long-time tail of a broadly stretched α-process but a separate relaxation of a different kind.

Asymmetric binary mixtures are, according to the MCT results, likely to show a slow process in coherent scattering, Sec. 5.2.1, of the center of mass of the fast species, analogous to the above result for rotation.[86,402–404] The susceptibility of coherent translational motion becomes bimodal for the smaller particles, i.e., the correlation function decays in two steps. Figure 10.2 presents the results for 270 K for various wavenumbers. The decays in both, ISF and CSF, shift to longer times

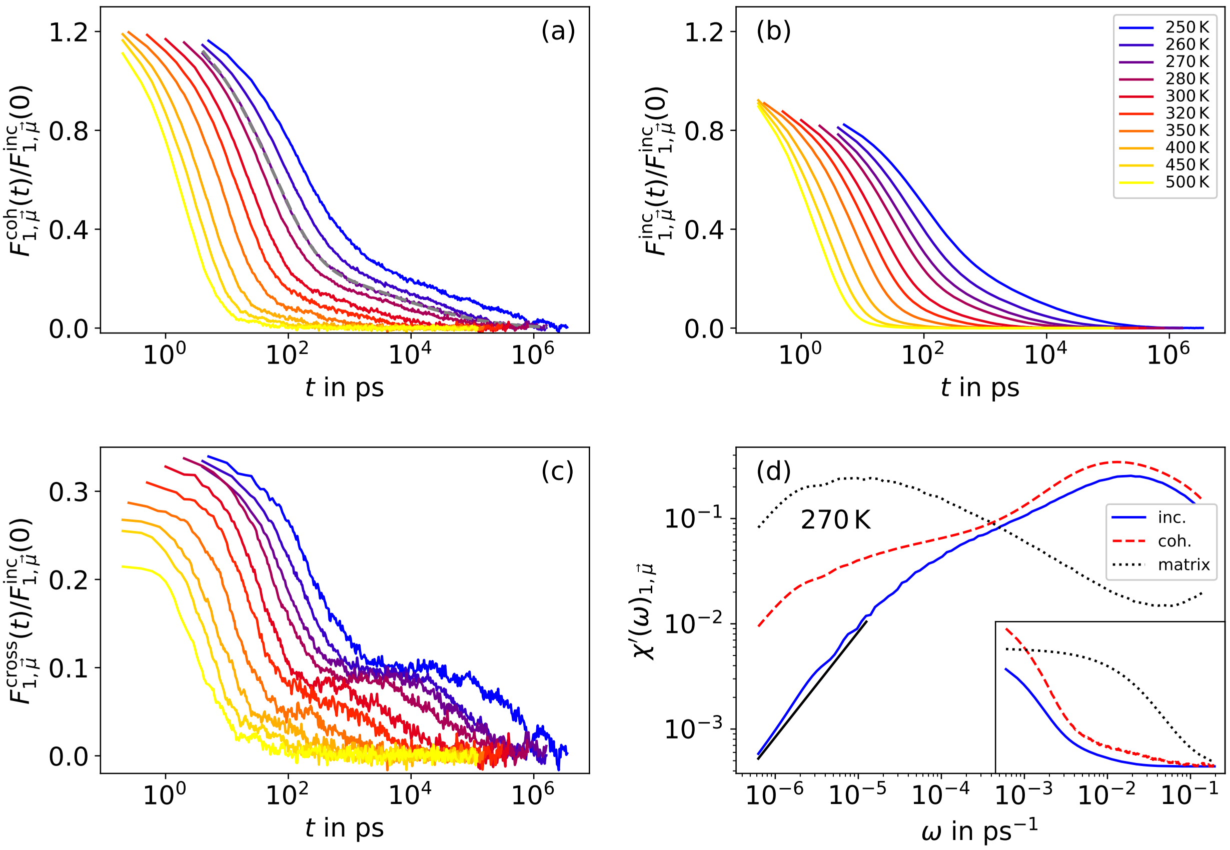

Figure 10.1.: Correlation functions F_1 of the dipole moment of picoline at various temperatures: (a) coherent, (b) incoherent and (c) cross contributions. The temperatures are the same in all three panels. Panel (d) presents the imaginary part of the susceptibility at 270 K, see Eq. (5.31). To reduce the noise of the coherent correlation function the data was fitted with a sum of two KWW functions, shown in (a) as dashed gray line, and then Fourier transformed. The black dotted line is $F^{\mathrm{inc}}_{1,\vec{\mu}}$ for polymer segments and the black solid line is a guide to the eye with slope $\sim \omega^1$. The inset shows the respective correlation functions.

with increasing length scale. The CSF exhibits two decays while only one decay is found for the ISF. The influence of anistropic reorientation found in $F^{\mathrm{inc}}_{1,\vec{\mu}}$ is reduced. The slow decay is at longer times than that of the incoherent measurement. No slow species is found in the incoherent studies of translation while the coherent measurement agrees with the theoretical expectation. The finding of cross contributions in both orientational and density-density correlations on the time scale of the segmental relaxation of the polymer suggests a relation of position and orientation. This phenomenon is investigated in detail in the following section.

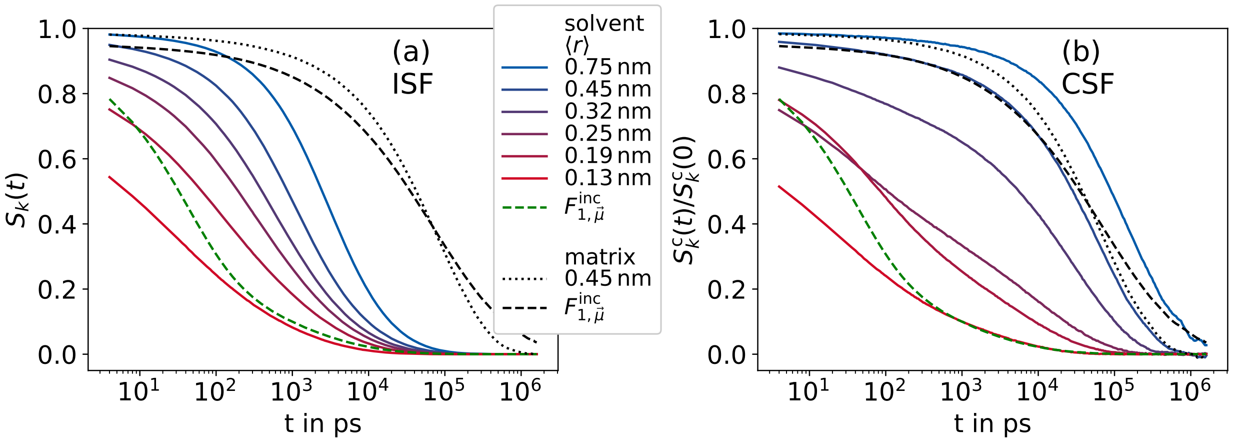

Figure 10.2.: Normalized scattering functions for the PMMA+picoline mixture at 270 K for various wavenumbers k: (a) ISF and (b) CSF. The scattering centers are the center of mass of either the picoline molecules or of the PMMA segments. The length scales in the legend are analytical average displacements $\langle r\rangle = 4/\sqrt{\pi}/k$ at τ_e for Gaussian propagation. The black and green dashed lines are normalized $F^{\mathrm{inc}}_{1,\vec{\mu}}$ for the dipole moment of picoline and PMMA segments, respectively.

10.3. Mechanism - fast replacement in a slowly relaxing energy landscape

The fast α-process in rotational correlation functions and the ISF indicate mutual replacement of solvent molecules on time scales faster than the segmental relaxation. The similarity of configurations in time can be probed by the configuration overlap correlation function (OCF), see Sec. 5.2.3. The distinct overlap Q_{dist}, i.e., the fraction of centers of mass of picoline molecules that are at time t within a cutoff radius of $r_\mathrm{c} = 0.2\,\mathrm{nm}$ of each other at time $t = 0$, is shown in Fig. 10.3(a).

The distinct overlap is by definition zero at the time origin and a finite value at infinite times, given by the density and cutoff radius r_c. For intermediate times, when translational motion sets in, the overlap increases. Contrary to the common finding in bulk, the distinct overlap in dynamically asymmetric mixtures overshoots the plateau value and decays afterwards. This enhanced distinct overlap exists at longer times than the self overlap, see the inset of Fig. 10.3(a). Thus, the matrix imprints a slowly changing energy landscape on the solvent and energetically preferred locations exist for some time. This is qualitatively different from the results for neutral pores in Ch. 9. There, the matrix is static for all times and the enhanced overlap does not decay.

Distinct replacements of particles are cross terms themselves and the rotational correlation function of the respective dipole moments can be calculated specifically for such distinct pairs. The correlation between the particle defining the sphere at $t = 0$ and the particle occupying this sphere at a later time is determined according to

$$F^{\mathrm{dist}}_{\ell,\vec{v}}(t) = \left\langle \frac{1}{N} \sum_{\substack{i,j \\ i\neq j}} n_{ij}(t) \cdot P_\ell(\vec{u}_i(0)\cdot\vec{u}_j(t)) \right\rangle \tag{10.1}$$

$$n_{ij}(t) = \begin{cases} 1 & |\vec{r}_i(0) - \vec{r}_j(t)| \leq r_\mathrm{c} \text{ and } i \neq j \\ 0 & \text{else,} \end{cases} \tag{10.2}$$

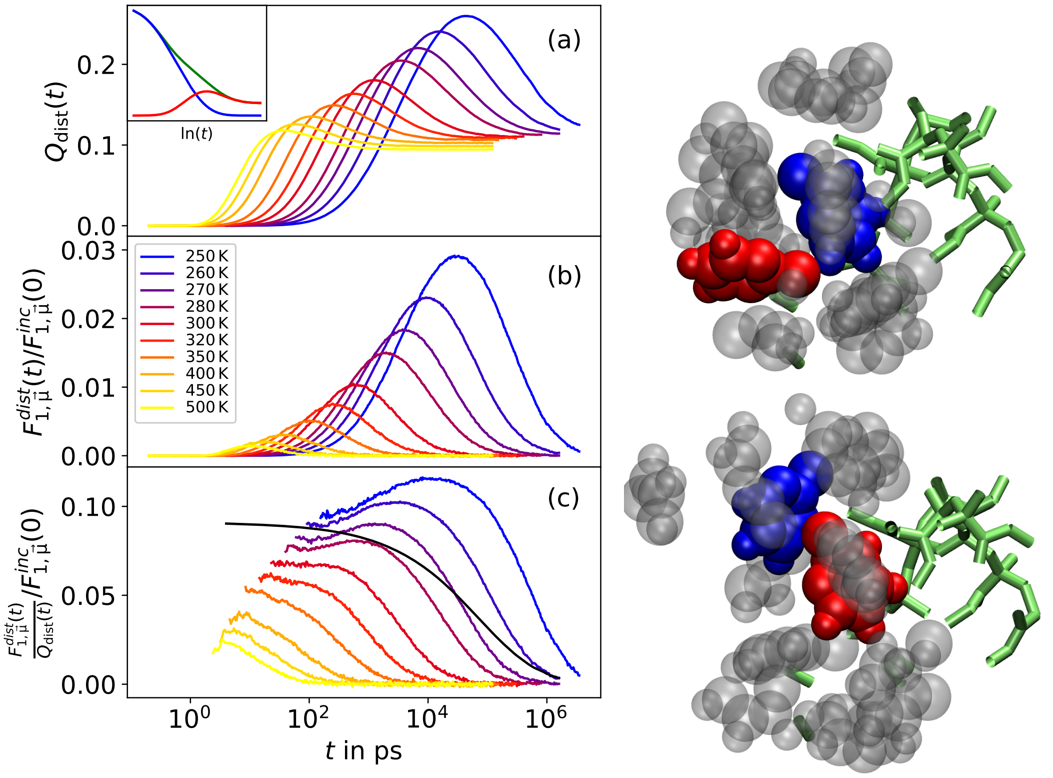

Figure 10.3.: Analysis of preferred locations and orientations of solvent molecules in the PMMA+picoline mixture. (a) Distinct part of the configuration overlap correlation function (OCF) Q_{dist} for various temperatures. A sphere of radius $r = 0.2$ nm was used to mark the initial center of mass positions of the picoline molecules. The inset shows the total OCF (green), self part (blue), and distinct part (red) for 270 K. (b) The total rotational cross correlation for distinct particle displacements $F^{\mathrm{dist}}_{1,\vec{\mu}}$, Eq. (10.1), weighted by the strength of the dipole moments. The data in (b) divided by the occurrence of distinct replacement in (a) is shown in (c) for data points $Q_{\mathrm{dist}} > 0.01$. This quantifies the average correlation per distinct replacement. The black solid line is $F^{\mathrm{inc}}_{1,\vec{\mu}}$ for PMMA segments, scaled for clarity. The temperatures are the same in all panels.
On the right side are two snapshots at 250 K and separated by 670 ps. Atoms of solvent molecules are shown as spheres and the matrix is represented by green tubes. The blue molecule is replaced by the red molecule, assuming a similar orientation, at later times (bottom). The displacements of the matrix are insignificant on this time scale.

Here, P_ℓ is the Legendre polynomial of rank ℓ, $\vec{u}_i$ are unit vectors $\vec{u}_i = \frac{\vec{v}_i}{|\vec{v}_i|}$, N is the number of particles, and $\vec{r}_i$ denotes their positions. The total amount of cross correlations by distinct replacement is shown in Fig. 10.3(b). It is zero at short times, when no replacements have happened, and long times, when correlation is lost. At intermediate times, this specific cross correlation exhibits a maximum. This is the **most important result** regarding the origin of long-lived cross correlations in this mixture. Not only do energetically preferred locations exist, but there are also preferred orientations at these locations. Note, that cross correlations from distinct replacement are only a fraction of all cross correlations. They may be much lower or even higher than the full cross correlations depending on the correlation with all next neighbor shells, i.e., depending on the Kirkwood factor g_K.[405]

By dividing the distinct correlations by the occurrence of distinct replacements, the average correlation per replacement can be determined, Fig. 10.3(c). This distinct correlation is significant and decays in a fashion similar to common correlation functions. Relaxation of the matrix and decorrelation of the orientation for distinct replacements happens on approximately the same time scale. For the lowest temperatures, the correlation per distinct replacement increases at intermediate times. Preferred locations with fast replacement, giving rise to Q_dist at shorter times, have lower energy barriers compared to locations with longer residence times. It is reasonable to expect the local energy potential for orientation to also be shallower and rotational cross correlations to be weaker at these sites. Preferred locations with longer residence times have stronger correlations and, thus, average distinct correlation increases on time scales shorter than the relaxation of the matrix. Furthermore, distinct replacement can also happen in bulk phases but is likely to have weaker cross correlations on shorter time scales. The amplitude of cross correlations caused by replacements on the surface of the matrix relative to the self correlation of the solvent overall depends on the concentration of the mixture and ratio of interface and bulk solvent molecules.

This mechanism is depicted on the right side of Fig. 10.3, and for a schematic diagram see Böhmer et al.[400] A necessary condition is that the translation of solvent molecules in contact with the matrix is significantly faster than the relaxation of the latter. In particular, for solvent molecules with anisotropic shapes and low enough temperatures, the solvent-matrix interaction leads to correlated orientation at preferred locations relative to the matrix.

10.4. Spatially resolved contributions to BDS relaxation strength

The mechanism for cross correlations as found for distinct replacements in the previous section only includes two particles, one defining the location and orientation and one replacing it. However, cross correlations between neighboring molecules can be significant, even on longer length scales. The intensity in Fig. 10.3(b) is highly dependent on the cutoff radius but remains less than half of the respective cross correlations in Fig. 10.1 even for less restrictive cutoff of $r_\mathrm{c} = 0.3$. Hence, the spatial distribution as well as the temporal evolution of cross correlations of the dipole moment of molecules is investigated in Fig. 10.4. Presented is the cumulative integral for scalar products of the dipole moment of solvent-molecule i, or segment i for PMMA, with solvent-molecule j at distance r_{ij},

$$F_{1,\vec{v}}^{\mathrm{cross}}(r,t) = \left\langle \frac{1}{N} \sum_{\substack{i,j \\ i\neq j}} \int_0^r \vec{v}_i(0) \cdot \vec{v}_j(t) \cdot \delta(r_{ij}(t) - r)\,\mathrm{d}r \right\rangle , \tag{10.3}$$

with $r_{ij}(t) = |\vec{r}_i(0) - \vec{r}_j(t)|$. The full integral at $r \to \infty$ is the total cross correlation, as shown in Fig. 10.1(c). At the time origin (red), total cross correlations are positive but correlations and anti-correlations alternate, seen as oscillations. Note, that these results are system dependent. As no

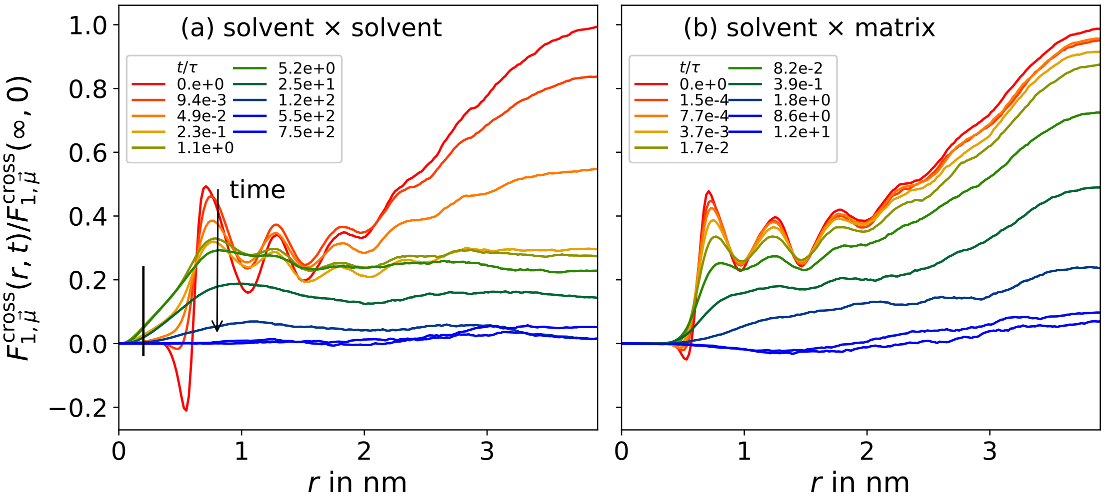

Figure 10.4.: Spatial and temporal resolved cross correlations in the PMMA+picoline mixture at 270 K. Cross correlations are between solvent molecules (a) and solvent and matrix molecules (b), see the main text for details. Curves are normalized by each total cross correlation at time zero. Cross correlations at different logarithmically spaced times t are represented by the coloring from red to green to blue, identical in (a) and (b). The legend denotes the ratio of time t and τ from Fig. 10.9 for the slow process in $F^{\mathrm{inc}}_{1,\vec{\mu}}$ of the solvent in (a) and the fast process in $F^{\mathrm{inc}}_{1,\vec{\mu}}$ of the PMMA segments in (b). The black line indicates the cut-off radius used for the configuration overlap correlation function.

distinct replacements have happened, there are no cross correlations at distances shorter than the next neighbor distance. Since correlation decreases with distance in amorphous liquids, one may expect only significant contributions at short distances. However, the particle number increases with $N \sim r^2$ and weak correlations at longer distances are weighted more strongly. In the case of PMMA, the segments of the polymer have a dipole moment as well. The cross correlations between solvent and matrix are qualitatively the same. Note, that the intensity of these effects as measured by for example dielectric spectroscopy depends not only on dipole-dipole but all other interactions and the strength of the dipole moments as well.

Including the temporal aspect, the decorrelation from short times to long times can be studied in detail. At intermediate times (green) cross correlations within the cutoff radius appear, as found in the previous section. These cross correlations do not account for the value of the integral at longer distances. Especially at the next neighbor distance long lived cross correlations exist. Similarly, cross correlations between solvent and matrix decay on comparable time scales. Hence, the total cross correlations at long times giving signal to the slow process of the solvent stem not only from distinct replacements but from neighboring preferred locations as well. Trivially, if preferred locations exist and on average a positive or negative correlation between them is found, then the mechanism from the previous section, correlated orientations for distinct replacements, will lead to long-lived correlations between them irrespective of the identity of the occupying particles. Of course, as seen in Fig. 10.4, the localization and orientation are smeared out with time by the relaxation of the matrix.

The exact details of the discussed observations are system dependent. Moreover, these cross correlations can depend on the used reference vectors and Legendre polynomials. Hence, such variations are investigated in the next section. Note that the mechanism as described above is the relevant foundation of long-lived cross correlations but not the entire contribution by itself.

10.5. Legendre polynomial and choice of vector

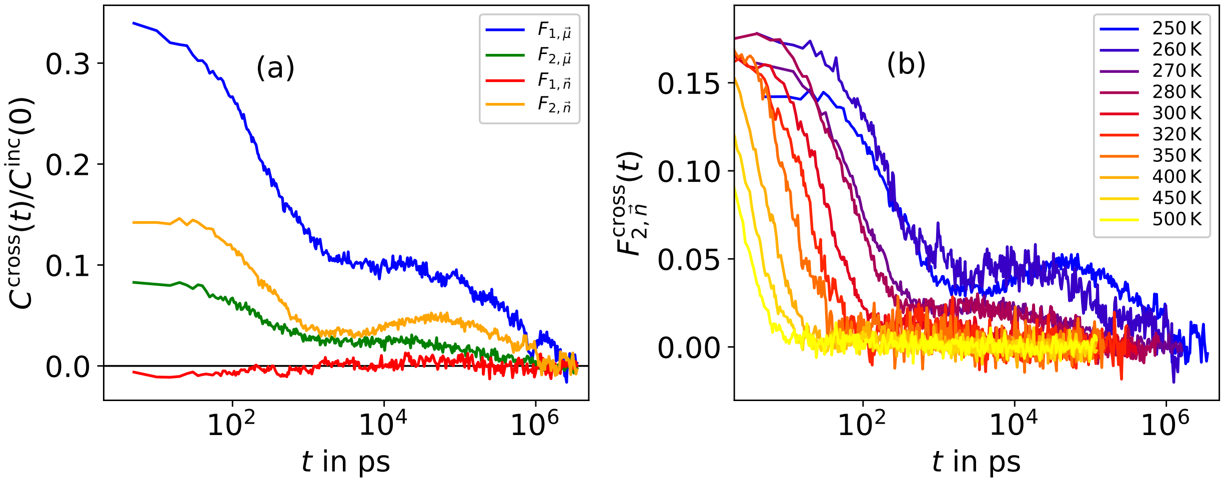

Figure 10.5.: (a) Normalized cross correlations at 250 K of the Legendre polynomials of rank 1 and 2 for two vectors of the solvent molecule, dipole moment $\vec{\mu}$ and plane normal $\vec{n}$. The coherent and incoherent correlation functions are scaled to the latter at $t = 0$ and then subtracted from each other. (b) The cross correlations for $F_{2,\vec{n}}$ as in (a) for all temperatures.

In case of experimental measurements of molecular motion, many methods probe only specific parts or properties of the molecule. Broadband dielectric spectroscopy (BDS) is sensitive to charges and dipole moments, photon correlation spectroscopy (PCS) is sensitive to the optical anisotropy tensor and nuclear magnetic resonance (NMR) often measures one or several specific internuclear vectors. Commonly, the vector within the molecule cannot be chosen freely and different methods can be sensitive to different rotations of the molecule. For example for monohydroxy alcohols BDS is dominated by the reorientation of the hydroxyl group while PCS can be dominated by the nonpolar rest of the molecule. Because parts of a flexible molecule can behave differently, both methods measure different correlation decays. Additionally, the methods vary in the rank of the Legendre polynomial measured, $\ell = 1$ for BDS and $\ell = 2$ for PCS and NMR. For self correlation, this problem is well known and studied. It is however less clear how cross correlations, especially in mixtures like the one studied here, are probed by different methods.

Therefore, two distinct vectors within the picoline molecule, the dipole moment $\vec{\mu}$ and the normal on the plane produced by the ring $\vec{n}$, correlated with F_1 and F_2 are compared in Fig. 10.5(a). $F_{1,\vec{\mu}}$ and $F_{2,\vec{n}}$ are comparable to observations with BDS and PCS, respectively, while the other two combinations are only accessible in the simulation. Note, that the cross correlation is shown for normalized vectors but the experimentally measured intensity depends on more factors. For the dipole moment, both Legendre polynomials produce qualitatively the same correlation function. Because P_2 is more sensitive to small angular displacements the cross correlations are weakened. However, for P_1 in combination with $\vec{n}$ cross correlations are negligible for all times.

Ring-like molecules have been found to perform π-stacking, t-stacking, and staggered π-stacking.[406]

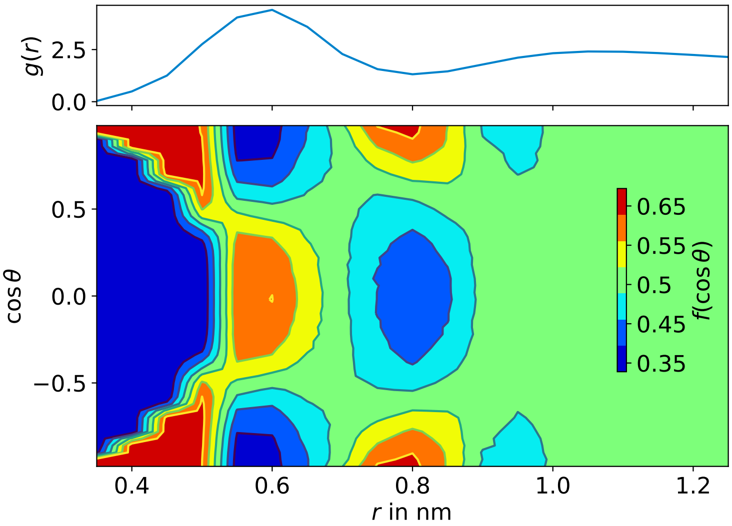

Figure 10.6.: Probability density $f(\cos\theta)$ where θ is the angle between the plane normal $\vec{n}$ of two picoline molecules at a center of mass distance of r. The probability is normalized for each distance r. The top graph shows the RDF for the center of mass.

The ring planes of neighboring molecules are parallel in π-stacking and orthogonal in t-stacking. Figure 10.6 presents the probability density of finding picoline molecules in different arrangements with respect to $\vec{n}$ at distance r. While π-stacking dominates at $r < 0.5\,\mathrm{nm}$ and around 0.8 nm, it is overshadowed by t-stacking at the peak in $g(r)$. P_1 is zero for t-stacking and since $f(\cos\theta)$ is symmetric around zero, it cancels out for π-stacking as well. The Coulomb interaction and the asymmetry of dipole moment and steric interaction of the methyl group are too weak at this temperature to cause asymmetric distributions. Hence, $F_{1,\vec{n}}$ is negligible for the solvent molecules. For stronger supercooling and distinct replacement stronger cross correlations may be possible.

In contrast, the Legendre polynomial of rank 2 has stronger cross correlations for $\vec{n}$ than for $\vec{\mu}$. One possible reason is the π-stacking and t-stacking. The symmetric Legendre polynomial P_2 is one in both cases and insensitive to π-flips, flips by 180°, of picoline around an axis within the ring plane. Therefore, measurements with P_1 and P_2 can differ. Another possibility are the interactions leading to similar orientations for distinct replacements. The steric interaction for tight packing at strong supercooling may be more influential than the dipole-dipole interaction. The cross correlations $F_{2,\vec{n}}^{\mathrm{cross}}$ appear to increase on the time scale of distinct replacement. This is not an artifact and instead follows from the decomposition of the coherent correlation function. When picoline molecules move and there is a significant fraction of t-stacking, then the new orientation is likely to negatively contribute and the average self correlation decays quickly. In contrast, rotational correlation of $\vec{n}$ is strong for picoline molecules replacing each other at time scales shorter than the relaxation of the matrix and cross correlations increase. The mechanism of distinct replacements transfers correlation from the self part to the cross part while the total correlation decays monotonously. That $F_{2,\vec{n}}^{\mathrm{cross}}$ increases at intermediate times is a sign that interactions of ring orientations is quite significant at lower temperatures.

Finally, the temperature dependence of cross correlations in $F_{2,\vec{n}}$ is investigated, see Fig. 10.5(b). Compared to Fig. 10.1(c), the temperature dependence of the long time cross correlations appears to be much higher. While the perceived intensity depends on the separation of correlation times of the fast and slow process, it is evident that the slow process, that exists in $F_{1,\vec{\mu}}$ at all temperatures, disappears for $F_{2,\vec{n}}$ at the highest temperatures. The weak interaction energy for the orientation compared to thermal fluctuations leads to significant vibrations. The higher sensitivity of P_2 to angular displacements leads to a stronger temperature dependence of the intensity. This may explain the strong temperature dependence of the relaxation strength seen in DDLS for the same system.[400]

Thus, three factors are relevant for the relaxation strength of the slow process: the interaction strength, property or part of the molecule probed and the correlation function (e.g., F_1 or F_2). In particular, it depends on the combination of all three. For example a vector related to the interaction will have a higher relaxation strength or while P_2 is more sensitive it may give better results in case of symmetries.

10.6. Fast and slow Picoline

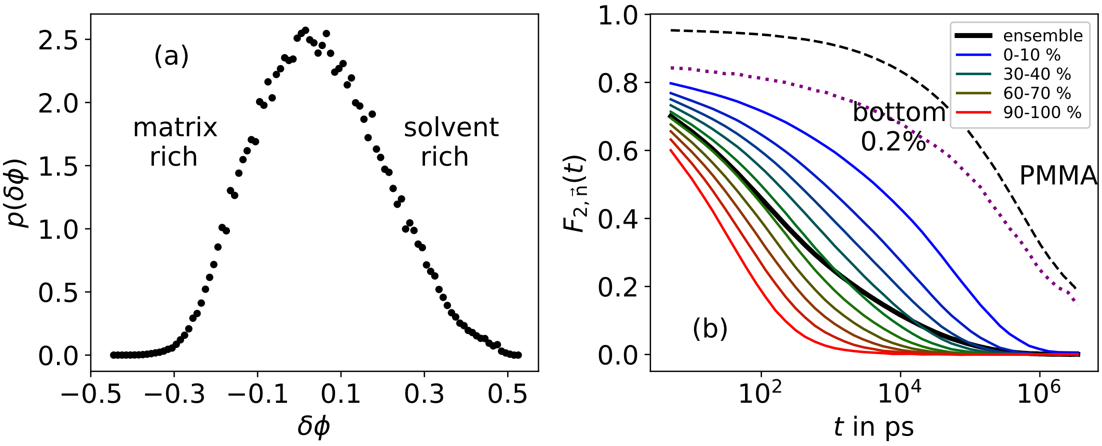

Figure 10.7.: (a) Probability distribution of the local concentration fluctuations $\delta\phi$, i.e., of the deviations of the local concentration ϕ_i from the average concentration at 250 K. Hereby, ϕ_i is the concentration of solvent molecules in a sphere of radius $r_c = 0.7$ nm around the center of mass position of solvent molecule i. (b) The correlation function $F_{2,\vec{n}}(t)$ is averaged for subsets of molecules with different local concentrations ϕ_i at $t = 0$. Specifically, each subset comprises 10 % of solvent molecules with similar values of $\delta\phi$, e.g., the 10 % fraction of solvent molecules with the lowest local concentration are labeled 0-10 %. The purple dotted line is the average correlation function for the lowest 0.2 %. The black solid and dashed line are the ensemble average and $F_{1,\mathrm{PMMA}}$, respectively.

In dynamically asymmetric binary mixtures the slow component in general shows regular supercooled behavior. The fast component, however, has strongly stretched correlation functions as a consequence of a broad distribution of dynamics. This can be observed, for example, as a wide temperature range for the line shape transition in NMR, indicating a broad distribution of mobilities that shifts through the experimental time scale.[309,407] Furthermore, so called four-time correlation functions can be employed in BDS and NMR to filter out fast molecules and obtain correlation functions of a slower subset.[408–410]

The varying degree of contact of solvent molecules with the matrix leads to significant differences in mobility that are not attenuated by relaxation of the neighboring particles, as in bulk. Thus, the dynamical heterogeneity may be linked to the structural heterogeneity. Indeed, resolving correlation functions by the local concentration leads to separation of mobilities in case of a binary mixture of water-like molecules.[317] Hence, the same concept and the definition of the local solvent concentration ϕ_i in Sec. 5.1.5 are applied here. Reference positions are the center of mass of picoline molecules and a cutoff of $r_c = 0.7\,\mathrm{nm}$ was used for the calculation. Correlation functions are then separately calculated for different local concentration around the respective solvent molecule, averaged over short times to reduce vibrational noise. Figure 10.7(a) shows the distribution of solvent fluctuations as deviation $\delta\phi$ from the average solvent concentration at 250 K. It is unimodal for all temperatures, suggesting no demixing at the investigated temperatures and concentration.

Figure. 10.7(b) shows correlation functions as obtained for various local concentrations, characterized by $\delta\phi$, in ascending steps of 10 % at 250 K. The solvent mobility, as measured by $F_{2,\vec{n}}(t)$ to avoid anisotropic reorientation, depends monotonically on the local concentration with the slowest solvent molecules being the ones with the lowest local concentration. The correlation functions of the 10 % solvent molecules with the lowest local concentration decays more than three orders of magnitude slower that that of the 10 % solvent molecules with the highest local concentration. Hence, the local concentration and mobility are correlated. The correlation functions are still stretched and each subset in itself is dynamically heterogeneous. There is no significant gap between subsets and the probability distribution of $\delta\phi$ itself is unimodal, suggesting that indeed no two dynamically separated solvent species caused by different local environments exist. The slowest subset, the lowest 10 %, is still significantly faster than the matrix. Only for solvent molecules with the lowest 0.2 % of local concentration dynamics on the same time scale as the matrix can be found. These molecules are essentially surrounded entirely by the polymer within the next neighbor shell. Thus, a very minor fraction of self correlation on the time scale of the matrix exists. However, the fraction of molecules is too low to cause two peaks in the susceptibility.

The fact that local concentration does not lead to bimodal mobility is even more evident from distributions of mean correlation times obtained by fitting correlation functions of subsets with KWW functions. In this analysis, the distribution of local concentrations $p(\delta\phi)$ is divided into 20 equidistant bins and the mean correlation time $\langle\tau\rangle$ is determined from the correlation function $F_{2,\vec{n}}^{\mathrm{inc}}$ resulting for each of these bins. Then, a pseudo probability density function $G(\ln(\langle\tau\rangle))$ can be determined by weighting the respective $\langle\tau\rangle$ values with the probability of the bins and normalizing over $\ln(\langle\tau\rangle)$, shown in Fig. 10.8(a). Note that the actual distribution of correlation times may be different. For all temperatures, $G(\langle\tau\rangle)$ has a unimodal shape. With decreasing temperature the probability density function shifts to longer times and strongly broadens, indicating that the dependence on the rotational dynamics on the local concentration increases.

Finally, the restoration of ergodicity concerning the local concentration and the solvent mobility can be determined. The former is obtained by standard autocorrelation. For the latter, solvent molecules are separated into 20 subsets according to their local concentration and tracked over time. $F_{2,\vec{n}}(t)$ is calculated for each subset and several logarithmically shifted time origins Δt_0. With time, if ergodicity holds, all subsets will approach and eventually equal the ensemble average. Figure 10.8(b) shows this evolution for the lowest temperature of 250 K, which was not simulated long enough for full ergodicity. However, it was assured that the ensemble average is fully recovered at higher temperatures. The differences of the correlation functions for each bin to the ensemble average are multiplied by their sign, summed up and then normalized to the value at $\Delta t_0 = 0$. This $C_{\Delta F_{2,\vec{n}}}$ characterizes the decay of the dynamical heterogeneity as created by different local concentrations. Its decay is significantly slower than the ensemble averaged dynamics and comparable to the dynamics of the slowest subset. This effect is different than for bulk OTP just above T_g, where four-time correlation functions revealed the so called ”rate memory” to last only about two τ.[409,410] For hard confinement, e.g., neutral pores

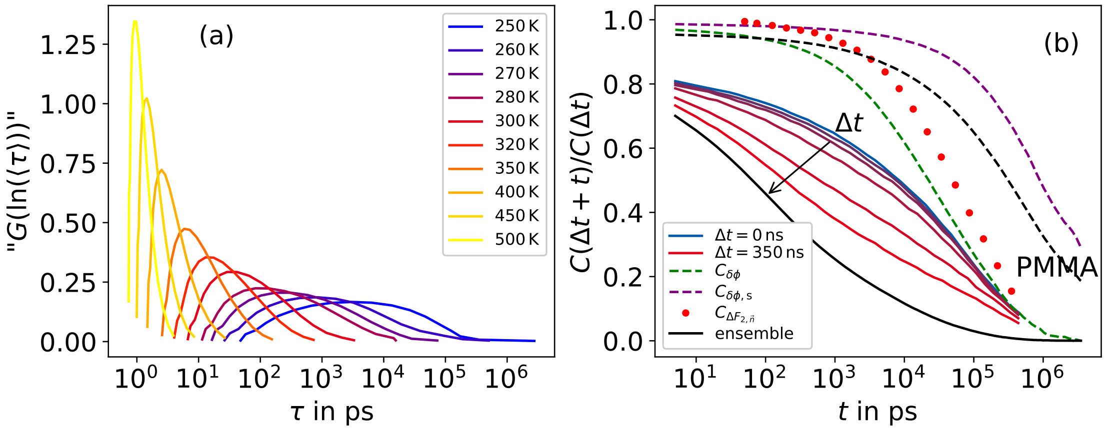

Figure 10.8.: (a) Pseudo probability density function of correlation times obtained by averaging correlation functions $F_{2,\vec{n}}$ over equidistantly binned values of $\delta\phi$. The mean correlation times are obtained by fits with KWW functions and their "probability" results from the sum of occurrences of the bin. (b) The temporal evolution of $F_{2,\vec{n}}(t)$ for following a fixed subset of particles for Δt, see main text for details. Shown is the correlation function of particles with the 5 % lowest local concentration, colored solid lines. The shift for the time origin of the correlation function is indicated by colors from blue to red and logarithmically distributed. The black solid and dashed line are the ensemble average and $F_{1,\mathrm{PMMA}}$, respectively. The green and purple dashed lines are the autocorrelation of $\delta\phi$ for reference positions following the solvent molecules and static in space, respectively. The red dots are the time evolution of the quantitative difference of $F_{2,\vec{n}}(t)$ for all subsets along the shift δt.

in Ch. 9, the ensemble average can only be recovered when the slowest particles at the pore surface exchange with faster particles by translation. However, in the case of soft confinement the time scale of ergodicity of the solvent could be limited by the relaxation of the matrix itself. $C_{\Delta F_{2,\vec{n}}}$ decays comparable or faster than the segmental relaxation of the polymer.

Because the mobility was resolved with respect to the local concentration, it should be compared to the autocorrelation of the latter. In case of reference positions following the center of mass of solvent molecules, the autocorrelation $C_{\delta\phi}$ decays with the same time constant as $C_{\Delta F_{2,\vec{n}}}$, Fig. 10.8(b). The restoration of ergodicity should follow $C_{\delta\phi}$ and, thus, the simple definition of $C_{\Delta F_{2,\vec{n}}}$ is sufficient. For static reference points, the density fluctuations $\delta\phi$ can only decay with the rearrangement of the matrix. Indeed, the correlation function $C_{\delta\phi,\mathrm{s}}$ decays significantly slower and comparable to the segmental relaxation of PMMA.

10.7. Relaxation map

Finally, correlation times of the investigated processes can be compared in an Arrhenius plot. However, the correlation functions are significantly stretched and are in most cases comprised of several decays beyond the trivial vibrational regime. As discussed in App. A.5.1, several fast processes of the solvent molecule are likely related to anisotropic reorientation. The slower isotropic reorientation process causes loss of the entire correlation. In case of cross correlations, the slow step is associated with the relaxation of the matrix. The latter should also cause a full decay of all solvent correlation. Hence, in

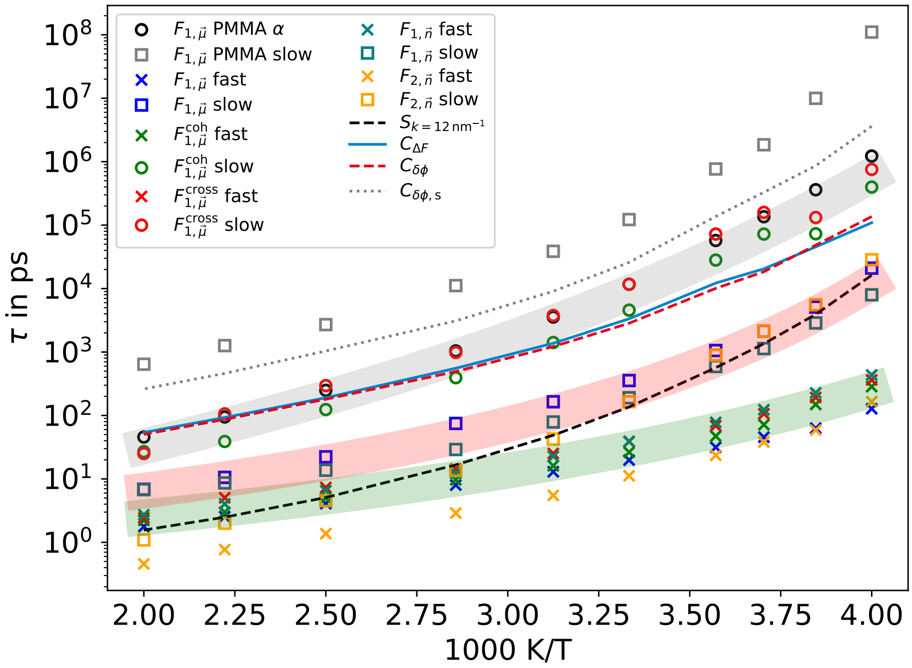

Figure 10.9.: Mean correlation times of the PMMA+picoline binary mixture. Fast and slow refer to the two processes in Eq. (10.4). The shaded areas are guides to the eye and depict the following: fast anisotropic picoline reorientation (green shaded area), isotropic picoline reorientation (red shaded area) and segmental relaxation of the matrix (gray shaded area). $C_{\Delta F}$ denotes the average of correlation times from $C_{\Delta F_{1,\vec{\mu}}}$ and $C_{\Delta F_{2,\vec{n}}}$.

both cases a multiplicative combination of KWW functions is employed:

$$C(t) = A\left(fe^{-(t/\tau_1)^{\beta_1}} + 1 - f\right) e^{-(t/\tau_2)^{\beta_2}}, \tag{10.4}$$

where A is the total amplitude and f its fraction that only the fast process acts upon. The slower decay characterized by τ_2 and β_2 and acts on both amplitudes. This approach is known as the Williams–Watts ansatz and was usually applied to the isotropic α and anisotropic β relaxation.[411] Note that fits with a sum of two KWW functions describe the data as well. The ambiguity of the fitting model and the complex correlation functions as well as the weak separation of time scales lead to only approximate correlation times. The results in Fig. 10.9 are rather a relaxation map to qualitatively understand the system. To obtain effective mean correlation times for the fast process, the integral $\langle\tau_1\rangle = \int_0^\infty e^{-(t/\tau_1)^{\beta_1}} e^{-(t/\tau_2)^{\beta_2}}\,\mathrm{d}t$ is calculated numerically.

The correlation times show three clusters: fast anisotropic picoline reorientation (green shaded area), isotropic picoline reorientation (red shaded area) and segmental relaxation of the matrix (gray shaded area). $F_{1,\vec{\mu}}$ is dominated in all variants, coherent, incoherent, and cross correlations, by the fast anisotropic reorientation. Fast anisotropic reorientations of the plane normal $\vec{n}$ fall into the same cluster at low temperatures. Note, that their anistropic process is not necessarily the same, i.e., discrepancies exist when resolved by local concentration (App. A.5.1), and the underlying dynamics are broadly distributed. The terminal decay of self correlation of picoline is also the same for all rotational correlation functions. Evidence of this being the α-process is provided by the agreement with correlation times from incoherent scattering functions for $k = 12\,\mathrm{nm}^{-1}$, the position of the next neighbor peak in the structure factor at the lowest temperature. At low temperatures, translation agrees well with the isotropic reorientation. This process cannot be fitted in the coherent variant of $F_{1,\vec{\mu}}$ because of its weak amplitude, strong stretching, and higher noise. Finally, the slow process in the coherent or cross correlations of $F_{1,\vec{\mu}}$ agrees well with the segmental relaxation of the polymer. The correlation function of the latter was fitted including a small long-time contribution that is likely caused by lower Rouse modes of polymer relaxation, e.g., end-to-end vector reorientation.

The correlation functions of the local concentration $\delta\phi$ can be compared as well. For static reference points the concentration fluctuations decay slower than the segmental motion of the polymer. In case of the reference points following the solvent molecule, the correlation time well agrees with the decorrelation of dynamical heterogeneity, again confirming the correlation of both. The latter correlation time is independent of the vector and Legendre polynomial used. Restoration of ergodicity quantified in this way is comparable to the matrix relaxation time. A weak decoupling is observed for the lowest temperatures. Because the translation of solvent molecules within the matrix causes decay of $C_{\delta\phi}$, it is dominated by the slowest solvent molecules but not slaved by the matrix. In mixtures with trapped solvent a strong coupling may be expected. For static confinements, e.g., silica pores, or below the glass transition of the matrix, ergodicity is also restored among the mobile solvent molecules despite the infinite time scale of matrix relaxation.

10.8. Outlook – solvent cross correlations in other mixtures

To show that the phenomena found for the PMMA+picoline system are more common, several other systems simulated by colleagues have been investigated to some extent. The simulation details are given in the appendix, App. A.5.2. The first two systems are chosen in order to investigate the necessity of molecular dipole moments. To derive a system close to the one studied so far, the partial charges of picoline have been redistributed such that the dipole moment is negligible. Still, long-lived cross correlations in $F_{2,\vec{n}}$ that decay on a time scale comparable to the segmental relaxation of the polymer exist while the self correlation decays orders of magnitude earlier, Fig. 10.10(a). Cross correlations in case of distinct overlap also agree with the previous findings. Hence, a long-ranged Coulomb interaction of permanent dipole moments is not necessary. A similar system is benzene mixed with oligo-styrene. All dipole moments are weak, in particular for the highly symmetric benzene ring. Also in this system long-lived solvent cross correlations exist, Fig. 10.10(b). The discrepancy for distinct overlap will be discussed further below. The increase of cross correlations at intermediate times agrees with observations in Sec. 10.5. Static cross correlations in $F_{2,\vec{n}}$ are slightly negative. Distinct overlap with time causes a shift from self correlation to cross correlations. The coherent and incoherent correlation functions decay as expected.

Hydrogen bonded systems have strong Coulomb interaction. Two examples shown here are aqueous mixtures of poly-ϵ-lysine (pϵL), a polymerized amino acid, and of the protein myoglobin, Fig. 10.10(c) and (d). Both have donor and acceptor groups for hydrogen bonds with water molecules. Here, the investigated correlation function is again $F_{1,\vec{\mu}}$ for the water dipole moment $\vec{\mu}$. Consistent with the results found for all mixtures studied in this chapter, the self correlation of the solvent decays orders of magnitude faster than the segmental relaxation of the solute. Solvent cross correlations that decay on the time scale of the matrix rearrangement exist.

Note, that the cross correlations per distinct overlap, $F^{\mathrm{dist}}(t)/Q_{\mathrm{dist}}(t)$, have a decay comparable to that of the self correlation. Non-surface water, of which both system have a lot, has a short lived hydrogen bonded network that promotes strong cross correlation before it is rearranged by structural relaxation. Intensity beyond this time scale may be related to the mechanism of fast replacement in a slowly changing energy landscape. Indeed, water in pϵL shows long-lived cross correlations for

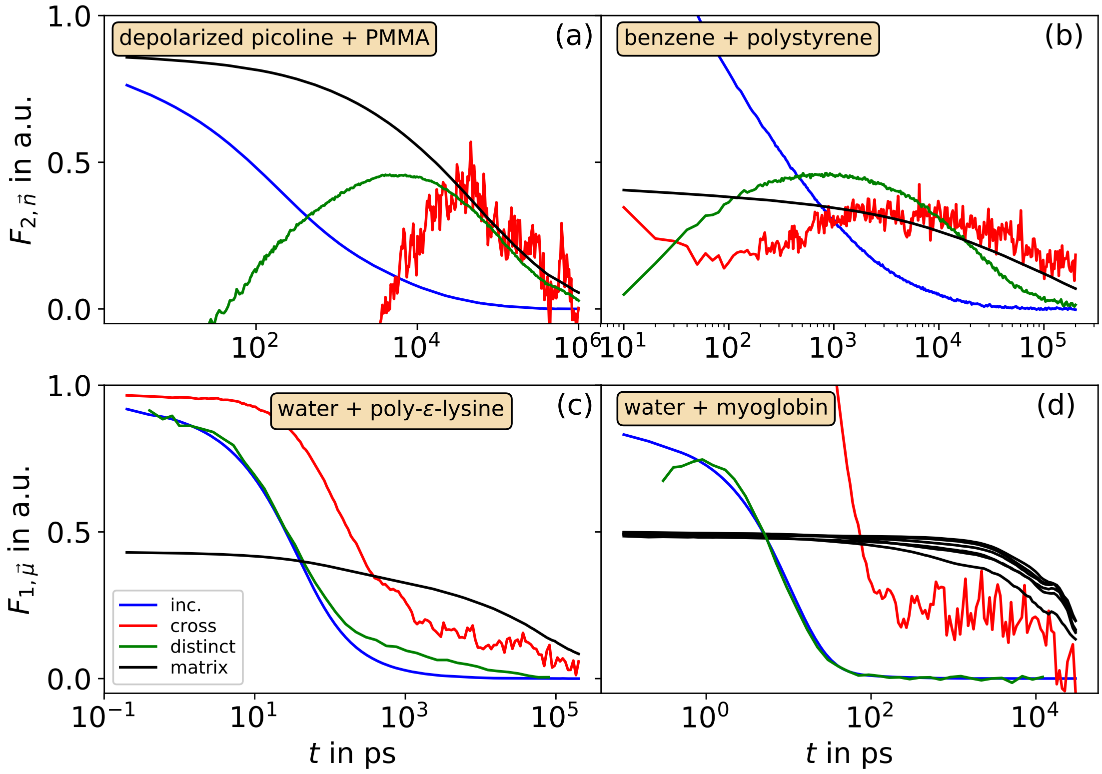

Figure 10.10.: Long-lived cross correlations in other asymmetric binary mixtures: (a) nonpolar picoline and PMMA, (b) benzene and polystyrene, (c) water and poly-ϵ-lysine, and myoglobin in water. The correlation functions are arbitrarily scaled to increase visibility of relevant features. Each plot shows the same functions: solvent self correlation (blue), solvent cross correlations (red), cross correlations per distinct replacement (green), and segmental relaxation of the solute (black). Nonpolar picoline and benzene have negligible dipole moment and instead F_2 and the ring plane normal $\vec{n}$ are analyzed.

distinct overlap. Similarly to benzene, they decay faster than the matrix process. No long-lived distinct cross correlations are found for myoglobin. Since myoglobin has a tertiary structure the orientation of segments is correlated with the overall orientation of the protein and, thus, decorrelates on the time scale of reorientation of the entire protein.

One might therefore conclude that the mechanism is not general and instead the electric field imposed by the dipole moment of the solute causes the cross correlations in the case of myoglobin. The LJ mixture of benzene and polystyrene showed however that such effects are not necessary. The simple approach to measure cross correlations of molecules occupying favorable sites within the matrix is likely insufficient. Only minor translation of the matrix on time scales before its reorientation leads to shifts in the laboratory frame that causes the correlation of space and orientation to decay. In particular, the protein can easily perform minor drifts because of the high hydration level of 8.45 g/g water per protein. The cutoff for water molecules is only 0.1-0.2 nm, a distance the surface atoms of such a large molecule cover far ahead of isotropic reorientation. A more sophisticated analysis could for example follow preferred locations in the coordinate frame of the macromolecule, in particular donor and acceptor groups for hydrogen bonds, to determine distinct overlap and cross correlations. In this case, the distinct overlap would be expected to be higher than the random value for all times while the cross correlations decay with the reorientation of the macromolecule.

10.9. Summary

Broadband spectroscopy experiments on the mixture of picoline and PMMA revealed a solvent process much slower than its α-relaxation.[400] The perfect selectivity in simulations performed here confirm this observation. The option to calculate coherent and incoherent correlation functions reveals that in this dynamically asymmetric binary mixture the solvent contribution at low frequencies in coherent measurements is almost entirely traced back to cross correlations. This agrees well with the discrepancies between ^{2}H NMR and BDS measuring incoherent and coherent correlation functions, respectively. In particular, the self correlation of the solvent does not consist of two dynamically separate species. Translation measured with the ISF also shows only one stretched exponential decay. Coherent scattering contains solvent density fluctuations and their decay on the time scale of the matrix. This observation for density–density fluctuations is consistent with theoretical calculations based on the MCT.[402]

This long-lived preferred localization in coherent scattering and the significantly faster decay of the ISF imply that solvent molecules exchange locations multiple times before the matrix relaxes. Point-to-set correlations show an increased likelihood of distinct overlap above the long-time random value, a feature nonexistent in pure bulk. A combination of distinct overlap and coherent rotational correlation functions reveals the relevant mechanism, fast replacement of solvent molecules within a slowly changing energy landscape. Cross correlations in case of distinct overlap are significant and decay only with the structural relaxation of the matrix. Solvent–solvent and solvent–matrix interactions not only cause energetically favorable locations but also orientations. The interaction is weak enough to allow translation and exchange of solvent molecules. The energy landscape imprinted on the solvent by the matrix causes these favorable locations to be long-lived.

The total intensity of long-lived cross correlations consists of not only distinct overlap but also solvent–matrix cross correlations, if applicable for the system and experiment, and cross correlations among favorable locations. Latter appear trivially since cross correlations between favorable locations will exist independent of the identity of the occupying molecules because of the above mechanism. Furthermore, three factors are relevant to whether or not and how strongly a coherent measurement will observe cross correlations: the interaction and the energy difference for correlated orientation, the vector of the molecule that is probed, and the correlation function on said vector. In particular, the combination of all three is important and determines the sensitivity to cross correlations.

As expected, the solvent mobility correlates strongly with the local environment, e.g., the local concentration. This allowed the resolution of a broad distribution of mobilities that is nevertheless unimodal. The time scale on which ergodicity in terms of solvent mobility is recovered could be identified and agrees with the autocorrelation of local concentration. This happens on significantly longer times than the solvent α-relaxation, on the edge of the broad distribution, and appears to decouple from the matrix relaxation. In general, it should not be longer than the structural relaxation of the matrix. While this process is most likely not spectrally active, i.e., is not detectable by most experiments, it is relevant in NMR. The relaxation of magnetization caused by spin-lattice interaction becomes non-exponential at low temperatures, when dynamical exchange becomes slower than T_1, the spin-lattice relaxation time. How this plays a role in the interpretation of data, e.g., for ^{2}H NMR of hydrated proteins,[52] remains to be studied.

Finally, these two phenomena, solvent cross correlations but absent self correlation on long time scales and the mechanism, have been superficially investigated for several other mixtures. The former occurs in nonpolar polymer-plasticizer mixtures and hydrogen bonding biological systems. The latter is not always observable with the simple algorithms applied here but cannot be ruled out. It may be worthwhile to develop a more general approach that tracks positions relative to the matrix. In any case, the findings presented here can be relevant in a wide variety of systems and revisiting them is important.[52,53,58,59,412,413] It may be that truly bimodal solvent self-dynamics are rarer than expected, more specifically when the slow subset is on the time scale of the solute. However, they may exist in more complex systems for example for structurally integrated solvent molecules like hydrogen bonded water stabilizing the tertiary structure of proteins or larger solvent molecules like trimethyl phosphate.[414] Even then, interpretation of the relaxation strength of slow processes in coherent measurements has to be done with great care as to not overestimate the fraction of slow particles. The mechanism itself could be general, since minor details in local configurations and the related energy differences take over at sufficiently low temperatures, where entropy becomes less relevant. However, it may be ill defined or absent for larger solvent molecules with internal degrees of freedom. In that case investigation of molecule fragments might be necessary. A better understanding of these phenomena is necessary for correct interpretations of coherent measurements. Clever series of experiments or complementary incoherent measurements, e.g., with NMR, are crucial.

11. Summary

In this work, extensive MD simulations were performed to investigate the properties of supercooled liquids. A main focus was the polyamorphism of water in its supercooled regime. Furthermore, the effects of nanoscopic confinements on the structure and dynamics of liquids was studied and corresponding length scales were determined. Finally, liquid mixtures composed of molecules with strongly different dynamics were investigated and the interpretation of results from various experimental methods was critically discussed. In several of these analyses, it was exploited that charge scaling allows for a systematic variation of the liquids' structure and dynamics.

It was possible to confirm the polyamorphism of water-like systems, which is supposed to exist in real water but be hidden in the *no-man's land*. The temperature dependence of the structural relaxation was investigated across a large temperature range and with constant or evolving structural properties. In particular, the relation between fragile-to-strong transitions in the supercooled regime and the existence of two water phases was explored.

The mobility of charge-scaled water was found to decrease significantly with increasing charge-scaling factor q. The high-temperature activation energy E_∞ and the glass transition temperature T_g show a similar q dependence so that $E_\infty/T_\mathrm{g} \sim 11$ is constant. Hence, E_∞ appears to be a relevant energy scale for the entire temperature range of supercooled liquids. The evolution of local structure with temperature remained qualitatively similar in a significant range of q values. However, the density maximum disappeared for the highest values of q because the expanding second next-neighbor shell can no longer compensate the common contraction upon cooling.

Furthermore, charge scaling enabled a thorough exploration of the polyamorphism of water-like systems. Isochore crossing showed that a liquid-liquid phase transition (LLPT) line ending in a liquid-liquid critical point (LLCP) exists for the TIP4P/2005 water model at charge scaling factors from $q = 0.86$ to $q = 0.91$. The data was characterized with the two-structure equation of state (TSEOS) formalism which not only allows for a reliable determination of the location of the LLCP but also for extra- and interpolations in the phase diagram. The critical temperature T_c, pressure P_c, and density ρ_c were all found to shift to lower values with decreasing q and it was confirmed that for models of water-like systems an LLCP at negative pressure can exist. Charge scaling and an extrapolation may be taken into consideration for estimation of the LLCP location in systems that are otherwise too viscous for current simulation studies. Given the abundance of simulations of water-like models that have an LLCP, it is likely that the same is true for real water.

Because reducing q led to faster dynamics at the LLCP, it was possible to observe high-density (HDL) and low-density liquid (LDL) phases in coexistence. Dynamics within each phase could be determined since the phases below the LLCP are stable on time and length scales greater than the structural relaxation. The results revealed that the high fragility of water at pressures below the LLCP is caused by rapid transition across isomorphs with constant fractions of high-density and low-density local structures. Along isomorphs the water-like systems behave like very strong liquids. The explanation of the suspected fragile-to-strong transition (FST) of real water as the transition from a fragile to a strong liquid could not be confirmed. However, two-state models for water dynamics by Tanaka and coworkers and by Caupin and coworkers[120,218] also failed to describe all observations.

Hence, a good description of dynamics within reactive binary mixtures is still missing.

The temperature dependence in the high-temperature regime and close to the LLCP cannot be attributed to either the HDL or the LDL phase. However, their stable coexistence in elongated systems allowed the analysis of short-range dynamics. The translational and rotational mobility was found to decrease by about two orders of magnitude from HDL to LDL and follow Arrhenius behavior for both phases in the temperature range studied, consistent with experimental observations for HDA and LDA above their glass transitions.[13] The results support the notion that translational and rotational motion do not decouple within the *no-man's land*.

A family of functional forms for the temperature dependence of structural relaxation of liquids was derived from a suitable series expansion and basic requirements for the temperature dependent activation energy $E(T)$. The resulting functions are capable of describing the dynamics in the full temperature regime from the boiling point to the glass transition for a large number of model and real liquids. In particular, the approach allows one to capture the existence of an FST. When deviations from a Vogel-Fulcher-Tammann (VFT) behavior do not occur, first-order solutions suffice. The second-order parameter becomes necessary if deviations from VFT behavior or even an FST exist. The Cohen-Grest model also adequately describes the low-temperature regime for systems with moderate deviations from VFT behavior and without, but it fails at higher temperatures. The derived functional forms of second order feature an inflection point in the Arrhenius plot, a maximum in $E_\mathrm{a} = \mathrm{d}\ln(\tau/\tau_\infty)/\mathrm{d}T^{-1}$, and a second Arrhenius regime at stronger supercooling, i.e., they describe strong-fragile-strong behavior (SFSB). The difference in activation energies of the high- and low-temperature Arrhenius laws determines whether the inflection point and the low-temperature Arrhenius regime are observable above T_g. The inflection point is missing from the Cohen-Grest model, which has no maximum in E_a but in its derivative, and thus a qualitatively different FST. Knowing whether the existence of a low-temperature limit of the activation energy is universal to all liquids and, subsequently, unraveling its microscopic origin is an important step towards a full understanding of the dynamics of supercooled liquids.

In addition, the effects of nanoscopic confinements on charge-scaled water models were analyzed. For this purpose, neutral confinements were used to avoid spurious liquid-matrix interactions and significant alterations of the structure of the liquid at the interface. The generally observed strong gradients of structural and dynamical properties at the liquid-matrix interface were found and the related static and dynamic correlation lengths were determined. Their relation to bulk-like behavior in the pore center was investigated. For all studied charge-scaled water models the dynamic correlation length at isokinetic points was the same. It was analyzed to which extent the growing length scales in neutral confinement can be used to explain the increasing activation energy of the bulk liquids in their supercooled regimes. For example, the RFOT theory[91] was be applied and the data collapsed with the static correlation lengths and universal parameters for $q \geq 0.9$, whereas deviations occurred for smaller charge-scaling factors. Also, the ratio of E_∞ to the onset temperature below which the slowdown at the interface becomes increasingly relevant differs between these two sets of charge-scaled variants. The results for the vibrational correlation length and the dynamical gradient are not reconcilable with the shoving model. Thus, a universal understanding in these models is still missing.

The relative slowdown ζ of the structural relaxation at the pore wall with respect to the pore center was analyzed in more detail. Firstly, ζ appears to follow an Arrhenius law for sufficient supercooling and its temperature dependence can be characterized using a constant activation energy ΔE_ζ and an onset temperature T_0. This constant activation energy can explain the reduced fragility of dynamics at interfaces. Additionally, $\Delta E_\zeta / E_\infty$ was found to be approximately the same for all charge-scaled systems suggesting that the high temperature activation energy in the bulk is also relevant in neutral confinements. Future work could investigate whether $\Delta E_\zeta(d)$ is independent of the distance to the pore wall and a self-consistent set of equations for $\tau(d, T)$ can be derived. However, due to the limited temperature range and moderate supercooling of simulation studies, it is also possible that ΔE_ζ has a weak temperature dependence.

Moreover, the static energy landscape imposed by the atoms of the confinement on the neighboring liquid was investigated. For this purpose, the persistent fluctuations of the local particle density in the interfacial region were determined and Boltzmann statistics was used to obtain the energy landscape from the spatially resolved density distribution. Good agreement with the mobility gradient across the pore was observed when assuming that translation of molecules requires overcoming the energy barriers within this PEL in addition to those in bulk. Thus, the slowdown at the pore wall can quantitatively be rationalized based on the additional static energy landscape resulting from the liquid-matrix interaction.

Lastly, dynamically asymmetric binary mixtures were simulated to determine the origin of a slow solvent process observed, e.g., with broadband dielectric spectroscopy BDS.[400] Using the capabilities of MD simulations, it was shown that the slow process cannot be attributed to a fraction of slow solvent molecules but is caused by their long-lived cross correlations, which explains the discrepancies between incoherent measurement methods, e.g., ^{2}H NMR, and coherent measurement methods, e.g., BDS. The slow relaxation of the solute molecules causes long-lived density fluctuations for the solvent molecules, which are probed via cross correlations in coherent measurements. The energy landscape imposed by the solute on the solvent creates preferred locations and orientations, as was confirmed using point-to-set correlation functions in combination with rotational correlation functions. Hence, cross correlations result because several solvent molecules occupy the same location and show the same orientation before a renewal of the preferred configurations is brought about by solute relaxation. This mechanism was confirmed by further analyses, which revealed that the distribution of correlation times of solvent dynamics is unimodal but very broad due to a significant spatial variation of the local concentration. Because of all of this complexity, identification of a slow solvent process from coherent measurements has to be done with great care and should be scrutinized by performing incoherent measurements.

Both the neutral confinements as hard confinements and the solute molecules in mixtures as soft confinements imprint a PEL on the liquid. Future studies could extend the analysis of the PEL based on Boltzmann statistics not only to hard confinements of other geometries, but also to macromolecules. An analysis that includes orientations in such systems could help rationalizing the amplitudes of cross correlations in rotational correlation functions. In addition, further studies could attempt to calculate the temporary PEL contribution of dynamic heterogeneities in supercooled liquids, with suitable artificial interactions or even in bulk directly. Moreover, short-lived structures in bulk that may cause cross correlations at intermediate times and their relation to self correlation could be studied in more detail with simulations.

Furthermore, the charge-scaled silica and water models share many features, e.g., their density anomalies and their pronounced or at least indicated FSTs. Hence, it is likely that the findings for the charge-scaled TIP4P/2005 systems with confirmed LLPT are also important to the other silica- and water-like and systems and, in general, to all liquids with competing compressed high-energy and spacious low-energy local structures. Moreover, a true liquid polyamorphism with an LLPT may not be required for SFSB. In fact, it could be that an FST generally occurs in liquids with a rapid change in local structures with temperature followed by a weaker temperature dependence upon further supercooling but still above T_g. Such behavior should leave traces in the temperature dependence of the configurational specific heat and entropy, as is the case for the charge-scaled TIP4P/2005 water models. In particular, it is important to know whether HDL also exhibits SFSB and if this is due to saturation of a high-density local structure, as opposed to the low-density tetrahedral structure of LDL. This would mean that differences in local structure do not have to be large in density. In addition, the functional forms of second order could be used to identify other promising molecular glass formers from the literature. Expanding the analyses within this work to a broader variation of liquids could reveal if the SFSBs with and without inflection point share a common origin. To this end, systematic modifications such as charge scaling of existing molecules as well as their adaption as model systems could make the relevant temperature regimes more accessible and advance the understanding of supercooled liquids.

Bibliography

[1] X. F. Pang. *Water*. WORLD SCIENTIFIC, 2014. DOI: `10.1142/8669` (cit. on pp. 1, 18, 19, 26).

[2] P. G. Debenedetti. “Supercooled and glassy water”. In: *J. Phys.: Condens. Matter* 15.45 (2003), R1669–R1726. DOI: `10.1088/0953-8984/15/45/r01` (cit. on pp. 1, 19, 21, 67, 69, 81).

[3] V. V. Vasisht, S. Saw, and S. Sastry. “Liquid–liquid critical point in supercooled silicon”. In: *Nat. Phys.* 7.7 (2011), pp. 549–553. DOI: `10.1038/nphys1993` (cit. on pp. 1, 21, 24, 68).

[4] E. Lascaris, M. Hemmati, S. V. Buldyrev, H. E. Stanley, and C. A. Angell. “Search for a liquid-liquid critical point in models of silica”. In: *J. Chem. Phys.* 140.22 (2014), p. 224502. DOI: `10.1063/1.4879057` (cit. on pp. 1, 21, 24, 25, 68, 74, 97, 127).

[5] P. H. Poole, F. Sciortino, U. Essmann, and H. E. Stanley. “Phase behaviour of metastable water”. In: *Nature* 360.6402 (1992), pp. 324–328. DOI: `10.1038/360324a0` (cit. on pp. 2, 19, 21, 67, 68).

[6] O. Mishima and H. E. Stanley. “The relationship between liquid, supercooled and glassy water”. In: *Nature* 396.6709 (1998), pp. 329–335. DOI: `10.1038/24540` (cit. on pp. 2, 20, 67, 68).

[7] H. Tanaka. “Liquid–liquid transition and polyamorphism”. In: *J. Chem. Phys.* 153.13 (2020), p. 130901. DOI: `10.1063/5.0021045` (cit. on pp. 2, 20, 23–25, 68).

[8] M. Togaya. “Pressure Dependences of the Melting Temperature of Graphite and the Electrical Resistivity of Liquid Carbon”. In: *Phys. Rev. Lett.* 79.13 (1997), pp. 2474–2477. DOI: `10.1103/physrevlett.79.2474` (cit. on pp. 2, 23, 68).

[9] Y. Katayama, T. Mizutani, W. Utsumi, O. Shimomura, M. Yamakata, and K. ichi Funakoshi. “A first-order liquid–liquid phase transition in phosphorus”. In: *Nature* 403.6766 (2000), pp. 170–173. DOI: `10.1038/35003143` (cit. on pp. 2, 23, 68).

[10] Y. Katayama, Y. Inamura, T. Mizutani, M. Yamakata, W. Utsumi, and O. Shimomura. “Macroscopic Separation of Dense Fluid Phase and Liquid Phase of Phosphorus”. In: *Science* 306.5697 (2004), pp. 848–851. DOI: `10.1126/science.1102735` (cit. on pp. 2, 23, 68).

[11] L. Henry, M. Mezouar, G. Garbarino, D. Sifré, G. Weck, and F. Datchi. “Liquid–liquid transition and critical point in sulfur”. In: *Nature* 584.7821 (2020), pp. 382–386. DOI: `10.1038/s41586-020-2593-1` (cit. on pp. 2, 23, 68).

[12] L. Heckmann and B. Drossel. “Common Features of Simple Water Models”. In: *J. Chem. Phys.* 138 (2013), p. 234503. DOI: `10.1063/1.4810875` (cit. on pp. 2, 24, 68).

[13] K. Amann-Winkel, C. Gainaru, P. H. Handle, M. Seidl, H. Nelson, R. Bohmer, and T. Loerting. “Water's second glass transition”. In: *Proc. Natl. Acad. Sci. U.S.A.* 110.44 (2013), pp. 17720–17725. DOI: `10.1073/pnas.1311718110` (cit. on pp. 2, 20, 24–26, 28, 68, 69, 92, 96, 98, 126, 184).

[14] A. K. Soper. “Continuous trends”. In: *Nat. Mater.* 13.7 (2014), pp. 671–673. DOI: `10.1038/nmat4019` (cit. on pp. 2, 21, 68).

[15] J. Swenson. “Possible relations between supercooled and glassy confined water and amorphous bulk ice”. In: *Phys. Chem. Chem. Phys.* 20.48 (2018), pp. 30095–30103. DOI: `10.1039/c8cp05688a` (cit. on pp. 2, 68).

[16] J. J. Shephard and C. G. Salzmann. “Molecular Reorientation Dynamics Govern the Glass Transitions of the Amorphous Ices”. In: *J. Phys. Chem. Lett.* 7.12 (2016), pp. 2281–2285. DOI: `10.1021/acs.jpclett.6b00881` (cit. on pp. 2, 26, 69).

[17] S. Cerveny, F. Mallamace, J. Swenson, M. Vogel, and L. Xu. “Confined Water as Model of Supercooled Water”. In: *Chem. Rev.* 116.13 (2016), pp. 7608–7625. DOI: `10.1021/acs.chemrev.5b00609` (cit. on pp. 2, 28, 69).

[18] S. Lemke, P. H. Handle, L. J. Plaga, J. N. Stern, M. Seidl, V. Fuentes-Landete, K. Amann-Winkel, K. W. Köster, C. Gainaru, T. Loerting, and R. Böhmer. “Relaxation dynamics and transformation kinetics of deeply supercooled water: Temperature,

pressure, doping, and proton/deuteron isotope effects". In: *J. Chem. Phys.* 147.3 (2017), p. 034506. DOI: `10.1063/1.4993790` (cit. on pp. 2, 25, 26, 67).

[19] R. S. Smith and B. D. Kay. "The existence of supercooled liquid water at 150?K". In: *Nature* 398.6730 (1999), pp. 788–791. DOI: `10.1038/19725` (cit. on pp. 2, 26).

[20] Y. Xu, N. G. Petrik, R. S. Smith, B. D. Kay, and G. A. Kimmel. "Growth rate of crystalline ice and the diffusivity of supercooled water from 126 to 262 K". In: *Proc. Natl. Acad. Sci. U.S.A.* 113.52 (2016), pp. 14921–14925. DOI: `10.1073/pnas.1611395114` (cit. on pp. 2, 19, 24, 26, 27, 85).

[21] F. Perakis, K. Amann-Winkel, F. Lehmkühler, M. Sprung, D. Mariedahl, J. A. Sellberg, H. Pathak, A. Späh, F. Cavalca, D. Schlesinger, A. Ricci, A. Jain, B. Massani, F. Aubree, C. J. Benmore, T. Loerting, G. Grübel, L. G. M. Pettersson, and A. Nilsson. "Diffusive dynamics during the high-to-low density transition in amorphous ice". In: *Proc. Natl. Acad. Sci. U.S.A.* 114.31 (2017), pp. 8193–8198. DOI: `10.1073/pnas.1705303114` (cit. on pp. 2, 21, 27).

[22] F. Sciortino, E. L. Nave, and P. Tartaglia. "Physics of the Liquid-Liquid Critical Point". In: *Phys. Rev. Lett.* 91.15 (2003), p. 155701. DOI: `10.1103/physrevlett.91.155701` (cit. on pp. 2, 22, 68).

[23] D. Frenkel and B. Smit. *Understanding Molecular Simulation*. Elsevier Science Publishing Co Inc, 2001, pp. 241–267. 664 pp. ISBN: 0122673514 (cit. on pp. 2, 29, 31).

[24] R. Horstmann. "Dynamics of bulk and confined waters: A molecular dynamics simulations study on the effects of molecular polarity". MA thesis. TU Darmstadt, 2016 (cit. on pp. 2, 57).

[25] E. Lascaris. "Tunable Liquid-Liquid Critical Point in an Ionic Model of Silica". In: *Phys. Rev. Lett.* 116.12 (2016), p. 125701. DOI: `10.1103/physrevlett.116.125701` (cit. on pp. 2, 21, 24, 39, 68, 70, 74, 81, 97).

[26] C. A. Angell, K. L. Ngai, G. B. McKenna, P. F. McMillan, and S. W. Martin. "Relaxation in glassforming liquids and amorphous solids". In: *J. Appl. Phys.* 88.6 (2000), pp. 3113–3157. DOI: `10.1063/1.1286035` (cit. on pp. 3, 101).

[27] A. Cavagna. "Supercooled liquids for pedestrians". In: *Phys. Rep.* 476.4-6 (2009), pp. 51–124. DOI: `10.1016/j.physrep.2009.03.003` (cit. on pp. 3, 12–15, 101, 138).

[28] J. H. Gibbs and E. A. DiMarzio. "Nature of the Glass Transition and the Glassy State". In: *J. Chem. Phys.* 28.3 (1958), pp. 373–383. DOI: `10.1063/1.1744141` (cit. on pp. 3, 13, 101, 138).

[29] G. Adam and J. H. Gibbs. "On the Temperature Dependence of Cooperative Relaxation Properties in Glass-Forming Liquids". In: *J. Chem. Phys.* 43.1 (1965), pp. 139–146. DOI: `10.1063/1.1696442` (cit. on pp. 3, 13, 85, 101, 103, 138).

[30] J. Dudowicz, K. F. Freed, and J. F. Douglas. "Generalized Entropy Theory of Polymer Glass Formation". In: *Adv. Chem. Phys*. John Wiley & Sons, Inc., 2008, pp. 125–222. DOI: `10.1002/9780470238080.ch3` (cit. on pp. 3, 14, 101).

[31] J. C. Dyre. "Colloquium: The glass transition and elastic models of glass-forming liquids". In: *Rev. Mod. Phys.* 78.3 (2006), pp. 953–972. DOI: `10.1103/revmodphys.78.953` (cit. on pp. 3, 16, 101, 145).

[32] W. Götze. *Complex Dynamics of Glass-Forming Liquids: A Mode-Coupling Theory*. Oxford University Press, 2008. 656 pp. ISBN: 9780199235346. DOI: `10.1093/acprof:oso/9780199235346.001.0001` (cit. on pp. 3, 101, 103).

[33] S. Mirigian and K. S. Schweizer. "Unified Theory of Activated Relaxation in Liquids over 14 Decades in Time". In: *J. Phys. Chem. Lett.* 4.21 (2015), pp. 3648–3653. DOI: `10.1021/jz4018943` (cit. on pp. 3, 101).

[34] G. B. McKenna and S. L. Simon. "50th Anniversary Perspective: Challenges in the Dynamics and Kinetics of Glass-Forming Polymers". In: *Macromolecules* 50.17 (2017), pp. 6333–6361. DOI: `10.1021/acs.macromol.7b01014` (cit. on pp. 3, 101, 102).

[35] K. Niss and T. Hecksher. "Perspective: Searching for simplicity rather than universality in glass-forming liquids". In: *J. Chem. Phys.* 149.23 (2018), p. 230901. DOI: `10.1063/1.5048093` (cit. on pp. 3, 101, 102).

[36] J. C. Martinez-Garcia, J. Martinez-Garcia, S. J. Rzoska, and J. Hulliger. "The new insight into dynamic crossover in glass forming liquids from the apparent enthalpy analysis". In: *J. Chem. Phys.* 137.6 (2012), p. 064501. DOI: `10.1063/1.4739750` (cit. on pp. 3, 101).

[37] B. Schmidtke, N. Petzold, R. Kahlau, M. Hofmann, and E. A. Rössler. "From boiling point to glass transition temperature: Transport coefficients in molecular liquids follow three-parameter scaling". In: *Phys. Rev. E* 86.4 (2012), p. 041507. DOI: `10.1103/physreve.86.041507` (cit. on pp. 3, 17, 18, 102, 103, 107, 112, 114, 117, 122–124, 154).

[38] H. Tanaka. "Two-order-parameter model of the liquid–glass transition. I. Relation between glass transition and crystallization". In: *J. Non-Cryst. Solids* 351.43-45 (2005), pp. 3371–3384. DOI: `10.1016/j.jnoncrysol.2005.09.008` (cit. on pp. 3, 18, 102).

[39] W.-S. Xu, J. F. Douglas, and K. F. Freed. “Generalized entropy theory of glass-formation in fully flexible polymer melts”. In: *J. Chem. Phys.* 145.23 (2016), p. 234509. DOI: `10.1063/1.4972412` (cit. on pp. 3, 14, 25, 102, 104).

[40] K. Ito, C. T. Moynihan, and C. A. Angell. “Thermodynamic determination of fragility in liquids and a fragile-to-strong liquid transition in water”. In: *Nature* 398.6727 (1999), pp. 492–495. DOI: `10.1038/19042` (cit. on pp. 3, 21, 25, 69).

[41] M. Alcoutlabi and G. B. McKenna. “Effects of Confinement on Material Behavior at the Nanometre Size Scale”. In: *J. Phys. Condens. Matter* 17.15 (2005), R461–R524. ISSN: 0953-8984. DOI: `10.1088/0953-8984/17/15/r01` (cit. on pp. 3, 27, 137).

[42] R. Richert. “Dynamics of Nanoconfined Supercooled Liquids”. In: *Annu. Rev. Phys. Chem.* 62.1 (2011), pp. 65–84. DOI: `10.1146/annurev-physchem-032210-103343` (cit. on pp. 3, 27, 137).

[43] P. Horng, M. R. Brindza, R. A. Walker, and J. T. Fourkas. “Behavior of Organic Liquids at Bare and Modified Silica Interfaces”. In: *J. Phys. Chem. C* 114.1 (2009), pp. 394–402. DOI: `10.1021/jp908444x` (cit. on pp. 3, 137).

[44] D. Demuth, M. Sattig, E. Steinrücken, M. Weigler, and M. Vogel. “2H NMR Studies on the Dynamics of Pure and Mixed Hydrogen-Bonded Liquids in Confinement”. In: *Z. Phys. Chem.* 232.7-8 (2018), pp. 1059–1087. DOI: `10.1515/zpch-2017-1027` (cit. on pp. 3, 27, 137).

[45] L. D. Gelb, K. E. Gubbins, R Radhakrishnan, and M Sliwinska-Bartkowiak. “Phase separation in confined systems”. In: *Rep. Prog. Phys.* 62.12 (1999), pp. 1573–1659. DOI: `10.1088/0034-4885/62/12/201` (cit. on pp. 3, 137).

[46] J. Geske, M. Harrach, L. Heckmann, R. Horstmann, F. Klameth, N. Müller, E. Pafong, T. Wohlfromm, B. Drossel, and M. Vogel. “Molecular Dynamics Simulations of Water, Silica, and Aqueous Mixtures in Bulk and Confinement”. In: *Z. Phys. Chem.* 232.7-8 (2018), pp. 1187–1225. DOI: `10.1515/zpch-2017-1042` (cit. on pp. 3, 4, 39, 68, 69, 137, 143).

[47] B. Kumari, M. Brodrecht, H. Breitzke, M. Werner, B. Grünberg, H.-H. Limbach, S. Forg, E. P. Sanjon, B. Drossel, T. Gutmann, and G. Buntkowsky. “Mixtures of Alcohols and Water confined in Mesoporous Silica: A Combined Solid-State NMR and Molecular Dynamics Simulation Study”. In: *J. Phys. Chem. C* 122.34 (2018), pp. 19540–19550. DOI: `10.1021/acs.jpcc.8b04745` (cit. on pp. 3, 137).

[48] F. Klameth and M. Vogel. “Structure and dynamics of supercooled water in neutral confinements”. In: *J. Chem. Phys.* 138.13 (2013), p. 134503. DOI: `10.1063/1.4798217` (cit. on pp. 3, 4, 137–139, 142, 151, 161, 162).

[49] K. Kim, K. Miyazaki, and S. Saito. “Slow dynamics, dynamic heterogeneities, and fragility of supercooled liquids confined in random media”. In: *J. Phys. Condens. Matter* 23.23 (2011), p. 234123. DOI: `10.1088/0953-8984/23/23/234123` (cit. on pp. 3, 42, 137).

[50] F. Klameth. “From Brownian motion to supercooled water in confinements-a molecular dynamics simulation study”. PhD thesis. TU Darmstadt, 2015 (cit. on pp. 4, 38, 160).

[51] T. Blochowicz, C. Karle, A. Kudlik, P. Medick, I. Roggatz, M. Vogel, C. Tschirwitz, J. Wolber, J. Senker, and E. Rössler. “Molecular Dynamics in Binary Organic Glass Formers”. In: *J. Phys. Chem. B* 103.20 (1999), pp. 4032–4044. ISSN: 1520-6106. DOI: `10.1021/jp983754x` (cit. on pp. 4, 44, 165, 166).

[52] S. Capaccioli, L. Zheng, A. Kyritsis, A. Paciaroni, M. Vogel, and K. L. Ngai. “The Dynamics of Hydrated Proteins Are the Same as Those of Highly Asymmetric Mixtures of Two Glass-Formers”. In: *ACS Omega* 6.1 (2020), pp. 340–347. DOI: `10.1021/acsomega.0c04655` (cit. on pp. 4, 165, 166, 181, 182).

[53] S. Cerveny and J. Swenson. “Water dynamics in the hydration shells of biological and non-biological polymers”. In: *J. Chem. Phys.* 150.23 (2019), p. 234904. DOI: `10.1063/1.5096392` (cit. on pp. 4, 166, 182).

[54] B. Pötzschner, F. Mohamed, A. Lichtinger, D. Bock, and E. A. Rössler. “Dynamics of asymmetric non-polymeric binary glass formers—A nuclear magnetic resonance and dielectric spectroscopy study”. In: *J. Chem. Phys.* 143.15 (2015), p. 154506. DOI: `10.1063/1.4932981` (cit. on pp. 4, 166).

[55] T. Körber, F. Krohn, C. Neuber, H.-W. Schmidt, and E. A. Rössler. “Main and secondary relaxations of non-polymeric high-Tg glass formers as revealed by dielectric spectroscopy”. In: *Phys. Chem. Chem. Phys.* 22.16 (16 2020), pp. 9086–9097. DOI: `10.1039/d0cp00930j` (cit. on pp. 4, 166).

[56] T. Blochowicz, S. Schramm, S. Lusceac, M. Vogel, B. Stühn, P. Gutfreund, and B. Frick. “Signature of a Type-A Glass Transition and Intrinsic Confinement Effects in a Binary Glass-Forming System”. In: *Phys. Rev. Lett.* 109.3 (3 2012), p. 035702. DOI: `10.1103/physrevlett.109.035702` (cit. on pp. 4, 166).

[57] B. Pötzschner, F. Mohamed, C. Bächer, E. Wagner, A. Lichtinger, R. Minikejew, K. Kreger, H.-W. Schmidt, and E. A. Rössler. "Non-polymeric asymmetric binary glass-formers. I. Main relaxations studied by dielectric, 2H NMR, and 31P NMR spectroscopy". In: *J. Chem. Phys.* 146.16 (2017), p. 164503. DOI: `10.1063/1.4980084` (cit. on pp. 4, 166).

[58] S. Cerveny, I. Combarro-Palacios, and J. Swenson. "Evidence of Coupling between the Motions of Water and Peptides". In: *J. Phys. Chem. Lett.* 7.20 (2016), pp. 4093–4098. DOI: `10.1021/acs.jpclett.6b01864` (cit. on pp. 4, 166, 182).

[59] M. Weigler, I. Combarro-Palacios, S. Cerveny, and M. Vogel. "On the microscopic origins of relaxation processes in aqueous peptide solutions undergoing a glass transition". In: *J. Chem. Phys.* 152.23 (2020), p. 234503. DOI: `10.1063/5.0010312` (cit. on pp. 4, 166, 182).

[60] W. Kauzmann. "The Nature of the Glassy State and the Behavior of Liquids at Low Temperatures." In: *Chem. Rev.* 43.2 (1948), pp. 219–256. DOI: `10.1021/cr60135a002` (cit. on p. 8).

[61] F. H. Stillinger and P. G. Debenedetti. "Phase transitions, Kauzmann curves, and inverse melting". In: *Biophys. Chem.* 105.2-3 (2003), pp. 211–220. DOI: `10.1016/s0301-4622(03)00089-9` (cit. on p. 8).

[62] A. L. Greer. "Too hot to melt". In: *Nature* 404.6774 (2000), pp. 134–135. DOI: `10.1038/35004689` (cit. on p. 8).

[63] H. Vogel. "Das Temperaturabhängigkeit Gesetz der Viskosität von Flüssigkeiten". In: *Phys. Z.* 22 (1921), p. 645 (cit. on pp. 8, 13, 110).

[64] F. H. Stillinger and P. G. Debenedetti. "Glass Transition Thermodynamics and Kinetics". In: *Annu. Rev. Condens. Matter Phys.* 4.1 (Jan. 2013), pp. 263–285. DOI: `10.1146/annurev-conmatphys-030212-184329` (cit. on pp. 9, 12).

[65] A. Khintchine. "Korrelationstheorie der stationären stochastischen Prozesse". In: *Math. Ann.* 109.1 (1934), pp. 604–615. DOI: `10.1007/bf01449156` (cit. on p. 10).

[66] R. Kohlrausch. "Theorie des elektrischen Rückstandes in der Leidener Flasche". In: *Ann. Phys. (Berlin)* 167.2 (1854), pp. 179–214. DOI: `10.1002/andp.18541670203` (cit. on p. 11).

[67] G. Williams and D. C. Watts. "Non-symmetrical dielectric relaxation behaviour arising from a simple empirical decay function". In: *Trans. Faraday Soc.* 66 (1970), p. 80. DOI: `10.1039/tf9706600080` (cit. on p. 11).

[68] P. Lunkenheimer, U. Schneider, R. Brand, and A. Loid. "Glassy dynamics". In: *Contemp. Phys.* 41.1 (2000), pp. 15–36. DOI: `10.1080/001075100181259` (cit. on p. 11).

[69] T. Blochowicz, E. A. Rössler, and M. Vogel. "Relaxation Processes in Molecular Liquids". In: Wiley, 2021, pp. 1013–1029. DOI: `10.1002/9781118801017.ch8.6` (cit. on p. 11).

[70] H. Jansson, R. Bergman, and J. Swenson. "Slow dielectric response of Debye-type in water and other hydrogen bonded liquids". In: *J. Mol. Struct.* 972.1-3 (2010), pp. 92–98. DOI: `10.1016/j.molstruc.2010.01.072` (cit. on p. 11).

[71] A. Einstein. "On the theory of the Brownian movement". In: *Ann. Phys. (Berlin)* 19.4 (1906), pp. 371–381 (cit. on p. 12).

[72] P. J. W. Debye. *Polar molecules*. Chemical Catalog Company, Incorporated, 1929 (cit. on p. 12).

[73] S. F. Swallen, P. A. Bonvallet, R. J. McMahon, and M. D. Ediger. "Self-Diffusion ofitris/i-Naphthylbenzene near the Glass Transition Temperature". In: *Phys. Rev. Lett* 90.1 (2003), p. 015901. DOI: `10.1103/physrevlett.90.015901` (cit. on pp. 12, 84).

[74] M. G. Mazza, N. Giovambattista, H. E. Stanley, and F. W. Starr. "Connection of translational and rotational dynamical heterogeneities with the breakdown of the Stokes-Einstein and Stokes-Einstein-Debye relations in water". In: *Phys. Rev. E* 76.3 (2007), p. 031203. DOI: `10.1103/physreve.76.031203` (cit. on pp. 12, 65, 84, 85).

[75] R. Meier, E. Schneider, and E. A. Rössler. "Change of translational-rotational coupling in liquids revealed by field-cycling sup1/supH NMR". In: *J. Chem. Phys.* 142.3 (2015), p. 034503. DOI: `10.1063/1.4904719` (cit. on pp. 12, 84).

[76] M. Becher, E. Steinrücken, and M. Vogel. "On the relation between reorientation and diffusion in glass-forming ionic liquids with microheterogeneous structures". In: *J. Chem. Phys.* 151.19 (2019), p. 194503. DOI: `10.1063/1.5128420` (cit. on pp. 12, 85).

[77] H. Cummins, G. Li, Y. Hwang, G. Shen, W. Du, J. Hernandez, and N. Tao. "Dynamics of supercooled liquids and glasses: comparison of experiments with theoretical predictions". In: *Z. Phys. B Con. Mat.* 103.3 (1997), pp. 501–519. DOI: `10.1007/s002570050405` (cit. on p. 12).

[78] G. S. Fulcher. "ANALYSIS OF RECENT MEASUREMENTS OF THE VISCOSITY OF GLASSES". In: *J. Am. Ceram. Soc.* 8.6 (1925), pp. 339–355. DOI: `10.1111/j.1151-2916.1925.tb16731.x` (cit. on pp. 13, 110).

[79] G. Tammann and W. Hesse. “Die Abhängigkeit der Viscosität von der Temperatur bie unterkühlten Flüssigkeiten”. In: *Z. Anorg. Allg. Chem.* 156.1 (1926), pp. 245–257. DOI: `10.1002/zaac.19261560121` (cit. on pp. 13, 110).

[80] V. N. Novikov and A. P. Sokolov. “Temperature Dependence of Structural Relaxation in Glass-Forming Liquids and Polymers”. In: *Entropy* 24.8 (2022), p. 1101. DOI: `10.3390/e24081101` (cit. on pp. 13, 101, 102).

[81] P. J. Flory. “Statistical thermodynamics of semi-flexible chain molecules”. In: *Proc. R. Soc. Lond. A* 234.1196 (1956), pp. 60–73. DOI: `10.1098/rspa.1956.0015` (cit. on p. 13).

[82] H.-P. Wittmann. “On the validity of the Gibbs–di-Marzio theory of the glass transition of lattice polymers”. In: *J. Chem. Phys.* 95.11 (1991), pp. 8449–8458. DOI: `10.1063/1.461274` (cit. on pp. 14, 102).

[83] M. Wolfgardt, J. Baschnagel, W. Paul, and K. Binder. “Entropy of glassy polymer melts: Comparison between Gibbs-DiMarzio theory and simulation”. In: *Phys. Rev. E* 54.2 (1996), pp. 1535–1543. DOI: `10.1103/physreve.54.1535` (cit. on pp. 14, 102).

[84] J. Baschnagel, M. Wolfgardt, W. Paul, and K. Binder. “Entropy theory and glass transition: A test by Monte Carlo simulation”. In: *J. Res. Natl. Inst. Stand. Technol.* 102.2 (1997), p. 159. DOI: `10.6028/jres.102.012` (cit. on pp. 14, 102).

[85] J.-P. Eckmann and I. Procaccia. “Ergodicity and slowing down in glass-forming systems with soft potentials: No finite-temperature singularities”. In: *Phys. Rev. E* 78.1 (2008), p. 011503. DOI: `10.1103/physreve.78.011503` (cit. on pp. 14, 102, 104).

[86] W. Gotze and L. Sjogren. “Relaxation processes in supercooled liquids”. In: *Rep. Prog. Phys.* 55.3 (1992), pp. 241–376. DOI: `10.1088/0034-4885/55/3/001` (cit. on pp. 14, 110, 167).

[87] W. Kob. “Course 5: Supercooled Liquids, the Glass Transition, and Computer Simulations”. In: *Slow Relaxations and nonequilibrium dynamics in condensed matter*. Ed. by J.-L. Barrat, M. Feigelman, J. Kurchan, and J. Dalibard. Vol. 199. Berlin, Heidelberg: Springer Berlin Heidelberg, 2003, pp. 199–269. ISBN: 978-3-540-44835-8. DOI: `10.1007/978-3-540-44835-8_5` (cit. on pp. 14, 110).

[88] L. M. C. Janssen. “Mode-Coupling Theory of the Glass Transition: A Primer”. In: *Front. Phys.* 6 (2018). DOI: `10.3389/fphy.2018.00097` (cit. on p. 14).

[89] G. Szamel. “Colloidal Glass Transition: Beyond Mode-Coupling Theory”. In: *Phys. Rev. Lett.* 90.22 (2003), p. 228301. DOI: `10.1103/PhysRevLett.90.228301` (cit. on p. 15).

[90] P. Mayer, K. Miyazaki, and D. R. Reichman. “Cooperativity beyond Caging: Generalized Mode-Coupling Theory”. In: *Phys. Rev. Lett* 97.9 (2006), p. 095702. DOI: `10.1103/PhysRevLett.97.095702` (cit. on p. 15).

[91] T. R. Kirkpatrick, D. Thirumalai, and P. G. Wolynes. “Scaling concepts for the dynamics of viscous liquids near an ideal glassy state”. In: *Phys. Rev. A* 40.2 (1989), pp. 1045–1054. DOI: `10.1103/physreva.40.1045` (cit. on pp. 15, 16, 138, 148, 162, 184).

[92] G. Biroli and J.-P. Bouchaud. “The Random First-Order Transition Theory of Glasses: A Critical Assessment”. In: Wiley, 2012, pp. 31–113. DOI: `10.1002/9781118202470.ch2` (cit. on pp. 15, 16).

[93] V. Lubchenko and P. G. Wolynes. “Theory of Structural Glasses and Supercooled Liquids”. In: *Annu. Rev. Phys. Chem.* 58.1 (2007), pp. 235–266. DOI: `10.1146/annurev.physchem.58.032806.104653` (cit. on pp. 15, 101).

[94] A. K. Doolittle. “Studies in Newtonian flow. II. The dependence of the viscosity of liquids on free-space”. In: *J. Appl. Phys.* 22.12 (1951), pp. 1471–1475. DOI: `10.1063/1.1699894` (cit. on p. 16).

[95] M. H. Cohen and D. Turnbull. “Molecular transport in liquids and glasses”. In: *J. Chem. Phys.* 31.5 (1959), pp. 1164–1169. DOI: `10.1063/1.1730566` (cit. on p. 16).

[96] D. Turnbull and M. H. Cohen. “Free-volume model of the amorphous phase: glass transition”. In: *J. Chem. Phys.* 34.1 (1961), pp. 120–125. DOI: `10.1063/1.1731549` (cit. on p. 16).

[97] M. H. Cohen and G. Grest. “Liquid-glass transition, a free-volume approach”. In: *Phys. Rev. B* 20.3 (1979), p. 1077. DOI: `10.1103/physrevb.26.6313` (cit. on pp. 16, 102, 110, 128).

[98] F. W. Starr, S. Sastry, J. F. Douglas, and S. C. Glotzer. “What do we learn from the local geometry of glass-forming liquids?” In: *Phys. Rev. Lett* 89.12 (2002), p. 125501. DOI: `10.1103/PhysRevLett.89.125501` (cit. on pp. 16, 52).

[99] R. W. Hall and P. G. Wolynes. “The aperiodic crystal picture and free energy barriers in glasses”. In: *J. Chem. Phys.* 86.5 (1987), pp. 2943–2948. DOI: `10.1063/1.452045` (cit. on p. 16).

[100] J. C. Dyre, N. B. Olsen, and T. Christensen. “Local elastic expansion model for viscous-flow activation energies of glass-forming molecular liquids”. In: *Phys. Rev. B* 53.5 (1996), p. 2171. DOI: `10.1103/PhysRevB.53.2171` (cit. on p. 17).

[101] J. C. Dyre, T. Christensen, and N. B. Olsen. “Elastic models for the non-Arrhenius viscosity of glass-forming liquids”. In: *J. Non-Cryst. Solids* 352.42 (2006), pp. 4635–4642. DOI: `10.1016/j.jnoncrysol.2006.02.173` (cit. on p. 17).

[102] F. Puosi and D. Leporini. “Communication: Correlation of the instantaneous and the intermediate-time elasticity with the structural relaxation in glassforming systems”. In: *J. Chem. Phys.* 136.4 (2012), p. 041104. DOI: `10.1063/1.3681291` (cit. on p. 17).

[103] F. Puosi and D. Leporini. “The kinetic fragility of liquids as manifestation of the elastic softening”. In: *Eur. Phys. J. E* 38.8 (2015), pp. 1–7. DOI: `10.1140/epje/i2015-15087-2` (cit. on p. 17).

[104] D. S. Simmons, M. T. Cicerone, Q. Zhong, M. Tyagi, and J. F. Douglas. “Generalized localization model of relaxation in glass-forming liquids”. In: *Soft Matter* 8.45 (2012), pp. 11455–11461. DOI: `10.1039/C2SM26694F` (cit. on p. 17).

[105] B. A. P. Betancourt, P. Z. Hanakata, F. W. Starr, and J. F. Douglas. “Quantitative relations between cooperative motion, emergent elasticity, and free volume in model glass-forming polymer materials”. In: *Proc. Natl. Acad. Sci. U.S.A.* 112.10 (2015), pp. 2966–2971. DOI: `10.1073/pnas.1418654112` (cit. on p. 17).

[106] F. Puosi, A. Pasturel, N. Jakse, and D. Leporini. “Communication: Fast dynamics perspective on the breakdown of the Stokes-Einstein law in fragile glassformers”. In: *J. Chem. Phys.* 148.13 (2018), p. 131102. DOI: `10.1063/1.5025614` (cit. on p. 17).

[107] S. Mirigian and K. S. Schweizer. “Elastically cooperative activated barrier hopping theory of relaxation in viscous fluids. I. General formulation and application to hard sphere fluids”. In: *J. Chem. Phys.* 140.19 (2014), p. 194506. DOI: `10.1063/1.4874842` (cit. on pp. 17, 162).

[108] S. Mirigian and K. S. Schweizer. “Elastically cooperative activated barrier hopping theory of relaxation in viscous fluids. II. Thermal liquids”. In: *J. Chem. Phys.* 140.19 (2014), p. 194507. DOI: `10.1063/1.4874843` (cit. on pp. 17, 162).

[109] H. A. Kramers. “Brownian motion in a field of force and the diffusion model of chemical reactions”. In: *Physica* 7.4 (1940), pp. 284–304. DOI: `10.1016/S0031-8914(40)90098-2` (cit. on p. 17).

[110] P. Hänggi, P. Talkner, and M. Borkovec. “Reaction-rate theory: fifty years after Kramers”. In: *Rev. Mod. Phys.* 62.2 (1990), p. 251. DOI: `10.1103/revmodphys.62.251` (cit. on p. 17).

[111] A. D. Phan and K. S. Schweizer. “Elastically Collective Nonlinear Langevin Equation Theory of Glass-Forming Liquids: Transient Localization, Thermodynamic Mapping, and Cooperativity”. In: *J. Chem. Phys. B* 122.35 (2018), pp. 8451–8461. DOI: `10.1021/acs.jpcb.8b04975` (cit. on p. 17).

[112] B. Schmidtke, N. Petzold, R. Kahlau, and E. A. Rössler. “Reorientational dynamics in molecular liquids as revealed by dynamic light scattering: From boiling point to glass transition temperature”. In: *J. Chem. Phys.* 139.8 (2013), p. 084504. DOI: `10.1063/1.4817406` (cit. on pp. 18, 102, 103, 112, 113, 117, 122, 123, 154, 229, 232).

[113] C. Alba-Simionesco, D. Kivelson, and G. Tarjus. “Temperature, density, and pressure dependence of relaxation times in supercooled liquids”. In: *J. Chem. Phys.* 116.12 (2002), pp. 5033–5038. DOI: `10.1063/1.1452724` (cit. on pp. 18, 103).

[114] N. Petzold, B. Schmidtke, R. Kahlau, D. Bock, R. Meier, B. Micko, D. Kruk, and E. A. Rössler. “Evolution of the dynamic susceptibility in molecular glass formers: Results from light scattering, dielectric spectroscopy, and NMR”. In: *J. Chem. Phys.* 138.12 (2013), 12A510. DOI: `10.1063/1.4770055` (cit. on pp. 18, 102, 112, 122).

[115] B. Schmidtke, M. Hofmann, A. Lichtinger, and E. A. Rössler. “Temperature Dependence of the Segmental Relaxation Time of Polymers Revisited”. In: *Macromolecules* 48.9 (2015), pp. 3005–3013. DOI: `10.1021/acs.macromol.5b00204` (cit. on pp. 18, 102, 112, 122, 123, 134, 154).

[116] L. Hecht, R. Horstmann, B. Liebchen, and M. Vogel. “MD simulations of charged binary mixtures reveal a generic relation between high-and low-temperature behavior”. In: *J. Chem. Phys.* 154.2 (2021), p. 024501. DOI: `10.1063/5.0031417` (cit. on pp. 18, 39, 64, 68, 102, 103, 107, 113, 114, 120, 123, 134).

[117] R. Horstmann and M. Vogel. “Common behaviors associated with the glass transitions of water-like models”. In: *J. Chem. Phys.* 147.3 (2017), p. 034505. DOI: `10.1063/1.4993445` (cit. on pp. 18, 39, 68, 69, 72, 102, 114, 118, 138, 163).

[118] E. P. Sanjon, B. Drossel, and M. Vogel. “Effects of the bond polarity on the structural and dynamical properties of silica-like liquids”. In: *J. Chem. Phys.* 148.10 (2018), p. 104506. DOI: `10.1063/1.5017681` (cit. on pp. 18, 39, 64, 68, 102, 103, 126–128, 138).

[119] R. Shi, J. Russo, and H. Tanaka. “Common microscopic structural origin for water’s thermodynamic and dynamic anomalies”. In: *J. Chem. Phys.* 149.22 (2018), p. 224502. DOI: `10.1063/1.5055908` (cit. on pp. 18, 26, 85, 92, 94, 99).

[120] R. Shi, J. Russo, and H. Tanaka. "Origin of the emergent fragile-to-strong transition in supercooled water". In: *Proc. Natl. Acad. Sci. U.S.A.* 115.38 (2018), pp. 9444–9449. DOI: `10.1073/pnas.1807821115` (cit. on pp. 18, 25, 26, 85, 92, 94, 99, 102, 103, 109, 124, 183).

[121] R. Shi and H. Tanaka. "The anomalies and criticality of liquid water". In: *Proc. Natl. Acad. Sci. U.S.A.* 117.43 (2020), pp. 26591–26599. DOI: `10.1073/pnas.2008426117` (cit. on pp. 18, 25, 26, 83, 85, 94, 99, 102).

[122] F. Mallamace, C. Branca, M. Broccio, C. Corsaro, C.-Y. Mou, and S.-H. Chen. "The anomalous behavior of the density of water in the range 30 K < T < 373 K". In: *Proc. Natl. Acad. Sci. U.S.A.* 104.47 (2007), pp. 18387–18391. DOI: `10.1073/pnas.0706504104` (cit. on p. 19).

[123] C. G. Salzmann. "Advances in the experimental exploration of water's phase diagram". In: *J. Chem. Phys.* 150.6 (2019), p. 060901. DOI: `10.1063/1.5085163` (cit. on pp. 19, 20, 22).

[124] T. C. Hansen. "The everlasting hunt for new ice phases". In: *Nat. Commun.* 12.1 (2021). DOI: `10.1038/s41467-021-23403-6` (cit. on pp. 19, 22).

[125] P. Gallo, K. Amann-Winkel, C. A. Angell, M. A. Anisimov, F. Caupin, C. Chakravarty, E. Lascaris, T. Loerting, A. Z. Panagiotopoulos, J. Russo, J. A. Sellberg, H. E. Stanley, H. Tanaka, C. Vega, L. Xu, and L. G. M. Pettersson. "Water: A Tale of Two Liquids". In: *Chem. Rev.* 116.13 (2016), pp. 7463–7500. DOI: `10.1021/acs.chemrev.5b00750` (cit. on pp. 19–21, 67, 68).

[126] P. Gallo, J. Bachler, L. E. Bove, R. Böhmer, G. Camisasca, L. E. Coronas, H. R. Corti, I. de Almeida Ribeiro, M. de Koning, G. Franzese, V. Fuentes-Landete, C. Gainaru, T. Loerting, J. M. M. de Oca, P. H. Poole, M. Rovere, F. Sciortino, C. M. Tonauer, and G. A. Appignanesi. "Advances in the study of supercooled water". In: *Eur. Phys. J. E* 44.11 (2021). DOI: `10.1140/epje/s10189-021-00139-1` (cit. on p. 19).

[127] R. J. Speedy and C. A. Angell. "Isothermal compressibility of supercooled water and evidence for a thermodynamic singularity at -45°C". In: *J. Chem. Phys.* 65.3 (1976), pp. 851–858. DOI: `10.1063/1.433153` (cit. on pp. 19, 67).

[128] D. Rosenfeld and W. L. Woodley. "Deep convective clouds with sustained supercooled liquid water down to -37.5 °C". In: *Nature* 405.6785 (2000), pp. 440–442. DOI: `10.1038/35013030` (cit. on p. 19).

[129] K. H. Kim, K. Amann-Winkel, N. Giovambattista, A. Späh, F. Perakis, H. Pathak, M. L. Parada, C. Yang, D. Mariedahl, T. Eklund, T. J. Lane, S. You, S. Jeong, M. Weston, J. H. Lee, I. Eom, M. Kim, J. Park, S. H. Chun, P. H. Poole, and A. Nilsson. "Experimental observation of the liquid-liquid transition in bulk supercooled water under pressure". In: *Science* 370.6519 (2020), pp. 978–982. DOI: `10.1126/science.abb9385` (cit. on pp. 19, 21, 67).

[130] H. Pathak, A. Späh, N. Esmaeildoost, J. A. Sellberg, K. H. Kim, F. Perakis, K. Amann-Winkel, M. Ladd-Parada, J. Koliyadu, T. J. Lane, C. Yang, H. T. Lemke, A. R. Oggenfuss, P. J. M. Johnson, Y. Deng, S. Zerdane, R. Mankowsky, P. Beaud, and A. Nilsson. "Enhancement and maximum in the isobaric specific-heat capacity measurements of deeply supercooled water using ultrafast calorimetry". In: *Proc. Natl. Acad. Sci. U.S.A.* 118.6 (2021). DOI: `10.1073/pnas.2018379118` (cit. on p. 19).

[131] H. Kanno, R. J. Speedy, and C. A. Angell. "Supercooling of Water to -92°C Under Pressure". In: *Science* 189.4206 (1975), pp. 880–881. DOI: `10.1126/science.189.4206.880` (cit. on p. 19).

[132] A. Hallbrucker, E. Mayer, and G. P. Johari. "Glass-liquid transition and the enthalpy of devitrification of annealed vapor-deposited amorphous solid water: a comparison with hyperquenched glassy water". In: *J. Phys. Chem.* 93.12 (1989), pp. 4986–4990. DOI: `10.1021/j100349a061` (cit. on p. 19).

[133] G. P. Johari, A. Hallbrucker, and E. Mayer. "The glass–liquid transition of hyperquenched water". In: *Nature* 330.6148 (1987), pp. 552–553. DOI: `10.1038/330552a0` (cit. on p. 19).

[134] K. Yoshida, T. Yamaguchi, S. Kittaka, M.-C. Bellissent-Funel, and P. Fouquet. "Thermodynamic, structural, and dynamic properties of supercooled water confined in mesoporous MCM-41 studied with calorimetric, neutron diffraction, and neutron spin echo measurements". In: *J. Chem. Phys.* 129.5 (2008), p. 054702. DOI: `10.1063/1.2961029` (cit. on pp. 19, 27).

[135] S. Kittaka, S. Ishimaru, M. Kuranishi, T. Matsuda, and T. Yamaguchi. "Enthalpy and interfacial free energy changes of water capillary condensed in mesoporous silica, MCM-41 and SBA-15". In: *Phys. Chem. Chem. Phys.* 8.27 (2006), pp. 3223–3231. DOI: `10.1039/b518365k` (cit. on pp. 19, 27).

[136] E. Mamontov. "Diffusion Dynamics of Water Molecules in a LiCl Solution: A Low-Temperature Crossover". In: *J. Phys. Chem. B* 113.43 (2009), pp. 14073–14078. DOI: `10.1021/jp904734y` (cit. on pp. 19, 25).

[137] S. Schneider and M. Vogel. “NMR studies on the coupling of ion and water dynamics on various time and length scales in glass-forming LiCl aqueous solutions”. In: *J. Chem. Phys.* 149.10 (2018), p. 104501. DOI: `10.1063/1.5047825` (cit. on p. 19).

[138] T. Loerting, V. Fuentes-Landete, P. H. Handle, M. Seidl, K. Amann-Winkel, C. Gainaru, and R. Böhmer. “The glass transition in high-density amorphous ice”. In: *J. Non-Cryst. Solids* 407 (2015), pp. 423–430. DOI: `10.1016/j.jnoncrysol.2014.09.003` (cit. on pp. 19, 25, 26).

[139] K. Amann-Winkel, R. Böhmer, F. Fujara, C. Gainaru, B. Geil, and T. Loerting. “Colloquium: Water’s controversial glass transitions”. In: *Rev. Mod. Phys.* 88.1 (2016), p. 011002. DOI: `10.1103/revmodphys.88.011002` (cit. on pp. 19–21, 67, 68).

[140] H. Whiting. “A New Theory of Cohesion Applied to the Thermodynamics of Liquids and Solids”. In: *Am. Acad. Arts Sci.* 19 (1883), p. 353. DOI: `10.2307/25138738` (cit. on p. 19).

[141] W. C. Röntgen. “Über die Constitution des flüssigen Wassers”. In: *Ann. Phys. (Berlin)* 281.1 (1892), pp. 91–97. DOI: `10.1002/andp.18922810108` (cit. on p. 19).

[142] H. E. Stanley, S. V. Buldyrev, M. Canpolat, O. Mishima, M. R. Sadr-Lahijany, A. Scala, and F. W. Starr. “The puzzling behavior of water at very low temperature”. In: *Phys. Chem. Chem. Phys.* 2.8 (2000), pp. 1551–1558. DOI: `10.1039/b000058m` (cit. on pp. 20, 67, 68).

[143] Y. Katayama, T. Hattori, H. Saitoh, T. Ikeda, K. Aoki, H. Fukui, and K. Funakoshi. “Structure of liquid water under high pressure up to 17 GPa”. In: *Phys. Rev. B* 81.1 (2010), p. 014109. DOI: `10.1103/physrevb.81.014109` (cit. on p. 20).

[144] O. Mishima and Y. Suzuki. “Propagation of the polyamorphic transition of ice and the liquid–liquid critical point”. In: *Nature* 419.6907 (2002), pp. 599–603. DOI: `10.1038/nature01106` (cit. on pp. 20, 67, 68).

[145] O. Mishima, L. D. Calvert, and E. Whalley. “An apparently first-order transition between two amorphous phases of ice induced by pressure”. In: *Nature* 314.6006 (1985), pp. 76–78. DOI: `10.1038/314076a0` (cit. on p. 20).

[146] L. E. Bove, F. Pietrucci, A. M. Saitta, S. Klotz, and J. Teixeira. “On the link between polyamorphism and liquid-liquid transition: The case of salty water”. In: *J. Chem. Phys.* 151.4 (2019), p. 044503. DOI: `10.1063/1.5100959` (cit. on p. 21).

[147] F. W. Starr, C. Angell, and H. Stanley. “Prediction of entropy and dynamic properties of water below the homogeneous nucleation temperature”. In: *Physica A* 323 (2003), pp. 51–66. DOI: `10.1016/s0378-4371(03)00012-8` (cit. on pp. 21, 69, 85, 103).

[148] M. D. Marzio, G. Camisasca, M. Rovere, and P. Gallo. “Microscopic origin of the fragile to strong crossover in supercooled water: The role of activated processes”. In: *J. Chem. Phys.* 146.8 (2017), p. 084502. DOI: `10.1063/1.4975387` (cit. on pp. 21, 69).

[149] I. Saika-Voivod, P. H. Poole, and F. Sciortino. “Fragile-to-Strong Transition and Polyamorphism in the Energy Landscape of Liquid Silica”. In: *Nature* 412.6846 (2001), pp. 514–517. DOI: `10.1038/35087524` (cit. on pp. 21, 25, 69, 138).

[150] P. G. Debenedetti and F. H. Stillinger. “Supercooled liquids and the glass transition”. In: *Nature* 410.6825 (2001), pp. 259–267. DOI: `10.1038/35065704` (cit. on pp. 21, 29, 31, 69, 101, 138).

[151] H.-O. May, P. Mausbach, and G. Ruppeiner. “Thermodynamic geometry of supercooled water”. In: *Phys. Rev. E* 91.3 (2015), p. 032141. DOI: `10.1103/physreve.91.032141` (cit. on p. 21).

[152] R. J. Speedy. “Stability-limit conjecture. An interpretation of the properties of water”. In: *J. Phys. Chem.* 86.6 (1982), pp. 982–991. DOI: `10.1021/j100395a030` (cit. on p. 21).

[153] P. H. Poole, F. Sciortino, T. Grande, H. E. Stanley, and C. A. Angell. “Effect of Hydrogen Bonds on the Thermodynamic Behavior of Liquid Water”. In: *Phys. Rev. Lett.* 73.12 (1994), pp. 1632–1635. DOI: `10.1103/physrevlett.73.1632` (cit. on p. 21).

[154] C. A. Angell. “Insights into Phases of Liquid Water from Study of Its Unusual Glass-Forming Properties”. In: *Science* 319.5863 (2008), pp. 582–587. DOI: `10.1126/science.1131939` (cit. on pp. 21, 25).

[155] S. Sastry, P. G. Debenedetti, F. Sciortino, and H. E. Stanley. “Singularity-free interpretation of the thermodynamics of supercooled water”. In: *Phys. Rev. E* 53.6 (1996), pp. 6144–6154. DOI: `10.1103/physreve.53.6144` (cit. on p. 21).

[156] M. Matsumoto, S. Saito, and I. Ohmine. “Molecular dynamics simulation of the ice nucleation and growth process leading to water freezing”. In: *Nature* 416.6879 (2002), pp. 409–413. DOI: `10.1038/416409a` (cit. on p. 21).

[157] J. C. Palmer, P. H. Poole, F. Sciortino, and P. G. Debenedetti. “Advances in Computational Studies of the Liquid–Liquid Transition in Water and Water-Like Models”. In: *Chem. Rev.* 118.18 (2018), pp. 9129–9151. DOI: `10.1021/acs.chemrev.8b00228` (cit. on pp. 21, 68).

[158] J. L. F. Abascal and C. Vega. “Widom line and the liquid–liquid critical point for the TIP4P/2005 water model”. In: *J. Chem. Phys.* 133.23 (2010), p. 234502. DOI: `10.1063/1.3506860` (cit. on pp. 21, 68, 77, 97).

[159] T. Sumi and H. Sekino. “Effects of hydrophobic hydration on polymer chains immersed in supercooled water”. In: *RSC Adv.* 3.31 (2013), pp. 12743–12750. DOI: `10.1039/c3ra41320a` (cit. on pp. 21, 68, 77, 97).

[160] R. S. Singh, J. W. Biddle, P. G. Debenedetti, and M. A. Anisimov. “Two-state thermodynamics and the possibility of a liquid-liquid phase transition in supercooled TIP4P/2005 water”. In: *J. Chem. Phys.* 144.14 (2016), p. 144504. DOI: `10.1063/1.4944986` (cit. on pp. 21, 49, 68–72, 74, 77, 81, 97).

[161] J. Russo and H. Tanaka. “Understanding water’s anomalies with locally favoured structures”. In: *Nat. Commun.* 5.1 (2014), p. 3556. DOI: `10.1038/ncomms4556` (cit. on pp. 21, 23, 68–70, 74).

[162] P. G. Debenedetti, F. Sciortino, and G. H. Zerze. “Second critical point in two realistic models of water”. In: *Science* 369.6501 (2020), pp. 289–292. DOI: `10.1126/science.abb9796` (cit. on pp. 21, 68, 77, 97).

[163] Y. Li, J. Li, and F. Wang. “Liquid–liquid transition in supercooled water suggested by microsecond simulations”. In: *Proc. Natl. Acad. Sci. U.S.A.* 110.30 (2013), pp. 12209–12212. DOI: `10.1073/pnas.1309042110` (cit. on pp. 21, 68).

[164] Y. Ni and J. L. Skinner. “Evidence for a liquid-liquid critical point in supercooled water within the E3B3 model and a possible interpretation of the kink in the homogeneous nucleation line”. In: *J. Chem. Phys.* 144.21 (2016), p. 214501. DOI: `10.1063/1.4952991` (cit. on pp. 21, 68).

[165] P. H. Poole, I. Saika-Voivod, and F. Sciortino. “Density minimum and liquid–liquid phase transition”. In: *J. Phys.: Condens. Matter* 17.43 (2005), pp. L431–L437. DOI: `10.1088/0953-8984/17/43/l01` (cit. on p. 21).

[166] Y. Liu, A. Z. Panagiotopoulos, and P. G. Debenedetti. “Low-temperature fluid-phase behavior of ST2 water”. In: *J. Chem. Phys.* 131.10 (2009), p. 104508. DOI: `10.1063/1.3229892` (cit. on pp. 21, 68, 97).

[167] Y. Liu, J. C. Palmer, A. Z. Panagiotopoulos, and P. G. Debenedetti. “Liquid-liquid transition in ST2 water”. In: *J. Chem. Phys.* 137.21 (2012), p. 214505. DOI: `10.1063/1.4769126` (cit. on pp. 21, 68).

[168] V. Holten, J. C. Palmer, P. H. Poole, P. G. Debenedetti, and M. A. Anisimov. “Two-state thermodynamics of the ST2 model for supercooled water”. In: *J. Chem. Phys.* 140.10 (2014), p. 104502. DOI: `10.1063/1.4867287` (cit. on pp. 21, 23, 68–70, 74).

[169] R. Chen, E. Lascaris, and J. C. Palmer. “Liquid–liquid phase transition in an ionic model of silica”. In: *J. Chem. Phys.* 146.23 (2017), p. 234503. DOI: `10.1063/1.4984335` (cit. on pp. 21, 24, 68, 70, 74).

[170] D. T. Limmer and D. Chandler. “The putative liquid-liquid transition is a liquid-solid transition in atomistic models of water. II”. In: *J. Chem. Phys.* 138.21 (2013), p. 214504. DOI: `10.1063/1.4807479` (cit. on pp. 22, 68).

[171] S. D. Overduin and G. N. Patey. “Fluctuations and local ice structure in model supercooled water”. In: *J. Chem. Phys.* 143.9 (2015), p. 094504. DOI: `10.1063/1.4929787` (cit. on pp. 22, 68).

[172] D. T. Limmer and D. Chandler. “Comment on “Spontaneous liquid-liquid phase separation of water””. In: *Phys. Rev. E* 91.1 (2015), p. 016301. DOI: `10.1103/physreve.91.016301` (cit. on p. 22).

[173] V. Holten, D. T. Limmer, V. Molinero, and M. A. Anisimov. “Nature of the anomalies in the supercooled liquid state of the mW model of water”. In: *J. Chem. Phys.* 138.17 (2013), p. 174501. DOI: `10.1063/1.4802992` (cit. on pp. 22, 23, 68, 69, 97).

[174] A. Imre, K. Martinás, and L. P. N. Rebelo. “Thermodynamics of Negative Pressures in Liquids”. In: *J. Non-Equilib. Thermodyn.* 23.4 (1998). DOI: `10.1515/jnet.1998.23.4.351` (cit. on p. 22).

[175] G. Pallares, M. E. M. Azouzi, M. A. González, J. L. Aragones, J. L. F. Abascal, C. Valeriani, and F. Caupin. “Anomalies in bulk supercooled water at negative pressure”. In: *Proc. Natl. Acad. Sci. U.S.A.* 111.22 (2014), pp. 7936–7941. DOI: `10.1073/pnas.1323366111` (cit. on pp. 22, 68).

[176] F. Caupin and M. A. Anisimov. “Thermodynamics of supercooled and stretched water: Unifying two-structure description and liquid-vapor spinodal”. In: *J. Chem. Phys.* 151.3 (2019), p. 034503. DOI: `10.1063/1.5100228` (cit. on pp. 22, 69, 72).

[177] Q. Zheng, D. J. Durben, G. H. Wolf, and C. A. Angell. “Liquids at Large Negative Pressures: Water at the Homogeneous Nucleation Limit”. In: *Science* 254.5033 (1991), pp. 829–832. DOI: `10.1126/science.254.5033.829` (cit. on p. 22).

[178] A. Mitus, A. Patashinskii, and B. Shumilo. “The liquid-liquid phase transition”. In: *Phys. Lett. A* 113.1 (1985), pp. 41–44. DOI: `10.1016/0375-9601(85)90602-4` (cit. on p. 22).

[179] E. Ponyatovsky and O. Barkalov. “Pressure—induced amorphous phases”. In: *Mater. Sci. Rep.* 8.4 (1992), pp. 147–191. DOI: `10.1016/0920-2307(92)90007-n` (cit. on p. 22).

[180] P. H. Poole, T. Grande, C. A. Angell, and P. F. McMillan. “Polymorphic Phase Transitions in Liquids and Glasses”. In: *Science* 275.5298 (1997), pp. 322–323. DOI: `10.1126/science.275.5298.322` (cit. on p. 22).

[181] F. Caupin and M. A. Anisimov. “Minimal Microscopic Model for Liquid Polyamorphism and Water-like Anomalies”. In: *Phys. Rev. Lett.* 127.18 (2021), p. 185701. DOI: `10.1103/physrevlett.127.185701` (cit. on pp. 22, 23).

[182] M. A. Anisimov, M. Duška, F. Caupin, L. E. Amrhein, A. Rosenbaum, and R. J. Sadus. “Thermodynamics of Fluid Polyamorphism”. In: *Phys. Rev. X* 8.1 (2018), p. 011004. DOI: `10.1103/physrevx.8.011004` (cit. on pp. 22, 23, 69, 70).

[183] J. C. Palmer, F. Martelli, Y. Liu, R. Car, A. Z. Panagiotopoulos, and P. G. Debenedetti. “Metastable liquid–liquid transition in a molecular model of water”. In: *Nature* 510.7505 (2014), pp. 385–388. DOI: `10.1038/nature13405` (cit. on pp. 23, 69).

[184] L. G. Pettersson and A. Nilsson. “The structure of water from ambient to deeply supercooled”. In: *J. Non-Cryst. Solids* 407 (2015), pp. 399–417. DOI: `10.1016/j.jnoncrysol.2014.08.026` (cit. on pp. 23, 69).

[185] V. Holten and M. A. Anisimov. “Entropy-driven liquid–liquid separation in supercooled water”. In: *Sci. Rep.* 2.1 (2012), pp. 1–7. DOI: `10.1038/srep00713` (cit. on pp. 23, 69).

[186] C. E. Bertrand and M. A. Anisimov. “Peculiar Thermodynamics of the Second Critical Point in Supercooled Water”. In: *J. Phys. Chem. B* 115.48 (2011), pp. 14099–14111. DOI: `10.1021/jp204011z` (cit. on pp. 23, 69).

[187] H. Tanaka. “Thermodynamic anomaly and polyamorphism of water”. In: *Europhys. Lett.* 50.3 (2000), pp. 340–346. DOI: `10.1209/epl/i2000-00276-4` (cit. on pp. 23, 69).

[188] J. W. Biddle, R. S. Singh, E. M. Sparano, F. Ricci, M. A. González, C. Valeriani, J. L. F. Abascal, P. G. Debenedetti, M. A. Anisimov, and F. Caupin. “Two-structure thermodynamics for the TIP4P/2005 model of water covering supercooled and deeply stretched regions”. In: *J. Chem. Phys.* 146.3 (2017), p. 034502. DOI: `10.1063/1.4973546` (cit. on pp. 23, 69–72, 74).

[189] P. F. McMillan, G. N. Greaves, M. Wilson, M. C. Wilding, and D. Daisenberger. “Polyamorphism and Liquid–Liquid Phase Transitions in Amorphous Silicon and Supercooled Al2O3–Y2O3 Liquids”. In: *Liquid Polymorphism*. John Wiley & Sons, Ltd, 2013, pp. 309–353. ISBN: 9781118540350. DOI: `10.1002/9781118540350.ch12` (cit. on p. 23).

[190] R. Li, G. Sun, and L. Xu. “Anomalous properties and the liquid-liquid phase transition in gallium”. In: *J. Chem. Phys.* 145.5 (2016), p. 054506. DOI: `10.1063/1.4959891` (cit. on p. 23).

[191] W. Tang and J. H. Perepezko. “Polyamorphism and liquid-liquid transformations in D-mannitol”. In: *J. Chem. Phys.* 149.7 (2018), p. 074505. DOI: `10.1063/1.5041757` (cit. on p. 24).

[192] M. Zhu and L. Yu. “Polyamorphism of D-mannitol”. In: *J. Chem. Phys.* 146.24 (2017), p. 244503. DOI: `10.1063/1.4989961` (cit. on p. 24).

[193] F. Sciortino. “Silicon in silico”. In: *Nature Physics* 7.7 (2011), pp. 523–524. DOI: `10.1038/nphys2038` (cit. on p. 24).

[194] D. Dhabal, C. Chakravarty, V. Molinero, and H. K. Kashyap. “Comparison of liquid-state anomalies in Stillinger-Weber models of water, silicon, and germanium”. In: *J. Chem. Phys.* 145.21 (2016), p. 214502. DOI: `10.1063/1.4967939` (cit. on pp. 24, 68).

[195] G. Zhao, Y. J. Yu, J. L. Yan, M. C. Ding, X. G. Zhao, and H. Y. Wang. “Phase behavior of metastable liquid silicon at negative pressure: Ab initio molecular dynamics”. In: *Phys. Rev. B* 93.14 (2016), p. 140203. DOI: `10.1103/physrevb.93.140203` (cit. on pp. 24, 68, 97).

[196] A. Ben-Naim. “One-dimensional model for water and aqueous solutions. I. Pure liquid water”. In: *J. Phys. Chem.* 128.2 (2008), p. 024505. DOI: `10.1063/1.2818051` (cit. on pp. 24, 68).

[197] F. Smallenburg, L. Filion, and F. Sciortino. “Erasing no-man’s land by thermodynamically stabilizing the liquid–liquid transition in tetrahedral particles”. In: *Nat. Phys.* 10.9 (2014), pp. 653–657 (cit. on pp. 24, 68).

[198] L. Xu, S. V. Buldyrev, C. A. Angell, and H. E. Stanley. “Thermodynamics and dynamics of the two-scale spherically symmetric Jagla ramp model of anomalous liquids”. In: *Phys. Rev. E* 74.3 (2006), p. 031108. DOI: `10.1103/physreve.74.031108` (cit. on pp. 24, 68).

[199] V. Bianco, O. Vilanova, G. Franzese, V. Bianco, O. Vilanova, and G. Franzese. “Polyamorphism and polymorphism of a confined water monolayer: liquid-liquid critical point, liquid-crystal and crystal-crystal phase transitions”. In: *Perspectives and Challenges in Statistical Physics and Complex Systems for the Next Decade*. WORLD SCIENTIFIC, 2014, pp. 126–149. DOI: `10.1142/9789814590143_0008` (cit. on p. 24).

[200] F. H. Stillinger and T. A. Weber. “Computer simulation of local order in condensed phases of silicon”. In: *Phys. Rev. B* 31.8 (1985), pp. 5262–5271. DOI: `10.1103/physrevb.31.5262` (cit. on pp. 24, 68).

[201] V. Molinero, S. Sastry, and C. A. Angell. “Tuning of Tetrahedrality in a Silicon Potential Yields a Series of Monatomic (Metal-like) Glass Formers of Very High Fragility”. In: *Phys. Rev. Lett.* 97.7 (2006), p. 075701. DOI: `10.1103/physrevlett.97.075701` (cit. on pp. 24, 68).

[202] C. A. Angell and V. Kapko. “Potential tuning in the S–W system. (i) BringingiT/isubc,2/subto ambient pressure, and (ii) collidingiT/isubc,2/subwith the liquid–vapor spinodal”. In: *J. Stat. Mech: Theory Exp.* 2016.9 (2016), p. 094004. DOI: `10.1088/1742-5468/2016/09/094004` (cit. on pp. 24, 68).

[203] F. Smallenburg and F. Sciortino. “Tuning the Liquid-Liquid Transition by Modulating the Hydrogen-Bond Angular Flexibility in a Model for Water”. In: *Phys. Rev. Lett.* 115.1 (2015), p. 015701. DOI: `10.1103/physrevlett.115.015701` (cit. on pp. 24, 39, 68).

[204] P. F. McMillan, M. Wilson, M. C. Wilding, D. Daisenberger, M. Mezouar, and G. N. Greaves. “Polyamorphism and liquid–liquid phase transitions: challenges for experiment and theory”. In: *J. Phys. Condens* 19.41 (2007), p. 415101. DOI: `10.1088/0953-8984/19/41/415101` (cit. on p. 24).

[205] J. Qvist, C. Mattea, E. P. Sunde, and B. Halle. “Rotational dynamics in supercooled water from nuclear spin relaxation and molecular simulations”. In: *J. Chem. Phys.* 136.20 (2012), p. 204505. DOI: `10.1063/1.4720941` (cit. on p. 24).

[206] O. Andersson and A. Inaba. “Dielectric properties of high-density amorphous ice under pressure”. In: *Phys. Rev. B* 74.18 (2006), p. 184201. DOI: `10.1103/physrevb.74.184201` (cit. on pp. 24, 25, 96, 98).

[207] E. Steinrücken, M. Weigler, V. Schiller, and M. Vogel. “Evolution of Dynamical Susceptibilities of Confined Water from Room Temperature down to the Glass Transition” (cit. on pp. 24, 28).

[208] C. A. Angell. “Liquid Fragility and the Glass Transition in Water and Aqueous Solutions”. In: *Chem. Rev.* 102.8 (2002), pp. 2627–2650. DOI: `10.1021/cr000689q` (cit. on pp. 25, 26, 85, 103).

[209] J. Bachler, J. Giebelmann, K. Amann-Winkel, and T. Loerting. “Pressure-annealed high-density amorphous ice made from vitrified water droplets: A systematic calorimetry study on water’s second glass transition”. In: *J. Chem. Phys.* 157.6 (2022), p. 064502. DOI: `10.1063/5.0100571` (cit. on pp. 25, 26).

[210] P. H. Poole, S. R. Becker, F. Sciortino, and F. W. Starr. “Dynamical Behavior Near a Liquid–Liquid Phase Transition in Simulations of Supercooled Water”. In: *J. Phys. Chem. B* 115.48 (2011), pp. 14176–14183. DOI: `10.1021/jp204889m` (cit. on pp. 25, 50, 69, 72, 83, 98).

[211] P. H. Poole, M. Hemmati, and C. A. Angell. “Comparison of Thermodynamic Properties of Simulated Liquid Silica and Water”. In: *Phys. Rev. Lett.* 79.12 (1997), pp. 2281–2284. DOI: `10.1103/PhysRevLett.79.2281` (cit. on p. 25).

[212] D. J. Lacks. “First-Order Amorphous-Amorphous Transformation in Silica”. In: *Phys. Rev. Lett.* 84.20 (2000), pp. 4629–4632. DOI: `10.1103/physrevlett.84.4629` (cit. on p. 25).

[213] E. Lascaris, M. Hemmati, S. V. Buldyrev, H. E. Stanley, and C. A. Angell. “Diffusivity and short-time dynamics in two models of silica”. In: *J. Chem. Phys.* 142.10 (2015), p. 104506. DOI: `10.1063/1.4913747` (cit. on pp. 25, 69, 83, 109).

[214] J. Geske, B. Drossel, and M. Vogel. “Fragile-to-strong transition in liquid silica”. In: *AIP Advances* 6.3 (2016), p. 035131. DOI: `10.1063/1.4945445` (cit. on pp. 25, 102, 126–128, 138).

[215] P. Richet. “Viscosity and configurational entropy of silicate melts”. In: *GCA* 48.3 (1984), pp. 471–483. DOI: `10.1016/0016-7037(84)90275-8` (cit. on p. 25).

[216] J. Engstler and N. Giovambattista. “Heating- and pressure-induced transformations in amorphous and hexagonal ice: A computer simulation study using the TIP4P/2005 model”. In: *J. Chem. Phys.* 147.7 (2017), p. 074505. DOI: `10.1063/1.4998747` (cit. on pp. 25, 69).

[217] O. Andersson. “Relaxation Time of Water’s High-Density Amorphous Ice Phase”. In: *Phys. Rev. B* 95.20 (2005), p. 205503. DOI: `10.1103/physrevlett.95.205503` (cit. on pp. 25, 96, 98).

[218] L. P. Singh, B. Issenmann, and F. Caupin. "Pressure dependence of viscosity in supercooled water and a unified approach for thermodynamic and dynamic anomalies of water". In: *Proc. Natl. Acad. Sci. U.S.A.* 114.17 (2017), pp. 4312–4317. DOI: 10.1073/pnas.1619501114 (cit. on pp. 25, 85, 92, 94, 95, 99, 183).

[219] P. M. de Hijes, E. Sanz, L. Joly, C. Valeriani, and F. Caupin. "Viscosity and self-diffusion of supercooled and stretched water from molecular dynamics simulations". In: *J. Chem. Phys.* 149.9 (2018), p. 094503. DOI: 10.1063/1.5042209 (cit. on pp. 25, 70, 83, 85, 92, 94–96).

[220] H. Tanaka. "Simple physical model of liquid water". In: *J. Chem. Phys.* 112.2 (2000), pp. 799–809. DOI: 10.1063/1.480609 (cit. on pp. 26, 85, 95, 102).

[221] S. Cukierman. "Et tu, Grotthuss! and other unfinished stories". In: *Biochim. Biophys. Acta* 1757.8 (2006), pp. 876–885. DOI: 10.1016/j.bbabio.2005.12.001 (cit. on pp. 26, 37).

[222] Y. Yue and C. A. Angell. "Clarifying the glass-transition behaviour of water by comparison with hyperquenched inorganic glasses". In: *Nature* 427.6976 (2004), pp. 717–720. DOI: 10.1038/nature02295 (cit. on p. 26).

[223] S. Capaccioli and K. L. Ngai. "Resolving the controversy on the glass transition temperature of water?" In: *J. Chem. Phys.* 135.10 (2011), p. 104504. DOI: 10.1063/1.3633242 (cit. on p. 26).

[224] J. H. Melillo and S. Cerveny. "Isotope Effect on the Dynamics of Hydrophilic Solutions at Supercooled Temperatures". In: *ACS Symposium Series*. American Chemical Society, 2021, pp. 263–281. ISBN: 9780841298484. DOI: 10.1021/bk-2021-1375.ch012 (cit. on p. 26).

[225] C. Gainaru, A. L. Agapov, V. Fuentes-Landete, K. Amann-Winkel, H. Nelson, K. W. Köster, A. I. Kolesnikov, V. N. Novikov, R. Richert, R. Böhmer, T. Loerting, and A. P. Sokolov. "Anomalously large isotope effect in the glass transition of water". In: *Proc. Natl. Acad. Sci. U.S.A.* 111.49 (2014), pp. 17402–17407. DOI: 10.1073/pnas.1411620111 (cit. on p. 26).

[226] E. H. Hardy, A. Zygar, M. D. Zeidler, M. Holz, and F. D. Sacher. "Isotope effect on the translational and rotational motion in liquid water and ammonia". In: *J. Chem. Phys.* 114.7 (2001), pp. 3174–3181. DOI: 10.1063/1.1340584 (cit. on p. 26).

[227] G. H. Findenegg, S. Jähnert, D. Akcakayiran, and A. Schreiber. "Freezing and Melting of Water Confined in Silica Nanopores". In: *ChemPhysChem* 9.18 (2008), pp. 2651–2659. DOI: 10.1002/cphc.200800616 (cit. on p. 27).

[228] A. Faraone, L. Liu, C.-Y. Mou, C.-W. Yen, and S.-H. Chen. "Fragile-to-strong liquid transition in deeply supercooled confined water". In: *J. Chem. Phys.* 121.22 (2004), p. 10843. DOI: 10.1063/1.1832595 (cit. on p. 27).

[229] M. Rosenstihl, K. Kämpf, F. Klameth, M. Sattig, and M. Vogel. "Dynamics of interfacial water". In: *J. Non-Cryst. Solids* 407 (2015), pp. 449–458. DOI: 10.1016/j.jnoncrysol.2014.08.040 (cit. on pp. 27, 28, 137, 141, 143, 156).

[230] J. Swenson, H. Jansson, and R. Bergman. "Relaxation Processes in Supercooled Confined Water and Implications for Protein Dynamics". In: *Phys. Rev. Lett.* 96.24 (2006), p. 247802. DOI: 10.1103/physrevlett.96.247802 (cit. on p. 27).

[231] S. Pawlus, S. Khodadadi, and A. P. Sokolov. "Conductivity in Hydrated Proteins: No Signs of the Fragile-to-Strong Crossover". In: *Phys. Rev. Lett.* 100.10 (2008), p. 108103. DOI: 10.1103/physrevlett.100.108103 (cit. on p. 27).

[232] M. Vogel. "Origins of Apparent Fragile-to-Strong Transitions of Protein Hydration Waters". In: *Phys. Rev. Lett.* 101.22 (2008), p. 225701. DOI: 10.1103/physrevlett.101.225701 (cit. on p. 27).

[233] J. Swenson. "The glass transition and fragility of supercooled confined water". In: *J. Phys.: Condens. Matter* 16.45 (2004), S5317–S5327. DOI: 10.1088/0953-8984/16/45/002 (cit. on p. 27).

[234] S. Cerveny, F. Barroso-Bujans, Á. Alegría, and J. Colmenero. "Dynamics of Water Intercalated in Graphite Oxide". In: *J. Phys. Chem. C* 114.6 (2010), pp. 2604–2612. DOI: 10.1021/jp907979v (cit. on pp. 27, 28).

[235] F. Bruni, R. Mancinelli, and M. A. Ricci. "Multiple relaxation processes versus the fragile-to-strong transition in confined water". In: *Phys. Chem. Chem. Phys.* 13.44 (2011), pp. 19773–19779. DOI: 10.1039/c1cp22029b (cit. on p. 27).

[236] M. Sattig and M. Vogel. "Dynamic Crossovers and Stepwise Solidification of Confined Water: A sup2/supH NMR Study". In: *J. Phys. Chem. Lett.* 5.1 (2014), pp. 174–178. DOI: 10.1021/jz402539r (cit. on p. 27).

[237] C. Lederle, M. Sattig, and M. Vogel. "Effects of Partial Crystallization on the Dynamics of Water in Mesoporous Silica". In: *J. Phys. Chem. C* 122.27 (2018), pp. 15427–15434. DOI: 10.1021/acs.jpcc.8b03815 (cit. on p. 27).

[238] S. Cerveny, G. A. Schwartz, R. Bergman, and J. Swenson. "Glass Transition and Relaxation Processes in Supercooled Water". In: *Phys. Rev. Lett.* 93.24 (2004), p. 245702. DOI: `10.1103/physrevlett.93.245702` (cit. on pp. 27, 28).

[239] J. Hedström, J. Swenson, R. Bergman, H. Jansson, and S. Kittaka. "Does confined water exhibit a fragile-to-strong transition?" In: *Eur. Phys. J. Special Topics* 141.1 (2007), pp. 53–56. DOI: `10.1140/epjst/e2007-00016-0` (cit. on p. 27).

[240] S. Capaccioli, K. L. Ngai, and N. Shinyashiki. "The Johari-Goldstein -Relaxation of Water". In: *J. Chem. Phys. B* 111.28 (2007), pp. 8197–8209. DOI: `10.1021/jp071857m` (cit. on pp. 27, 28).

[241] G. Buntkowsky and M. Vogel. "Small Molecules, Non-Covalent Interactions, and Confinement". In: *Molecules* 25.14 (2020), p. 3311. DOI: `10.3390/molecules25143311` (cit. on p. 28).

[242] T. H. G. Carr, J. J. Shephard, and C. G. Salzmann. "Spectroscopic Signature of Stacking Disorder in Ice I". In: *J. Phys. Chem. Lett.* 5.14 (2014), pp. 2469–2473. DOI: `10.1021/jz500996p` (cit. on p. 28).

[243] Y. Yao, V. Fella, W. Huang, K. A. I. Zhang, K. Landfester, H.-J. Butt, M. Vogel, and G. Floudas. "Crystallization and Dynamics of Water Confined in Model Mesoporous Silica Particles: Two Ice Nuclei and Two Fractions of Water". In: *Langmuir* 35.17 (2019), pp. 5890–5901. DOI: `10.1021/acs.langmuir.9b00496` (cit. on p. 28).

[244] J. Swenson and S. Cerveny. "Dynamics of deeply supercooled interfacial water". In: *J. Phys.: Condens. Matter* 27.3 (2014), p. 033102. DOI: `10.1088/0953-8984/27/3/033102` (cit. on p. 28).

[245] M. Sattig, S. Reutter, F. Fujara, M. Werner, G. Buntkowsky, and M. Vogel. "NMR studies on the temperature-dependent dynamics of confined water". In: *Phys. Chem. Chem. Phys.* 16.36 (2014), pp. 19229–19240. DOI: `10.1039/c4cp02057j` (cit. on pp. 28, 92).

[246] K. Elamin, H. Jansson, and J. Swenson. "Dynamics of aqueous binary glass-formers confined in MCM-41". In: *Phys. Chem. Chem. Phys.* 17.19 (2015), pp. 12978–12987. DOI: `10.1039/c5cp00751h` (cit. on p. 28).

[247] S. Capaccioli, K. L. Ngai, S. Ancherbak, M. Bertoldo, G. Ciampalini, M. S. Thayyil, and L.-M. Wang. "The JG b/b-relaxation in water and impact on the dynamics of aqueous mixtures and hydrated biomolecules". In: *J. Chem. Phys.* 151.3 (2019), p. 034504. DOI: `10.1063/1.5100835` (cit. on p. 28).

[248] M. Allen and D. Tildesley. *Computer Simulation of Liquids*. Oxford: Clarendon, 2017. 640 pp. ISBN: 9780198803195 (cit. on pp. 29, 30).

[249] M. J. Abraham, T. Murtola, R. Schulz, S. Páll, J. C. Smith, B. Hess, and E. Lindahl. "GROMACS: High performance molecular simulations through multi-level parallelism from laptops to supercomputers". In: *SoftwareX* 1-2 (2015), pp. 19–25. DOI: `10.1016/j.softx.2015.06.001` (cit. on p. 29).

[250] S. Páll and B. Hess. "A flexible algorithm for calculating pair interactions on SIMD architectures". In: *Comput. Phys. Commun.* 184.12 (2013), pp. 2641–2650. DOI: `10.1016/j.cpc.2013.06.003` (cit. on p. 29).

[251] D. van der Spoel, E. Lindahl, B. Hess, G. Groenhof, A. E. Mark, and H. J. C. Berendsen. "GROMACS: Fast, flexible, and free". In: *J. Comput. Chem.* 26.16 (2005), pp. 1701–1718. DOI: `10.1002/jcc.20291` (cit. on p. 29).

[252] H. Berendsen, D. van der Spoel, and R. van Drunen. "GROMACS: A message-passing parallel molecular dynamics implementation". In: *Comput. Phys. Commun.* 91.1-3 (1995), pp. 43–56. DOI: `10.1016/0010-4655(95)00042-e` (cit. on p. 29).

[253] E. Lindahl, B. Hess, and D. van der Spoel. "GROMACS 3.0: a package for molecular simulation and trajectory analysis". In: *J. Mol. Model.* 7.8 (2001), pp. 306–317. DOI: `10.1007/s008940100045` (cit. on p. 29).

[254] B. Hess, C. Kutzner, D. van der Spoel, and E. Lindahl. "GROMACS 4: Algorithms for Highly Efficient, Load-Balanced, and Scalable Molecular Simulation". In: *J. Chem. Theory Comput.* 4.3 (2008), pp. 435–447. DOI: `10.1021/ct700301q` (cit. on p. 29).

[255] E. Lindahl, M. J. Abraham, B. Hess, and D. van der Spoel. "GROMACS 2020.6 Manual". In: *Zenodo* (2021). DOI: `10.5281/ZENODO.4576060` (cit. on p. 29).

[256] M. Born and R. Oppenheimer. "Zur Quantentheorie der Molekeln". In: *Ann. Phys. (Berlin)* 389.20 (1927), pp. 457–484. DOI: `10.1002/andp.19273892002` (cit. on p. 30).

[257] W. C. Swope, H. C. Andersen, P. H. Berens, and K. R. Wilson. "A computer simulation method for the calculation of equilibrium constants for the formation of physical clusters of molecules: Application to small water clusters". In: *J. Chem. Phys.* 76.1 (1982), pp. 637–649. DOI: `10.1063/1.442716` (cit. on p. 30).

[258] H. J. C. Berendsen. "Transport Properties Computed by Linear Response through Weak Coupling to a Bath". In: *Model Simul Mat Sci Eng* (1991), pp. 139–155. DOI: `10.1007/978-94-011-3546-7_7` (cit. on p. 32).

[259] S. Nosé. “A molecular dynamics method for simulations in the canonical ensemble”. In: *Mol. Phys.* 52.2 (1984), pp. 255–268. doi: 10.1080/00268978400101201 (cit. on p. 32).

[260] S. Nosé. “A unified formulation of the constant temperature molecular dynamics methods”. In: *J. Chem. Phys.* 81.1 (1984), pp. 511–519. doi: 10.1063/1.447334 (cit. on p. 32).

[261] W. G. Hoover. “Canonical dynamics: Equilibrium phase-space distributions”. In: *Phys. Rev. A* 31.3 (1985), pp. 1695–1697. doi: 10.1103/physreva.31.1695 (cit. on p. 32).

[262] G. J. Martyna, M. L. Klein, and M. Tuckerman. “Nosé–Hoover chains: The canonical ensemble via continuous dynamics”. In: *J. Chem. Phys.* 97.4 (1992), pp. 2635–2643. doi: 10.1063/1.463940 (cit. on p. 33).

[263] G. Bussi, D. Donadio, and M. Parrinello. “Canonical sampling through velocity rescaling”. In: *J. Chem. Phys.* 126.1 (2007), p. 014101. doi: 10.1063/1.2408420 (cit. on p. 33).

[264] M. Parrinello and A. Rahman. “Polymorphic transitions in single crystals: A new molecular dynamics method”. In: *J. Appl. Phys.* 52.12 (1981), pp. 7182–7190. doi: 10.1063/1.328693 (cit. on p. 33).

[265] S. Nosé and M. Klein. “Constant pressure molecular dynamics for molecular systems”. In: *Mol. Phys.* 50.5 (1983), pp. 1055–1076. doi: 10.1080/00268978300102851 (cit. on p. 33).

[266] T. Darden, D. York, and L. Pedersen. “Particle mesh Ewald: An N·log(N) method for Ewald sums in large systems”. In: *J. Chem. Phys.* 98.12 (1993), pp. 10089–10092. doi: 10.1063/1.464397 (cit. on p. 34).

[267] J. E. Jones. “On the determination of molecular fields. —II. From the equation of state of a gas”. In: *Proc. R. Soc. Lond. A* 106.738 (1924), pp. 463–477. doi: 10.1098/rspa.1924.0082 (cit. on p. 35).

[268] B. Hess, H. Bekker, H. J. C. Berendsen, and J. G. E. M. Fraaije. “LINCS: A linear constraint solver for molecular simulations”. In: *J. Comput. Chem.* 18.12 (1997), pp. 1463–1472. doi: 10.1002/(sici)1096-987x(199709)18:12<1463::aid-jcc4>3.0.co;2-h (cit. on p. 36).

[269] J.-P. Ryckaert, G. Ciccotti, and H. J. Berendsen. “Numerical integration of the cartesian equations of motion of a system with constraints: molecular dynamics of n-alkanes”. In: *J. Comput. Phys.* 23.3 (1977), pp. 327–341. doi: 10.1016/0021-9991(77)90098-5 (cit. on p. 36).

[270] S. Miyamoto and P. A. Kollman. “Settle: An analytical version of the SHAKE and RATTLE algorithm for rigid water models”. In: *J. Comput. Chem.* 13.8 (1992), pp. 952–962. doi: 10.1002/jcc.540130805 (cit. on p. 36).

[271] A. Grossfield, P. N. Patrone, D. R. Roe, A. J. Schultz, D. Siderius, and D. M. Zuckerman. “Best Practices for Quantification of Uncertainty and Sampling Quality in Molecular Simulations [Article v1.0]”. In: *Living J. Comp. Mol. Sci.* 1.1 (2019). doi: 10.33011/livecoms.1.1.5067 (cit. on p. 36).

[272] E. Braun, J. Gilmer, H. B. Mayes, D. L. Mobley, J. I. Monroe, S. Prasad, and D. M. Zuckerman. “Best Practices for Foundations in Molecular Simulations [Article v1.0]”. In: *Living J. Comp. Mol. Sci.* 1.1 (2019). doi: 10.33011/livecoms.1.1.5957 (cit. on p. 36).

[273] P. A. Hunt, C. R. Ashworth, and R. P. Matthews. “Hydrogen bonding in ionic liquids”. In: *Chem. Soc. Rev.* 44.5 (2015), pp. 1257–1288. doi: 10.1039/c4cs00278d (cit. on p. 37).

[274] V. Molinero and E. B. Moore. “Water Modeled As an Intermediate Element between Carbon and Silicon”. In: *J. Chem. Phys. B* 113.13 (2008), pp. 4008–4016. doi: 10.1021/jp805227c (cit. on p. 37).

[275] H. J. C. Berendsen, J. R. Grigera, and T. P. Straatsma. “The missing term in effective pair potentials”. In: *J. Phys. Chem.* 91.24 (1987), pp. 6269–6271. doi: 10.1021/j100308a038 (cit. on pp. 37, 138).

[276] J. L. F. Abascal and C. Vega. “A general purpose model for the condensed phases of water: TIP4P/2005”. In: *J. Chem. Phys.* 123.23 (2005), p. 234505. doi: 10.1063/1.2121687 (cit. on pp. 37, 70).

[277] C. Vega and J. L. F. Abascal. “Simulating water with rigid non-polarizable models: a general perspective”. In: *Phys. Chem. Chem. Phys.* 13.44 (2011), p. 19663. doi: 10.1039/c1cp22168j (cit. on pp. 37, 38, 57).

[278] S. Chatterjee, P. G. Debenedetti, F. H. Stillinger, and R. M. Lynden-Bell. “A computational investigation of thermodynamics, structure, dynamics and solvation behavior in modified water models”. In: *J. Chem. Phys.* 128.12 (2008), p. 124511. doi: 10.1063/1.2841127 (cit. on pp. 38, 57).

[279] L. A. Báez and P. Clancy. “Existence of a density maximum in extended simple point charge water”. In: *J. Chem. Phys.* 101.11 (1994), pp. 9837–9840. doi: 10.1063/1.467949 (cit. on pp. 38, 57).

[280] C. Vega and J. L. F. Abascal. “Relation between the melting temperature and the temperature of maximum density for the most common models of water”. In: *J. Chem. Phys.* 123.14 (2005), p. 144504. DOI: `10.1063/1.2056539` (cit. on pp. 38, 57).

[281] A. A. Milischuk and B. M. Ladanyi. “Structure and dynamics of water confined in silica nanopores”. In: *J. Chem. Phys.* 135.17 (2011), p. 174709. DOI: `10.1063/1.3657408` (cit. on p. 38).

[282] J. L. F. Abascal, E. Sanz, R. G. Fernández, and C. Vega. “A potential model for the study of ices and amorphous water: TIP4P/Ice”. In: *J. Chem. Phys.* 122.23 (2005), p. 234511. DOI: `10.1063/1.1931662` (cit. on p. 38).

[283] T. Pal and M. Vogel. “On the Relevance of Electrostatic Interactions for the Structural Relaxation of Ionic Liquids: A Molecular Dynamics Simulation Stuyd”. In: *J. Chem. Phys.* 150.12 (2019), p. 124501. DOI: `10.1063/1.5085508` (cit. on pp. 39, 68, 113, 114).

[284] M. Flämig, M. Hofmann, N. Fatkullin, and E. A. Rössler. “NMR Relaxometry: The Canonical Case Glycerol”. In: *J. Phys. Chem. B* 124.8 (2020), pp. 1557–1570. DOI: `10.1021/acs.jpcb.9b11770` (cit. on p. 39).

[285] M. Becher, T. Wohlfromm, E. A. Rössler, and M. Vogel. “Molecular dynamics simulations vs field-cycling NMR relaxometry: Structural relaxation mechanisms in the glass-former glycerol revisited”. In: *J. Chem. Phys.* 154.12 (2021), p. 124503. DOI: `10.1063/5.0048131` (cit. on p. 39).

[286] R. Chelli, P. Procacci, G. Cardini, R. G. D. Valle, and S. Califano. “Glycerol condensed phases Part I. A molecular dynamics study”. In: *Phys. Chem. Chem. Phys.* 1.5 (1999), pp. 871–877. DOI: `10.1039/a808958b` (cit. on p. 39).

[287] R. Chelli, P. Procacci, G. Cardini, and S. Califano. “Glycerol condensed phases Part II.A molecular dynamics study of the conformational structure and hydrogen bonding”. In: *Phys. Chem. Chem. Phys.* 1.5 (1999), pp. 879–885. DOI: `10.1039/a808957d` (cit. on p. 39).

[288] J. Blieck, F. Affouard, P. Bordat, A. Lerbret, and M. Descamps. “Molecular dynamics simulations of glycerol glass-forming liquid”. In: *Chem. Phys.* 317.2-3 (2005), pp. 253–257. DOI: `10.1016/j.chemphys.2005.05.045` (cit. on p. 39).

[289] A. V. Egorov, A. P. Lyubartsev, and A. Laaksonen. “Molecular Dynamics Simulation Study of Glycerol–Water Liquid Mixtures”. In: *J. Phys. Chem. B* 115.49 (2011), pp. 14572–14581. DOI: `10.1021/jp208758r` (cit. on p. 39).

[290] W. Kob and H. C. Andersen. “Scaling behavior in the β-relaxation regime of a supercooled Lennard-Jones mixture”. In: *Phys. Rev. Lett.* 73.10 (1994), pp. 1376–1379. DOI: `10.1103/physrevlett.73.1376` (cit. on pp. 40, 68).

[291] W. Kob and H. C. Andersen. “Testing mode-coupling theory for a supercooled binary Lennard-Jones mixture I: The van Hove correlation function”. In: *Phys. Rev. E* 51.5 (1995), pp. 4626–4641. DOI: `10.1103/physreve.51.4626` (cit. on pp. 40, 68).

[292] G. Biroli, B. Clark, L. Foini, and F. Zamponi. “Leggett’s bound for amorphous solids”. In: *Phys. Rev. B* 83.9 (2011), p. 094530. DOI: `10.1103/physrevb.83.094530` (cit. on p. 40).

[293] T. A. Weber and F. H. Stillinger. “Local order and structural transitions in amorphous metal-metalloid alloys”. In: *Phys. Rev. B* 31.4 (1985), pp. 1954–1963. DOI: `10.1103/physrevb.31.1954` (cit. on p. 40).

[294] D. Coslovich, M. Ozawa, and W. Kob. “Dynamic and thermodynamic crossover scenarios in the Kob-Andersen mixture: Insights from multi-CPU and multi-GPU simulations”. In: *Eur. Phys. J. E* 41.5 (2018). DOI: `10.1140/epje/i2018-11671-2` (cit. on pp. 40, 41, 102).

[295] A. S. S and S. Sastry. “Low-temperature behaviour of the Kob Andersen binary mixture”. In: *J. Phys.: Condens. Matter* 15.11 (2003), S1253–S1258. DOI: `10.1088/0953-8984/15/11/343` (cit. on pp. 41, 102).

[296] D. Fragiadakis and C. M. Roland. “Molecular dynamics simulation of the Johari-Goldstein relaxation in a molecular liquid”. In: *Phys. Rev. E* 86.2 (2012), p. 020501. DOI: `10.1103/physreve.86.020501` (cit. on p. 41).

[297] D. Fragiadakis and C. M. Roland. “Characteristics of the Johari-Goldstein process in rigid asymmetric molecules”. In: *Phys. Rev. E* 88.4 (2013), p. 042307. DOI: `10.1103/physreve.88.042307` (cit. on p. 41).

[298] T. S. Ingebrigtsen, T. B. Schrøder, and J. C. Dyre. “Isomorphs in Model Molecular Liquids”. In: *J. Phys. Chem. B* 116.3 (2012), pp. 1018–1034. DOI: `10.1021/jp2077402` (cit. on p. 41).

[299] D. Fragiadakis and C. M. Roland. “Participation in the Johari-Goldstein Process: Molecular Liquids versus Polymers”. In: *Macromolecules* 50.10 (2017), pp. 4039–4042. DOI: `10.1021/acs.macromol.7b00621` (cit. on p. 41).

[300] R. J. Greet and D. Turnbull. “Glass Transition in *o*-Terphenyl”. In: *J. Chem. Phys.* 46.4 (1967), pp. 1243–1251. DOI: `10.1063/1.1840842` (cit. on p. 41).

[301] L. J. Lewis and G. Wahnström. “Relaxation of a molecular glass at intermediate times”. In: *Solid State Commun* 86.5 (1993), pp. 295–299. DOI: `10.1016/0038-1098(93)90376-x` (cit. on p. 41).

[302] U. R. Pedersen, T. S. Hudson, and P. Harrowell. “Crystallization of the Lewis-Wahnström *ortho*-terphenyl model”. In: *J. Chem. Phys.* 134.11 (2011), p. 114501. DOI: `10.1063/1.3559153` (cit. on p. 41).

[303] R. Horstmann, L. Hecht, S. Kloth, and M. Vogel. “Structural and Dynamical Properties of Liquids in Confinements: A Review of Molecular Dynamics Simulation Studies”. In: *Langmuir* 38.21 (2022), pp. 6506–6522. DOI: `10.1021/acs.langmuir.2c00521` (cit. on pp. 42, 137).

[304] M. Lingenheil, R. Denschlag, R. Reichold, and P. Tavan. “The “Hot-Solvent/Cold-Solute” Problem Revisited”. In: *J. Chem. Theory Comput.* 4.8 (2008), pp. 1293–1306. DOI: `10.1021/ct8000365` (cit. on p. 44).

[305] A. Cheng and K. M. Merz. “Application of the Nosé-Hoover Chain Algorithm to the Study of Protein Dynamics”. In: *J. Chem. Phys.* 100.5 (1996), pp. 1927–1937. DOI: `10.1021/jp951968y` (cit. on p. 44).

[306] T. Blochowicz and E. A. Rössler. “Beta Relaxation versus High Frequency Wing in the Dielectric Spectra of a Binary Molecular Glass Former”. In: *Phys. Rev. Lett.* 92.22 (2004), p. 225701. DOI: `10.1103/physrevlett.92.225701` (cit. on p. 44).

[307] A. N. Gaikwad, E. R. Wood, T. Ngai, and T. P. Lodge. “Two Calorimetric Glass Transitions in Miscible Blends Containing Poly(ethylene oxide)”. In: *Macromolecules* 41.7 (2008), pp. 2502–2508. ISSN: 0024-9297. DOI: `10.1021/ma702429r` (cit. on pp. 44, 165).

[308] J. Biroš, T. Larina, J. Trekoval, and J. Pouchlý. “Dependence of the glass transition temperature of poly (methyl methacrylates) on their tacticity”. In: *Colloid Polym. Sci.* 260.1 (1982), pp. 27–30. DOI: `10.1007/bf01447672` (cit. on p. 44).

[309] M. Vogel, P. Medick, and E. Rössler. “Slow molecular dynamics in binary organic glass formers”. In: *J. Mol. Liq.* 86.1-3 (2000). Dynamical processes in condensed molecular systems: Proceedings of the Polish-Israel-German symposium, pp. 103–108. ISSN: 0167-7322. DOI: `10.1016/s0167-7322(99)00131-2` (cit. on pp. 44, 165, 175, 239).

[310] D. Bingemann, N. Wirth, J. Gmeiner, and E. A. Rössler. “Decoupled Dynamics and Quasi-Logarithmic Relaxation in the Polymer-Plasticizer System Poly(methyl methacrylate)/Tri-m-cresyl Phosphate Studied with 2D NMR”. In: *Macromolecules* 40.15 (2007), pp. 5379–5388. ISSN: 0024-9297. DOI: `10.1021/ma070519g` (cit. on pp. 44, 165).

[311] A. K. Malde, L. Zuo, M. Breeze, M. Stroet, D. Poger, P. C. Nair, C. Oostenbrink, and A. E. Mark. “An Automated Force Field Topology Builder (ATB) and Repository: Version 1.0”. In: *J. Chem. Theory Comput.* 7.12 (2011), pp. 4026–4037. DOI: `10.1021/ct200196m` (cit. on pp. 44, 241).

[312] M. Stroet, B. Caron, K. M. Visscher, D. P. Geerke, A. K. Malde, and A. E. Mark. “Automated Topology Builder Version 3.0: Prediction of Solvation Free Enthalpies in Water and Hexane”. In: *J. Chem. Theory Comput.* 14.11 (2018), pp. 5834–5845. DOI: `10.1021/acs.jctc.8b00768` (cit. on pp. 44, 241).

[313] M. Bartelmeß. “Accessing structure and dynamics of Elastin in isoviscous solvents”. MA thesis. TU Darmstadt, 2015 (cit. on p. 47).

[314] N. A. Müller. “Molecular dynamics simulations of concentration fluctuations in binary mixtures”. PhD thesis. TU Darmstadt, 2021 (cit. on p. 47).

[315] P. Kumar, S. V. Buldyrev, and H. E. Stanley. “A tetrahedral entropy for water”. In: *Proc. Natl. Acad. Sci. U.S.A.* 106.52 (2009), pp. 22130–22134. DOI: `10.1073/pnas.0911094106` (cit. on p. 49).

[316] E. Shiratani and M. Sasai. “Growth and collapse of structural patterns in the hydrogen bond network in liquid water”. In: *J. Chem. Phys.* 104.19 (1996), pp. 7671–7680. DOI: `10.1063/1.471475` (cit. on pp. 49, 72).

[317] N. Müller and M. Vogel. “Relation between concentration fluctuations and dynamical heterogeneities in binary glass-forming liquids: A molecular dynamics simulation study”. In: *J. Chem. Phys.* 150.6 (2019), p. 064502. DOI: `10.1063/1.5059355` (cit. on pp. 50, 176).

[318] S. Elliott. “Interpretation of the principal diffraction peak of liquid and amorphous water”. In: *J. Chem. Phys.* 103.7 (1995), pp. 2758–2761. DOI: `10.1063/1.470510` (cit. on p. 51).

[319] V. Voloshin, N. Medvedev, Y. I. Naberukhin, A Geiger, and M Klene. “Radial distribution functions of atoms and voids in large computer models of water”. In: *J. Struct. Chem.* 46.3 (2005), pp. 438–445. DOI: `10.1007/s10947-006-0122-1` (cit. on p. 51).

[320] S. Hunklinger. “Festkörperphysik”. In: Munich, Germany: Oldenbourg Verlag, 2011, pp. 106–107. ISBN: 9783486705478 (cit. on pp. 52, 145).

[321] I.-C. Yeh and G. Hummer. “System-Size Dependence of Diffusion Coefficients and Viscosities from Molecular Dynamics Simulations with Periodic Boundary Conditions”. In: *J. Phys. Chem. B* 108.40 (2004), pp. 15873–15879. DOI: `10.1021/jp0477147` (cit. on p. 52).

[322] N. Lačević, F. W. Starr, T. B. Schrøder, and S. C. Glotzer. “Spatially heterogeneous dynamics investigated via a time-dependent four-point density correlation function”. In: *J. Chem. Phys.* 119.14 (2003), pp. 7372–7387. DOI: `10.1063/1.1605094` (cit. on p. 54).

[323] F. Klameth, P. Henritzi, and M. Vogel. “Static and Dynamic Length Scales in Supercooled Liquids: Insights from Molecular Dynamics Simulations of Water and Tri-Propylene Oxide”. In: *J. Chem. Phys.* 140.14 (2014), p. 144501. DOI: `10.1063/1.4870089` (cit. on pp. 54, 137, 138, 142, 144, 151, 161, 162).

[324] E. Duboué-Dijon and D. Laage. “Characterization of the Local Structure in Liquid Water by Various Order Parameters”. In: *J. Chem. Phys. B* 119.26 (2015), pp. 8406–8418. DOI: `10.1021/acs.jpcb.5b02936` (cit. on p. 60).

[325] M. Sasai. “Spatiotemporal heterogeneity and energy landscape in liquid water”. In: *Physica A* 285.3-4 (2000), pp. 315–324. DOI: `10.1016/s0378-4371(00)00288-0` (cit. on p. 60).

[326] K. T. Wikfeldt, A. Nilsson, and L. G. M. Pettersson. “Spatially inhomogeneous bimodal inherent structure of simulated liquid water”. In: *Phys. Chem. Chem. Phys.* 13.44 (2011), p. 19918. DOI: `10.1039/c1cp22076d` (cit. on pp. 60, 79).

[327] P. Kumar, S. V. Buldyrev, S. R. Becker, P. H. Poole, F. W. Starr, and H. E. Stanley. “Relation between the Widom line and the breakdown of the Stokes–Einstein relation in supercooled water”. In: *Proc. Natl. Acad. Sci. U.S.A.* 104.23 (2007), pp. 9575–9579. DOI: `10.1073/pnas.0702608104` (cit. on pp. 65, 84, 85).

[328] L. Xu, F. Mallamace, Z. Yan, F. W. Starr, S. V. Buldyrev, and H. E. Stanley. “Appearance of a fractional Stokes–Einstein relation in water and a structural interpretation of its onset”. In: *Nat. Phys.* 5.8 (2009), pp. 565–569. DOI: `10.1038/nphys1328` (cit. on pp. 65, 85).

[329] C. Goy, M. A. Potenza, S. Dedera, M. Tomut, E. Guillerm, A. Kalinin, K.-O. Voss, A. Schottelius, N. Petridis, A. Prosvetov, G. Tejeda, J. M. Fernández, C. Trautmann, F. Caupin, U. Glasmacher, and R. E. Grisenti. “Shrinking of Rapidly Evaporating Water Microdroplets Reveals their Extreme Supercooling”. In: *Phys. Rev. Lett.* 120.1 (2018), p. 015501. DOI: `10.1103/physrevlett.120.015501` (cit. on p. 67).

[330] F. Caupin. “Escaping the No Man’s Land: Recent Experiments on Metastable Water”. In: *J. Non-Cryst. Solids* 407 (2015), pp. 441–448. DOI: `10.1016/j.jnoncrysol.2014.09.037` (cit. on p. 67).

[331] K. H. Kim, A. Späh, H. Pathak, F. Perakis, D. Mariedahl, K. Amann-Winkel, J. A. Sellberg, J. H. Lee, S. Kim, J. Park, K. H. Nam, T. Katayama, and A. Nilsson. “Maxima in the thermodynamic response and correlation functions of deeply supercooled water”. In: *Science* 358.6370 (2017), pp. 1589–1593. DOI: `10.1126/science.aap8269` (cit. on p. 67).

[332] L. Kringle, W. A. Thornley, B. D. Kay, and G. A. Kimmel. “Reversible structural transformations in supercooled liquid water from 135 to 245 K”. In: *Science* 369.6510 (2020), pp. 1490–1492. DOI: `10.1126/science.abb7542` (cit. on p. 67).

[333] V. Holten, J. V. Sengers, and M. A. Anisimov. “Equation of State for Supercooled Water at Pressures up to 400 MPa”. In: *J. Phys. Chem. Ref. Data* 43.4 (2014), p. 043101. DOI: `10.1063/1.4895593` (cit. on p. 69).

[334] P. Mausbach, H.-O. May, and G. Ruppeiner. “Thermodynamic metric geometry of the two-state ST2 model for supercooled water”. In: *J. Chem. Phys.* 151.6 (2019), p. 064503. DOI: `10.1063/1.5101075` (cit. on p. 69).

[335] J. Guo and J. C. Palmer. “Fluctuations near the liquid–liquid transition in a model of silica”. In: *Phys. Chem. Chem. Phys.* 20.39 (2018), pp. 25195–25202. DOI: `10.1039/c8cp04237c` (cit. on p. 70).

[336] R. Shi and H. Tanaka. “Microscopic structural descriptor of liquid water”. In: *J. Chem. Phys.* 148.12 (2018), p. 124503. DOI: `10.1063/1.5024565` (cit. on pp. 72, 83, 98).

[337] A. Skibinsky, S. V. Buldyrev, G. Franzese, G. Malescio, and H. E. Stanley. “Liquid-liquid phase transitions for soft-core attractive potentials”. In: *Phys. Rev. E* 69.6 (2004), p. 061206. DOI: `10.1103/physreve.69.061206` (cit. on p. 74).

[338] T. Yagasaki, M. Matsumoto, and H. Tanaka. “Spontaneous liquid-liquid phase separation of water”. In: *Phys. Rev. E* 89.2 (2014), p. 020301. DOI: `10.1103/physreve.89.020301` (cit. on pp. 77, 87, 97).

[339] P. H. Handle and F. Sciortino. “Potential energy landscape of TIP4P/2005 water”. In: *J. Chem. Phys.* 148.13 (2018), p. 134505. DOI: `10.1063/1.5023894` (cit. on pp. 77, 97).

[340] R. Horstmann and M. Vogel. “Relations between thermodynamics, structures, and dynamics for modified water models in their supercooled regimes”. In: *J. Chem. Phys.* 154.5 (2021), p. 054502. DOI: `10.1063/5.0037080` (cit. on pp. 83, 109).

[341] T. A. Kesselring, E. Lascaris, G. Franzese, S. V. Buldyrev, H. J. Herrmann, and H. E. Stanley. “Finite-size scaling investigation of the liquid-liquid critical point in ST2 water and its stability with respect to crystallization”. In: *J. Chem. Phys.* 138.24 (2013), p. 244506. DOI: `10.1063/1.4808355` (cit. on pp. 83, 87).

[342] D. Demuth, M. Reuhl, M. Hopfenmüller, N. Karabas, S. Schoner, and M. Vogel. “Confinement Effects on Glass-Forming Aqueous Dimethyl Sulfoxide Solutions”. In: *Molecules* 25.18 (2020), p. 4127. DOI: `10.3390/molecules25184127` (cit. on p. 84).

[343] F. Pabst, J. Kraus, S. Kloth, E. Steinrücken, M. Kruteva, A. Radulescu, M. Vogel, and T. Blochowicz. “Evidence of supercoolable nanoscale water clusters in an amorphous ionic liquid matrix”. In: *J. Chem. Phys.* 155.17 (2021), p. 174501. DOI: `10.1063/5.0066180` (cit. on p. 84).

[344] Z. Shi, P. G. Debenedetti, and F. H. Stillinger. “Relaxation processes in liquids: Variations on a theme by Stokes and Einstein”. In: *J. Chem. Phys.* 138.12 (2013), 12A526. DOI: `10.1063/1.4775741` (cit. on p. 85).

[345] R. S. Singh, J. C. Palmer, A. Z. Panagiotopoulos, and P. G. Debenedetti. “Thermodynamic analysis of the stability of planar interfaces between coexisting phases and its application to supercooled water”. In: *J. Chem. Phys.* 150.22 (2019), p. 224503. DOI: `10.1063/1.5097591` (cit. on p. 87).

[346] G. Camisasca, N. Galamba, K. T. Wikfeldt, and L. G. M. Pettersson. “Translational and rotational dynamics of high and low density TIP4P/2005 water”. In: *J. Chem. Phys.* 150.22 (2019), p. 224507. DOI: `10.1063/1.5079956` (cit. on p. 98).

[347] L. Berthier and G. Biroli. “Theoretical perspective on the glass transition and amorphous materials”. In: *Rev. Mod. Phys.* 83.2 (2011), pp. 587–645. DOI: `10.1103/revmodphys.83.587` (cit. on p. 101).

[348] M. D. Ediger, C. A. Angell, and S. R. Nagel. “Supercooled Liquids and Glasses”. In: *J. Chem. Phys.* 100.31 (1996), pp. 13200–13212. DOI: `10.1021/jp953538d` (cit. on p. 101).

[349] R. Richert and C. A. Angell. “Dynamics of glass-forming liquids. V. On the link between molecular dynamics and configurational entropy”. In: *J. Chem. Phys.* 108.21 (1998), pp. 9016–9026. DOI: `10.1063/1.476348` (cit. on p. 101).

[350] H. Tanaka. “Relation between Thermodynamics and Kinetics of Glass-Forming Liquids”. In: *Phys. Rev. Lett.* 90.5 (2003), p. 055701. DOI: `10.1103/physrevlett.90.055701` (cit. on pp. 101, 104).

[351] T. Hecksher, A. I. Nielsen, N. B. Olsen, and J. C. Dyre. “Little evidence for dynamic divergences in ultraviscous molecular liquids”. In: *Nat. Phys.* 4.9 (2008), pp. 737–741. DOI: `10.1038/nphys1033` (cit. on p. 101).

[352] F. Stickel, E. W. Fischer, and R. Richert. “Dynamics of glass-forming liquids. I. Temperature-derivative analysis of dielectric relaxation data”. In: *J. Chem. Phys.* 102.15 (1995), pp. 6251–6257. DOI: `10.1063/1.469071` (cit. on p. 101).

[353] F. Stickel, E. W. Fischer, and R. Richert. “Dynamics of glass-forming liquids. II. Detailed comparison of dielectric relaxation, dc-conductivity, and viscosity data”. In: *J. Chem. Phys.* 104.5 (1996), pp. 2043–2055. DOI: `10.1063/1.470961` (cit. on pp. 101, 132, 133).

[354] F. Mallamace, C. Branca, C. Corsaro, N. Leone, J. Spooren, S.-H. Chen, and H. E. Stanley. “Transport properties of glass-forming liquids suggest that dynamic crossover temperature is as important as the glass transition temperature”. In: *Proc. Natl. Acad. Sci. U.S.A.* 107.52 (2010), pp. 22457–22462. DOI: `10.1073/pnas.1015340107` (cit. on p. 101).

[355] J. Zhao, S. L. Simon, and G. B. McKenna. “Using 20-million-year-old amber to test the super-Arrhenius behaviour of glass-forming systems”. In: *Nat. Commun.* 4.1 (2013). DOI: `10.1038/ncomms2809` (cit. on p. 101).

[356] V. N. Novikov and A. P. Sokolov. “Qualitative change in structural dynamics of some glass-forming systems”. In: *Phys. Rev. E* 92.6 (2015), p. 062304. DOI: `10.1103/physreve.92.062304` (cit. on pp. 102, 127, 128).

[357] F. Kremer and A. Loidl. “The Scaling of Relaxation Processes—Revisited”. In: *Advances in Dielectrics*. Springer International Publishing, 2018, pp. 1–21. DOI: `10.1007/978-3-319-72706-6_1` (cit. on p. 102).

[358] R. R. Nigmatullin, S. I. Osokin, and G Smith. “New approach in the description of dielectric relaxation phenomenon: correct deduction and interpretation of the Vogel–Fulcher–Tamman equation”. In: *J. Phys.: Condens. Matter* 15.20 (2003), pp. 3481–3503. DOI: `10.1088/0953-8984/15/20/309` (cit. on p. 102).

[359] J. C. Mauro, Y. Yue, A. J. Ellison, P. K. Gupta, and D. C. Allan. “Viscosity of glass-forming liquids”. In: *Proc. Natl. Acad. Sci. U.S.A.* 106.47 (2009), pp. 19780–19784. DOI: `10.1073/pnas.0911705106` (cit. on pp. 102, 110).

[360] I. Avramov and A. Milchev. "Effect of disorder on diffusion and viscosity in condensed systems". In: *J. Non-Cryst. Solids* 104.2-3 (1988), pp. 253–260. DOI: `10.1016/0022-3093(88)90396-1` (cit. on pp. 102, 110).

[361] H. Bässler. "Viscous flow in supercooled liquids analyzed in terms of transport theory for random media with energetic disorder". In: *Phys. Rev. Lett.* 58.8 (1987), pp. 767–770. DOI: `10.1103/physrevlett.58.767` (cit. on pp. 102, 110).

[362] Y. S. Elmatad, D. Chandler, and J. P. Garrahan. "Corresponding States of Structural Glass Formers". In: *J. Phys. Chem. B* 113.16 (2009), pp. 5563–5567. DOI: `10.1021/jp810362g` (cit. on pp. 102, 110).

[363] J. Souletie and D. Bertrand. "Glasses and spin glasses: a parallel". In: *J. phys., I* 1.11 (1991), pp. 1627–1637. DOI: `10.1051/jp1:1991230` (cit. on pp. 102, 110).

[364] V. V. Ginzburg. "A simple mean-field model of glassy dynamics and glass transition". In: *Soft Matter* 16.3 (2020), pp. 810–825. DOI: `10.1039/c9sm01575b` (cit. on p. 102).

[365] S. Corezzi, S. Capaccioli, R. Casalini, D. Fioretto, M. Paluch, and P. A. Rolla. "Check of the temperature- and pressure-dependent Cohen–Grest equation". In: *Chem. Phys. Lett.* 320.1-2 (2000), pp. 113–117. DOI: `10.1016/s0009-2614(00)00185-8` (cit. on p. 102).

[366] M. Paluch, R. Casalini, and C. M. Roland. "Cohen-Grest model for the dynamics of supercooled liquids". In: *Phys. Rev. E* 67.2 (2003), p. 021508. DOI: `10.1103/physreve.67.021508` (cit. on pp. 102, 128, 132, 133).

[367] V. A. Zykova, S. V. Adichtchev, V. N. Novikov, and N. V. Surovtsev. "Second-order-derivative analysis of structural relaxation time in the elastic model of glass-forming liquids". In: *Phys. Rev. E* 101.5 (2020), p. 052610. DOI: `10.1103/physreve.101.052610` (cit. on pp. 102, 127, 128).

[368] A. Kudlik, S. Benkhof, T. Blochowicz, C. Tschirwitz, and E. Rössler. "The dielectric response of simple organic glass formers". In: *J. Mol. Struct.* 479.2-3 (1999), pp. 201–218. DOI: `10.1016/s0022-2860(98)00871-0` (cit. on pp. 102, 123).

[369] A. Kudlik, C. Tschirwitz, S. Benkhof, T. Blochowicz, and E. Rössler. "Slow secondary relaxation process in supercooled liquids". In: *EPL* 40.6 (1997), pp. 649–654. DOI: `10.1209/epl/i1997-00518-y` (cit. on pp. 102, 123).

[370] L. Santen and W. Krauth. "Absence of thermodynamic phase transition in a model glass former". In: *Nature* 405.6786 (2000), pp. 550–551. DOI: `10.1038/35014561` (cit. on pp. 102, 104).

[371] R. Verberg, I. M. de Schepper, and E. G. D. Cohen. "Viscosity of colloidal suspensions". In: *Phys. Rev. E* 55.3 (1997), pp. 3143–3158. DOI: `10.1103/physreve.55.3143` (cit. on p. 119).

[372] B. W. H. van Beest, G. J. Kramer, and R. A. van Santen. "Force fields for silicas and aluminophosphates based oniab initio/icalculations". In: *Phys. Rev. Lett.* 64.16 (1990), pp. 1955–1958. ISSN: 0031-9007. DOI: `10.1103/PhysRevLett.64.1955` (cit. on pp. 126, 138).

[373] T. L. Spehr, B. Frick, M. Zamponi, and B. Stühn. "Dynamics of water confined to reverse AOT micelles". In: *Soft Matter* 7.12 (2011), p. 5745. DOI: `10.1039/C1SM05204G` (cit. on p. 137).

[374] M. Agamalian, J. M. Drake, S. K. Sinha, and J. D. Axe. "Neutron diffraction study of the pore surface layer of Vycor glass". In: *Phys. Rev. E* 55.3 (1997), pp. 3021–3027. DOI: `10.1103/physreve.55.3021` (cit. on p. 137).

[375] R. Schmitz, N. Müller, S. Ullmann, and M. Vogel. "A molecular dynamics simulations study on ethylene glycol-water mixtures in mesoporous silica". In: *J. Chem. Phys.* 145.10 (2016), p. 104703. DOI: `10.1063/1.4962240` (cit. on p. 137).

[376] L. Berthier and W. Kob. "Static point-to-set correlations in glass-forming liquids". In: *Phys. Rev. E* 85.1 (1 2012), p. 011102. DOI: `10.1103/physreve.85.011102` (cit. on pp. 137, 138, 142, 144, 162).

[377] L. Hecht. "Charge and Composition Scaling of Binary Glass-Forming Liquids". MA thesis. TU Darmstadt, 2019 (cit. on pp. 137, 139, 154).

[378] M. F. Harrach, F. Klameth, B. Drossel, and M. Vogel. "Effect of the hydroaffinity and topology of pore walls on the structure and dynamics of confined water". In: *J. Chem. Phys.* 142.3 (2015), p. 034703. DOI: `10.1063/1.4905557` (cit. on pp. 137, 141, 156).

[379] J. Geske, B. Drossel, and M. Vogel. "Structure and dynamics of a silica melt in neutral confinement". In: *J. Chem. Phys.* 146.13 (2017), p. 134502. DOI: `10.1063/1.4979341` (cit. on pp. 137–139, 142, 143, 161, 162).

[380] P. Scheidler, W. Kob, and K. Binder. "The Relaxation Dynamics of a Supercooled Liquid Confined by Rough Walls". In: *J. Phys. Chem. B* 108.21 (2004), pp. 6673–6686. DOI: `10.1021/jp036593s` (cit. on pp. 138, 142, 161, 162).

[381] A. Cavagna, T. S. Grigera, and P. Verrocchio. "Mosaic Multistate Scenario Versus One-State Description of Supercooled Liquids". In: *Phys. Rev. Lett.* 98.18 (2007), p. 187801. ISSN: 1527-943X. DOI: `10.1103/physrevlett.98.187801` (cit. on p. 138).

[382] G. Biroli, J.-P. Bouchaud, A. Cavagna, T. S. Grigera, and P. Verrocchio. “Thermodynamic Signature of Growing Amorphous Order in Glass-Forming Liquids”. In: *Nat. Phys.* 4.10 (2008), pp. 771–775. doi: `10.1038/nphys1050` (cit. on pp. 138, 144).

[383] W. Kob, S. Roldán-Vargas, and L. Berthier. “Nonmonotonic temperature evolution of dynamic correlations in glass-forming liquids”. In: *Nat. Phys.* 8.2 (2012), pp. 164–167. doi: `10.1038/nphys2133` (cit. on pp. 138, 142).

[384] G. M. Hocky, T. E. Markland, and D. R. Reichman. “Growing Point-to-Set Length Scale Correlates with Growing Relaxation Times in Model Supercooled Liquids”. In: *Phys. Rev. Lett.* 108.22 (2012), p. 225506. doi: `10.1103/physrevlett.108.225506` (cit. on pp. 138, 144).

[385] F. Klameth and M. Vogel. “Slow Water Dynamics near a Glass Transition or a Solid Interface: A Common Rationale”. In: *J. Phys. Chem. Lett.* 6.21 (2015), pp. 4385–4389. doi: `10.1021/acs.jpclett.5b02010` (cit. on p. 138).

[386] P. Scheidler, W. Kob, and K. Binder. “The relaxation dynamics of a simple glass former confined in a pore”. In: *EPL* 52.3 (2000), pp. 277–283. doi: `10.1209/epl/i2000-00435-1` (cit. on p. 138).

[387] M. Vogel and S. C. Glotzer. “Spatially Heterogeneous Dynamics and Dynamic Facilitation in a Model of Viscous Silica”. In: *Phys. Rev. Lett.* 92.25 (2004), p. 255901. doi: `10.1103/physrevlett.92.255901` (cit. on p. 138).

[388] M. Vogel and S. C. Glotzer. “Temperature dependence of spatially heterogeneous dynamics in a model of viscous silica”. In: *Phys. Rev. E* 70.6 (2004), p. 061504. doi: `10.1103/physreve.70.061504` (cit. on p. 138).

[389] J. Horbach and W. Kob. “Static and dynamic properties of a viscous silica melt”. In: *Phys. Rev. B* 60.5 (1999), pp. 3169–3181. doi: `10.1103/physrevb.60.3169` (cit. on p. 138).

[390] I. Saika-Voivod, F. Sciortino, and P. H. Poole. “Free energy and configurational entropy of liquid silica: Fragile-to-strong crossover and polyamorphism”. In: *Phys. Rev. E* 69.4 (2004), p. 041503. doi: `10.1103/physreve.69.041503` (cit. on p. 138).

[391] A. Saksaengwijit, J. Reinisch, and A. Heuer. “Origin of the Fragile-to-Strong Crossover in Liquid Silica as Expressed by its Potential-Energy Landscape”. In: *Phys. Rev. Lett.* 93.23 (2004), p. 235701. doi: `10.1103/physrevlett.93.235701` (cit. on p. 138).

[392] R. Horstmann, E. P. Sanjon, B. Drossel, and M. Vogel. “Effects of confinement on supercooled tetrahedral liquids”. In: *J. Chem. Phys.* 150.21 (2019), p. 214704. doi: `10.1063/1.5095198` (cit. on pp. 138, 143, 144, 148, 154, 162, 163).

[393] G. Floudas, W. Steffen, E. W. Fischer, and W. Brown. “Solvent and polymer dynamics in concentrated polystyrene/toluene solutions”. In: *J. Chem. Phys.* 99.1 (1993), pp. 695–703. doi: `10.1063/1.465742` (cit. on p. 165).

[394] S. Schramm, T. Blochowicz, E. Gouirand, R. Wipf, B. Stühn, and Y. Chushkin. “Concentration fluctuations in a binary glass former investigated by x-ray photon correlation spectroscopy”. In: *J. Chem. Phys.* 132.22 (2010), p. 224505. doi: `10.1063/1.3431537` (cit. on pp. 165, 166).

[395] T. Blochowicz, S. A. Lusceac, P. Gutfreund, S. Schramm, and B. Stühn. “Two Glass Transitions and Secondary Relaxations of Methyltetrahydrofuran in a Binary Mixture”. In: *J. Chem. Phys. B* 115.7 (2011), pp. 1623–1637. issn: 1520-6106. doi: `10.1021/jp110506z` (cit. on pp. 165, 166).

[396] F. He and R. Richert. “Solvation dynamics in viscous polymer solution: Propylene carbonate confined by poly(methylmethacrylate)”. In: *Phys. Rev. B* 74.1 (1 2006), p. 014201. doi: `10.1103/physrevb.74.014201` (cit. on p. 165).

[397] T. Körber, R. Minikejew, B. Pötzschner, D. Bock, and E. A. Rössler. “Dynamically asymmetric binary glass formers studied by dielectric and NMR spectroscopy”. In: *Eur. Phys. J. E* 42.11 (2019), p. 143. issn: 1292-895X. doi: `10.1140/epje/i2019-11909-5` (cit. on p. 166).

[398] P. J. Hains and G. Williams. “Molecular motion in polystyrene-plasticizer systems as studied by dielectric relaxation”. In: *Polymer* 16.10 (1975), pp. 725–729. issn: 0032-3861. doi: `10.1016/0032-3861(75)90188-3` (cit. on p. 166).

[399] R. Kahlau, D. Bock, B. Schmidtke, and E. A. Rössler. “Dynamics of asymmetric binary glass formers. I. A dielectric and nuclear magnetic resonance spectroscopy study”. In: *J. Chem. Phys.* 140.4 (2014), p. 044509. doi: `10.1063/1.4861428` (cit. on p. 166).

[400] T. Böhmer, R. Horstmann, J. P. Gabriel, F. Pabst, M. Vogel, and T. Blochowicz. “Origin of Apparent Slow Solvent Dynamics in Concentrated Polymer Solutions”. In: *Macromolecules* 54.22 (2021), pp. 10340–10349. doi: `10.1021/acs.macromol.1c01414` (cit. on pp. 166, 167, 171, 175, 181, 185).

[401] L. Nilsson and B. Halle. “Molecular origin of time-dependent fluorescence shifts in proteins”. In: *Proc. Natl. Acad. Sci. U.S.A.* 102.39 (2005), pp. 13867–13872. DOI: `10.1073/pnas.0504181102` (cit. on p. 166).

[402] Y. Kaneko and J. Bosse. “Dynamics of binary liquids near the glass transition: a mode-coupling theory”. In: *J. Non-Cryst. Solids* 205-207 (1996), pp. 472–475. DOI: `10.1016/s0022-3093(96)00262-1` (cit. on pp. 167, 181).

[403] J. Bosse and Y. Kaneko. “Motion of Interacting Particles in a Disordered Medium”. In: *Prog. Theor. Phys. Supp.* 126.0 (1997), pp. 13–20. DOI: `10.1143/ptp.126.13` (cit. on p. 167).

[404] T. Voigtmann. “Multiple glasses in asymmetric binary hard spheres”. In: *EPL* 96.3 (2011), p. 36006. DOI: `10.1209/0295-5075/96/36006` (cit. on p. 167).

[405] J. G. Kirkwood. “The Dielectric Polarization of Polar Liquids”. In: *J. Chem. Phys.* 7.10 (1939), pp. 911–919. DOI: `10.1063/1.1750343` (cit. on p. 171).

[406] T. Sato, T. Tsuneda, and K. Hirao. “A density-functional study on π-aromatic interaction: Benzene dimer and naphthalene dimer”. In: *J. Chem. Phys.* 123.10 (2005), p. 104307. DOI: `10.1063/1.2011396` (cit. on p. 173).

[407] R. P. Kambour, J. M. Kelly, B. J. McKinley, B. J. Cauley, P. T. Inglefield, and A. A. Jones. “Spectroscopic studies of diluent motion in glassy plasticized blends”. In: *Macromolecules* 21.10 (1988), pp. 2937–2940. DOI: `10.1021/ma00188a008` (cit. on p. 175).

[408] R. Böhmer, B. Schiener, J. Hemberger, and R. V. Chamberlin. “Pulsed dielectric spectroscopy of supercooled liquids”. In: *Z. Phys. B Condens. Matter* 99.1 (1995). DOI: `10.1007/s002570050015` (cit. on p. 175).

[409] K. Schmidt-Rohr and H. W. Spiess. *Multidimensional Solid-State NMR and Polymers*. Elsevier, 1994. ISBN: 978-0-08-092562-2. DOI: `10.1016/c2009-0-21335-3` (cit. on pp. 175, 176).

[410] A. Heuer, M. Wilhelm, H. Zimmermann, and H. W. Spiess. “Rate Memory of Structural Relaxation in Glasses and Its Detection by Multidimensional NMR”. In: *Phys. Rev. Lett.* 75.15 (1995), pp. 2851–2854. DOI: `10.1103/physrevlett.75.2851` (cit. on pp. 175, 176).

[411] G. Williams and D. C. Watts. “Molecular motion in the glassy state. The effect of temperature and pressure on the dielectric βrelaxation of polyvinyl chloride”. In: *Trans. Faraday Soc.* 67 (1971), p. 1971. DOI: `10.1039/tf9716701971` (cit. on pp. 178, 238).

[412] S. Cerveny and J. Swenson. “Dynamics of supercooled water in a biological model system of the amino acid l-lysine”. In: *Phys. Chem. Chem. Phys.* 16.40 (2014), pp. 22382–22390. DOI: `10.1039/c4cp02487g` (cit. on p. 182).

[413] A. Nasedkin, S. Cerveny, and J. Swenson. “Molecular Insights into Dipole Relaxation Processes in Water–Lysine Mixtures”. In: *J. Chem. Phys. B* 123.28 (2019), pp. 6056–6064. DOI: `10.1021/acs.jpcb.9b01928` (cit. on p. 182).

[414] T. Körber, B. Pötzschner, F. Krohn, and E. A. Rössler. “Reorientational dynamics in highly asymmetric binary low-molecular mixtures—A quantitative comparison of dielectric and NMR spectroscopy results”. In: *J. Chem. Phys.* 155.2 (2021), p. 024504. DOI: `10.1063/5.0056838` (cit. on p. 182).

[415] J. Rieger. “The glass transition temperature of polystyrene”. In: *J. Therm. Anal.* 46.3-4 (1996), pp. 965–972. DOI: `10.1007/bf01983614` (cit. on p. 241).

[416] L. Heyer. “Investigation of L-lysine oligomer water solution properties using molecular dynamics simulations”. MA thesis. TU Darmstadt, 2019 (cit. on p. 241).

[417] R. B. Best, W. Zheng, and J. Mittal. “Balanced Protein–Water Interactions Improve Properties of Disordered Proteins and Non-Specific Protein Association”. In: *J. Chem. Theory Comput.* 10.11 (2014), pp. 5113–5124. DOI: `10.1021/ct500569b` (cit. on p. 241).

[418] J. Wang, R. M. Wolf, J. W. Caldwell, P. A. Kollman, and D. A. Case. “Development and testing of a general amber force field”. In: *J. Comput. Chem.* 25.9 (2004), pp. 1157–1174. DOI: `10.1002/jcc.20035` (cit. on p. 241).

[419] C. I. Bayly, P. Cieplak, W. Cornell, and P. A. Kollman. “A well-behaved electrostatic potential based method using charge restraints for deriving atomic charges: the RESP model”. In: *J. Chem. Phys.* 97.40 (1993), pp. 10269–10280. DOI: `10.1021/j100142a004` (cit. on p. 241).

[420] J. Reusing. “MD Simulationen zur Untersuchung der positionsaufgelösten Dynamik Myoglobins in topographischen Nanoporen MD simulations of position resolved dynamics for myoglobin in topographic nano pores”. BA thesis. TU Darmstadt, 2019 (cit. on p. 242).

[421] G. Kachalova, A. Popov, and H. Bartunik. *ATOMIC RESOLUTION CRYSTAL STRUCTURE ANALYSIS OF NATIVE DEOXY AND CO MYOGLOBIN FROM SPERM WHALE AT ROOM TEMPERATURE*. 1999. DOI: `10.2210/pdb1bzr/pdb` (cit. on p. 242).

Acronyms

MD	molecular dynamics
SPC/E	simple point charge extended
PME	particle-mesh Ewald
BDS	broadband dielectric spectroscopy
DSC	differential scanning calorimetry
NMR	nuclear magnetic resonance
DDLS	depolarized dynamic light scattering
AG	Adam-Gibbs
CRR	cooperatively rearranging regions
ECNLE	elastically collective nonlinear Langevin equation
MCT	mode-coupling theory
RFOT	random first-order transition theory
VFT	Vogel-Fulcher-Tammann
LDL	low-density liquid
HDL	high-density liquid
LDA	low-density amorphous ice
HDA	high-density amorphous ice
LDS	low-density structure
HDS	high-density structure
CP	critical point
LLCP	liquid-liquid critical point
LLPT	liquid-liquid phase transition
LVS	liquid-vapor spinodal
LSI	local structure index
KWW	Kohlrausch-Williams-Watts
ISF	incoherent intermediate scattering function
CSF	coherent intermediate scattering function
RCF	rotational correlation function
OCF	configuration overlap correlation function
MSD	mean square displacement
FT	Fourier transform
LJ	Lennard-Jones
MC	Monte-Carlo
NPT	isothermal-isobaric ensemble
NVT	canonical ensemble
NVE	microcanonical ensemble
LW-OTP	Lewis-Wahnström ortho-terphenyl
OTP	ortho-terphenyl
PBC	periodic boundary conditions
PEL	potential energy landscape
PMMA	poly-methylmethacrylate
RDF	radial pair-distribution function
SD	Stokes-Debye
SE	Stokes-Einstein
SED	Stokes-Einstein-Debye
TSEOS	two-structure equation of state
SLR	simple-liquid regime
HTR	high-temperature regime
LTA	low-temperature Arrhenius
HTA	high-temperature Arrhenius
eHTR	extended high-temperature regime
FST	fragile-to-strong transition
FOF	first-order function
rFOF	reciprocal first-order function
SOF	second-order function
rSOF	reciprocal second-order function
CG	Cohen & Grest
SFB	strong-to-fragile behavior
SFSB	strong-fragile-strong behavior

List of Figures

List of Tables

Curriculum Vitae

Name

Robin Thomas Horstmann

Year and Place of Birth

1991
in Heppenheim, Germany

Education

2017 – 2023	Doctorate Physics TU Darmstadt
2015 – 2017	M.Sc. Physics TU Darmstadt
2011 – 2015	B.Sc. Physics TU Darmstadt
2010 – 2011	B.Sc. Physics Ruprecht-Karls-Universität Heidelberg

Publications by the author

[1] R. Horstmann and M. Vogel. ”Common behaviors associated with the glass transitions of water-like models”. In: *J. Chem. Phys.* 147.3 (2017), p. 034505. DOI: 10.1063/1.4993445.

[2] J. Geske, M. Harrach, L. Heckmann, R. Horstmann, F. Klameth, N. Müller, E. Pafong, T. Wohlfromm, B. Drossel, and M. Vogel. ”Molecular Dynamics Simulations of Water, Silica, and Aqueous Mixtures in Bulk and Confinement”. In: *Z. Phys. Chem.* 232.7-8 (2018), pp. 1187–1225. DOI: 10.1515/zpch-2017-1042.

[3] R. Horstmann, E. P. Sanjon, B. Drossel, and M. Vogel. ”Effects of confinement on supercooled tetrahedral liquids”. In: *J. Chem. Phys.* 150.21 (2019), p. 214704. DOI: 10.1063/1.5095198.

[4] L. Hecht, R. Horstmann, B. Liebchen, and M. Vogel. ”MD simulations of charged binary mixtures reveal a generic relation between high-and low-temperature behavior”. In: *J. Chem. Phys.* 154.2 (2021), p. 024501. DOI: 10.1063/5.0031417.

[5] R. Horstmann and M. Vogel. ”Relations between thermodynamics, structures, and dynamics for modified water models in their supercooled regimes”. In: *J. Chem. Phys.* 154.5 (2021), p. 054502. DOI: 10.1063/5.0037080.

[6] T. Böhmer, R. Horstmann, J. P. Gabriel, F. Pabst, M. Vogel, and T. Blochowicz. ”Origin of Apparent Slow Solvent Dynamics in Concentrated Polymer Solutions”. In: *Macromolecules* 54.22 (2021), pp. 10340–10349. DOI: 10.1021/acs.macromol.1c01414.

[7] R. Horstmann, L. Hecht, S. Kloth, and M. Vogel. ”Structural and Dynamical Properties of Liquids in Confinements: A Review of Molecular Dynamics Simulation Studies”. In: *Langmuir* 38.21 (2022), pp. 6506-6522. DOI: 10.1021/acs.langmuir.2c00521.

[8] M. Becher, R. Horstmann, S. Kloth, E. A. Rössler, and M. Vogel. ”A Relation between the Formation of a Hydrogen-Bond Network and a Time-Scale Separation of Translation and Rotation in Molecular Liquids”. In: *J. Phys. Chem. Lett.* 13.20 (2022), pp. 4556–4562. DOI: 10.1021/acs.jpclett.2c00821.

[9] M. M. Hoffmann, M. D. Too, N. A. Paddock, R. Horstmann, S. Kloth, M. Vogel, and G. Buntkowsky. ”On the Behavior of the Ethylene Glycol Components of Polydisperse Polyethylene Glycol PEG200”. In: *J. Phys. Chem. B* (2023). DOI: 10.1021/acs.jpcb.2c06773.

Other contributions

a) ”Molecular dynamics study of modified SPC/e water in neutral confinements”, Poster, DPG, Regensburg Germany (2016)

b) ”Molecular dynamics simulations of water-like models from supercooled to superheated temperatures”, Poster, IDMRCS, Wisla Poland (2017)

c) ”Glasübergang von wasserartigen Molekülen im Bulk und Confinement”, Talk, AK Meeting, Lichtenfels Germany (2018)

d) ”Glass Transition of Water-Like Models in Bulk and Confinement”, Talk, DPG, Regensburg Germany (2019)

e) ”Solvent dynamics in glass-forming mixtures: an MDS perspective”, Talk, AK Meeting (2021)

A. Appendix

A.1. Charge scaled water models

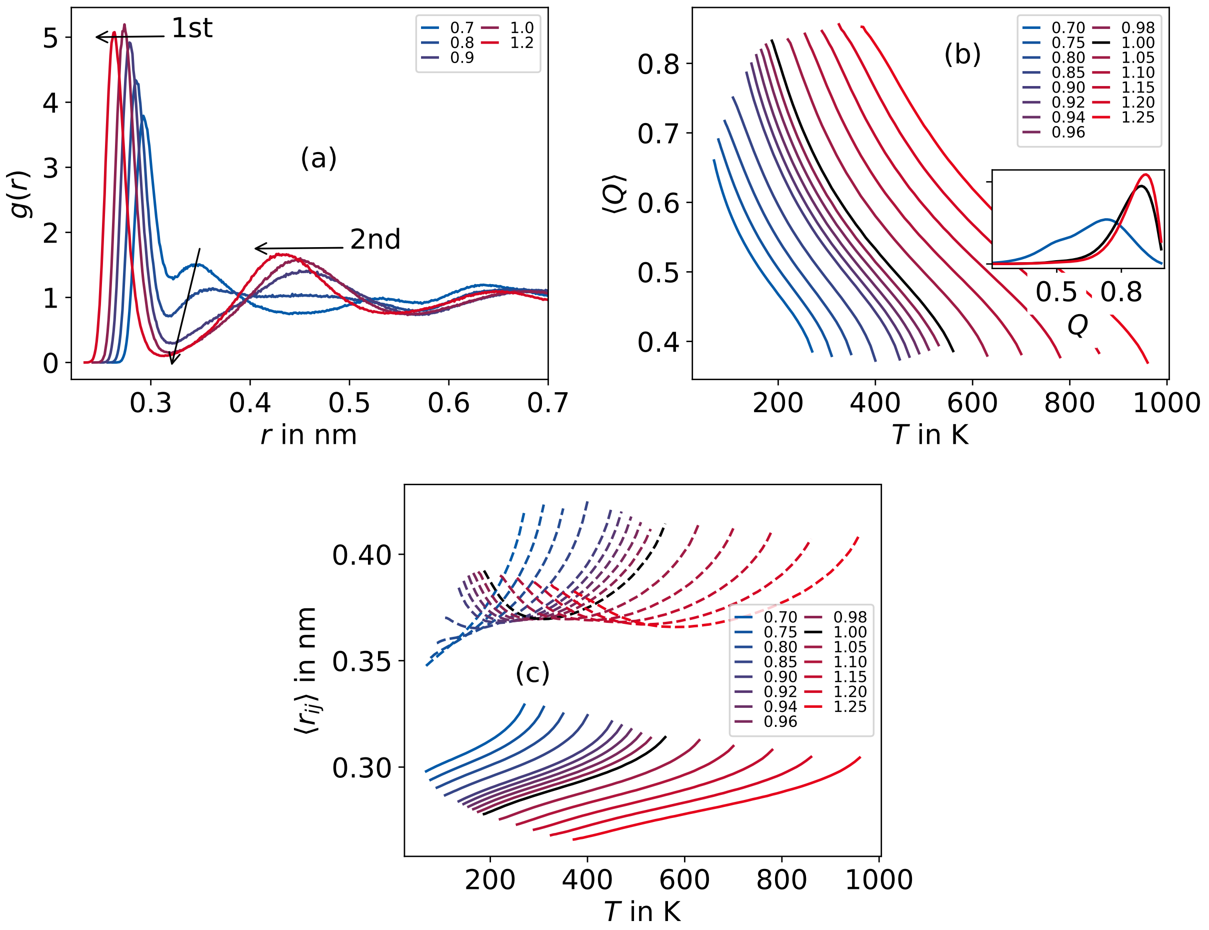

Figure A.1.: (a) Oxygen-oxygen radial pair-distribution functions $g(r)$, see Sec. 5.1.1, for several of the charge-scaled variants of the SPC/E water model at atmospheric pressure and the lowest simulated temperatures. (b) The average tetrahedral order parameter $\langle Q \rangle$, see Sec. 5.1.3, for the charge-scaled variants of SPC/E water model at atmospheric pressure. The inset shows the probability distribution of Q at the lowest temperature for $q = 0.7$, 1.0, and 1.25. (c) The average oxygen-oxygen distance to the first four (solid lines) and fifth to eighth (dashed lines) next neighbors of the charge-scaled variants of the SPC/E water model. The charge-scaling factor q is given in the legend. Figures 6.2(a), 6.3(a), and 6.4(a) of the main text present the data for the TIP4P/2005 water model, respectively.

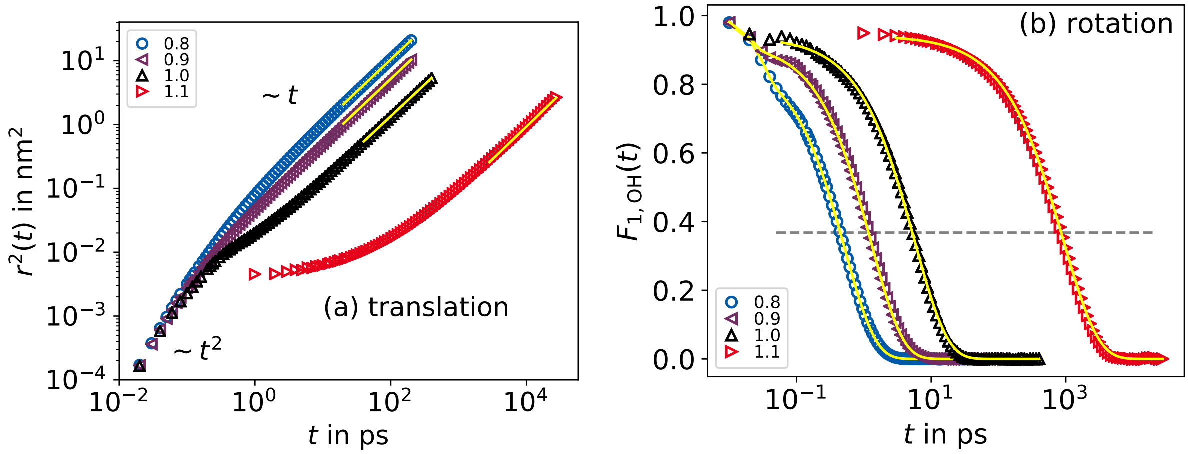

Figure A.2.: Measures of dynamics at 300 K for several charge-scaled variants of TIP4P/2005: (a) translation probed with the MSD of the oxygen atoms and (b) rotation probed by $F_{1,\mathrm{OH}}$, see Sec. 5.2.2 and 5.2.3, respectively. The charge-scaling factor q is given in the legend. In (a), solid yellow lines indicate fits to Eq. (5.24), yielding the self-diffusion coefficients D. In (b), solid yellow lines are fits to a KWW function, Eq. (2.5), and to a sum of two KWW functions for $q \leq 1$. The gray dashed line indicates the criterion for the determination of the correlation time τ_e. Figure 6.5 of the main text shows the respective results for the SPC/E variants.

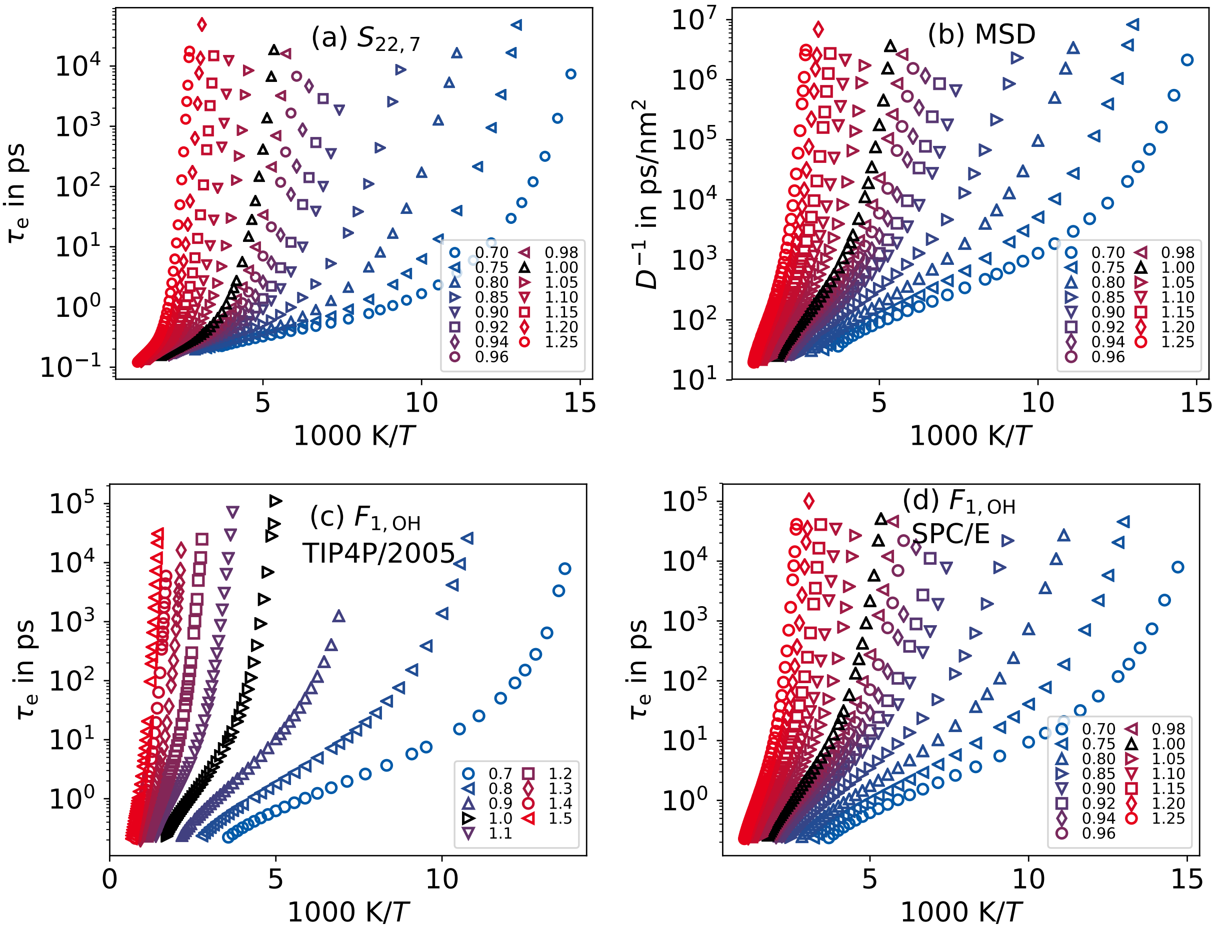

Figure A.3.: Dynamical properties of the charge-scaled variants of the TIP4P/2005 and SPC/E water models. (a) and (b) present respective SPC/E data to Fig. 6.6(b) and (c): (a) the correlation time τ_e for the ISF with wavenumber $22.7\,\mathrm{nm}^{-1}$ and (b) the self-diffusion coefficient determined with the MSD. (c) and (d) present the correlation time τ_e as determined with the rotational correlation function $F_{1,\mathrm{OH}}$ for the TIP4P/2005 and SPC/E variants, respectively. The charge-scaling factor q is given in the legends.

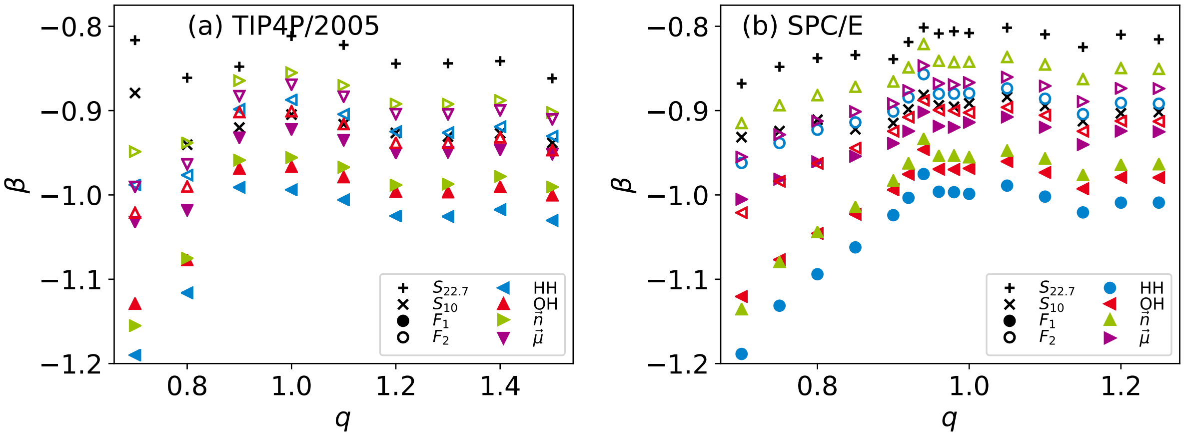

Figure A.4.: The exponent β of a power law fit $D = \alpha \cdot \tau_\mathrm{e}^\beta$ with the self-diffusion coefficient D and different correlation times τ_e for the charge-scaled variants of the TIP4P/2005 (a) and SPC/E (b) water models. Solid and open symbols represent rotational autocorrelation functions with Legendre polynomials of rank $\ell = 1$ and $\ell = 2$, respectively. The normal on the HOH plane is denoted $\vec{n}$. The power-law fit was limited to $2 \cdot 10^{-4}\,\frac{\mathrm{nm}^2}{\mathrm{ps}} > D > 5 \cdot 10^{-7}\,\frac{\mathrm{nm}^2}{\mathrm{ps}}$ to ensure supercooled dynamics and avoid data of poor statistics.

A.2. Polyamorphism in charge scaled TIP4P/2005

A.2.1. Pressure of isochores

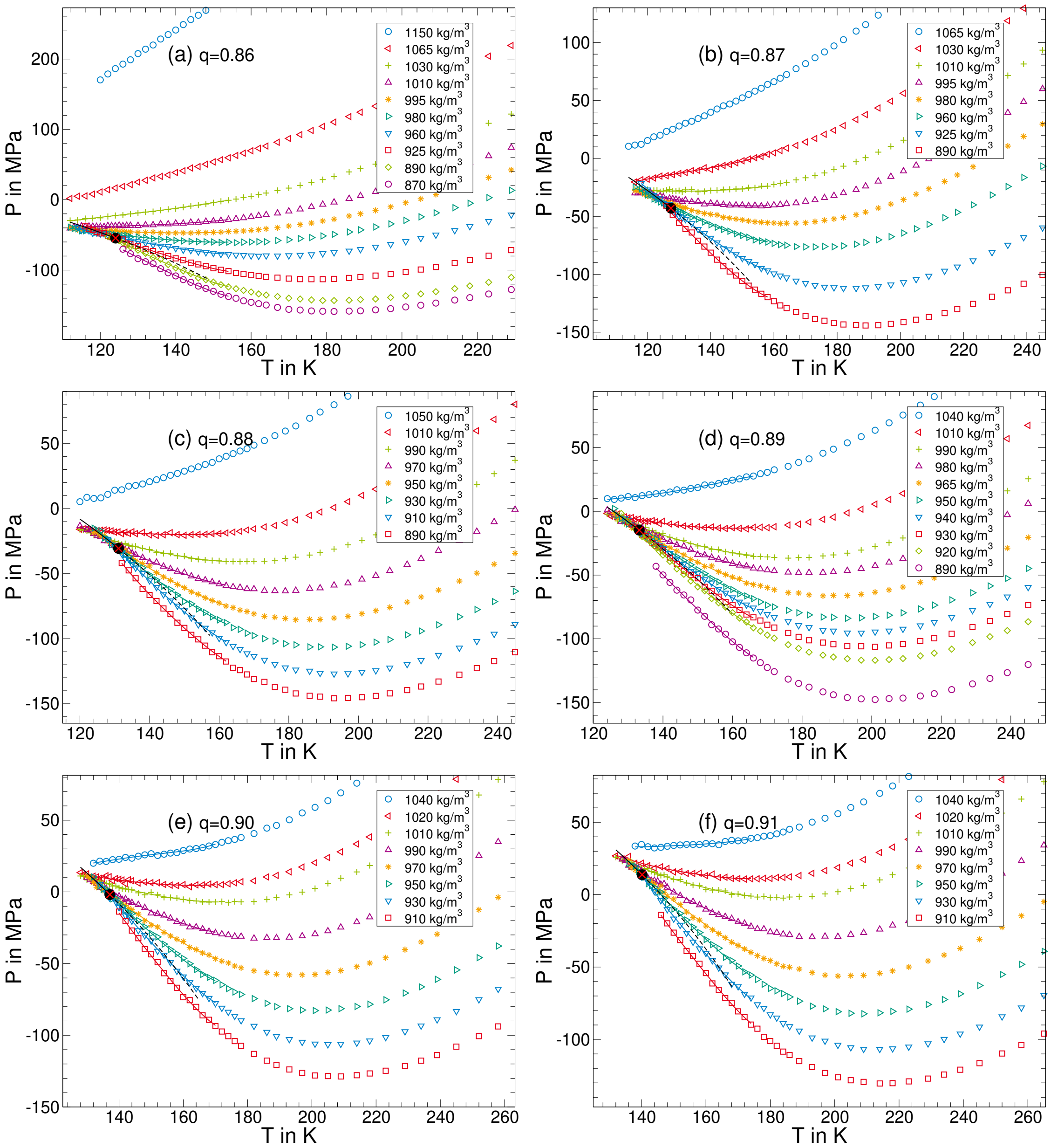

Figure A.5.: Isochore data of the charge-scaled TIP4P/2005 water model in the P-T diagram in ascending order from $q = 0.86$ (a) to $q = 0.91$ (f). The respective densities are given in the legend. The colored solid lines are the result of the TSEOS analysis and indicate the data points that were included in the fit routine. The red crosses on black circles mark the position of the LLCP, the black solid lines are the LLPT, and the black dashed lines the Widom line. Note, that the axis range varies between the graphs.

A.2.2. Pressure with phase separation

Knowing that phase separation occurs in the elongated systems, it may be questionable to compare them with the cubic systems directly. Since both simulation series follow isochores, the resulting pressure may be different. Figure A.6 presents the time averaged pressure P of elongated systems alongside TSEOS interpolations of data from cubic systems, see Fig. 7.1 (a). The data for both systems at the same density agrees within small scattering of the data. The pressure of other isochores with cubic geometry is significantly different.

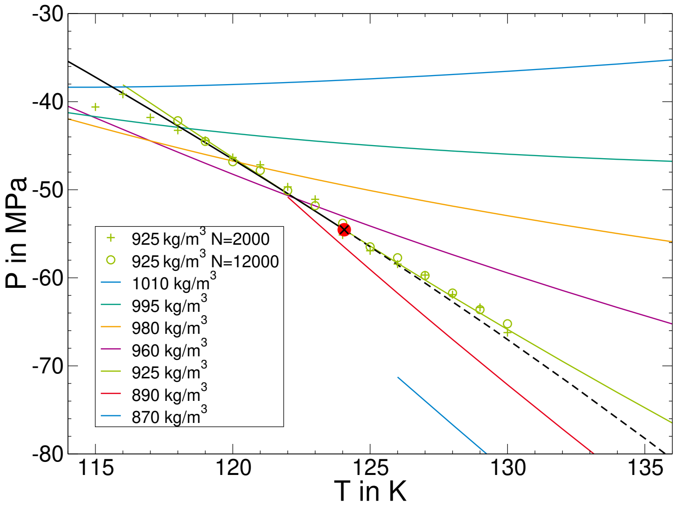

Figure A.6.: Time-averaged pressure P of simulations with the charge-scaled TIP4P/2005 water model with $q = 0.86$. The open circles are data for the elongated system with $\rho = 925\,\text{kg/m}^3 \approx \rho_c$, $N = 2000$ molecules and aspect ratio $1 : 1 : 3$. All isochores are shown to assess how well the data matches. For clarity, the data for cubic systems is shown as interpolations with the TSEOS from Fig. 7.1. The LLCP is marked as a black cross on a red circle and the LLPT line and Widom line are indicated by a solid black and dashed black line, respectively.

Spatially resolved density and structure

N=2000 molecules, $1:1:3$ **and** $T > T_c$

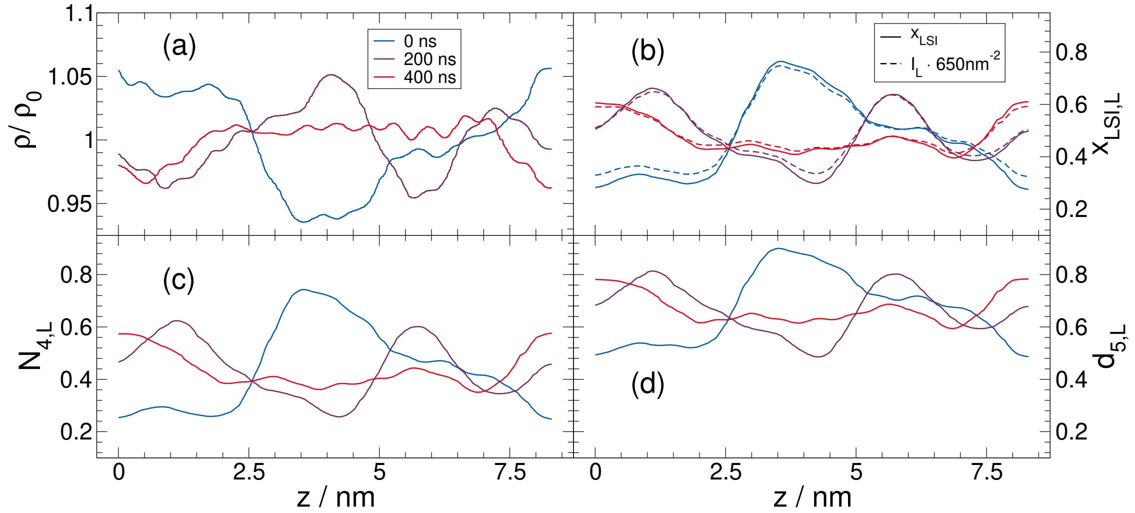

N=12000 molecules, $1:1:6$ **and** $T < T_c$

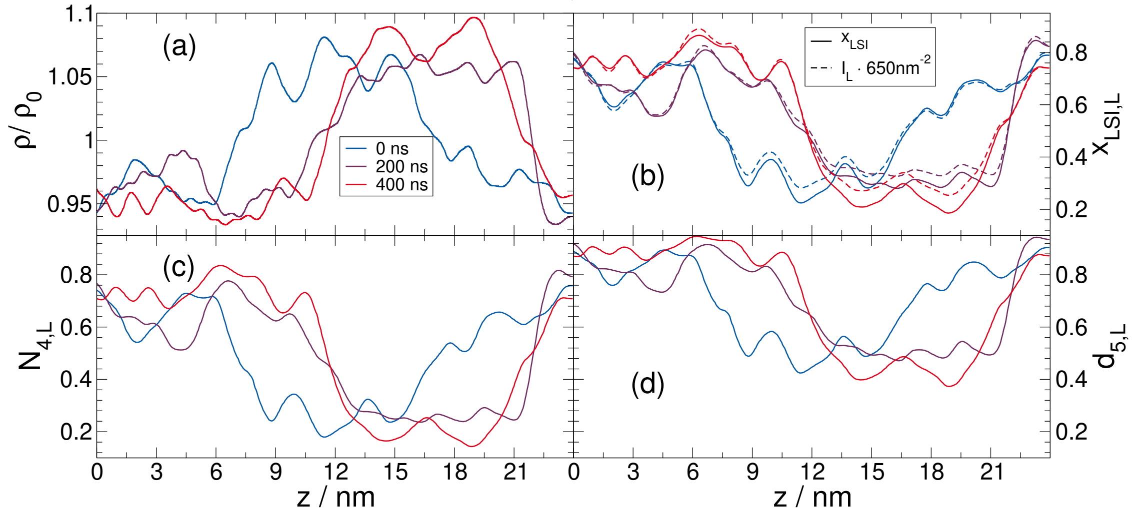

Figure A.7.: Spatially resolved structural properties of the charge-scaled TIP4P/2005 water model with $q = 0.88$ simulated at $\rho = 940$ kg/m^3, $T = 125$ K and in elongated geometry: (a) ρ_L/ρ, (b) I_L and $x_{LSI,L}$, (c) $N_{4,L}$, and $d_{5,L}$. Presented is data at the beginning, middle and end of the trajectory. The structural identifiers were averaged over $\delta z = 1$ nm thick layers centered on each oxygen and perpendicular to the z-axis. To reduce noise the properties were averaged over short periods of time and a low-pass filter was applied to further reduce artifacts caused by the discretization of the number of particles in a layer. At the top, data is shown for $L_x : L_y : L_z \equiv 1:1:3$ and $N = 2000$ molecules at $T = 132$ K $> T_c$. At the bottom, data is shown for $L_x : L_y : L_z \equiv 1:1:6$ and $N = 12000$ molecules at $T = 124$ K $< T_c$

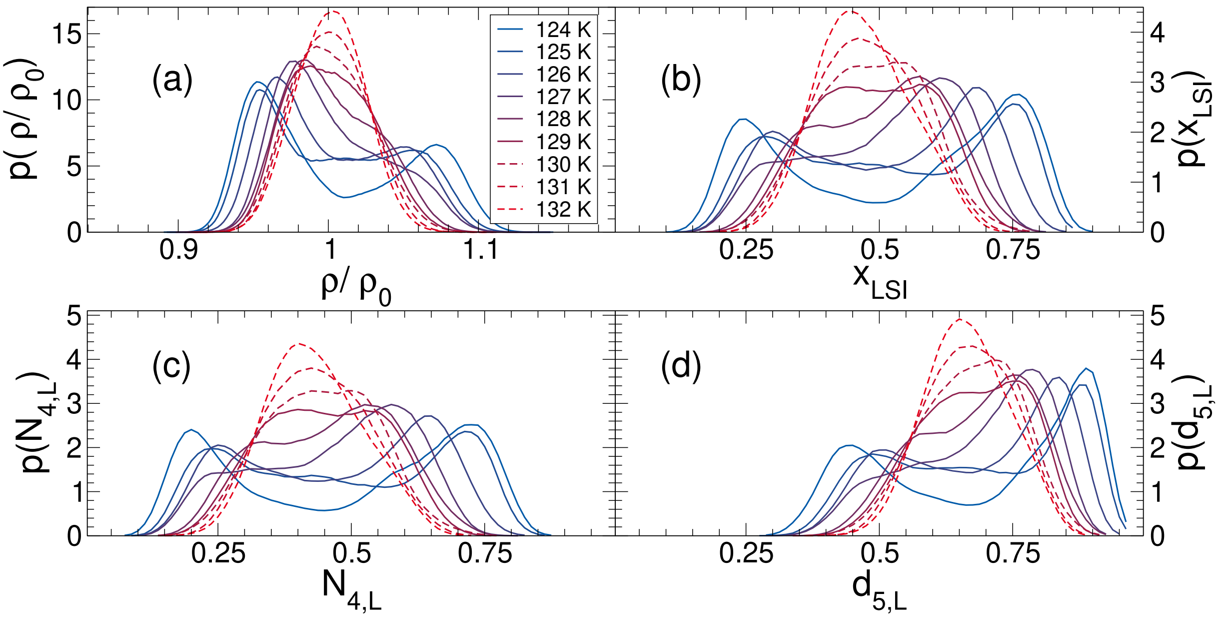

Figure A.8.: Probability distributions of the layer-averaged properties for the charge-scaled TIP4P/2005 water model with $q = 0.88$ and $\rho = 940$ kg/m^3 at the indicated temperatures: (a) ρ_L/ρ, (b) I_L, and (c) $N_{4,\mathrm{L}}$ d_5. The results were determined for the larger elongated system with aspect ratio $1:1:12$ and $N = 12000$ molecules. The critical temperature is $T_\mathrm{c} \approx 131$ K and dashed lines indicate results at and above this value in the one-phase region. For $N_{4,\mathrm{L}}$, $x_{\mathrm{I,L}}$, and $d_{5,\mathrm{L}}$ a moving average was applied to reduce artificial noise due to their discretized values. Figure A.8 in the appendix presents data for the larger system with $N = 12000$.

A.2.3. Spatially resolved correlation times for charge-scaling q=0.86

In Fig. 7.13 of the main text, data is shown for coexistence in elongated geometries and charge-scaled TIP4P/2005 with $q = 0.88$. Figure A.9 presents the corresponding data for the lowest charge-scaling factor studied, $q = 0.86$. Correlation functions $F_{1,\mathrm{OH}}(t)$ were averaged over subsets with different layer-averaged structural identifier $N_{4,\mathrm{L}}$, a measure of the LDS fraction. Consistent with $q = 0.86$, the correlation times follow Arrhenius-like behavior for subsets with lower LDS fraction while the temperature dependence appears to be higher for higher LDS fractions $N_{4,\mathrm{L}} \geq 0.7$. Again, the correlation time of $C_{\mathrm{N}4,\mathrm{L}}$ increases significantly below T_c. Only for sufficient cooling below the LLCP do layers with higher $N_{4,\mathrm{L}} \geq 0.7$ and lower $N_{4,\mathrm{L}} \leq 0.1$ LDS fraction appear. As the time scale of fluctuations of $N_{4,\mathrm{L}}$ grows stronger upon cooling below the LLCP, the correlation time of LDL-like environments can slow down further.

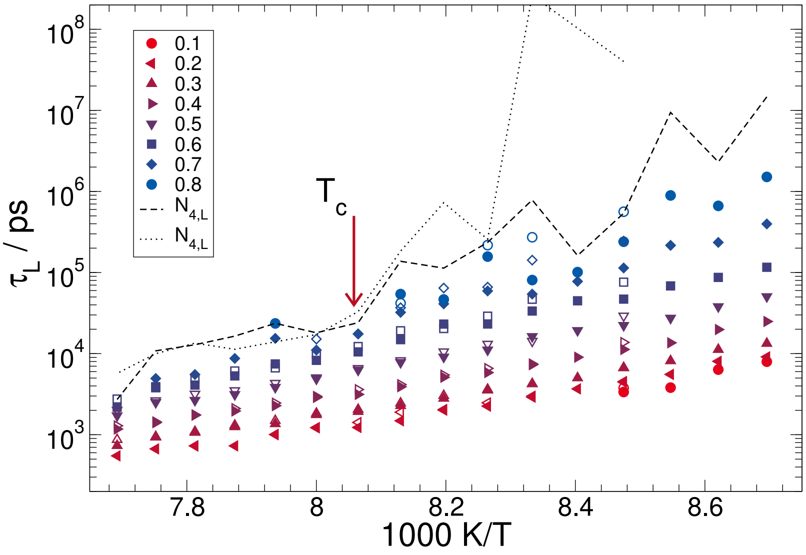

Figure A.9.: The temperature dependence of mean rotational correlation times τ_L measured with $F_{1,\mathrm{OH}}(t)$ for environments with the indicated layer-averaged structural identifier $N_{4,\mathrm{L}}$. The data is for charge-scaled TIP4P/2005 systems with $q = 0.86$ and elongated geometry with $N = 2000$ molecules and aspect ratio $1:3:3$ (solid symbols) and $N = 12000$ and $1:1:6$ (open symbols). Presented are results for simulations with density $\rho = 925$ kg/m^3. For comparison, the time scale τ_{N_4} of $N_{4,\mathrm{L}}$ fluctuations from fits of $C_{\mathrm{N}_{4,\mathrm{L}}}(t)$ to KWW functions is shown: (dashed) $N = 2000$ and (dotted) $N = 12000$. The arrow marks the critical temperature $T_\mathrm{c} \approx 124$ K. Poor statistics for the rarer cases of $N_{4,\mathrm{L}} = 0.1$ and $N_{4,\mathrm{L}} = 0.8$ allow their investigation only far below the LLCP.

Single and two-step decays in supercooled water

Rotational correlation times are presented in Sec. 7.4 for simulations into the metastable regime of charge-scaled TIP4P/2005 water models. They are determined by fits of $F_{1,\mathrm{OH}}(t)$ to KWW functions. It was assured that this is an acceptable model for all simulations in cubic geometry. Figure A.10(a) presents results on the example of $q = 0.86$ at $T = 116\,\mathrm{K} < T_\mathrm{c}$ and $\rho = 925\,\mathrm{kg/m^3} \approx \rho_\mathrm{c}$, i.e., in the metastable regime. A single KWW is able to characterize the stretched exponential decay. However, for elongated systems a double exponential decay characterized by a weighted superposition of two KWW functions becomes necessary at the same thermodynamic conditions. The reason is the promoted phase separation.

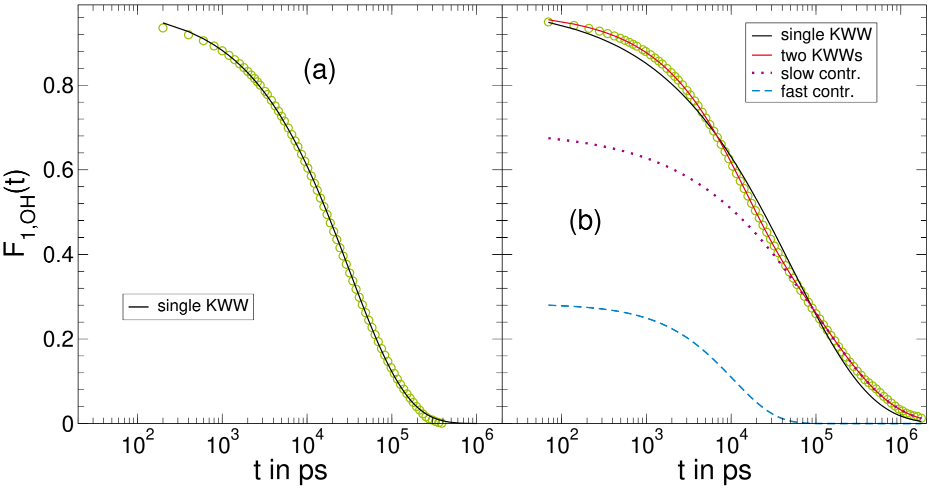

Figure A.10.: Rotational correlation functions $F_{1,\mathrm{OH}}(t)$ for the charge-scaled TIP4P/2005 water model with $q = 0.86$ at $T = 116\,\mathrm{K} < T_\mathrm{c}$ and $\rho = 925\,\mathrm{kg/m^3} \approx \rho_\mathrm{c}$ in (a) cubic and (b) elongated geometry with aspect ratio $1:1:3$ and $N = 2000$ molecules. The solid black and red lines are fits with a single KWW function and a weighted superposition of two KWW functions to the data, respectively. The dotted purple and dashed blue line show the slow and fast contributions, respectively, of the superposition. Their mean correlation times are $\langle\tau_\mathrm{fast}\rangle = 11.4\,\mathrm{ns}$ and $\langle\tau_\mathrm{slow}\rangle = 212\,\mathrm{ns}$.

A.2.4. Relation between self-diffusion coefficient and LDS fraction

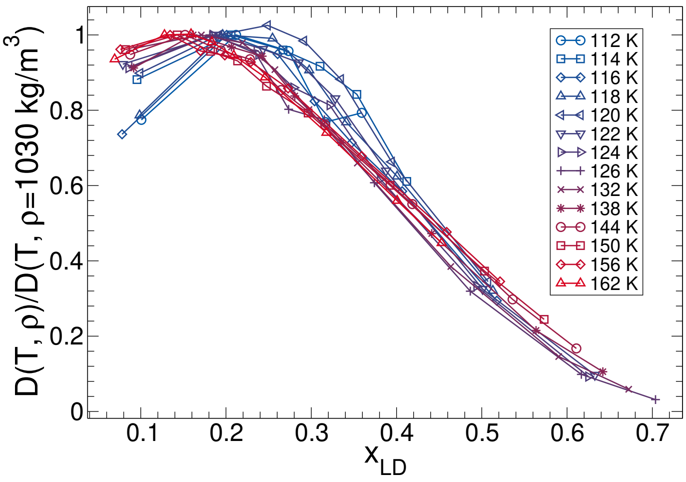

Figure A.11.: The dependence of the self-diffusion coefficient D on LDS fraction x_{LD} for isochores of the charge-scaled TIP4P/2005 with $q = 0.86$. $D(T, \rho)$ is normalized by the value at $\rho = 1030$ kg/m^3 and the same temperature for clarity. x_{LD} at each T and ρ is calculated from the TSEOS analysis. Solid lines only connect the points to increase the visibility of the x_{LD} dependence. Note, that the relation of D and x_{LD} is neither linear and nor monotonic at the lowest temperatures.

A.2.5. Test of the Model of Caupin for Isochores

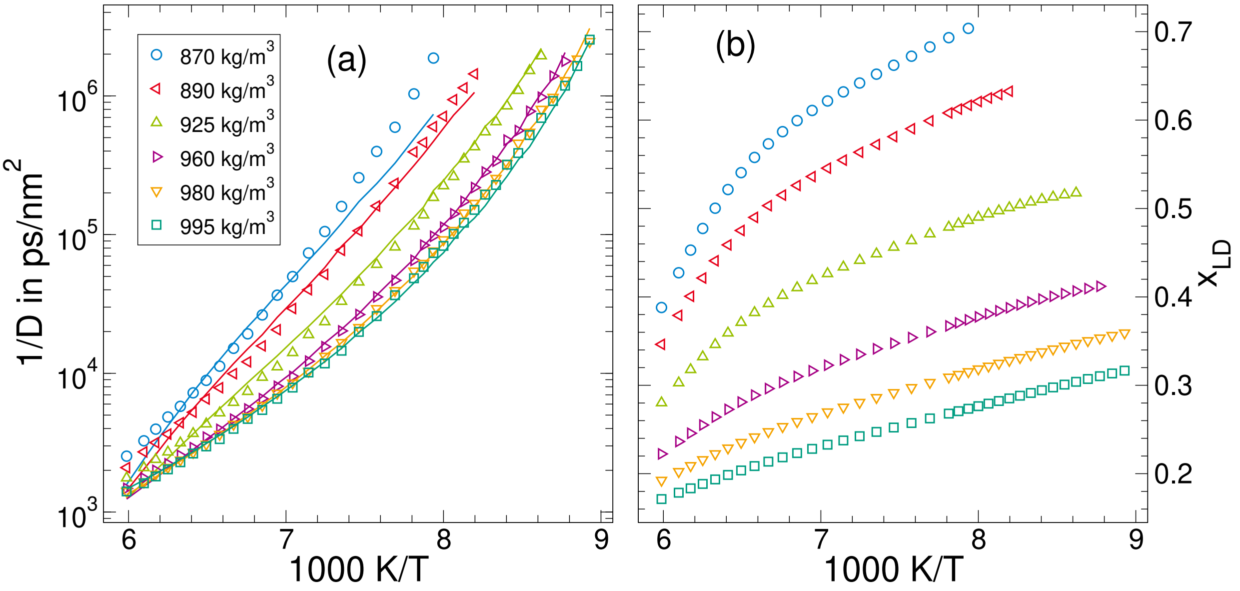

Figure A.12.: (a) The temperature-dependent self-diffusion coefficients $1/D$ of the charge-scaled TIP4P/2005 model with $q = 0.86$ at the indicated isochores (colored symbols and dotted lines). Solid lines are global fits of the data to Eq. (7.11). The LDS fraction f is given by the equilibrium concentration x_{LD} of the TSEOS for the same charge-scaled system. (b) Equilibrium concentration x_{LD} of the LDS component calculated from the TSEOS. Isochores with the highest densities were omitted because they are too far from the range of validity of the TSEOS. The colors in the legend apply to both graphs. The corresponding data for isobaric conditions is presented in Fig. 7.14.

A.3. Functional forms of $E(T)$

A.3.1. Definition of T_g for the self-diffusion coefficient

In Ch. 8, the self-diffusion coefficients D are often extrapolated to the glass transition to determine T_g. This is a non-standard investigation and a definition has to be defined. The official definition of T_g is given as the step in differential scanning calorimetry and the analysis and cooling rate are specified (ISO 11357-2:2020). In addition, the glass transition can be defined by threshold values for viscosity or structural relaxation time. The latter is a common practice in experimental studies where correlation times near T_g are available. Typical thresholds are $\eta(T_g) = 10^{12}$ Pa·s and $\tau(T_g) = 1000\,\mathrm{s}$, although $100\,\mathrm{s}$ have also been used.

D at T_g can be estimated from the Stokes-Einstein relation, Eq. (2.6). Using approximations for water of $T_g = 140\,\mathrm{K}$, $R_\mathrm{H} = 0.15\,\mathrm{nm}$, and the definition $\eta(T_g) = 10^{12}$ Pas, D is on the order of $10^{-19}\,\mathrm{nm}^2/\mathrm{ps}$. An alternative naive definition for T_g using the self-diffusion coefficient is the requirement that T_g is reached when D has the same slowdown relative to the prefactor of the high-temperature Arrhenius law. Typical values for τ_∞ are 10^{-14} to $10^{-13}\,\mathrm{s}$ resulting in a relative slowdown of 16 to 17 orders of magnitude.[112] D_∞ is on the order of $1\,\mathrm{nm}^2/\mathrm{ps}$ for the charge-scaled variants of the TIP4P/2005 and SPC/E water models in Fig. 8.9. This yields $D(T_g) \sim 10^{-17\pm1}\,\mathrm{nm}^2/\mathrm{ps}$, a more conservative threshold since it requires higher diffusivity at the glass transition.

However, the SED relations are often violated and the self-diffusion coefficients D and τ decouple. Their relation can often be described by a power law in the moderately supercooled regime. Data from simulations of various systems shown in Ch. 8 is fitted with power laws and extrapolated to correlation times of 1000 s. The corresponding self-diffusion coefficients are shown in Fig. A.13.

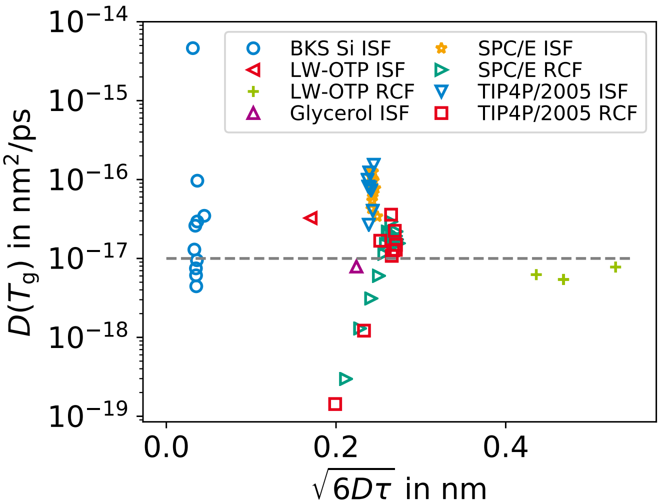

Figure A.13.: The self-diffusion coefficients D at the glass transition temperature T_g determined by fitting power laws to the relation of D and τ and extrapolating τ to 1000 s. The correlation times τ are either from the ISF or from rotational correlation functions with F_1. The wavenumber is $k = 10\,\mathrm{nm}^{-1}$ for all systems except silica, where it is $k = 20\,\mathrm{nm}^{-1}$. The x-axis marks the length scale of displacements as given by the MSD at $t = \tau$ in the high-temperature regime. The data for the BKS model of silica and the SPC/E and TIP4P/2005 water models include points for all charge-scaled variants.

The results for $D(T_g)$ scatter around $10^{-17\pm1}\,\mathrm{nm}^2/\mathrm{ps}$. Some of the charge-scaled variants of the two water models have even lower values, but they are the exception. There is no clear correlation with the length scale of the displacements at τ in the high-temperature regime. One would expect that higher self-diffusion coefficients would be required at T_g for larger molecules to experience significant displacements. The molecules studied in this work are small and deviations from the finally used value of D, given in Eq. (A.1), are small as well. Hence, a general definition of T_g using D should not cause significant issues. In particular, the steep temperature dependence near T_g leads to large differences in D at very minor temperature variations. Conversely, the definition of D should lead to errors for T_g of at most a few percent. This is sufficient for the analyses performed in this work.

With the relative slowdown given SED holds and the extrapolations in Fig. A.13, T_g is defined as

$$D(T_\mathrm{g}) = 10^{-17}\,\mathrm{nm}^2/\mathrm{ps} = 10^{-19}\,\mathrm{cm}^2/\mathrm{s}\,. \tag{A.1}$$

Thus, the MSD at 1000 s is about 0.01 nm^2 or 1 $\mathrm{\AA}^2$. The plateau value of the MSD at short times is, for example, 0.007 nm^2, 0.005 nm^2, and 0.003 nm^2 for LW-OTP, glycerol, and water, respectively, at the lowest temperatures of the simulations in this work. Thus, the system is still barely mobile and the definition satisfies the expectation that the liquid is indistinguishable from a solid upon further supercooling.

A.3.2. Additional figures

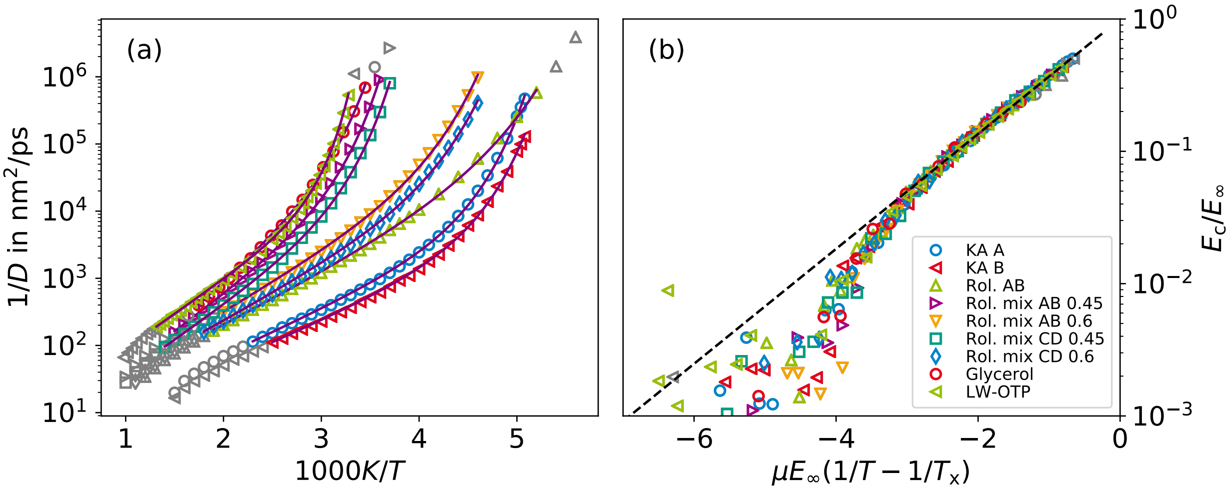

Figure A.14.: Complementary plots to Fig. 8.5. (a) Temperature dependence of the reciprocal self-diffusion coefficient $1/D(T)$ for several model LJ liquids, the Lewis-Wahnströhm model for OTP, and glycerol. The data for the model systems with reduced unit systems has been rescaled as detailed in Sec. 4.2.2. (b) Master curve of the data on the left with the rFOF, Eq. (8.17). E_c is calculated from the data and shown as a function of the exponent in Eq. (8.7). Solid purple lines are fits to Eq. (8.16) and the black dashed line is a guide to the eye. Gray symbols mark the eHTR and data points with $D \geq 10^{-6}$ nm^2/ps, and are excluded from the fit to avoid data of poor quality. The legend applies to both plots. The size-to-distance ratios of Roland's dumbbell mixtures are given in the legend.

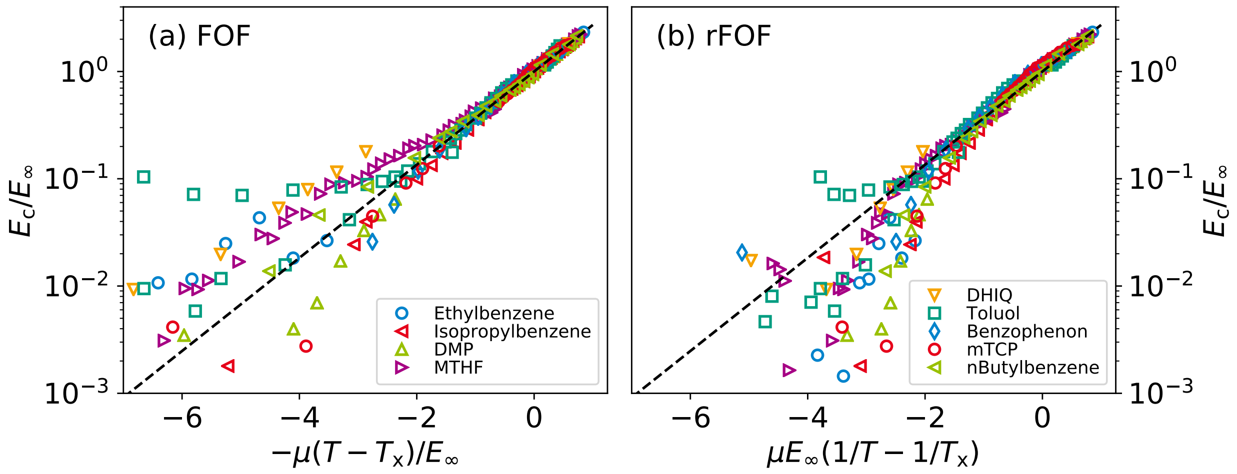

Figure A.15.: Complementary plots to Fig. 8.7(b). Shown are master curves for fits of the FOF (a) and rFOF (b) to rotational correlation times for various molecular glass formers from dielectric spectroscopy and light scattering experiments taken from the literature.[112] Here, the parametrization of the HTA was fixed during the fits. E_c is calculated from the data and shown as a function of the exponent in Eq. (8.6) and (8.8), respectively. The black dashed lines are a guides to the eye. The legends apply to both plots.

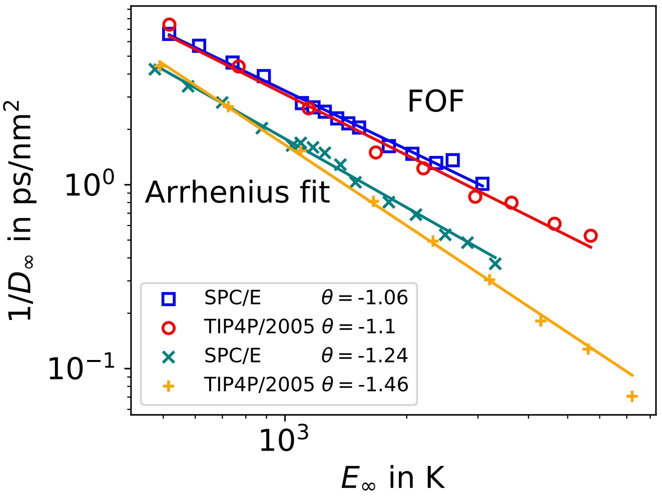

Figure A.16.: The dynamical prefactor $1/D_\infty$ shown as a function of E_∞ for the charge-scaled variants of the SPC/E and TIP4P/2005 water models. Solid lines are fits with a power law and the exponent θ is given in the legend. Fit parameters are shown for a fit with the FOF and for separate determination of the HTA. The curves for the latter are shifted downward by a factor of two.

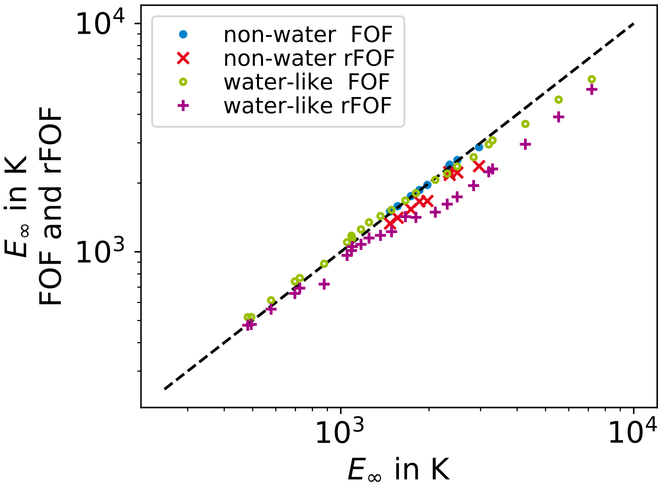

Figure A.17.: Comparison of E_∞ from fitting the HTA independently and from fitting the FOF and rFOF, Eq. (8.6) and (8.7), to the self-diffusion coefficients of several molecular glass formers. The data for water-like systems is the same as in Fig. 8.8 while the non-water systems are those in Fig. 8.5. The black dashed line is a guide to the eye.

A.4. Water in neutral confinements

A.4.1. Average static correlation length

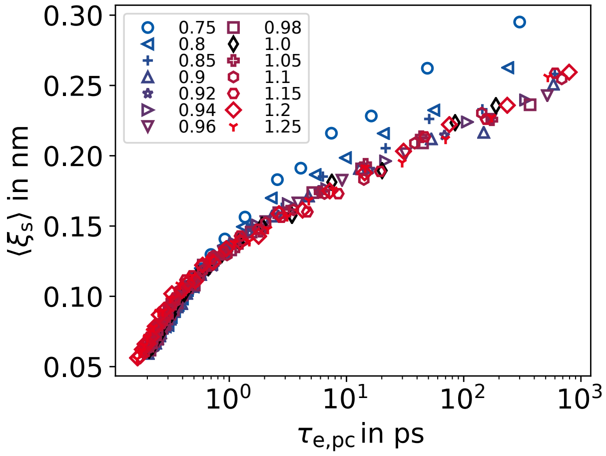

Figure A.18.: (a) Average static correlation lengths $\langle \xi_s \rangle = \xi_{\text{sta.}}/\beta \cdot \Gamma(1/\beta)$ as a function of the correlation time $\tau_{\text{e,pc}}$ in the pore center. The data is the result from fits with Eq. (9.2) to configurational overlap plateau profiles $Q_\infty(d)$, as in Fig. 9.6(b), for the charge-scaled SPC/E water model in neutral confinements. The charge scaling q is given in the legend. $\tau_{\text{e,pc}}$ is determined from $S_{22.7}$, Eq. (5.20), for the oxygen atoms.

A.4.2. Short-time angular displacement

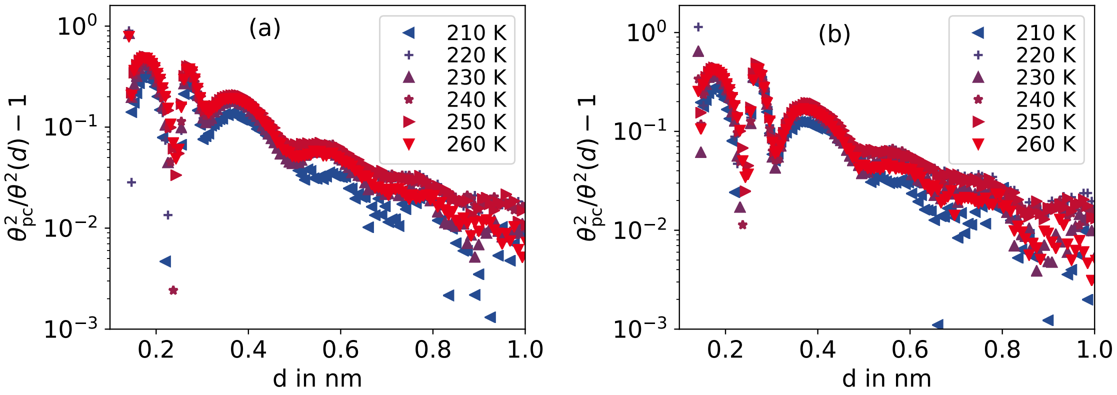

Figure A.19.: Distance resolved short-time angular displacement $\theta^2(d)$ in neutral pores of the original SPC/E water model for two different vectors, dipole moment $\vec{\mu}$ (a) and OH−bond vector (b). The angular displacement is taken at $t = 1$ ps. To demonstrate the underlying exponential behavior, the data is rescaled by the value in the pore center θ_{pc} and diminished by one.

A.4.3. The potential at the pore wall

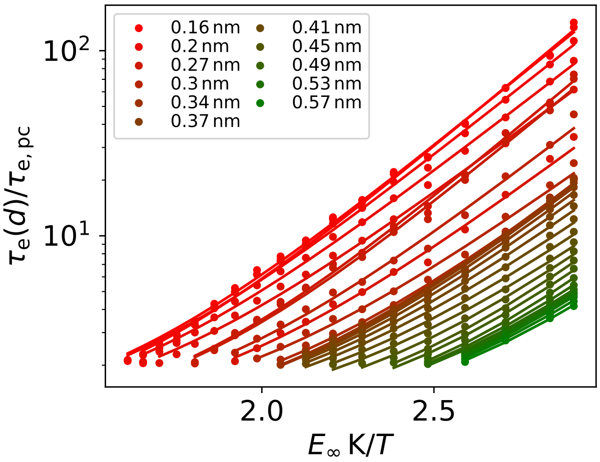

Figure A.20.: (a) The relative slowdown relative to the pore center at several distances to the pore wall. Correlation times are from the ISF with $k = 22.7\,\mathrm{nm}^{-1}$ and the system is a cylindrical neutral pore with the original SPC/E model of water. The distances to the pore wall are given in the legend and color-coded from red to green with increasing distance. The solid lines are fits with Eq. (9.5) to the data. Only temperatures with $\tau_\mathrm{e,pw}/\tau_\mathrm{e,pc} > 2$ are shown and distances with insufficient slowdown are omitted.

The fit of Eq. (9.5) to the temperature dependence of the relative slowdown $\zeta(d) = \tau(d)/\tau_\mathrm{pc}$ at different distances d to the pore surface can also be performed for rotational correlation times. Figure A.21 presents the resulting fit parameters for $F_{1,\mathrm{OH}}$ and all charge-scaled variants. ΔE_ζ and T_0 are rescaled by the high-temperature activation energy E_∞ of $F_{1,\mathrm{OH}}$. Despite the scatter of the data, $\Delta E_\zeta/E_\infty$ is close to unity. The ratio of E_∞ for both correlation functions given in the inset in Fig. A.21 (a) can be used to rescale the data. In this case, $\Delta E_\zeta/E_\infty$ is smaller than for correlation times measured with the ISF. The slowdown at the pore wall is further reduced by the lower T_0, indicating that stronger supercooling is required for the potential energy landscape to become relevant. In particular, longer correlation times imply greater distances, and thus more averaging over different dynamics.

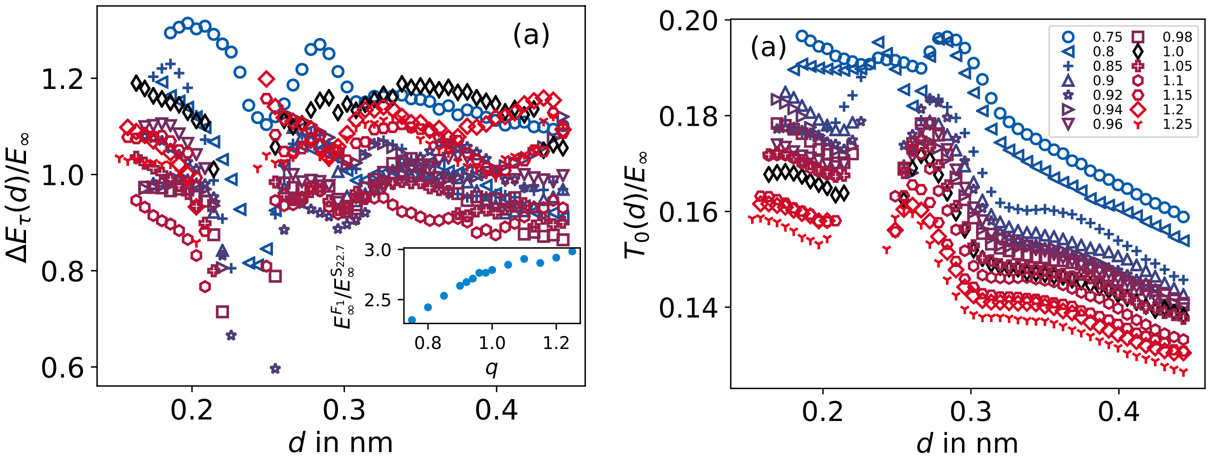

Figure A.21.: Analogous analysis to Fig 9.17. The distance resolved fit parameters (a) ΔE_τ and (b) T_0 in units of E_∞ from fits with Eq. (9.5) to correlation times $\tau_e(d,T)$ from $F_{1,\mathrm{OH}}$ within neutral pores. The charge scaling q is given in the legend. The inset in (a) displays the ratio of activation energies E_∞ of $F_{1,\mathrm{OH}}$ and the ISF and can be used to calculate the values for when the data is rescaled with E_∞ from the ISF instead.

A.5. Cross correlations in asymmetric binary mixtures

A.5.1. Anisotropic reorientation of picoline molecules mixed with PMMA

The incoherent correlation function $F_{1,\vec{\mu}}^{\mathrm{inc}}$ of the picoline dipole moment, shown in Fig. 10.1(b), shows two steps that could be interpreted as fast and slow solvent components. Here, the origin of the two steps in the correlation decay will be discussed. Molecules with a flat structure, as caused by aromatic rings or variants thereof, have a strong steric interaction. However, rotating the ring plane by 180°, also called π-flip, does not increase the potential energy in the case of symmetries. The activation energy for such a flip does not depend on cooperative processes as much as structural relaxation. Therefore, its temperature dependence is weak and the π-flip may decouple from the isotropic reorientation for strong supercooling.

The angular van Hove distribution function, the probability distribution of finding a vector at a later times with an angular deflection α from its original orientation, can be used to study such anistropic behavior. Usually, the angular van Hove evolves over time from a vibrationally broadened distribution at $\theta = 0°$ to a sine function for isotropic reorientation. Fig. A.22(a) shows the angular van Hove at intermediate times for three reference vectors, the dipole moment, the plane normal, and a C–C axis, from the methyl group carbon to its counterpart in the ring. A significant amount of large angular deflections at 140° and above appears for the latter two vectors indicating π-flips. The dipole moment also lies within the ring plane but at an angle of about 67° with respect to the presented C–C bond. In the case of π-flips of the plane normal around this C–C axis, the dipole moment flips by $2 \cdot (90° - 67°) = 46°$ resulting in a moderate decay of F_1 to 0.7. Indeed, the van Hove for the dipole moment shows increased probability of angular displacements in the range from 30° to over 90° compared to both other vectors.

The isotropic and π-flip contribution, denoted $p(\alpha)$ and $p(\beta)$ respectively, to the angular van Hove of the plane normal were quantified and are presented in Fig. A.22(d) alongside the $F_{1,\vec{n}}$ and $F_{2,\vec{n}}$. The correlation function for the α-process is $C_\alpha(t) = 1 - p(\alpha)$ while $p(\beta)$ decays again with isotropic reorientation at longer times and the correlation function is $C_\beta(t) = 1 - 2\frac{p(\beta)}{1-p(\alpha)}$. Good agreement is found between the α-process and $F_{2,\vec{n}}$, consistent with the expectation that the Legendre polynomial of rank 2 is insensitive to the π-flips. Correspondingly, the sensitive $F_{1,\vec{n}}$ agrees with C_β.

Because solvent mobility is broadly distributed and correlated with the local solvent concentration $\delta\phi$, see Sec. 10.6, the correlation function have to be investigated for smaller subsets identified by $\delta\phi$ to avoid smearing out features. The correlation function $F_{1,\vec{\mu}}$ shifts with $\delta\phi$ as strongly as $F_{2,\vec{n}}$ in Fig. 10.7. However, as the local concentration decreases, a slow decay becomes more prominent. Both correlation times and possibly also both amplitudes do not have the same dependence on $\delta\phi$. The correlation functions are fitted by a sum of two KWW functions and a multiplicative sum:

$$C(t) = Afe^{-(t/\tau_1)^{\beta_1}} + A(1-f)e^{-(t/\tau_2)^{\beta_2}} \tag{A.2}$$

$$C(t) = A\left(fe^{-(t/\tau_1)^{\beta_1}} + 1 - f\right)e^{-(t/\tau_2)^{\beta_2}} \tag{A.3}$$

The latter is also referred to as the Williams–Watts ansatz and may be more appropriate since the slower isotropic reorientation causes a complete loss of correlation.[411] However, the fits with both functions show no discernible differences in quality. Both imply a dependence of the relative amplitude of the two steps on $\delta\phi$. A full quantitative analysis is not performed because of the ambiguity of the fitting model. Nevertheless, the contributions to the ensemble average are obviously nontrivial.

To determine the identity of the two steps they can be compared with the correlation function of the plane normal with the Legendre polynomials of rank 1 and 2. Figure. A.22(c) shows for one subset of local concentrations both KWW fit components to $F_{1,\vec{\mu}}$ according to Eq. (A.2) and the scaled $F_{1,\vec{n}}$ and $F_{2,\vec{n}}$. The slow decay of $F_{1,\vec{\mu}}$ is comparable to $F_{2,\vec{n}}$, which is insensitive to π-flips. Hence, $F_{2,\vec{n}}$ and the slow component of $F_{1,\vec{\mu}}$ probe the isotropic reorientation associated with the α-process. The correlation function $F_{1,\vec{n}}$ should decay for π-flips with half the correlation time. However, the fast component of $F_{1,\vec{\mu}}$ decays on shorter time scales and could be related to different anisotropic reorientation. For example, benzene was found to rotate rapidly about its symmetry axis.[309] Further analysis of the anisotropic reorientation is beyond the interest of this study, which attempts to identify general features of asymmetric binary mixtures.

To emphasize the complexity of this system, the dependence of $F_{1,\vec{n}}$ and $F_{2,\vec{n}}$ on $\delta\phi$ is shown in Fig. A.22(e). At high local concentrations, the decays of both correlation functions are faster. However, the concentration dependence is different for both Legendre polynomials. This suggests that π-flips have a weaker dependence on $\delta\phi$ than isotropic reorientation. That they depend on the local concentration at all implies that either the energy barrier depends on ϕ or that the small asymmetry of picoline leads to slightly different energies for the two flipped orientations in different local configurations. Either case leads to a suppression of π-flips.

Note that only one picoline α-process is visible in BDS. The observations made here may be exaggerated in the simulation and not consistent with the real system. However, the picoline spectra are only visible at strong supercooling where the asymmetry and subsequent interactions could be significant enough to suppress π-flips, or they are simply not yet in the measured frequency window.

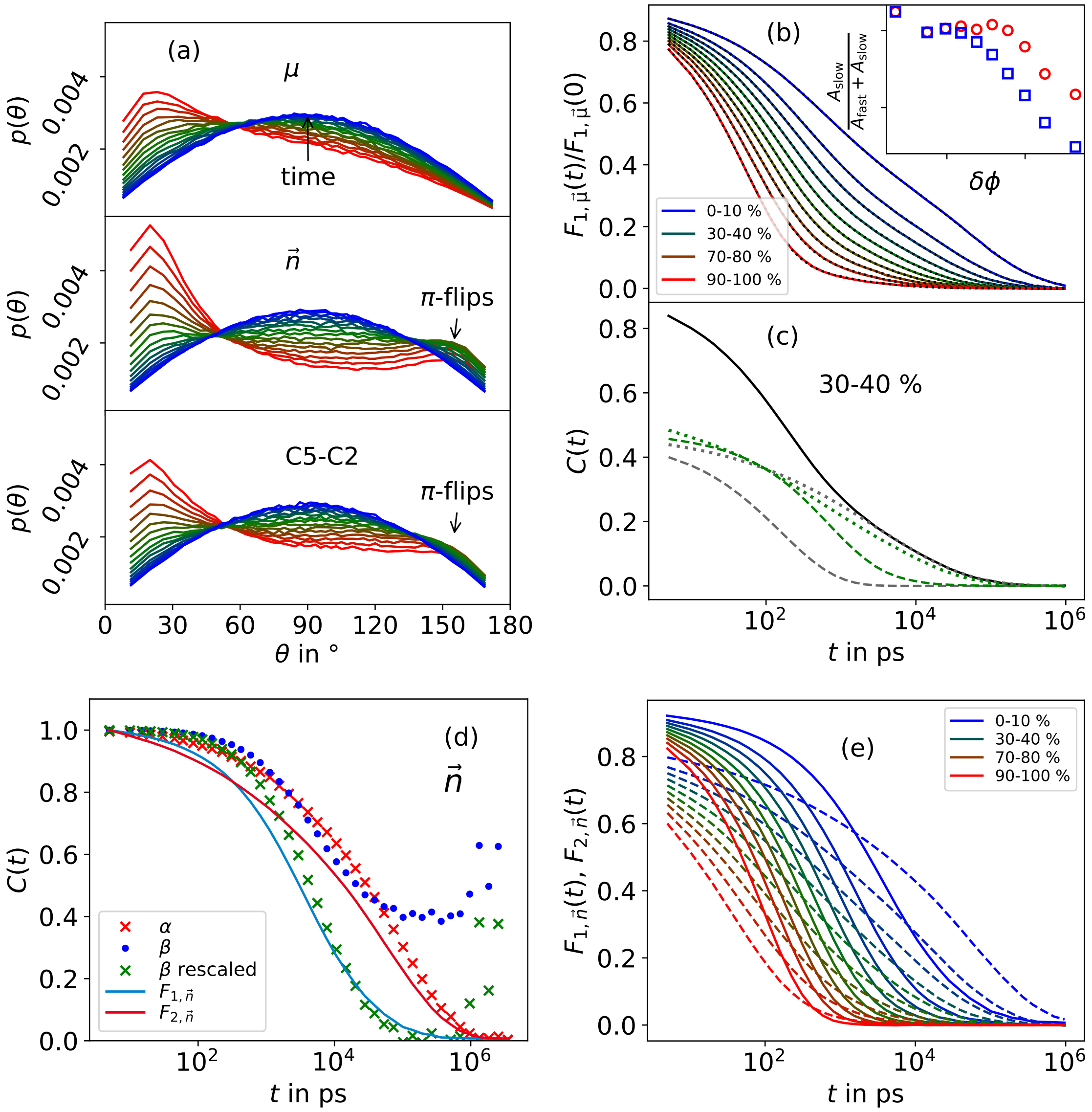

Figure A.22.: (a) Angular van Hove distribution function for three different vectors of the picoline molecule at 250 K. Only the subset of particles with 25 to 30 % of values for the local density $\delta\phi$ is shown. The time differences are indicated by colors from red to green to blue and range from 4 to 140 ns. The resulting correlation functions are shown in (d) for the plane normal. (b) Normalized correlation function $F_{1,\vec{\mu}}$ at 250 K resolved by local concentration and averaged over subsets each involving 10 % of the ensemble. The black dotted lines are fits with Eq. (A.2). The inset shows the relative amplitude of the slow process determined by fits with Eq. (A.2) (red circles) and (A.3) (blue squares). (c) The normalized correlation function $F_{1,\vec{\mu}}$ for 30 to 40 % of local concentrations (black solid line) is compared with its two KWW fit components (gray lines), as in (b), $F_{1,\vec{n}}$ (green dashed line) and $F_{2,\vec{n}}$ (green dotted line) for the same subset. The latter two are scaled to match the amplitude of the fast and slow KWW components, respectively. (e) The correlation functions $F_{1,\vec{n}}$ (solid lines) and $F_{2,\vec{n}}$ (dashed lines) for the same subsets as in (b).

A.5.2. Simulation details on the additional binary mixtures

Nonpolar picoline The binary mixture of PMMA and picoline, Sec. 4.4, was simulated with a nonpolar version of picoline. Removing the dipole moment from the solvent potentially reduces long-range Coulomb interactions. In order not to change the short-range Coulomb interaction too much, the sum of the absolute partial charges was kept the same. Thus, there are higher-order interactions, e.g., quadrupolar interactions. There are infinitely many different solutions for such a parametrization. Additional constraints were applied, e.g., grouping equivalent atoms and restricting hydrogen atoms to positive charges. The new parametrization of the partial charges was found by numerical minimization of the dipole moment and is shown in Fig. A.23. The simulation protocol and parameters were the same as for the original parametrization.

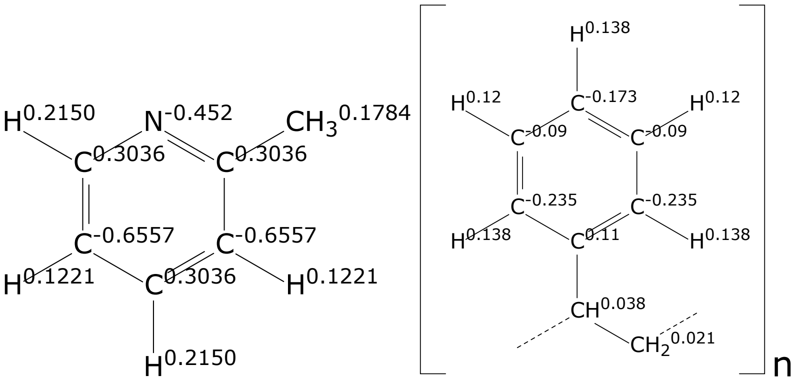

Figure A.23.: Chemical formula of picoline (left) and repeat unit of poly-styrol (right). The numbers indicate the partial charges. In the case of picoline, the partial charges are shown for the nonpolar version, i.e., without a permanent dipole moment. Created with BKchem by Beda Kosata.

Oligomerized styrene in benzene As a weakly charged binary mixture, oligomerized styrene was mixed with benzene. The former has a high T_g of about $\sim$363 K,[415] for high molecular weights, and the latter acts as a plasticizer. Analogous to the PMMA+picoline mixture in Sec. 4.4, the simulation consisted of 500 benzene molecules and 10 oligo-styrene chains with a length of 50 repeat units. The simulation protocols and parameters are the same as for the mixture of PMMA and picoline. In the same way, topologies from the ”automated topology builder” web service were obtained.[311,312] The topology for benzene (molid: 804; hash: 536ff) was adopted as is while the parametrization of oligomerized styrene was combined from topologies of a short (molid: 573883, hash: 068c7) and a long chain (molid: 345971, hash: b893d). The former has more accurate partial charges while the latter was used for parameters of bonded interactions. Again, a charge-neutral monomer topology was derived to allow polymerization of arbitrary length, see Fig. A.23.

Poly-ϵ-lysine in water Simulations of a mixture of poly-ϵ-lysine and water were performed by Lisa Heyer as part of her master’s thesis.[416] In poly-ϵ-lysine, the amino acid lysine is linked via its ϵ-amino group and α-carboxyl group. The force field is based on AMBER ff03ws.[417] Missing bonded parameters were taken from the general AMBER force field[418] and partial charges had to be recalculated using RESP.[419] The force field for water is TIP4P/2005. The length of the polymer is 32 monomers and the degree of hydration is 200 wt%. For more details, see the original work.

Myoglobin in water Simulations of the hydrated protein myoglobin were performed by Jessica Reusing as part of her bachelor's thesis.[420] Myoglobin is related to the protein hemoglobin and binds oxygen and iron. It is found in muscle tissue of mammals. It is composed of 153 amino acids and 1608 atoms. The structure was taken from scattering experiments.[421] It was simulated with the GROMOS54a7 united atom force field and mixed with 8000 SPC/E water molecules, giving a degree of hydration of about 10 wt%. For more details, see the original work.

Danksagung

Diese Arbeit ist natürlich auch durch die Unterstützung und Zusammenarbeit, wissenschaftlich aber auch freundschaftlich, mit anderen Menschen möglich geworden.

Deshalb möchte ich zuallererst Michael Vogel für das Vertrauen in mich und die Übernahme nach dem Bachelor und dem Master danken. So konnte ich ein Thema, das ich sehr gerne mag, verfolgen. Er hat immer einen Rahmen geschaffen, in dem man sich wissenschaftlich entfalten konnte. Man konnte spontan mit Ergebnissen vorbeikommen und er hatte häufig auch ein Ohr für wilde Ideen. Und gerade dann konnte sein enormes Literaturwissen auf hilfreiche Paper verweisen.

Die Reise fing natürlich nicht erst mit der Promotion an. Ich möchte meinem Oberstufen-Mathelehrer Herrn Felden danken, dem es wirklich wichtig war, uns für ein mögliches Studium vorzubereiten und wegen dem ich zu Beginn des Studiums nicht maßlos überfordert war. Ich möchte Patrick Wieth für seine sehr spaßige und von viel auf den Tisch hauen geprägte Betreuung meiner Bachelorarbeit danken. Bei ihm habe ich Simulationen und kondensierte Materie kennen- und lieben gelernt. Ich möchte dem Ansprechpartner im Studienbüro danken, der mir versichert hat, dass der Master in Physik viel mehr Spaß machen wird. Verrückt, aber vielleicht hätte ich statt einem Doktortitel sonst nur einen Bachelor. Und ich möchte Kai Stroh danken für die gegenseitige Betreuung unserer Masterarbeiten als uns Doktoranden fehlten.

Ich möchte den tollen Menschen der AG Vogel für diese besondere Zeit danken. Ohne dieses tolle Umfeld hätte ich wahrscheinlich nicht mehr die Doktorarbeit angefangen. Die vielen Kaffeepausen, Feierabendbiere, Grillabende und sonstige Feiern, Abende im Hobbit oder in der Uni und vieles mehr haben die Jahre deutlich aufgebessert. Und auch danke dafür, dass ihr mich nicht verstoßen habt, wenn ich zum wiederholten Male eure PCs für meine Analysen ausgenutzt habe. Der viele wissenschaftliche Austausch und auch die Einblicke in die Experimente haben immer Spaß gemacht. Und auch das Teilen von gemeinsamem Leid war sehr hilfreich. Da hier über die vielen Jahre hinweg zig Personen in Frage kommen, werde ich nicht alle aufzählen. Aber fühlt euch nicht vergessen.

Vielen Dank auch an Sebastian, der als sehr guter Büropartner immer für wissenschaftliche aber auch nerdige Gespräche zu haben war. Ich bin sehr froh ihn als beständigen Teil meines Alltags gehabt zu haben. Und vielen Dank an Jessica, die auch eine Bereicherung war und mit der ich über echt vieles reden konnte.

Danke auch an die Blochowiczs für die spannende wissenschaftliche Zusammenarbeit. Die abendlichen Diskussionen mit euch und anderen über Physik, die manchmal auch gut angetrunken an der Tafel stattfanden, haben echt Spaß gemacht. Und Entschuldigung an diejenigen, die wir damit genervt haben.

Ich möchte auch Austin Angell für die Inspiration und Literatur danken, die mich tiefer in den Wahnsinn des Polyamorphismus von Wasser hat abtauchen lassen. Und es macht mich traurig, nicht mehr die Chance gehabt zu haben ihm meine Ergebnisse mitteilen zu können.

Viel Dank gilt auch Markus, dem ich mit meinen Stresstests des Clusters, Netzwerks und NAS viel Arbeit gemacht habe. Wer das Wettrüsten gewonnen hat, werden wir wegen meinem Ende der Simulationszeit wohl nie erfahren. Außerdem waren die vielen Gespräche über technische Details sehr spannend und wertvoll für die Entwicklung meiner amateurhaften IT-Kenntnisse. Vielen Dank auch an Matthias und Niels, die mit dem Python-Package dafür gesorgt haben, dass ich mich seit der Masterarbeit vor allem auf Forschung und weniger auf segmentation faults fokussieren konnte. Und außerdem möchte ich den vielleicht leblosen, aber trotzdem von mir liebgewonnen PCs, insbesondere Rudi und Primus, und Nodes, die meine Belastung ertragen haben, danken.

Ich möchte natürlich auch meinen Eltern und Geschwistern danken. Sie haben mich immer in meinen Entscheidungen im Studium unterstützt und waren immer für mich da, wenn ich mal zurück in die Heimat wollte. Danke auch an meine alten Freunde in Heppenheim, die immer für eine Auszeit von der Uni zu haben waren.

Ich danke allen Korrekturleser/-innen und Zuhörer/-innen meiner Probevorträge: Dominik, Elisa, Sebastian, Christoph, Verena, Sandra, Sarah, und allen, die ich hier vergessen habe. Euer Feedback war unglaublich wertvoll, weil ich gerne mal blind für meine umständlichen Herangehensweisen und Erklärungen bin.

Sehr besonders möchte ich Dominik danken. Dass er in der finalen Schreibphase mir Gesellschaft geleistet hat, wenn ich in die Uni gekommen bin, war unermesslich wertvoll. Auch wenn sein wichtigster Beitrag die überwachende Präsenz war, so hat er dadurch und auch durch seinen Charakter dafür gesorgt, dass ich produktiv gearbeitet habe. Außerdem hat er immenses Wissen über unsere wissenschaftlichen Themen als auch über Abschlussarbeiten und Präsentationen. Dadurch hat er immer mit konstruktivem Rat beigestanden. Außerdem war er der hauptsächliche Korrekturleser, was vor allem vielen unverständlichen Sätzen und ganzen unnützen Abschnitten zum Verhängnis wurde.

Und zu guter Letzt möchte ich meiner besten Freundin Elisa danken. Sie hat für viele gute Zeiten, die den Stress der Doktorarbeit kompensieren, gesorgt und mir in schlechten Zeiten beigestanden. Vor allem auch in der Coronazeit, als der Großteil des Zusammenseins der AG zum Erliegen gekommen war, konnte ich mich auf sie verlassen. Ihre vielen guten Zusprüche und Versuche mich zu motivieren, als das Schreiben der Thesis nicht gut voran kam, haben dazu beigetragen, dass ich unbedingt noch fertig werden wollte. Das Finale der Schreibphase und der Prüfungsvorbereitung hat sie mir deutlich erträglicher gemacht.

Vielen lieben Dank an euch alle. Ich wünsche euch nur das Beste in eurer Zukunft und hoffe, dass wir uns immer wieder über den Weg laufen werden.